

Characterisation and evolution of Au mineralisation in the Loulo mining district, Western Mali

David Matthew Lawrence

A thesis submitted in partial fulfilment of the requirements of Kingston University for the
degree of Doctor of Philosophy

This research programme was carried out in collaboration with Randgold Resources Ltd

August 2010



PAGES NOT SCANNED AT THE
REQUEST OF THE UNIVERSITY

SEE ORIGINAL COPY OF THE THESIS
FOR THIS MATERIAL

Lawrence, D.M. 2010
ETHOS ID: 525102

Please do NOT digitise the following images/figures

Figure 1.6	p.13
Figure 1.7	p.14
Figure 2.1	p.19
Figure 2.2	p.20
Figure 2.3	p.22
Figure 2.4	p.24
Figure 2.5	p.25
Figure 2.6	p.28
Figure 2.8	p.30
Figure 3.1	p.48
Figure 3.2	p.50
Figure 3.4	p.55
Figure 3.21	p.74
Figure 3.22	p.75
Figure 4.1	p.90
Figure 4.8	p.105
Figure 5.19	p.183
Figure 6.21	p.236
Figure 7.8	p.261
Figure 8.1	p.269
Figure 8.2	p.269

ABSTRACT

Loulo is a world-class orogenic gold district in SW Mali. The mining district is comprised of two major operational mines at Yalea (6.5 Moz at 4.7 g/t) and Gara (3.7 Moz at 4.1 g/t), plus numerous satellite deposits and other prospective targets, which takes Loulo's overall resource to 14.4 Moz. Two distinct types of ore deposit are recognised. Gara-style deposits are Fe-rich and characterised by a Fe-Cu-REE-Au-Ni-W-As \pm Co-Ag-Pd metal association. Yalea-style, As-rich, deposits exhibit more typical orogenic gold features with a metal signature consisting of Fe-As-Cu-W-Au-Pb-Sb-Ag.

Investigations into the source and composition of the auriferous fluids indicate two styles of ore fluid were responsible for mineralisation: (1) a 'Gara-style' oxidised (FM-buffered), high temperature (>400 °C), hypersaline (35-55 wt.% NaCl equiv.), Na-Fe-Cl-B-bearing magmatic fluid; and (2) a 'Yalea-style' reduced (QFM-buffered), lower temperature (300-350 °C), low-salinity (<10 wt.% NaCl equiv.) CO₂-N₂-H₂S-rich metamorphic fluid. The identification of hypersaline Na-Fe chloride-rich fluid inclusions questions the metamorphic fluid paradigm for orogenic gold deposits. Field, petrographic and isotopic studies also provide convincing evidence that magmatic fluids played an integral role in gold mineralisation. These include: (1) the presence of a significant boron anomaly along the length of the Senegal-Mali Shear Zone (which hosts Loulo and other large gold deposits such as Sadiola), typified in Loulo by the presence of large volumes of replacive epigenetic tourmaline; (2) widespread pink sodic alteration; (3) the spatial association with iron oxide-copper-gold (IOCG) deposits in the adjacent Falémé district in Senegal; (4) the presence of Ni-Co sulphides and abundant REE-W minerals in the ore paragenetic assemblage; and (5) carbon isotopes overlapping the magmatic field (e.g. Gara vein ankerites show $\delta^{13}\text{C}$ compositions from -14.4 to -4.5‰).

Both metamorphic and magmatic fluids were capable of carrying gold as either bi-sulphide complexes or oxidised chloride complexes, respectively. In the Gara-style orebodies, mineralisation was controlled by the mixing of these two fluids, which resulted in changes in temperature, pH and $f\text{O}_2$, and caused retrograde boiling of the CO₂ component. This style of Loulo orebody contains distinct mineralogical and fluid inclusion characteristics, and it is therefore proposed that Gara-style orebodies represent a new sub-class of orogenic gold deposit, with evidence suggesting possible links with IOCG/skarn mineralisation. In the Yalea-style orebodies, mineralisation is confined to metamorphic fluids with the principal mineralisation trap linked to fluid immiscibility during fluctuations in pressure and/or temperature, and fluid-rock interactions with reduced host sediments. Chemisorption processes may also have played a role in gold deposition to account for the high levels of refractory gold in arsenopyrite.

ACKNOWLEDGEMENTS

This research project was fully funded by Randgold Resources. I gratefully acknowledge the help and support the company gave me during the three and half year's research, and I am thankful for the opportunity to work on such a world-class mining district. I would especially like to thank senior geologists Joel Holliday, Reinet Harbidge, Rod Quick and Ken King for their input and advice, as well as the numerous junior geologists that helped during my field visits to Mali.

I would also like to acknowledge several members of staff (past and present) at Kingston University, including Kym Jarvis, Benoit Disch, Kevin Attree, Simon de Mars and Ian Jarvis for their help in lithochemistry preparation and analysis; Richard Giddens for his assistance in SEM probe analysis; Simon Crust for technical guidance on microscopy issues; Ian Gill for sample preparation; and Claire Ivison for her advice on cartography issues. A special thanks must go to Adrian Boyce and the technical staff at SUERC, East Kilbride, for their help with stable isotope analysis and interpretation.

I would also like to acknowledge the support from my family, girlfriend and fellow post-graduate students. Lastly, and most importantly, many thanks to my supervisors Peter Treloar, Andy Rankin and Paul Harbidge for their contribution, support and guidance during the project.

TABLE OF CONTENTS

ABSTRACT	I
ACKNOWLEDGEMENTS.....	II
CHAPTER 1: INTRODUCTION AND PROJECT OUTLINE	1
1.1 Introduction to Mali and Malian gold mining	1
1.1.1 Mali	1
1.1.2 Gold mining in Mali.....	3
1.2 The Loulo mining district	6
1.2.1 Location	6
1.2.2 Mining district layout.....	7
1.2.3 Exploration and development history	8
1.2.4 Randgold Resources.....	10
1.2.5 Previous work	10
1.3 Orogenic gold mineralisation.....	11
1.3.1 Spatial distribution	11
1.3.2 Temporal distribution.....	14
1.3.3 Fluid source(s).....	15
1.4 Project outline	15
1.4.1 Project background.....	15
1.4.2 Principal objectives	16
1.4.3 Approach and methodology	16
1.5 Layout of thesis.....	17
CHAPTER 2: THE BIRIMIAN OF WEST AFRICA- A REVIEW	19
2.1 Regional setting of the West African Craton	19
2.2 Archaean domains.....	22
2.3 Birimian geology	23
2.3.1 Birimian volcano-plutonic belts and sedimentary basins	25
2.3.2 Birimian granitoids.....	26
2.3.3 Birimian lithostratigraphic succession.....	26
2.4 Tarkwaian geology	27
2.5 Birimian crustal evolution.....	28
2.5.1 Introduction	28
2.5.2 Magmatic accretion and basin opening (stages 1-3).....	30
2.5.2.1 Tectonic setting	30
2.5.2.2 Subprovince model	32
2.5.3 Eburnean orogeny (stage 4).....	34
2.5.3.1 Structural history	34
2.5.3.2 Tarkwaian sedimentation.....	35
2.5.3.3 Emplacement of basin-type granitoids	36
2.5.3.4 Tectonic model.....	36
2.5.4 Emplacement of post-tectonic granitoids (stage 5).....	37
2.6 Birimian metallogenesis.....	37
2.6.1 Gold mineralisation	37
2.6.1.1 Ghana	38
2.6.1.2 Mali-Senegal	40
2.6.1.3 Burkina Faso.....	41
2.6.1.4 Côte d'Ivoire.....	42
2.6.1.5 Reguibat Shield	42
2.6.2 Iron ore mineralisation	42
2.6.3 Other Birimian resources.....	43
2.6.4 Birimian mineralisation history	43
2.6.4.1 Syn-orogenic stage	43
2.6.4.2 Late-orogenic stage.....	44
2.7 Conclusions.....	44

CHAPTER 3: GEOLOGY OF THE LOULO AREA	46
3.1 Regional geology of the Kédougou-Kéniéba inlier.....	46
3.1.1 Mako Series.....	46
3.1.2 Dialé-Daléma Series.....	47
3.1.3 Eastern parts of the KKI.....	47
3.2 Geological and structural setting of the Loulo district.....	49
3.2.1 Loulo stratigraphy.....	49
3.2.1.1 Falémé belt.....	49
3.2.1.2 Kofi Series.....	51
3.2.1.3 Dialé-Daléma Series.....	51
3.2.2 Structural setting.....	54
3.2.2.1 Outline.....	54
3.2.2.2 Structural evolution.....	54
3.3 Lithological descriptions.....	59
3.3.1 Carbonates.....	59
3.3.2 Argillaceous greywackes.....	61
3.3.3 Tourmaline-bearing quartz-wackes.....	62
3.3.4 Feldspar-rich sandstones.....	63
3.3.5 Hydrothermal-tectonic breccias.....	64
3.3.6 Minor intrusive rocks.....	64
3.3.7 Kofi basin-type plutons.....	67
3.3.8 Moussala basin-type pluton.....	68
3.3.9 Balangouma plutons.....	68
3.4 Lithogeochemistry.....	72
3.4.1 Sampling and data integrity.....	72
3.4.2 Results.....	73
3.4.2.1 Intrusive rocks.....	73
3.4.2.2 Kofi sediments.....	79
3.5 Discussion.....	82
3.5.1 Birimian granitoid compositions.....	82
3.5.2 Tectonic setting.....	82
3.5.3 Provenance setting for the Kofi sediments.....	84
3.5.4 Depositional setting and depth of burial for the Kofi Series.....	86
3.5.5 Crustal evolution at the Archaean-Proterozoic boundary.....	86
3.6 Conclusions.....	87
CHAPTER 4: MINERALISATION AT LOULO.....	89
4.1 Introduction.....	89
4.2 Gara.....	89
4.2.1 Orebody parameters.....	89
4.2.2 Mineralisation styles.....	90
4.2.3 Vein mineralogy.....	92
4.2.4 Ore mineralogy.....	92
4.2.4.1 Paragenesis.....	92
4.2.4.2 Ore-related sulphides and accessory phases.....	93
4.2.4.3 Gold.....	100
4.2.5 Gara West.....	103
4.3 Yalea & P-125.....	103
4.3.1 Orebody parameters.....	103
4.3.2 Yalea Main.....	105
4.3.2.1 Mineralisation styles.....	105
4.3.2.2 Ore mineralogy.....	108
4.3.3 Yalea North.....	115
4.3.3.1 Mineralisation styles.....	115
4.3.3.2 Ore mineralogy and paragenesis.....	115
4.3.3.3 Gold/ silver grains.....	120
4.3.4 P-125.....	121
4.3.4.1 Mineralisation styles.....	121
4.3.4.2 Ore mineralogy and paragenesis.....	122
4.4 Faraba.....	126
4.4.1 Orebody parameters.....	126

4.4.2	Mineralisation styles	126
4.4.3	Ore mineralogy and paragenesis	126
4.4.4	Supergene alteration	131
4.5	Other deposits	131
4.5.1	Loulo-3.....	131
4.5.2	Baboto.....	132
4.5.3	P-129.....	133
4.5.4	P-64.....	133
4.5.5	Goukoto.....	135
4.6	Discussion.....	136
4.6.1	Deposit summary	136
4.6.2	Comparative mineralogy model for the Loulo district	137
4.6.3	Geothermometry	138
4.6.3.1	Arsenopyrite geothermometry	138
4.6.3.2	Telluride geothermometry	141
4.7	Conclusions.....	141
CHAPTER 5: HYDROTHERMAL ALTERATION AT LOULO		143
5.1	Alteration characteristics of orogenic gold deposits	143
5.2	Alteration characteristics at Loulo	144
5.2.1	Hydrothermal alteration	144
5.2.2	Regional metamorphism	144
5.3	Alteration mineralogy	144
5.3.1	Gara.....	145
5.3.1.1	Sodic alteration	145
5.3.1.2	Tourmalinisation.....	148
5.3.2	Yalea Main.....	164
5.3.2.1	Sodic \pm ankerite alteration	164
5.3.2.2	Phyllic alteration.....	167
5.3.3	Other types of alteration in the Loulo district	172
5.4	Alteration geochemistry.....	173
5.4.1	Isocon method of Grant (1986)	173
5.4.2	Mass transfers during alteration	174
5.4.2.1	Tourmalinisation.....	174
5.4.2.2	Albitisation	176
5.4.3	Alteration profiles	176
5.5	Discussion.....	179
5.5.1	Gara- vs. Yalea-style summary	179
5.5.2	Tourmalinisation	179
5.5.2.1	Chemical compositions.....	179
5.5.2.2	Fluid source	182
5.5.3	Sodic alteration	185
5.5.4	Alteration geothermometry	185
5.6	Conclusions.....	187
CHAPTER 6: FLUID INCLUSION STUDIES AT LOULO.....		188
6.1	Introduction.....	188
6.2	Aims and objectives.....	188
6.3	Previous fluid inclusion studies	189
6.4	Methodology.....	190
6.4.1	Sample preparation.....	190
6.4.2	Microthermometry	191
6.4.3	Laser Raman Spectroscopy	191
6.4.4	SEM analysis of opened inclusions.....	191
6.5	Fluid inclusion petrography	192
6.5.1	Classification schemes	192
6.5.2	Timing and origin of inclusions	192
6.5.3	Fluid inclusion types and occurrence	194
6.5.4	Fluid inclusion populations	201
6.6	Microthermometry and Raman spectroscopy	202
6.6.1	Equations of state	202

6.6.2	Microthermometry and Raman results	204
6.6.2.1	CO ₂ -(N ₂)-(CH ₄) inclusions (type 1)	204
6.6.2.2	H ₂ O-NaCl inclusions (type 2)	211
6.6.2.3	H ₂ O-CO ₂ -NaCl inclusions (type 3)	215
6.6.2.4	Multiphase solid H ₂ O-CO ₂ -NaCl inclusions (type 4)	220
6.7	Discussion	224
6.7.1	Fluid immiscibility	225
6.7.2	Fluid mixing	229
6.7.3	P-V-T modelling	233
6.7.4	Source of ore-forming fluids	239
6.8	Conclusions	239
CHAPTER 7: STABLE ISOTOPE STUDIES AT LOULO		241
7.1	Introduction and objectives	241
7.2	Methodology	241
7.2.1	Mineral separation	241
7.2.2	Analytical procedures	241
7.3	Oxygen isotope studies	242
7.3.1	Previous studies	243
7.3.2	Sample selection and objectives	246
7.3.3	Results	247
7.4	Carbon isotope studies	251
7.4.1	Previous studies	251
7.4.2	Sample selection and objectives	251
7.4.3	Results	252
7.5	Sulphur isotope studies	254
7.5.1	Previous studies	254
7.5.2	Sample selection and objectives	255
7.5.3	Results	256
7.6	Discussion	257
7.6.1	Oxygen isotopes	257
7.6.2	Carbon isotopes	258
7.6.3	Sulphur isotopes	260
7.7	Conclusions	262
CHAPTER 8: ORE GENETIC MODEL FOR LOULO		264
8.1	Introduction	264
8.2	The northern Loulo orebodies	264
8.2.1	Gara- vs. Yalea-style orebodies	264
8.2.2	Yalea-style orebodies	266
8.2.2.1	Ore mineralisation	266
8.2.2.2	Fluid origin and chemistry	267
8.2.2.3	Source of volatile components	268
8.2.2.4	Source of metals	268
8.2.2.5	Metal transport	268
8.2.2.6	Gold precipitation	270
8.2.2.7	Alteration associated with Yalea-style mineralisation	271
8.2.3	Gara-style orebodies	272
8.2.3.1	Ore mineralisation	272
8.2.3.2	Fluid chemistry, origin and evolution	273
8.2.3.3	Metal transport	276
8.2.3.4	Gold precipitation	277
8.2.3.5	Alteration associated with Gara-style mineralisation	277
8.2.3.6	Possible sources for magmatic fluids	278
8.2.4	Post-mineralisation fluids	280
8.2.5	Barren fluids	280
8.3	The southern Loulo orebodies	281
8.3.1	Ore mineralisation	281
8.3.3	P-T conditions of mineralisation at Loulo	283
8.4	Controls on mineralisation at Loulo	285

8.5	Implications	285
8.5.1	Implications for orogenic gold mineralisation	285
8.5.2	Insights into Birimian gold mineralisation	287
8.5.3	Exploration strategies.....	288
CHAPTER 9: CONCLUSIONS.....		289
9.1	Project objectives and conclusions	289
9.2	Suggestions for future work.....	294
REFERENCES.....		296
APPENDICES		324
A-1	Microprobe analysis.....	324
A-2	Geochemical sample preparation and analysis	324
A-3	Geochemistry data presented in chapter 3 and chapter 5	332
A-4	Paragenesis charts for the smaller Loulo prospects	338
A-5	WinClastour methodology	340
A-6	Microthermometric data.....	340

LIST OF FIGURES

CHAPTER 1: INTRODUCTION

Fig. 1.1. Map of Mali showing the location of the major gold deposits within the country.....	2
Fig. 1.2. Artisanal workings in the Faraba region of the Loulo permit.....	4
Fig. 1.3. Mali's annual gold production (modified from Holliday, 2009).....	6
Fig. 1.4. The landscape surrounding Loulo (looking NNW).....	7
Fig. 1.5. A) Plan view of the Gara pit, looking south. B) Plan view of the Yalea pit, looking north.....	9
Fig. 1.6. Map showing the relationship between the distribution of crust of a given age and the location of significant orogenic gold deposits (Goldfarb <i>et al.</i> , 2001a).....	13
Fig. 1.7. Timing of orogenic gold mineralisation vs. periods of crustal growth (Groves <i>et al.</i> , 2005a).....	14

CHAPTER 2: THE BIRIMIAN OF WEST AFRICA- A REVIEW

Fig. 2.1. The distribution of African cratons and Pan-African orogenic belts (Dallmeyer & Lécorché, 1991).....	19
Fig. 2.2. Geological setting of West Africa showing the position of the Leo-Man and Reguibat shields, and surrounding Pan-African orogenic belts (from Feybesse <i>et al.</i> , 2006, modified after Dallmeyer & Lécorché, 1991).....	20
Fig. 2.3. Schematic reconstruction of the West Gondwana assembly (Klein & Moura, 2008).....	21
Fig. 2.4. Schematic lithotectonic map of the Leo-Man Shield of the West African Craton, showing the location of Birimian gold deposits (adapted from Feybesse & Milési, 1994).....	24
Fig. 2.5. The geology of Birimian terranes in central and western Ghana (modified from Pigois <i>et al.</i> , 2003).....	25
Fig. 2.6. Schematic lithostratigraphic column for Birimian and Tarkwaian rocks in Ghana (modified from Pigois <i>et al.</i> , 2003).....	28
Fig. 2.7. Histogram summarising the geochronology data collected in the past few decades on Palaeoproterozoic rocks of the WAC.....	29
Fig. 2.8. Abouchami <i>et al.</i> (1990) oceanic plateau growth model for the Birimian crust.....	30
Fig. 2.9. Histograms showing the growth of the Birimian crust during stages 1-3 of crustal evolution. A) Eastern subprovince, B) Western subprovince.....	32
Fig. 2.10. Histogram showing the detrital zircon ages of Tarkwaian sediments from the Ashanti and Sefwi belts in Ghana, and from the Hounde belt in Burkina Faso (data from Davis <i>et al.</i> , 1994; Pigois <i>et al.</i> , 2003; Bossiere <i>et al.</i> , 1996).....	35
Fig. 2.11. Map of the West Mali Gold Belt showing the Loulo study area.....	41

CHAPTER 3: GEOLOGY OF THE LOULO AREA

Fig. 3.1. Regional geology map of the Kédougou-Kéniéba inlier (scale 1:250,000).....	48
Fig. 3.2. Regional geology map of the Loulo mining district (scale- 1:65,000).....	50
Fig. 3.3. Schematic stratigraphic columns for Gara (A) and Yalea (B).....	52
Fig. 3.4. Orientations of structures associated with sinistral strike slip faults (modified from Davis & Reynolds, 1996).....	55
Fig. 3.5. Plan (A) and cross sections (B) of the Gara fold system.....	56
Fig. 3.6. A structural evolution model for the Loulo district. A) D ₂ Transpression- <i>part 1</i> , B) D ₂ Transpression- <i>part 2</i> , C) D ₃ Transtension.....	58
Fig. 3.7. Drill-core photos and transmitted light images (PPL) of the schistose carbonate sediments.....	60

Fig. 3.8. Drill-core photo and transmitted light image (XPL) of the schistose argillaceous greywacke.....	61
Fig. 3.9. Drill-core photos and transmitted light images (XPL) of the various quartz-wacke units. A) to B) Weakly tourmalinised quartz-wacke. C) to D) Tourmalinite.....	62
Fig. 3.10. Drill-core photos and transmitted light images (XPL) of the feldspar-bearing sandstones. A) to B) Arkoses, C) to D) Feldspathic greywackes.....	63
Fig. 3.11. Field photograph of hydrothermal-tectonic breccias from wall-rock at P-125.....	64
Fig. 3.12. Drill-core photo and transmitted light images (XPL) of the Kofi Birimian mafic dykes.....	65
Fig. 3.13. Transmitted light image (XPL) of the P-129 porphyry dyke.....	66
Fig. 3.14. Drill-core photo and transmitted light image (XPL) of a Mesozoic mafic dyke.....	66
Fig. 3.15. A feldspar ternary plot for the Birimian and post-Birimian dykes.....	67
Fig. 3.16. Hand specimen and transmitted light (XPL) images of the Kofi basin-type intrusions.....	67
Fig. 3.17. Hand specimen and transmitted light (XPL) images of the Moussala syeno-granite.....	68
Fig. 3.18. XPL images showing the varying degrees of albitisation of plagioclase within the Balangouma plutons.....	69
Fig. 3.19. Hand specimen photos and transmitted light images (XPL) showing the composition of the Balangouma plutons. A) Granodiorite, B) Quartz-diorite, C) Tonalite.....	70
Fig. 3.20. Mineralogical classification of major Birimian intrusive rocks at Loulo and the surrounding areas. A) QAPF diagram, B) Feldspar ternary plot.....	71
Fig. 3.21. Geochemical classification and nomenclature for the major Birimian intrusive rocks within and around the Loulo property. A) TAS diagram, B) An-Ab-Or plot, C) AFM diagram, D) Na ₂ O/K ₂ O diagram.....	74
Fig. 3.22. Geochemical classification and nomenclature for minor Birimian intrusive rocks within and around the Loulo property. A) TAS diagram, B) AFM diagram.....	75
Fig. 3.23. MORB-normalised trace element distribution patterns for the Loulo intrusive rocks. A) Balangouma plutons. B) Basin-type plutons, C) Minor intrusive rocks.....	77
Fig. 3.24. Chondrite-normalised REE patterns for the Loulo intrusive rocks. A) Balangouma plutons. B) Basin-type plutons, C) Minor intrusive rocks.....	78
Fig. 3.25. Classification of the Kofi clastic sediments according to the Herron diagram.....	79
Fig. 3.26. MORB-normalised distribution patterns for the Kofi sediments. A) Gara argillaceous greywackes, B) Yalea argillaceous greywackes. C) Arkoses and feldspathic greywackes.....	80
Fig. 3.27. Chondrite-normalised REE distribution patterns for the Kofi sediments. A) Gara argillaceous greywackes, B) Yalea argillaceous greywackes. C) Arkoses and feldspathic greywackes.....	81
Fig. 3.28. Discrimination diagram for granitic rocks after Pearce <i>et al.</i> (1984) and Harris <i>et al.</i> (1986).....	83
Fig. 3.29. Discrimination diagrams for the Birimian Kofi sediments after Bhatia (1983) and Bhatia & Crook (1986).....	84
Fig. 3.30. La _N /Yb _N vs. Yb _N and Eu/Eu* vs. Gd _N /Yb _N plots for the Loulo intrusive and sedimentary rocks, respectively, showing Archaean geochemical affinities.....	87

CHAPTER 4: MINERALISATION AT LOULO

Fig. 4.1. A block model for the Gara deposit.....	90
Fig. 4.2. Pit and drill-core samples of the Gara vein stockwork. A) to B) Ankerite-pyrite veins. C) Sigmoidal grey quartz mineralized veins reactivating early ankerite veins. D) Brecciated ankerite vein. E) Straight barren milky quartz veins. F) Folded barren calcite vein.....	91

Fig. 4.3. Back-scattered electron (BSE) images of the major and minor sulphide phases present at Gara. A) to B) Highly altered pyrites. C) Zoned pyrite crystal showing lighter zones of As-Ni bearing pyrite. D) Arsenopyrite intergrowth with pyrite. E) Chalcopyrite-I inclusions within pyrite. F) Late chalcopyrite-II sealing fractures within pyrite or located along pyrite-gersdorffite contacts.....	95
Fig. 4.4. BSE images of rare earth phosphates and tungstate phases at Gara. A) to D) Monazite inclusions and intergrowths associated with pyrite. E) Late monazite grain situated along fracture plane in pyrite. F) Xenotime. G) Deformed scheelite porphyroblast.....	97
Fig. 4.5. A BSE image showing Ti replacement of pyrite at Gara.....	100
Fig. 4.6. BSE images showing the various gold locations at Gara. A) to B) GI, C) to E) GII, F) GIII, G) GIV, H) GV	101
Fig. 4.7. The structural setting for the Yalea & P-125 deposits.....	104
Fig. 4.8. A block model for Yalea-P-125 deposits.....	105
Fig. 4.9. Drill core photos of the various tectonic and hydrothermal textures present within the Yalea orezone.....	107
Fig. 4.10. BSE images of the ore phases present at Yalea Main. A) to B) Contemporaneous pyrite-II and arsenopyrite-I formation. C) to F) Arsenopyrite-II after pyrite-II. G) Chalcopyrite-I inclusion along pyrite-II growth boundary. H) to I) Chalcopyrite-II after pyrite-II. J) Zoned tennantite overprinting arsenopyrite-II. K) Scheelite intergrowths with pyrite-II. L) Late-stage scheelite post-dating pyrite-II.....	111
Fig. 4.11. Gold grains associated with numerous sulphide phases at Yalea Main (BSE images). A) GI in pyrite-II. B) GI in arsenopyrite-II. C) GII associated with chalcopyrite-II. D) GII associated with tennantite.....	114
Fig. 4.12. BSE images of the ore phases at Yalea North. A) Contemporaneous pyrite and arsenopyrite formation. B) Cobaltite intergrowth with pyrite-II. C) to D) Idiomorphic gersdorffite crystals surrounding pyrite. E) Small gersdorffite crystals within fracture cutting pyrite. F) Chalcopyrite-I and chalcopyrite-II associated with pyrite-II.....	118
Fig. 4.13. Co-Ni-Fe ternary diagram (atomic wt.%) showing the composition of cobaltite and gersdorffite minerals from the Yalea North orezone.....	119
Fig. 4.14. Drill core images showing the disseminated sulphides at P-125.....	121
Fig. 4.15. BSE images showing the major sulphide phases at P-125. A) Arsenopyrite-I intergrown with disseminated pyrite. B) to D) Arsenopyrite-II after pyrite. E) Disseminated pyrite replaced by tennantite. F) Chalcopyrite-II overprinting pyrite.....	123
Fig. 4.16. Drill-core and reflected light (PPL) images showing the magnetite replacement of the P-125 sulphides.....	125
Fig. 4.17. Mineralisation styles at Faraba. A) Arsenopyrite-I-ankerite vein. B) Magnetite-chlorite-pyrite vein. C) Massive disseminated arsenopyrite-II. D) Massive disseminated pyrite-II rich zone.....	127
Fig. 4.18. BSE images of ore stage III and ore stage IV at Faraba. A) to B) Pyrite-II overprinting arsenopyrite-II. C) to D) Telluride minerals associated with arsenopyrite-II. E) to F) Native gold associated with pyrite-II.....	130
Fig. 4.19. Reflected light images (PPL) showing magnetite replacement of pyrite at Faraba South.....	131
Fig. 4.20. Histogram showing the composition of the Gara- and Yalea-style arsenopyrites.....	139
Fig. 4.21. Sulphidation curves in the system Fe-As-S in the stability range of arsenopyrite (Barton, 1969), with atomic wt.% As arsenopyrite-buffered curves from Kretschmar & Scott (1976).....	140

CHAPTER 5: HYDROTHERMAL ALTERATION AT LOULO

Fig. 5.1. Drill core images of the distal pink sodic alteration zones in wall-rock argillaceous greywacke sediments surrounding the Gara orezone.....	146
--	-----

Fig. 5.2. Photomicrographs of the distal pink sodic alteration zone at Gara.....	147
Fig. 5.3. Shear zones bounding the Gara tourmalinite alteration zone.....	148
Fig. 5.4. Photomicrographs and BSE images showing the relative timing of the various tourmaline phases at Gara. A) to B) E-stage tourmalines, C) to I) L-stage tourmalines.....	150
Fig. 5.5. The classification of tourmaline generations at Gara. A) Ca-X-site vacancy-Na + (K) ternary plot (Hawthorne & Henry, 1999). B) Al-Fe-Mg ternary diagram (Henry & Guidotti, 1985).....	155
Fig. 5.6. Field photos and photomicrographs of the various tourmaline phases in the hydrothermal-tectonic breccias host rocks at Yalea North.....	156
Fig. 5.7. BSE images showing the nature of the tourmaline crystals at Yalea North.....	158
Fig. 5.8. The classification of tourmaline generations at Yalea North. A) Ca-X-site vacancy-Na +(K) ternary plot (Hawthorne & Henry, 1999). B) Al-Fe-Mg ternary diagram (Henry & Guidotti, 1985).....	160
Fig. 5.9. The classification of tourmaline generations at P-129, P-64 and P-125. A) Ca-X-site vacancy-Na +(K) ternary plot (Hawthorne & Henry, 1999). B) Al-Fe-Mg ternary diagram (Henry & Guidotti, 1985).....	163
Fig. 5.10. Drill core photos of the pink distal albite alteration zone in footwall sediments at Yalea Main. A) Pervasive alteration of argillaceous greywacke sediments. B) Hydrothermal-tectonic breccias along footwall NNE splays.....	165
Fig. 5.11. Transmitted light images (XPL) of the albite ± ankerite alteration zones at Yalea Main. A) Proximal metasomatic albite-ankerite zone along the main N-S Yalea mineralised shear. B) Distal albite zone along a NNW splay off the main N-S shear.....	166
Fig. 5.12. Drill core photos of phyllic alteration at Yalea Main. A) Green sericite-chlorite shears overprinting pink albite altered rock in proximity to the orezone. B) Chlorite-carbonate-quartz veins cross cutting albite-altered rock.....	167
Fig. 5.13. Binary plots showing the compositions of the hydrothermal and metamorphic chlorites at Loulo. A) Fe/(Fe+Mg) vs. Si cation plot using the nomenclature of Hey (1954). B) Si/Al vs. Fe/(Fe+Mg) plot.....	169
Fig. 5.14. Drill core and transmitted light images of the silica alteration at Baboto.....	172
Fig. 5.15. A) Isocon diagram, after Grant (1986), showing mass changes involved during tourmalinisation at Gara. B) Elemental mass changes involved during tourmaline alteration.....	175
Fig. 5.16. A) to B) Isocon diagrams showing the mass changes involved during albitisation of argillaceous greywacke sediments at Gara and Yalea. C) to D) Elemental mass changes involved during albitisation at Gara and Yalea.....	177
Fig. 5.17. Al-Fe-Mg ternary diagram (Henry & Guidotti, 1985) showing the full tourmaline compositional dataset for Loulo.....	180
Fig. 5.18. Binary plots showing the major element chemistry of the Loulo tourmalines. A) Al vs. X-site vacancy plot. B) Mg vs. X-site vacancy binary plot.....	181
Fig. 5.19. Schematic diagrams illustrating the two possible fluid source models for the widespread tourmaline observed in the Loulo district. A) Syngenetic exhalative model of Dommanget <i>et al.</i> (1993). B) Epigenetic granitic model adopted during this present study.....	183
Fig. 5.20. Boron concentrations in the eastern parts of the Kédougou-Kéniéba inlier based on soil geochemistry surveys carried out by Randgold Resources.....	184
Fig. 5.21. Histogram showing the formation temperatures of hydrothermal chlorite at Yalea Main, Loulo-3 and Faraba, and metamorphic chlorite from sedimentary and intrusive rocks from the Loulo district.....	186

CHAPTER 6: FLUID INCLUSION STUDIES AT LOULO

Fig. 6.1. Fluid inclusion populations at various Birimian gold deposits.....	190
Fig. 6.2. Schematic drawings showing the distribution of the four fluid inclusion types at Gara (A) and Yalea (B).....	193
Fig. 6.3. Photomicrographs of the four fluid inclusion types at Loulo (at room temperature): CO ₂ inclusions (type 1) (A to B); H ₂ O-NaCl inclusion (type 2) (C to D); H ₂ O-CO ₂ -NaCl inclusions (type 3) (E to F); multiphase solid H ₂ O-CO ₂ -NaCl-FeCl ₂ inclusions (type 4) (G to H).....	196
Fig. 6.4. Electron microprobe images of opened, quartz-hosted type 4 inclusions (gold coated samples) from Gara and Yalea North. A) to B) halite; C) Fe chloride and magnetite; D) a range of solid phases including haematite, muscovite and carbonates. E) to F) evaporite components of the brine. H) BSE image of halite showing Cu concentration on the apex of the cube.....	198
Fig. 6.5. Fluid inclusion populations in the Loulo mining district.....	201
Fig. 6.6. The melting and homogenisation temperatures of CO ₂ -(N ₂)-(CH ₄) (type 1) inclusion at Loulo.....	207
Fig. 6.7. Representative Raman spectra of CO ₂ -(N ₂)-(CH ₄) inclusions from auriferous and barren quartz at Gara. A) CO ₂ inclusion from the main ore phase. B) CO ₂ -CH ₄ -N ₂ inclusion from reactivated quartz. C) CO ₂ -N ₂ fluid from barren veins.....	208
Fig. 6.8. Representative Raman spectra of CO ₂ -(N ₂)-(CH ₄) inclusions from auriferous and barren quartz at Yalea Main. A) CO ₂ -N ₂ -CH ₄ inclusion from Yalea South B) CO ₂ -N ₂ inclusion from Yalea Central. C) CO ₂ -N ₂ fluid from barren veins.....	209
Fig. 6.9. CO ₂ -N ₂ -CH ₄ ternary diagrams showing the gas fluid compositions of type 1 and type 3 inclusions at Loulo (mol.%). A) Gara-style deposits; B) Yalea-style deposits; C) Barren veins.....	210
Fig. 6.10. Freezing and heating measurements for H ₂ O-NaCl (type 2) inclusions at Loulo.....	213
Fig. 6.11. Homogenisation temperatures vs. salinity binary plots for H ₂ O-NaCl inclusions at Loulo. A) Gara-style deposits contain; B) Yalea-style deposits; C) Barren veins.....	214
Fig. 6.12. Freezing and heating measurements for H ₂ O-CO ₂ -NaCl inclusions (type 3) at Loulo.....	218
Fig. 6.13. Salinity vs. T _h total plots for H ₂ O-CO ₂ -NaCl inclusions at Loulo. A) Gara-style deposits. B) Yalea-style deposits and barren veins.....	220
Fig. 6.14. Freezing and heating measurements for hypersaline, multiphase solid, H ₂ O-CO ₂ (type 4) inclusions at Loulo.....	223
Fig. 6.15. Composition-temperature phase diagram for the system H ₂ O-CO ₂ -NaCl at 2 kbar, and 0 and 6 wt.% NaCl equivalent.....	226
Fig. 6.16. Bulk XH ₂ O vs. salinity plot for type 3 H ₂ O-CO ₂ inclusions from Yalea-style gold-bearing veins.....	227
Fig. 6.17. T _h total vs. salinity plot for H ₂ O-CO ₂ (type 3) inclusions from Gara-style auriferous veins (redrawn from Fig. 6.13a) showing strong evidence for fluid mixing.....	230
Fig. 6.18. H ₂ O-NaCl-CO ₂ ternary diagram showing the bulk molar compositions of type 1, type 3 and type 4 inclusions in the Gara-style deposits.....	230
Fig. 6.19. A schematic sketch of the fluid mixing model proposed for the Gara-style deposits.....	232
Fig. 6.20. Isochores for minimum, maximum and mean bulk densities for type 1 and type 2 inclusions from Yalea-style mineralised quartz veins. Intersections are also shown with chlorite temperatures determined in section 5.5.4, which are assumed to be coeval with mineralisation. A) Yalea Central, B) Loulo-3, C) Baboto.....	234
Fig. 6.21. Relationship between inclusion size and the pressure required to initiate re-equilibration in quartz-hosted fluid inclusions under atmosphere confining pressure. Data from Bodnar <i>et al.</i> (1989), Leroy (1979) and Swanenburg (1980). Figure from Bodnar (2003b).....	236

Fig. 6.22. Isochore plots of barren veins from Gara and Yalea. A) Isochores of type 1 and type 2 inclusions using minimum, maximum and average bulk densities (type 2 inclusions- 95% confidence level). B) Isochores of the highest and lowest bulk density of type 3 inclusions.....	238
---	-----

CHAPTER 7: STABLE ISOTOPE STUDIES AT LOULO

Fig. 7.1. A histogram showing the uniform silicate $\delta^{18}\text{O}$ compositions at Gara and the main Yalea orebody).....	247
Fig. 7.2. $\delta^{18}\text{O}_{\text{fluid}}$ vs. temperature plot for mineralised quartz at Gara and Yalea Main.....	248
Fig. 7.3. A histogram showing the carbonate $\delta^{18}\text{O}$ compositions at Loulo.....	249
Fig. 7.4. $\delta^{18}\text{O}_{\text{fluid}}$ vs. temperature plot for the Loulo carbonates.....	250
Fig. 7.5. A histogram showing the scattered distribution of $\delta^{13}\text{C}$ compositions of the Loulo carbonates.....	253
Fig. 7.6. Sulphur isotope compositions ($\delta^{34}\text{S}$) of Birimian and other Palaeoproterozoic orogenic gold deposits.....	255
Fig. 7.7. A histogram showing the bimodal isotopic compositions of the Loulo sulphides.....	256
Fig. 7.8. The variation of sulphide S isotopic compositions in sediment-hosted orogenic gold deposits, in correlation with the seawater sulphate curve through geological time (Chang <i>et al.</i> , 2008).....	261

CHAPTER 8: ORE GENETIC MODEL FOR LOULO

Fig. 8.1. Gold solubility (in molality, m , and in parts per billion) and speciation at 1 kbar, as a function of temperature for an aqueous solution containing 1.5 molal (m) NaCl and 0.5 m KCl, with pH buffered by the assemblage K-feldspar-muscovite-quartz. A) $f\text{O}_2$ buffered by the haematite-magnetite (HM) assemblage ($\Sigma\text{S} = 0.01$ m). B) ΣS and $f\text{O}_2$ buffered by the assemblage pyrite-pyrrhotite-magnetite ($\Sigma\text{S} = 0.1$ m). (figure from Williams-Jones <i>et al.</i> , 2009).....	269
Fig. 8.2. Gold solubility (in part per billion; solid lines) and speciation at 0.5 kbar and 250 °C, as a function of $\log f\text{O}_2$ and pH in a solution containing 1 m NaCl and ΣS of 0.01 m. (figure from Williams-Jones <i>et al.</i> , 2009).....	269
Fig. 8.3. Fluid model based on available fluid inclusions, geochemical and isotopic data for the Loulo hydrothermal system, identifying likely fluid sources, transport mechanisms and trapping conditions for orogenic gold mineralisation along the SMSZ.....	275
Fig. 8.4. A 2009 gravity map of the Loulo permit showing numerous low density anomalies in the northern part of the permit and in the south at Goukoto and P-64, indicating deep-seated granitic bodies exist within the Kofi sedimentary package. Image courtesy of Randgold Resources.....	279
Fig. 8.5. Depth of emplacement in the Loulo district based on mineralogy and fluid inclusion studies, showing shallower conditions to the south.....	284

LIST OF TABLES

CHAPTER 1: INTRODUCTION

Table 1.1. Summary of gold reserves and resources for the Loulo mining district (for year ending 2009).....	8
Table 1.2. General characteristics of Precambrian and Phanerozoic orogenic gold deposits (data summarised from Groves <i>et al.</i> , 2000; Ridley & Diamond, 2000; Goldfarb <i>et al.</i> , 2005; Duuring <i>et al.</i> , 2007).....	12

CHAPTER 2: THE BIRIMIAN OF WEST AFRICA- A REVIEW

Table 2.1. Characteristics of belt- and basin-type granitoids in Ghana (modified from Hirdes & Davis, 1998).....	26
Table 2.2. Crustal growth model for Birimian rocks of the WAC (Feybesse <i>et al.</i> , 2006).....	29
Table 2.3. Summary of Birimian geochronological data collected on various rock types across West Africa.....	33
Table 2.4. Tectonic phases of the Eburnean orogeny in Ghana based on structural and geochronological evidence collected by Feybesse <i>et al.</i> (2006).....	34
Table 2.5. A proposed classification scheme for Birimian and Tarkwaian gold mineralisation.....	38
Table 2.6. Birimian mineralisation history modified after Milési <i>et al.</i> (1992).....	43

CHAPTER 3: GEOLOGY OF THE LOULO AREA

Table 3.1. Outlining the major sediment types of the Kofi Series, with comparisons to mine terminology.....	51
Table 3.2. Differences between belt- and basin-type intrusions in the eastern parts of the KKI, based on field descriptions, mineralogy and chemistry.....	82
Table 3.3. A comparison of provenance elemental ratios from the Kofi sediments, granodiorites and quartz-diorites of the Balangouma pluton, and early Proterozoic volcanic rocks (EPC; Condie, 1993).....	85

CHAPTER 4: MINERALISATION AT LOULO

Table 4.1. Summary wall-rock alteration, vein and sulphide paragenesis for the Gara orebody.....	93
Table 4.2. Representative chemical composition of the Fe-Ni-As-S minerals at Gara by electron microprobe analysis.....	94
Table 4.3a. Chemical compositions of monazite at Gara by electron microprobe analysis.....	98
Table 4.3b. Chemical compositions of xenotime at Gara by electron microprobe analysis.....	99
Table 4.4. Representative electron microprobe analysis of native gold at Gara.....	102
Table 4.5. Schematic cartoons of the various textures present along the N-S Yalea Main orezone.....	106
Table 4.6. Summary of hydrothermal alteration, gangue and sulphide paragenesis for Yalea Main.....	109
Table 4.7. Chemical composition of tennantite at Yalea Main by electron microprobe analysis.....	110
Table 4.8. Representative electron microprobe analysis of native gold at Yalea Main.....	114
Table 4.9. Summary wall-rock alteration, gangue and sulphide paragenesis for the Yalea North oreshoot.....	115
Table 4.10. Representative chemical composition of the Fe-Ni-S and the As-Ni-Co-Fe-S minerals of the Yalea North oreshoot by electron microprobe analysis.....	117
Table 4.11. Representative chemical composition of monazite at Yalea North analysis.....	120

Table 4.12. Representative electron microprobe analysis of native gold and silver grains at Yalea North.....	120
Table 4.13. Summary paragenesis for wall-rock alteration and ore phases at P-125.....	122
Table 4.14. Representative electron microprobe analysis of native gold at P-125.....	124
Table 4.15. Summary mineral paragenesis for Faraba Main and Faraba South oreshoots.....	128
Table 4.16. Representative electron microprobe analysis of Bi-Te minerals at Faraba.....	129
Table 4.17. Representative electron microprobe analysis of native gold at the Faraba orebodies.....	129
Table 4.18. Representative microprobe analysis of Sb-Pb bearing trace sulphides at Baboto.....	133
Table 4.19. Representative electron microprobe analysis of native gold at a selection of minor Loulo orebodies.....	134
Table 4.20. Representative electron microprobe analysis of Au-Te minerals at Goukoto.....	135
Table 4.21. Deposit summary table for mineralisation in the Loulo mining district.....	136
Table 4.22. Summarising the two major petrogenetic types present in the Loulo district.....	137
Table 4.23. Estimated mineralisation temperatures at Loulo based on the arsenopyrite geothermometer (Kretschmar & Scott, 1976; Sharp <i>et al.</i> , 1985).....	139

CHAPTER 5: HYDROTHERMAL ALTERATION AT LOULO

Table 5.1. Representative chemical compositions of tourmaline phases at Gara by electron microprobe analysis.....	153
Table 5.2. Representative chemical composition of tourmaline phases at Yalea North by electron microprobe analysis.....	159
Table 5.3. Representative chemical composition of tourmaline at P-64, P-129 and P-125 orebodies by electron microprobe analysis.....	162
Table 5.4. Chemical composition of hydrothermal and metamorphic chlorites at Loulo by electron microprobe analysis.....	170
Table 5.5. Alteration characteristics of Gara- and Yalea-style orebodies in the Loulo mining district.....	179

CHAPTER 6: FLUID INCLUSION STUDIES AT LOULO

Table 6.1. Compositional classification of fluid inclusions present in the Loulo district, based on phases identified at room temperature.....	194
Table 6.2. Identification of solid phases by optical microscopy and electron microprobe analysis.....	199
Table 6.3. Notations and terminology used in this chapter (as used by Diamond, 2003).....	203
Table 6.4. Summary of microthermometric and Raman results for CO ₂ -(N ₂)-(CH ₄) (type 1) inclusions.....	206
Table 6.5. Summary of microthermometric results for H ₂ O-NaCl (type 2) inclusions at Loulo.....	212
Table 6.6. Summary of microthermometric and Raman results for H ₂ O-CO ₂ -NaCl (type 3) inclusions at Loulo.....	217
Table 6.7. Summary of microthermometric and Raman results for multiphase H ₂ O-CO ₂ (type 4) inclusions at Loulo.....	222
Table 6.8. Fluid inclusion characteristics of Gara- and Yalea-style orebodies in the Loulo district.....	224

CHAPTER 7: STABLE ISOTOPE STUDIES AT LOULO

Table 7.1. Isotopic compositions (O, C & S) of the Gara, Yalea Main and Faraba orebodies (data collected from present study).....	244
--	-----

Table 7.2. Selected data (O, C & S) from the Fouillac <i>et al.</i> (1993) stable isotope study.....	246
Table 7.3. Measured silicate $\delta^{18}\text{O}_{\text{V-SMOW}}$ (‰) and calculated values for coexisting fluid (all data from this study).....	248
Table 7.4. Measured carbonate $\delta^{18}\text{O}_{\text{V-SMOW}}$ (‰) and calculated values for coexisting fluid (all data from this study).....	250

CHAPTER 8: ORE GENETIC MODEL FOR LOULO

Table 8.1. Mineralogical and geochemical characteristics of the Gara- and Yalea-style orebodies at Loulo (data taken from Table 4.22, Table 5.5 & Table 6.8).....	265
Table 8.2. P-T estimates for Yalea-style mineralisation.....	267
Table 8.3. Te-Au mineral phases associated with Faraba style deposits.....	282

APPENDICES

Table A-1. Emission lines used for ICP-AES and association limits of detection.....	326
Table A-2. Quality controls on the ICP-AES data.....	326
Table A-3. Detection limits for the ICP-MS.....	328
Table A-4. Quality controls on the ICP-MS data.....	329
Table A-5. Whole rock geochemistry of the intrusive and sedimentary rock samples from Loulo.....	332
Table A-6. Summary vein and sulphide paragenesis for the Loulo-3 orebody.....	338
Table A-7. Summary wall-rock alteration, vein and sulphide paragenesis for the Baboto orebody.....	338
Table A-8. Summary vein and sulphide paragenesis for the P-129 orebody.....	339
Table A-9. Summary wall-rock alteration, vein and sulphide paragenesis for the P-64 orebody.....	339
Table A-10. Summary of the microthermometric and Raman spectrometric data for fluid inclusions from mineralised and barren veins at Gara.....	341
Table A-11. Summary of the microthermometric and Raman spectrometric data for fluid inclusions from mineralised and barren veins at Yalea Main.....	343
Table A-12. Summary of the microthermometric and Raman spectrometric data for fluid inclusions from mineralised veins at Yalea North.....	345
Table A-13. Summary of the microthermometric and Raman spectrometric data for fluid inclusions from mineralised veins at Loulo-3.....	346
Table A-14. Summary of the microthermometric and Raman spectrometric data for fluid inclusions from mineralised veins at Baboto.....	347

CHAPTER 1: INTRODUCTION AND PROJECT OUTLINE

In this thesis, the geology and genesis of the Loulo orogenic gold district in western Mali is investigated. Chapter 1 introduces the reader to gold mining in Mali, the setting and history of the Loulo mining district, the general characteristics of orogenic gold deposits, and the aims and objectives of the project. This chapter also acknowledges Randgold Resources, who funded the project and currently own the Loulo mine.

1.1 Introduction to Mali and Malian gold mining

1.1.1 Mali

The Republic of Mali is the largest country in West Africa with a land area of approximately 1,240,000 km², a third of which is covered by the Sahara Desert. The landlocked country is bordered to the west by Mauritania; to the north by Algeria; to the east by Niger; to the south by Burkina Faso, Côte d'Ivoire and Guinea; and to the SW by Senegal (Fig. 1.1). Loulo is situated in the Sahel zone; a semi-arid region that forms a transition between the Sahara Desert to the north and the sub-tropical Sudan savannah that covers the southern part of Mali.

The Malian landscape is flat, situated at relatively low altitudes (average 200-300 m above sea level) despite being located several hundred kilometres from the coast. The lowest elevation occurs along the Senegal River (23 m above sea level) and the highest elevation at Mount Hombori (1155 m above sea level) (Fig. 1.1). Mali's most important geographic feature is the great Niger River, which transverses the Sahel and southern regions of the country. The Niger River acts a major source of food, as well as transportation and trade routes with the capital, Bamako. Mali has a population of approximately 13.8 million, with an annual growth rate of 2.61% (U.S. Central Intelligence Agency, 2010). The population is unevenly distributed with nearly 90% of the population situated in the south, especially in the capital Bamako, which is estimated to be one of the fastest growing cities in Africa (~13% of overall population). Mali's official language is French, but around 80% of the population speak the native 'Bambara' language, plus numerous other African languages.

Mali was once part of three ancient West Africa empires (Ghana, Mali and Songhai empires) that controlled trans-Saharan trade in gold, salt and other precious commodities between 700 AD to 1591 (Velton, 2009). The empires arose in a region of Africa that became known as the western Sudan; a vast area of savannah that extended from the southern margin of the Sahara Desert to the rainforests of Guinea. The Ghana Empire (or Wagadou Empire) was located in present SE Mauritania and western Mali, and ruled from 790-1076. The introduction of the camel during this period expanded trade routes to North Africa, Middle East and Europe (Davidson, 2005). After the fall of the Ghana Empire, the Empire of Mali took control of West Africa, and during the 14th century stretched from the Atlantic Ocean to present-day Nigeria (an area larger

than western Europe). During the peak of the Mali Empire, Timbuktu (or Tombouctou) was built as the centre of commerce and Islamic culture. The Songhai Empire ruled West Africa during the 15th and 16th centuries and represents one of Africa largest historical empires. Central to the Songhai's success were the gold fields along the Niger River. The collapse of the Songhai Empire by a Moroccan mercenary uprising in 1591 ended the regions dominance in African and world trade.

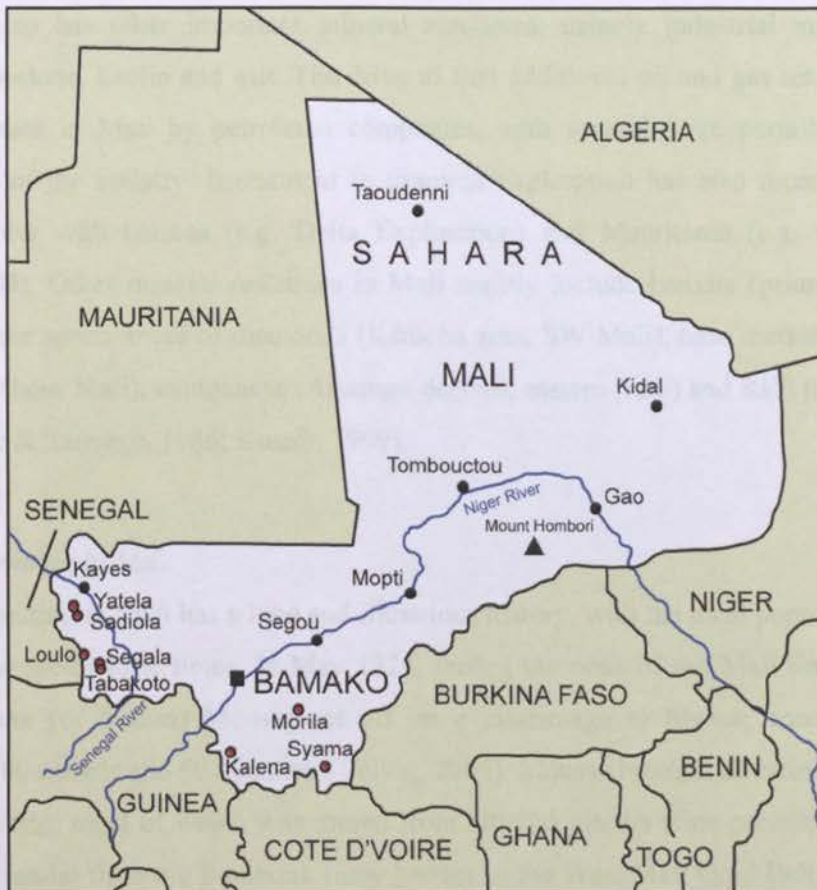


Fig. 1.1. Map of Mali showing the location of the major gold deposits (red circles) within the country.

Mali fell under French colonial rule in 1892 and became known as the Sudanese Republic. In 1959, the Sudanese Republic and Senegal combined to form the Mali Federation, which in 1960 gained independence from France. The Mali Federation lasted only a few months before Senegal withdrew, allowing the Sudanese Republic to form the independent nation of Mali. Mali's first president, Modibo Keita, moved quickly to establish a single-party state. During the 1960's, the economy severely declined and Keita was overthrown by a group of military officers led by Moussa Traore. The country suffered numerous coup attempts through the 1970's and 1980's. After the Tuareg uprising in 1990, Mali became a democratic, multiple-party state and has since become one of the most politically and socially stable countries in Africa. The former general, Amadou Toure, who led the Tuareg coup, was elected president in 2002 and re-elected in 2007.

Despite Mali's improving political system, it remains one of the poorest countries in Africa. The average worker's annual salary is currently (2009 est.) approximately US\$1,200 (U.S. Central Intelligence Agency, 2010). The country is heavily reliant on foreign aid and vulnerable to fluctuations in prices of gold and cotton (Mali's two leading exports). Mali's main industry is agriculture, employing around 80% of the labour force (U.S. Central Intelligence Agency, 2010). In addition to cotton, the country also exports rice, corn, vegetables, tobacco and tree crops. Although the mining sector is dominated by gold (~80% of all mining activities; Bermúdez-Lugo, 2006), Mali also has other important mineral resources; namely industrial minerals such as phosphate, limestone, kaolin and salt. The drive to find additional oil and gas reserves has led to recent investment in Mali by petroleum companies, with several large permits issued in the northern parts of the country. Investment in uranium exploration has also recently taken place along the border with Guinea (e.g. Delta Exploration) and Mauritania (e.g. Oklo Uranium) (Holliday, 2009). Other mineral resources in Mali mainly include bauxite (primarily in western Mali), and minor appearances of diamonds (Kéniéba area, SW Mali), base metals (Zn-Pb deposit at Tessalit, northern Mali), manganese (Ansongo deposit, eastern Mali) and REE minerals (eastern Mali) (Leblanc & Sauvage, 1986; Kusnir, 1999).

1.1.2 Gold mining in Mali

Gold mining in Mali has a long and illustrious history, with the local population exploiting the metal since pre-historic times. In May 1324, during the peak of the Mali Empire, legendary emperor Kankan (or Mansa) Moussa set off on a pilgrimage to Mecca, accompanied by an entourage of 100 camels and 60,000 men (Velton, 2009). Moussa brought an estimated 8 tonnes (t) of gold on his trip, most of which was mined from alluvial placers (fine particles of native gold found in river sands) from the Bambouk (now known as the West Mali Gold Belt; *see below*) and Buré (southern Guinea) goldfields. According to the historian al-Umari, Moussa spent so lavishly on his travels that Cairo's financial market crashed. Despite the fact it took a decade for the price of gold to fully recover, Moussa's visit alerted European and Arab rulers to the wealth of Mali and helped develop political, cultural and trade links between western Sudan and the rest of the world (Velton, 2009). The collapse of the Songhai Empire in the late 16th century ended the regions dominance in African and world gold trade. Thousands of artisanal miners are still active in Mali today (Fig. 1.2) and their production is estimated around 96,500 oz/year (Holliday, 2007).

Commercial mining started in Mali in the 1970's. The first industrial mine, Kalana, was discovered after a large exploration programme by Société Nationale de Recherche et d'Exploitation Minière (SONAREM) (Boltroukevitch, 1973). During the 1980's, a United Nations assisted project carried out extensive soil geochemistry surveys leading to the discovery of several gold occurrences, including the Syama deposit (Kusnir, 1999). Soil geochemistry surveys are a useful exploration tool in prospecting in the flat, outcrop poor, landscape that covers most of Mali

(Kusnir & Diallo, 1986). In 1991, Mali relaxed its mining codes after collaboration with the International Development Association. This led to renewed foreign interest and began the recent boom in Mali, which has seen the country become Africa's joint third leading gold producer, level with Tanzania, after Ghana and South Africa (Holliday, 2008). AngloGold Ashanti and Randgold Resources are the most active in the country, but other companies such as IAMGold, Merrex Gold, Axmin, Avion and Arnvel are also exploring.

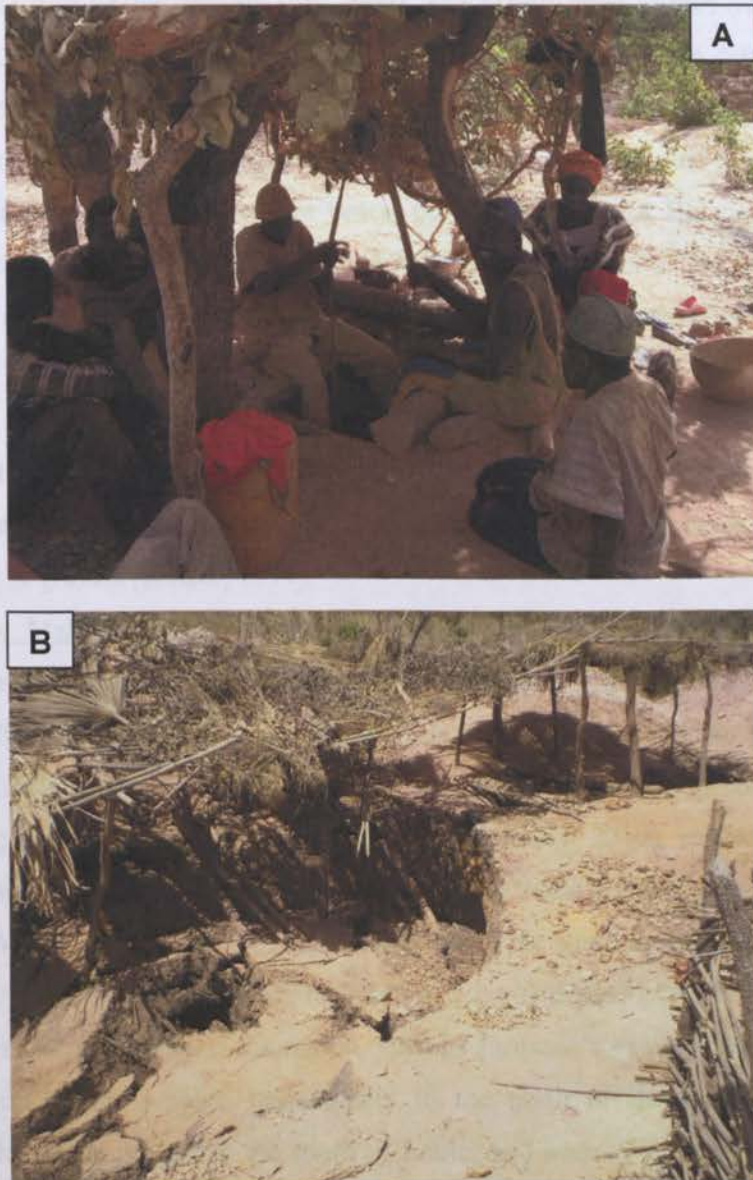


Fig. 1.2. Artisanal workings in the Faraba region of the Loulo permit. **A)** Local Malians mining for gold (picture taken in May 2006). **B)** A collapsed mine shaft (picture taken in January 2007).

Malian gold deposits outcrop in two distinct areas of the country, in the SW along the border with Senegal (West Mali Gold Belt) and in the Bougouni area, in southern Mali (Mali South) (Fig. 1.1). These deposits are associated with Palaeoproterozoic rocks (2.0-2.2 Ga) of the West African Craton, known as the Birimian (the regional setting, geology, crustal evolution and metallogenesis of the Birimian crust is discussed in *chapter 2*).

Mali South contains the giant Morila deposit (9.15 Moz resource; Randgold Resources, 2009), and the smaller Syama (4.5 Moz resource; Resolute Mining Ltd, 2009) and Kalana deposits (~1 Moz resource; Avnel Gold Mining Ltd, 2009). The Morila mine is part owned by Randgold Resources (40%), AngloGoldAshanti (40%) and the State of Mali (20%). To date, Morila is Mali's biggest single producer of gold, producing >5 Moz since the turn of the century. However, 2009 was Morila's last year of full production and now the deposit has become a stockpile treatment operation until closure in 2013. In recent years, the old Syama and Kalana mines have been brought back into production. In 2007, Resolute Mining took control of the Syama deposit with current reserves of 1.83 Moz at 3.12 g/t (grams per tonne), plus additional satellite reserves discovered along strike (e.g. Tabakoroni resource of 745, 000 oz at 2.53 g/t; Holliday, 2009). The Kalana mine has been owned by Avnel since 2004. Average grades of 13.1 g/t makes Kalana a profitable deposit despite its small size (Holliday 2009). A number of alluvial placers have been located in the rivers draining the Kalana area, with the largest, the Bale placer, containing around 0.14 Moz of gold in gravels (Kusnir, 1999).

The West Mali Gold Belt is the most productive gold region in West Africa outside Ghana, and the major deposits are shown in Fig. 2.11 and Fig. 3.1. This gold belt contains the two largest deposits/districts in Mali, at Loulo and Sadiola, which contain estimated resources of 14.4 Moz at 4.41 g/t (including the Goukoto deposit; Randgold Resources Ltd, 2009) and 14 Moz at 2.4 g/t (including production of >5 Moz since 1997; Holliday, 2010), respectively. AngloGold Ashanti and IAMGold own the northern permits including Sadiola and the nearby Yatela deposit (resource of 2.7 Moz; Holliday, 2010). Smaller deposits to the south include the Tabakoto (2 Moz resource at 2.2 g/t) and Segala (0.9 Moz resource at 2.2 g/t) deposits (Avion Gold Corp, 2009). Numerous projects are underway in the region, such as Etruscan's exciting Diba target just south of Sadiola; Axmin's Kofi project, immediately to the north of the Loulo permit; Papillion Resources Ltd Medinandi project to the south of Loulo; and Merrex Gold Siribaya targets in the southern part of the belt. Mali South and the West Mali Gold belt are discussed in further detail in *chapter 2 (section 2.6.1.2)*.

Gold has now become Mali's leading export product followed by cotton, and has seen a rapid increase since the turn of the century, accounting for 57% of the country's exports in 2003 (Bermúdez-Lugo, 2003), 65% in 2005 (Holliday, 2007) and up to 72% in 2008 (Holliday, 2008). This rise has seen the contribution to the gross domestic product (GDP) increase from 6% in 1998 to 15% in 2008 (Bermúdez-Lugo, 2006; Holliday, 2008). However, annual gold production has been on a steady decline in recent years from 62 tonnes in 2006 to 46 tonnes in 2009 (Fig. 1.3)

(Holliday, 2009). This drop in gold production reflects the fact that two of Mali's big three gold mines (Morila and Sadiola) are nearing closure, and emphasises the need for further exploration projects with real economic potential in the country (Holliday, 2008).

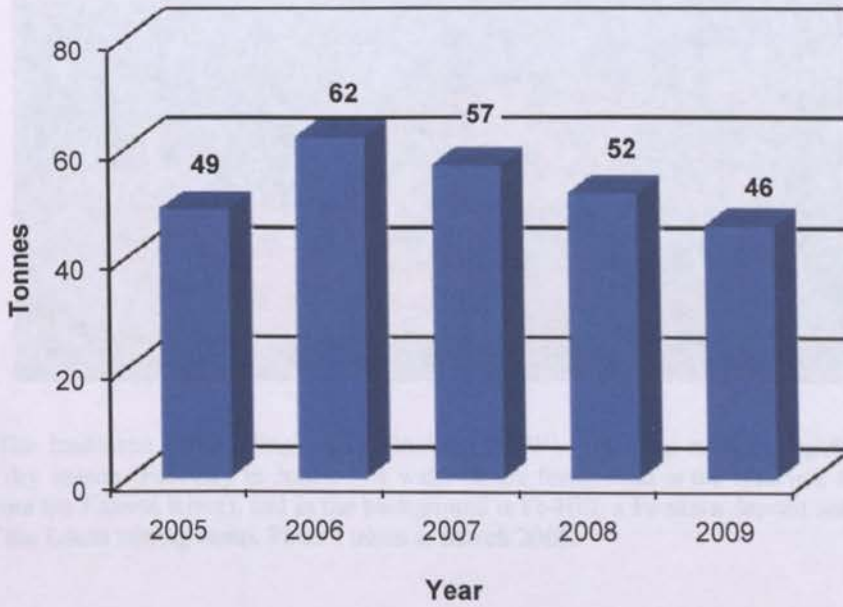


Fig. 1.3. Mali's annual gold production (modified from Holliday, 2009).

1.2 The Loulo mining district

1.2.1 Location

Loulo is situated approximately 13°N of the equator, in the semi-arid Kayes region of SW Mali, close to the border with Senegal. Loulo is located 350 km west of Bamako and 220 km south of Kayes (the nearest major town). In terms of major gold deposits, Loulo is situated 96 km south of Sadiola and 25 km west of Segala and Tabakoto (Fig. 1.1). Loulo can be accessed by road from Kayes and Bamako or by air from Bamako (an hour flight). The landscape surrounding Loulo is relatively flat (100-110 m above sea level). Higher elevations are observed over laterite plateaus, iron-ore deposits (preferentially in the Bambadji permit to the west of Loulo; up to 200 m above sea level) (Fig. 1.4), and north to NNE-trending ridges (e.g. Yalea ridge; elevations up to 165 m above sea level). The western margin of the permit is bounded by the Falémé River (a tributary of the Senegal River), which forms the border with Senegal to the west. The largest village in proximity to the mine is Djidjaan Kéniéba (3000-5000 inhabitants). Numerous smaller villages occur in the permit including Loulo (after which the mine is named), Baboto and Sakola.



Fig. 1.4. The landscape surrounding Loulo (looking NNW). The area remains lightly vegetated during the dry season (February to June). The water in the foreground is the reservoir for the mine (drained from the Falémé River), and in the background is Fe-Hill; a Fe skarn deposit situated just to the NW of the Loulo mining camp. Picture taken in March 2008.

1.2.2 Mining district layout

The Loulo mining permit is the largest land holding along the West Mali Gold Belt, covering an area of 1,270 km². The mining district layout (including location of permits and orebodies) are shown in Fig. 3.2. The concession consists of the original Loulo permit (371 km²) (where all the major gold orebodies exist at present) and neighbouring permits including the Clib holding to the north (91.2 km²) and the Bambadji and Daléma permits to the west in Senegal (404 km² and 402.9 km², respectively). The Loulo property currently consists of two major operational mines at Yalea (including the P-125 satellite deposit) and Gara, with current resources estimated at 6.5 Moz at 4.7 g/t and 3.7 Moz at 4.1 g/t, respectively (Table 1.1). In 2008, a significant orebody was discovered in the southern parts of the Loulo permit at Goukoto, with a current resource of 2.9 Moz at 6.8 g/t. The permit also includes numerous satellite and smaller orebodies (e.g. Loulo-3, Faraba, Baboto, P-129, P-64 and Gara West) that further highlights the high endowment of this area of Mali, and takes Loulo's mining resource to 14.4 Moz.

Table 1.1. Summary of gold reserves and resources for the Loulo mining district (for year ending 2009).

Orebody	Mineral reserves Proven and probable				Mineral resource			
	Tonnes (Mt)	Grade (g/t)	Contained Gold (tonnes)	Mozs	Tonnes (Mt)	Grade (g/t)	Contained Gold (tonnes)	Mozs
Stockpiles	1.11	1.78	1.97	0.06	1.11	1.78	1.97	0.06
Gara	19.22	4.15	79.72	2.56	27.99	4.11	115.12	3.70
Yalea (incl. P-125)	26.66	4.91	130.91	4.21	42.89	4.70	201.79	6.49
Goukoto	7.47	6.83	51.02	1.64	13.13	6.82	89.51	2.88
Loulo 3	1.00	2.94	2.94	0.09	2.30	3.31	7.63	0.25
Faraba	–	–	–	–	6.78	2.60	17.63	0.57
Baboto	–	–	–	–	5.30	1.71	9.06	0.29
Gara West	1.23	2.07	2.55	0.08	1.69	2.30	3.88	0.13
P-129	0.23	2.73	0.63	0.02	0.50	3.00	1.50	0.05
Total (not incl. Goukoto)	49.45	4.42	218.72	7.02	88.57	4.05	358.57	11.53
Total (incl. Goukoto)	56.92	4.74	269.74	8.66	101.70	4.41	448.08	14.41

Note- cut off grades of 1.5 g/t for underground mining

1.2.3 Exploration and development history

The ore potential of the Loulo mining district has long been recognised, but commercial mining only started in 2005. Artisanal workings were discovered at Yalea prior to the discovery of the deposit. Although they have not been dated, these workings are probably several hundred years old. Extensive soil geochemistry surveys in the area were carried out early in the 1980's by Syndicat Or, a joint venture between the French Bureau de Recherches Géologiques et Minières (BRGM) and the Malian Direction Nationale de la Géologie et des Mines (DNGM). This led to the discovery of the Gara deposit in 1981 (previously known as Loulo-0). Field mapping showed a clear relationship between mineralisation and quartz-tourmaline greywackes (termed quartz-wackes in this study). Drilling of the Gara deposit and nearby satellite deposits by the Syndicat Or took place between 1984 and 1987. They continued work in the area until 1989, concluding with a feasibility study suggesting the deposit was sub-economic. Based on the evaluation of the earlier data, BHP Minerals entered into an option and share purchase agreement with Syndicat Or in June 1992. BHP carried out fieldwork and drilling programmes during 1993 and acquired BRGM shares in Syndicat Or. The new joint venture became known as Société des Mines de Loulo (SOMILO). BHP estimated Loulo's gold resource at 1.28 Moz.

BHP Minerals ended their interest in Loulo in October 1996, when Randgold Resources acquired BHP's Malian projects for US\$20 million (including the Morila and Syama deposits). Randgold Resources then carried out an intensive exploration programme, which led to the discovery of the Yalea deposit in 1996/1997. After the acceptance of a feasibility study in 1999,

the company acquired enough shares to take their stake in the Loulo mine to 80%, with the Government of Mali holding the remaining 20%. In 2003, the company re-established its exploration programme and a revision of the feasibility study was undertaken to meet the board of director's investment criteria. In November 2005, the Loulo mine was officially open, twenty-four years after the first discovery by the Syndicat Or. Open-pit mining commenced at the Gara and Yalea deposits (Fig. 1.5), as well as smaller pits at P-125 and P-129. In June 2008, the first ore was mined at Yalea's underground project, which is currently mining 60,000 t/month and scheduled to produce 120,000 t/month by July 2010. In July 2009, overground mining started at Loulo-3, taking Loulo past the 1 Moz production mark. Underground mining is scheduled to start at Gara in 2010. The significant recent discovery at Goukoto has extended Loulo mining beyond 2025, outlasting many other known gold deposits in Mali.



Fig. 1.5. **A)** Plan view of the Gara pit, ~1.2 km in length, looking south (photo taken in February 2008). **B)** Plan view of the Yalea pit, ~1.5 km in length, looking north (photo taken in February 2008).

1.2.4 Randgold Resources

Randgold Resources is a gold focused mining and exploration company established in the Channel Islands in 1995. The company was listed on the London Stock Exchange in 1997, on Nasdaq (GOLD) in 2002, and is now a FTSE 100 company, making a profit of US\$84.3 million in 2009. Randgold are currently active in West and Central Africa. Their West African projects include the Loulo and Morila mines in Mali, the Massawa deposit in Senegal (3 Moz resource at 4.0 g/t; Randgold Resources Ltd, 2009) and the Tongon project in northern Côte d'Ivoire (4.58 Moz resource at 2.8 g/t; Randgold Resources Ltd, 2009) (locations are shown in the following chapters in Fig. 2.4 and Fig. 3.1). In 2008, Randgold acquired the world-class Kibali permit in the Democratic Republic of Congo (DRC), with current reserve and resource estimates of 9.19 Moz at 4.48 g/t and 19.76 Moz at 3.36 g/t, respectively.

In social terms, Randgold believe heavily in aiding local communities. The company have helped to build schools surrounding Loulo (in the Loulo, Baboto and Djidjaan Kéniéba villages), as well as the construction of a local health clinic. Furthermore, Randgold supply health support in the form of an effective malaria indoor spraying programme, which decreased annual malaria cases by 30% surrounding Loulo. They also assist local farmers to improve agriculture in the area and have started sustainability projects, replanting over a thousand indigenous trees and plants destroyed through mining activities.

1.2.5 Previous work

Previous work on the Loulo deposits is largely confined to unpublished internal company reports. Structural studies on the Loulo area have been carried out by Harris (1998), Allibone (2004), Allibone & Cameron (2006), and more locally on the Faraba and P-64 targets (Coffey Mining Pty, 2007). Other consultancy work includes an Aster imaging report (Cameron & Moolman, 2004) and a sensitive high-resolution ion microprobe (SHRIMP) report on mineralisation at Gara (Vielreicher, 2006). Very little published data exists for Loulo, all of which dates back to late 1980's and early 1990's. Early work outlining the main aspects and controls on mineralisation at Loulo include Milési (1989a, b; 1992) and Dommanget *et al.* (1993). A stable isotope study has also been carried out at Loulo (Fouillac *et al.*, 1993). This early work was carried out when there was a restricted database and a limited understanding of the controls on mineralisation (e.g. limited drill core and no open pits). The majority of the data collected in this present study questions the conclusions raised by Milési and others.

1.3 Orogenic gold mineralisation

Loulo and many other West African gold deposits classify as orogenic gold deposits. Orogenic gold deposits are epigenetic, structurally controlled lode deposits. They are the most common and significant type of gold deposit, accounting for over a quarter of the total historic gold production (Goldfarb *et al.*, 2005). A considerable proportion of mined placer deposits are erosional products of orogenic lodes, adding to their significance in terms of production. Two of the most productive orogenic gold provinces are Archaean deposits associated with the Yilgarn Craton, Western Australia, and the Superior Subprovince, Canada. Traditionally, this type of deposit has been referred to as ‘mesothermal’ gold deposits (e.g. Nesbitt *et al.*, 1986). More recently the term ‘orogenic gold’ has been used as these deposits occur over a continuum of depths from 15-20 km to within 2-3 km of the surface (Groves *et al.*, 1998). Orogenic gold deposits of all ages share common characteristics such as ore mineralogy, fluid composition, deposit geometry and host geology (Kerrick & Cassidy, 1994; Groves *et al.*, 1998, 2003; Kerrich *et al.*, 2000; Ridley & Diamond, 2000). These features are summarised in Table 1.2.

1.3.1 Spatial distribution

The geodynamic setting for orogenic gold deposits was established by a landmark paper by Kerrich & Wyman (1990). These deposits have a common association with accretionary orogens or Cordilleran-style tectonic settings, where several allochthonous terranes are progressively accreted to a continental margin along major ‘docking’ faults. The absence of large gold deposits from collisional orogens (e.g. Himalayan and Alpine belts) is likely due to higher rates of uplift and erosion (lower preservation potential), and smaller, shallower and less connected structural networks compared to the deep-seated plumbing systems that develop in terrane boundaries of transpressive orogens (Kerrick *et al.*, 2000). Archaean and Palaeoproterozoic deposits are situated in large equidimensional cratons (~1000-1500 km diameter) while Phanerozoic examples exist within elongate metamorphic belts attached to the margins of these cratons or older Phanerozoic belts (Fig. 1.6). These differences in geological settings are attributed to the different tectonic regimes that may have occurred in the past, from possible mantle plume-related tectonics in the Archaean to modern cyclic tectonics during the Phanerozoic (Groves *et al.*, 2005a, b).

Table 1.2. General characteristics of Precambrian and Phanerozoic orogenic gold deposits (data summarised from Groves *et al.*, 2000; Ridley & Diamond, 2000; Goldfarb *et al.*, 2005; Duuring *et al.*, 2007).

Characteristics	Descriptions
Geological Setting	Mainly associated with accretionary orogens where several allochthonous terranes are progressively accreted to a continental margin along major 'docking' faults (Cordilleran-style tectonics). Limited appearance in collisional orogens.
Host geology: - rock type - metamorphic grade	Extremely variable- Archaean deposits tend to be in volcanic or intrusive rocks, while Phanerozoic deposits are mainly sedimentary-hosted. Majority of deposits are found in greenschist facies rocks, however, some significant Archaean deposits occur in higher-grade terranes extending into amphibolite to granulite facies.
Emplacement conditions	Epizonal (<6km, 150-300°C); mesozonal (6-12km, 300-475°C); hypozonal (>12km, >475°C).
Geometry and mineralogy of deposits: - structural setting - mineralisation styles - wall-rock alteration - ore mineralogy	Shear-hosted, usually situated within 2 nd or higher order splays off major terrane-bounding faults. Deposits are usually emplaced near the brittle-ductile transition showing a range of brecciation and ductile shearing textures. Many deposits are vein-hosted but breccia and disseminated-hosted deposits also occur. Addition of significant amounts of CO ₂ , S, K, H ₂ O, SiO ₂ ± Na + LILE. Quartz dominant vein systems with up to 10 % sulphide minerals (mainly Fe & As-bearing) and ≤ 3-15% carbonate minerals. Pyrite is generally the most dominant sulphide phase in intrusive or volcanic terranes, while arsenopyrite is dominant in sedimentary-hosted deposits. Base metal concentrations are extremely low, with minor amounts of Ag, As, Cu, Te, W, and Sb.
Timing of mineralisation	Occur in the late stages of orogenesis, mainly during D ₃ -D ₄ of a D ₁ -D ₄ deformation sequence, with most deposits post-dating peak metamorphism (up to 10-20 m.y.).
Ore fluid composition	Typically low-moderate salinity (<10 wt% NaCl equiv), reduced, near neutral to slightly alkaline, mixed H ₂ O-CO ₂ (5 to 50 mol % CO ₂) fluid. Minor amounts of CH ₄ and N ₂ , especially in sediment-hosted deposits.

Fig. 1.6. Map showing the relationship between the distribution of crust of a given age and the location of significant orogenic gold deposits (Goldfarb *et al.*, 2001a).

1.3.2 Temporal distribution

Orogenic gold deposits also have a heterogeneous temporal distribution. Orogenic gold formation has a strong correlation with major peaks in crustal growth (Fig. 1.7) and record secular changes in global tectonic processes through time (Groves *et al.*, 2005a, b). Two major Precambrian peaks exist: one during the Late Archaean between 2800-2550Ma, associated with the configuration of Kenorland; and the other during the Palaeoproterozoic between 2100-1800 Ma, related to the formation of the Birimian crust in West Africa (host to the Loulo deposits) and related South American terranes (Goldfarb *et al.*, 2001a, b). These periods in crustal growth are presumed to be associated with plume influenced mantle overturn events (Davies, 1995). A continuous genesis from 600-50 Ma correlates to the widely accepted secular decrease in global heat flow to a more continuous crustal growth of modern tectonics during the Phanerozoic (Groves *et al.*, 2005a).

Fig. 1.7. Timing of orogenic gold mineralisation vs. periods of crustal growth. **A)** Shows the temporal distribution of major orogenic gold deposits. **B)** Shows periods of crustal growth from Condie (2000). Note the clear positive relationship between crustal growth and orogenic gold formation. Figure from Groves *et al.* (2005a).

The temporal distribution of orogenic gold deposits is largely agreed to be the result of the preservational characteristics of the host terrane (e.g. Kesler & Wilkinson, 2006; Groves *et al.*, 2005b). Late Archaean and Palaeoproterozoic deposits were preserved in the centre of buoyant equidimensional cratons. During the onset of modern tectonics in the Meso-and-Neoproterozoic, continental crust became denser (Poudjom Djomani *et al.*, 2001) and more prone to uplift and erosion, with many orogens now eroded down to higher metamorphic roots, explaining the distinct absence of gold deposits from 1800-600 Ma (Kerrich *et al.*, 2000; Goldfarb *et al.*, 2001a; Groves *et al.*, 2003, 2005a). The presence of gold deposits between 600-50 Ma implies that 600 Ma is an approximate threshold for preservation, or lack of complete erosion, of a deposit in modern-style

orogenic belts (Groves *et al.*, 2005a). The high abundance of Phanerozoic placer deposits in collisional belts is strong evidence for the continuous erosion of orogenic deposits. The complete absence of deposits in the last 50 Ma suggests this is a minimum period to uplift and expose a productive province (Goldfarb *et al.*, 2001a).

1.3.3 Fluid source(s)

Despite the economic importance of orogenic gold, the origin of the gold transporting fluids remains unclear (Ridley & Diamond, 2000; Groves *et al.*, 2003). The release of low-salinity CO₂-H₂O metamorphic fluids during greenschist facies regional metamorphism is the generally accepted model (e.g. Koons & Craw, 1991; Powell *et al.*, 1991; Stüwe *et al.*, 1993; Jamison *et al.*, 1998; Pettke *et al.*, 2000; Pitcairn *et al.*, 2006), although exsolution of fluids from granitic magmas has also been suggested to be a potential fluid source (e.g. Campbell & Hill, 1988; Burrow & Spooner, 1989; Spooner, 1993; de Ronde *et al.*, 2000). The origin of orogenic gold-bearing fluids is examined in detail in *chapter 8*, where it is shown that petrographic, fluid inclusion and isotopic work at Loulo can contribute significantly to the metamorphic vs. magmatic fluid source debate.

1.4 Project outline

1.4.1 Project background

The Birimian terranes of West Africa are highly endowed in gold and represent the richest orogenic gold province in Africa (Cameron, 2006), with deposits comparable in size to the well-known gold districts in Canada and Western Australia. Ghana is well known for its large Birimian aged orogenic and palaeoplacer gold deposits (e.g. Schmidt Mumm *et al.*, 1997; Pigois *et al.*, 2003; Tunks *et al.*, 2004; Willie & Klemd, 2004; Feybesse *et al.*, 2006). However, other parts of the Birimian crust are also gold enriched, including the West Mali Gold Belt (*section 1.1.2*). A detailed review of Birimian gold mineralisation is included in *chapter 2 (section 2.6.1.2)*. Although gold production is thought to date back over 2,500 years, the Birimian of West Mali is largely under-explored in terms of commercial mining and thus this gold province has considerable potential for future exploration. Whilst an abundance of detailed literature exists on orogenic gold deposits from other parts of the globe, documentation of the geology and genesis of Birimian gold deposits is lacking outside Ghana. Given the absence of detailed studies in Mali, and in particular in the Loulo district, Randgold Resources initiated and sponsored a geological research project aimed at understanding the fluid evolution of the Loulo hydrothermal system.

1.4.2 *Principal objectives*

The main aim of this research project is to develop an ore genetic model for the Loulo gold deposits, based on analysis of the lithological, petrogenetic and fluid controls of mineralisation. The main objectives are:

1. to determine the mineralogical characteristics of mineralisation and alteration, and to establish paragenetic sequences for individual orebodies;
2. to develop a comprehensive dataset of fluid chemistries and PVT properties to model the various hydrothermal mineralising fluids.
3. to constrain the potential source(s) of fluid and ore-related components;
4. to understand the controls on fluid migration, subsequent alteration and mineralisation;
and
5. to use these data to develop local and regional exploration strategies.

In summary, this study is designed to characterise the geology of the Loulo area, to determine the paragenesis and evolution of the orebodies, and to constrain the origin and nature of the various mineralising fluids. In a wider context, the distinct features of some of the Loulo orebodies may have important implications for the understanding of orogenic gold deposits, such as the potential fluid source(s) for this deposit type. Furthermore, data collected in this study will increase the knowledge and understanding of Birimian gold mineralisation.

1.4.3 *Approach and methodology*

Fieldwork consisted of two field seasons spent on site at Loulo. Due to intense laterisation of the region, field exposure is very poor in the Loulo district and most of the work was carried out logging extensive diamond drill core. Limited work was undertaken underground because mining at Yalea was only in its infancy during the field visits. The first field season (Jan-Mar 2007) included an introduction to the Loulo geology. This involved visiting the major deposits as well as the prospective targets within the permit. A preliminary sample suite of host rocks, altered rocks and mineralised zones were collected from the Gara and Yalea deposits. Subsequent laboratory work employed transmitted and reflected light microscopy, and electron microprobe analysis, to determine mineralogical and textural characteristics of the samples. The second field season (Jan-Mar 2008) involved more detailed logging of new drill core from the main deposits, as well as investigating the satellite deposits and other prospects. Representative samples were collected for geochemical, mineralogical and textural analysis, as well as for fluid inclusion and isotope work.

Sampling within the Loulo district was designed to provide a wide spatial coverage of gold mineralisation within the district and at individual deposits. Ten different orebodies are investigated in this study from across the permit. At the main deposits (Gara and Yalea),

representative samples were collected from all parts of the orebody (at least 15 different drill cores from each deposit), as well as from surrounding barren zones for comparison. The overall sample suite included over 300 samples collected from drill core, accompanied by approximately 40 samples from field outcrop.

1.5 Layout of thesis

- *Chapter 2* provides a comprehensive literature review on the Birimian, summarising the regional setting, the geology and tectonic evolution of the Birimian crust. Birimian metallogenesis is also discussed with particular reference to orogenic gold mineralisation.
- The geology of the Loulo area is discussed in *chapter 3*. The regional geology of the Kédougou-Kéniéba inlier (the host terrane of the Loulo gold deposits) is briefly summarised and the structural setting for gold mineralisation at Loulo is outlined. The stratigraphy of the Loulo district is also described. Detailed petrographic descriptions of the various lithologies and geochemical analysis of the rock types are presented to understand the evolution of the local geology.
- *Chapter 4* documents the mineralisation characteristics of the Loulo orogenic gold deposits, highlighting the various styles of mineralisation, ore mineralogy and paragenesis, using a combination of field observations, standard optical microscopy studies and detailed scanning electron microscope analysis. A comparative mineralogical model for the Loulo district is also proposed.
- *Chapter 5* outlines the mineralogical and geochemical characteristics of hydrothermal alteration at Loulo, concentrating on the Gara and Yalea deposits.
- *Chapter 6* documents the petrographic, microthermometric, laser Raman and electron microprobe properties of fluid inclusions from the Loulo deposits. These data are used to distinguish the nature and source of the fluid and metal components; to give estimates on P-T-X conditions at the time of ore deposition; and to provide information on metal transport and depositional mechanisms.
- Oxygen, carbon and sulphur isotope data are discussed in *chapter 7*. These data are used to provide information on the physiochemical conditions of the ore fluid; to determine the source(s) of the fluids; and to understand the role of wall-rock interactions.
- The data collected in *chapters 3 to 7* are used to develop an ore genetic model for the

Loulo mining district (*chapter 8*). Data collected at Loulo are also considered in a wider context including their implications for orogenic gold mineralisation and Birimian metallogenesis; in particular ways in which the new data may be used to guide future local and regional exploration strategies are outlined.

- *Chapter 9* summarises the main conclusions and topics for future research.

CHAPTER 2: THE BIRIMIAN OF WEST AFRICA- A REVIEW

The Loulo mining district is situated in Palaeoproterozoic (Birimian) rocks of the West African Craton. This chapter represents a comprehensive literature review on the Birimian summarising the regional setting of the West African Craton, the geology of the Birimian terranes and the tectonic evolution of the Birimian crust. Lastly, Birimian metallogenesis is discussed with particular reference to orogenic gold mineralisation.

2.1 Regional setting of the West African Craton

The geology of Africa is complex and consists of numerous Archaean-Palaeoproterozoic cratons, Neoproterozoic Pan-African mobile belts and Phanerozoic cover sequences (Olsen, 2000; Cameron, 2006). The Precambrian crust of Africa is dominated by the Kaapvaal Craton, Congo, Tanzanian and West Africa cratons (Fig. 2.1). The West African Craton (WAC) forms an extensive portion of Precambrian crust covering ~4,500,000 km² (Rocci *et al.*, 1991), with an estimated lithospheric thickness of 240 km (Attoh & Ekwueme, 1997; Priestley *et al.*, 2008).

Fig. 2.1. The distribution of African cratons and Pan-African orogenic belts: 1 Archaean-Palaeoproterozoic crystalline basement; 2 Meso- to Neoproterozoic epicontinental clastic sedimentary sequences; 3 Pan-African orogens; 4 Palaeozoic basins; 5 Post-Palaeozoic cover successions (Dallmeyer & Lécorché, 1991). *Note-* the Kalahari Craton is also referred to as the Kaapvaal Craton; and the Zaire Craton is now referred to as the Congo Craton.

The WAC consists of two major Archaean-Palaeoproterozoic shields (Fig. 2.2): the Reguibat Shield to the north and the extensive Leo-Man Shield to the south. The Reguibat Shield extends for approximately 1500 km in a SW-NE direction across Mauritania, Morocco and western Algeria. This shield has received far less attention than its southern counterpart as the Precambrian crust is largely situated beneath unconsolidated superficial sediments of the Sahara Desert. The Leo-Man Shield is approximately 2000 km wide E-W, covering Liberia, Guinea, Côte

d'Ivoire, southern Mali, Burkina Faso, SW Niger and western Ghana. The shield comprises a western Archaean domain (known as the Man domain or the Guinea Rise) and a central and eastern Palaeoproterozoic domain (referred to as the Baoulé-Mossi domain). These two domains are separated by the N-S trending sinistral Sassandra Shear Zone (Camil, 1984) and an Archaean-Palaeoproterozoic transition zone (e.g. Kouamelan *et al.*, 1997; Egal *et al.*, 2002). Palaeoproterozoic inliers outcrop to the NW of the Leo-Man Shield. The Kédougou-Kéniéba inlier (KKI) is situated along the Mali-Senegal border (host to the Loulo deposits) and the Kayes inlier is located further to the north in western Mali (Fig. 2.4).

Fig. 2.2. Geological setting of West Africa showing the position of the Leo-Man and Reguibat shields, and surrounding Pan-African orogenic belts (from Feybesse *et al.*, 2006; modified after Dallmeyer & Lécorché, 1991).

The WAC stabilised during the Neoproterozoic (ca. 1.7 to 1 Ga; Black & Liegeois, 1993). The craton underwent extensional deformation during the early parts of this period along its boundaries (e.g. Volta basin; Nédélec *et al.*, 2007) and within the central regions of the craton (formation of the huge sub-circular Taoudeni intracratonic basin; Brooner *et al.*, 1990). These covers sequences consist of a mixture of marine, continental and glacial Neoproterozoic to Devonian sediments that reach up to 8 km in thickness (Villeneuve & Cornée, 1994). The occurrence of Palaeoproterozoic inliers in the western parts of the Taoudeni basin suggests continuity of the Palaeoproterozoic basement underneath this sedimentary sequence.

2.1.1 Correlation to South America

Palaeoproterozoic rocks of the São Luis Craton (SLC), in French Guyana, represent a rifted remnant of the southern tip of the WAC (Onstott & Hargraves, 1981; Gibbs & Olszewski, 1982; Grau *et al.*, 1985; Klein & Moura, 2008). These rocks contain the same lithological, tectonic and age (2240-2080 Ma) characteristics to Palaeoproterozoic rocks of the Baoulé-Mossi domain (Klein & Moura, 2001; 2008; Moura *et al.*, 2003; Klein *et al.*, 2005a; 2009). Palaeogeographic reconstructions based on these studies consistently put the SLC opposite the present-day coastline of Ghana and Togo (Cohen & Gibbs, 1989; Nomade *et al.*, 2001).

2.1.2 Pan-African orogenic belts

The WAC is totally surrounded by Pan-African mobile belts that represent a succession of collisional and accretion events that took place during the late Neoproterozoic (ca. 500-700 Ma) (Caby, 2003). The eastern margin of the craton is bounded by the Trans-Saharan mobile zone, which includes the Pharausian, Gourma (also referred to as Hoggar-Iforas belt), and Dahomeyide orogens (Black *et al.*, 1979, 1994; Attoh & Nudé, 2008) (Fig. 2.2). This suture zone is interpreted to represent oceanic closure at around 600 Ma between the WAC and the Tuareg-Nigeria platform (Hoggar and Benin-Niger shields; Black *et al.*, 1979). The Trans-Saharan mobile zone can be correlated over to South America with collision between the SLC and the São Francisco Craton from 500-650 Ma (Castellana & Long, 1998). The western margin of the WAC is a complex polyphase mobile zone, which can be traced from Liberia to Morocco. This zone consists of the Rockelide and Bassaride Neoproterozoic belts and the Hercynian Mauritanide belt (Villeneuve, 2008; Caby & Kienast, 2009) (Fig. 2.2). The southern tip of the WAC is bounded by the Gurupi belt (750-550 Ma), which separates the SLC from the Amazonian Craton. These Pan-African belts represent a branched system of orogens related to the formation of West Gondwana supercontinent (Klein & Moura, 2008) (Fig. 2.3).

Fig. 2.3. Schematic reconstruction (not to scale) of the West Gondwana assembly (Klein & Moura, 2008).

2.2 Archaean domains

The Archaean domains on the western sides of the Reguibat and Leo-Man shields have received little attention and their relationships with the Palaeoproterozoic rocks to the east are debatable (Camil, 1984; Delor *et al.*, 1994; Kouamelan *et al.*, 1997; Egal *et al.*, 2002). The Man domain (or Guinea Rise) has been affected by at least two thermo-tectonic events: the Leonian (~3050 Ma) and the Liberian (~2800-2900 Ma), the latter being the most marked (Bessoles, 1977). Evidence for pre-Leonian (3.2-3.6 Ga) crust also exists (Kouamelan *et al.*, 1997; Thiéblemont *et al.*, 2001). In Sierra Leone, the Precambrian crust is composed primarily of disrupted greenstone belts, granitoid gneisses and migmatites, with metasediments and banded iron formations (BIF's) increasing further to the east in Liberia (Cameron, 2006). The Man domain is metamorphosed to a greenschist to amphibolite grade, increasing to granulite facies to the west (Foster & Piper, 1993). In western Côte d'Ivoire, a small Palaeoproterozoic outlier (Ity) exists near the margin of the Archaean crust (Fig. 2.4).

The Reguibat Shield further to the north shows more widespread evidence of pre-Leonian crust (e.g. Potrel *et al.*, 1996) and thus has been divided into two separate Mesoarchaeoan terranes (Key *et al.*, 2008): an eastern Choum-Rag el Aboid Terrane showing Leonian to pre-Leonian ages

between 3.5-3.45 Ga and 3.2-2.99 Ga; and a western Tasiast-Tijirit Terrane showing dominantly Liberian ages around 2900 Ma. The crust shows similar compositions to the Man domain and likely represents a larger Achaean craton stretching from Liberia to Morocco, which is overlain centrally by Neoproterozoic to Phanerozoic cover sequences.

2.3 Birimian geology

The Palaeoproterozoic crust (2050-2200 Ma) of the Leo-Man shield is composed of rocks of the Birimian Supergroup and Tarkwaian System (the latter discussed in *section 2.4*). The term “Birimian” comes from the type locality where these rocks were first described along the Birim River in Ghana (Kitson, 1928; Junner, 1940). Birimian terranes form narrow (15-40 km), linear to arcuate, mainly NE to NNE-trending, volcano-plutonic belts and wider (60-200 km) intervening sedimentary basins, intruded by various generations of granitoids (Leube *et al.*, 1990). These rocks resemble Archaean granite-greenstone terranes (Abouchami *et al.*, 1990; Milési *et al.*, 1992; Sylvester & Attoh, 1992; Attoh & Ekwueme, 1997), such as the Superior Province of the Canadian Shield (Card, 1990). The structure of the Birimian crust is illustrated in Fig. 2.4, showing the location of various volcanic belts and gold deposits mentioned throughout this chapter.

Birimian rocks were accreted and metamorphosed to at least a greenschist facies grade during the Eburnean orogeny at ~2.1 Ga (Bonhomme, 1962; Black, 1980). Although the regional greenschist mineral assemblages are generally considered as prograde (e.g. Mumin & Fleet, 1995; Kribek *et al.*, 2008), some studies suggest a retrograde greenschist overprint path. Peak metamorphic conditions of amphibolite grade have been recorded in Ghana, in the southern Ashanti belt (500-650°C and 5-6 kbar; John *et al.*, 1999), NW Sefwi belt (490-580 °C and 4-6 kbar; Galipp *et al.*, 2003), and the southern Kibi-Winneba belt (500-610 °C and 4.5-6 kbar; Klemd *et al.*, 2002); and in parts of the Côte d’Ivoire and Burkina Faso (600 °C and 5 kbar; Ledru *et al.*, 1994). Amphibolite-facies assemblages are also observed in the contact aureoles of the Birimian granitoids (e.g. Debat *et al.*, 2003).

The structure of the Birimian crust is best distinguished in Ghana (Fig. 2.5), where five linear volcano-plutonic belts and four intervening sedimentary basins have been identified (Leube *et al.*, 1990; Taylor *et al.*, 1992; Hirdes *et al.*, 1992; Oberthür *et al.*, 1998; Feybesse *et al.*, 2006). In the northern half of the Baoulé-Mossi domain, the continuity, spacing and parallelism of the volcano-plutonic belts are not as clearly developed and reflect the increase in uplift and erosion towards the north (Bossière *et al.*, 1996).

Three main subjects of debate exist concerning the Palaeoproterozoic rocks of the WAC: (1) the stratigraphic position of metasedimentary units in relation to the metavolcanic rocks; (2) the tectonic setting for the initiation of crustal formation; and (3) the geotectonic evolution of the Birimian crust. The various models put forward for these three subjects will be discussed in detail in the following sections.

Fig. 2.4. Schematic lithotectonic map of the Leo-Man Shield of the West African Craton, showing location of Birimian gold deposits. Due to scaling factors, Birimian belt-type granitoids and Tarkwaian sediments are not shown (map adapted from Feybesse & Milési, 1994).

Fig. 2.5. The geology of Birimian terranes in central and western Ghana. Birimian terranes are characterised by narrow NE-SW-trending volcano-plutonic belts separated by intervening sedimentary basins. Both basins and belts are intruded by several generations of granitoids, which increase in size towards the northwest. Dixcove-type granitoids = belt-type plutons, Cape Coast-type granitoids = basin-type plutons, Bongo = post-tectonic K-rich plutons (*see section 2.3.2*). Map also shows location of Ghanaian gold deposits (*see section 2.6.1.1*). A majority of deposits are located along the western margin of Ashanti belt, including the giant Obuasi and Prestea deposits. Map modified from Pigios *et al.* (2003).

2.3.1 Birimian volcano-plutonic belts and sedimentary basins

Volcano-plutonic belts make up approximately 10 to 20 vol. % of the upper Birimian crust, and are estimated to have an original thickness of 4 to 12 km before subsequent uplift and erosion (Sylvester & Attoh, 1992). The belts consist of a bimodal suite, largely dominated by a thick sequence of tholeiitic basalts (locally pillowed), as well as dolerites and gabbroic intrusive rocks, overlain by calc-alkaline andesitic and dactylic tuffs and flows, with subordinate rhyolites (Abouchami *et al.*, 1990). The volcanic units are also interlayered with immature clastic sediments and carbonates (volcano-sedimentary terranes). The Birimian sedimentary basins consist of a package of isoclinal folded marine wackes, argillites and chemical sediments (e.g. Mn-rich carbonates and cherts), interbedded with calc-alkaline volcanic rocks. Leube *et al.* (1990) established a sedimentary facies model for the Ghanaian Birimian basins. These authors recognised that volcanic/volcaniclastic, chemical sediments and wackes are situated along the transition with the volcano-plutonic belts, while argillites are observed within the central regions of the basins.

2.3.2 Birimian granitoids

The Birimian crust is composed of large volumes of granitoids (~70%). At least three generations of calc-alkaline granitoids have been distinguished (e.g. Leube *et al.*, 1990; Hirdes *et al.*, 1992; Taylor *et al.*, 1992; Oberthür *et al.*, 1998): (1) **belt-type**: numerous small-scale (10's of km's) pre-tectonic, Na-rich tonalite-trondhjemite-granodiorite (TTG) plutons; (2) **basin-type**: syn-tectonic to late-kinematic extensive batholiths (max. 100's of km's) that typically have a granodioritic-granitic composition; and (3) rare **K-rich post-tectonic** plutons, which have a clear intrusive relationship with Tarkwaian rocks (*see section 2.4*). In Ghana, these three generations of granitoids have been traditionally referred to as Dixcove, Cape Coast and Bongo granitoids, respectively (Junner, 1940; Kesse, 1985). The characteristics of the two main generations (basin- and belt-type granitoids) are summarised in Table 2.1.

Table 2.1. Characteristics of belt- and basin-type granitoids in Ghana (modified from Hirdes & Davis, 1998).

Belt-type granitoids	Basin-type granitoids
Small to medium-sized plutons (10s of km), restricted to Birimian volcano-plutonic belts	Large batholiths (max 100s of km) generally restricted to basin sediments
Contact aureoles less than a few tens of metres	Extensive contact aureoles
Mafic component dominated by hornblende	Mafic component dominated by biotite
Metaluminous	Peraluminous
Typically dioritic to granodioritic in composition	Typically granodioritic-granitic in composition
$\text{Na}_2\text{O}, \text{CaO}_{\text{belt}} > \text{Na}_2\text{O}, \text{CaO}_{\text{basin}}$	$\text{Rb}, \text{K}_2\text{O}_{\text{basin}} > \text{Rb}, \text{K}_2\text{O}_{\text{belt}}$
Similar geochemical characteristics to tholeiitic basalts in belts for some elements	No evidence for geochemical similarity to tholeiitic basalts in the belts

Note- these characteristics can be used to describe belt- and basin-type granitoids in other areas of the Baoulé-Mossi domain and related inliers.

2.3.3 Birimian lithostratigraphic succession

The lithostratigraphic position of the Birimian metasediments and metavolcanic units has long been debated across the whole Baoulé-Mossi domain (summarised in Pouclet *et al.*, 2006). In Ghana, anglophone geologists such as Junner (1935, 1940) divided the successions into a lower Birimian (B1) unit dominated by sedimentary rocks and an upper Birimian (B2) unit composed mainly of volcanic rocks. Francophone geologists opted for a reverse stratigraphy, maintaining the sediments are younger than the volcanic rocks (e.g. Papon, 1973). A third model established by Leube *et al.* (1990) suggested the sediments and volcanic rocks formed quasi-contemporaneously as lateral facies equivalents.

The controversy concerning the lithostratigraphic position of the Birimian sedimentary basins and volcano-plutonic belts can be explained by a combination of factors. In many cases, the belt-basin contact is fault-bounded and thus the two neighbouring rock formations may not have

been adjacent to each other at time of formation. In addition, the confusion in identifying the correct stages of volcanism and sedimentation may also play apart, with the sedimentary basin sequences containing layers of calc-alkaline volcanic rocks and the volcano-plutonic belts interbedded with occasional sediments (Pouclet *et al.*, 2006). Furthermore, the disruption by granitoid emplacement and an increase in the rate of erosion of the Birimian sequences in the northern regions of the Leo-Man Shield enhances the difficulty in understanding the original lithostratigraphic succession. However, it is now generally agreed the sedimentary basins are younger than the volcano-plutonic belts (Hirdes *et al.*, 1996; Pouclet *et al.*, 1996). Geochronological data on the various rock types in Ghana and other parts of the Baoulé-Mossi domain indicate the sediment deposition ages are younger than the volcano-plutonic belts (Hirdes *et al.*, 1992; Davis *et al.*, 1994; Oberthür *et al.*, 1998). Furthermore, provenance modelling using isotopic and geochemical data clearly shows that the sediments were mostly derived from the volcanic belts (Taylor *et al.*, 1992; Asiedu *et al.*, 2004; Roddaz *et al.*, 2007).

2.4 Tarkwaian geology

A subordinate group of sediments, known as the Tarkwaian System, unconformably overlie the Birimian volcano-plutonic belts in Ghana, Burkina Faso and Côte d'Ivoire. The Tarkwaian System was initially defined in the Tarkwa gold mine in the Ashanti belt, Ghana, and the lithological succession is shown in Fig. 2.6. Tarkwaian rocks consist of a clastic sequence of conglomerates, sandstones and minor argillites, metamorphosed to a greenschist facies grade during the Eburnean orogeny (Davis *et al.*, 1994). They are thought to represent erosional products of the volcano-plutonic belts that were deposited in narrow intramontane grabens during local rifting, preferentially in the central regions of the belts (Leube *et al.*, 1990). Sestini (1973) described these sediments as alluvial fan deposits deposited during crustal uplift (molasse deposits). In Burkina Faso, Tarkwaian sediments also contain acid pyroclastics suggesting that Birimian volcanic activity was at least partly coeval with Tarkwaian sedimentation (Bossière *et al.*, 1996).

Fig. 2.6. Schematic lithostratigraphic column for Birimian and Tarkwaian rocks in Ghana. The Birimian crust is composed of an early generation of volcanism and belt magmatism, overlain by basin sediments and basin-type granitoids. The Tarkwaian System unconformably overlies the Birimian volcanic-plutonic belts. The Tarkwaian is composed of four rock formations: a basal Kawere Group; the Blanket Series, host to significant gold paleoplacer deposits (*see section 2.6.1.1*); and upper units known as the Tarkwa Phyllite and Huni Sandstone. Geochronological data are mainly from zircon dating, excluding tholeiite lava date of 2166 ± 66 Ma (Rb/Sr whole rock method). Figure modified from Pigois *et al.* (2003).

2.5 Birimian crustal evolution

2.5.1 Introduction

The formation of the WAC represents one of the largest crustal formation events in the history of Africa (Olson, 2000). Available geochronological data (Fig. 2.7) shows the Birimian represents a juvenile crustal formation event that mainly took place between 2050-2200 Ma, with little or no Archaean inheritance. The only recorded evidence of an Archaean input to the Birimian crust is from the Winneba basin-type granitoid in SE Ghana, on the margin of the craton, with Sm/Nd whole rock ages of ~ 2600 Ma (Taylor *et al.*, 1992). Taking into account Palaeoproterozoic rocks of the SLC, Boher *et al.* (1992) suggests the minimum crustal growth rate for the Birimian was $1.6 \text{ km}^3/\text{yr}$, which is approximately 60% higher than the Phanerozoic growth rate estimated by Reyner & Schubert (1984).

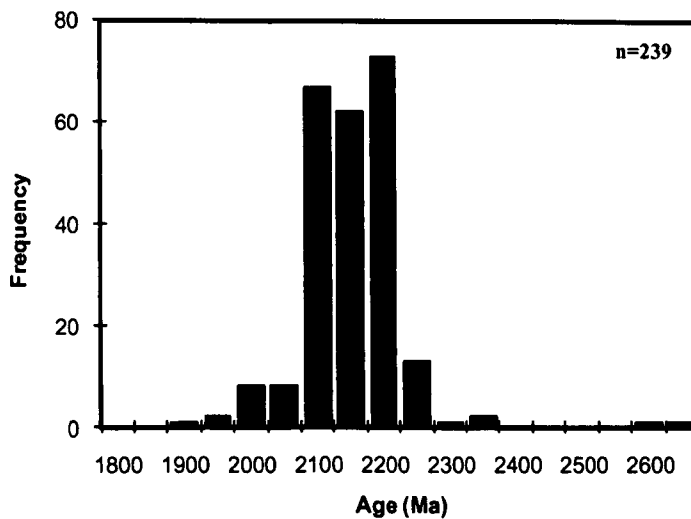


Fig. 2.7. Histogram summarising the geochronology data collected in the past few decades on Palaeoproterozoic rocks of the WAC. The graph shows a majority of rocks were formed between 2050-2200 Ma. See text for references.

In agreement with geochronological data, isotopic studies show limited inheritance from earlier Proterozoic or Archaean material. Granitoids and volcanic rocks from across the Baoulé-Mossi domain show juvenile features, such as low initial Sr isotopic compositions (0.700-0.702 ‰), positive ϵ_{Nd} values (+1.2 to +4.3‰), and short crustal residence ages less than 200 m.y. (Abouchami *et al.*, 1990; Boher *et al.*, 1990; Doumbia *et al.*, 1998; Pawlig *et al.*, 2006). Radiogenic isotopic studies on a variety of mineral deposits also indicate a short pre-mineralisation crustal history (Marcoux & Milési, 1993). Most researchers agree that the Birimian crust grew in at least five stages as shown in Table 2.2.

Table 2.2. Crustal growth model for Birimian rocks of the WAC (Feybesse *et al.*, 2006).

Birimian events		Description
Magmatic accretion	Stage 1	Eruption and emplacement of tholeiitic, dominantly mafic, volcano-plutonic belts.
	Stage 2	The creation of the first segments of Palaeoproterozoic continental crust with the emplacement of small, pre-orogenic, Na-rich, calc-alkaline, TTG plutons (belt-type).
Basin opening	Stage 3	The deposition of Birimian basin sediments through the erosion of rocks formed during stages 1-2.
Eburnean orogeny	Stage 4	Crustal shortening and emplacement of major syn-tectonic to late-kinematic peraluminous granitoids (basin-type), as well as the deposition of Tarkwaian molasse sediments.
Post-orogenic magmatism	Stage 5	Minor, K-rich, granitoid stocks.

2.5.2 Magmatic accretion and basin opening (stages 1-3)

2.5.2.1 Tectonic setting

The tectonic setting for Birimian volcanism and pre-orogenic magmatism is a debated subject. Many authors envisage the role of subduction processes, either as a result of plume-related tectonics (Abouchami *et al.*, 1990; Boher *et al.*, 1992) or volcanic-arc tectonics (e.g. Sylvester & Attoh, 1992; Beziat *et al.*, 2000). Other authors believe the initiation of Birimian crustal growth grew in extensional settings, such as an intracontinental rift (e.g. Leube *et al.*, 1990) or back-arc basin setting (e.g. Vidal & Alric, 1994).

2.5.2.1.1 Oceanic Plateau model

Abouchami *et al.* (1990) proposed that the initiation of Birimian crustal growth started in a within-plate environment, based on geochemical studies carried out on tholeiitic lavas from across the whole WAC. Trace element patterns show Nb enrichment with low Ce/Nb ratios, which are the opposite of island arc basalt (IAB) where Nb depletion is usually present (Pearce *et al.*, 1984). Strong isotopic heterogeneities (ϵ_{Nd} ranging from +1.2 to +4.3 ‰) are inconsistent with a mid-ocean ridge basalt (MORB) mantle source. The depletion in Ti and the slightly depleted light rare earth element (LREE) patterns are suggested by these authors to have close similarities to oceanic flood basalts found in modern oceanic plateau settings, such as the Nauru basin in the Pacific (e.g. Castillo *et al.*, 1986). A geochemical study by Boher *et al.* (1992) showed that belt-type granitoids have similar ϵ_{Nd} values to tholeiite lava's in the same area, implying that mafic and felsic magmas came from the same mantle protolith. Abouchami *et al.* (1990) and Boher *et al.* (1992) suggested the Birimian volcanic-plutonic belts formed as a result of a mantle plume event that produced extensive oceanic plateaus (Fig. 2.8). The presence of komatiite lavas in Ghana (Leube *et al.*, 1990) further supports such a model.

Fig. 2.8. Abouchami *et al.* (1990) oceanic plateau growth model for the Birimian crust. The crust grew in the following steps: (1) plume-related tholeiites are emplaced in an oceanic realm to form thick piles of oceanic plateaus; (2) overloading of plateaus or collision with micro-continental fragments cause plateaus to sink with subduction processes triggering melting and the emplacement of calc-alkaline belt-type granitoids; (3) the final stage involves the collision of the plateaus with an Archaean continental nucleus.

2.5.2.1.2 *Island-arc model*

In contrast to the work of Abouchami *et al.* (1990) and Boher *et al.* (1992), the majority of the geochemical studies carried out on the Birimian crust indicate a volcanic-arc setting. They include data collected from volcanic and granitic rocks from Ghana (Sylvester & Attoh, 1992; Dampare *et al.*, 2008); Burkina Faso (Beziat *et al.*, 2000); Guinea (Lahondere *et al.*, 2002; Egal *et al.*, 2002); the Kédougou-Kéniéba inlier (KKI) (Dia *et al.*, 1997; Pawlig *et al.*, 2006; Dioh *et al.*, 2006); and the São Luis Craton (SLC) (Klein *et al.*, 2005a; 2009). Trace-element and REE patterns show typical features of arc magmatism (Pearce *et al.*, 1984): (1) LREE enriched patterns; (2) strong enrichment in the large-ion lithophile elements (LILE; Rb, Ba, Th) relative to high field strength elements (HFSE; Nb ± Ta); and (3) high Ce/Nb and Th/Nb ratios. The dominant tholeiitic affinity of the Birimian rocks is a typical feature of Archaean arc magmatism (incompatible element poor mantle sources), compared to most Proterozoic and Palaeozoic arc basalts, which are characterised by calc-alkaline magmatism (incompatible element rich mantle sources) (Condie, 1989). Furthermore, several investigations have suggested the ultramafic components of the volcanic-plutonic belts may represent fragments of the subducted oceanic crust (ophiolite complex) (Attoh *et al.*, 2006; Pouclet *et al.*, 2006).

The large extension of the Baoulé-Mossi domain means it's not unreasonable to expect variability in tectonic settings (Hirdes *et al.*, 1996; Beziat *et al.*, 2000; Galipp *et al.*, 2003). The heterogeneous nature of the Birimian crust is not unique. Modern examples where arc and plateaus have accreted onto each other occur in the Solomon arc, along the southern margin of the Ontong-Java Plateau (Tejada *et al.*, 1996), and numerous arcs on the Caribbean Plateau (White *et al.*, 1999).

2.5.2.1.3 *Extensional models*

An intracontinental rift setting for the Birimian volcanic rocks has been proposed by several workers (e.g. Junner, 1940; Kesse, 1985; Milési *et al.*, 1989b; Leube *et al.*, 1990; Alric, 1990) to explain the apparent lack of evidence for subduction zones. Alternatively, Vidal & Alric (1994) suggested a transtensional back-arc setting for volcanic rocks in the Haute-Comoé region of Côte d'Ivoire, based on geochemical signatures showing both IAB and MORB characteristics. However, extensional models for the Birimian have been heavily criticised by many authors (e.g. Sylvester & Attoh, 1992; Beziat *et al.*, 2000). Firstly, there is no evidence of voluminous continental material older than the Birimian terranes. Secondly, alkaline mafic and felsic volcanism are voluminous in continental-rift settings but are largely absent in Birimian volcanic rocks (Sylvester & Attoh, 1992).

2.5.2.2 Subprovince model

The initiation of Birimian crustal growth (stages 1-3) occurred between 2050-2200 Ma. Hirdes *et al.* (1996) and Hirdes & Davis (2002) proposed that the volcanic belts and detrital sediments show a progressive westward younging across the Baoulé-Mossi domain. These authors divided the Birimian domain into an older eastern subprovince (2150-2200 Ma) and a younger western subprovince (2050-2120 Ma) (Fig. 2.9). The eastern subprovince covers Ghana, SW Niger, Burkina Faso and eastern Côte d'Ivoire, while the western subprovince extends over central Côte d'Ivoire, eastern Guinea, southern Mali and the KKI. Hirdes *et al.* (1996) suggested that the boundary between these Birimian subprovinces occurs along the Ouango Fitini shear zone, a sinistral NNE-trending high strain zone situated in central Côte d'Ivoire.

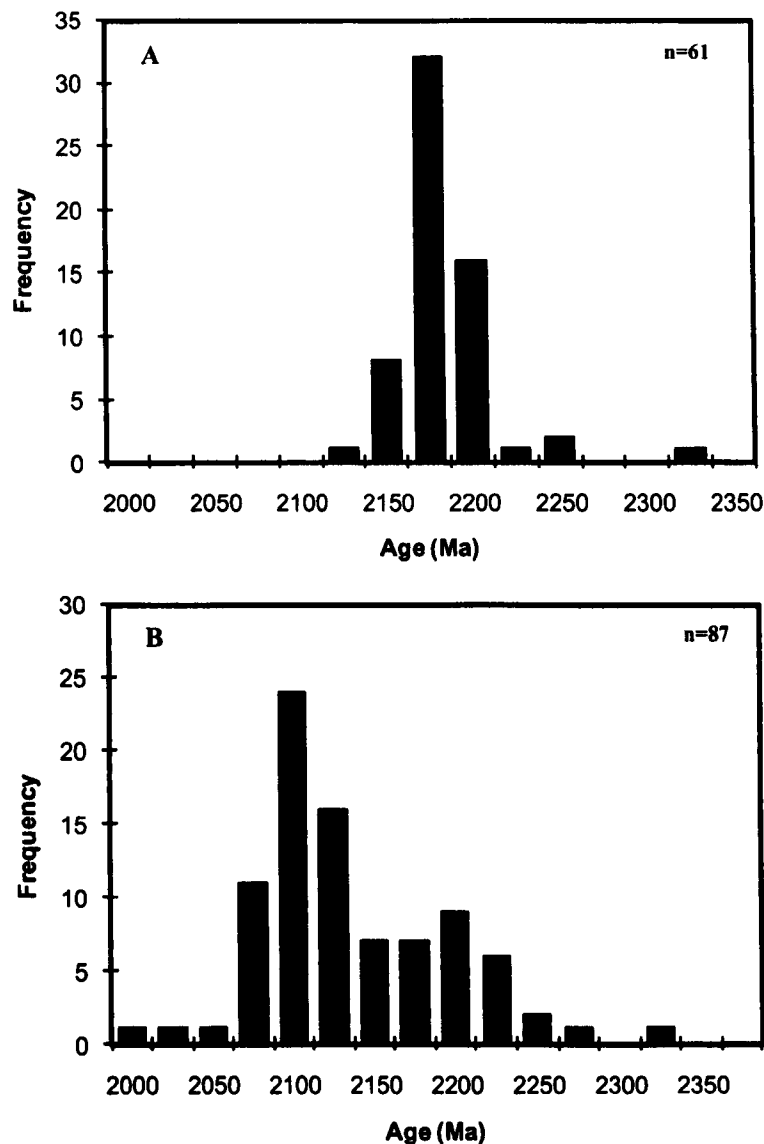


Fig. 2.9. Histograms showing the growth of the Birimian crust during stages 1-3 of crustal evolution, based on reliable geochronological data (mainly U/Pb or Pb/Pb dates). **A) Eastern subprovince-**clustering between 2175-2225 Ma. Note ~2600 Ma ages recorded from the Winneba granitoid are not shown (see Fig. 2.7). **B) Western subprovince-**clustering between 2075-2125 Ma. Although Tarkwaian deposits formed during stage-4 of Birimian crustal growth, they are largely erosional products of rocks formed during stages 1-2 and so are included in the histograms. See Hirdes *et al.* (1996) and Hirdes & Davis (2002) (and references therein).

The subprovince model is scrutinised by the local appearance of early Birimian activity (2150-2200 Ma) and pre-Birimian ages (>2200 Ma) within the western subprovince (Dia, 1988; Lemoine, 1988; Hirdes *et al.*, 1996; Dia *et al.*, 1997; Lahondère *et al.*, 2002; Gasquet *et al.*, 2003; Pawlig *et al.*, 2006; Gueye *et al.*, 2007). Hirdes & Davis (2002) suggested a continuous or local substratum of 2150-2200 Ma old rocks may occur underneath the late Birimian volcano-plutonic belts. The appearance of pre-Birimian ages (2200-2312 Ma) found locally across the whole Baoulé-Mossi domain (Fig. 2.9) suggests that the formation of the Birimian crust may have started earlier than first thought, with major peaks in crustal development occurring later (Hirdes & Davis, 2002; Gasquet *et al.*, 2003). A summary of all the available geochronological data is presented in Table 2.3.

Table 2.3. Summary of Birimian geochronological data collected on various rock types across West Africa. See Hirdes *et al.* (1996), Hirdes & Davis (2002) and Gueye *et al.* (2008) (and references therein).

Rock type	Eastern subprovince				Western subprovince			
	Ghana	Burkina Faso	Niger	E.Côte d'Ivoire	C. Côte d'Ivoire	Guinea	S. Mali	KKI
Belt volcanism (stage 1)	2189 ± 1 to 2200 ± 4	2158-2238	-	2195 2195 ± 10	2104 ± 2 2105 ± 1	2093 ± 2 2212 ± 6	2098 ± 5	2063-2155 (2063-2099)
Belt-type granitoids (stage 2)	2137-2179	2122-2194 (2160-2194)	2135-2188	2150-2152	2092—2312 (2092-2123)	-	2074 +9/-8	2045-2254 (2045-2110)
Basin sediments (stage 3)	2134-2184	2120-2162	-	2141-2188	2100-2133	-	-	2093-2165
Tarkwaian sediments (stage 4)	2132-2245 (2132-2195)	2124-2171	-	-	-	-	-	-
Basin-type granitoids (stage 4)	2068-2115	2097-2109	2112-2118	2079-2110	2079-2109	2020-2096 (2072-2096)	-	2008-2079
Post-tectonic granitoids (stage 5)	1968 ± 49	1991 ± 12	-	-	-	-	-	1973 ± 33
Pre-Birimian ages	2245 ± 4 2300-2600	-	-	-	2208-2312	2212 ± 6	-	2205-2254

Note- the Birimian and Tarkwaian sediment data given here are detrital ages rather than depositional ages. Brackets refer to the modal age range.

2.5.3 Eburnean orogeny (stage 4)

Rocks formed during the early stages of Birimian crustal growth were deformed and metamorphosed during the Eburnean orogeny around 2.1 Ga (Black, 1980). During the orogeny, large volumes of new crust were added in the form of large peraluminous granitoids (basin-type). Crustal thickening and uplift also led to the deposition of the Tarkwaian molasse sediments within the volcano-plutonic belts.

2.5.3.1 Structural history

The Eburnean orogeny contains a polycyclic evolution with a collisional D₁ phase and later transcurrent phases (D₂-D₃ stage) (e.g. Milési *et al.*, 1992; Feybesse *et al.*, 2006). This change in tectonic style is common in other orogenic belts (e.g. Shackleton, 1986). The tectonic textures associated with each stage of the Eburnean orogeny in Ghana are summarised in Table 2.4. The D₁-D₃ structural history for the Ghanaian Birimian terranes is probably too simplistic for an orogenic event that occurred over a ~50 m.y. period. In other areas of the Birimian crust, slightly different structural histories are observed (e.g. Loulo; *section 3.2.2*) or more complex tectonics are suggested (e.g. Naba *et al.*, 2004; Hein *et al.*, 2004).

Table 2.4. Tectonic phases of the Eburnean orogeny in Ghana based on structural and geochronological evidence collected by Feybesse *et al.* (2006).

Stage	Tectonic style	Textures	Timing
D ₁	Collisional thrust tectonics	Complex array of collisional fractures including fold and thrust geometries. NE-trending S ₁ cleavage and F ₁ folding and development of thrust faults mainly along contacts between volcano-plutonic belt and sedimentary basin.	2130-2095 Ma
D ₂	Crustal shortening & sinistral strike-slip	Upright F ₂ folds with horizontal or slightly dipping hinges, and associated ENE-WSW-trending S ₂ cleavage. Earlier thrusts reactivated during ductile sinistral ductile movement.	2095-1980 Ma
D ₃	Crustal shortening & dextral strike-slip	Reverse movement and deformation at shallower crustal levels with the dominance of brittle dextral F ₃ folds with axes trending N-S to NNE-SSW and associated S ₃ cleavage in same direction.	

The collisional phase involved the accretion of the volcano-plutonic belts and sedimentary basins during the initial collision between Archaean and Palaeoproterozoic blocks. Leube & Hirdes (1986) indicated crustal shortening associated with the Eburnean orogeny decreased the spacing between the volcano-plutonic belts to less than one-third of their original separation. Supracrustal rocks underwent regional peak metamorphism (greenschist or amphibolite facies) during this stage. Metamorphism has been dated in Ghana, Burkina Faso, Niger and Côte d'Ivoire between 2092 ± 3 to 2107 ± 93 Ma by various dating methods, including U-Pb dating of titanite

(Oberthür *et al.*, 1998), Sm-Nd whole rock dating (Boher *et al.*, 1992), and K-Ar dating of hornblende and amphibole (Cheilletz *et al.*, 1994; Feybesse *et al.*, 2006). Timing of D_1 deformation in Ghana (2130-2095 Ma; Feybesse *et al.*, 2006) generally predates many of the rocks of the western subprovince suggesting the Eburnean orogeny affected these rocks at a latter date. Timing of D_1 deformation in southern Mali is dated at 2098 ± 5 Ma (Liegeois *et al.*, 1991), agreeing with a westerly progressing accretion event.

Later transcurrent movement lead to further crustal shortening and magmatism, which caused retrograde metamorphism of the syn- D_1 metamorphic paragenesis and reopening of the K-Ar system. This change in tectonic style from a collisional to a transcurrent regime had an important control on Birimian metallogenesis (discussed in section 2.6.4; Milési *et al.*, 1992; Feybesse *et al.*, 2006).

2.5.3.2 Tarkwaian sedimentation

Uplift during the Eburnean orogeny caused the volcano-plutonic belts to rise above sea level. Local rifting, preferentially in the central regions of the volcano-plutonic belts (Leube *et al.*, 1990), provided a basin for Tarkwaian molasse deposits to form. Geochronological data available for Tarkwaian sediments (Table 2.3; Fig. 2.10) agree with sedimentological evidence that these rocks are erosional products of the Birimian volcano-plutonic belts. Davis *et al.* (1994) established an age range for sedimentation within the Tarkwa basin in the Ashanti belt. Using the youngest detrital zircon age (2132 ± 3 Ma; Davis *et al.*, 1994; Pigois *et al.*, 2003) and the emplacement age of the Tarkwaian-hosted Bansa pluton (2097 ± 2 Ma; Oberthür *et al.*, 1998), Tarkwaian sedimentation took place between 2100-2130 Ma. This implies a D_1 -timing for the Tarkwaian System, as suggested by structural studies of Eisenlohr & Hirdes (1992), Hirdes *et al.* (1992), and Hirdes & Nunoo (1994).

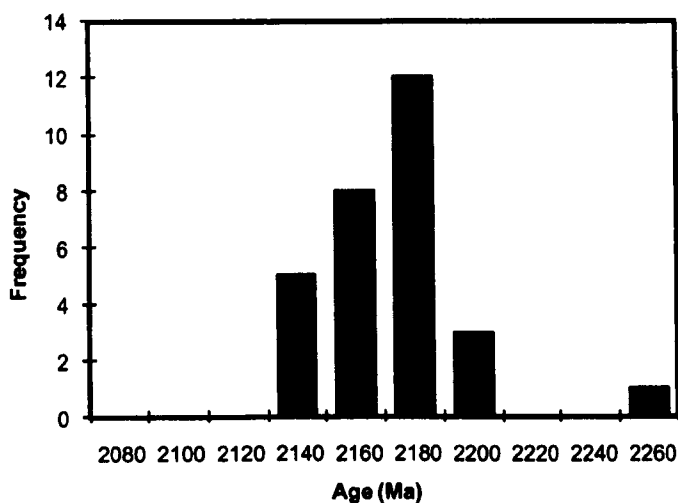


Fig. 2.10. Histogram showing the detrital zircon ages of Tarkwaian sediments from the Ashanti and Sefwi belts in Ghana, and from the Hounde belt in Burkina Faso (data from Davis *et al.*, 1994; Pigois *et al.*, 2003; Bossiere *et al.*, 1996). Detrital ages closely resemble the ages of underlying volcano-plutonic belts and belt-type granitoids. No Archaean inheritance is observed.

2.5.3.3 Emplacement of basin-type granitoids

The second generation of Birimian granitoids (basin-type) was emplaced throughout the Eburnean orogeny (Allibone *et al.*, 2002a; Feybesse *et al.*, 2006) and generally outlasted Tarkwaian sedimentation. Although these granitoids are predominately confined to the sedimentary basins, they also have also been observed intruding Tarkwaian rocks in the Ashanti belt (Banso pluton; Oberthür *et al.*, 1998). Similar to the metamorphic ages, basin-type granitoids show a SE-directed convergence across the Baoulé-Mossi domain, over a 50 m.y. period between 2070 to 2118 Ma (Table 2.3).

In the eastern subprovince, basin-type granitoids from Ghana, Niger and Burkina Faso are significantly younger than the first generation of granitoids (stage-2; ~70 m.y.) and volcano-plutonic rocks (stage 1; max. 130 m.y.) (Boher *et al.*, 1992; Taylor *et al.*, 1992; Davis *et al.*, 1994; Hirdes *et al.*, 1996; Oberthür *et al.*, 1998; Castaing *et al.*, 2003; and references therein). This indicates Birimian crustal growth took place over a maximum period of 200 m.y. in the eastern parts of the craton. However, Birimian rocks in the western parts of the Baoulé-Mossi domain formed over a much shorter time period (<50 m.y.). Basin-type plutons contain similar ages (e.g. KKI) or slightly younger ages (10-40 m.y.) than rocks of the neighbouring volcanic belts (Yao *et al.*, 1995; Hirdes *et al.*, 1996; Ndiaye *et al.*, 1997; Doumbia *et al.*, 1998; Hirdes & Davis, 2002; Gueye *et al.*, 2007; and references therein). This short crustal history for the western parts of the Birimian crust can be explained by the formation of rocks in a narrowing oceanic basin (rocks of the eastern subprovince were already accreting onto an Archaean continental mass). This argument could be scrutinised by the local appearance of pre-2150 Ma rocks in the western subprovince, but still suggests the main part of crustal development occurred over a short time period.

2.5.3.4 Tectonic model

The Eburnean orogeny represents a large ocean closure orogen (as described by Leahy *et al.*, 2005), where multiple arcs, oceanic plateaus and marine sediments progressively amalgamated onto a growing Archaean continental mass(s) over tens to millions of years. Closure of the oceanic basin is likely to have taken place between the Man Archaean craton, situated to the west of the Baoulé-Mossi domain (*section 2.2*) (e.g. Attoh & Ekwueme, 1997), and Archaean rocks of the SLC, placed to SE of Ghana (Feybesse *et al.*, 2006). Geochronological data for all stages of Birimian crustal growth imply a dominance of SE directed convergence (i.e. the majority of the Birimian terranes amalgamated onto the SLC). Remnants of this eastern contact zone can be seen in southern Ghana on the edge of the WAC: (1) the Winneba basin-type pluton contains the only Archaean inheritance in the Birimian crust (~2600 Ma; Taylor *et al.*, 1992); and (2) the possible discovery of late-Archaean to early Proterozoic banded iron formation (BIF) supracrustal rocks (Feybesse *et al.*, 2006).

There is also evidence that the western margin of the basin was active during the Birimian/Eburnean. The Kakadian batholith intruding the Mako volcanic belt in the KKI

(discussed in *section 3.1.1*) show some of the oldest emplacement ages in the Birimian crust (2079-2213 Ma). After oceanic closure, the western contact of the Birimian crust sheared against (Sassandra Fault; Camil, 1984) or subducted beneath the Man Archaean crust (Delor *et al.*, 1994; Feybesse & Milési, 1994; Kouamelan *et al.*, 1997; Egal *et al.*, 2002) during the time period of ~2070-2095 Ma.

2.5.4 Emplacement of post-tectonic granitoids (stage 5)

The termination of Birimian crustal formation is marked by the intrusion of minor, K-rich, post-tectonic granitoids. They are generally confined to the volcano-plutonic belts and intrude Tarkwaian sediments. They have been dated between 1910-1990 Ma in Ghana and Burkina Faso (Hirdes *et al.*, 1987; Chalokwu *et al.*, 1997).

2.6 Birimian metallogenesis

Birimian terranes are highly endowed with respects to gold and represent the richest orogenic gold province in Africa (Cameron, 2006), with deposits comparable in size to the well-known gold districts in Canada and Western Australia. In terms of other types of mineral deposit, the Birimian crust contains widespread manganese deposits, infrequent iron oxide deposits (e.g. the Falémé iron ore district), and extremely rare base metal deposits. In contrast, the Archaean domains of the WAC are highly deficient in gold and enriched with respects to bauxite and iron (mainly banded iron formations). Further comparisons between Birimian and Archaean mineralisation of the WAC, and the surrounding Pan-African terranes are not discussed here (*see* Milési *et al.*, 1992; Foster *et al.*, 2000; Cameron, 2006).

2.6.1 Gold mineralisation

Gold production has a long history in West Africa, thought to date back over 2,500 years (Pigois *et al.*, 2003). Two of the most productive and prospective gold regions are the Ashanti belt, in Ghana, and the West Mali Gold Belt in the KKI (host to the Loulo deposits). Gold districts also occur elsewhere in western Ghana, Côte d'Ivoire, Burkina Faso, SW Niger, southern Mali and eastern Senegal (Fig. 2.4). Based on host rock and ore mineralogy, Birimian orogenic gold deposits can be further divided into several different types (Table 2.5). As well orogenic gold, the Birimian crust is also host to modified palaeoplacers of the Tarkwaian System and reduced intrusion-related gold systems (RIRGS). A proposed classification scheme for Birimian gold mineralisation is summarised in Table 2.5. Size classification of gold deposits given in the following sections is based on ranges stated in Groves *et al.* (2003): supergiant deposits >75 Moz; giant deposits 9 to 75 Moz; world-class deposits 3 to 9 Moz; and sub-world-class deposits <3 Moz.

Table 2.5. A proposed classification scheme for Birimian and Tarkwaian gold mineralisation. Deposits consist of palaeoplacers (type 1), orogenic gold (types 2-5) and RIRGS (type 6).

Deposit type		Example(s)
Tarkwaian conglomerate-hosted palaeoplacers		Type 1 Tarkwa & Bippo Bin (Ghana).
Orogenic gold deposits	Ashanti-type shear-hosted deposits (volcanic-hosted). Quartz-sulphide mineralised veins (pyrite and/or arsenopyrite) and disseminated sulphide ore in vicinity to quartz veins.	Type 2 Obuasi, Prestea, Bogosu, Konongo & Akyem (Ashanti belt, Ghana); Bibiani (Sefwi belt, Ghana); Syama (S. Mali); Massawa (Senegal)
	Sediment-hosted shear deposits. Quartz + carbonate mineralised veins.	Type 3 Loulo (tourmaline-rich turbidites); Sadiola & Yatela (carbonates; Mali)
	Shear-hosted quartz vein deposits, with rare polymetallic sulphides (Pb, Cu, Zn) and sulphosalts (Cu, Ag).	Type 4 Larafella & Poura (Burkina Faso); Hire (Côte d'Ivoire); Kalena (Mali); Sabodala (Senegal)
	Granitoid-hosted deposits concordant with major faults and shear zones (post-date host intrusions).	Type 5 Ahafo, Ayanfuri, Nysiaso, Ayankeyerim & Chirano (Ghana)
Reduced intrusion-related gold systems (RIRGS)		Type 6 Morila (S. Mali)

Note- numerous deposits are difficult to classify (e.g. Lero & Sigui in Guinea; Diabatou, Guibaré and Fété Kolé deposits in Burkina Faso).

2.6.1.1 Ghana

Ghana (previously known as the Gold Coast) is the most gold productive region of West Africa and includes the world famous gold deposits along the Ashanti belt, such as Obuasi and Prestea. Numerous organisations are involved in the country, including AngloGold Ashanti, Gold Fields Ltd., Newmont, GoldenStar Resources and Mwana Africa. The well-studied Ghanaian terranes include numerous types of orogenic gold deposits and paleoplacers. Their locations are shown in Fig. 2.5.

Palaeoplacers (type 1)

Palaeoplacers of the Tarkwaian System are confined to Ghana (possibly just a function of exploration?). Gold exists in the matrix of quartz-pebble conglomerates of the Banket Series (Fig. 2.6). Six, fining upwards, conformable auriferous horizons exist within this sequence (Strogen, 1988). These horizons are locally known as the 'Banket Reefs' (Blenkinsop *et al.*, 1994), with the three richest horizons termed the Basal/Main Reef, the Middle Reef and the Breccia Reef. Heavy minerals including haematite, magnetite, rutile and zircon are associated with gold but are not necessary for gold appearance (Hirdes & Nunoo, 1994). The source of the Tarkwaian gold is controversial, and similar to that concerning the larger Archaean Witwatersrand quartz-pebble conglomerates (e.g. Kirk *et al.*, 2001; Frimmel *et al.*, 2002). Most workers believe the deposits to

be modified palaeoplacers (e.g. Sestini, 1973; Kesse, 1985; Klemd *et al.*, 1993), although an epigenetic-hydrothermal origin has also been suggested (e.g. Ledru *et al.*, 1988). The palaeoplacer model is preferred by many authors because of the close spatial association between gold and conglomerates, and the silver depleted nature of the gold (a typical characteristic for transported gold) (Klemd *et al.*, 1993).

A majority of deposits are situated in the Tarkwa basin, including Tarkwa (resource of 16.2 Moz at 1.4 g/t; Gold Fields Ltd, 2009) and smaller deposits including the Bippo Bin, Teberebi, Iduaprim and Damang deposits (the latter also host to lode mineralisation). Palaeoplacer gold is present in other volcanic belts in Ghana (e.g. the Bui belt), but has yet to be explored in any great detail.

Ashanti-style mineralisation (type 2)

Type 2 deposits are the most common and significant type of deposit in Ghana. They are hosted in Birimian volcanic rocks along the margins of the belts, and to a lesser extent, in Tarkwaian sediments (e.g. Damang). Ghanaian type 2 deposits can be subdivided into two dominant styles: (1) higher-grade quartz lodes (>10 g/t) associated with brittle fractures along controlling faults (e.g. Allibone *et al.*, 2002b); and (2) generally lower grades (2 to 10 g/t) associated with disseminated arsenopyrite and/or pyrite in graphitic mylonite fault rocks or relatively undeformed wall-rock (e.g. Oberthür *et al.*, 1994). The Ashanti-style deposits include the giant Obuasi (37.4 Moz resource at 5.1 g/t; AngloGold Ashanti Ltd, 2008) and Prestea (including Bosgou and Mampon) (~15 Moz resource at 3.1 g/t; Golden Star Resources Ltd, 2009) deposits, the world-class Akyem (7.6 Moz reserve; Newmont Mining Corp, 2009) and Damang deposits (4.3 Moz resource at 1.8 g/t; Gold Fields Ltd, 2009), plus smaller deposits such as Konongo (past production of 1.65 Moz at 11.8 g/t; Signature Metals Ltd, 2010).

Granitoid-hosted deposits (type 5)

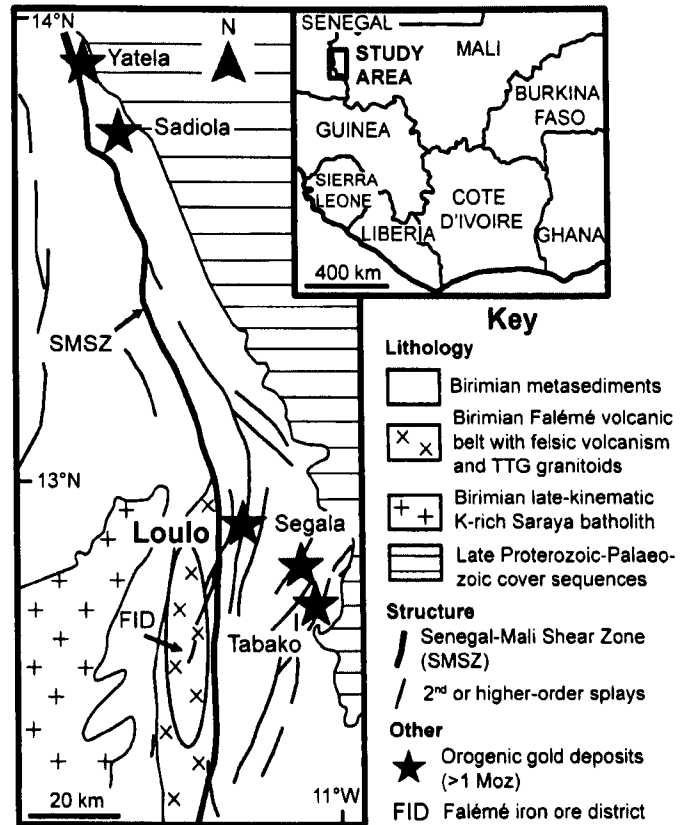
Gold deposits in Ghana are also hosted in Birimian basin- and belt-type granitoids. Mineralised granitoids occur as small, steeply dipping intrusive stocks, concordant with regional shear directions along belt-basin contacts or along shears away from these transition zones (Yao *et al.*, 2001). Gold mineralisation seems to be only spatially related with their host intrusions. Mineralisation postdates their hosts by 5-20 m.y. (Oberthür *et al.*, 1998; Yao & Robb, 1999). Mineralisation is similar to Ashanti-style deposits characterised by quartz-sulphide veins +/- stockworks, and disseminated ore in pervasive alteration halos, with the dominance of arsenopyrite and pyrite sulphides (Yao *et al.*, 2001). Examples include the giant Ahafo deposit (9.4 Moz reserve; Newmont Mining Corp, 2009) and the smaller Chirano mine (4.07 Moz resource; Redback Mining Inc, 2009).

2.6.1.2 Mali-Senegal

Malian gold mining is summarised in *section 1.1.2*, and thus this section only discusses the structural controls on mineralisation and the range of deposit types present. Birimian rocks outcrop in two large areas of Mali and Senegal: the KKI along the border between Mali and Senegal; and the Bougouni area in southern Mali, situated on the NW extremities of the Leo-Man Shield (Fig 2.4). Mineralisation in the KKI is controlled by two major shear zones. The West Mali Gold Belt is controlled by the regionally important Senegal-Mali Shear Zone (SMSZ; Fig. 2.11). This belt is the second leading gold productive region in West Africa (behind the Ashanti belt in Ghana), producing greater than 1 Moz annually (Merrex Gold Inc, 2009). The high gold endowment of the KKI is also outlined by targets in volcanic rocks in the Senegalese part of the inlier, controlled by the Main Transcurrent Shear Zone (MTZ), including the Sabodala (3.5 Moz resource; Mineral Deposits Ltd, 2009) and Massawa projects (3 Moz resource at 4.0 g/t; Randgold Resources, 2009). The geology of the KKI is discussed in *chapter 3*.

The Bougouni area (Mali South) contains the giant, complex Morila deposit. This deposit, situated in the Massigui (or Bougouni) greenstone belt, is unique in terms of Birimian mineralisation (type 6 deposit). Mcfarlane *et al.* (2008) established a genetic relationship between mineralisation and granodiorite-tonalite plutons and suggested Morila has similar characteristics to reduced intrusion-related gold systems (RIRGS) (e.g. Hart, 2007), with ore assemblages dominated by pyrrhotite and gold in association with As-Bi-Sb-Te and W. The second largest gold deposit in the region is the breccia-vein hosted Syama deposit, situated in altered mafic volcanics of the Senoufou greenstone belt, to the SE of Morila. The deposit has similar characteristics to Ashanti-style type 2 deposits (Olson *et al.*, 1992). The Kalana deposit situated in the Bale (or Kalana) volcano-plutonic belt, close to the Guinean border, is classified as a type 4 deposit, with a mineral paragenesis consisting of polymetallic (Pb, Cu, Zn) sulphides, cupro-argentiferous sulphosalts and accessory bismuth and matildite (Blagonadezhdin, 1975; Milési *et al.*, 1992). The small size of Kalana (~1 Moz; Holliday 2009) is typical of type 4 deposits (Milési *et al.*, 1992).

Fig. 2.11. Map of the West Mali Gold Belt, showing the Loulo study area. Orogenic gold deposits (type 3) are controlled by the regionally important Senegal-Mali Shear Zone, with a majority of the mineralisation confined to metasediments on the eastern side of the shear zone, within 2nd or higher order splays. On the western side of the shear, along the Falémé volcanic belt, a different style of mineralisation occurs, known as the Falémé iron ore deposits (FID) (discussed in section 2.6.2).



2.6.1.3 Burkina Faso

Past gold production in Burkina Faso is minimal compared to that of Ghana and Mali (Beziat *et al.*, 2008). The only significant mining operation that has occurred in the country was at the Poura mine, where 0.4 Moz of Au and 53,000 Oz of Ag were produced during the 1980's (Sanogo & Prost, 1993). However, with a major recent drive to promote minerals investment in the country, Burkina Faso could potentially be one of the most productive regions in West Africa for future exploration. Over \$100 million has been invested in the past few years in Burkina Faso on 130 prospecting licenses (Lepage, 2007), identifying numerous gold prospects (Fig. 2.4). Several projects are under development including Essakane (IAMGold/ Orezone); Youga (Etruscan); Taparko (High River Gold Mines); Kalsaka (Cluff Gold); and Belahouro (Volta Resource)

The various deposit types in Burkina Faso have been summarised by Beziat *et al.* (2008). Many of the deposits share similarities to the Ashanti-style deposits. However, Burkina Faso also contains a range of other types of gold deposit, such as small polymetallic quartz-sulphide vein orebodies (type 4 deposits, such as Larafella and Poura; Klemd & Ott, 1997); gold-telluride mineralisation (Diabatou; Klemd *et al.*, 1997); and quartz-tourmaline vein deposits (e.g. Guibaré and Fété Kolé deposits; Beziat *et al.*, 1999; Dubois *et al.*, 2001). Unlike Ghana, no significant palaeoplacers (type 1) have been discovered in the Tarkwaian conglomerates. Bossière *et al.* (1996) noted that zircons from Tarkwaian sediments in Burkina Faso are euhedral indicating relatively short transport distances, thus not allowing secondary concentration of the gold.

2.6.1.4 Côte d'Ivoire

Côte d'Ivoire is largely undeveloped in terms of mineral production compared to other areas of the Baoulé-Mossi domain (agricultural based economy). Since the military coup in December 1999, political and social issues have delayed mineral production in the country. In the last few years rebel soldiers have begun disarming with peace being restored. As a result, there has been a renewal of mineral interest in the country. The first gold was poured at Lihir Gold Ltd. Bonikro project (<1 Moz resource) in southern Côte d'Ivoire, which has an estimated lifespan of eight years (Lihir Gold Ltd, 2009). Numerous other exploration permits have been issued or are pending from companies such as Newmont, Etruscan, Caystar, Cluff Gold, EquiGold and Taurian (Lepage, 2007). The major projects under development include Randgold Resources Tongon project in the prospective Nielle permit of the Senoufou belt, south of Syama (4.58 Moz resource at 2.8 g/t; Randgold Resources, 2009), and Cluff Gold's Angovia gold mine in the Yaoure region (0.45 Moz resource at 1.5 g/t; Cluff Gold PLC, 2009).

2.6.1.5 Reguibat Shield

The Palaeoproterozoic portion of the Reguibat Shield is largely unexplored compared to its southern counterpart. Most of the exploration has occurred in Moroccan terranes and include gold deposits such as Iourim and Tafrent; the latter with a resource of 220,000 oz at 1.22 g/t (Cameron, 2006).

2.6.2 Iron ore mineralisation

Iron ore deposits are largely absent from Birimian rocks of West Africa. An exception is the Falémé iron district located in the KKI (Fig. 3.1; Fig. 3.2), which is the only large Palaeoproterozoic stratiform iron deposit of West Africa. The district is comprised of 28 individual endo- and exo-skarn deposits (9 major and 19 minor orebodies) distributed in a 65 km long and 15 km wide belt in eastern Senegal (one orebody situated in western Mali), to the SW of Loulo. Many of the deposits are situated on the margins of granodiorites-dioritic intrusions. Schwartz & Melcher (2004) suggested that these deposits show similar geological characteristics to iron oxide-copper-gold (IOCG) districts and may be representative of the iron oxide-rich end-member of the iron oxide-copper-gold system.

The Falémé iron district has current reserves of 750 Mt of magnetite (250 Mt at 45% Fe) and haematite (500 Mt at 58% Fe) (values from Herbert & Senghor 2007, Randgold internal report). The Senegalese part of the district was explored during periods in the late 1950's to early 1980's by various organisations, including the Bureau de Recherches Géologiques Minières (BRGM) and Société des Mines de Fer de Sénégal Oriental (MIFERSO). Arcelor Mittal currently owns the licence and exploration is ongoing. Sporadic iron appearances occur elsewhere in the Birimian, in oolitic ironstones from the Bougouni area of Mali (Kusnir, 1999) and in several deposits related to mafic or felsic magmatic rocks in Burkina Faso (Neyberg *et al.*, 1980).

2.6.3 Other Birimian resources

Carbonate-hosted manganese deposits are widespread in central and eastern parts of the Baoulé-Mossi domain (e.g. Mücke, 2005; Nyame, 2008). In Ghana, manganiferous beds are common along the transition zone between volcano-plutonic belts and sedimentary basins, and have a close spatial association with orogenic gold deposits (Leube *et al.*, 1990). Other mineral types include major bauxite deposits (Kusnir, 1999); rare polymetallic deposits in Burkina Faso, including the epigenetic Perkoa zinc deposit (Schwartz & Melcher, 2003), plus minor copper and lead deposits (e.g. Marcoux & Milési, 1992); diamonds (e.g. Pouclet *et al.*, 2004); and uranium deposits throughout the Leo-Man Shield.

2.6.4 Birimian mineralisation history

A clear understanding of the Birimian mineralisation history is hindered by a lack of available geochronological data. However, the relative timings of mineralisation in relation to the different tectonic phases of the Eburnean orogeny can be distinguished. Milési *et al.* (1992) identified a polyphase mineralisation history for the Birimian (Table 2.6). This model has been modified to include more recent data.

Table 2.6. Birimian mineralisation history modified after Milési *et al.* (1992), showing a three-fold evolution. Examples of deposit types are given and described in the text below.

Mineralisation stage	Description	Examples
Stage 1	Pre-orogenic , sedimentary-exhalative mineralisation	Mn deposits
Stage 2	Syn-orogenic post-D ₁ to syn-D ₂ mineralisation	Gold palaeoplacer deposits, Perkoa Zn deposit
Stage 3	Late-orogenic , main mineralisation stage associated with the D ₂ -D ₃ transcurrent tectonic regime	Orogenic gold deposits, Falémé iron district, reduced intrusion-related gold systems (RIRGS)

2.6.4.1 Syn-orogenic stage

Mineralisation associated with the pre-orogenic stage is confined to the widespread Mn-deposits associated with stage 3 of Birimian crustal growth (not discussed here; see Milési *et al.*, 1992). Syn-orogenic mineralisation is largely controlled by Tarkwaian gold palaeoplacers, which appear to pre-date Birimian orogenic gold mineralisation. This statement is based on three fundamental lines of evidence: (1) regional structural studies have established Tarkwaian rocks underwent D₁ deformation (Eisenlohr & Hirdes, 1992; Hirdes *et al.*, 1992; Hirdes & Nunoo, 1994), whereas Birimian gold mineralisation has a D₂-D₃ origin (e.g. Feybesse *et al.*, 2006); (2) some Birimian gold lodes crosscut and overprint Tarkwaian palaeoplacers (e.g. Damang deposit;

Pigois *et al.*, 2003; Tunks *et al.*, 2004); and (3) radiometric ages attained from paleoplacers pre-date available ages of Birimian gold deposition (Pigois *et al.*, 2003). Evidence for the third point is limited in extent. Deposition ages for the Tarkwa basin is estimated between 2100-2130 Ma (Davis *et al.*, 1994), which is older than hydrothermal xenotime ages from vein mineralisation at Damang (2063 ± 9 Ma; Pigois *et al.*, 2003).

The exact source of Tarkwaian gold remains uncertain; however, it must be older than the Banket Series (maximum age of 2132 ± 3 Ma; Davis *et al.*, 1994). Pigois *et al.* (2003) implied that the source of the Tarkwaian gold was intrusion-related gold deposits related to belt magmatism (stage 2 of crustal growth) or, yet unknown, orogenic gold deposits formed early in the Eburnean, broadly synchronous with Tarkwaian sedimentation. In some cases, the Tarkwaian palaeoplacers may actually be the metal source for known Birimian lode deposits (Tunks *et al.*, 2004).

2.6.4.2 Late-orogenic stage

Orogenic gold mineralisation took place towards the end of the Eburnean orogeny (a typical characteristic for orogenic gold deposits; Groves *et al.*, 2000) during retrograde metamorphism (Leube *et al.*, 1990; Milési *et al.*, 1992; Mumin & Fleet, 1995; Klemd & Hides, 1997; Klemd *et al.*, 1997; 2002; John *et al.*, 1999). The change from compressional (D_1) to transcurrent tectonics (D_2 - D_3) presumably increased fluid focussing and led to the formation of numerous gold deposits along major shear zones that mainly occur at the lithological contact between volcano-plutonic belts and sedimentary basins (Milési *et al.*, 1992; Feybesse *et al.*, 2006). The absolute timing for Birimian lode-gold emplacement is not well constrained. Granitoid hosted deposits in Ghana have been dated using hydrothermal rutile between 2086-2110 Ma (Yao & Robb, 1999). Other radiometric ages for gold mineralisation include Damang (U-Pb monazite age of 2063 ± 9 Ma; Pigois *et al.*, 2003); Loulo (combined monazite and xenotime Pb/Pb age of $2028 \text{ Ma} \pm 10 \text{ Ma}$; Vielreicher, 2006); and Poura and Kalana deposits (Pb/Pb age of $2001 \pm 17 \text{ Ma}$; Milési *et al.*, 1989b). The skarn deposits of the Falémé iron district are also suggested to have occurred late in the Eburnean orogeny (Schwartz & Melcher, 2004).

2.7 Conclusions

The major conclusions made from this review on the Birimian of West Africa are summarised below:

1. The Birimian crust is composed of linear to arcuate, bimodal volcano-plutonic belts and intervening sedimentary basins, intruded by several generations of granitoids. Birimian terranes resemble Archaean granite-greenstone terranes (e.g. dominance of tholeiitic basalts and granitoids with I-type characteristics).
2. Available geochronological and isotopic studies suggest the Birimian marks a major juvenile crustal formation event that took place between 2050-2200 Ma,

with little or no Archaean inheritance.

3. The Birimian crust grew in at least five stages: (1) eruption and emplacement of tholeiitic, dominantly mafic, volcano-plutonic belts in a volcanic-arc or oceanic plateau setting; (2) subduction triggered melting and the formation of the first segments of Palaeoproterozoic continental crust, with the emplacement of small, pre-orogenic, Na-rich, calc-alkaline tonalite-trondhjemite-granodiorite (TTG) plutons; (3) erosion of the volcano-plutonic belts resulted in the deposition of Birimian basin sediments; (4) crustal shortening associated with the Eburnean orogeny led to emplacement of major syn-tectonic to late-kinematic peraluminous granitoids, as well as the deposition of Tarkwaian molasse sediments; and (5) emplacement of minor, K-rich, post-tectonic granitoid stocks.
4. Available geochronological data for stages 1-3 of Birimian crustal growth show an apparent progressive westward younging across the Birimian crust and thus can be subdivided into an older eastern subprovince (2150-2200 Ma) and a younger western subprovince (2075-2120 Ma). Local inheritance of older Birimian material can be seen in the western subprovince.
5. The Eburnean orogeny (stage 4) represents the amalgamation of multiple volcanic-arcs and oceanic plateaus onto a growing Archaean mass, probably the São Luis Craton (SLC), situated to SE of the West African Craton (WAC), during closure of a large ocean basin (Pacific sized).
6. The Eburnean underwent a polycyclic evolution consisting of two separate tectonic phases: a collisional D₁ phase and a later transcurrent D₂-D₃ stage. However, a more complex deformation history for the Eburnean cannot be ruled out. The orogeny affected Birimian rocks from ~2070-2130 Ma, with progressive younging to the west.
7. The Palaeoproterozoic crust of West Africa is highly endowed with respects to gold and manganese, and relatively deficient in base metals and iron (excluding the Falémé iron district). Several types of Birimian lode gold deposits exist (mainly orogenic gold with rare intrusion-related gold), as well as modified Tarkwaian palaeoplacers.
8. Recent exploration has led to the discovery of numerous world-class orogenic gold deposits, similar in scale to those in the well-known gold districts of Western Australia and Canada. Two of the most productive/prospective regions are the Ashanti belt in Ghana, and the West Mali Gold Belt in the Kédougou-Kéniéba inlier (host to the Loulo gold deposits).
9. A polyphase mineralisation history exists for the Birimian with a majority of orogenic gold deposits emplaced in the late stages of the Eburnean orogeny during transcurrent movement.

CHAPTER 3: GEOLOGY OF THE LOULO AREA

In this chapter, the regional geology of the Kédougou-Kéniéba inlier is briefly summarised and the structural setting for gold mineralisation at Loulo is considered. The Loulo stratigraphy is also discussed including detailed petrographic descriptions of the various lithologies. Lastly, geochemical compositions of the rock types are presented and discussed.

3.1 Regional geology of the Kédougou-Kéniéba inlier

The Loulo mining district is situated in the eastern part of the Kédougou-Kéniéba inlier (KKI). Birimian rocks of the KKI occupy an area of 15,000 km² in eastern Senegal and a small part of western Mali, to the NW of the Leo-Man Shield (Fig. 2.4). The inlier is bounded on its western margin by the Hercynian Mauritanide belt and is unconformably overlain by flat lying Neoproterozoic sediments of the Taoudeni basin on all other sides. The KKI has attracted much geological interest since the discovery of the giant Loulo and Sadiola orogenic gold deposits.

Previous studies separated the KKI into two lithostratigraphic successions: the Mako Series consisting of a NE-trending volcano-plutonic belt, which is overlain to the east by sediments of the Dialé-Daléma Series (Bassot & Caen-Vachette, 1984; Bassot, 1987). The Dialé-Daléma sedimentary basin consists of a western Dialé Series, which is separated by rocks of the Daléma Series to the east by the large basin-type Saraya batholith. However, recent exploration in the eastern parts of the KKI has recognised a N-trending volcano-sedimentary terrane, known as the Falémé belt. To avoid confusion, rocks of Dialé-Daléma basin are referred to here as sediments located to the west of the Falémé belt. Sediments located to the east of the Falémé belt are referred to as the Kofi Series. A geological map of the KKI is shown in Fig. 3.1, accompanied by available geochronological data.

3.1.1 Mako Series

The Mako volcano-plutonic belt has a complex history and structural relationships are difficult to interpret due to the intense deformation associated with the Hercynian Mauritanide orogenic belt (Gueye *et al.*, 2008). Several petrographic, geochemical and geochronological studies have been carried out in the area (Dia *et al.*, 1997; Diallo, 2001; Hirdes & Davis, 2002; Dioh *et al.*, 2006; Pawlig *et al.*, 2006; Gueye *et al.*, 2007, 2008). The belt is mainly composed of carbonate altered basaltic lavas and andesites of tholeiitic affinity, and widespread intercalated volcanoclastic rocks and sediments (Fig. 3.1).

The Mako Series is intruded by numerous granitoids of various generations, compositions and sizes. The large Kakadian batholith, along the western margin of the belt, is composed of numerous coalescent ultramafic (e.g. the Sandikounda Layered Complex) and felsic plutons (e.g. Lamina-Kaourou Plutonic Complex). This batholith has a complex geological history with a wide

range of emplacement ages (2079-2213 Ma; Dia *et al.*, 1997; Gueye *et al.*, 2007). The upper age range is significantly older than other rocks of the KKI and other areas of the western subprovince (*see section 2.5.2.2*). Hirdes & Davis (2002) suggested that early activity occurred on the margin of the Birimian crust in this particular part of the West African Craton (WAC). The Mako belt is also centrally intruded by smaller, sub-circular granitoids with similar characteristics to other Birimian volcanic belt-type plutons (*see section 2.3.2*). In contrast to the Kakadian batholith, available geochronological data show these granitoids have much younger emplacement ages (2070-2080 Ma; Hirdes & Davis, 2002; Gueye *et al.*, 2007).

The boundary between the Mako belt and the Dialé-Daléma sedimentary basin is tectonic and marked by a major terrane-bounding shear zone, known as the Main Transcurrent Zone (MTZ). This important regional structure trends NE and curves northward as it crosses the Falémé River into Mali (Milési *et al.*, 1989a). Ongoing exploration along the MTZ has led to discoveries of the Massawa and Sabodala gold deposits.

3.1.2 Dialé-Daléma Series

Following Hirdes & Davis (2002), the Dialé and Daléma series are considered here to be part of the same sedimentary basin. The basin consists of detrital (quartz and feldspar-bearing wackes and argillites) and chemical sediments (carbonates) interbedded with calc-alkaline volcanoclastic sediments, some of which contain lapilli-sized fragments (Bassot, 1987; Hirdes & Davis, 2002). Wackes increase towards the margins of the basin. The sedimentary pile was isoclinally folded during the Eburnean orogeny, with upright to slightly overturned folds to the SE. The basin is centrally intruded by the large (~2000 km²), K-rich, Saraya batholith. This batholith is interpreted to be syn-tectonic to late-kinematic in origin and is composed of several coalescent, biotite-bearing, quartz-monozite and granitic plutons (Pons *et al.*, 1992).

3.1.3 Eastern parts of the KKI

The Falémé belt has only recently been recognised as an entity because of poor exposure and extensive lateritisation of the terrane in the eastern parts of the KKI. It's debatable to whether the Falémé district is a volcano-plutonic belt (similar to the Mako Series) or an igneous complex within the Dialé-Daléma Series. However, geochemical analysis (*section 3.4*) implies a volcanic belt origin. According to ongoing exploration work, the Falémé belt is composed primarily of TTG granitoids (associated with Fe skarn deposits) with intercalated volcanoclastic, clastic and carbonate sediments, plus minor andesite (occasionally pillowed) and felsic volcanic rocks (Fig. 3.1 & Fig. 3.2). The Boboti and South Falémé plutons in the southern parts of the belt have been studied by Ndiaye *et al.* (1997) and Hirdes & Davis (2002), and are composed of biotite + hornblende + clinopyroxene-bearing, Na-rich, tonalities and granodiorites.

The Falémé belt is cut to the north and east by the Senegal-Mali Shear Zone (SMSZ), which forms the contact with the Kofi Series in Mali. The SMSZ is the principal fluid pathway for

gold mineralisation in the Kofi sediments and hosts deposits along the West Mali Gold Belt (*section 2.6.1.2*) (Fig. 2.11 & Fig. 3.1). The Kofi Series is composed of folded detrital sandstones and chemical sediments (similar to Dialé-Daléma Series), plus several granitic intrusions which increase in abundance towards the south. The geology of the Falémé belt and Kofi Series is described in greater detail in the following sections.

3.2 Geological and structural setting of the Loulo district

3.2.1 Loulo stratigraphy

The Loulo district is situated in the eastern parts of the KKI, straddling the border of western Mali (Loulo-Clib permits) and eastern Senegal (Bambadji-Daléma permits). The geology of the Loulo district is shown in Fig. 3.2 and consists of sediments of the Kofi Series, the northern half of the Falémé belt, and a small section of the Dialé-Daléma Series.

3.2.1.1 Falémé belt

The Falémé belt is a granitoid dominated terrane. The Balangouma pluton outcrops in the western margin of the Loulo property. This pluton is a large irregular-shaped body (~300 km²) trending in a NE direction, thinning northward. Recent mapping has shown that the Balangouma pluton is a collective term for smaller individual plutons (Fig. 3.2) of varying compositions (diorites-granodiorites). The northern half of the Boboti tonalite pluton outcrops in the southern part of the Daléma permit. The granitoids of the Falémé belt are spatially and genetically associated with iron skarn deposits (Fig. 3.2; *section 2.6.3*). The Balangouma plutons are associated with the Senegalese Karakaene, Kouroudiako and Kabelea iron deposits, and one further deposit towards the north in Mali (NNW of the Gara deposit; referred to here as 'Fe Hill').

Other rock types include widespread clastic and carbonate sedimentary rocks intercalated with volcanoclastic sediments; the latter common to the north in the Clib permit or as small outcrops on isolated hills and laterite plateaus. Hydrothermal-tectonic ferruginous breccias are observed on the eastern border of the Falémé belt; known in Senegal as the Cargneule. Minor basaltic/andesite volcanic rocks have been mapped around the villages of Bambadji, Lengeya and Mandankhoto. Leucocratic felsic volcanic rocks are less common and outcrop along the southern Bambadji border, where they form a brecciated contact with the mafic volcanic rocks. All rock types have experienced greenschist facies metamorphism associated with the Eburnean orogeny. The Bambadji and Daléma permits were acquired by Randgold in last few years and as a result the majority of the data collected in this chapter comes from the Loulo permit in Mali. However, the Balangouma pluton is discussed further to compare with intrusions of the Kofi Series.

3.2.1.2 Kofi Series

The Kofi Series is composed largely of alternating metasediments, metacarbonates and hydrothermal-tectonic breccias, as well as pink granites (basin-type) and minor intrusive rocks. Sediments strike N-S to NNE-SSW and dip moderately to steeply (60-80°) to the east (predominately). Locally, the sediments are tightly isoclinally folded (e.g. Gara). The Kofi sedimentary sequence is composed of a variety of arenaceous sediments including argillaceous greywackes, quartz-wackes, tourmalinites, arkoses and feldspathic greywackes. This sediment terminology differs to previous work (e.g. Dommanget *et al.*, 1993) and mine terminology (Table 3.1). The stratigraphy at Gara and Yalea is shown in Fig. 3.3.

Table 3.1. Outlining the major sediment types of the Kofi Series, with comparisons to mine terminology

Mine terminology	Terminology used in this study
Carbonates	Carbonates (limestones and dolostones)
Argillaceous quartzites (SQR)	Argillaceous greywackes
Greywackes	Quartz-wackes
Quartz-tourmaline greywackes (QT)	Tourmalinites
Grey quartzites (QG)	Arkoses
Quartzites	Feldspathic greywackes
QR-tourmaline breccias	Hydrothermal-tectonic breccias
Quartz rosé units (QR)	Albite-altered zones (mainly after argillaceous greywackes)

Note- lithology descriptions are given in section 3.3. The latter rock type is described in chapter 5.

The Kofi sediments are intruded by several basin-type granitoids within and around the Loulo area. The largest mappable intrusion is a 40 km² circular pink Birimian granitoid, approximately 25 km to the east of the Gara deposit, situated to the south of Sitakili, referred to as the Yatea granite (just outside of the permit area; Fig. 3.1). This pluton is spatially associated with the Segala gold deposit. An isolated pink granitoid stock is also observed to the NE of Gara, along the transition zone with the Falémé belt. Larger intrusions are seen to the south of the Loulo permit (e.g. the B-rich Gamaye pluton). The Kofi sediments are also intruded by numerous generations of dykes (Birimian to Mesozoic) of variable thicknesses (tens of centimetres to hundreds of metres). The most prominent dyke is an E-W trending dolerite intrusion (~200 m thick) near Djidian Keneiba village (Fig. 3.2), which transects all rock-types in the eastern half the KKI.

3.2.1.3 Dialé-Daléma Series

A small portion of the Dialé-Daléma Series outcrops in the western parts of the Clib permit, where Birimian basin sediments are intruded by the highly-altered Moussala basin-type pluton. This pluton represents the northern extension of the Saraya batholith (Fig. 3.1 & Fig. 3.2).

Fig. 3.3. A) Schematic Gara stratigraphic column, showing the major rock lithologies (not to scale).


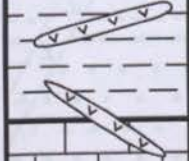

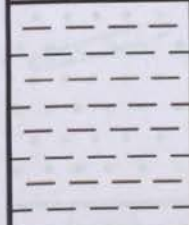

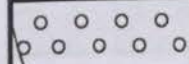
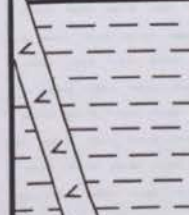
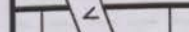
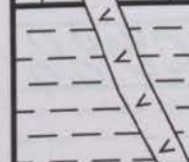
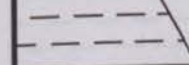
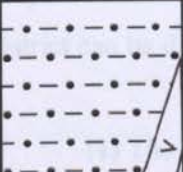

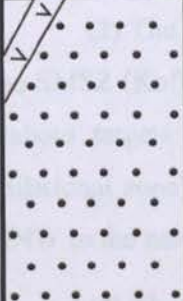
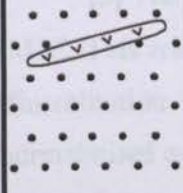
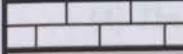
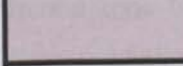
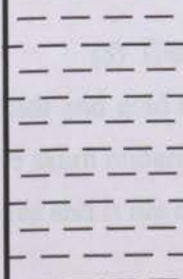
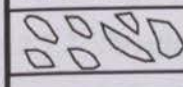
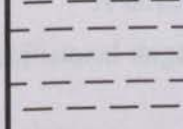
Lithology	Terminology used in this study	Thickness (m)	Description
	Argillaceous greywackes	minimum of 250 m	An upper unit of argillaceous greywackes consisting of alternating layers of greywackes (rich in carbonate cement) and argillites. High degrees of pink albite alteration is present, particularly around the Gara West orebody. Thin (<15 m) limestone beds are intercalated in this sequence.
	Birimian dolerite & Si-poor diorite dykes	<2 m to 12 m	Thin, discontinuous, mafic dykes showing strong schistosity and greenschist facies metamorphic overprint. Common in the argillaceous greywackes and upper part of the limestone unit.
	Limestones	140 m	Foliated limestones intercalated with thin organic-rich clay horizons and lenses. Locally, more massive limestone beds are observed.
	Argillaceous greywackes	variable thickness of 10-140 m	Argillaceous greywackes, with high carbonate cement content, border the orezone. Pink albite alteration largely targets the arenaceous laminae rather than altering the whole rock. This unit becomes notably thinner at the hinge of the vertical F_2 folds.
	Tourmalinites	5-20 m	The Gara orezone is confined to a thin unit of strongly tourmalinised (>30% tur) quartz-wacke. Rather than forming one bed, this unit contains thin (<1 m) interbeds of less-tourmalinised (10-15% tur) quartz-wacke associated with low grade (<1 g/t). A thicker low-tourmalinised quartz-wacke unit occurs below the orezone.
	Quartz-wackes	10-35 m	
	Argillaceous greywackes	variable thickness of 25-130 m	Sediments to the east of the orezone are mainly argillaceous greywackes. Pink albite alteration occurs close to the orezone, largely targeting the arenaceous laminae rather than altering the whole rock. This unit becomes notably thinner at the hinge of the vertical F_2 folds.
	Limestones	15 m	A thin unit of schistose limestone separates a thick sequence of argillaceous greywackes.
	Argillaceous greywackes	minimum of 120 m	
	Post-Birimian dolerite dyke	5-20 m	Sub-horizontal Mesozoic dolerite dyke intrudes all units.

Fig 3.3. B) Schematic Yalea stratigraphic column, showing the major rock lithologies (not to scale).

Lithology	Terminology used in this study	Thickness (m)	Description
	Post-Birimian dolerite dyke	20 m	Sub-horizontal, unaltered, Mesozoic dolerite dyke intrudes all units.
	Feldspathic greywackes	minimum of 150 m	HW feldspathic greywackes- massive, unaltered rocks with an argillaceous-rich matrix and carbonate cement.
	Arkoses	~100 to 200 m	Unaltered, clast-supported, feldspar-rich sandstones. This package is extremely heterogeneous in composition with sediments often grading into feldspathic greywackes and carbonate-rich sandstones. Thin (~10 m) albite alteration zones occur along HW second-order splays.
	Birimian dolerite & Si-poor diorite dykes	<5 m	Thin, discontinuous, altered and deformed mafic dykes, occasionally observed in both HW and FW lithologies.
	Dolostones	12-15 m	Thin foliated dolostone unit caps the orezone in the southern parts of Yalea. This unit splays off the orezone further to the north where it is displaced further into the HW.
	Orezone	10-30 m	The Yalea N-S shear zone is associated with a proximal metasomatic albite-carbonate alteration zone.
	Argillaceous greywackes	minimum of 150 m	FW package of altered and sheared argillaceous greywackes with a carbonate cement. A distal pink albite alteration zone (<60 m) borders the orezone.
	Hydrothermal-tectonic breccias	<10-20 m	Brecciation of the argillaceous greywackes occurs along FW second-order splays, accompanied by a high fluid flux of albite and, lesser, tourmaline alteration.
			

Note- HW = hangingwall; FW = footwall.

3.2.2 Structural setting

3.2.2.1 Outline

The structural geology of the Loulo area is beyond the scope of this project and the proposed models are only discussed briefly here. In terms of structural setting, the Loulo mining district can be divided into five sub-areas:

(1) The N-S-trending **Senegal-Mali Shear Zone (SMSZ)** (Fig. 3.2) is the main controlling shear (first-order), separating the Falémé volcano-sedimentary terrane to the west from the Kofi sedimentary terrane to the east. Although the SMSZ controls the regional fluid flow, the greatest ore flux occurs in higher order shears, faults and folds. This is a common characteristic for orogenic gold deposits (e.g. the Yilgarn Craton, Western Australia; Groves *et al.*, 2000).

(2) The NNE (020°) **Yalea-trend** is a major second-order lineament on the eastern wall of the SMSZ (Kofi Series) and hosts the Yalea mine, and the P-125, Loulo-3, Loulo-2, Loulo-1 and Baboto targets (Fig. 3.2). Yalea is situated in a N-S, left-hand flexure along this structure (dilatational zone). The Yalea-trend rotates to an N-S direction around the Baboto targets and then NNW to the north of the permit area.

(3) The **Gara area** is associated with macroscopic folds close to the eastern border of the SMSZ. This zone occurs to the NW of the Yalea-trend and includes the Gara and P-129 deposits. Mineralisation at Gara is hosted in a thin (5-20 m), folded and fractured unit of highly tourmalinised quartz-wacke (Fig. 3.3a; Fig. 3.5).

(4) The N-S **Faraba area** in the southern parts of the Loulo permit can be treated as a discrete zone from the Gara and Yalea areas. This zone is characterised by strain partitioning (discussed below).

(5) The **Falémé belt** to the west of the SMSZ shows a lack of NNE structures, related folds and gold mineralisation (several minor targets). This terrane is associated with replacement Fe skarn mineralisation genetically linked to felsic intrusions. This zone is outside the main study area and is not discussed further in this section.

3.2.2.2 Structural evolution

A three stage structural model can be implied for the Loulo district consisting of an early collisional stage (D_1) and later transcurrent stages (D_2 - D_3) (Treloar, pers. comm.).

1. Collisional phase (D_1)

The initial accretion of the Birimian terranes during the Eburnean orogeny caused the development of F_1 folds within the Kofi sediments. F_1 folds occur as sub-horizontal to gently-inclined (axial planes dipping at 30°), close to open folds (interlimb angle between 40 to >100°

with wavelengths up to 600 m) (Fig. 3.5). At Gara, these folds are superimposed (refolded) by younger vertical F_2 folds associated with the D_2 transpression phase. Harris (1998) proposed these F_1 folds are linked to early thrusts.

2. Transpression phase (D_2)

The N-S-trending SMSZ was initiated as a sinistral transpressional fault. Fig. 3.4 shows the likely structures associated with a left-lateral strike-slip fault. At low strain rates, folds and thrusts developed on the eastern wall of the SMSZ. These thrusts formed parallel to the P-shear direction and were accompanied with the development of hangingwall antiforms with NNE-trending axes (initiation of F_2 folding; Fig. 3.6a). These early thrusts and folds formed a simple compressional duplex (positive flower structure). As strain accumulated in the Kofi sediments, it became increasingly accommodated by NNE-striking sinistral P-shears. The F_2 folds developed further during this stage with the formation of synforms and short WSW limb geometries (Gara model; Fig 3.5a; Fig. 3.6b). The F_2 folds control the surface geometry of the Gara orezone (Fig. 3.5a). They occur as vertical, isoclinal folds, with wavelengths <200 m and amplitudes of ~ 50 m (Fig. 3.5b). Axial planes trend NNE ($\sim 030^\circ$) plunging moderately to the SSW.

Fig. 3.4. Orientations of structures associated with sinistral strike slip faults. **A)** Simple brittle regime- PSZ = principal shear zone; P = primary shear; R = reidel shear; σ_1 = principal stress direction; σ_3 = minimum stress direction. **B)** More ductile (higher temperature, lower strain rates) regime- showing development of normal faults parallel to R-shear direction in a transtensional setting and thrusts and hangingwall antiforms parallel to P-shear direction in transpressional settings. Figure modified from Davis & Reynolds (1996).

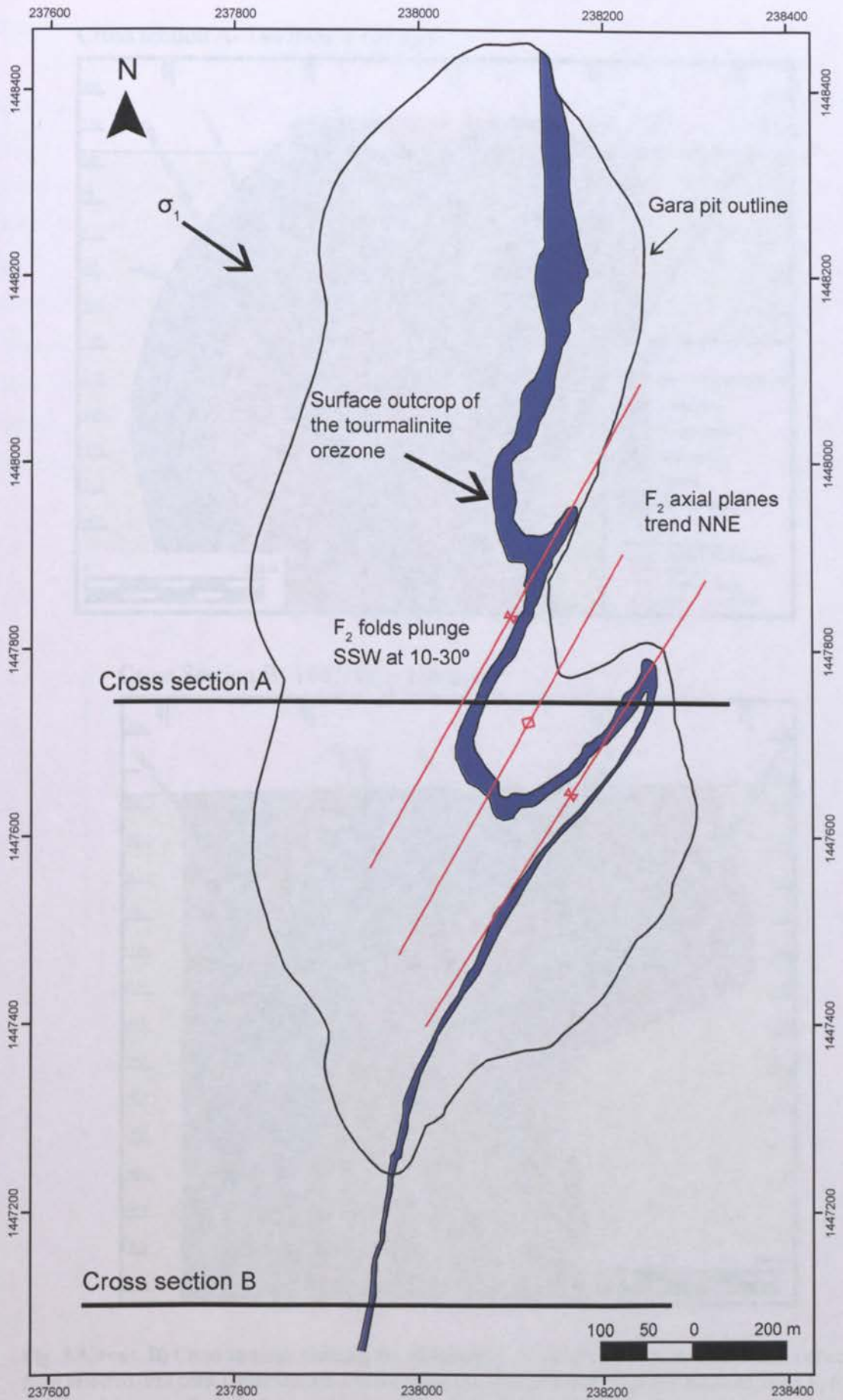
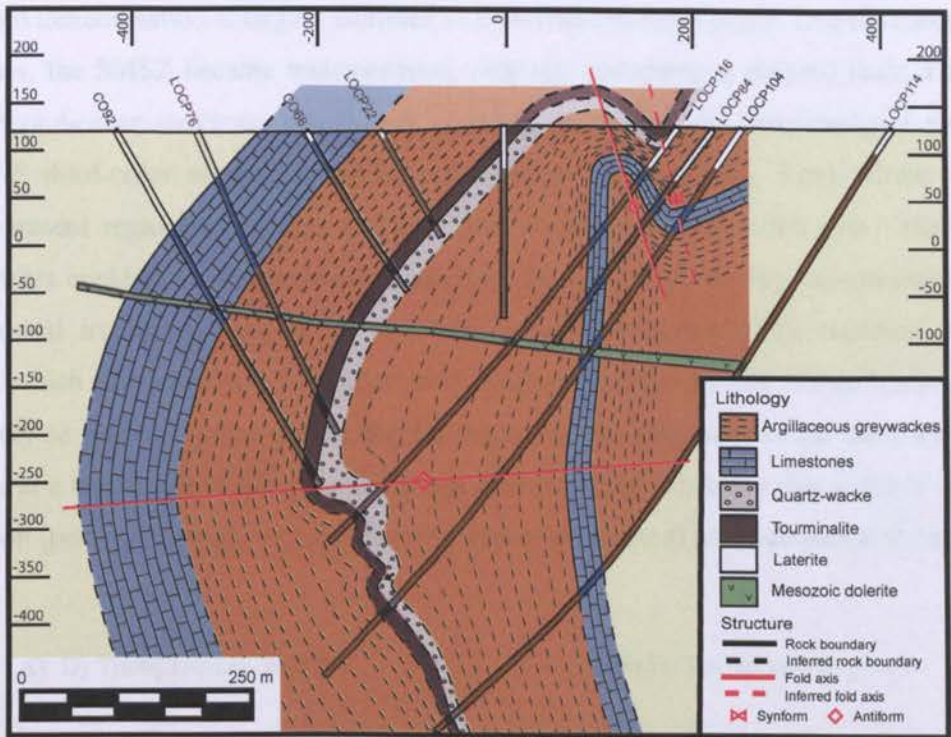


Fig. 3.5. Plan and cross sections of the Gara fold system. **A)** Plan section of the Gara orebody showing the surface expression of the tourmalinite orezone controlled by F₂ folding. Cross section lines are shown in Fig. 3.5b. Grid: UTM29 WGS84.

Cross section A- 1447800 ± 100 mN



Cross Section B- 1447100 ± 100 mN

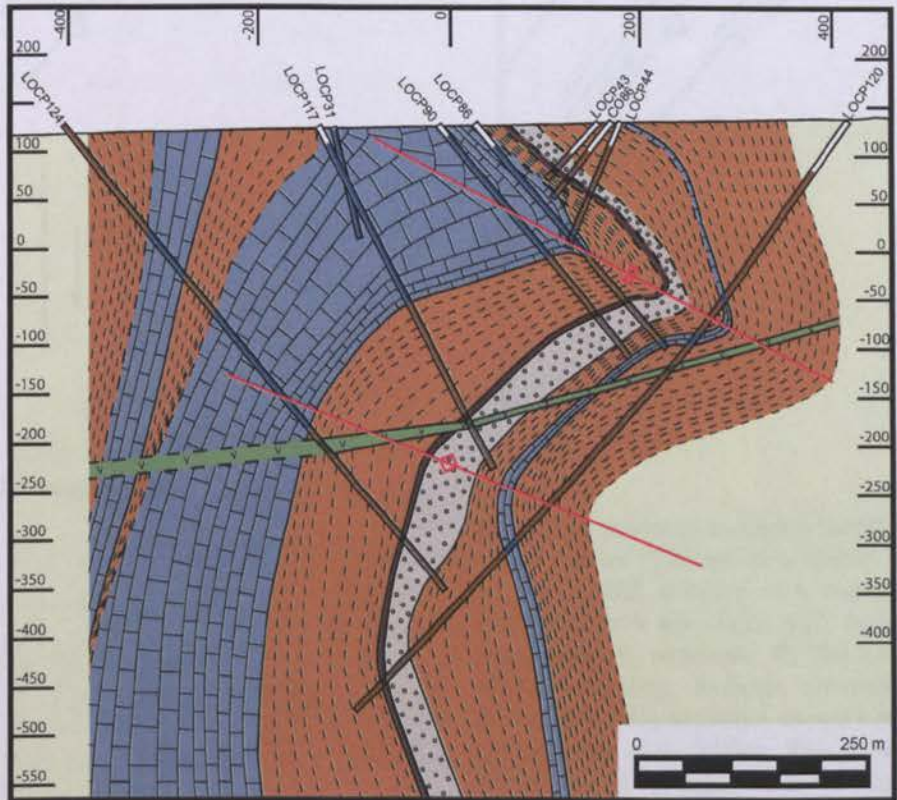


Fig. 3.5. cont. B) Cross sections showing the morphology of the Gara folds. Structural data collected from selected drill core. Cross section A shows both the sub-horizontal to gently inclined, open F_1 folds and the tighter, vertical, F_2 folds; with the latter controlling surface outcrop shown in Fig. 3.5a. In outcrop and in cross section the F_2 fold axes dip steeply to east; however the eastern limb of the synform shown above seems to flatten to the east. Cross section B is from south of the Gara pit and only shows the F_1 folds. Vertical and horizontal scale in meters.

3. Transtension phase (D_3)

Gold mineralisation is largely confined to a D_3 transtensional phase. Due to changes in far field stresses, the SMSZ became transtensional, although remaining a sinistral fault. The NNE-trending second-order structures reactivated as principal shears with transtensional movement forming N-S third-order structures that have a R-shear geometry (Fig. 3.6c). These left-hand flexures represent regions of dilation and preferred zones of mineralisation (the Yalea model). These R-shears could be new structures or reactivate fabrics formed during transpression. During further sinistral transtension along the N-S structures, fourth-order NNW-trending structures developed, which accommodates late-stage mineralisation (e.g. Goukoto). Mineralisation at Gara is also likely to have occurred during the D_3 stage. As the long-axis of the tourmalinite host sediment is at a high angle to the principal stress direction (Fig. 3.5a), the unit is likely to deform via extension (post- F_2 folding), with the development of extensional and extensional shear veins.

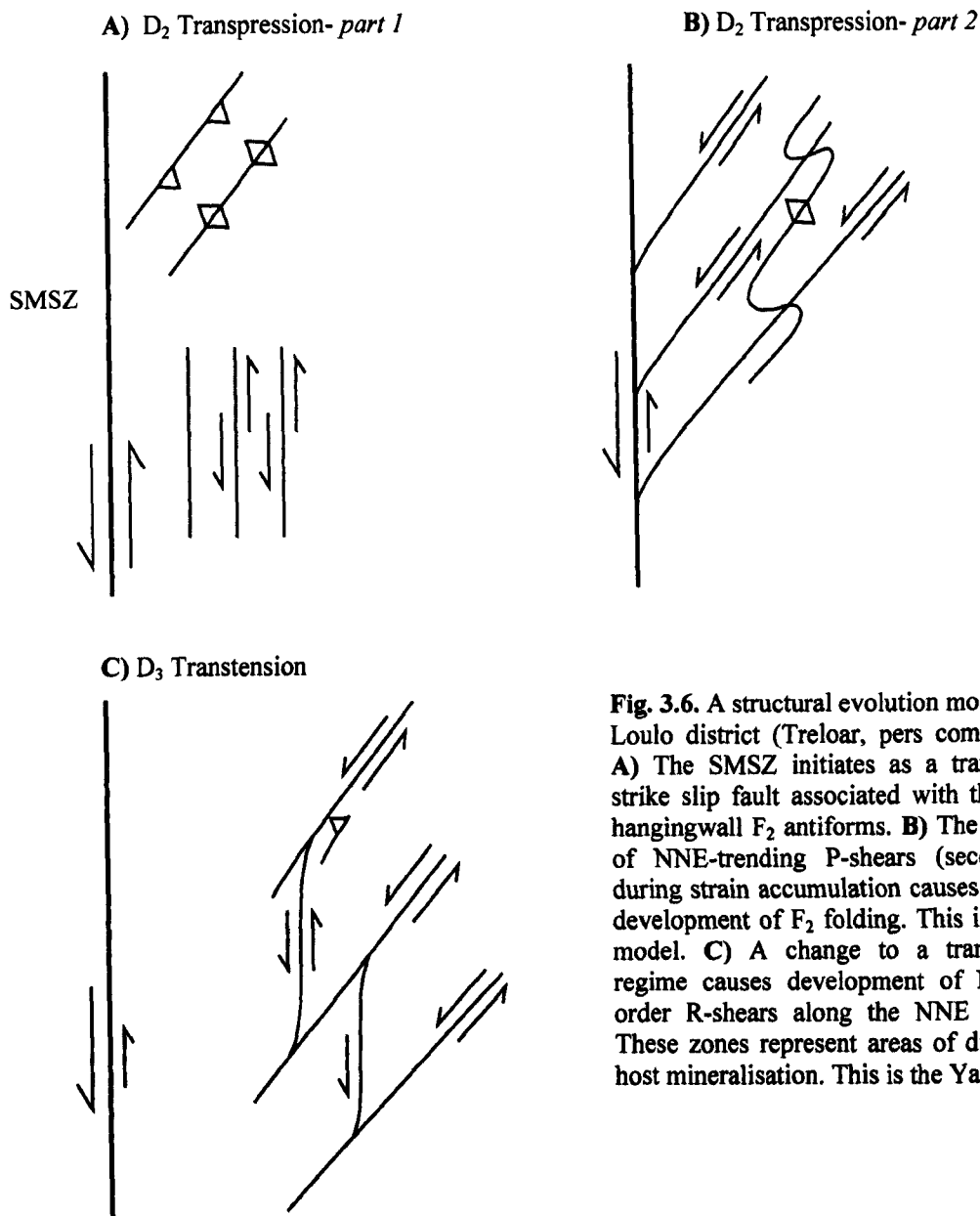


Fig. 3.6. A structural evolution model for the Loulo district (Treloar, pers comm. 2010). **A)** The SMSZ initiates as a transpressive strike slip fault associated with thrusts and hangingwall F_2 antiforms. **B)** The formation of NNE-trending P-shears (second-order) during strain accumulation causes continued development of F_2 folding. This is the Gara model. **C)** A change to a transtensional regime causes development of N-S third-order R-shears along the NNE structures. These zones represent areas of dilation and host mineralisation. This is the Yalea model.

Faraba model

Structures related to the Faraba targets can be explained by a strain partitioning model. Sediments at Faraba consist of steeply dipping, alternating coarse to gritty sandstones and finer argillaceous sediments, with mineralisation confined to the former. During sinistral strike-slip movement, the finer-grained sediments will incorporate most of strain and create boundins around low strain coarser sediments. Shear stresses will partition into a simple shear component in the high strain incompetent units, while a pure shear component will occur in the low strain competent units, which creates zones of dilatancy for mineralisation (fracture development).

3.3 Lithological descriptions

This section mainly describes the lithologies of the Kofi Series, in terms of field relations, rock characteristics and mineralogy. The Balangouma pluton of the Falémé belt and the Moussala pluton of the Dialé-Daléma Series are also discussed to show similarities/contrasts with intrusive rocks of the Kofi Series.

-Kofi Series

3.3.1 Carbonates

Chemical sediments in the Loulo district consist of limestones and dolostones rich in carbonaceous matter. They are strongly foliated (schistose carbonates) showing prominent ductile deformation features (Fig. 3.7b), and form sharp contacts with the siliciclastic sedimentary units. Limestone wall-rocks surrounding the Gara deposit are composed primarily of recrystallised calcite with intercalated dolomite grains, while Yalea wall-rock can be fully dolomitised (Table A-3 in the appendices). In comparison to the widespread carbonate units in the Leo-Man Shield (*see section 2.6.3*), the Loulo carbonates are notably depleted in manganese (<0.2% MnO).

The carbonates are composed of alternating layers of silica-poor (<10%) and silica-rich (up to 35%) horizons between 0.5 to 5 mm in thickness (Fig. 3.7a, b). Silicates occur in a granular form (20-130 μm) consisting of variable amounts of orthoclase, quartz and sericite. The cyclic distribution of these minerals represents a sedimentary feature (i.e. bedding/lamination) rather than a post-depositional introduction of silica. A characteristic feature of this rock type is the presence of regular, black layers rich in carbonaceous matter, which have often brecciated during deformation (Fig. 3.7c). Carbon exists in an amorphous form, coating clay-sized particles (<40 μm) primarily composed of mica. Prior to metamorphism, these layers probably represented original organic-rich clay interbeds or lenses. The carbonates contain a diverse range of trace minerals (that increase in abundance in the silica-rich horizons). In order of decreasing abundance they include: pyrrhotite (10-100 μm), reticulated rutile, apatite, pyrite (20 μm - 2 mm), zircon, skeletal parisite (90 μm) (replacing apatite), and fluorite. Parisite ($\text{Ca}[\text{Ce,La}]_2[\text{CO}_3]_3\text{F}_2$) is dominantly a hydrothermal mineral phase and implies hydrothermal fluids interacted with these

carbonate units (possible use as an important mineralised fluid tracer).

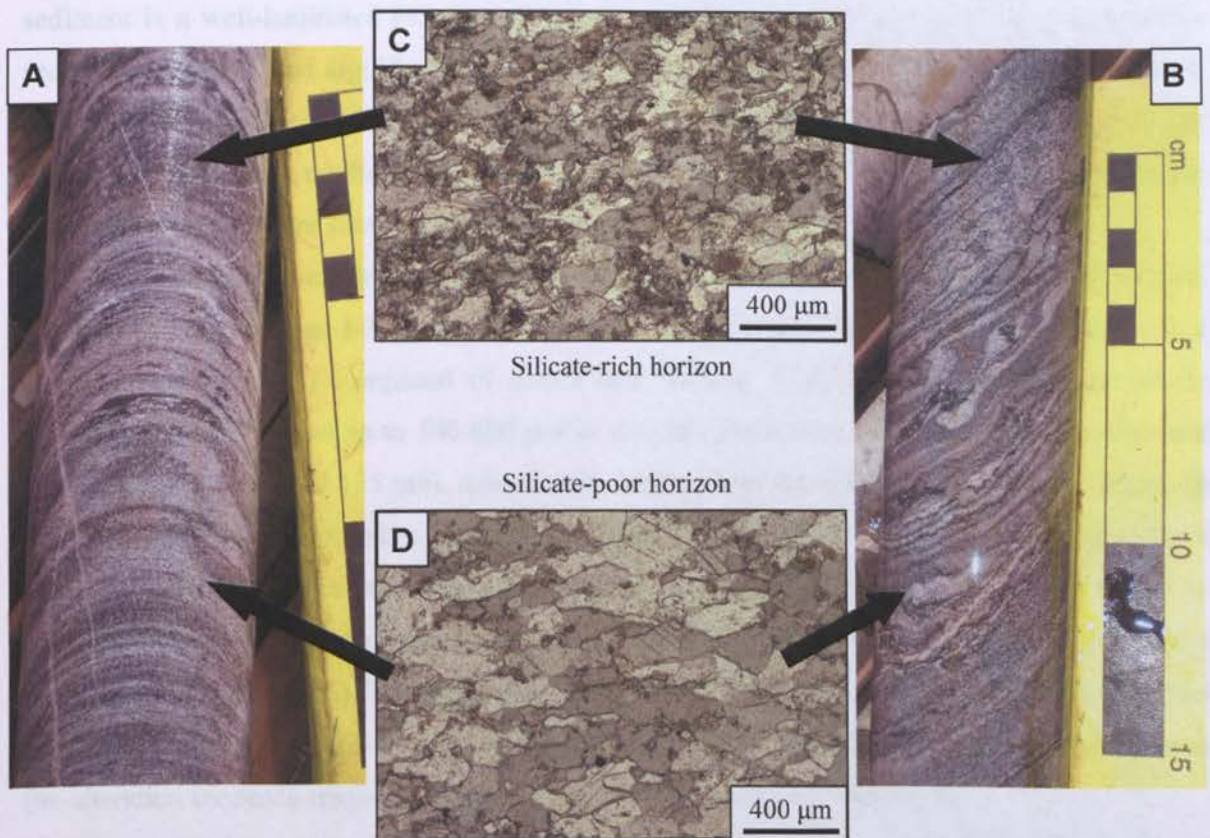


Fig. 3.7. Drill core photos and transmitted light images (PPL) of the schistose carbonates. **A)** Well-laminated rock with alternating light grey layers consisting of silica-poor beds and darker layers composed of silica-rich beds (LOCP120, 561 m). **B)** A strongly ductile deformed carbonate unit (LOCP117, 154 m). **C)** Transmitted light photomicrograph of the silicate-rich horizons. Silicates occur as granular minerals along the crystal boundaries of larger carbonate minerals. **D)** Transmitted light image of the silicate-poor horizons.

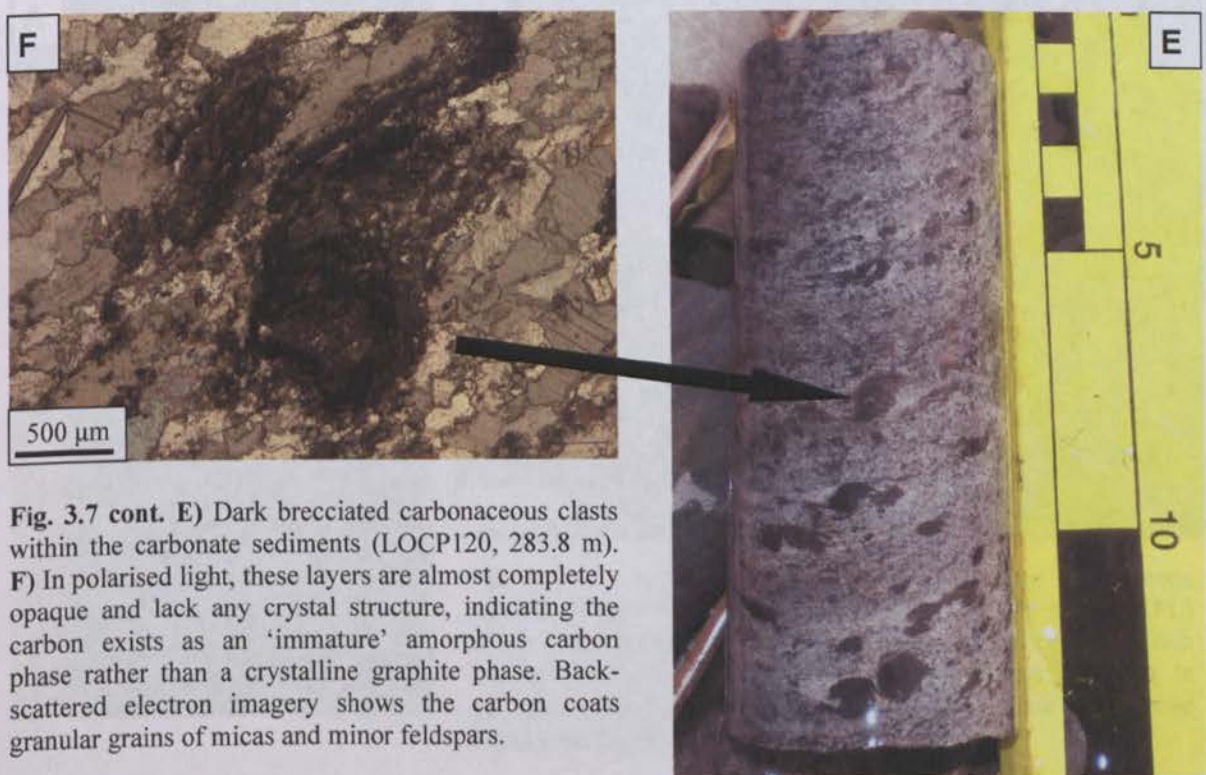


Fig. 3.7 cont. **E)** Dark brecciated carbonaceous clasts within the carbonate sediments (LOCP120, 283.8 m). **F)** In polarised light, these layers are almost completely opaque and lack any crystal structure, indicating the carbon exists as an 'immature' amorphous carbon phase rather than a crystalline graphite phase. Back-scattered electron imagery shows the carbon coats granular grains of micas and minor feldspars.

3.3.2 Argillaceous greywackes

Argillaceous greywackes are the most common sedimentary lithology at Loulo. The sediment is a well-laminated (<1 mm to 2 cm), green-grey sandstone consisting of a turbidite sequence of wackes and argillites (Fig. 3.8). This rock type contains well-preserved soft sediment deformation features such as slumps, water escapes and intrasedimentary faults. Similar to the carbonate beds, the argillaceous greywackes are strongly foliated (schistose argillaceous greywackes) and at Gara show pronounced microfolds within the larger macrofolds.

Arenaceous layers are light grey in colour and are generally thicker than the argillite layers (300 μm to 2 cm, average 1-3 mm). These layers are carbonate-rich units (ankeritic cement) with a clast fraction (20-60%) composed of quartz and feldspar. Quartz clasts can exist as detrital anhedral/subhedral grains up to 500-600 μm in size, but more commonly they occur as fine-sand sized angular grains (100-125 μm). Albite clasts tend to form more equant grains up to 100 μm in size. The matrix is composed of granular quartz and sericite (30-80 μm). The carbonate cement forms poikiloblastic clusters surrounding larger clasts of quartz and albite, or exists as intergranular crystals between smaller grains of the matrix. The cement can vary in abundance between laminae (20-60%). The arenaceous layers are rich in haematite (~10%), which exist as tabular and blocky grains (5-150 μm) commonly completely or partially transformed to leucoxene (an alteration sequence frequently seen in the Loulo orebodies- see chapter 4).

Argillite layers are green in colour with thicknesses between 150 μm to 5 mm. These layers represent original clay-rich horizons, which have metamorphosed to a sericite-chlorite-albite assemblage. Carbonaceous layers observed in the carbonates are rarely seen in this rock type.

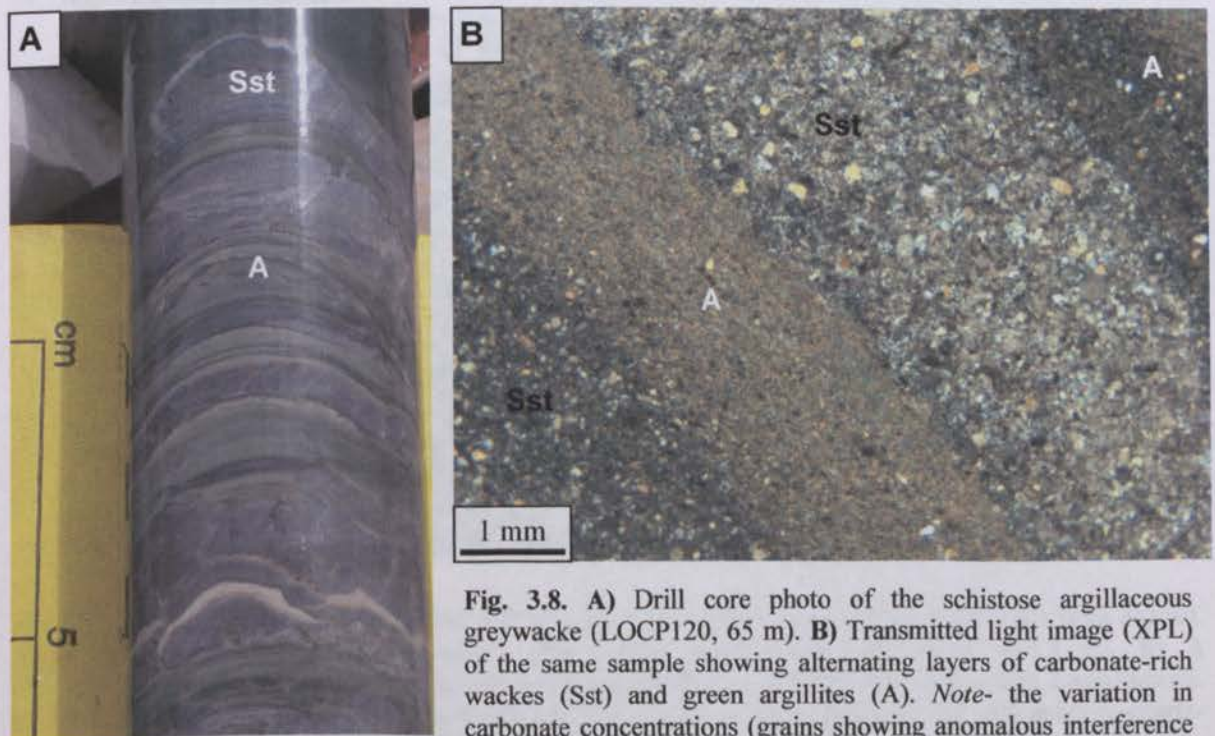


Fig. 3.8. A) Drill core photo of the schistose argillaceous greywacke (LOCP120, 65 m). B) Transmitted light image (XPL) of the same sample showing alternating layers of carbonate-rich wackes (Sst) and green argillites (A). *Note-* the variation in carbonate concentrations (grains showing anomalous interference colours) between wacke laminae.

3.3.3 Tourmaline-bearing quartz-wackes

The most Si-rich sediments of the Kofi Series classify as quartz-wackes. This rock type is a massive, dark grey, matrix-supported, poorly sorted, fine-to-coarse sand sediment (100 μm to 2.2 mm) (Fig. 3.9a). Quartz exists as subhedral detrital clasts, often heavily recrystallised showing polycrystalline textures with rolling extinction. The matrix is composed of microcrystalline quartz (50-100 μm), minor platy sericite (up to 130 μm) and sporadic grains of chlorite. Quartz-wackes are cemented together by carbonate (<20%) and variable amounts of post-depositional cryptocrystalline tourmaline (5 to >30% tur). At Gara, quartz-wackes can be divided into a weakly tourmalinised (5-20% tur) and a tourmalinite sequence (>30% tur). The latter rock type is finer-grained (100-500 μm) than the less-tourmalinised quartz-wackes (Fig. 3.9b). Tourmaline forms part of the hydrothermal alteration sequence and is examined in detail in *chapter 5*.

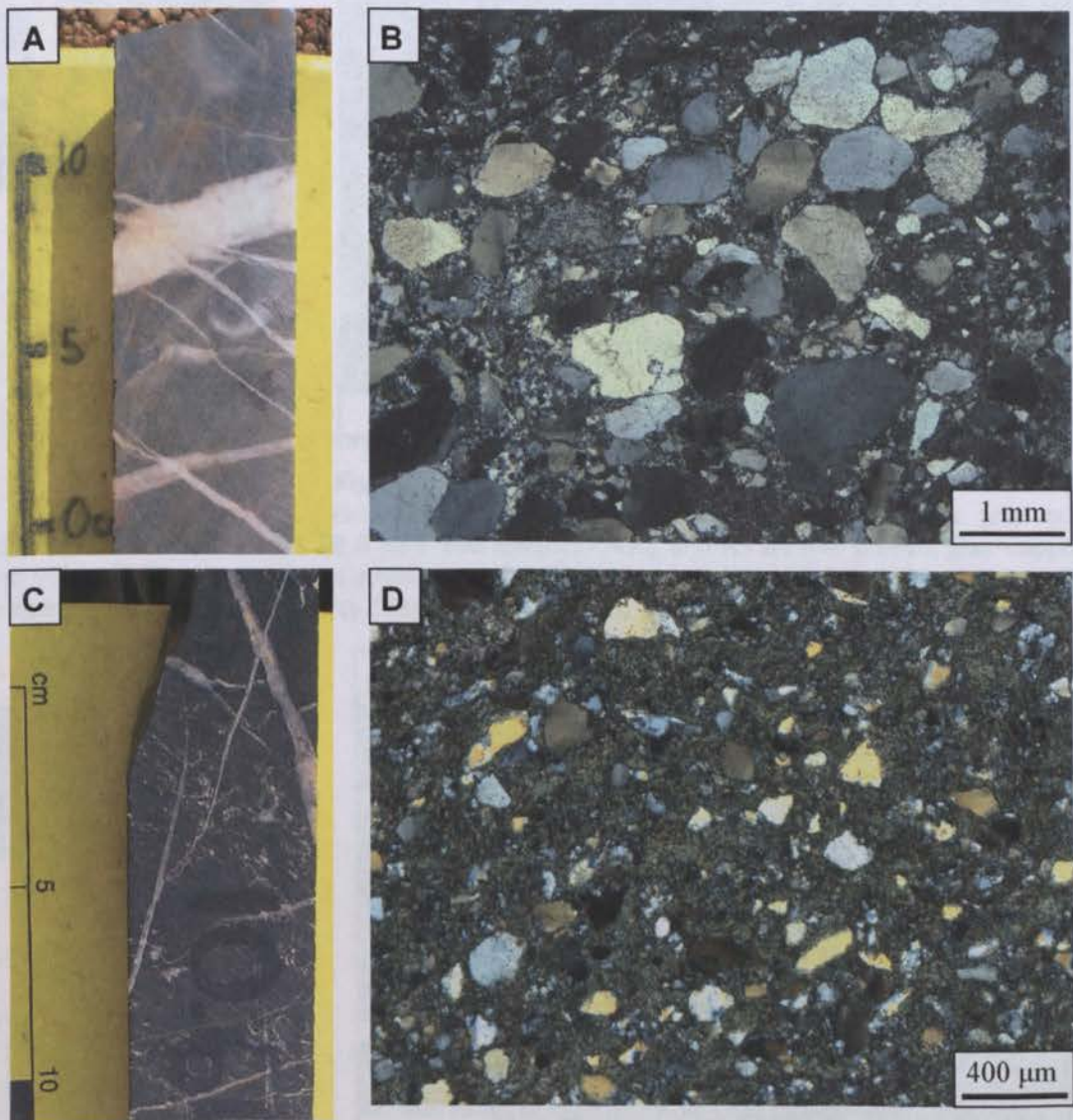


Fig. 3.9. Drill core photos and associated XPL images of the quartz-wacke units present at the Gara deposit. **A)** Weakly-tourmalinised rock associated with barren quartz veins (LOCP119, 434.8 m). **B)** A photomicrograph shows that the rock is composed dominantly of coarse-grained (500 μm to 2 mm) quartz. **C)** Dark grey-black tourmalinite sandstone (LOCP40, 261 m). This unit is associated with ankerite-quartz-pyrite mineralising veins (not shown here). **D)** Tourmalinites occur as finer-grained (<200 μm) sediments. Tourmaline occurs as an olive green mineral in XPL, which makes up a large portion of the rock (~60%).

3.3.4 Feldspar-rich sandstones

The Kofi Series also contains feldspar-rich sandstones as well as carbonate and quartz-bearing wackes. Grain-supported varieties classify as arkoses (90:10 to 80:20 clast-matrix ratio). These units have previously been termed grey quartzites; however, they contain equal proportions of quartz and feldspar. Arkoses are rather heterogeneous in composition often grading into feldspathic greywackes (30-35% matrix) or carbonate-rich sandstones (ankerite and dolomite cement up to 20%). Matrix-supported varieties (35:65 clast-matrix ratio) can be termed feldspathic greywackes. These sediments are more homogenous and argillaceous in composition compared to the arkoses. The composition of the arkoses and feldspathic greywackes is illustrated in Fig. 3.10. Thin millimetre-scale lenticular argillite interbeds are irregularly observed within these rocks.

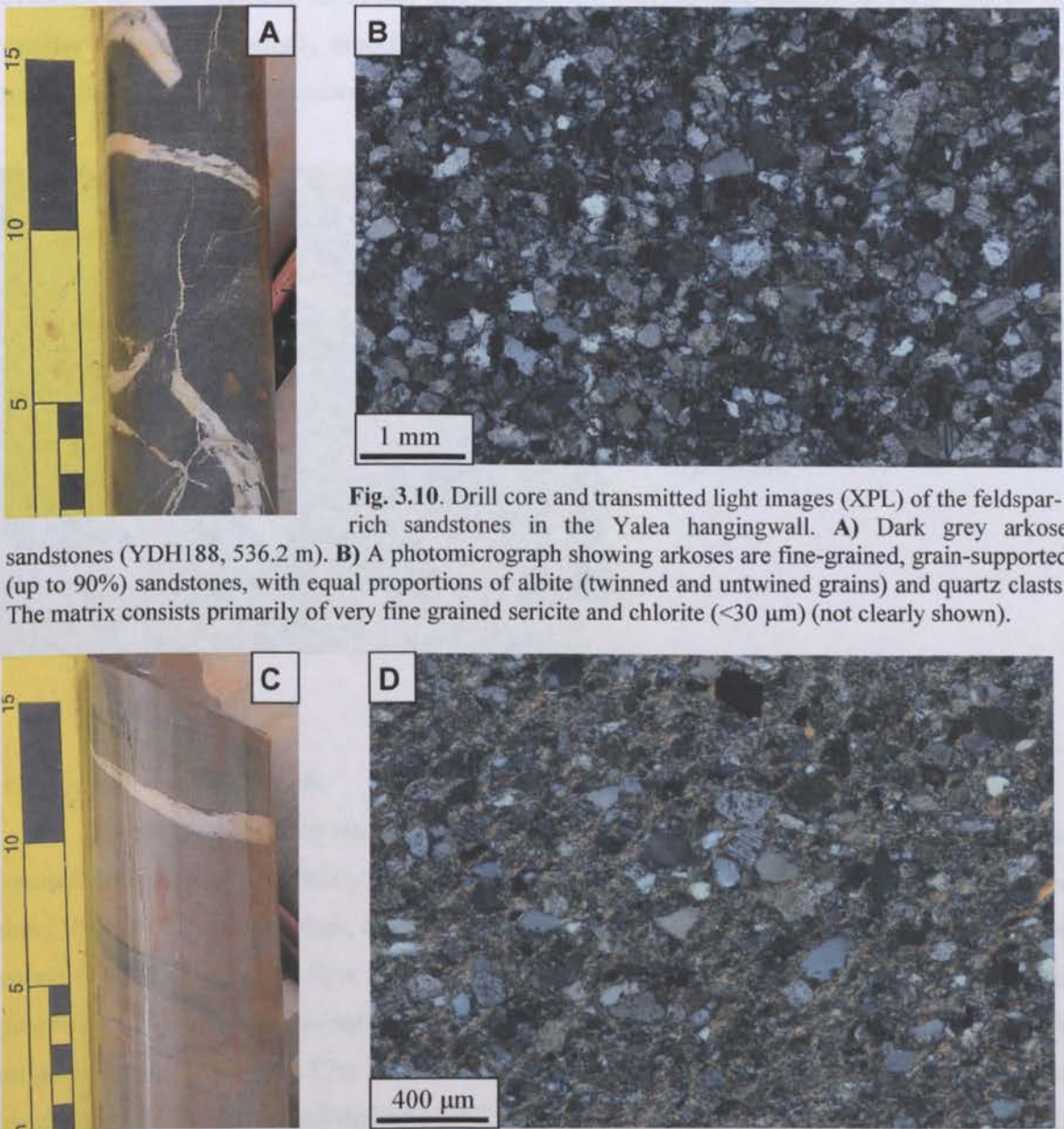


Fig. 3.10. Drill core and transmitted light images (XPL) of the feldspar-rich sandstones in the Yalea hangingwall. **A)** Dark grey arkose sandstones (YDH188, 536.2 m). **B)** A photomicrograph showing arkoses are fine-grained, grain-supported (up to 90%) sandstones, with equal proportions of albite (twinned and untwined grains) and quartz clasts. The matrix consists primarily of very fine grained sericite and chlorite (<30 µm) (not clearly shown).

Fig. 3.10. C) Light grey/green, massive feldspathic greywacke (YHD188, 215.2 m). **D)** Transmitted light image showing these sediments are fine-grained, matrix-supported sediments. The clast fraction consists of sub-rounded, very fine-to-fine sand sized (50 to 230 µm) quartz and albite (equal proportions) and an argillaceous matrix primarily of sericite, chlorite and minor quartz. This rock type shows moderate to strong schistosity, with the alignment of the matrix material and occasionally the clast fraction.

3.3.5 Hydrothermal-tectonic breccias

Breccia units are frequently seen along the Loulo shear zones and form as a result of multiple fluid events and deformation. These rocks contain clasts of all the sediment lithologies discussed above (heavily altered), as well as additional hydrothermal material (e.g. pink albite and tourmaline) (Fig. 3.11). The breccias are commonly matrix-supported (40:60 clast-matrix ratio) with sub-rounded to angular clasts between <1 cm to 10 cm in size (mainly <5 cm). These units are termed hydrothermal-tectonic breccias for several reasons: (1) *hydrothermal*- breccias contain large amounts of alteration material (high fluid movement caused some degree of hydraulic fracturing) and (2) *tectonic* - clasts are commonly stretched and aligned parallel to shear fabric; in many instances the development of cataclasites (progressive fracturing) occurs; and there is strong evidence for ultra-mylonite formation, where breccia fragments have been milled into smaller and smaller fragments. Tectonic brecciation is considered the most dominant process. Albite and tourmaline alteration is discussed in *chapter 5*.



Fig. 3.11. Field photograph of the hydrothermal-tectonic breccias from wall-rock at P-125. Clasts consist mainly of pink albite-altered argillaceous greywacke rock fragments and black, Fe-rich, tourmaline clasts. The matrix is composed of milled rock fragments with a tourmaline cement (multiple tourmaline alteration events occurred). In places, these units are host to mineralisation (e.g. Yalea North).

3.3.6 Minor intrusive rocks

Three types of minor intrusive rocks occur in the Kofi Series. **Birimian mafic dykes** are intermittently observed intruding wall-rock at both Gara and Yalea deposits (Fig. 3.3). They are thin (50 cm to 13 m thick), dark, discontinuous dykes (hard to correlate between neighbouring drill cores) (Fig. 3.12a), which form sharp contacts with the host sediments (no baked margins are observed). They are characterised by high degrees of deformation and metamorphism (pre to syn-orogenic intrusions) (Fig. 3.12c). The intensity of alteration makes primary compositions difficult to interpret. Least-altered and deformed dykes are saturated with respect to silica (<10% quartz) and classify as dolerites and Si-poor diorites. Intrusions are rich in plagioclase (up to 50%), biotite and/or hornblende (Fig. 3.12b). Mafic dykes crystallised from an oxidised melt (quartz-fayalite-magnetite buffered melt- QFM) with magnetite (~5%) often zoned with Zn-bearing chromite.

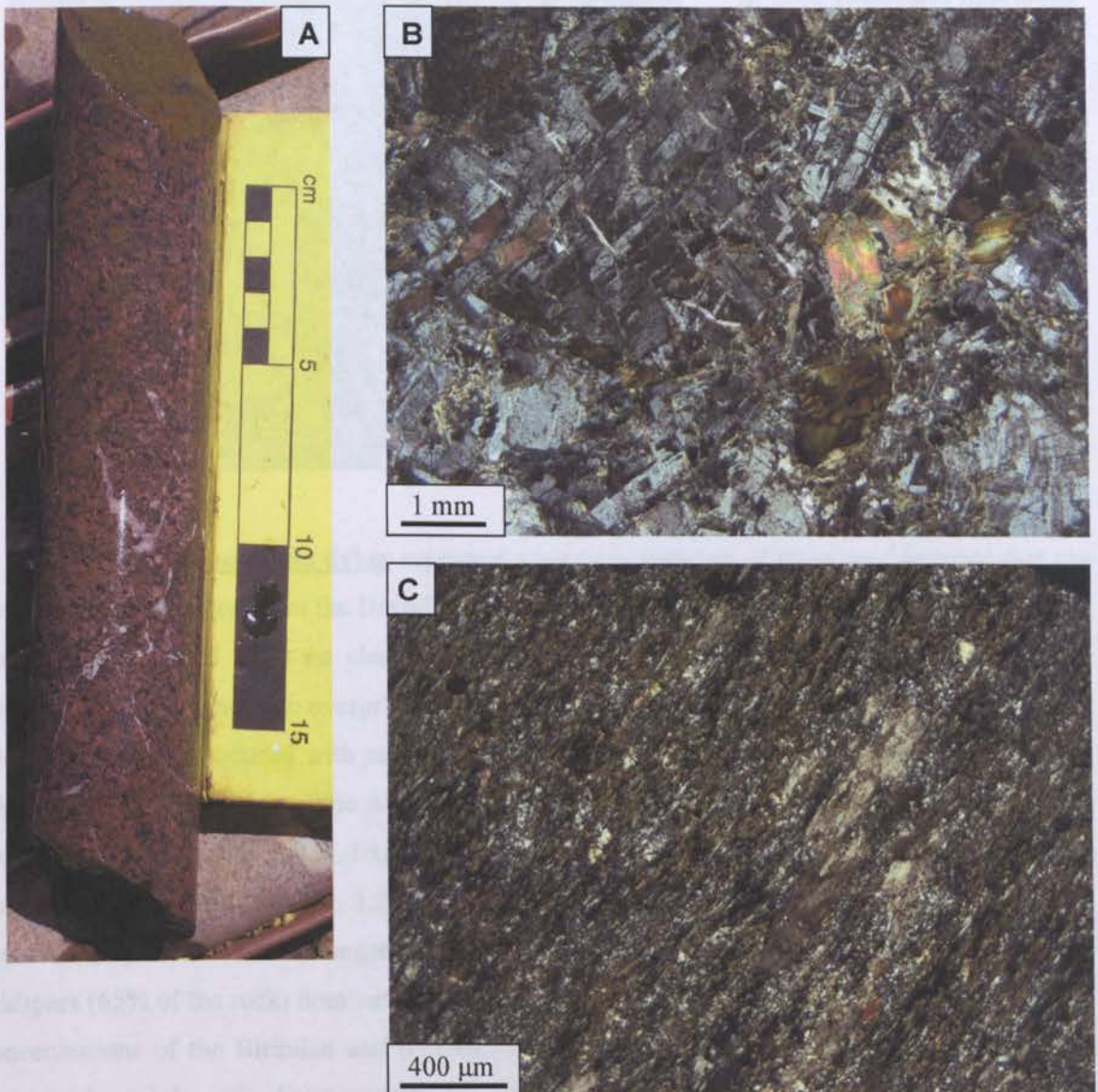


Fig. 3.12. Birimian mafic dykes cutting Kofi sediments. **A)** Drill core photo of less-altered mafic dyke with minor veining (LOCP124, 38 m). **B)** XPL image of A). The intrusion shows a phaneritic texture composed primarily of plagioclase (60%) and biotite (30%). **C)** XPL image of a Birimian dolerite schist showing strong chlorite (“green-schist”) replacement (green mineral; 30% of the rock) of biotite (brown mineral). The greenschist facies assemblage also consists of carbonate, which occurs as lenses parallel to the fabric. Magnetite (opaques) is associated with the mafic components (sample taken from LOCP120, 442.7 m).

Birimian felsic dykes are commonly spatially associated with mineralisation in the Loulo district. Porphyritic diorites and granodiorites are observed at P-129, Loulo-3, Goukoto, Gara (northern face of the open pit) and Yalea deposits. They are sub-vertical intrusions that are notably thicker than the mafic Birimian dykes (up to 130 m thick). Felsic dykes are composed of phenocrysts of plagioclase (partially to completely altered to albite) within a fine-grained quartz-albite-biotite matrix (Fig. 3.14). Accessory phases vary between intrusions; some are magnetite-rich (oxidised series), while others are ilmenite-pyrrhotite rich (reduced series).

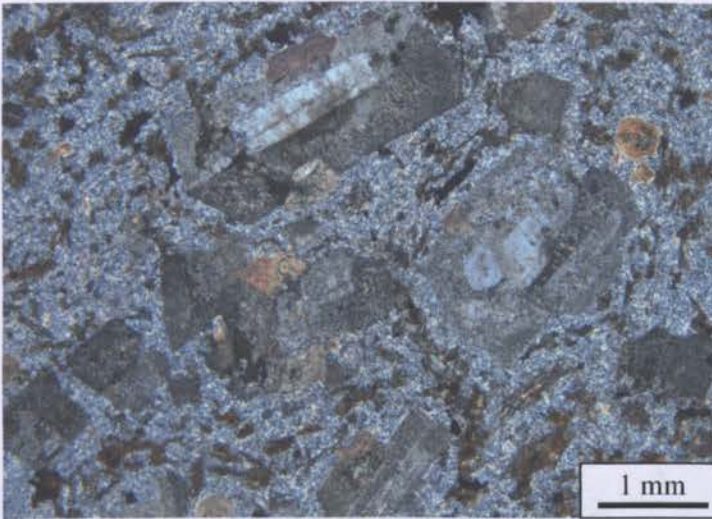


Fig. 3.13. Transmitted light image (XPL) of the P-129 porphyry dyke, showing a seriate texture (P129DH12, 179 m). The dyke is composed of blocky, rhombic and tabular phenocrysts (600 μm to 3.7 mm) of plagioclase (occasionally containing quartz cores) and a groundmass of fine-grained quartz, albite, biotite, chlorite and carbonate. Plagioclase is partially altered along its margins by albite.

Post-Birimian mafic dykes represent a young generation of dyke emplacement that can be clearly distinguished from the Birimian dykes. These dolerites are remarkably fresh (prominent ophitic textures) and show no clear evidence of being affected by the Eburnean orogeny (no deformation or metamorphic overprint) and related hydrothermal fluids (Fig. 3.14). They are likely Mesozoic in age, associated with partial crustal thinning on the edges of the West African Craton (WAC) during the opening of the Atlantic. They are more continuous than the Birimian dykes and vary in thickness from 2-200 m. Examples include the E-W trending dyke cross cutting sediments immediately north of Gara (Fig. 3.2) and the sub-horizontal intrusions cutting the Gara and Yalea orezones (Fig. 3.3). These younger dykes are more Ca-rich than Birimian intrusive units, with feldspars (65% of the rock) dominated by bytownite (71 to 79 An%). Fig. 3.15 shows the feldspar concentrations of the Birimian and post-Birimian dykes. The mafic component of the dykes is composed mainly of clinopyroxene (25-30%) and rare orthopyroxenes (<5%). Opaque assemblages are rich in ilmenite (oxidised melt), which tends to rim clinopyroxenes.

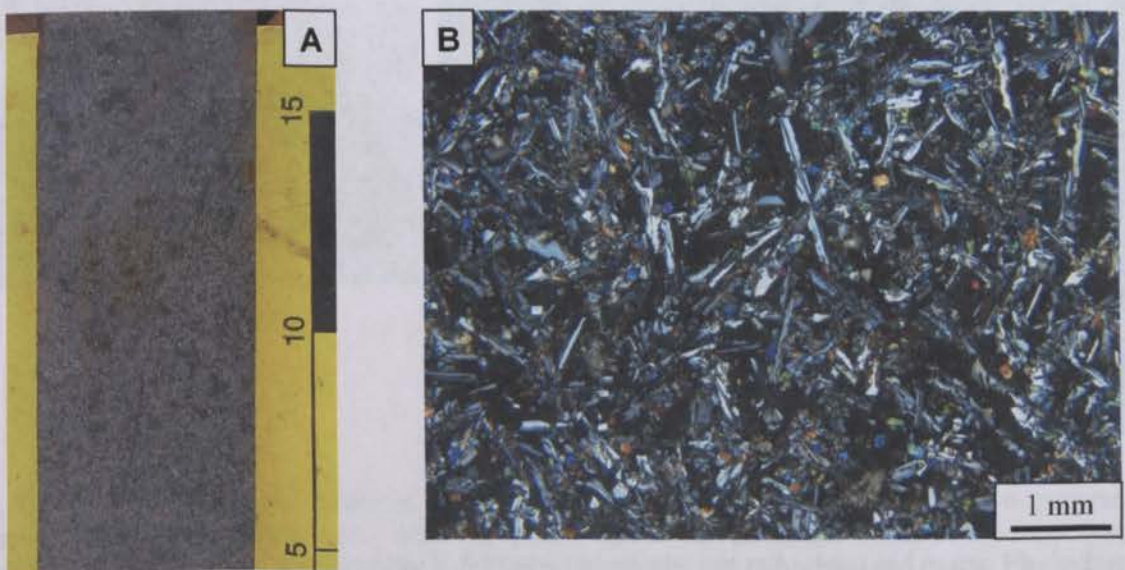


Fig. 3.14. Mesozoic mafic dyke. **A)** Drill core photo (YDH187, 521.8m). **B)** An XPL image of A). The dyke shows strong ophitic textures with plagioclase (bytownite) laths enclosed by anhedral pyroxenes (mainly clinopyroxene).

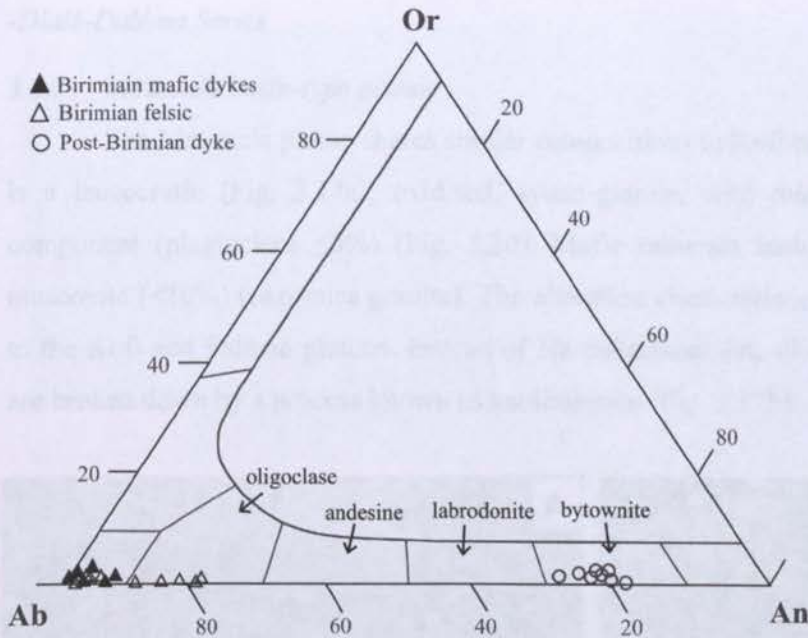


Fig. 3.15. A feldspar ternary plot for Birimian and post-Birimian dykes, showing the dominance of the Ab-An series. Post-Birimian feldspars plot away from the Birimian feldspars into the Ca-rich fields. This emphasises the high Na-alteration of the Birimian dykes. Data determined by Energy Dispersive X-ray Spectroscopy on the Scanning Electron Microscope (SEM-EDS) (methodology given in the appendices in section A-1).

3.3.7 Kofi basin-type plutons

The Yatea granite and the small granite stock just to the NE of Gara are pink, medium-grained (1-3 mm crystal size), K-rich intrusions. They classify as monzogranites, where orthoclase and microcline (45%) are dominant over plagioclase (up to 25%) (Fig. 3.16; Fig. 3.20a). The feldspar compositions of these plutons are shown in Fig. 3.20b. The mafic assemblage of the intrusions is predominated by biotite (<10%), with accessory phases including magnetite (oxidised melt), monazite and sphene. The plutons are metamorphosed to a greenschist facies (biotite → chlorite + epidote) and show evidence of Na metasomatism (discussed in section 3.4.1).

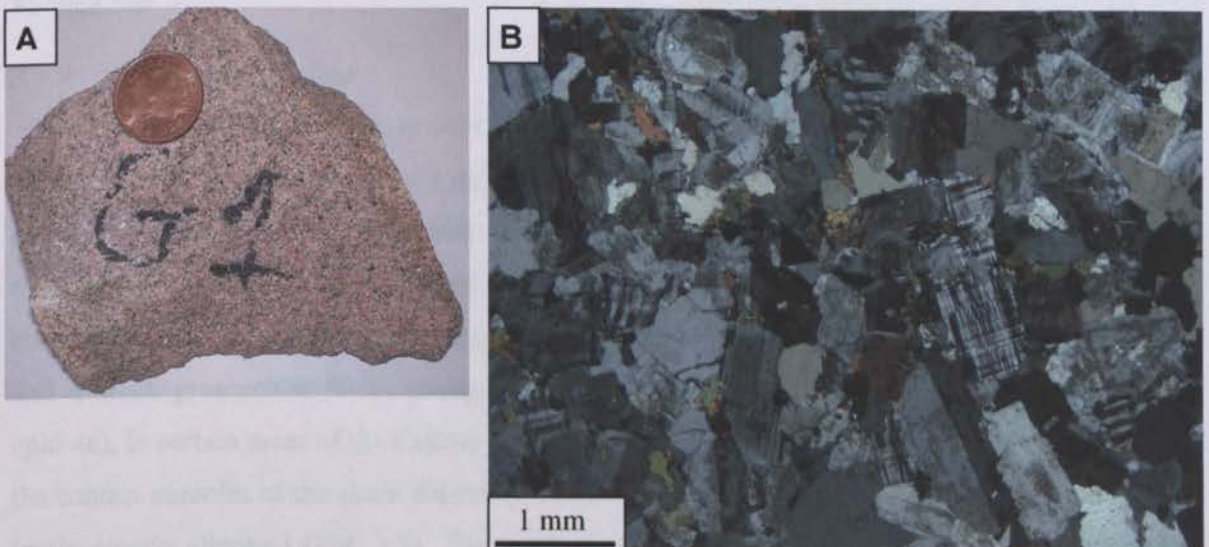


Fig. 3.16. The Kofi basin-type intrusions. **A)** Hand specimen of the pink homogeneous Yatea monzogranite (sample PTG1 in geochemical study- section 3.4). **B)** Transmitted light image (XPL) of the same sample showing a felsic component dominated by K-feldspars (microcline and orthoclase) and quartz. Plagioclase is rarer and usually altered showing a speckled texture (top right). The mafic component occupies <10% of the rock and is composed primarily of biotite (small minerals with green/brown interference colours).

*-Dialé-Daléma Series*3.3.8 *Moussala basin-type pluton*

The Moussala pluton shares similar compositions to Kofi basin-type intrusions. The pluton is a leucocratic (Fig. 3.17a), oxidised, syeno-granite, with microcline the principal feldspar component (plagioclase $\leq 5\%$) (Fig. 3.20). Mafic minerals include biotite ($>90\%$) and minor muscovite ($<10\%$) (two-mica granite). The alteration characteristics of the Moussala pluton differ to the Kofi and Falémé plutons. Instead of Na metasomatism, silicates (K-feldspars and biotites) are broken down by a process known as kaolinisation (Fig. 3.17b).

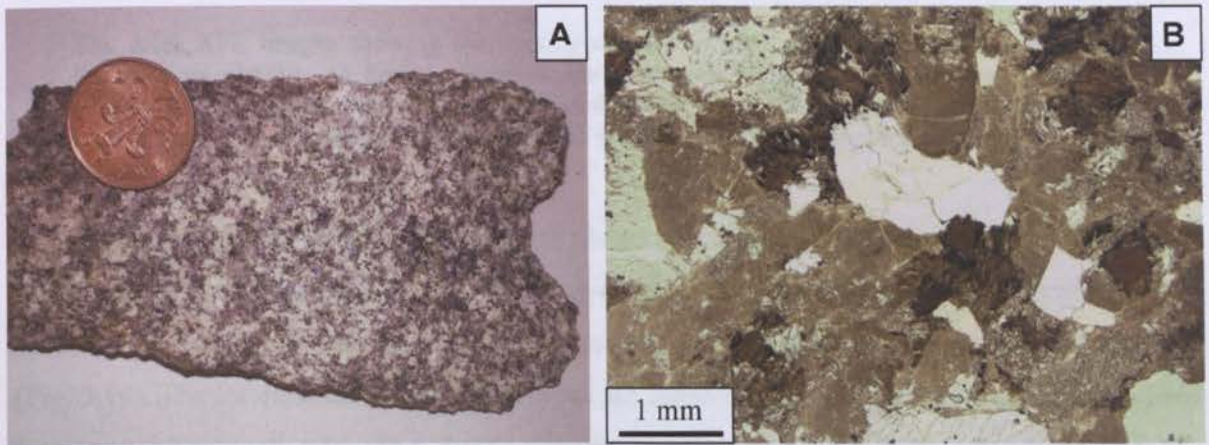


Fig. 3.17. The Moussala syeno-granite. **A)** Hand-specimen of sample R39 in geochemical study- section 3.4). **B)** Transmitted light image (PPL) of A) showing the highly-altered nature of the Moussala pluton. K is extremely mobile and is leached (along with Fe & Mg) from biotite and K-feldspars to leave behind kaolin (the light brown material). Biotites (dark brown minerals) are commonly altered along cleavage planes.

*Falémé belt*3.3.9 *Balangouma plutons*

Within the Falémé belt, numerous isolated outcrops of the Balangouma plutons exist in the western and northern parts of the Loulo property. Due to poor exposure and the absence of any drill core from this part of the permit, the exact size and shape of these plutons and their contact relationships with the volcanic and sedimentary host rocks are unclear. The plutons are characterised by variable degrees of hydrothermal alteration, most notably albitisation (Fig. 3.18), and a weak greenschist facies overprint (biotite + hornblende + clinopyroxene \rightarrow chlorite + epidote). In certain areas of the Falémé belt (preferentially along the margin with the SMSZ and in the contact aureoles of the skarn deposits), albite can be the dominant component of the intrusions (metasomatic albitites) (Fig. 3.2). The northern extent of the Falémé belt has been cut by the SMSZ. This is clearly observed in the Clib permit where intrusive rocks are strongly sheared showing inequigranular and strong foliated textures, with the alignment of finer-grained mafic minerals around felsic phenocrysts. Magmatic textures prevail in others areas of the Falémé belt.

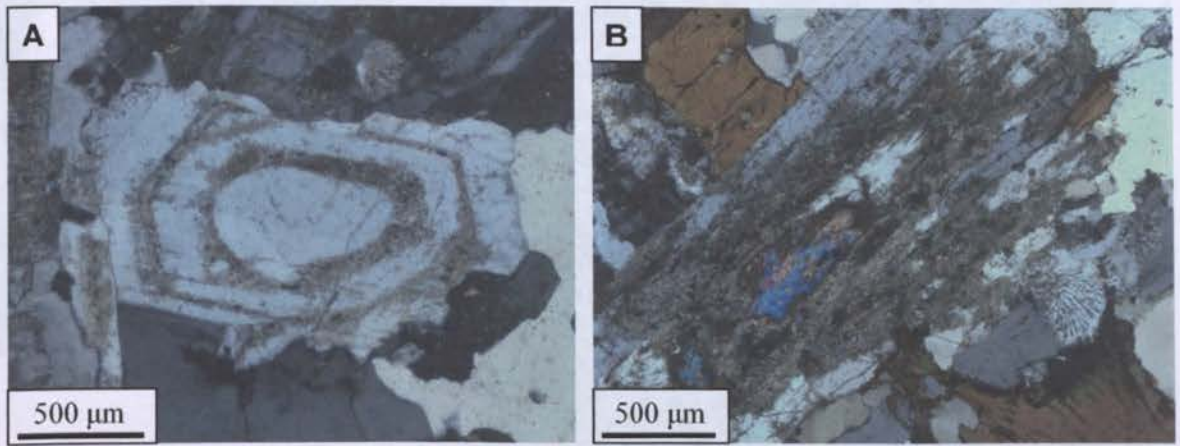


Fig. 3.18. XPL images showing the varying degrees of albitisation of plagioclase within the Balangouma plutons. **A)** Partial alteration along zonation boundaries. **B)** Pervasive alteration occasionally associated with sericite (high birefringence mineral in the centre of image). Images taken from sample R5 on the western border of the Bambadji permit (Fig. 3.2).

The compositions of the Balangouma plutons are notably different to the Kofi plutons and Moussala granite. Three intrusive rock types are observed: (1) granodiorites rich in hornblende; (2) biotite + hornblende-bearing quartz-diorites; and (3) rare clinopyroxene (cpx)-bearing tonalities (Fig. 3.19). The composition of these rock types are shown in Fig. 3.20. All rock-types crystallised from an oxidised melt, with the common occurrence of anhedral Cr ± V bearing magnetite (~5% of the rocks).

1. **Granodiorites** are phaneritic intrusions (crystal size between 0.5 to 2 mm) showing prominent hypidiomorphic textures away from the SMSZ. The least-altered rocks are plagioclase-rich (40-45%), with quartz and alkali-feldspar contents of 15-25% and 15%, respectively (Fig. 3.19a). Hornblende (300-500 µm) occurs as the predominant mafic mineral phase (~15-20%). Accessory phases include sphene, monazite, pyrite, zircon, gersdorffite and extremely rare chalcopyrite.

2. **Quartz-diorites** are darker and generally coarser (up to 6 mm) than more felsic varieties, characterised by more inequigranular textures. They are also plagioclase rich (45-55%), with lower concentrations of quartz (~10%) and minor alkali feldspars (mainly microcline, ≤5%) (Fig. 3.19b). The mafic component of the quartz-diorites (35%) is rich in biotite (up to 2 mm) and hornblende (300-500 µm) (former more dominant) and minor quantities of clinopyroxene (<5%).

3. **Tonalites** outcrop in the central regions of the Bambadji permit and exist as leucocratic, aphanitic (crystals <1 mm) intrusive rocks. The feldspar component of these rocks is predominately plagioclase (altered to albite), with very limited K-feldspar (≤ 1%). Quartz constituents are up to 35%. The mafic assemblage is largely dominated by sub-rounded clinopyroxene (augite; 5-10% of the rock), with minor hornblende. Scheelite represents a common accessory phase. Hand specimen and thin section images of this rock type is shown in Fig. 3.19c.

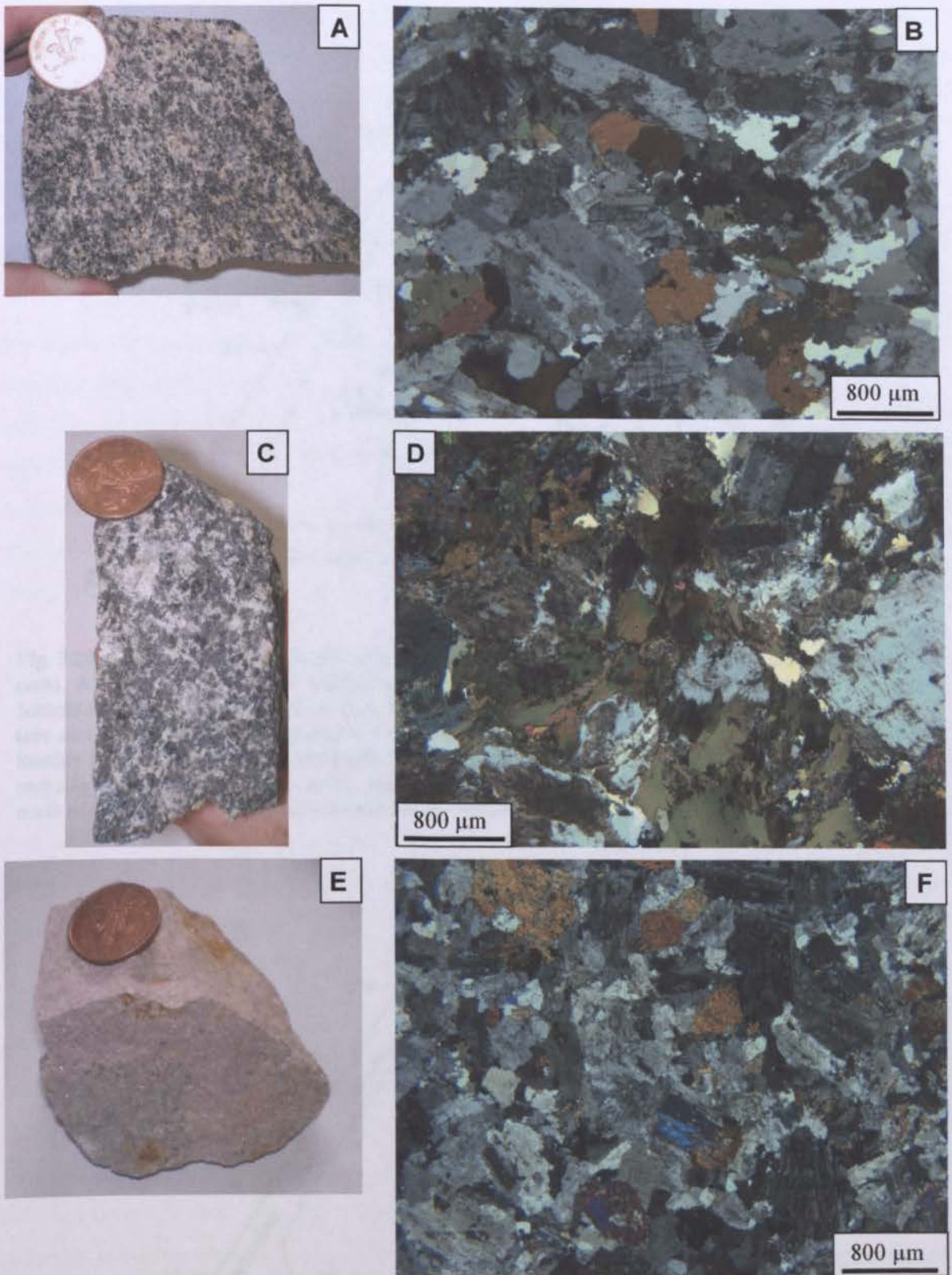


Fig. 3.19. Hand specimens and photomicrographs (XPL) showing the composition of the Balangouma plutons. **A)** Granodiorite (sample LR5). **B)** Transmitted light image of A) showing a felsic component dominated by plagioclase (simple twinned minerals). Quartz is the second dominant mineral (grains showing grey/white interference colours on the right side of image), plus minor K-feldspar (cross hatched microclines). Mafic minerals (<20%) are hornblende (brown-green minerals). **C)** Quartz-diorite (sample R37). **D)** Transmitted light image of C) showing the rock is composed largely of plagioclase and biotite (green mineral in the centre and bottom of picture). Altered plagioclase is seen in the bottom left. Hornblende is less dominant than biotite, occurring as smaller (300-500 μm) equant grains (aggregates of brown-green minerals seen in top left). **E)** Cpx-bearing leucocratic tonalite (sample R8). **F)** Transmitted light image of E) showing a rock composed mainly of plagioclase and quartz, with anhedral augite (high birefringence minerals).

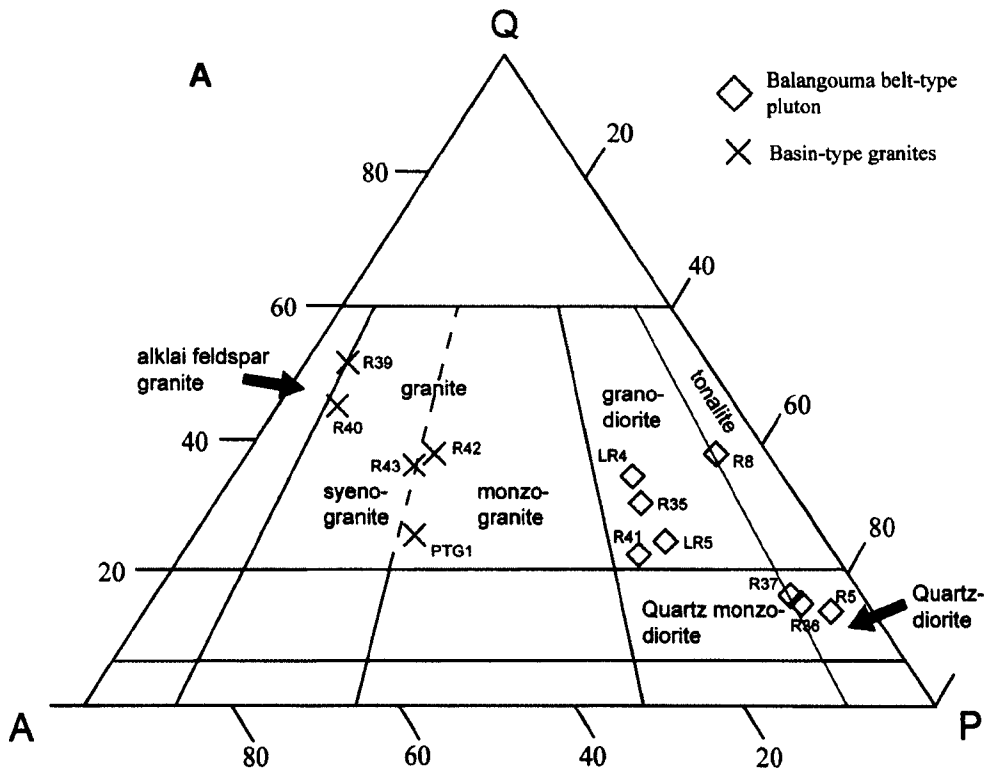


Fig. 3.20. Mineralogical classification of major Birimian intrusive rocks at Loulo and the surrounding areas. **A)** QAPF diagram (the feldspathoid triangle is omitted here) based on mineral estimates. Sample numbers are given to show correlation between rock classifications based on geochemistry (see section 3.4.2). The Balangouma belt-type plutons plots into the granodiorite, quartz-diorite and tonalite fields, while the Kofi and Moussala basin-type plutons are more Si & K-rich, falling into the monzogranite and syenogranite fields. Kofi Series- Yatea pluton (PTG1) and isolated outcrop just north of Gara (R42 & R43); Dialé-Daléma Series- Moussala pluton (R39 & R40).

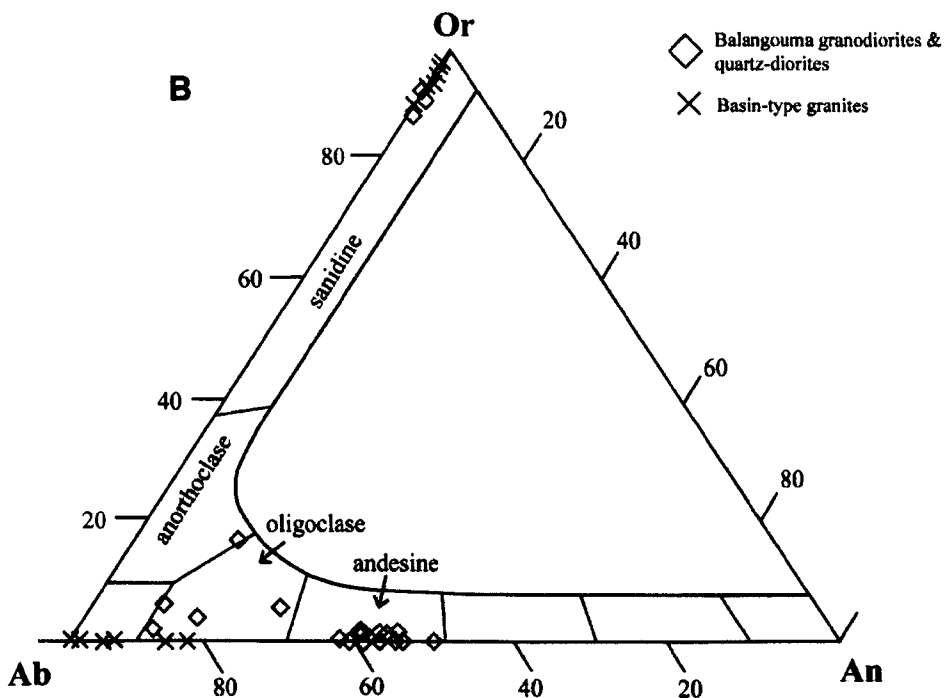


Fig. 3.20 cont. B). Ternary feldspar plot showing the mineral compositions of the major intrusive rocks (mineral chemistries determined by SEM-EDS analysis). Balangouma plutons are dominated by plagioclase feldspars (Ab-An series), mainly andesine; while the Kofi and Moussala granites are composed largely of alkali feldspars (Ab-Or series).

The iron skarn deposits, situated along the margins of the intrusions are intruded by a late generation of felsic magmatism. Thin (<10 m) dark, finely crystalline, porphyritic dioritic dykes show similar compositions to the Balangouma plutons, with a dominance of plagioclase over K-feldspar (ratio 10:1). These dykes contain hornblende, biotite and clinopyroxene (the latter more dominant), all altered to chlorite.

3.4 Lithochemochemistry

In order to better constrain the composition of the various igneous and sedimentary rocks present in the Loulo area, a geochemical study was carried out on the major rock types (59 samples) from across the permit (to add to petrography and field data). The sample suite were analysed on the ICP-AES (major and minor elements) and ICP-MS (trace and REE data) instruments at Kingston University. Methodologies and detection limits are given in the appendices (*section A-2*). As well as their use in rock classifications, these data can also help to distinguish the tectonic setting for the various rock types and data can be compared to tectonic and crustal growth models for other parts of the Birimian crust.

3.4.1 Sampling and data integrity

The locations of the intrusive rock samples collected in the field are shown in Fig. 3.2. Other samples collected for this geochemical study are from drill core, open pits or underground shafts. Basin-type granitoid samples include the two Kofi plutons (Yatea granite- PTG1; granite outcrop NE of Gara- R42 & R43) and the Moussala granite (R39 & R40). Eight suitable samples (least-altered) of the Balangouma plutons were used in this section from different outcrops in the Bambadji-Daléma permits (R5 & R8), along the northwest border of the Loulo permit (R41, LR4 & LR5), and from the Clib permit to the north (R35, R36 & R37). Two further samples (R21 & R25) were collected from felsic intrusions that transect the Karakaena iron ore deposit. A variety of minor intrusions were also analysed, including three felsic porphyritic dykes from the north face of the Gara open pit (GP1), from P-129 (P129.10) and Yalea underground (UYP1), and four mafic dykes from Gara drill core (LD9, LD14 & LD23) and Yalea underground (UYP2). A sample of the post-Birimian dykes was also collected from Yalea wall-rock (YD36). Sediments collected from Gara and Yalea wall-rock were also analysed (least hydrothermally altered samples). Although the compositions of the quartz-wackes are reported, limited interpretations were made of these data due to the intense alteration associated with this rock type (toumalinisation). The major, minor and REE compositions of the Birimian intrusive rocks and sediments are presented in the appendices (Table A-5).

Element mobility

Petrographic data shows the Birimian intrusive rocks have undergone variable degrees of Na ± K hydrothermal alteration, as well as regional greenschist facies metamorphism.

Geochemistry also shows clear evidence of alteration: (1) the majority of the intrusive samples plot in the alkaline field on the TAS diagram (Fig. 3.21a); (2) a cluster of samples fall within the trondhjemite field (most Na-altered samples) on the Ab-An-Or plot (Fig. 3.21b); and (3) the scattered pattern of large ion lithophile elements (mobile elements) on the MORB-normalised trace element spider diagrams (Fig. 3.23). Classification of the intrusive rocks using alkali elements is done with caution. Despite the Na-K alteration, original mineral assemblages are still preserved in most samples. The albitites observed at Bambadji were not analysed in this study.

The Kofi sediments have undergone similar styles of alteration to the intrusive rocks. Sediment samples show pervasive greenschist facies metamorphism (sericitisation and chloritisation). All samples show varying degrees of albitisation, carbonate and silica alteration. Calculating the degree of palaeoweathering and metasomatism of these samples using the Chemical Index of Alteration (CIA) (Nesbitt & Young, 1982) and the Plagioclase Index of Alteration (PIA) (Fedo *et al.*, 1995) is extremely difficult due to their high carbonate contents. These indices use CaO values within the silicate fraction and it will be near impossible to correct for this as each sample contains variable, and high, abundances of calcite, ankerite and dolomite.

3.4.2 Results

3.4.2.1 Intrusive rocks

3.4.2.1.1 Major element data

Basin-type granitoids

The basin-type granitoids are more silica-rich (70-77% SiO₂) than the Falémé Balangouma plutons (Fig. 3.21a, b). Granites are K-rich (3-5.5% K₂O), peraluminous (A/CNK ratios of ~1.1) and calc-alkaline in composition (Fig. 3.21c), with lower Na and Ca contents than the Balangouma plutons. The Moussala pluton is extremely peraluminous (A/CNK ratios of 3 to 4) due to the intense alteration of this intrusion. Using the diagram of Chappell & White (1974) (Fig. 3.21d), the least-altered samples plot along the boundary between I- and S-type granitoids.

Balangouma plutons

The Balangouma plutons are classified as Na-rich (4-8.6% Na₂O), calc-alkaline, I-type intrusions (Fig. 3.21c,d). The high Na contents are partially down to the high degrees of albitisation in some samples. However, petrographic data shows the dominance of Ab-An series over the Ab-Or feldspar series. They plot in the syeno-diorite (quartz-diorite samples) and granodiorite fields on the TAS diagram of Cox *et al.* (1979) (Fig. 3.21a), with a few samples plotting into the granite field (e.g. cpx-bearing tonalite sample- R8). Using normative plots of Ab-An-Or (Barker, 1979) (Fig. 3.21b), these rocks have a TTG composition (granodiorites, tonalities and trondhjemites). However, the 'trondhjemite' samples are the most pervasive Na-altered

samples and they represent original granodiorites-tonalites-diorites. The Balangouma pluton is generally metaluminous in composition (A/CNK ratios of 0.65 to 1). One sample from the Bambadji permit (R5) shows a peraluminous composition (A/CNK ratios of 1.25).

Fig. 3.21. Geochemical classification and nomenclature for the major Birimian intrusive rocks within and around the Loulo property. **A)** TAS diagram of Cox et al. (1979) adapted by Wilson (1989). Dotted line subdivides the alkalic rocks from subalkalic rocks. **B)** Classification of granitic rocks according to their normative (CIPW) An-Ab-Or composition after Barker (1979). **C)** AFM diagram (Irvine & Baragar, 1971; Barker & Arth, 1976). Fields: CA = calc-alkaline, T = tholeiite. **D)** Na₂O/K₂O diagram to distinguish I- and S-type granitoids (boundary from Chappell & White, 1974).

Minor intrusions

Geochemical classification of the minor intrusions is shown in Fig. 3.22. The P-129 felsic dyke is a Na-rich (5.4% Na₂O), calc-alkaline, I-type granodiorite, with similar compositions to the Balangouma belt-type pluton. Other Birimian felsic dykes classify as calc-alkaline, Si-rich, syenodiorites. Birimian mafic dykes include calc-alkaline diorites and dolerites, with Si contents between 48-55 wt.% SiO₂. These Birimian dykes are clearly distinguished from the post-Birimian dolerite dyke on the AFM diagram (Irvine & Baragar, 1971; Barker & Arth, 1976), where the younger dyke generation plots into the tholeiite field (Fig. 3.22b). The post-Birimian dyke plots well into the sub-alkaline field on the TAS diagram (Fig. 3.22a) compared to the Birimian dykes, which plot in the alkaline field or along the alkaline-sub-alkaline boundary, representing lower degrees of alteration of the former.

Fig. 3.22. Geochemical classification and nomenclature for minor Birimian intrusive rocks within and around the Loulo property. **A)** TAS diagram of Cox *et al.* (1979) adapted by Wilson (1989). Dotted line subdivides the alkalic rocks from subalkalic rocks. **B)** AFM diagram (Irvine & Baragar, 1971; Barker & Arth, 1976). Fields: CA = calc-alkaline, T = tholeiite.

3.4.2.1.2 Trace and REE patterns

Trace element concentrations for the intrusive rock samples are normalised to Mid-Ocean Ridge Basalts (MORB) (values from Pearce, 1983), while REE's are normalised to Chondrite (values from Sun & McDounough, 1989). Trace element plots presented in Fig. 3.23 show similar patterns for all intrusive rock types, with enrichment of large ion lithophile elements (LILE; K, Rb, Ba, Th) relative to high field strength elements (HFSE; Ta, Nb, Ce, Hf, Zr, Sm, Y, Yb). On average, LILE enrichment is ten orders of magnitude higher compared to MORB, with Rb concentrations reaching up to a hundred times greater in basin-type granites. Basin-type granites generally have more fractionated patterns ($K_2O/Yb_{(N)}$ of 21-75 and $Ta/Yb_{(N)}$ of 85-267) compared to Balangouma samples ($K_2O/Yb_{(N)}$ of 2-57 and $Ta/Yb_{(N)}$ of 5-20). Most rocks show marked negative Nb anomalies, with high $Ce/Nb_{(N)}$ ratios mainly between 1 to 5.3. Tantalum depletions are also seen in some samples (especially the minor intrusions). Also, all studied samples show minor depletions in Hf and Zr relative to MORB.

Chondrite-normalised REE patterns (Fig. 3.24) are also similar for all rock types. They are fractionated with a clear negative slope, showing strong enrichment in light rare earth elements (LREE) relative to heavy rare earth elements (HREE). This fractionation is greater in more felsic rocks such as the basin-type granitoids ($La/Lu_{(N)}$ ratios of 4-54, mean of 32) compared to the Balangouma quartz-diorites and granodiorites, and Kofi mafic dykes ($La/Lu_{(N)}$ of 4-20, mean of 12). Minor felsic dykes that intrude the Karakaena iron ore deposit (samples R21 & R25) show slightly different REE trends with flat LREE patterns (Fig. 3.24a). The Si-rich basin-type granitoids show stronger negative Eu anomalies (Eu/Eu^* ratio of 0.3 to 0.85, mean of 0.57) compared to the Balangouma and minor intrusive rocks (Eu/Eu^* ratios of 0.75 to 1, mean of 0.85), implying limited plagioclase is present in the former (Taylor & McLennan, 1985). This is consistent with petrographic studies, which show feldspar components in the basin-type granites are dominated by K-feldspar. Total REE content is extremely variable (25-250 $\sum REE$), but on average REE concentrations increase towards more mafic-rich rocks.

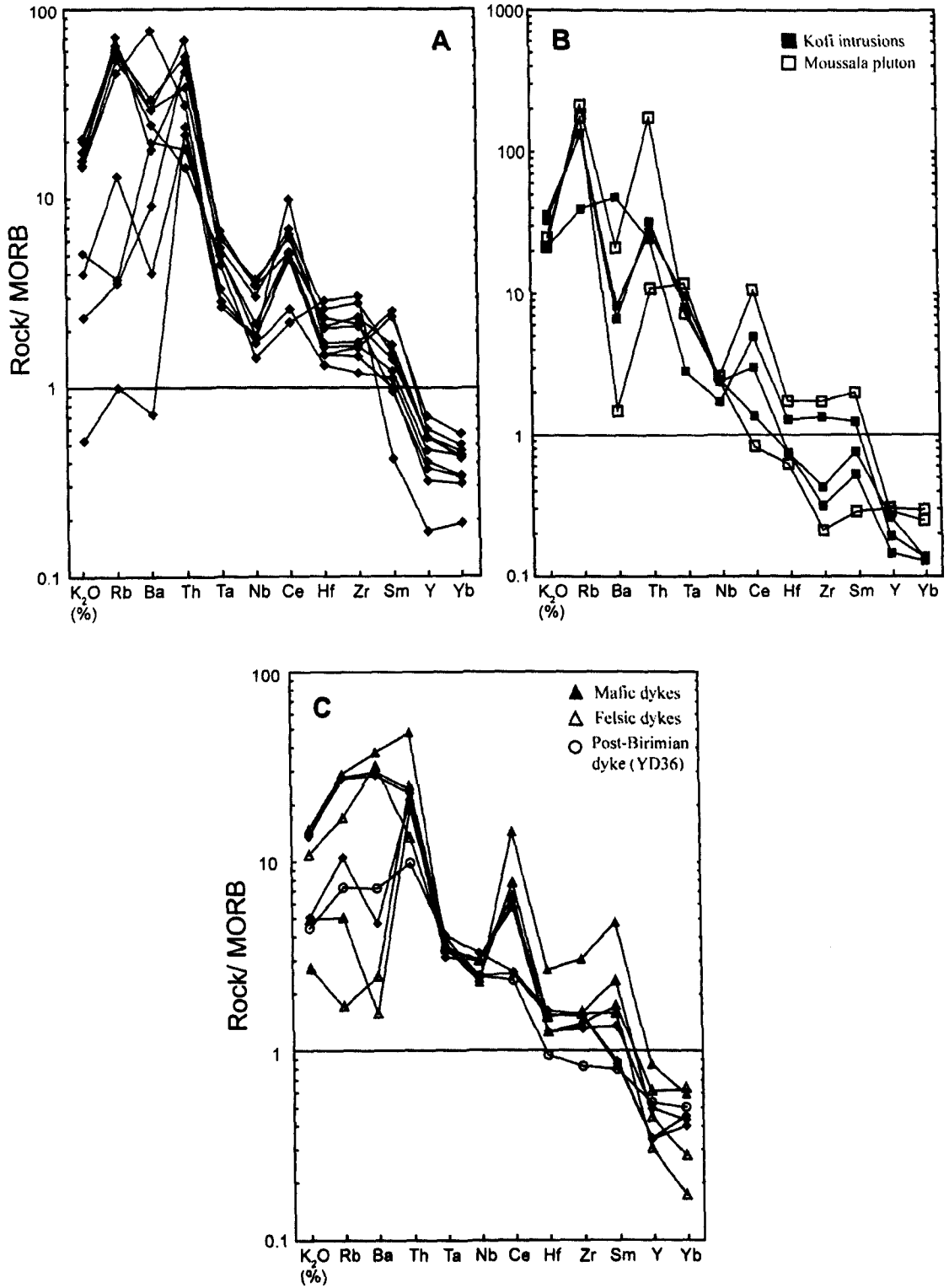


Fig. 3.23. MORB-normalised trace element distribution patterns for the Loulo intrusive rocks. **A)** Balangouma plutons. **B)** Basin-type granitoids. **C)** Birimian and Post-Birimian dykes. The scattered LILE pattern is indicative of alteration. MORB-normalised values from Pearce (1983).

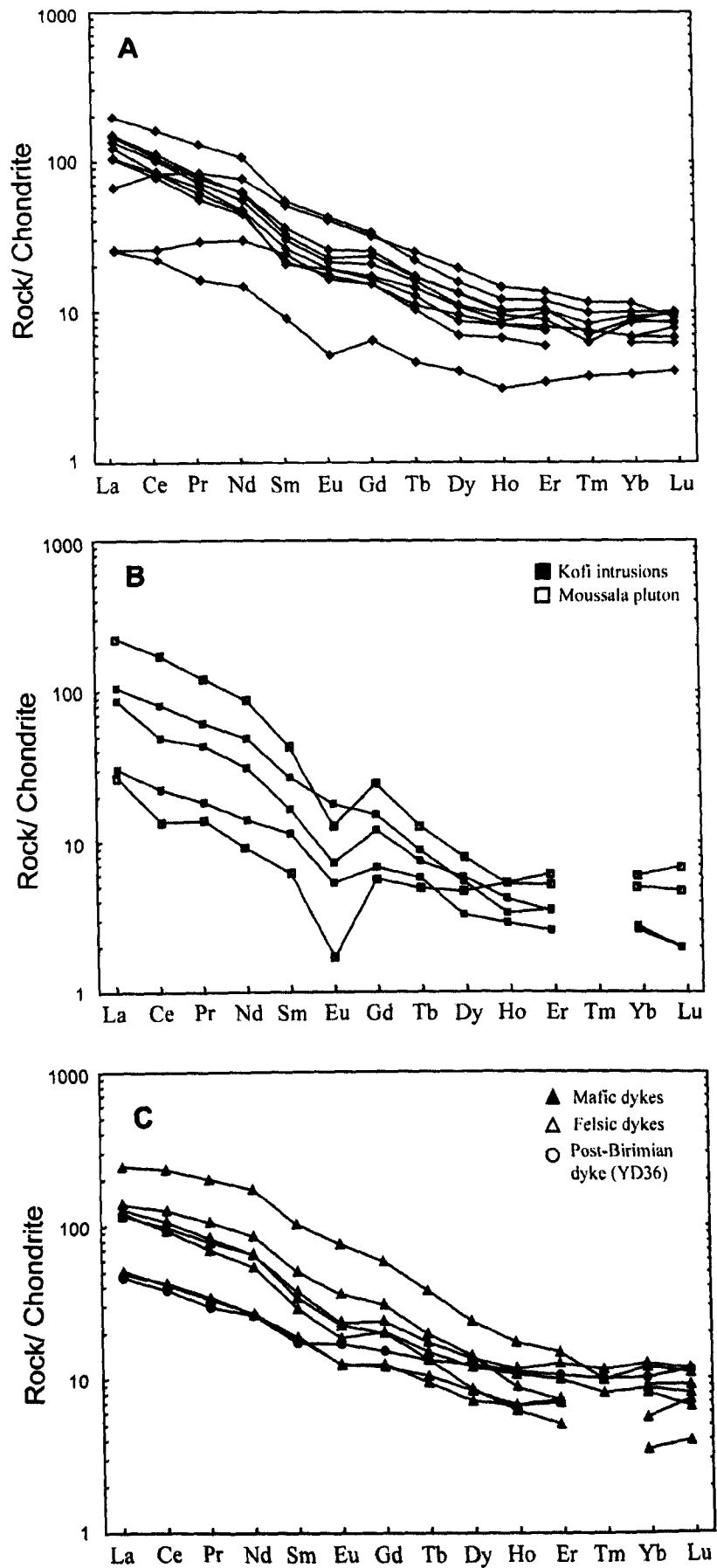


Fig. 3.24. Chondrite-normalised REE patterns for the Loulo intrusive rocks. A) Balangouma plutons. B) Basin-type granitoids. C) Mafic/felsic dykes. Chondrite values from Sun & McDonough (1989).

3.4.2.2 Kofi sediments

3.4.2.2.1 Major element data

The quartz-wacke and tourmalinite units are the most Si-rich sediments in the Kofi Series, with SiO_2 contents of 77-88% and 72-74% respectively. These sediments are depleted in alkali elements compared to other rock units ($\text{Na}_2\text{O}+\text{K}_2\text{O} < 3\%$). The remainder of the quartz-wackes and tourmalinites are composed primarily of Al, Fe and Mg, which are accounted for by the widespread tourmaline cement. Limited interpretations are made in the following sections on the major, minor and trace element data of these rocks due to high degrees of tourmaline alteration.

The various types of greywacke sediments and arkoses are plotted on the Herron (1988) diagram (Fig. 3.25). The schistose argillaceous greywackes and feldspathic greywackes plot in a tight cluster in the narrow greywacke field, with the former extending into the shale field. The argillaceous greywackes contain lower and more variable SiO_2 contents (45-59%) than feldspathic greywackes (57-59%). Both greywacke units contain high CaO contents (5-13%, mainly between 6-8%) reflecting the high concentrations of carbonate cement within these rocks. The more clastic-rich arenaceous sediments (termed arkoses during petrographic studies) plot over a wide range on the Herron diagram, falling mainly in the arkose field but also into the wacke and Fe-sand fields. These sediments also contain variable CaO contents between 0.8-7.5%. The heterogeneous nature to this rock type was also observed during petrographic studies, where it is evident that the sediment grades into greywackes of varying composition.

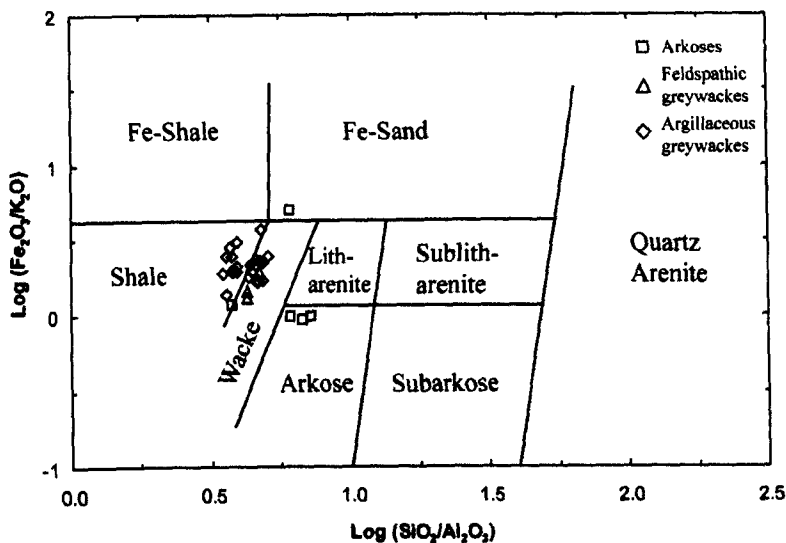


Fig. 3.25. Classification of the Kofi clastic sediments according to the Herron diagram (Herron, 1988).

Gara wall-rock carbonates are composed predominately of calcite, with low FeO-MgO contents (<3%), and contain high concentrations of Sr (1400-3000 ppm) and Zn (800-1100 ppm). Carbonate units at Yalea are dolomitised with similar FeO concentrations (1 to 1.6%) and higher MgO contents (1.6 to 19.5%). The high silicate fraction present in these rocks is shown by SiO_2 contents between 4 and 38% (mainly <16%) and Al_2O_3 contents between 1-10% (mainly <5%).

3.4.2.2.2 Trace and REE data

Trace and REE distribution patterns are similar for all the analysed sediments. The trace element data are normalised to MORB for comparison with the intrusion data shown in section 3.4.2.1.2. All rock types show similar patterns to the least-altered Birimian intrusive rocks, with enrichment in LILE and depletion in HFSE (Fig. 3.26), with Ta/Yb ratios of 4.5 to 10 closely matching quartz-diorites and granodiorites of the Balangouma plutons (Ta/Yb ratios of 5 to 20). Strong depletions in Ta and Nb are observed, with high Ce/Nb ratios of 0.7 to 5.9. Only the arkoses show any notable variation in concentration between samples. Chondrite-normalised REE patterns (Fig. 3.27) are also very similar to REE patterns seen in the intrusive rocks. They contain typical Archaean chondrite-normalised REE distribution patterns, with LREE enrichment ($La_N/Sm_N = 2.22-4.22$) relative to HREE ($La_N/Yb_N = 3.35-14.65$), minor negative Eu anomalies ($Eu/Eu^* = 0.74-1.07$; mean of 0.87) and fairly flat HREE patterns ($Gd_N/Yb_N = 1.23-2.58$).

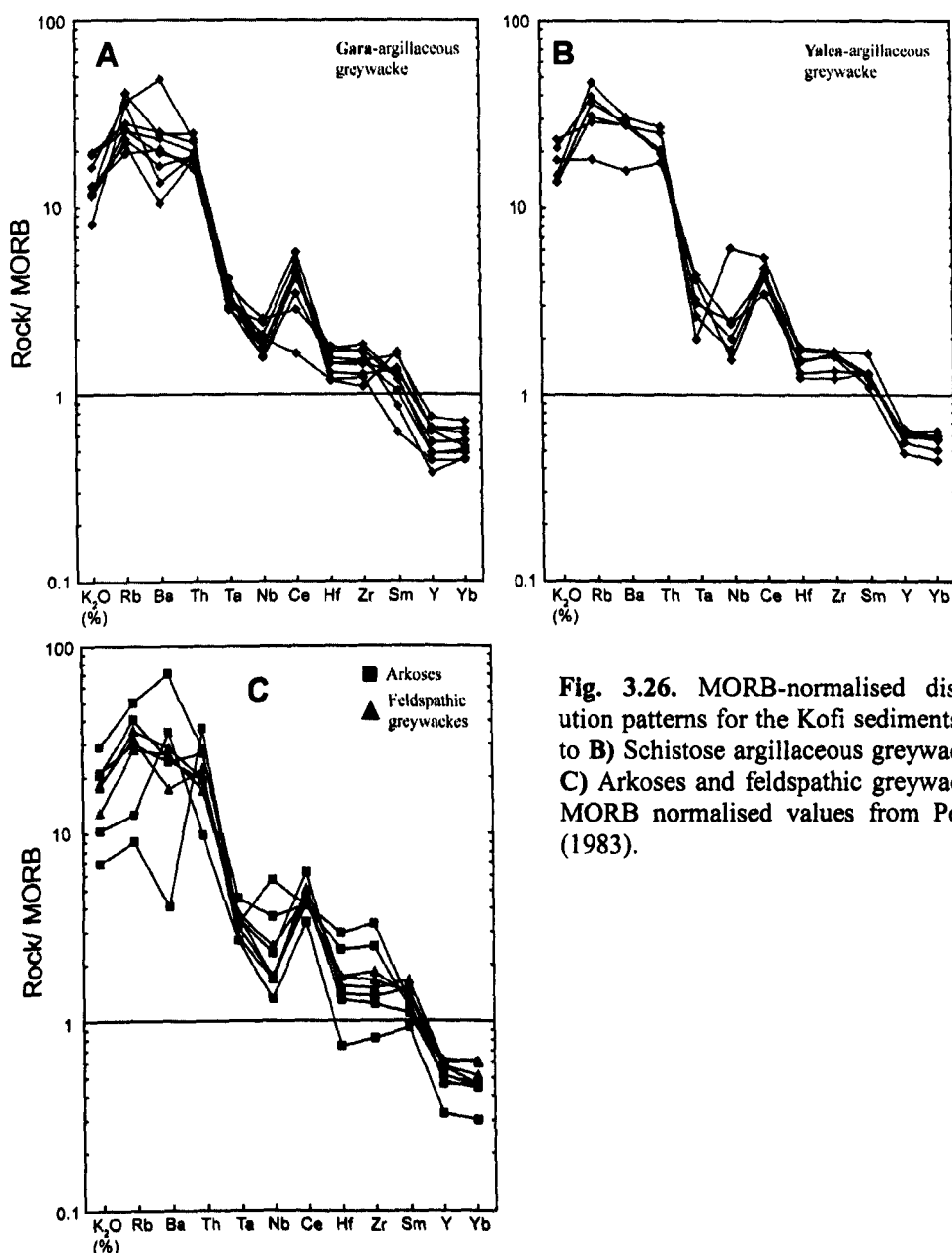


Fig. 3.26. MORB-normalised distribution patterns for the Kofi sediments. A) to B) Schistose argillaceous greywackes. C) Arkoses and feldspathic greywackes. MORB normalised values from Pearce (1983).

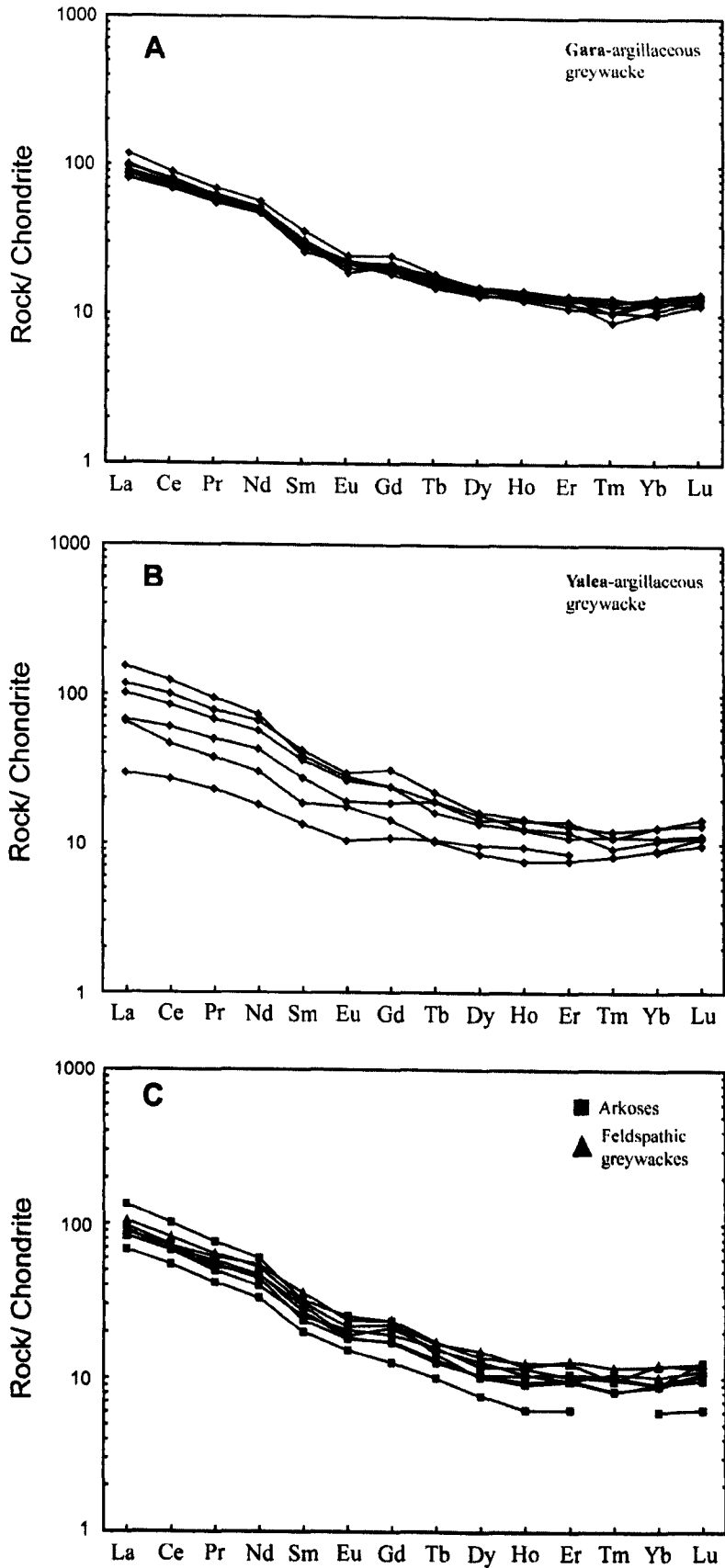


Fig. 3.27. Chondrite-normalised REE distribution patterns for the Kofi sediments A) to B) Schistose argillaceous greywackes. C) Arkoses and feldspathic greywackes. Chondrite values from Sun & McDonough (1989).

3.5 Discussion

3.5.1 Birimian granitoid compositions

The clear mineralogical and chemical compositional differences between the Balangouma plutons of the Falémé belt and the various granitoids intruding the Birimian basin sediments in and around the Loulo property suggests separate generations of granitoid emplacement. The compositions of the Balangouma and basin-type plutons are similar to granitoids in Ghana (e.g. Leube *et al.*, 1990; Hirdes *et al.*, 1992) and other parts of the Birimian crust (e.g. Doumbia *et al.*, 1998; Gasquet *et al.*, 2003; Naba *et al.*, 2004) (see section 2.3.2). The major comparisons between the Balangouma pluton and the basin-type intrusions from the eastern parts of the KKI are shown in Table 3.2.

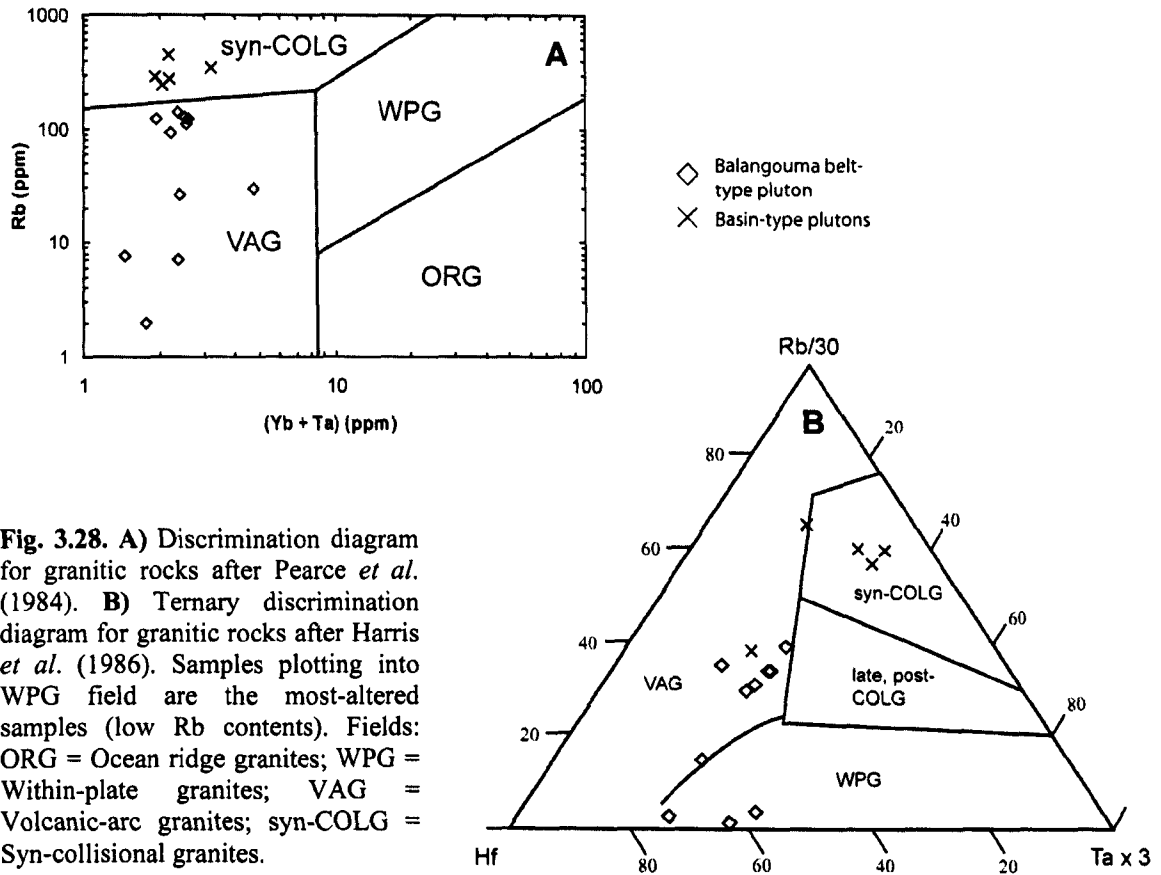
Table 3.2. Differences between belt- and basin-type intrusions in the eastern parts of the KKI, based on field descriptions, mineralogy and geochemistry.

Balangouma belt-type granitoids	Basin-type granitoids
Moderately dark intrusions (mafic component >20%)	Leucocratic to pink intrusions (mafic component <10%)
Na-rich, calc-alkaline, TTG intrusions	K-rich, calc-alkaline granites
I-type granitoids (magnetite-series)	Show I-type characteristics (magnetite-series), with samples plotting along I-S type boundary
Mainly quartz-diorite to granodiorite compositions	Granitic compositions
Metaluminous	Peraluminous
Feldspar dominated by plagioclase	Feldspars dominated by microcline and orthoclase
Mafic component dominated by hornblende and biotite	Mafic component dominated by biotite
Diorites- cpx-bearing	No pyroxene present
Low LILE concentrations (e.g. Rb levels of 5 to 145ppm- the lowest values come from most altered samples)	High LILE concentrations (e.g. Rb levels of 80 to 450ppm)
Minor mineral phases dominated by Cr-bearing magnetite, monazite (in granodiorites), scheelite, minor gersdorffite and sphene	Minor mineral phases dominated by Cr-depleted magnetite, monazite and less so ilmenite and sphene

3.5.2 Tectonic setting

Trace-element spider diagrams for the intrusive rocks (Fig. 3.23) show a clear enrichment in LILE (K, Rb, Ba, Th) compared to HFSE, with prominent negative Ta and Nb anomalies and high Ce/Nb ratios, and REE patterns with strong LREE enrichment (Fig. 3.24). These patterns are distinctive for intrusive rocks emplaced in modern day active margin environments (Pearce *et al.*, 1984). Discrimination diagrams of Pearce *et al.* (1984), presented in Fig. 3.28, clearly show separate generations of emplacement for the belt- and basin-type granitoids, with the Balangouma

samples plotting in the volcanic-arc field and the basin-type samples in the syn-collisional field. This is consistent with the Birimian crustal growth model shown in *section 2.5*, which suggests that belt-type plutons form prior to orogenesis (magmatic accretion event; stage 2) and basin-type plutons form later during the accretion of the volcanic belts during the Eburnean orogeny (stage 4).



Comparisons with previous studies

The geochemical data collected in this study closely matches other Birimian geochemical work on volcanic rocks (Sylvester & Attoh, 1992; Beziat *et al.*, 2000; Dampare *et al.*, 2008) and granitoids (Dioh *et al.*, 2006; Pawlig *et al.*, 2006), who all suggest a volcanic-arc geodynamic setting for the Birimian volcanic belts. In contrast, these data differ to the oceanic plateau model of Abouchami *et al.* (1990) and Boher *et al.* (1992) (LREE depletion, positive Nb anomalies and low Ce/Nb ratios). See *section 2.5.2.1* for direct comparison.

3.5.3 Provenance setting for the Kofi sediments

Very few geochemical studies have been carried out on the Birimian sediments (Asiedu *et al.*, 2004; Roddaz *et al.*, 2007) and the origin and timing of sediment formation (pre- or post-volcanic belt formation) is still debatable (*section 2.3.3*). The near identical sediment and plutonic (especially the Balangouma plutons) trace and REE patterns imply the Kofi sediments were deposited in similar environments to the Birimian intrusions (i.e. a volcanic-arc setting). Discrimination diagrams also show the sediments plot into the volcanic-arc field (Fig. 3.29).

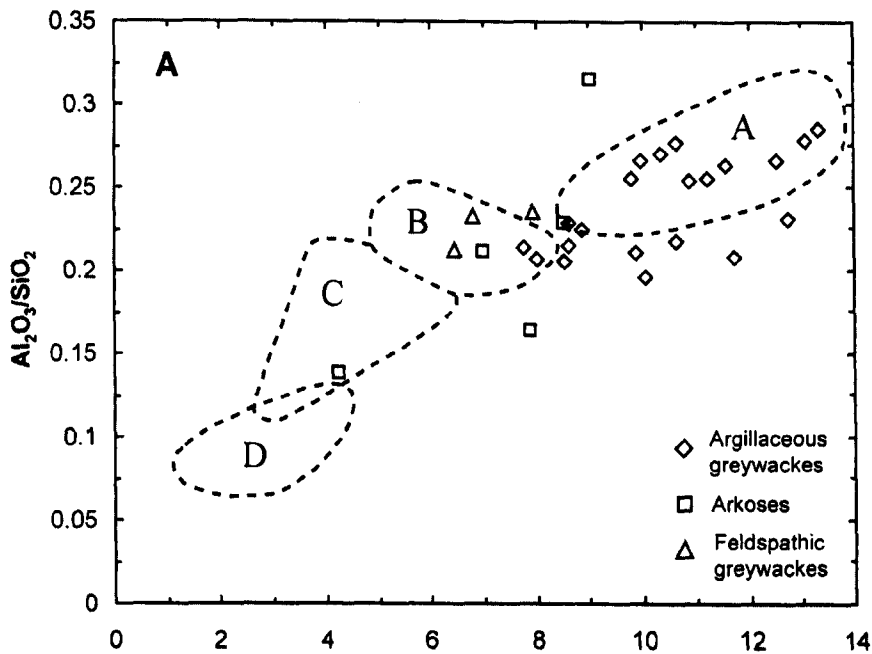
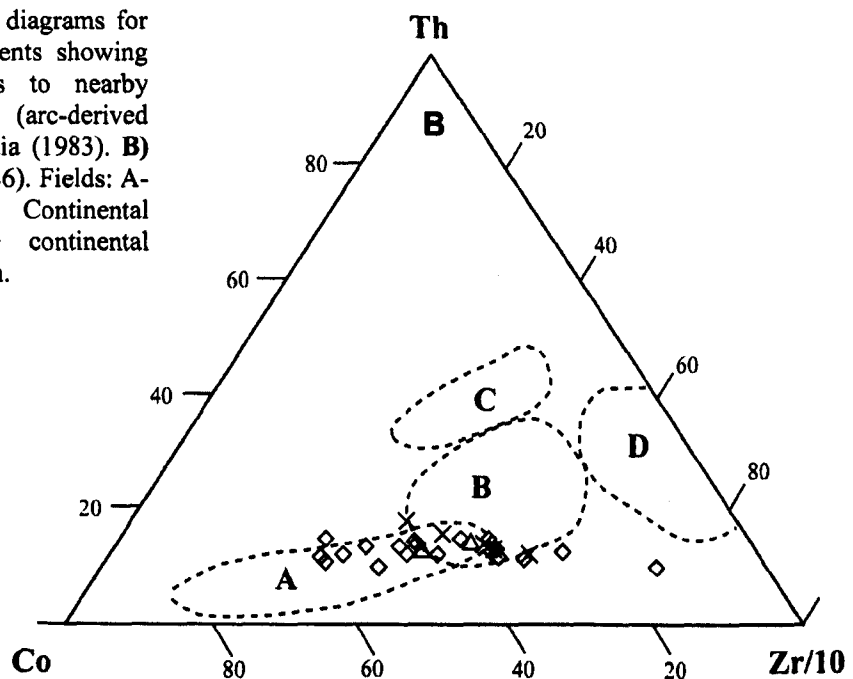


Fig. 3.29. Discrimination diagrams for the Birimian Kofi sediments showing similar tectonic settings to nearby Birimian intrusive rocks (arc-derived sediments). **A)** after Bhatia (1983). **B)** after Bhatia & Crook (1986). Fields: A- Oceanic island arc, B- Continental island arc, C- Active continental margin, D- Passive margin.



Provenance modelling of the Kofi sediments can be achieved by using elemental ratios such as La/Cr, La/Co, Th/Cr and Th/Co (Cullers *et al.*, 1988; Cullers 2000) and comparing them to different rocks types of the Balangouma plutons (Table 3.3). To make the modelling more robust, the data are also compared to a range of early Proterozoic volcanic rocks (EPC) from Condie (1993). The Kofi sediments contain similar ratios to Balangouma plutons, with compositions matching diorite Balangouma samples (lower-end range). Compared to EPC, the analysed sediments show La/Co and Th/Co ratios intermediate between felsic and andesite rocks (nearer andesite values) and La/Cr and Th/Cr ratios similar to andesites (Table 3.3).

Table 3.3. A comparison of provenance elemental ratios from the Kofi sediments, granodiorites and quartz-diorites of the Balangouma pluton, and early Proterozoic volcanic rocks (EPC; Condie, 1993).

	Kofi sediments		Balangouma pluton		Volcanic rocks of Condie (2003)		
	Range	Mean	Range	Mean	Felsic Mean	Andesites Mean	Basalts Mean
La/Cr	0.06-0.66	0.27	0.06-0.58	0.32	3	0.31	0.08
La/Co	0.01-3.07	1.58	1.29-4.05	2	5	0.74	0.29
Th/Cr	0.03-0.08	0.05	0.01-0.18	0.09	0.8	0.05	0.02
Th/Co	0.01-0.62	0.29	0.25-1.44	0.67	1.33	0.12	0.06

REE distribution patterns are also widely used in sediment provenance studies. The degree of fractionation of LREE over HREE is considered to be the measure of the proportion of felsic over mafic component in the source region, while the size of the Eu anomaly relates to the abundance of plagioclase in the source region (Taylor & McLennan, 1985). The near identical REE patterns for the argillaceous greywackes, feldspathic greywackes and arkoses (Fig. 3.27) suggest they were all derived from the same source. La_N/Yb_N ratios (mean of 8.01) for the analysed sediments are similar to the Balangouma plutons and felsic EPC rocks ($La_N/Yb_N = 13.19$ and 8.1 respectively) implying the dominance of felsic/intermediate source rocks over mafic source rocks. The small Eu anomalies (Eu/Eu^* mean = 0.87) suggest a lack of widespread K-rich granites in the source region.

Both trace and REE data for the Kofi sediments suggest a mixed source with a dominant intermediate to lower-end felsic contribution. Most of the Birimian volcanic belts are dominantly composed of tholeiitic basalts (e.g. the Mako belt further to the east; Dia *et al.*, 1997). However, the neighbouring Falémé belt is more felsic than other belts, with the dominance of TTG granitoids. This implies the Kofi sediments were sourced from the neighbouring Falémé belt or a volcano-plutonic belt of similar composition (depending on displacement along the SMSZ). These data agree with many structural and geochronological studies (e.g. Hirdes *et al.*, 1992; Davis *et al.*, 1994; Oberthür *et al.*, 1998; Pouclet *et al.*, 2006) that show the Birimian sediments are younger than, and ultimately the erosional products of, Birimian volcano-plutonic belts.

3.5.4 *Depositional setting and depth of burial for the Kofi Series*

Sediments of the Kofi Series were deposited in a marine environment in the fore-arc or back-arc region of the Falémé volcano-plutonic belt or a volcanic belt of similar composition. Weathering and erosion of the volcanic belt supplied detrital sediment to the Kofi basin mainly in the form of fine-grained turbidites. The argillaceous greywacke units probably represent more distal turbidite sequences (thinner greywacke beds) than the quartz-wackes and feldspathic greywackes, with regular deposition of background argillites. The carbonate units mark a change in sedimentation conditions within the basin from mostly clastic to dominantly chemical ('calm environments').

The amorphous state of the widespread carbon present within the Kofi Series carbonate units implies a low degree of burial for the sedimentary sequence. Amorphous carbon is stable into zeolite to lower greenschist facies metamorphic grade rocks, while more ordered graphite is present in upper greenschist to amphibolite facies (Landis, 1971; Grew, 1973; Diessal *et al.*, 1978). Metamorphic mineral assemblages (chlorite-sericite-calcite-epidote) from the Loulo district imply greenschist metamorphic conditions. The lack of metamorphic biotite implies temperatures were below 420 °C (Elisenlohr & Hirdes, 1992) and chlorite geothermometry (discussed in section 5.5.4; Cathelineau & Nieva, 1985; Cathelineau, 1988) indicate metamorphic temperatures of 268-294 °C (lower greenschist facies conditions).

3.5.5 *Crustal evolution at the Archaean-Proterozoic boundary*

The Archaean-Proterozoic boundary is recognised as a fundamental break-point in the chemical evolution of the upper continental crust, with notable differences in trace and REE compositions from Archaean and post-Archaean rocks worldwide (e.g. Taylor & McLennan 1985; Condie, 1993). Geochemical analysis of Birimian rocks, which is one of the world's least studied shields (Sylvester & Attoh, 1992), provides a good opportunity to study this boundary. Both igneous and metasedimentary rocks from this part of the KKI show affinities to Archaean granite-greenstone terranes. Using the La_N/Yb_N vs. Yb_N plot, both belt- and basin-type granitoids fall mainly within the Archaean field, with a slight overlap into the post-Archaean field (Fig. 3.30a). Analysis of the sedimentary data shows more convincing results (Fig. 3.30b). Similar data have been collected elsewhere in the Birimian (Abouchami *et al.*, 1990; Leube *et al.*, 1990; Sylvester & Attoh, 1992; Taylor *et al.*, 1992; Doumbia *et al.*, 1998; Gasquet *et al.*, 2003; Asiedu *et al.*, 2004; Dioh *et al.*, 2006) and imply that the Archaean-Proterozoic boundary may not necessarily coincide with a worldwide change in crustal evolution.

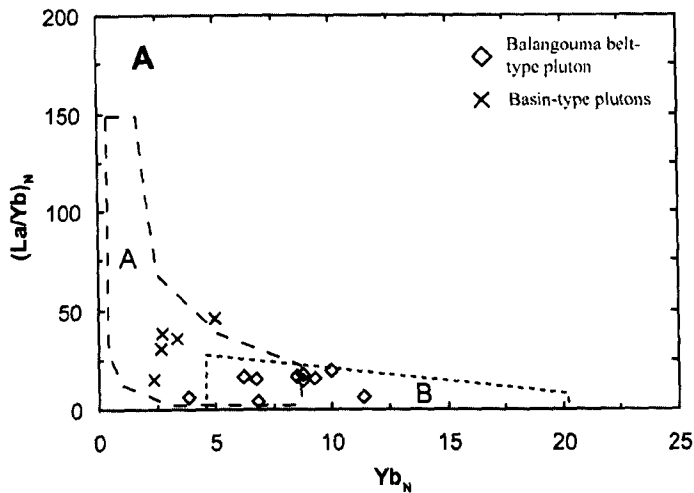
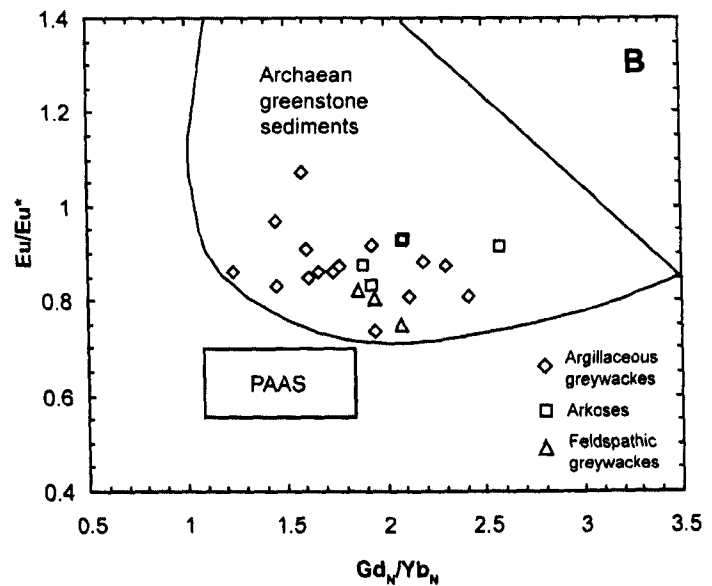


Fig. 3.30. A) La_N/Yb_N vs. Yb_N diagram after Martin (1987), showing similarities between Loulo intrusive rocks and Archaean TTG rocks. Fields of Archaean (A) and Post-Archaean (B). B) Eu/Eu^* vs. Gd_N/Yb_N plot for the Kofi metasedimentary series showing similarities to Archaean greenstone sediments. Fields of Archaean greenstone sediments and post-Archaean average Australian Shale (PAAS) from McLennan *et al.* (1993).



3.6 Conclusions

The main aspects of the geology of the Loulo area are summarised below:

1. The Loulo mining district is situated in the eastern parts of the Birimian Kédougou-Kéniéba inlier, along a belt-basin contact controlled by the Senegal-Mali Shear Zone (SMSZ).
2. The SMSZ acted as an important pathway for regional fluid flow with the greatest orogenic gold flux situated in second or higher splays on the eastern wall of the shear, in sediments of the Kofi Series. Mineralisation is linked to a change in crustal movement from a transpressional to transtensional regime.
3. The Loulo wall-rock sediments consist of alternating limestones/dolostones and sandstones of varying compositions (argillaceous greywackes, feldspathic greywackes, quartz-wackes and arkoses). These sediments are intruded by leucocratic to pink homogeneous, calc-alkaline, peraluminous, K-rich (3-5.5% K_2O), biotite-bearing granites.

The Kofi Series is also composed of several generations of Birimian and Mesozoic felsic and mafic dykes.

4. The Falémé volcano-plutonic belt (west of the SMSZ) is a granitoid-dominated terrane consisting of Na-rich (4-8.6% Na₂O), calc-alkaline, I-type, metaluminous intrusions (referred to as the Balangouma plutons) composed mainly of biotite + hornblende bearing quartz-diorites and granodiorites, and rare clinopyroxene-bearing tonalities. Siliciclastic sediments, volcanoclastic rocks and minor andesite flows make up the remainder of the volcano-plutonic belt in the Loulo area.
5. The Falémé belt is marked by a contrasting style of mineralisation, with endo- and exo-iron skarn deposits of the Falémé district located along the margins of the Balangouma plutons (iron oxide-copper-gold systems), associated with strong sodic alteration zones. Orogenic gold is largely absent from the western wall of the SMSZ (intrusive rocks acted as a possibly barrier to mineralisation).
6. The Balangouma plutons (belt-type) and plutons intruding the sedimentary basins (basin-type) show distinct compositional differences. This is seen elsewhere in the Birimian and indicates separate generations of intrusion emplacement. However, both types of granitoids appear to have crystallised from a QFM-buffered melt.
7. Trace and REE patterns of the intrusive rocks show a clear enrichment in LILE compared to HFSE, with prominent negative Ta and Nb anomalies and high Ce/Nb ratios. These patterns are distinctive of rocks emplaced into modern day volcanic-arc environments.
8. The Kofi sediments contain similar trace and REE patterns to the Balangouma plutons, which suggest they were deposited in a similar tectonic setting. Provenance modelling implies a mixed felsic/mafic source similar to the Falémé belt, suggesting that weathering and erosion of the neighbouring volcanic belt or a belt of similar composition supplied sediment to a fore-arc or back-arc Kofi basin, prior to emplacement of the basin-type syn-orogenic to late-kinematic intrusions.

CHAPTER 4: MINERALISATION AT LOULO

The aim of this chapter is to document the mineralisation characteristics of the Loulo orogenic gold deposits, highlighting the various styles of mineralisation, ore mineralogy and paragenesis. The opening sections describes in detail the data collected from the working Gara and Yalea deposits, and the prospective Faraba deposit in the southern parts of the mining district, using a combination of field observations, standard optical microscopy studies and detailed Scanning Electron Microscope (SEM) analysis (SEM operating conditions and detection limits are given in the appendices *section A-1*). The second part of the chapter briefly summarises the mineralisation characteristics of a selection of other Loulo orebodies. Lastly, a comparative mineralogical model for the Loulo district is discussed.

4.1 Introduction

Gold mineralisation in the Loulo mining district is generally restricted to the eastern wall of the Senegal-Mali Shear Zone (SMSZ), in sediments of the Kofi Series. The western side of the shear zone, along the Falémé belt, is less explored and only a few prospects currently exist within the Bambadji permit (not discussed here). The Loulo orebodies contain a range of mineralisation styles including: vein-hosted deposits (e.g. Gara, Faraba & Loulo-3); disseminated sulphide mineralisation (e.g. P-125); breccia-hosted deposits (e.g. Yalea North); and mineralisation confined to sulphide veinlets and stringers along brittle-ductile shear zones (e.g. Yalea & Baboto). In many cases, numerous styles of mineralisation are present within a single deposit (e.g. P-125 & P-64). Coupled with the range in mineralisation styles, Loulo contains diverse ore assemblages throughout the permit and these are discussed in detail in the following sections. The locations of the Loulo gold deposits mentioned in this chapter are shown in Fig. 3.2.

4.2 Gara

4.2.1 Orebody parameters

The Gara deposit (previously known as Loulo-0) is situated close to the Falémé River, to the west of the Loulo mining camp. Gara is currently the second largest deposit at Loulo with a reserve and resource of 2.56 Moz at 4.15 g/t and 3.71 Moz at 4.11 g/t, respectively (for year ending 2009). Open pit mining started in 2006, but approximately 80% of the ore resource sits underneath the current pit, with underground mining scheduled for 2010. Mineralisation is situated within a 5-20 m thick unit of extensively folded tourmalinite rocks (Fig. 3.5). The structural history of the Gara folds is summarised in *section 3.2.2.2*. The tourmalinite units acted as a favourable host lithology for mineralisation. An early tourmaline alteration event (*chapter 5*) increased the brittleness of the host and during D₂-D₃ deformation the rock fractured to form the Gara stockwork. High-grade zones are controlled by NNE-striking sinistral P-shears on the limbs

of the SSW plunging F_2 folds. A block model for the Gara orebody is shown in Fig. 4.1.

Fig. 4.1. A block model for the Gara deposit. The highest grades occur in the southern parts of the orebody, situated along NNE structures that occur on the limbs of the F_2 folds. Grid 200:200 m. Figure courtesy of Randgold Resources (2010).

4.2.2 Mineralisation styles

Gara forms a carbonate-quartz-sulphide vein stockwork deposit, with strong evidence of hydraulic fracturing and brittle-ductile deformation. Vein geometries include straight centimetre to millimetre veins (dominant; Fig. 4.2a, b & e), breccias (Fig. 4.2c to d), lenticular veins and sigmoidal vein arrays (Fig. 4.2c). Other vein morphologies include folded veins (Fig. 4.2f) and tension cracks which are generally barren and situated outside the main stockwork generation (confined to weakly tourmalinised sediments). Previous studies by Dommanget *et al.* (1993) identified five silica-carbonate influxes and two sulphide networks, while Allibone (2004) recognised several dominant trending veinsets, including a consistently developed NW-striking veinset and other sets such as E- ($080-090^\circ$) and NE-striking veins present in the hinge and limbs of the F_2 folds. However, evidence collected in this study implies a more complex stockwork generation with multiple stages of quartz-carbonate-sulphide formation (multiple trending veinsets; impossible to interpret the relative timing of each vein generation).

Several grade controls can be identified in the Gara stockwork. Firstly, gold concentration shows a positive relationship with sulphide abundance (Fig. 4.2b). Secondly, the vein composition (described in *section 4.2.3*) acts as an important grade control, with the presence of carbonate an important precursor for mineralisation. Quartz-rich veins are generally weakly mineralised (<0.5 g/t) or barren (Fig. 4.2e). Furthermore, the number of veinsets (veins with different orientations) appears to be more important than the intensity of the stockwork (Fig. 4.2e), implying the bulk of mineralisation targeted particular veinsets. Finally, high-grade zones (5 to 40 g/t) are also associated with brecciated veins (zones of dilatancy).

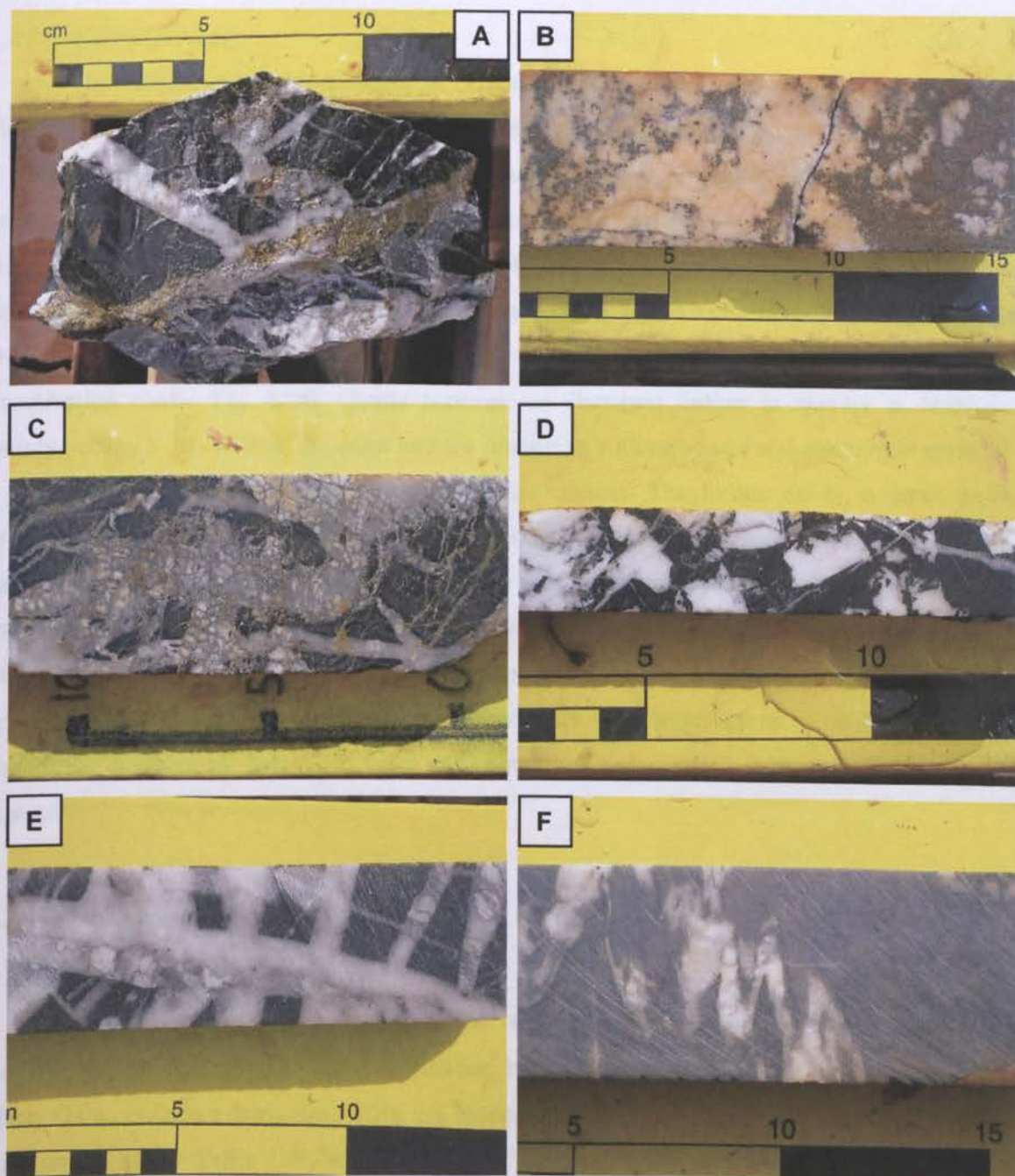


Fig. 4.2. Grab and drill core samples of the Gara vein stockwork. The photographs illustrate the composition of the veins and the range of vein morphologies that occur in the tourmalinite host. **A)** A pit sample from a high-grade zone showing the presence of ankerite-pyrite veins. **B)** A sulphide-rich ankerite vein associated with high-grade (90.3 g/t), showing clearly the link between gold concentrations and carbonate-pyrite abundance. Limonite alteration (brown material on the right of the image) occurs after pyrite (LOCP124, 552 m). **C)** Sigmoidal mineralised vein showing reactivation and brecciation of an early carbonate vein (white material) by later dull grey quartz, with both vein phases associated with sulphide generation (LOCP97, 347 m). **D)** A strongly brecciated carbonate vein with the vein structure no longer present (LOWDH23, 441 m). **E)** Straight barren (0.11 g/t) milky quartz veins (minor carbonate). The low-grade can be attributed to the lack of the vein carbonate and the low number of veinsets (2 vein directions, perpendicular to each other) (LOCP49, 180.6m). **F)** A folded barren calcite vein (LOCP81, 676.55m). Folded veins usually occur within the weakly-tourmalinised quartz-wacke (note the lighter colour of the host rock compared to A to D) and pre-date mineralisation (D₁ to D₂ origin).

4.2.3 Vein mineralogy

The Gara stockwork contains high carbonate concentrations (60-70 vol.% of the veins). This is an atypical characteristic for vein-hosted orogenic gold deposits, where carbonate concentrations are usually ≤ 5 to 15 vol.%. Mineralised veins are composed of Fe-Mg bearing carbonates (ankerites), while carbonate constituents of the barren veins are mainly composed of calcite. Quartz is the second major component of the Gara veins. Two separate styles of quartz generation are observed. A broad milky quartz generation exists as a cogenetic phase with ankerite or calcite, while a late grey quartz generation can be seen sealing brecciated ankerite veins (reactivation phase; Fig. 4.2c). Quartz textures are discussed further in *chapter 6*. Sulphides mainly occupy 5-30 vol.% of the veins and are situated in both carbonate and quartz vein material.

Gangue minerals include albite and minor chlorite. The former exists as small grains (<100 μm) trapped between larger quartz crystals, while the latter occurs as fibrous grains throughout the mineralisation history at Gara. The most common accessory minerals are rutile and apatite. Rutile exists as acicular, blocky and skeletal grains (20-80 μm) dispersed within quartz-carbonate vein material. Apatite shows rounded or rare irregular-shaped habits (80-200 μm grain size) situated within ankerite or as rarer intergrowths with larger pyrite. Apatite increases in abundance in carbonate-dominated veins and contain micro-inclusions (<10 μm) of scheelite and monazite.

4.2.4 Ore mineralogy

4.2.4.1 Paragenesis

Representative samples from different vein generations throughout the deposit show a similar ore petrography, implying a continuous, homogenous, mineralising fluid flow event took place. Gara contains a fairly distinctive ore assemblage that differs from many reported orogenic gold deposits (*see* Table 1.2), with a Fe-Cu-REE-Au-Ni-W-As metal association. In terms of sulphide phases, Gara contains a fairly simple ore petrogenetic history with pyrite occurring as the principal sulphide mineral (95-99% of total sulphides) and the only gold-bearing sulphide phase. Chalcopyrite is the main accessory sulphide, occurring as a trace phase (<5%). Two generations of chalcopyrite are observed: an early phase forming contemporaneously with pyrite (chalcopyrite-I); and a later, more dominant, phase post-dating pyrite formation (chalcopyrite-II). Other accessory sulphides, in order of decreasing abundance, include: pyrrhotite, gersdorffite, pentlandite and arsenopyrite. No Sb, Pb or Zn-bearing sulphides are observed at Gara. The Gara mineralised veins also contain common rare earth minerals with similar concentration levels to chalcopyrite (monazite and xenotime coexist with pyrite). Other accessory minerals include scheelite (a common ore phase at Loulo). A summary of the paragenesis is presented in Table 4.1, and the evidence is discussed in the following section.

Table 4.1. Summary wall-rock alteration, vein and sulphide paragenesis for the Gara orebody.

Mineral	Pre-ore stage	Main ore stage	Post-main ore stage	Supergene stage
Wall-rock alteration				
Tourmaline	██████████	—————	—————	
Albite	██	██████████	██	██
Ankerite	-----	-----		
Haematite	-----			
Chlorite		—————		
Sericite		—————		
Vein material				
Calcite			-----	
Ankerite		██████████		
Quartz		██████████	-----	
Gangue				
Albite		—————		
Rutile		—————		
Apatite		—————		
Chlorite			—————	
Imenite			—————	
Sulphides/Opaques				
Pyrite		██████████		
Arsenopyrite		—————		
Pyrrhotite		—————		
Gersdorffite		—————		
Pentlandite		———		
Monazite		██████████	—————	
Xenotime		—————		
Scheelite		—————		
Chalcopyrite-I		—————		
Chalcopyrite-II			██████████	
Gold		██████████	-----	
Supergene				
Leucoxene				██████████
Limonite				—————

Note- Wall-rock alteration is discussed in detail in *chapter 5*.

4.2.4.2 Ore-related sulphides and accessory phases

Minerals of the Fe-Ni-As-S system

Pyrite is present in numerous forms, including aggregates (up to several centimetres), single pyritohedral crystals (<200 µm), or as rare massive pyrite in carbonate-dominated veins (Fig. 4.2b). Pyrite is also frequently observed as post-schistosity disseminations in the host rock situated along the vein walls. Locally, pyrite contains diffusive zonation patterns with As (arsenian pyrite) ± Ni bearing zones (Fig. 4.3c; Table 4.2). Pyrite often shows a vuggy texture, where the mineral has been partially altered by leucoxene and/or more commonly by late-stage tourmaline (Fig. 4.3a, b; *see chapter 5*). Micro-fissures are frequent in deformed pyrite and are commonly host to late-stage sulphides or remobilised gold (Fig. 4.6).

Pyrite is host to a range of trace Fe-Ni-As sulphides (Table 4.2). Pyrrhotite and gersdorffite are the most common phases. **Pyrrhotite** occurs as small (10 µm) subhedral inclusions, preferentially in the cores of pyrite crystals. Iron-bearing **gersdorffite** (NiAsS) form subhedral to tabular inclusions (20-50 µm) (Fig. 4.3f) and tend to have a positive relationship with monazite abundance. **Pentlandite** ([Fe,Ni]₉S₈) forms a rare ore constituent of the reactivated veins (grey quartz vein phase) and exists as rare subhedral grains intergrown with pyrrhotite (<25 µm) or occur as granular grains within the quartz vein material. **Arsenopyrite** occurs as extremely rare (only seen in a few samples) euhedral inclusions (2 to 20 µm) within pyrite cores or as larger intergrowths (up to 70 µm) (Fig. 4.3d). Back-scattered electron (BSE) images of the Loulo Ni-bearing sulphides are best illustrated at Yalea North.

Table 4.2. Representative chemical composition of the Fe-Ni-As-S minerals at Gara by SEM-EDS analysis (wt.%).

N	Mineral	Fe	As	Ni	S	Σ
1	Py	46.61	–	–	51.81	98.42
2	Py	46.98	–	–	53.15	100.13
3	Py	45.32	1.60	0.71	52.66	100.30
4	Py	45.46	1.97	0.69	52.87	100.99
5	Po	60.45	–	0.23	38.12	98.80
6	Po	60.56	–	–	38.99	99.55
7	Pn	33.89	–	34.90	33.10	101.89
8	Pn	33.97	–	33.71	32.78	100.46
9	Gf	4.40	42.97	31.73	20.00	99.10
10	Gf	9.64	42.06	26.67	19.81	98.18
11	Gf	11.55	42.48	24.09	20.00	98.12
12	Gf	8.78	43.76	28.90	19.67	101.11
13	Aspy	34.98	43.89	–	20.75	99.62
14	Aspy	33.99	44.23	–	21.02	99.24
15	Aspy	33.13	45.62	–	22.12	100.88

Py- pyrite, Po- pyrrhotite, Pn- pentlandite, Gf- gersdorffite, Aspy- arsenopyrite. Blank-not detected.

Accessory sulphides

Chalcopyrite-I forms a minor constituent of the Cu sulphide phases at Gara. It usually occurs as small (7-20 µm) anhedral to tabular inclusions within pyrite (Fig. 4.3e). Along with monazite, chalcopyrite is the most common inclusion-type within the main sulphide phase. The second generation of chalcopyrite (**chalcopyrite-II**) forms the primary sulphide phase in the last stages of sulphide paragenesis. Chalcopyrite-II occurs as small (<20 µm) elongate grains within narrow discontinuous deformation cracks in pyrite, or more frequently observed filling continuous micro-fracture networks (Fig. 4.3f). Rarely, chalcopyrite is seen as large (up to 3 mm in size) irregular-shaped grains situated away from pyrite. Chalcopyrite-II is usually inclusion free and increases in abundance towards the southern parts of the deposit. This polyphase paragenesis for chalcopyrite is a common feature throughout the northern regions of the Loulo district. No systematic compositional difference between the two generations has been detected.

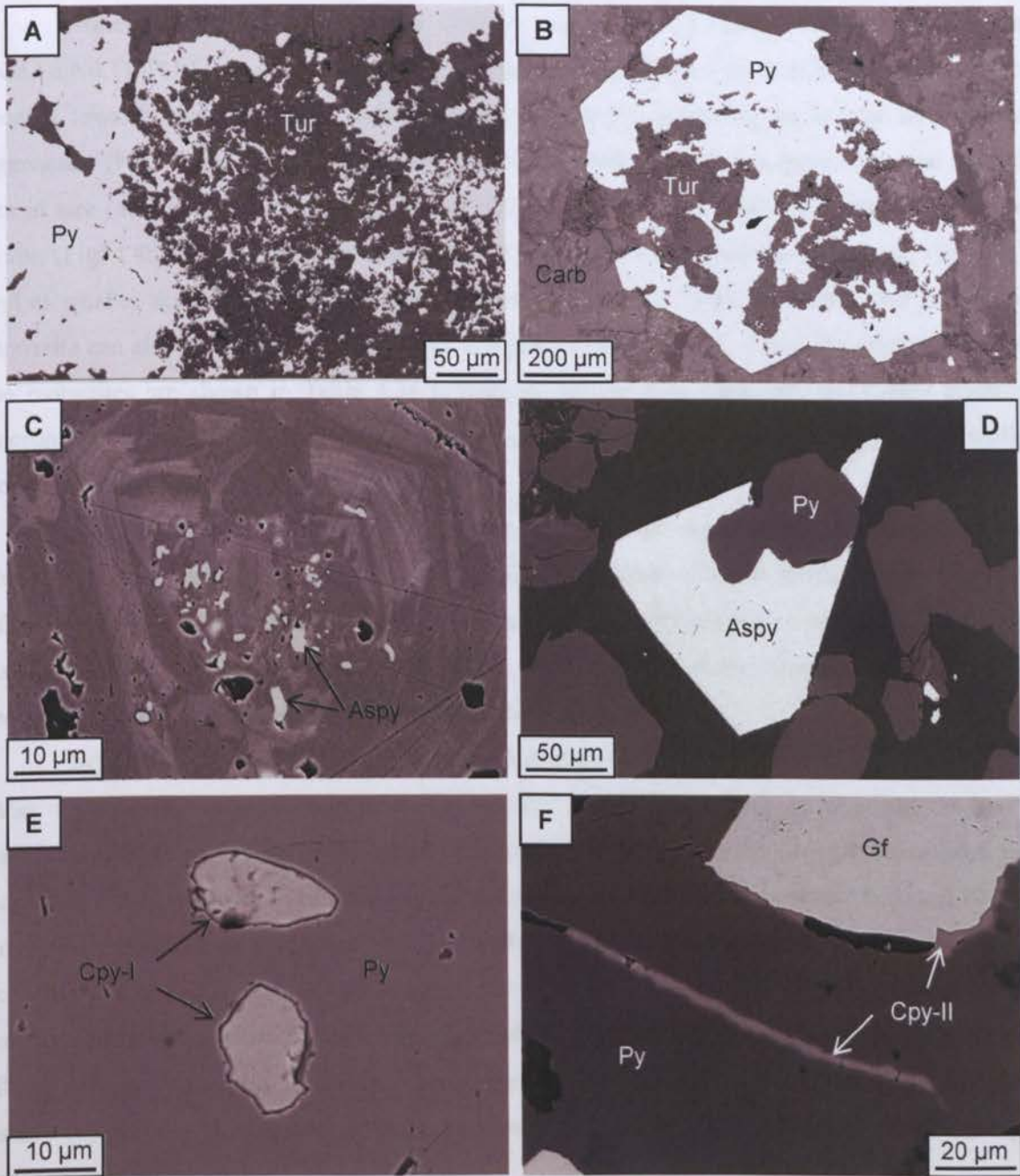


Fig. 4.3. Back-scattered electron (BSE) images of the major and minor sulphide phases present at Gara. **A)** Highly altered pyrites replaced by late stage tourmaline (discussed in *chapter 5*) (LOCP117, 338.4 m). **B)** Vuggy pyrite replaced by tourmaline (LOCP117, 338.4 m). **C)** Zoned pyrite crystal showing lighter zones of As-Ni bearing pyrite. Small inclusions of arsenopyrite are associated with these As-Ni bearing zones (LOCP124, 557.6 m). **D)** Euhedral arsenopyrite intergrowth with pyrite (LOCP59, 535.4 m). **E)** Anhedral chalcopyrite-I inclusions situated within the core of a pyrite crystal (LOWDH23, 438.05 m). **F)** Late chalcopyrite-II sealing fractures within pyrite or located along pyrite-gersdorffite contacts (LOWDH23, 438.05 m). Abbreviations- Carb = carbonate; Tur = tourmaline; Py = pyrite; Aspy = arsenopyrite; Cpy = chalcopyrite; Gf = gersdorffite.

Phosphates and tungstates

Mineralised veins at Gara are rich in rare earth phosphates, including monazite ($[\text{Ce,La,Nd,Th}]\text{PO}_4$) and xenotime (YPO_4). **Monazite** is predominately confined to pyrite, often located towards the margins as individual grains or more commonly as two or three phase aggregates (Fig. 4.4a). These grains occur as spherical and/or polygonal grains between 10-500 μm in size (mainly $<100 \mu\text{m}$). Deformation cracks running through pyrite also transect monazite grains (Fig. 4.4b). Monazite is also observed as intergrowths with pyrite (up to 200 μm ; Fig. 4.4c) and as smaller skeletal grains (20-50 μm) rimming pyrite (Fig. 4.4d). Extremely rare late-phase monazite can also be seen post-dating pyrite and gangue material (Fig. 4.4e). The compositions of the monazites are shown in Table 4.3a (energy dispersive X-ray spectroscopy (EDS) electron microprobe data). They classify as Ce-rich monazites (monazite [-Ce]), depleted in Th (usually below detection limits).

Xenotime is present in much lower concentrations than monazite (a 10 fold decrease), but shows a positive relationship with monazite abundance. It occurs as small anhedral inclusions (10-30 μm) within pyrite and apatite, and as larger grains (up to 100 μm) in vein carbonate (Fig. 4.4f). Its composition is fairly uniform (Table 4.3b), with Y replaced by a range of other REE's including Gd, Dy, Er, Yb (combined total $<5 \text{ wt.}\%$).

Scheelite (CaWO_4) is present in lower abundances than the rare earth phosphates. Like other Ca-bearing accessory minerals (e.g. apatite), scheelite abundance is greater in more carbonate-rich veins (absent from quartz-rich veins). However, its appearance throughout the deposit is rather sporadic. In reflected light, it occur as grey anisotropic minerals between 20-160 μm , mainly confined to pyrite and vein-carbonate as aggregates of three or more grains. Larger scheelite grains ($>200 \mu\text{m}$) hosted in carbonate are often heavily deformed (Fig. 4.4g). In the southern parts of the Gara deposit, late-stage scheelite is common (along with chalcopyrite-II), filling deformation cracks in pyrite. These scheelite-rich zones are associated with high gold assays (up to 90 g/t). Conversely, high gold grade zones are not always associated with high scheelite concentrations.

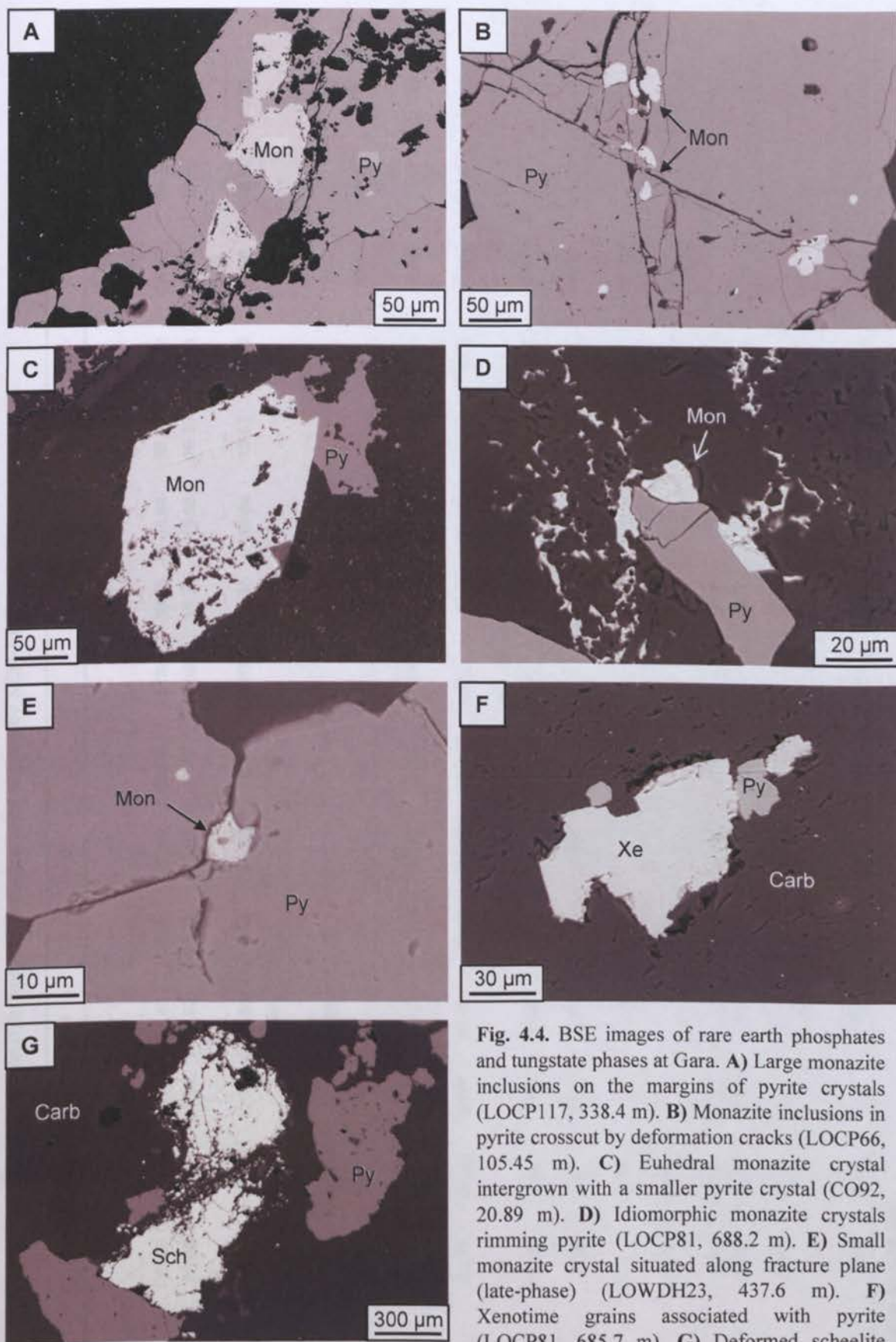


Fig. 4.4. BSE images of rare earth phosphates and tungstate phases at Gara. **A)** Large monazite inclusions on the margins of pyrite crystals (LOCP117, 338.4 m). **B)** Monazite inclusions in pyrite crosscut by deformation cracks (LOCP66, 105.45 m). **C)** Euhedral monazite crystal intergrown with a smaller pyrite crystal (CO92, 20.89 m). **D)** Idiomorphic monazite crystals rimming pyrite (LOCP81, 688.2 m). **E)** Small monazite crystal situated along fracture plane (late-phase) (LOWDH23, 437.6 m). **F)** Xenotime grains associated with pyrite (LOCP81, 685.7 m). **G)** Deformed scheelite porphyroblast (LOCP124, 557.6 m). Mon- monazite, Xe- xenotime, Sch- scheelite, Py- pyrite, Carb- carbonate.

Table 4.3a. Chemical composition of monazite from mineralising veins at Gara by SEM-EDS analysis (wt.%).

	1	2	3	4	5	6	7	8	9	10	11	12	13	14	15	
SiO ₂	-	-	-	-	-	-	-	-	0.23	-	-	-	0.78	-	-	
ThO ₂	-	-	-	-	-	-	-	-	-	-	0.89	-	2.16	-	-	
Ce ₂ O ₃	33.48	36.61	35.15	34.40	36.85	37.40	35.67	36.09	33.85	36.64	36.37	36.22	34.73	36.28	36.68	
La ₂ O ₃	20.08	21.36	21.34	17.92	20.23	18.28	17.40	17.50	15.39	16.68	19.23	21.18	19.54	19.55	19.25	
Pr ₂ O ₃	-	-	-	-	-	-	-	-	-	-	-	-	2.70	-	-	
Nd ₂ O ₃	13.74	12.15	12.29	13.61	13.63	14.38	15.41	15.80	16.35	14.69	13.53	11.75	10.86	12.90	13.53	
Sm ₂ O ₃	-	-	-	1.37	-	-	1.89	-	2.28	-	-	-	-	-	-	
Gd ₂ O ₃	-	-	-	-	-	-	-	-	1.69	-	-	-	-	-	-	
Fe ₂ O ₃	-	0.23	-	0.83	-	-	-	-	-	-	-	-	1.67	-	-	
CaO	0.39	0.34	-	-	-	-	-	-	1.02	0.71	-	-	0.34	0.49	0.64	
NiO	-	-	-	-	-	-	-	-	-	0.31	-	-	-	-	-	
P ₂ O ₅	30.88	29.33	29.26	29.82	29.20	29.15	29.77	29.64	29.32	30.34	30.00	28.90	27.20	30.08	29.59	
Total	98.56	100.02	98.04	97.96	99.91	99.20	100.13	99.04	100.13	99.37	100.02	98.05	99.98	99.30	99.68	
									Number of ions on the basis of 16 (O).							
P	4.08	3.93	3.98	4.00	3.93	3.95	3.97	3.99	3.91	4.01	3.99	3.95	3.70	4.00	3.95	
Si	4.08	3.93	3.98	4.00	3.93	3.95	3.97	3.99	0.04	4.01	3.99	3.95	0.13	4.00	3.95	
Sum	-	-	-	-	-	-	-	-	3.95	4.01	3.99	3.95	3.83	4.00	3.95	
Fe ³⁺	-	0.03	-	0.10	-	-	-	-	-	-	-	-	0.20	-	-	
Ni	0.07	0.06	-	-	-	-	-	-	0.17	0.12	-	-	0.06	0.08	0.11	
Ca	-	-	-	-	-	-	-	-	-	-	0.03	-	0.08	-	-	
Th	1.91	2.12	2.07	2.00	2.15	2.19	2.06	2.10	1.95	2.10	2.09	2.14	2.04	2.09	2.12	
Ce	1.15	1.25	1.26	1.05	1.19	1.08	1.01	1.03	0.90	0.96	1.12	1.26	1.16	1.13	1.12	
La	-	-	-	-	-	-	-	-	-	-	-	-	0.16	-	-	
Pr	0.77	0.69	0.71	0.77	0.77	0.82	0.87	0.90	0.92	0.82	0.76	0.68	0.62	0.72	0.76	
Nd	-	-	-	0.07	-	-	0.10	-	0.12	-	-	-	-	-	-	
Sm	-	-	-	-	-	-	-	-	0.09	-	-	-	-	-	-	
Gd	-	-	-	-	-	-	-	-	-	-	-	-	-	-	-	
Sum	3.90	4.14	4.04	3.99	4.11	4.09	4.04	4.02	4.15	4.03	4.00	4.08	4.32	4.03	4.11	

Blank- below detection limit

Table 4.3b. Chemical composition of xenotime from mineralising veins at Gara by SEM-EDS analysis (wt.%).

	1	2	3	4	5	6	7	8
Rb ₂ O ₃	1.40	1.40	1.49	1.28	1.26	–	1.17	0.95
Y ₂ O ₃	44.76	46.83	46.85	46.13	47.28	47.12	47.02	45.90
Gd ₂ O ₃	2.86	1.72	1.56	2.67	1.63	1.18	1.74	2.60
Dy ₂ O ₃	5.53	5.21	4.36	5.21	4.53	5.53	5.75	6.59
Er ₂ O ₃	3.65	3.88	–	–	4.21	4.46	4.41	4.38
Yb ₂ O ₃	5.00	3.73	4.09	4.53	3.59	4.76	4.08	–
Fe ₂ O ₃	–	–	0.54	–	1.03	1.16	1.00	1.48
CoO	0.19	–	1.30	1.55	–	–	–	–
CaO	–	–	2.09	–	–	–	–	–
PbO	–	–	0.68	–	–	–	–	–
P ₂ O ₅	36.06	36.95	36.41	37.97	35.69	35.08	35.50	37.21
Total	99.46	99.71	99.36	99.35	99.23	99.29	100.67	99.11
Number of ions on the basis of 16 (O)								
P	4.02	4.05	3.96	4.10	3.96	3.94	3.93	4.05
Fe ³⁺	–	–	0.05	–	0.10	0.12	0.10	0.14
Co	0.02	–	0.13	0.16	–	–	–	–
Rb	0.10	0.10	0.10	0.09	0.09	–	0.08	0.07
Y	3.14	3.22	3.20	3.13	3.30	3.32	3.27	3.14
Ca	–	–	0.29	–	–	–	–	–
Gd	0.12	0.07	0.07	0.11	0.07	0.05	0.08	0.11
Dy	0.23	0.22	0.18	0.21	0.19	0.24	0.24	0.27
Er	0.15	0.16	–	–	0.17	0.19	0.18	0.18
Yb	0.20	0.15	0.16	0.18	0.14	0.19	0.16	–
Pb	–	–	0.02	–	–	–	–	–
Sum	3.97	3.92	4.21	3.88	4.07	4.11	4.12	3.91

Blank-below detection limit

Supergene alteration

Leucoxene (TiO₂) forms as a replacement phase after pyrite often forming atoll-like textures surrounding the sulphide (Fig. 4.5). Leucoxene replacement is a typical feature of the Kofi Series; observed in the surrounding sediments and minor intrusive rocks (*section 3.3*), as well as within the orebodies. Leucoxene commonly contain micro-inclusions (<5 µm) of ilmenite with elevated W concentrations (up to 3 wt.% WO₃), implying an alteration history as follows:



Limonite [FeO(OH)·nH₂O] (after pyrite) is occasionally seen (Fig. 4.2b), especially within the vicinity of the weathered zone (30 to 60 m deep).

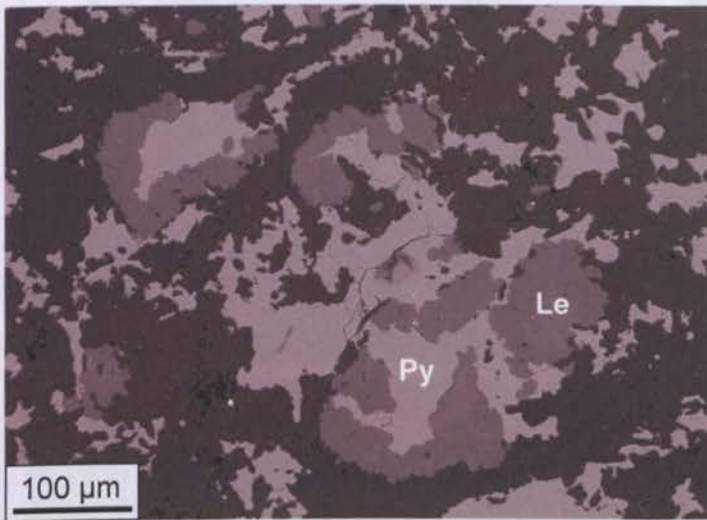


Fig. 4.5. A BSE image showing Ti replacement of pyrite at Gara. Skeletal pyrite (Py) altered along its margins by leucoxene (Le) (LOCP117, 338.4 m).

4.2.4.3 Gold

All gold particles at Gara exist as native gold. In the weathered zone, pyrite and carbonate have been removed leaving free gold in quartz stockworks (Dommanget *et al.*, 1993). At depth, 93% of the gold is associated with pyrite (the only Au-bearing sulphide). Gold is located in various sites (Fig. 4.6): (1) occluded in pyrite (45%; GI); (2) randomly distributed individual grains situated along micro-fissures in pyrite (41%; GIIa); (3) forming discrete veinlets in deformed pyrite (4%; GIIb); (4) nucleated on the margins of the pyrite crystals (3%; GIII); and lastly (5) as free gold in quartz-carbonate vein material (7%; GIV).

The majority of the gold at Gara is present in the first two gold sites (GI & GII). Occluded gold (coeval with pyrite mineralisation) is ultrafine-to-medium grained (2 to 70 μm , average grain size of 15 μm) occurring as subhedral to anhedral equidimensional grains, mainly situated towards the rims of pyrite crystals (Fig. 4.6a, b). Occluded gold is generally confined to pyrite and Ni-bearing pyrite rather than arsenian pyrite zones. Rarely, occluded gold is seen along the contacts between pyrite and their inclusion minerals (e.g. pyrrhotite and chalcopyrite-I). Fracture-bound gold (Fig. 4.6c to e) is a common feature in many orogenic gold deposits. This late-phase mineralisation is argued by some workers to represent a separate second hydrothermal event in these gold systems (e.g. Vallance *et al.*, 2004). However, fracture-bound gold is often interpreted to reflect local remobilisation of the ductile metal during subsequent deformation and/or vein recrystallisation (e.g. Dube *et al.*, 2004). The latter model is favoured for the Loulo deposits, with clear evidence of post-mineralisation deformation and partial vein recrystallisation.

In places, gold veinlets can be observed infilling sections or whole micro-fracture networks in deformed pyrite, over lengths of 50 to 340 μm (Fig. 4.6f). Within the Loulo permit, these discrete gold veinlets are almost exclusively confined to the Gara deposit and are associated with high grade zones (>10 g/t). Gold is occasionally observed attached to the margins of pyrite crystals in pressure shadows (Fig. 4.6g) or along fracture terminations. Free gold (<10 to 100 μm) is rarely observed in quartz and carbonate vein material in close proximity to pyrite (Fig. 4.6h).

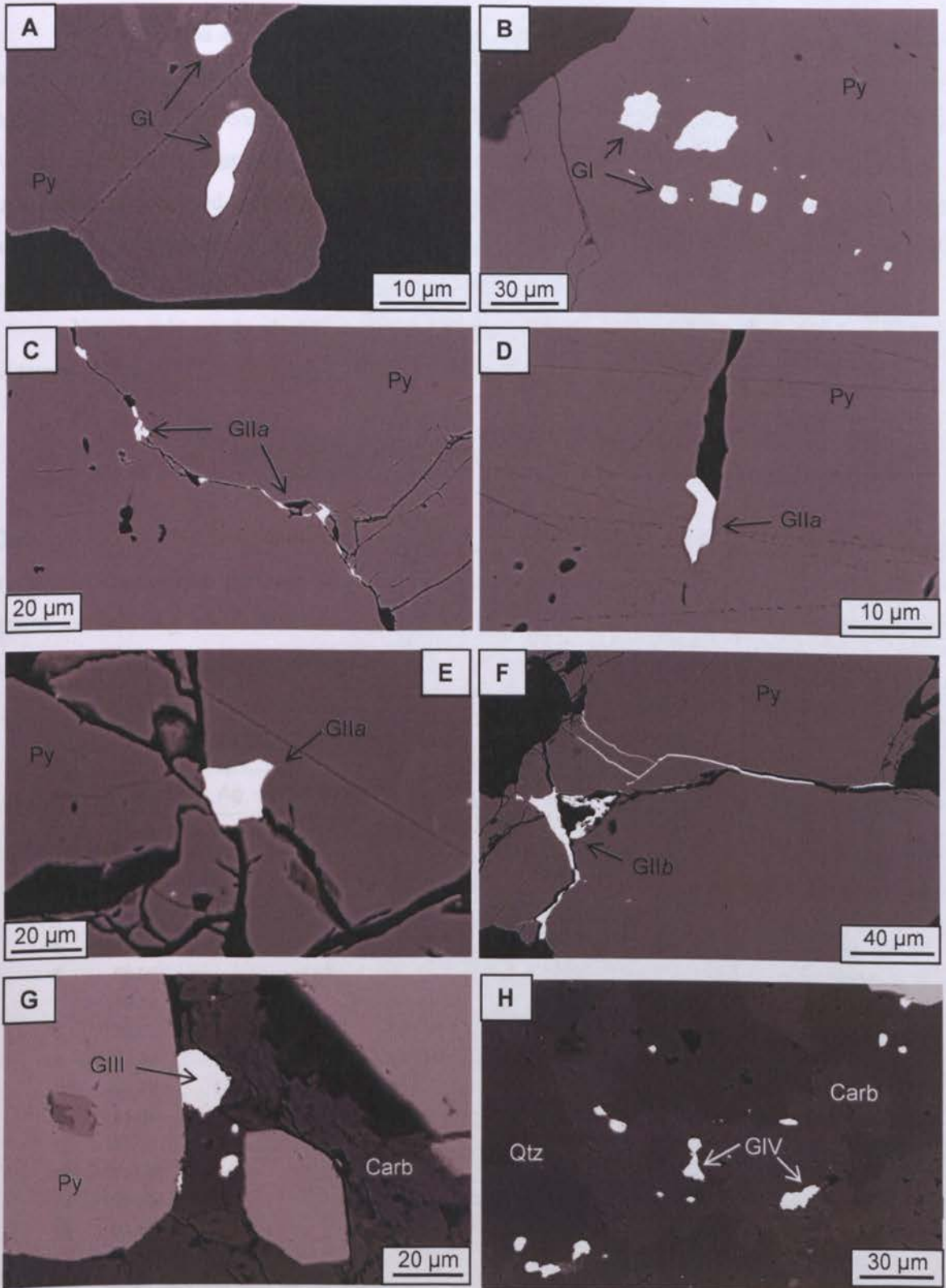


Fig. 4.6. BSE images showing the various gold locations at Gara: A) to G) hosted in pyrite and H) in vein material). **A)** Small anhedral occluded gold grains on pyrite margins (LOCP107, 738.7 m). **B)** Occluded gold also exists as larger grains in multiphase aggregates on the margins of pyrite crystals (LOCP117, 338.4 m). **C)** Trails of elongate, ultra-fine, remobilised gold along a deformation crack (LOWDH23, 438.05m). **D)** Remobilised gold situated at a fracture termination (LOCP81, 688.2 m). **E)** Larger, more equidimensional, remobilised gold grain situated along the intersection of multiple fractures (dilation zone). Similar sized gold can also exist along fractures bends (LOCP59, 535.4 m). **F)** Gold veinlets infilling micro-fissures in deformed pyrite, associated with high-grade of 21.9 g/t (LOCP44, 210.3 m). **G)** Equant subhedral gold grain attached to the margin of pyrite (LOCP40, 273.5 m). **H)** Aggregates of free anhedral gold in vein material, mainly confined to carbonate, in close proximity to pyrite (LOCP40, 272.5 m). Abbreviations same as *section 4.2.4.3* and Fig. 4.3.

As well as the strong relationship between sulphide abundance and gold grade, there also seems to be a clear relationship between grade and gold location at Gara. Although the remobilisation event(s) concentrated the gold locally (GIIb; Fig. 4.6f), many low-grade (<10 g/t) regions of the orezone are dominated by GIIa gold particles within deformation cracks (60-65%). In contrast, remobilised gold is less frequent in higher grade zones (>10 g/t), with equal or greater abundances of occluded gold. Ironically, this implies that the remobilisation event(s), in most cases, may have diluted the Gara mineralised system.

Native gold nearly always occurs as an alloy with silver and the Au/Ag ratio is described in terms of fineness (Hough *et al.*, 2009), which is generally represented by the formula:

$$1000 * \text{wt.\% Au} / (\text{wt.\% Au} + \text{wt.\% Ag}) \quad (\text{Eq. 4.2})$$

Gara gold is Ag-depleted, containing a fineness of 983 to >995 (Table 4.4), with silver levels highest in the northern parts of the deposit and in remobilised grains (up to 1.2 wt% Ag). Some grains contain Ag concentrations that are below the detection limits of EDS analysis (see appendices *section A-1* for detection limits).

Table 4.4. Representative SEM-EDS analyses of native gold at Gara (wt.%).

N	Au	Ag	Fe	Σ	N	Au	Ag	Fe	Σ
1	99.44	0.82	–	100.25	16	99.40	0.90	–	100.30
2	98.76	0.80	–	99.56	17	99.98	0.78	–	100.76
3	98.38	0.76	–	99.14	18	96.81	0.48	0.94	98.22
4	99.80	–	–	99.81	19	98.42	1.11	0.38	99.91
5	99.99	0.31	0.92	100.22	20	101.36	0.18	–	101.55
6	98.06	–	1.62	99.60	21	100.88	–	–	100.88
7	99.39	0.33	–	99.71	22	98.74	0.34	–	99.08
8	99.05	1.15	–	100.19	23	97.99	0.45	1.06	99.50
9	97.25	1.17	0.93	99.35	24	97.66	0.35	0.69	98.71
10	98.79	1.18	–	99.97	25	99.97	0.28	–	100.25
11	98.04	1.06	0.64	99.74	26	98.65	1.08	–	99.72
12	98.13	1.00	–	99.13	27	99.08	0.64	–	99.72
13	99.10	0.89	–	99.99	28	99.77	–	–	99.78
14	99.89	–	–	98.89	29	98.09	0.41	–	98.50
15	98.54	1.67	–	100.21	30	100.40	0.30	–	100.71

Blank- below detection limit. Fe from background pyrite.

4.2.5 Gara West satellite orebody

Gara West is a minor satellite deposit situated in argillaceous greywacke wall-rock approximately 0.5 km west of the main Gara orezone, with a mining resource (indicated and inferred) of 48,000 oz at average grades of 3 g/t (for year ending 2009). Gara West contains both vein and coarse disseminated sulphide (200-600 μm) styles of mineralisation. Apart from the appearance of replacement magnetite (a replacement phase discussed further in *section 4.3.4*), both mineralisation stages show similar mineralogy to Gara: pyrite is the principal sulphide phase (~99%); numerous stages of chalcopyrite formation are observed; trace assemblages dominated by monazite; and gold (<20 μm) confined to pyrite with low Ag concentrations (fineness >980).

4.3 Yalea & P-125

In this section the mineralisation styles and ore mineralogy of the world-class Yalea deposit (Randgold Resources primary discovery at Loulo) and its high-grade satellite deposit at P-125 are discussed.

4.3.1 Orebody parameters

Yalea lies 6 km to the SE of Gara and lies on a third-order, N-S brittle-ductile shear (R-shear geometry), formed during transpressional movement (D_3 deformation) along the NNE Yalea-trend that hosts mineralisation further to the north at Loulo-3, Loulo-2 and Loulo-1 (the last two deposits are not discussed in this study). Based on differences in mineralisation styles, petrogenetic history and alteration assemblages, the northern parts of the Yalea deposit can be divided into a separate entity, distinct from the main Yalea orezone (the Yalea North oreshoot). Yalea North occurs at the intersection between the N-S and NNE-trending shears. The P-125 satellite deposit is situated 0.5 km north of Yalea along another N-S Reidal shear. The location of the orebodies and their structural setting is illustrated in Fig. 4.7.

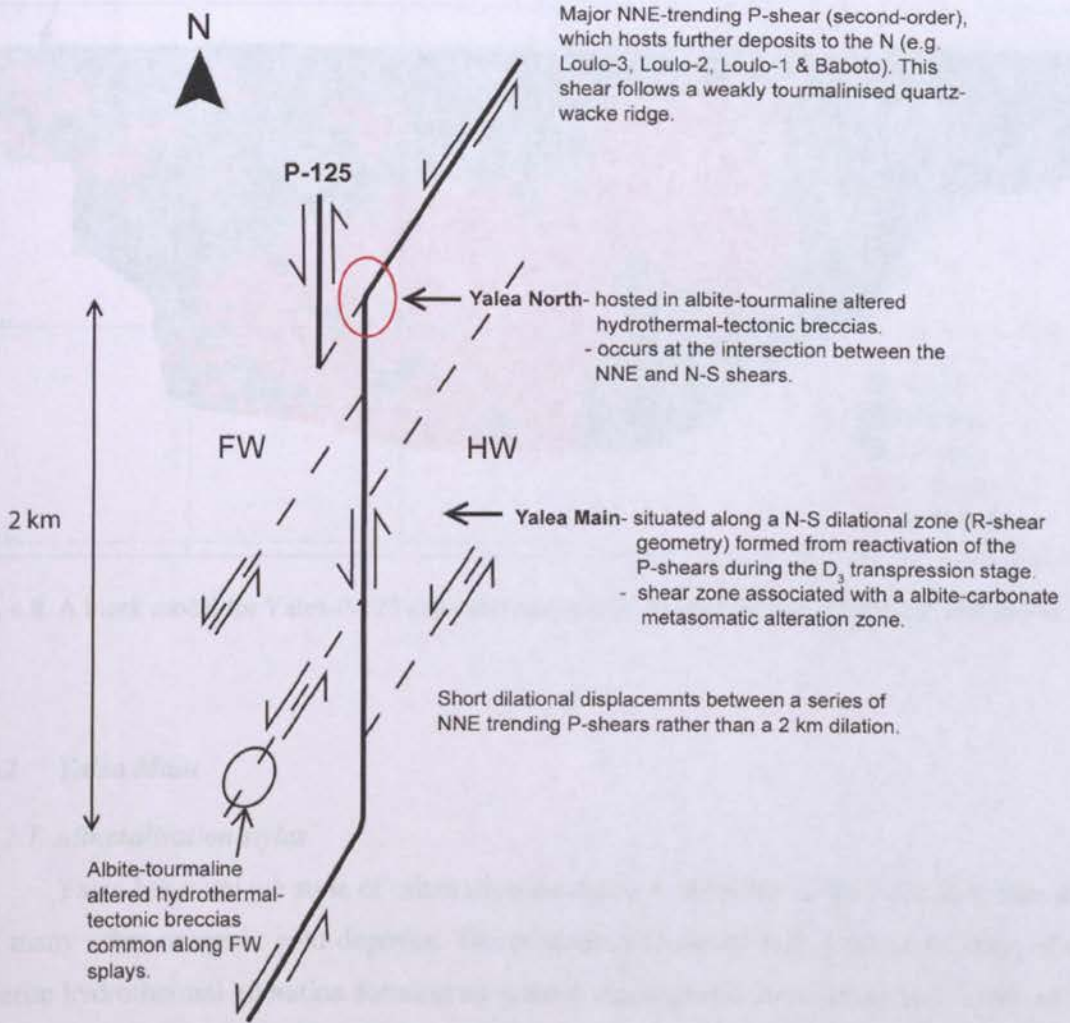


Fig. 4.7. The structural setting for the Yalea & P-125 deposits. See *section 3.2.2* for further details. FW = footwall and HW = hangingwall.

Currently, the Yalea mineralised structure is the largest orebody at Loulo, with a mining reserve and resource of 4.21 Moz at 4.91 g/t and 6.49 Moz at 4.77 g/t, respectively (for year ending 2009). Open-pit mining started in November 2005 and in June 2008 the first ore was mined from Yalea underground project (approximately 90% of the ore sits underground). Gold grades vary throughout the orebody, but the highest grades occur in the central and southern parts of the Yalea deposit (Fig. 4.8). The high-grade zone in the central parts of the deposit occurs along a vertical flexure of the N-S Yalea shear, where the shear steepens from 60° to the east to sub-vertical (a possible localised dilational zone).

Fig. 4.8. A block model for Yalea-P-125 deposits (courtesy of Randgold Resources). Grid 500:500 m.

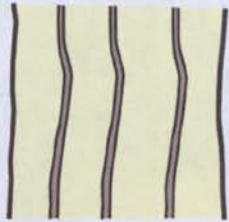
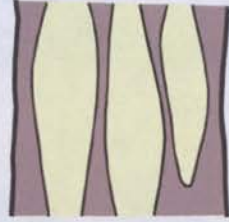
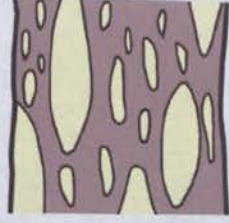
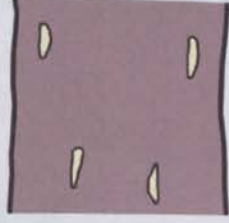


4.3.2 Yalea Main

4.3.2.1 Mineralisation styles

Yalea has a unique style of mineralisation that is remarkably different to that seen at Gara and many other orogenic gold deposits. The orezone is characterised by an early stage of albite-ankerite hydrothermal alteration forming an intense metasomatic zone (maximum width of 30 m) along the N-S shear (*see chapter 5*). Very minor sulphides are associated with this alteration phase (<1 vol.%). The main mineralisation phase occurs late in the fluid history, located in narrow ductile and brittle sulphide \pm quartz shears that overprint and deform the early alteration material, rather than forming distinct carbonate-quartz veining as observed at Gara (although minor ankerite-quartz mineralised are seen). A variety of tectonic and hydrothermal textures are observed in the mineralisation zone (Table 4.5; Fig. 4.9). These textures are controlled by rheological contrasts (albite-rich zones show more brittle textures, while carbonate-rich zones exhibit ductile shearing) and possible differences in strain along the shear. Barren calcite-quartz veining is observed in wall-rock surrounding the orezone, post-dating the textures shown in Table 4.5.

Grade controls at Yalea Main differ to those observed at Gara. At Yalea, high sulphide abundance is not always associated with strongly mineralised zones (a weaker sulphide-Au relationship). Yalea gold is associated with multiple sulphide phases (*section 4.3.2.2.3*) and consequently, the number of different sulphides present is a more important mineralisation control than the amount of the sulphides present. Gangue phases at Yalea Main are similar to Gara, with accessory apatite, rutile, ilmenite and leucoxene (the last two are alteration products of pyrite; Eq. 4.1).

Table 4.5. Schematic cartoons of the various textures present along the N-S Yalea Main orezone.

Texture	Description	Schematic
Type 1	Tectonic fabric- narrow (mm scale), parallel to sub-parallel, N-S sulphide shears crosscutting early albite-carbonate alteration. Common in albite-rich zones and often overprinted by type 4 hydrothermal textures.	
Type 2a	Tectonic fabric- carbonate-rich zones deform in a ductile manner with the formation of pronounced boudins aligned parallel to the main shear. This allows mineralisation fluids to occupy the space left open during deformation (Fig. 4.9a).	
Type 2b	Tectonic fabric- carbonate-rich boudins in type 2a stretch and brecciate. Commonly seen with texture type 2a (Fig. 4.9b).	
Type 3	Tectonic fabric- albite-carbonate alteration material deforms sufficiently enough to allow space for massive sulphides to be deposited. Rare texture associated with high-grade (>20 g/t) (Fig. 4.9c).	
Type 4a	Hydrothermal overprint of type 1- network of sulphide ± quartz veinlets cross cutting albite-carbonate alteration zone. Commonly seen in albite-rich zones (Fig. 4.9d).	
Type 4b	Hydrothermal fabric- albite-carbonate material becciates as a result of hydrothermal stress (jigsaw texture). Confined to albite-rich zones (Fig. 4.9e).	

Note- light yellow represents the albite-carbonate metasomatic zone, while the grey material signifies the sulphide mineralisation.

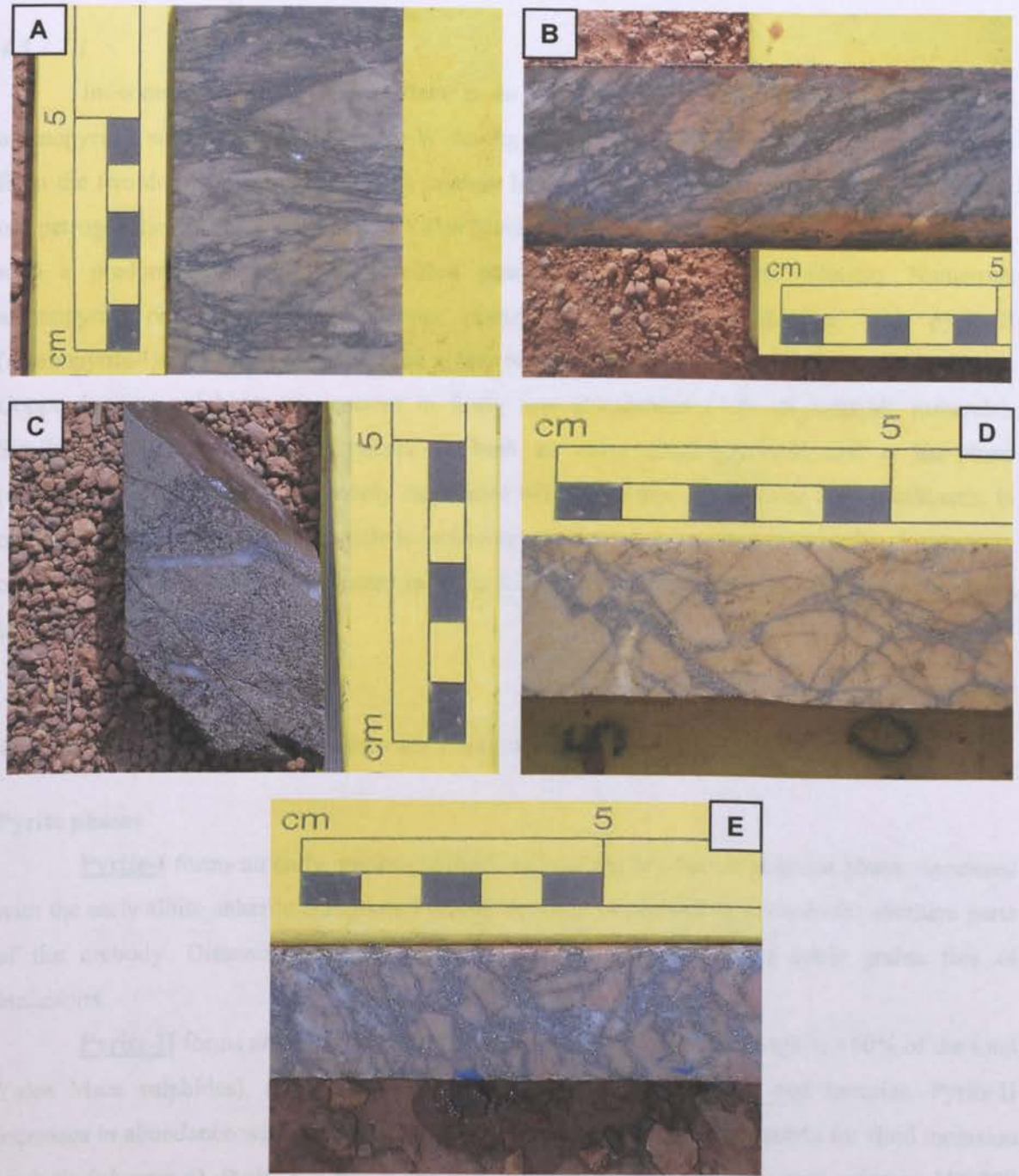


Fig. 4.9. Drill core photos of the various tectonic and hydrothermal textures present within the Yalea Main orezone. **A)** A carbonate-rich section of the shear showing strong ductile deformation features. Sulphides (dark material) are wrapped around carbonate-albite boudins (texture 2a) (YDH191, 678.6 m). **B)** Carbonate-rich boudins deformed further creating extra space for mineralisation (texture 2b) (YDH191, 676 m). **C)** Locally, the Yalea alteration zone deforms sufficiently enough to allow deposition of massive sulphides, associated with high grade of 26.8 g/t (texture 3) (YDH189, 597.2 m). **D)** An albite-rich part of the Yalea shear showing the dominance of hydrothermal textures- network of arsenopyrite veinlets (texture 4a) (YDH191, 683.3 m). **E)** Pink albite-rich zones also characterised by hydrothermal breccias with sulphides and quartz situated in the matrix (texture 4b) (YDH143, 622.25 m). The range of ductile and brittle textures observed at Yalea Main are summarised in Table 5.5.

4.3.2.2 Ore mineralogy

4.3.2.2.1 Paragenesis

In contrast to Gara, Yalea Main is an As-rich deposit (20- to 30-fold increase in arsenopyrite) with a typical Fe-As-Cu-W-Au-Ag-Pb metal association. Pyrite and arsenopyrite form the two dominant sulphide phases (mainly between 70:30 to 60:40 ratio). A more complex ore petrogenetic history is observed at Yalea Main. Two generations of pyrite formation are seen, with a predominant pyrite-II mineralised phase (~95% of the pyrite phases). Numerous arsenopyrite phases are also apparent, occurring in textural equilibrium with pyrite-II (arsenopyrite-I) and more commonly as a late replacement phase of pyrite-II (arsenopyrite-II). Copper-bearing sulphides are present in fairly low abundances (<5% of sulphide minerals). Similar to Gara, chalcopyrite occurs as both an early (chalcopyrite-I) and a late-phase (chalcopyrite-II); the latter commonly associated with tennantite. Other trace ore constituents, in order of decreasing abundances, include: scheelite, pyrrhotite, galena and jamesonite. A summary of the mineral paragenesis is presented in Table 4.6, and the evidence is discussed in the following section.

4.3.2.2.2 Ore-related sulphides and accessory phases

Pyrite phases

Pyrite-I forms an early, minor (<1% of the total pyrite), barren sulphide phase associated with the early albite-ankerite alteration. Pyrite-I increases in abundance towards the southern parts of the orebody. Disseminated pyrite occurs as granular (30-300 μm) cubic grains free of inclusions.

Pyrite-II forms an extensive sulphide mineralisation phase (ore stage 1; ~60% of the total Yalea Main sulphides), associated with the late brittle-ductile shears and breccias. Pyrite-II increases in abundance with depth, and is usually accompanied by minor quartz for fluid inclusion analysis (*chapter 6*). Pyrite exhibits cubic or pyritohedral habits (30 μm -1 mm, average 150-200 μm) and also exists as rare massive pyrite (Fig. 4.9d). Pyrite-II frequently shows diffusive and, less commonly, concentric zonation patterns with arsenian pyrite (0.5-2 wt.%), and has a close association with numerous arsenopyrite phases (Fig. 4.10). This pyrite phase contains inclusions of chalcopyrite and pyrrhotite, and other minerals including gold (approximately 80% of Yalea's visible gold). Pyrite-II has undergone similar deformation features to pyrite at Gara, with abundant micro-fissures dissecting the sulphides.

Table 4.6. Summary of hydrothermal alteration, gangue and sulphide paragenesis for Yalea Main.

Mineral	Pre-ore stage	Main ore stage		Post-main ore stage	Supergene
		1	2		
Wall-rock alteration					
Albite	██████████				
Ankerite	██████████	—————			
Quartz	—————				
Haematite	—————				
Sericite		██████████			
Chlorite		██████████			
Vein material					
Calcite		—————			
Ankerite		—————			
Quartz		—————			
Gangue					
Rutile		—————			
Apatite		—————			
Ilmenite				—————	-----
Sulphides/Opaques					
Pyrite-I	—————				
Pyrite-II		██████████			
Arsenopyrite-I		██████████			
Jamesonite		—————			
Chalcopyrite-I		—————			
Pyrrhotite		—————			
Sayrite		—————			
Arsenopyrite-II			██████████		
Galena			—————		
Scheelite		—————			
Monazite				—————	
Tennantite				██████████	
Chalcopyrite-II				██████████	
Gold		██████████		-----	
Supergene					
Leucoxene					██████████
Covellite					—————
Chalcocite					—————

Note- alteration history discussed in detail in chapter 5.

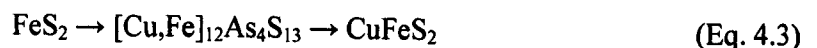
Arsenopyrite phases

At Yalea Main, arsenopyrite accounts for approximately 30-35% of the sulphide minerals. **Arsenopyrite-I** forms around 30% of the arsenic phases and coexists with pyrite-II in ore stage 1, forming euhedral tabular inclusions or intergrowths (10-100 μm) with pyrite (and vice-versa) (Fig. 4.10a, b). **Arsenopyrite-II** forms the dominant As-phase (same composition as arsenopyrite-I) and is the main sulphide phase in ore stage 2. Arsenopyrite-II is often massive, occurring as overgrowths along the margins of pyrite-II stringers and veinlets (Fig. 4.10e), existing as pseudomorphs of pyrite-II (Fig. 4.10c, d), or crosscutting pyrite-II (Fig. 4.10f). This sulphide phase contains inclusions of scheelite, galena and gold. Both arsenopyrite phases are less deformed than the pyrite phases. No optical or compositional zoning is observed.

Copper-bearing sulphides

Cu-bearing sulphides occur in similar concentrations to Gara (~5% of the sulphide assemblage). **Chalcopyrite-I** occurs as minor inclusions within pyrite-II and less so in arsenopyrite-I. They exist as tabular to anhedral grains (up to 50 µm), occasionally located along pyrite growth boundaries (Fig. 4.10h). **Chalcopyrite-II** (same composition as earlier phase) represents the last stage of sulphide paragenesis and can be observed infilling fractures cutting mainly pyrite-II (Fig. 4.10g), and less commonly in arsenopyrite-I and arsenopyrite-II. The distribution of chalcopyrite-II throughout the deposit is variable and largely controlled by the deformation history of the major sulphide phases. This late chalcopyrite phase is also observed as a minor replacement phase of pyrite-II (Fig. 4.10i). Gold is occasionally seen in chalcopyrite-II (<2% of the overall visible gold).

Tennantite ($[\text{Cu,Fe}]_{12}\text{As}_4\text{S}_{13}$) forms another late Cu-bearing mineral stage at Yalea Main, where it commonly forms an intermediate phase during the transformation of pyrite-II to chalcopyrite-II (Fig. 4.10i):



Tennantites contain elevated Fe contents (Table 4.7) and zonation patterns reflecting variations in Sb and Zn concentrations (Fig. 4.10j). They also occur without chalcopyrite-II, in discrete veinlets cutting all pyrite and arsenopyrite sulphide phases.

Table 4.7. Chemical composition of tennantite at Yalea determined by SEM-EDS analysis (wt.%).

	1	2	3	4	5	6	7	8	9	10
S	28.26	27.52	28.81	27.08	28.51	27.08	28.70	27.54	28.81	28.86
Fe	7.61	6.80	7.19	6.60	7.20	6.13	8.22	6.46	7.14	8.14
Cu	43.46	41.85	43.90	41.37	43.23	41.47	43.70	42.22	43.69	42.70
Zn	–	1.18	0.71	1.48	1.02	1.59	–	1.87	0.96	–
As	18.94	13.53	19.23	12.04	19.82	12.72	19.31	11.91	20.11	19.55
Sb	1.52	9.75	–	11.97	–	10.68	–	11.80	–	–
Σ	99.78	100.62	99.91	100.55	99.74	99.68	99.93	101.81	100.72	99.24

Blank- below detection limit

Accessory sulphides

Accessory sulphides (<1%) at Yalea Main are composed of Fe-Sb-Pb bearing minerals. **Pyrrhotite** (<30 µm) forms the most common inclusion-type within pyrite (after arsenopyrite-I and chalcopyrite-I), occurring as a trace phase. **Galena**, absent from Gara, is present as rare spherical micro-inclusions (2-15 µm) in arsenopyrite-II. Along with tennantite, **jamesonite** ($\text{Pb}_4\text{FeSb}_4\text{S}_{14}$) occurs as a rare Sb-phase, usually present as flame-shaped inclusions (10-25 µm) confined to pyrite.

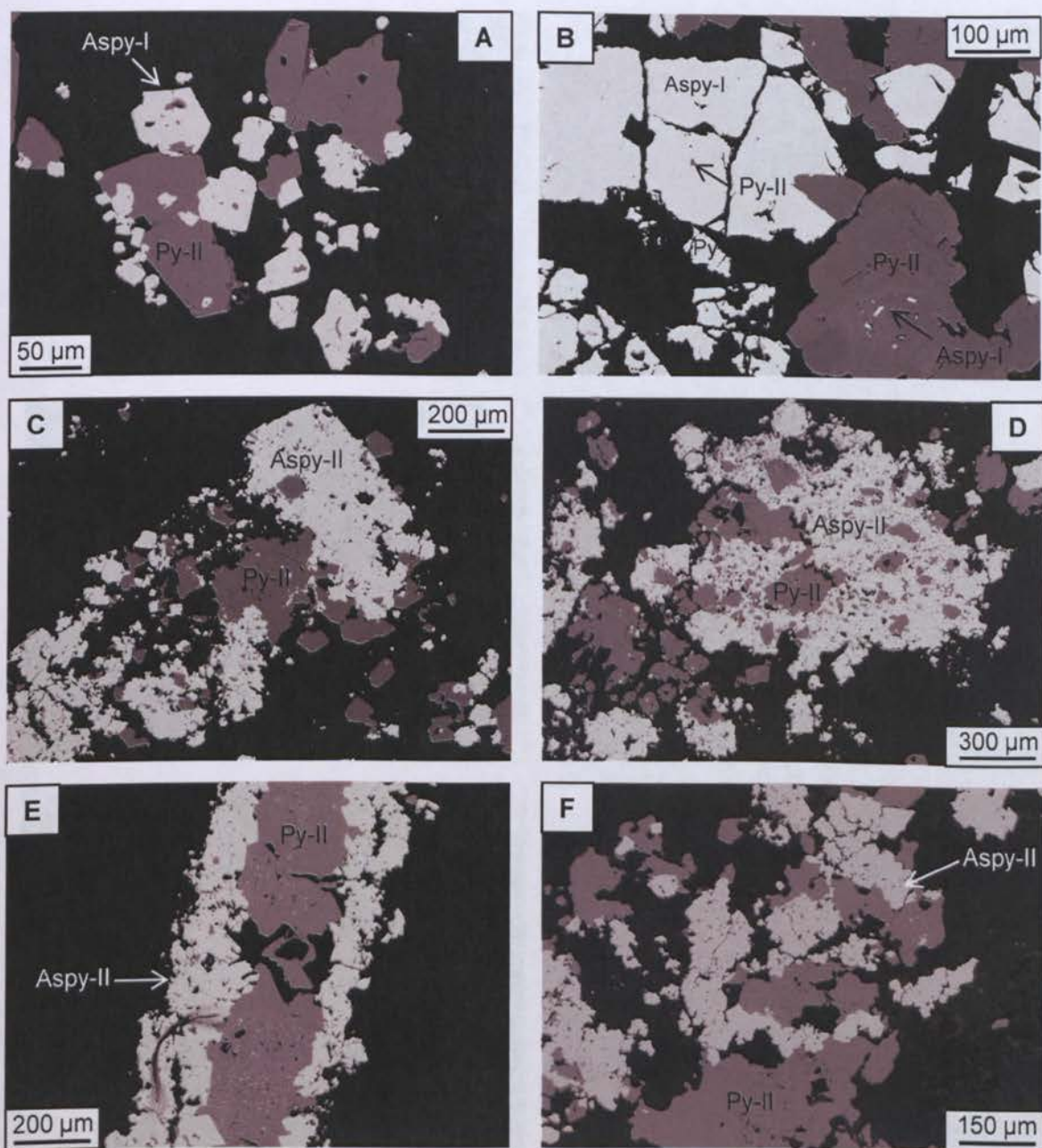


Fig. 4.10. BSE images of the ore phases present at Yalea Main. **A)** Euhedral arsenopyrite-I crystals intergrown with larger pyrite-II (YDH143, 622.25 m). **B)** Contemporaneous pyrite-II and arsenopyrite-I formation showing intergrowths and inclusions of pyrite in arsenopyrite (and vice-verse) (YDH159W, 596.0 m). **C)** Late-phase arsenopyrite-II existing as partial pseudomorphs of pyrite-II (YDH189, 591.3 m). **D)** Pyrite-II grain extensively replaced by arsenopyrite-II (YDH248, 489.4 m). **E)** Arsenopyrite-II overprinting pyrite-II along vein margins (YDH132, 518.8 m). **F)** Arsenopyrite-II crosscutting pyrite-II grain (YDH223, 789.0 m). Abbreviations same as Fig. 4.3.

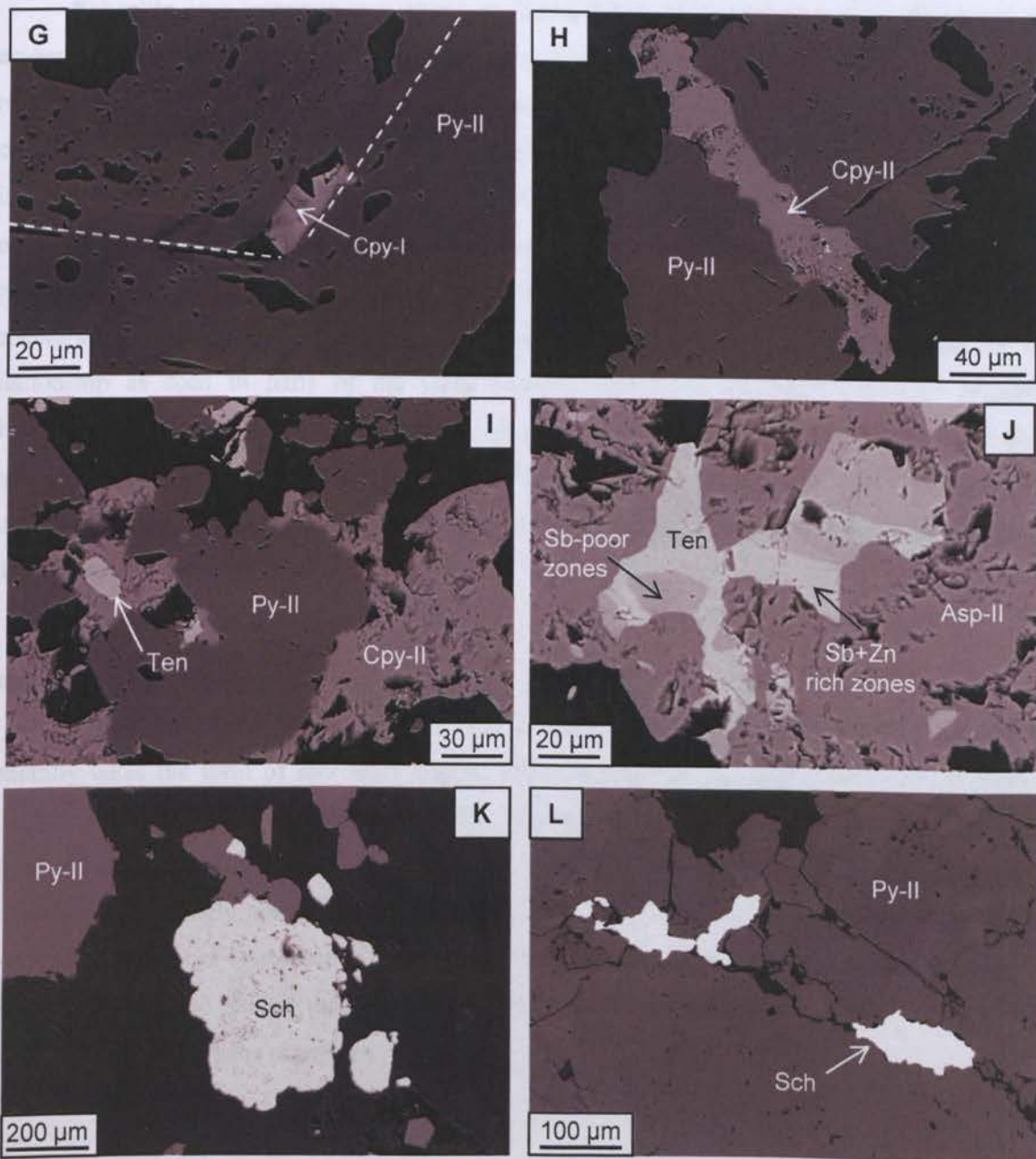


Fig. 4.10. cont. **G**) Chalcopyrite-I inclusion situated along pyrite-II growth boundary (YDH159W, 596.0 m). **H**) More common late-stage chalcopyrite-II veinlet cross cutting pyrite-II (YDH237, 743.55 m). **I**) Pyrite-II replaced by chalcopyrite-II; the latter containing inclusions of tennantite (YDH189, 591.3 m). **J**) Zoned tennantite overprinting arsenopyrite-II (YDH143, 622.25 m). **K**) Scheelite porphyroblast and smaller grains intergrown with pyrite-II. **L**) Late-stage, irregular-shaped scheelite post-dating pyrite-II (YDH231, 464.65 m). Ten = tennantite; other abbreviations same as Fig. 4.3 and Fig. 4.4.

Tungstates, oxides and phosphates

Scheelite is a common ore phase at Yalea Main. Scheelite occurs in all stages of paragenesis, as inclusions and intergrowths in pyrite-II (Fig. 4.10k), arsenopyrite-I and arsenopyrite-II, and situated in late fractures cutting all the above sulphide phases (Fig. 4.10l). Scheelite often forms multiphase aggregates or exists as granular grains. They have a bimodal size distribution across the deposit, with most grains between 2-100 µm in size and rarer larger porphyroblasts up to 2 mm (Fig. 4.10k). Disseminated scheelite within hydrothermal quartz is also common. Scheelite abundance varies significantly throughout the deposit, with higher concentrations in more As-rich zones (up to ~5% of the ore minerals). There is no apparent Au-W relationship as seen in parts of the Gara deposit. Rare U-Pb minerals (probably **savrite**- $\text{Pb}_2[\text{UO}_2]_5\text{O}_6[\text{OH}]_2 \cdot 4[\text{H}_2\text{O}]$) occur as tiny (<10 µm) subhedral inclusions within pyrite-II and replacement arsenopyrite-II. Monazite, present in significant amounts at Gara, forms an extremely rare mineral phase at the main Yalea orebody, where it exists as fine crystalline grains (<10 µm) with a close association with chalcopyrite-II.

Supergene minerals

Supergene alteration at Yalea is only a minor feature below the laterite cover and generally takes the form of secondary copper minerals, such as **covellite** (CuS) and **chalcocite** (Cu₂S) (pseudomorphous after chalcopyrite-II). The presence of these supergene minerals has led to ore recovery issues. Copper is present as Cu¹⁺ and Cu²⁺ ions within covellite and chalcocite. These ions are strongly reactive with cyanide (used as gold ligand in mineral processing), while chalcopyrite (Cu³⁺) is less reactive. To resolve this problem, an extra step was included in the mineral processing to oxidise the Cu. No apparent secondary concentration of gold is observed as a result of these supergene processes.

4.3.2.2.3 Gold

Numerous mineralisation events are interpreted at Yalea Main, with gold situated in multiple sulphide phases including pyrite-II (Fig. 4.11a), arsenopyrite-I, arsenopyrite-II (Fig. 4.11b), chalcopyrite-II (Fig. 4.11c) and tennantite (Fig. 4.11d). Gold occurs as occluded gold in the sulphides (GI; 40%); as small, randomly distributed remobilised grains within deformation cracks (GII; 55%); and rarely as grains attached to the margins of pyrite and arsenopyrite grains (GIII; <5%). Approximately 80% of all visible gold is associated with pyrite phases. However, arsenopyrite abundance does not seem to affect the grade at Yalea Main, suggesting a majority of the gold associated with arsenopyrite exists as refractory gold (locked up in the crystal lattice; GIV). Similar observations are made at other As-rich orebodies along the Yalea-trend (e.g. P-125, Loulo-3 and Baboto). Wavelength dispersive spectra (WDS) analysis of the arsenopyrite grains shows no evidence of refractory gold (detection limit for Au on the WDS is ~40 ppm), which

implies gold either exists as nanoparticles or that refractory gold is irregularly distributed throughout the arsenopyrite phases. Yalea gold is extremely fine-grained (twice as fine as Gara gold), with average grain sizes of 8-10 μm . Silver concentrations of the gold grains are distinctly higher than Gara, with a gold fineness of 920 to 990 (average 950; Table 4.8).

Table 4.8. Representative SEM-EDS analyses of native gold at Yalea Main (wt.%).

N	Au	Ag	Fe	As	Σ	N	Au	Ag	Fe	Σ
1	95.87	6.55	—	—	102.43	13	94.56	4.99	—	99.55
2	96.12	1.04	0.68	0.89	98.73	14	91.97	6.76	0.22	98.95
3	93.59	6.14	0.80	—	100.53	15	97.12	3.49	—	100.61
4	93.83	4.38	—	—	98.21	16	96.10	3.10	—	99.20
5	98.74	1.59	—	—	100.33	17	98.40	1.20	0.23	99.83
6	92.34	7.87	0.23	—	100.44	18	93.82	5.18	—	99.00
7	99.38	1.54	—	—	100.92	19	95.17	3.63	—	98.80
8	96.78	4.20	—	—	100.98	20	95.55	3.35	—	98.90
9	97.56	2.68	0.26	—	100.50	21	98.12	1.48	—	99.60
10	99.12	1.64	—	—	100.76	22	97.23	2.84	—	100.07
11	94.43	4.98	0.46	0.83	100.70	23	92.32	6.44	—	98.76
12	93.96	6.12	—	—	100.08	24	94.78	5.13	—	99.91

Blank- below detection limit. Fe & As from background sulphides

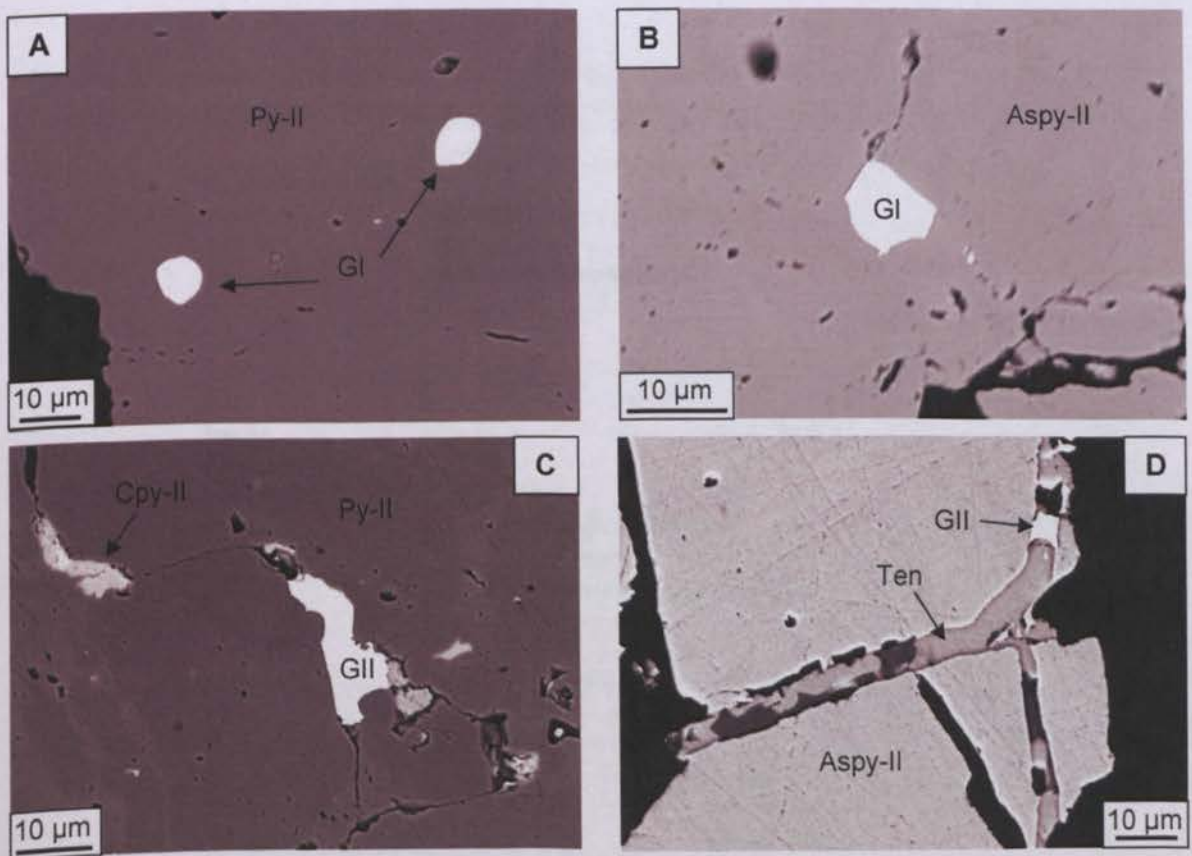


Fig. 4.11. Gold grains associated with numerous sulphide phases at Yalea Main (BSE images). **A)** Anhedral occluded gold in pyrite-II (YDH132, 508.0 m). **B)** Subhedral gold grain in core of arsenopyrite-II (YDH237, 741.68 m). **C)** Fracture-bound gold in pyrite-II, spatially associated with chalcopyrite-II (YDH248, 489.4 m). **D)** Gold within late tennantite crosscutting arsenopyrite-II (remobilised?) (YDH143, 622.25 m). Abbreviations same as in text and Fig. 4.10.

4.3.3 Yalea North

4.3.3.1 Mineralisation styles

The Yalea North oreshoot is hosted within highly-altered (albite + tourmaline) hydrothermal-tectonic breccias (described in *section 3.3.5*; Fig. 3.11) along the intersection of the NNE trending P shear and the N-S Yalea structure. This oreshoot is associated with lower gold grades than other parts of the Yalea orebody (<4 g/t; Fig. 4.8). These breccia host rocks are frequently observed between Yalea North and P-125, as well as along footwall splays in the main Yalea orezone (Fig. 4.7). Mineralisation is confined to the matrix of the breccias or within minor pyrite stringers or quartz-ankerite veining which crosscuts the breccia fragments. The alteration characteristics of the hydrothermal-tectonic breccias are discussed in *chapter 5*.

4.3.3.2 Ore mineralogy and paragenesis

The breccia-hosted Yalea North orebody shows strong petrogenetic differences from the main Yalea orebody and other deposits situated along the Yalea-trend. Mineral assemblages are characterised by a Fe-Cu-Ni-Co-As-REE-Au-Ag-Pd metal association, similar to Gara (with the addition of Co & Ag). A summary of the mineral paragenesis is presented in Table 4.9 and the evidence is discussed below.

Table 4.9. Summary wall-rock alteration, gangue and sulphide paragenesis for the Yalea North oreshoot.

Mineral	Pre-ore stage	Main ore stage	Post-main ore stage	Supergene stage
Wall-rock alteration				
Albite	██████████	██████████		
Ankerite	██████████	██████████		
Tourmaline	██████████	██████████		
Quartz		██████████		
Gangue				
Apatite			██████████	
Rutile			██████████	
Ilmenite				██████████
Sulphides/Opaques				
Pyrite-I	██████████			
Pyrite-II		██████████		
Arsenopyrite		██████████		
Cobaltite		██████████		
Pentlandite		██████████		
Pyrrhotite		██████████		
Monazite		██████████		
Xenotime		██████████		
Chalcopyrite-I		██████████		
Gersdorffite			██████████	
Chalcopyrite-II			██████████	
Tennantite			██████████	
Gold		██████████	-----	
Supergene				
Leucoxene				██████████
Limonite				██████████

Note- alteration discussed in *chapter 5*.

Minerals in the Fe-Ni-S system

The dominant sulphide phase at Yalea North is pyrite (major decrease in arsenopyrite abundance compared to Yalea Main). Pyrite occurs as a minor barren pyrite phase (**pyrite-I**; <2% of total sulphides) associated with the albite-ankerite alteration material (clast fragments). The mineralised pyrite generation (**pyrite-II**; ~90% of total sulphides) exists in the matrix of the breccias or situated within veinlets that overprint these rocks. Pyrite-II occurs as aggregates of euhedral pyritohedral vuggy grains (80 μm -1 mm, average 200-300 μm) that lack the extensive tourmaline replacement textures seen at Gara (pre- to syn-mineralisation tourmaline events). As well as gersdorffite (discussed below), pyrite is host to several Fe-Ni sulphides (Table 4.10) including Ni-bearing **pyrrhotite** (~10 μm) and rare **pentlandite** (<10 μm); the latter associated with Ni-rich cobaltite. Pyrite is also host to a range of other inclusions (<20 μm) including common chalcopyrite-I, arsenopyrite and monazite, and rare Se-bearing galena, ilmenite, rutile, apatite, xenotime, barite and zircon. Locally, pyrite is heavily replaced by skeletal and acicular leucoxene (with an intermediate ilmenite stage) similar to Gara.

Minerals in the As-Co-Ni-Fe-S system

Yalea North contains a variety of Ni-Co-Fe sulphur-arsenides (5-10% of the overall sulphides). **Arsenopyrite** occurs as anhedral micro-inclusions (<5-15 μm) or larger euhedral grains (up to 500 μm) intergrown with pyrite-II (Fig. 4.12a). Pyrite inclusions are also frequently observed in arsenopyrite indicating both sulphide phases formed contemporaneously. No late replacement arsenopyrite is observed at Yalea North (contrast to Yalea Main).

Cobalt and nickel sulphur-arsenides occur as minor ore phases (1-5% of the sulphide population) with similar concentration levels to arsenopyrite. Cobaltite (CoAsS) and gersdorffite (NiAsS) form a continuous compositional series (Fig. 4.13), with increasingly Ni-rich minerals towards the late stages of paragenesis. **Cobaltite** forms in textural equilibrium with the main pyrite phase as blocky grains (10 to 40 μm) on the margins of larger pyrite (Fig. 4.12b). Two varieties of cobaltite are present: (1) an isomorphous cobaltite series (varying Fe contents; generally lower than gersdorffites); and (2) Fe-Ni rich cobaltite (intermediate in composition between cobaltite and gersdorffite). **Gersdorffite** is more abundant than cobaltite and occurs late in the petrogenetic history (post pyrite-II), occasionally associated with chalcopyrite-II. Gersdorffite forms subhedral to idiomorphic thin irregular-shaped grains (up to 100 μm) surrounding pyrite (Fig. 4.12c, d), or as smaller grains (<20 μm) within deformation cracks in pyrite (Fig. 4.12e). Two varieties of Co-depleted gersdorffite are detected: (1) Fe-rich (>9 wt.% Fe) gersdorffite; and (2) rarer, Fe-poor (<9 wt.% Fe), Sb-bearing gersdorffite. Cobalt and gersdorffite compositions are presented in Table 4.10 and Fig. 4.13.

Table 4.10. Representative chemical composition of the Fe-Ni-S and the As-Ni-Co-Fe-S minerals of the Yalea North oreshoot by SEM-EDS analysis (wt.%).

N	Mineral	Fe	As	Co	Ni	Sb	S	Σ
1	Py-II	53.27	-	-	-	-	46.54	99.81
2	Py-II	53.2	-	-	-	-	46.23	99.43
3	Po	60.09	-	-	0.23	-	38.18	98.50
4	Po	58.89	-	-	0.42	-	36.90	96.21
5	Pn	42.45	-	-	25.89	-	33.45	101.79
6	Pn	40.34	-	-	26.45	-	33.12	99.91
7	Pn	39.21	-	-	27.99	-	33.65	100.85
8	Aspy	34.81	42.46	-	-	-	22.12	99.40
9	Aspy	34.53	45.40	-	-	-	21.68	101.61
10	Aspy	34.46	44.93	-	-	-	21.92	101.31
11	Aspy	35.17	44.28	-	-	-	21.72	101.17
12	Aspy	35.09	43.73	-	-	-	20.47	99.30
13	Aspy	35.34	43.73	-	-	-	21.23	100.31
14	Aspy	34.75	44.17	-	-	-	20.67	99.60
15	Gf	15.87	42.63	-	19.86	-	20.33	98.68
16	Gf	14.68	44.17	-	21.06	-	21.03	100.94
17	Gf	10.17	44.59	-	24.83	-	19.43	99.02
18	Gf	8.80	45.86	-	26.64	-	19.79	101.09
19	Gf	14.87	43.78	1.52	19.53	-	21.04	100.74
20	Gf	12.82	43.66	1.57	22.42	-	20.07	100.52
21	Gf	13.73	42.45	2.40	19.32	-	20.45	99.33
22	Gf	15.56	43.61	-	19.69	-	20.32	99.19
23	Gf	14.78	41.47	1.99	19.44	-	21.79	99.48
24	Gf	5.40	42.21	-	28.88	3.45	18.29	101.06
25	Gf	9.30	44.46	-	25.60	0.57	19.80	99.74
26	Ni-Cb	9.92	41.27	14.26	11.25	-	20.43	97.12
27	Ni-Cb	9.24	41.84	18.14	9.18	-	20.54	98.93
28	Ni-Cb	9.82	42.45	12.90	12.81	-	20.40	98.39
29	Ni-Cb	15.63	38.32	9.85	12.15	-	23.06	99.02
30	Ni-Cb	9.74	41.85	13.86	12.64	-	20.13	98.21
31	Ni-Cb	11.22	41.74	14.69	10.58	-	20.81	99.03
32	Cb	3.72	41.10	32.32	1.31	-	20.94	99.39
33	Cb	7.64	41.96	22.09	6.17	-	20.22	98.09
34	Cb	11.53	35.74	26.27	0.92	-	25.30	99.77
35	Cb	4.24	41.17	31.92	0.85	-	21.04	99.22
36	Cb	7.79	41.85	24.68	5.39	-	20.59	100.30
37	Cb	10.47	38.23	21.83	5.05	-	22.76	98.34
38	Cb	5.57	40.49	30.77	1.15	-	20.83	98.81
39	Cb	7.87	41.71	23.99	5.01	-	21.46	100.05
40	Cb	3.43	42.45	32.51	1.05	-	20.35	99.79
41	Cb	6.02	42.65	24.94	5.14	-	19.80	98.56
42	Cb	3.67	42.37	32.24	1.13	-	20.71	100.13

Py- pyrite, Po- pyrrhotite, Pn- pentlandite, Asp- arsenopyrite, Gf- gersdorffite, Cb- cobaltite; Ni-Cb- Ni-rich cobaltite. Blank- below detection limit.

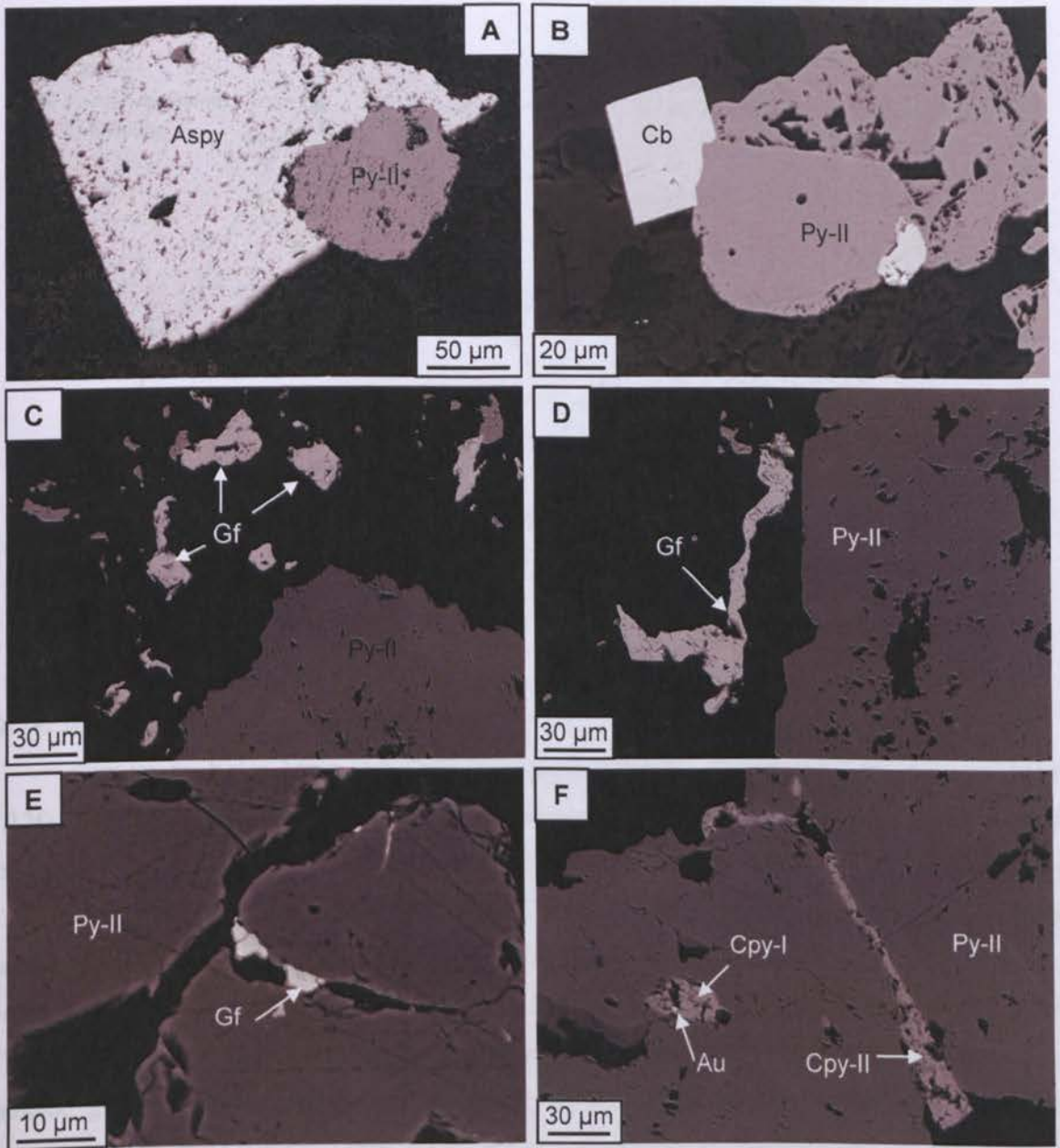


Fig. 4.12. BSE images of the ore phases at Yalea North. **A)** Contemporaneous pyrite and arsenopyrite formation (YDH149, 473.9 m). **B)** Blocky cobaltite crystal with mutually interpenetrating crystal boundaries with larger pyrite (YDH149, 468.8 m). **C)** Aggregate of idiomorphic gersdorffite crystals surrounding pyrite (YDH149, 476.8 m). **D)** Thin irregular-shaped gersdorffite crystal on the margin of vuggy pyrite (YDH254, 90.65 m). **E)** Small gersdorffite crystals within fracture cutting pyrite (YDH149, 476.8 m). **F)** Showing two-stage evolution of chalcopyrite common in the northern half of the Loulo permit (YDH254, 98.7 m). Same abbreviations as Table 4.10.

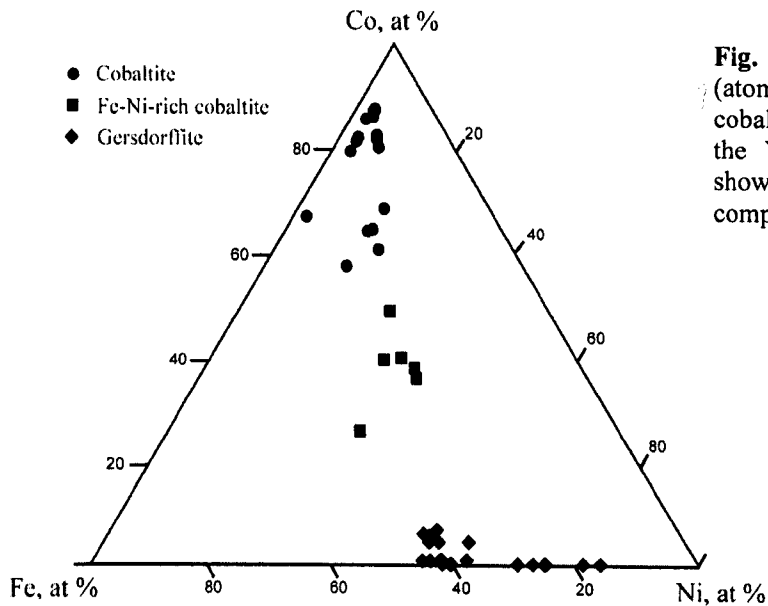


Fig. 4.13. Co-Ni-Fe ternary diagram (atomic %) showing the composition of cobaltite and gersdorffite minerals from the Yalea North orezone. Table 4.10 shows a representative chemical composition of these minerals.

Other ore phases

Similar to Yalea Main and Gara, two generations of **chalcopyrite** are observed (Fig. 4.12f). **Tennantite** is also associated with the chalcopyrite-II, but its relationship is more difficult to interpret compared to Yalea Main. Tennantite compositions are identical to those presented in Table 4.7. Yalea North is rich in REE minerals, with **monazite** forming at all stages of mineral paragenesis. Monazites exist as skeletal grains nucleated on sulphide margins and as micro-inclusions within pyrite-II (<10 μm), and in places are pseudomorphously replaced by apatite. They also occur late in the petrogenetic history infilling micro-fissures in deformed pyrite-II or as isolated grains (<10 μm) within the fractures. They have similar compositions to the Gara monazites (Monazite (-Ce); Table 4.11), and no systematic compositional difference occur between different generations. **Xenotime** is a rare phase associated with pyrite-II.

Table 4.11. Representative chemical composition of monazite at Yalea North by SEM-EDS analysis (wt.%).

	1	2	3	4	5	6	7	8	
SiO ₂	–	–	1.41	–	–	–	–	–	
Ce ₂ O ₃	20.14	16.50	16.12	16.61	18.36	18.05	16.04	16.79	
La ₂ O ₃	35.93	37.96	35.21	36.11	35.98	36.42	37.81	34.73	
Nd ₂ O ₃	11.89	14.46	15.13	14.48	14.12	14.70	13.97	16.35	
Fe ₂ O ₃	–	1.13	2.85	1.99	–	–	0.75	1.02	
CaO	0.49	–	–	–	0.51	1.12	0.49	0.50	
NiO	0.23	–	–	–	–	–	0.25	–	
P ₂ O ₅	29.84	29.61	28.78	29.58	30.49	29.27	29.33	30.49	
Total	98.42	99.66	99.50	98.77	99.47	99.56	98.53	99.89	
			Number of ions on the basis of 16 (O).						
P	4.00	3.94	3.77	3.94	4.02	3.92	3.94	3.99	
Si	–	–	0.22	–	–	–	–	–	
Sum	4.00	3.94	3.99	3.94	4.02	3.92	3.94	3.99	
Fe ³⁺	–	0.13	0.33	0.24	–	–	0.09	0.12	
Ni	0.03	–	–	–	–	–	0.03	–	
Ca	0.08	–	–	–	0.08	0.19	0.08	0.08	
Ce	1.17	0.95	0.91	0.96	1.05	1.05	0.93	0.95	
La	2.10	2.20	2.01	2.10	2.07	2.13	2.21	1.98	
Nd	0.67	0.81	0.84	0.81	0.79	0.83	0.79	0.90	
Sum	4.05	4.10	4.09	4.10	3.99	4.19	4.14	4.04	

Blank- below detection limit

4.3.3.3 Gold/ silver grains

Gold grains at Yalea North occur mainly as free gold within the matrix of the breccias or occluded in pyrite-II. Gold is rarely observed in arsenopyrite, chalcopyrite-I, chalcopyrite-II and gersdorffite. The fineness of the majority of the gold is between 920 to 990, with higher Ag concentrations in more As-rich zones (Table 4.12). As well as native gold, occasional native silver (<10 µm) and rare Pd-bearing gold grains are observed in this oreshoot (Table 4.12).

Table 4.12. Representative SEM-EDS analyses of native gold and silver grains at Yalea North (wt.%).

N	Au	Ag	Pd	Fe	Σ	N	Au	Ag	Fe	Σ
1	80.23	1.18	17.82	–	99.23	9	95.55	2.66	0.30	98.51
2	92.34	6.38	–	–	98.72	10	91.11	6.20	1.50	98.81
3	93.78	7.99	–	–	101.77	11	92.21	5.95	0.62	98.77
4	97.18	2.12	–	1.46	100.75	12	96.80	2.44	–	99.24
5	92.12	5.02	–	–	97.14	13	96.92	3.54	0.37	100.83
6	94.47	4.65	–	–	99.12	14	94.20	4.06	0.48	98.74
7	89.66	5.18	4.03	–	98.87	15	2.33	97.49	–	99.82
8	96.19	1.75	–	0.91	98.85	16	1.89	98.34	–	100.23

Blank- below detection limit. Fe from background pyrite. Analyses 15 & 16 are native silver grains.

4.3.4 P-125

4.3.4.1 Mineralisation styles

The P-125 satellite deposit is a shallow, high-grade (average grade of 5.4 g/t; as high as 78 g/t), orebody situated <0.5 km north of the Yalea pit. P-125 classifies as a massive disseminated sulphide-style deposit (a fourth style of Loulo mineralisation) (Fig. 4.14). Disseminated style mineralisation occurs on a smaller scale at Gara West, Faraba and P-64. P-125 also contains a minor ankerite-quartz vein stage (Fig. 4.14b). The relative timing of the disseminated- and vein-stage mineralisation is difficult to interpret, but in places the former seems to predate the latter (disseminated sulphides situated within fractures cutting the veins). The margins of the P-125 ore shoot (top and bottom) are characterised by typical Yalea ore, where mineralisation is confined to pyrite stringers or pyrite-quartz-ankerite veinlets situated in brittle shears that crosscut an early albite-ankerite (+ chlorite) metasomatic zone.



Fig. 4.14. Drill core images showing the main mineralisation style at P-125. **A)** Massive disseminated sulphides (pyrite and arsenopyrite; the latter too fine-grained to see with the naked eye) (P125DH12, 141 m). **B)** A weaker disseminated zone showing clearly the presence of both pyrite (70%) and arsenopyrite (greyish minerals; 30%). Arsenopyrite contains a brown halo where they have altered to goethite. Disseminated sulphides cut across a weakly mineralised quartz-carbonate vein (P125DH12, 154.9 m).

4.3.4.2 Ore mineralogy and paragenesis

The ore mineralogy and paragenesis at P-125 is similar to Yalea Main (Fe-As-Cu-W-Au-Pb-Ag metal signature) rather than Yalea North (Table 4.13). The minor vein stage shares identical features to the disseminated sulphides and so is included as one mineralisation event for the purpose of this study.

Table 4.13. Summary paragenesis for wall-rock alteration and ore phases at P-125.

Mineral	Pre-ore stage	Main ore stage 1	2	Post-main ore stage	Supergene
Wall-rock alteration					
Albite	██████████				
Ankerite	██████████				
Tourmaline				_____	
Chlorite	██████████	██████████		██████████	
Magnetite				██████████	
Veining					
Ankerite		██████████	██	██	
Quartz		██████████	██	██	
Sulphides/Opaques					
Pyrite		██████████			
Arsenopyrite-I		██████████			
Chalcopyrite-I		_____			
Pyrrhotite		_____			
Scheelite		_____			
Arsenopyrite-II			██████████		
Galena			_____		
Chalcopyrite-II				_____	
Tennantite				_____	
Gold		██████████	██████████	██████████	
Supergene					
Haematite					██████████
Goethite					_____

Note- A more complex paragenesis is possible if the massive sulphide phase and minor vein stage represent separate mineralisation events. Wall-rock alteration is discussed further in *chapter 5*.

Although in hand-specimen pyrite seems to be the pre-dominant sulphide phase (Fig. 4.14a), fine-grained arsenopyrite (<500 µm) is extremely common (15-30% of total sulphides in the disseminated phase and up to 50% in the minor vein phase). Like the main Yalea orebody, a two-stage arsenopyrite growth occurs (Fig. 4.15a to d). Pyrite and arsenopyrite contain inclusions of chalcopyrite-I, scheelite, galena and pyrrhotite. The last stages of sulphide paragenesis are associated with tennantite and chalcopyrite-II formation; both minor phases (<5%) replacing the major sulphide phases (Fig. 4.15e, f). Visible gold grains at P-125 (5-70 µm; average <20 µm) are largely confined to pyrite and its secondary products (*see below*), but also seen in arsenopyrite-I and arsenopyrite-II. Gold fineness is extremely uniform between 975 and 990 (Table 4.14).

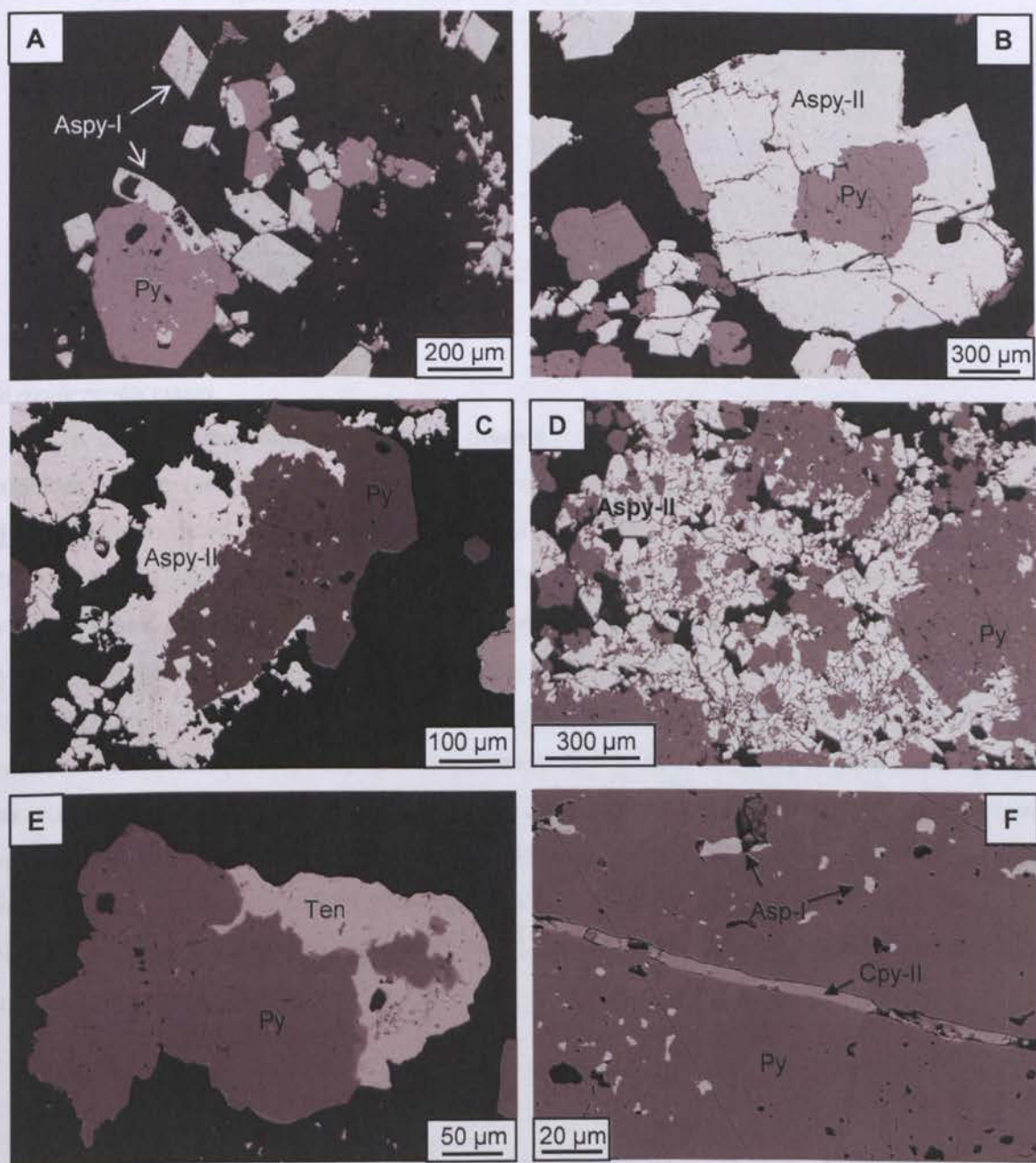


Fig. 4.15. BSE images showing the major sulphide phases at P-125. **A)** Rhombic arsenopyrite-I grains intergrown with disseminated pyrite (P125DH12, 143.35 m). **B)** Arsenopyrite-II pseudomorphously replacing a disseminated pyrite grain (P125DH12, 144.2 m). **C)** Arsenopyrite-II replacing the rim of a vein-phase pyrite grain (P125DH12, 146.6 m). **D)** Arsenopyrite-II overprinting disseminated pyrite (P125DH16, 150.1 m). **E)** Disseminated pyrite replaced by tennantite (P125DH12, 154.9 m). **F)** Chalcopyrite-II filling fracture cutting disseminated pyrite (P125DH12, 144.2 m). Same abbreviations as Fig. 4.10

Table 4.14. Representative SEM-EDS analyses of native gold at P-125 (wt.%).

<i>N</i>	Au	Ag	Fe	Σ	<i>N</i>	Au	Ag	Fe	Σ
1	99.85	1.28	–	101.12	7	97.74	1.48	0.29	99.50
2	96.77	2.03	0.82	99.62	8	97.94	1.29	–	99.23
3	96.65	2.56	–	99.21	9	98.23	1.47	–	99.70
4	97.33	2.20	0.30	99.83	10	97.58	1.51	–	99.09
5	97.56	1.21	0.51	99.28	11	99.06	1.39	–	100.46
6	97.93	1.44	–	99.37	12	98.71	2.29	–	101.00

Blank- below detection limit. Fe from background sulphides

Fe oxide replacement

A characteristic feature of the P-125 deposit is the extensive alteration of the disseminated sulphides. Pyrite (and less so arsenopyrite-II) has been replaced by several mineral phases. **Magnetite** (considered part of the hydrothermal system) is the most common replacement mineral (20-40% of the sulphides altered to magnetite) (Fig. 4.16a). Magnetite forms rhombic and prismatic grains (mainly 350 µm-1 mm) on the margins of sulphide grains (Fig. 4.16b, c), or in pyrite-rich zones exist as aggregates of radiating fibres. Magnetite overprints all major sulphide phases (Fig. 4.16d, e). Excluding the P-125 deposit, magnetite replacement is a characteristic feature of the southern Loulo orebodies (e.g. Faraba, P-64). Approximately 70% of the magnetite has oxidised to **haematite** (supergene process), mainly along the margins of the grains (a texture known as martite; Fig. 4.16c). The intense oxidation of the sulphides seems to have caused secondary gold enrichment, with higher grades associated with more extensive alteration zones. Disseminated sulphides are also extensively replaced by Fe-rich chlorite and tourmaline (discussed further in *chapter 5*).

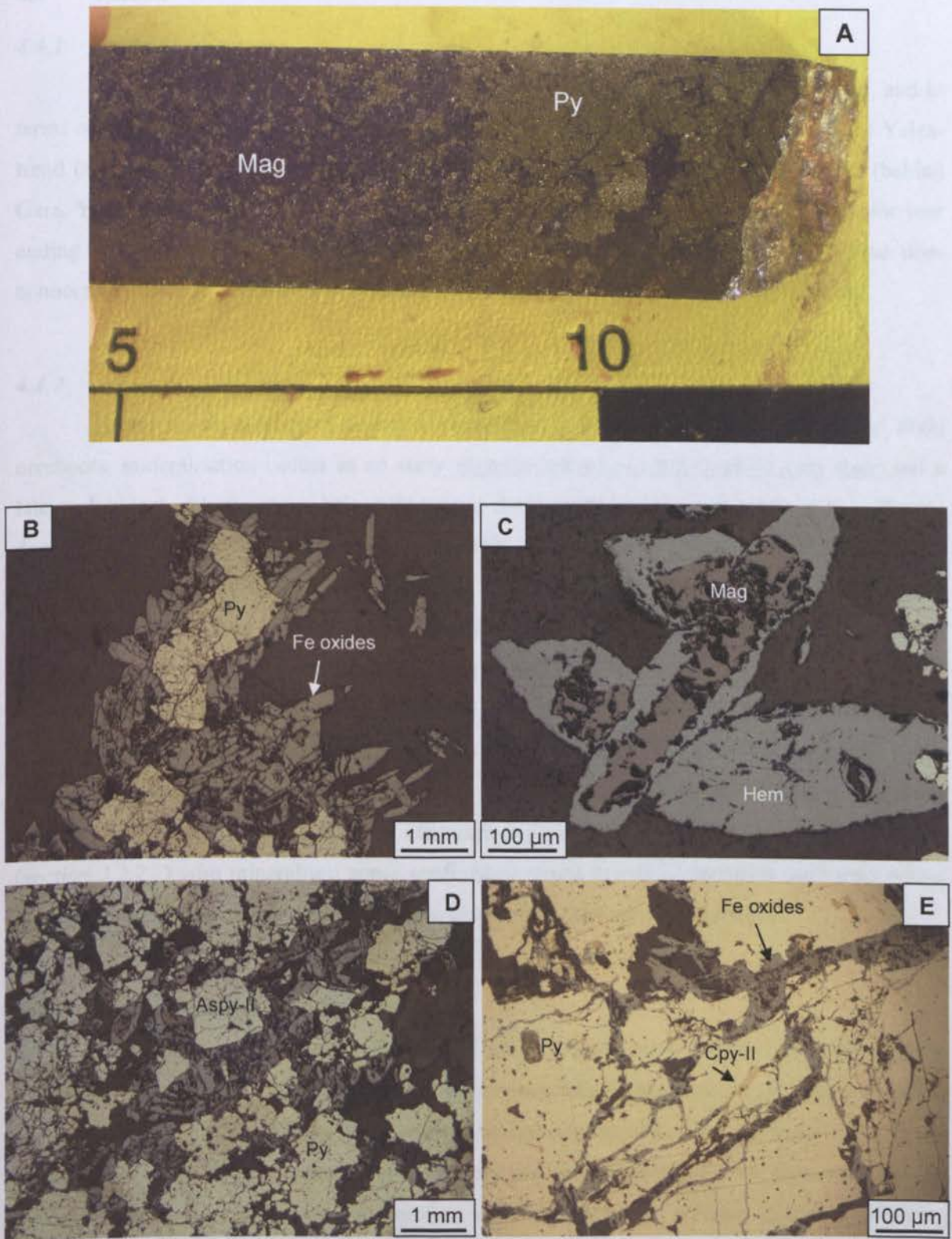


Fig. 4.16. Drill core and reflected light (PPL) images showing the magnetite replacement of the P-125 sulphides. **A)** Magnetite replacing massive disseminated pyrite (P125DH12, 142.5 m). Replacement textures are more distinct in thin section. **B)** Radiating prismatic magnetite grains surrounding pyrite grains (P125DH12, 144.2 m). **C)** Martite texture showing haematite alteration of the magnetite rims (P125DH12, 144.2 m). **D)** Magnetite (partially altered to haematite) crosscutting arsenopyrite-II (lighter grains) and pyrite (yellow grains) (P125DH12, 146.6 m). **E)** Magnetite (completely replaced by haematite) veinlets overprinting pyrite (P125DH12, 157.8 m). Magnetite associated with late chalcopyrite-II (brass coloured mineral). Mag = magnetite; Hem = haematite; other abbreviations as in Fig. 4.3.

4.4 Faraba

4.4.1 Orebody parameters

Faraba is situated in the southern regions of the Loulo district, 30 km from Gara, and in terms of structural setting is considered a separate sub-area to Gara and deposits along the Yalea-trend (*section 3.2.2*). Faraba is currently the fourth largest deposit in the Loulo district (behind Gara, Yalea and Goukoto) with a resource of 566,952 oz at average grades of 2.60 g/t (for year ending 2009). Faraba occurs over a strike length of 2.5 km and is composed of three non-connecting oreshoots: Faraba North, Faraba Main (most of the resource) and Faraba South.

4.4.2 Mineralisation styles

Faraba shows a range of complex mineralisation styles. In the Faraba North and Main oreshoots, mineralisation occurs as an early ankerite-dolomite-quartz-sulphide vein stage and a later sulphide ± chlorite stage. Mineralisation in the vein stage is largely confined to carbonate dominated veins (Fig. 4.17a), and towards the north form sheeted veins parallel to the shear fabric in the host rock. Sulphide mineralisation in the second ore phase exist as either coarse disseminated (millimetre in size) massive sulphides, which overprint the earlier vein stage (Fig. 4.17c, d), or as finer-grained minerals (<500 µm) in black chlorite veinlets and stringers. Sulphide-chlorite veinlets reactivate the carbonate-quartz veins and occur along the interface between the veins and the host rock, within fractures in the veins, or situated in the matrix of brecciated veins. This phase is also common in the Faraba South oreshoot, with the notable addition of magnetite (Fig. 4.17b). Mineralisation and related alteration is patchy and controlled by strain partitioning (*section 3.2.2.2*) with mineralised zones confined to coarse-grained arenaceous sediments within an alternating package of sandstones and fine-grained argillaceous-rich sediments.

4.4.3 Ore mineralogy and paragenesis

The mineralogical evolution at Faraba is distinctly different to deposits discussed so far in the northern parts of the Loulo district. The most noteworthy differences are: (1) the widespread occurrence of telluride minerals; (2) a reverse paragenetic sequence for major sulphide phases compared to other As-rich orebodies (e.g. Yalea Main & P-125); and (3) Cu concentrations are markedly lower than the northern deposits, with the complete absence of late Cu-bearing sulphides. A summary mineral paragenesis for Faraba is shown in Table 4.15.

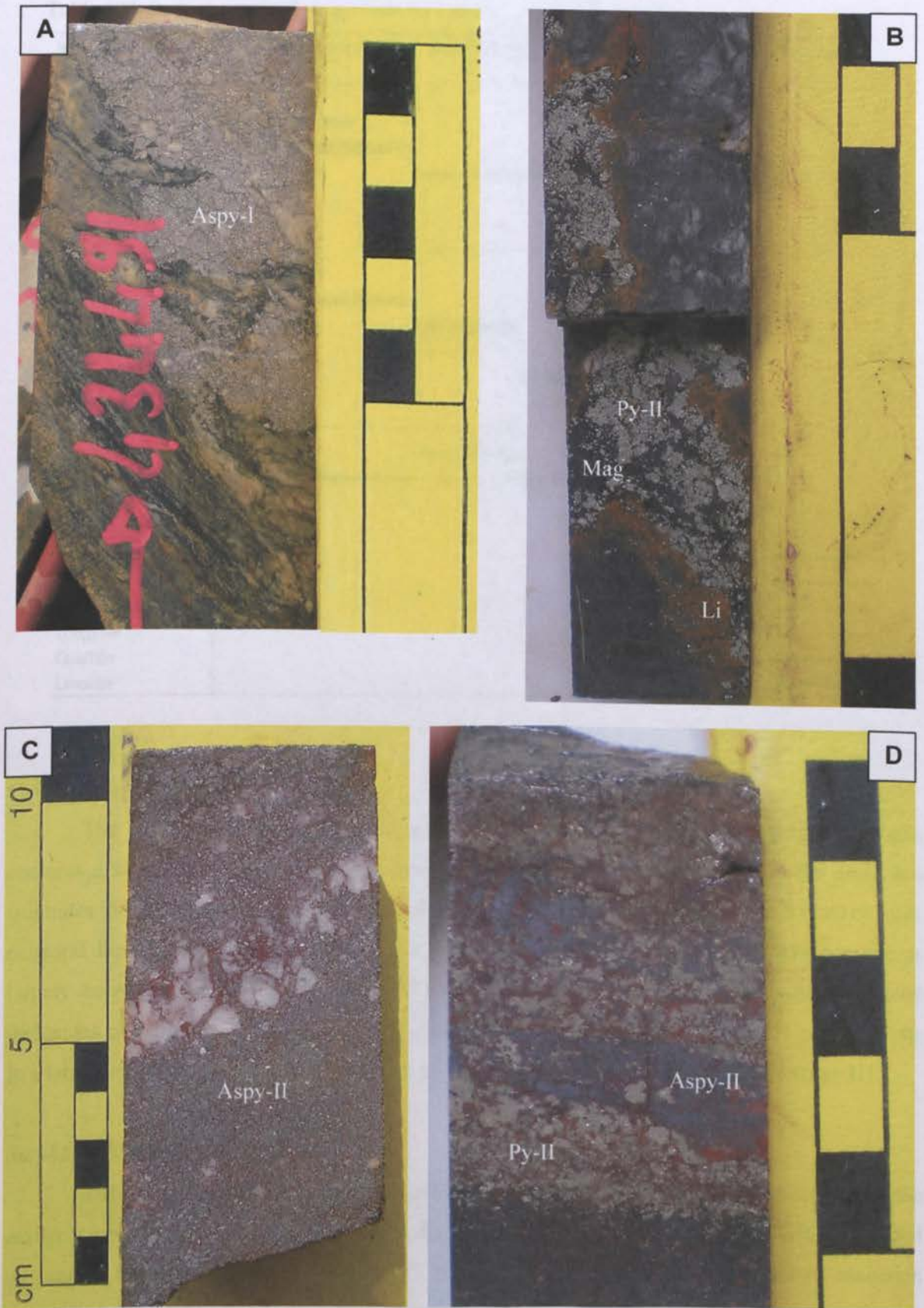


Fig. 4.17. Mineralisation styles at Faraba. **A)** Sulphide (mainly arsenopyrite-I)-rich ankerite vein cross cutting strongly sheared sediments (1.45 g/t) (FADH015, 189 m). **B)** Magnetite-chlorite-pyrite vein with a thin 0.5 cm halo of iron staining (limonite) along the vein walls (4.43 g/t) (FADH018, 68.6 m). **C)** Massive disseminated arsenopyrite overprinting quartz vein, associated with low-grade (<0.1 g/t) (FADH009, 155.95 m). **D)** Massive disseminated pyrite-rich zone associated with high-grade (20.86 g/t). Arsenopyrite also seen (grey minerals), altered to goethite (red mineral) (FADH002, 162.8 m).

Table 4.15. Summary mineral paragenesis for Faraba.

Mineral	Vein stage		Sulphide-chlorite stage		Post-main ore stage	Supergene
	I	II	III	IV		
Vein material						
Quartz	██████████					
Carbonate	██████████					
Chlorite			██████████			
Sulphides/Opaques						
Arsenopyrite-I	██████████					
Galena			██████████			
Sayrite						
Pyrite-I		██████████				
Arsenopyrite-II			██████████			
Chalcopyrite					██████████	
Pyrite-II				██████████		
Scheelite					██████████	
Pyrrhotite					██████████	
Tellurides			██████████			
Gold		██████████		██████████		
Magnetite					██████████	
Supergene						
Leucoxene						██████████
Haematite						██████████
Barite						██████████
Tungstite						██████████
Goethite						██████████
Limonite						██████████

Carbonate-rich vein phase

The Faraba vein-stage is only described briefly as the sulphide-chlorite-magnetite phase contains a similar and more interesting paragenesis. Pyrite and arsenopyrite from the dominant sulphides (50:50 ratio). Arsenopyrite-I exists as aggregates of several grains (up to 5 mm) or form euhedral hexagonal individual grains (140 μm - 2 mm, average 500-600 μm). Arsenopyrite is largely barren in terms of gold but contain minor telluride mineralisation, with occasional inclusions of tsumoite (BiTe) (**ore stage I**). Gold (fineness of 910-945; Table 4.17) mainly exists in a later pyrite-I phase, which often moulds around and replaces arsenopyrite-I (**ore stage II**).

Sulphide-chlorite-magnetite phase

The mineral paragenesis of the sulphide-chlorite-magnetite phase is a duplication of the earlier carbonate vein phase, with two distinct ore phases associated with different metal signatures. **Ore stage III** is characterised by massive arsenopyrite-II and suite of inclusion minerals (<20 μm) confined to the Bi-Te system, namely (in order of decreasing abundance) tsumoite (BiTe), hedleyite (Bi₇Te₃), altaite (PbTe), native bismuth and an unknown ternary Bi-Te (\pm Au) alloy (Fig. 4.18c, d). The composition of these telluride phases are presented in Table 4.16. This stage is associated with low Au-grade (<0.5 g/t) despite high sulphide abundance (Fig. 4.17c). Arsenopyrite-II contains regular inclusions of chalcopyrite, pyrrhotite and galena (10-30 μm).

Table 4.16. Representative SEM-EDS analyses of Bi-Te minerals at Faraba (wt.%).

N	Mineral	Au	Ag	Te	Pb	Bi	Fe	As	Σ
1	Ts	–	–	35.34	–	61.66	0.38	1.56	98.94
2	Ts	–	–	40.13	–	59.08	–	–	99.21
3	Ts	–	–	40.36	–	60.64	–	–	101.00
4	Ts	–	–	39.54	–	58.45	–	–	97.99
5	Ts	–	–	40.34	–	58.45	0.35	1.45	100.57
6	He	–	–	20.12	–	78.56	–	–	98.68
7	He	–	–	19.89	–	79.71	–	–	99.60
8	He	–	–	19.74	0.41	79.24	–	–	99.39
9	Al	–	–	41.45	59.98	–	–	–	101.43
10	Al	–	–	40.29	60.34	–	–	–	100.63
11	Al	–	–	37.98	61.07	–	–	–	99.05
12	NB	–	–	–	–	99.17	–	–	99.17
13	NB	–	–	–	–	100.98	–	–	100.98
14	Uk	4.99	–	40.81	–	53.08	0.42	1.91	101.21

Ts-tsumoite; He- hedleyite; Al-altaite, NB- native bismuth; Uk- unknown Te-Bi (±Au) mineral.
Blank- below detection limit. Fe & As from background sulphides

Ore stage IV is distinguished by a Fe-Au-W metal association and the notable absence of tellurides. Pyrite-II overprints and replaces the Te-Bi-bearing arsenopyrite-II phase (Fig. 4.18a, b). In the Faraba South oreshoot, this ore stage is the predominant sulphide generation. Gold particles are mainly occluded in pyrite (GI; 80%) (Fig. 4.18e) or remobilised in deformation cracks (GII), and contain a slightly lower gold fineness compared to ore stage II between 850 to 920 (Ag levels increase towards the south; Table 4.17). At Faraba South, gold can form discrete veinlets within deformation fractures over lengths of 170 µm (a texture only seen elsewhere at Gara) (Fig. 4.18f). Occluded gold is fine to medium in size (3 to 5 times coarser than observed at Yalea and Gara) between <10 µm to 140 µm (average 20-50 µm). Tungstates are common ore minerals (2% of the opaque phases) including scheelite and ferberite (FeWO₄). The Faraba orebodies are distinguished by the extensive oxidation of the sulphide phases. Magnetite extensively replaces pyrite-II; either as a massive phase (Faraba South; Fig. 4.19) or as globular grains (Faraba Main). In contrast to P-125, magnetite formation has not caused secondary gold enrichment, with barren magnetite-only veinlets seen outside the orezone.

Table 4.17. Representative SEM-EDS analyses of native gold at the Faraba orebodies (wt.%).

N	Au	Ag	Σ	N	Au	Ag	Σ
1	92.08	8.38	100.46	7	90.80	8.59	99.39
2	92.26	7.96	100.22	8	91.52	8.68	100.20
3	90.57	9.05	99.61	9	84.73	14.50	99.23
4	92.95	8.27	101.23	10	84.99	15.25	100.24
5	91.19	8.00	99.19	11	88.23	11.65	99.88
6	90.32	8.52	98.83	12	86.78	12.48	99.26

Note- analyses (9) to (12) from Faraba South oreshoot.

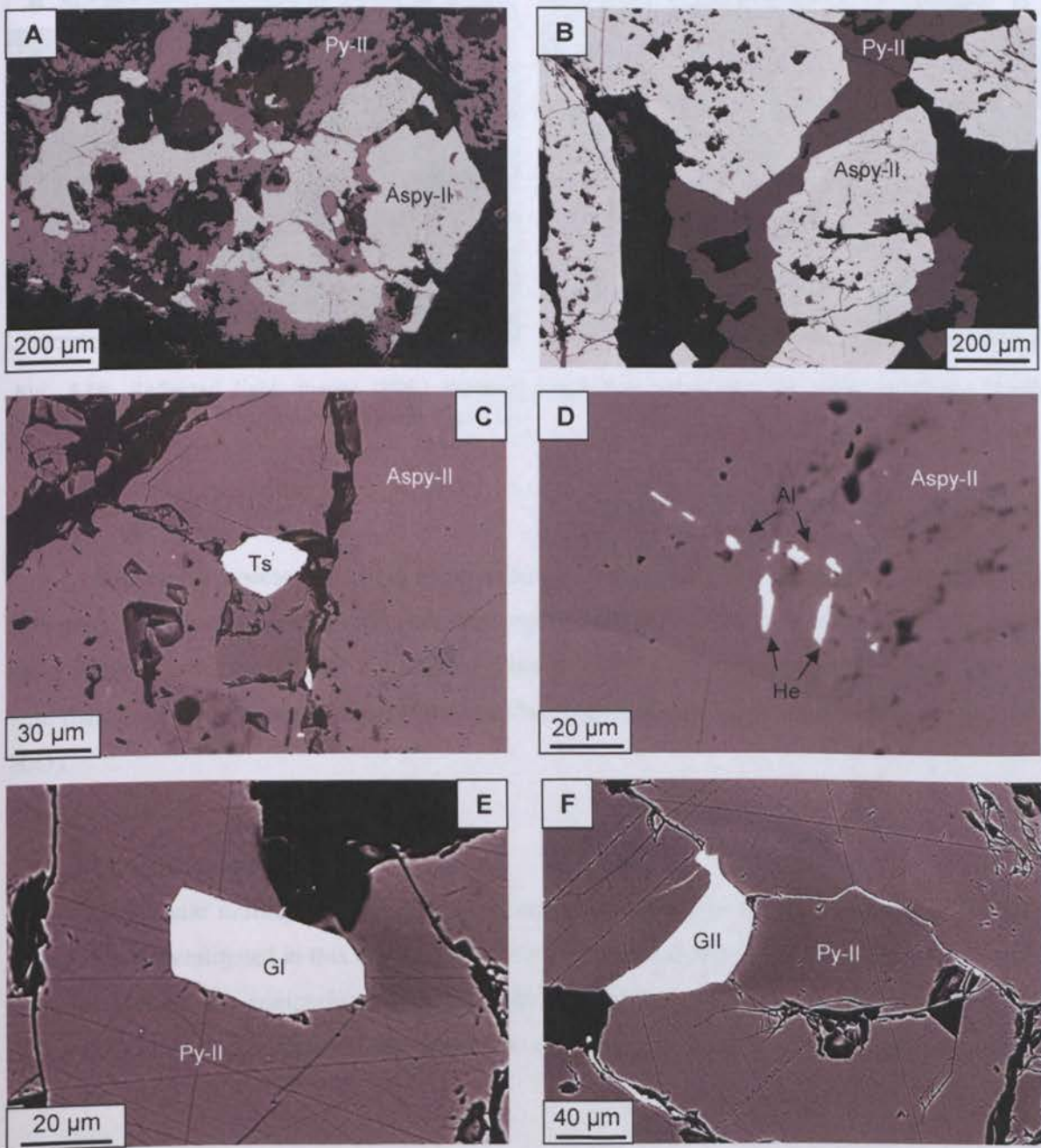


Fig. 4.18. BSE images of Faraba ore stages III and IV. **A)** Pyrite-II replacing arsenopyrite-II (reverse paragenesis to Yalea Main & P-125) (FADH015, 256.9 m). **B)** Pyrite-II crosscutting arsenopyrite-II (FADH009, 155.95 m). **C)** Tsumoite inclusion within the core of arsenopyrite-II. These tellurides are slightly larger than other types and are commonly found as isolated inclusions (FADH015, 265.7 m). **D)** A cluster of ultra-fine telluride inclusions within arsenopyrite-II. Alaite occurs as subhedral equidimensional grains, while heyleyite exist as more elongate inclusions (FADH015, 256.9 m). **E)** Coarse occluded gold (50 µm) in pyrite-II (FADH018, 75.9 m). **F)** Remobilised gold sealing micro-fracture in pyrite-II (FADH018, 75.9 m). Abbreviations as in text and in Table 4.16.

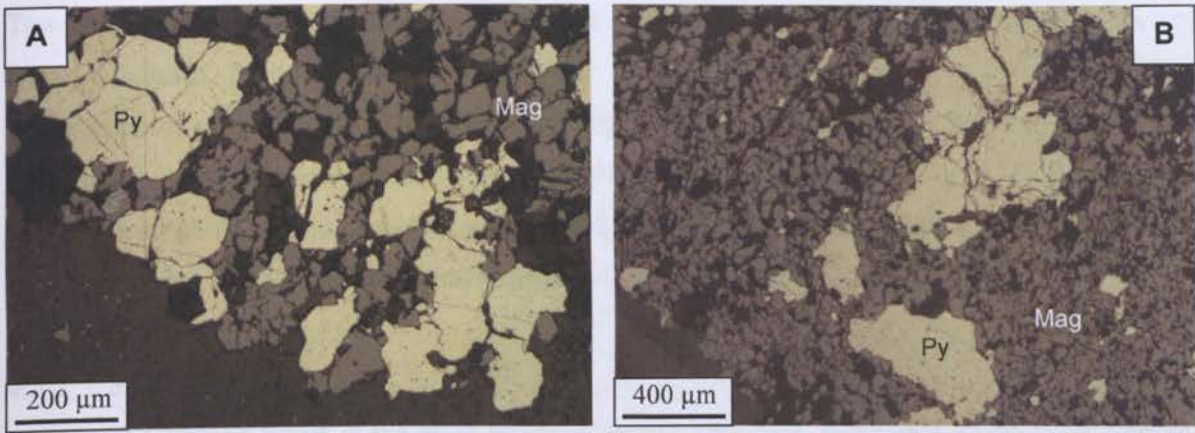


Fig. 4.19. Reflected light images (PPL) showing magnetite replacement of pyrite at Faraba South (FADH018, 68.6 m). Same abbreviations as Fig. 4.16.

Supergene alteration

Supergene processes are also widespread at Faraba. Pyrite and magnetite have altered to haematite, red brown goethite, leucoxene, and more commonly to limonite, which can be seen as halos along vein margins (Fig. 4.17b). Skeletal barite is also a common alteration phase associated with these supergene minerals. Furthermore, W-bearing ore phases have altered to tungstite ($\text{WO}_3 \cdot \text{H}_2\text{O}$).

4.5 Other deposits

The Loulo mining district contains several other orebodies within the Kofi Series and a selection are investigated in this section. The following data concentrates on the ore mineralogy of these orebodies for comparison with deposits discussed in *section 4.2 to 4.4*. Simplistic paragenesis charts are included in the appendices (*section A-4*) (no field photos or BSE images are shown here).

4.5.1 Loulo-3

The Loulo-3 orebody is situated 3 km north of Yalea, over a strike length strike of 1 km along the major NNE Yalea-trend (Fig. 3.2). The Yalea North-Loulo-3 segment of Yalea-trend has a strong association with weakly tourmalinised quartz-wackes. Domanget *et al.* (1993) indicated that Loulo-3 shared similar characteristics to Gara because of its spatial association between tourmaline and gold. However, tourmaline is largely unrelated to mineralisation (pre-mineralisation stage) and occurs in considerably lower abundances. The Loulo-3 mineralisation is largely associated with chlorite alteration zones (*see chapter 5*).

Loulo-3 is a quartz-carbonate vein-hosted stockwork deposit. Unlike Gara, mineralisation is largely associated with quartz-dominated veins. Barren or weakly mineralised ankerite-rich veins usually occur as an early fluid phase, which are reactivated by quartz-chlorite-sulphide veins.

The Loulo-3 ore paragenesis is analogous to Yalea Main and P-125 (Fe-As-Cu-W-Au-Pb-Ag metal signature). Pyrite and arsenopyrite (latter showing a two-stage growth history) form the major sulphide phases (70:30 ratio). Predominantly, Cu-phases represent the last stages of sulphide paragenesis. Multiple mineralisation events are observed, with native gold (<10 to 60 µm) situated in various sulphide phases including pyrite (85%), arsenopyrite-I, arsenopyrite-II, chalcopyrite-II and tennantite. Gold contains a fineness identical to Yalea Main (950 to 980; Table 4.19).

4.5.2 Baboto

The Baboto target is the most northern deposit along the Yalea-trend (Fig. 3.2). Baboto occurs over a strike-length of 3 km but contains consistently low-grades (average grade of 1.71 g/t). Mineralisation is uniform and mainly confined to quartz-dominated veins, plus sulphide stringers and veinlets, associated with large amounts of silica alteration (*section 5.3.3*). In terms of major sulphides, this deposit shares similar characteristics to Yalea Main, P-125 and Loulo-3, but the minor and trace ore assemblage is significantly more polymetallic than other Loulo orebodies. Mineralisation can be separated into two distinct mineral stages:

1. Fe-Sb-Au stage- is dominated by pyrite (~70% of the total sulphides) plus several Sb-bearing sulphides. Tetrahedrite ($[\text{Cu,Fe}]_{12}\text{Sb}_4\text{S}_{13}$) (1 to 10% of the sulphide minerals) is usually present in the cores of pyrite crystals (Tetrahedrite-I). Ullmannite (NiSbS) occurs as a trace phase as euhedral micro-inclusions (<10 µm) within pyrite. Other inclusion phases in pyrite include arsenopyrite-I, chalcopyrite-I, scheelite and pyrrhotite.

2. As-Pb-Sb-Au stage- consists predominately of arsenopyrite (~20% of the overall sulphides) and elevated concentrations of Pb. Arsenopyrite-II often occurs as multiphase aggregates (several hundreds of crystals) of euhedral idiomorphic overgrowths or less commonly pseudomorphously replacing pyrite. Like other As-rich orebodies, galena ($\pm\text{Sb}\pm\text{Se}\pm\text{Cu}$) is a trace mineral phase associated with arsenopyrite formation, but occurs in much higher concentrations (up to 1% of the sulphide population). They occur as aggregates of euhedral/subhedral inclusions (2-30 µm) in arsenopyrite or situated as trails of grains along pyrite-arsenopyrite grain boundaries. Ardaite ($\text{Pb}_{19}\text{Sb}_{13}\text{S}_{35}\text{Cl}_7$) and bournonite (PbCuSbS_3) (former more dominant) are commonly associated with galena in arsenopyrite-II (<20 µm). Ardaite inclusions are easily distinguished from galena by their more anhedral habits. The compositions of the various Sb-Pb minerals from both stages are shown in Table 4.21.

Visible gold at Baboto is associated with both stages, occluded (2-20 µm) in pyrite and both arsenopyrite phases (mainly pyrite). Baboto contains the most Ag-rich gold along the Yalea-trend with a fineness of 840-875 (Table 4.19; one grain with a Ag content of 3 wt.%). The last stages of sulphide paragenesis are distinguished by tetrahedrite-II and chalcopyrite-II (<5% of total sulphides), which overprint and replace all major sulphide phases.

Table 4.18. Representative SEM-EDS analyses of Sb-Pb bearing trace sulphides at Baboto (wt.%).

N	Mineral	Fe	Cu	Zn	Pb	Se	Ni	Sb	S	Cl	Σ
1	Tet-I	3.39	38.23	4.12	–	–	–	29.47	24.72	–	99.93
2	Tet-I	3.23	38.50	4.48	–	–	–	29.29	25.19	–	100.69
3	Tet-I	3.56	38.49	3.82	–	–	–	28.73	23.88	–	98.48
4	Tet-I	3.73	37.51	3.69	–	–	–	29.33	24.80	–	99.06
5	Tet-II	4.43	38.65	3.35	–	–	–	29.83	25.35	–	101.62
6	Tet-II	3.95	37.76	3.29	–	–	–	29.26	24.53	–	98.79
7	Tet-II	3.42	37.21	3.68	–	–	–	28.70	24.71	–	97.72
8	Ul	2.49	–	–	–	–	27.29	53.10	15.64	–	98.52
9	Ul	0.27	–	–	–	–	27.65	56.89	15.23	–	100.04
10	Ul	2.68	–	–	–	–	27.89	55.97	14.89	–	101.43
11	Bo	5.01	11.43	–	37.78	–	–	24.14	19.12	–	97.47
12	Bo	3.04	12.89	–	40.23	–	–	24.74	19.72	–	100.62
13	Ad	2.29	–	–	57.62	–	–	20.05	15.12	2.90	97.98
14	Ad	3.12	–	–	58.26	–	–	19.34	15.90	1.99	98.60
15	Gal	2.02	–	–	84.99	–	–	–	12.77	–	99.78
16	Gal	3.86	1.20	–	79.07	–	–	0.77	13.30	–	98.20
17	Gal	2.02	–	–	85.32	0.98	–	0.24	12.65	–	101.20
18	Gal	1.23	–	–	85.87	–	–	1.23	13.65	–	101.98

Tet- tetrahedrite, Ul- ullmannite, Bo- bourmonite, Ad- ardaite, Gal- galena. Blank- below detection limit.

4.5.3 P-129

P-129 is a minor deposit situated halfway between Gara and Yalea (part of the Gara subarea; *section 3.2.2*). The P-129 orebody is the only example of an intrusion-hosted deposit of notable grade in the Loulo property, with the majority of mineralisation (patchy) situated in a sub-vertical Birimian porphyry granodioritic dyke (*sections 3.3.6 & 3.4.2.1*). Mineralisation is situated in ankerite-rich veins and tourmaline-biotite veinlets/stringers (the latter reactivates the former), which post-date the host intrusion. The mineralogy of the sulphide ore is rather simple (similar to Gara and Yalea North). The predominant sulphide phase is pyrite (>95%) with an inclusion assemblage consisting of arsenopyrite (<5%), monazite, pentlandite, gersdorffite and scheelite. Chalcopyrite (<1%) occurs as a late stage replacing pyrite. Gold at P-129 (1-25 µm) is confined to pyrite, usually present as occluded gold (~90%) and less frequently as remobilised gold (~10%). Gold fineness is similar to Gara with very low Ag-contents (>985; Table 4.19).

4.5.4 P-64

P-64 is situated in the southern parts of the Loulo district, to the NW of Faraba. It shares similar features to Gara, Yalea North and P-129: (1) a strong association exists between gold and tourmaline (mineralisation confined to tourmaline-bearing sandstones); and (2) pyrite is the major component of the sulphide ore (95-99%). P-64 is characterised by two generations of pyrite, both showing a poor sulphide-Au relationship. Pyrite occurs as either pre-schistosity disseminations aligned parallel to host rock fabric; or as vuggy, skeletal and corroded grains located within a later

vein stockwork that either follows or crosscuts the host fabric. The P-64 stockwork (dominant towards top of the orezone) contains a complex vein history consisting of ankerite-pyrite veins, intensely recrystallised quartz-pyrite veins, extensional planar sulphide veins and late sinuous quartz-tourmaline-biotite-pyrite veins (higher pyrite abundance in carbonate-bearing veins). Minor and trace ore assemblage are analogous to Gara with a few exceptions. Gold occurs as native gold and calaverite (AuTe_2) (10:1 ratio) occluded in pyrite or its replacement phases (*see below*), and as free grains within the host rock, as ultrafine to fine (1-40 μm ; average 10 μm) particles. Native gold is extremely Ag-depleted with fineness values >995 (Table 4.19). Rare Pd-bearing gold grains are also observed in quartz-tourmaline-biotite-pyrite veins (similar to Yalea North) along with native bismuth (2 μm).

Similar to Faraba, vein pyrite has been heavily replaced by magnetite and subsequently by supergene minerals. Magnetite can exist as partial pseudomorphs of pyrite or form idiomorphic aggregates of fibrous grains (up to 200 μm) originating away from pyrite grain boundaries. Chromite is occasionally seen within the cores of magnetite. Magnetite is often oxidised to haematite along the margins of the grains, while in places pyrite, magnetite and haematite have altered to dark red/brown goethite. Some monazite grains (preferentially towards the top of the orezone) have completely altered to rare-earth hydrated carbonates (Ce-rich lanthanite- $(\text{Ce}, \text{La})_2[\text{CO}_3]_3 \cdot 8\text{H}_2\text{O}$) and/or calkinsite- $(\text{Ce}, \text{La})_2[\text{CO}_3]_3 \cdot 4\text{H}_2\text{O}$).

Table 4.19. Representative SEM-EDS analyses of native gold at a selection of minor Loulo orebodies (wt.%).

	N	Au	Ag	Fe	As	Σ		N	Au	Ag	Pd	Fe	Σ
Loulo-3	1	94.96	4.07	-	-	99.03	P-129	1	97.94	1.01	-	-	98.96
	2	98.90	2.65	-	-	101.54		2	98.73	0.48	-	0.71	99.92
	3	96.51	2.93	-	-	99.44		3	98.71	0.89	-	-	99.60
	4	96.21	3.19	-	-	100.41		4	99.29	0.97	-	-	100.26
	5	95.34	4.96	-	-	99.27		5	97.89	0.67	-	0.93	99.49
	6	96.98	1.97	-	-	99.04		6	98.58	0.99	-	0.74	99.60
	7	96.89	2.56	-	-	100.51		7	96.95	1.08	-	0.82	98.85
	8	98.34	2.88	-	-	98.81		8	98.11	0.70	-	0.51	98.18
	9	96.23	2.67	-	-	98.90		9	97.60	1.20	-	-	99.34
	10	94.78	4.41	-	-	99.19		10	98.21	0.64	-	-	99.30
Baboto	1	96.60	3.12	0.71	-	100.43	P-64	1	84.23	-	15.27	-	99.50
	2	84.71	14.18	0.92	-	99.81		2	86.45	-	14.89	-	101.34
	3	83.36	15.68	-	-	99.04		3	99.19	0.31	-	-	99.50
	4	84.70	13.74	0.76	1.21	100.41		4	99.35	0.36	-	-	99.71
	5	86.00	12.18	0.30	0.79	99.27		5	98.78	0.27	-	-	99.05
	6	84.62	13.95	0.47	-	99.04		6	99.38	0.22	-	-	99.60
	7	83.98	15.23	1.30	-	100.51		7	100.21	0.12	-	-	100.33
	8	83.22	15.60	-	-	98.81		8	97.87	0.31	-	-	98.18
	9	83.84	14.67	0.32	1.93	100.77		9	99.33	-	-	-	99.33
	10	85.62	13.06	0.31	-	98.99		10	99.11	0.19	-	-	99.30

Blanks below detection limit. Fe from background pyrite.

4.5.5 Goukoto

Goukoto is a significant new discovery situated in the southern parts of the Loulo permit between Faraba and P-64. The deposit contains a current resource of 2.88 Moz at high average grades of 6.82g/t. Drilling at Goukoto started after the field visits and thus this deposit is not discussed in great detail in this study. Goukoto formed during the late stages of D₃ transtension along a NNW trending R-shear. The mineralisation style is similar to Yalea Main, with mineralisation associated with a network of pyrite, carbonate-pyrite and quartz-pyrite veins/veinlets and stringers formed during shearing of an early albite alteration stage.

Goukoto shares characteristics of both P-64 and Faraba deposits. Pyrite is the principal sulphide phase (>95%), with trace assemblages consisting of chalcopyrite, pyrrhotite, monazite and xenotime (similar to P-64). Gold exists as native gold or as a variety of Au-bearing tellurides in the Au-Ag-Te system (different to the tellurides observed at Faraba). Telluride minerals include calaverite (AuTe₂), Bi-bearing sylvanite (AgAuTe₄) and petzite (Ag₃AuTe₂), which occur as small inclusions (≤10 to 15 μm) within the cores of pyrite crystals. Native gold (10:1 native gold/telluride ratio) is situated in numerous sites and is spatially associated with the tellurides. Native gold has a bimodal size distribution (10-30 μm to 100-150 μm) and is typically Ag-depleted (fineness >985). The composition of Au-Te minerals are presented in Table 4.20.

Table 4.20. Representative SEM-EDS analyses of Au-Te minerals at Goukoto (wt.%).

<i>N</i>	<i>Mineral</i>	Au	Ag	Te	Bi	Σ
1	NG	98.75	1.23	–	–	99.98
2	NG	99.02	0.78	–	–	99.80
3	NG	97.98	1.34	–	–	99.32
4	NG	98.34	1.23	–	–	99.57
5	NG	97.75	1.56	–	–	99.31
6	NG	97.67	1.45	–	–	99.12
7	Cv	43.23	–	56.23	–	99.46
8	Cv	44.78	0.27	55.78	–	100.83
9	Cv	44.10	–	56.45	–	100.55
10	Cv	43.67	0.67	55.98	–	100.32
11	Sv	37.89	3.12	58.81	2.34	102.16
12	Sv	35.90	4.90	57.34	3.56	101.70
13	Sv	34.65	5.34	57.23	3.67	100.89
14	Pt	25.23	40.98	33.56	–	99.77
15	Pt	27.89	39.79	33.12	–	100.80

NG-native gold; Cv-calaverite; Sv-sylvanite; Pt- petzite. Blank- below detection limit.

4.6 Discussion

4.6.1 Deposit summary

The different styles of mineralisation and ore petrogenesis observed in the Loulo orebodies investigated during this study are summarised in Table 4.21, and a comparative mineralogical model is discussed in *section 4.6.2*.

Table 4.21. Deposit summary table for mineralisation in the Loulo mining district.

Orebody	Major mineralisation style(s)	Dominant sulphide phase(s)	Minor to trace ore assemblages	Metal signature
Gara	ankerite-quartz veining	pyrite	chalcopyrite + monazite + native gold + gersdorffite + pyrrhotite + pentlandite + scheelite + arsenopyrite + xenotime	Fe-Cu-REE-Au- Ni-W-As
Gara West	ankerite-quartz veining & disseminated	pyrite	magnetite + chalcopyrite + monazite + xenotime + pyrrhotite + native gold	Fe-Cu-REE-Au
Yalea Main	sulphide veinlets/stringers	pyrite & arsenopyrite	chalcopyrite + tennantite + scheelite + pyrrhotite + native gold + galena + jamesonite + sayrite	Fe-As-Cu-W-Au-Ag-Pb-Sb-U
Yalea North	breccia-hosted	pyrite	chalcopyrite + gersdorffite + cobaltite + arsenopyrite + monazite + tennantite + native gold + pentlandite + xenotime + native silver	Fe-Cu-Ni-Co-As-REE-Au-Ag-Pd
P-125	massive disseminated	pyrite & arsenopyrite	magnetite + chalcopyrite + tennantite + scheelite + native gold + pyrrhotite + galena	Fe-As-Cu-W-Au-Pb-Ag
Faraba	ankerite-dolomite-quartz veining, sulphide-chlorite-magnetite veining & disseminated	pyrite & arsenopyrite	magnetite + chalcopyrite + scheelite + native gold + tsumoite + altaite + hedleyite + ferberite + pyrrhotite + galena + sayrite + native bismuth	Fe-As-Cu-W-Au-Te-Bi-Ag-Pb-Sb-U
Loulo-3	quartz-ankerite veining	pyrite & arsenopyrite	chalcopyrite + tennantite + scheelite + native gold + pyrrhotite + galena	Fe-As-Cu-W-Au-Pb-Ag
Baboto	quartz veins & sulphide veinlets/stringers	pyrite & arsenopyrite	tetrahedrite + chalcopyrite + galena + native gold + ardaite + bournonite + ullmannite + pyrrhotite	Fe-As-Cu-Pb-Sb-Au-Ag-Se
P-129	ankerite-quartz veining & chlorite-tourmaline veining	pyrite	Arsenopyrite + chalcopyrite + monazite + gersdorffite + pentlandite + scheelite + pyrrhotite + native gold	Fe-REE-As-Ni-W-Au
P-64	ankerite-quartz-tourmaline veining & disseminated	pyrite	magnetite + chalcopyrite + monazite + gersdorffite + scheelite + arsenopyrite + pentlandite + pyrrhotite + native gold + calaverite + native bismuth	Fe-Cu-REE-Ni-W-As-Au-Te-Bi-Pd
Goukoto	sulphide veinlets/stringers	pyrite	magnetite + chalcopyrite + monazite + pyrrhotite + native gold + calaverite + sylvanite + petzite + xenotime	Fe-Cu-REE-Au-Te-Bi-Ag

4.6.2 Comparative mineralogy model for the Loulo district

The principal sulphides at Loulo are arsenopyrite and/or pyrite. Little or no Pb-Zn-Mo bearing sulphides are observed (rare galena), which is typical of the low base-metal content of orogenic gold deposits (Ridley & Diamond, 2000). As shown in Table 4.21, the Loulo mining district contains a diverse range of ore mineralogy. In the northern parts of Loulo, two distinct petrogenetic assemblages are seen: (1) a **Gara-style** Fe-rich assemblage, with a typical Fe-Cu-REE-Au-Ni-W-As \pm Co-Ag-Pd metal association; and (2) a **Yalea-style** As-rich assemblage, with a prominent Fe-As-Cu-W-Au-Pb-Sb-Ag signature.

Gara-style deposits show atypical orogenic gold characteristics (*see* Table 1.2), including orezones dominated by pyrite (principal sulphide phase); abundant monazite and, less so, xenotime; a range of Ni-bearing sulphides; and Ag-depleted gold mainly confined to pyrite. In contrast, Yalea-style deposits exhibit similar ore mineralogy to many reported orogenic gold deposits. Orebodies are characterised by a more complex paragenesis, with dominant sulphide phases of pyrite and arsenopyrite (latter showing several generations of sulphide growth); a trace assemblage consisting of pyrrhotite, galena and a range of minor Sb-bearing phases; a lack of REE phosphates and Ni-bearing sulphides; and Ag-rich gold situated in numerous sulphide phases. The major differences between Gara- and Yalea-style deposits are documented in Table 4.22. In both deposit styles, chalcopyrite \pm other Cu-bearing sulphides represent the last stages of sulphide paragenesis.

Table 4.22. Summarising the two major petrogenetic types present in the Loulo district.

Characteristics	Gara-style	Yalea-style
Examples	Gara, Gara West, Yalea North, P-129 & P-64?	Yalea, P-125, Loulo-3 & Baboto
Mineralisation styles	Ankerite-quartz vein-hosted, breccia-hosted & disseminated deposits.	Quartz vein-hosted, ankerite-quartz vein-hosted, sulphide veinlets/ stringers & massive disseminated styles.
Major sulphides	Pyrite (>90%; mainly >99%)	Pyrite & arsenopyrite (>90%)
Minor sulphides	Chalcopyrite + gersdorffite + pentlandite + pyrrhotite + arsenopyrite \pm cobaltite	Chalcopyrite + tennantite + pyrrhotite + galena \pm tetrahedrite \pm jamesonite \pm bournonite \pm ullmannite
Other ore minerals of interest	Monazite + xenotime + minor scheelite \pm magnetite	Range of tungstates (mainly scheelite) + sayrite \pm magnetite
Metal association	Fe-Cu-REE-Au-Ni-W-As \pm Co-Ag-Pd	Fe-As-Cu-W-Au-Pb-Sb-Ag
Gold location	Gold mainly confined to pyrite in numerous sites. Free gold is generally minor (except P-64).	Gold situated in a range of sulphide phases.
Gold fineness	>980 (an exception is Yalea North). Rare Pd-bearing grains.	840-960 (5 to 15 fold increase in Ag with respect to Gara-style deposits). An exception is P-125.

Note- alteration assemblages are notably different between these styles of deposit (discussed in chapter 5).

A third style of Loulo deposit (referred to as **Faraba-style**) occurs in the southern parts of the mining district and shows a distinctive Au-Te-Bi metal signature (Faraba, Goukoto & P-64). These orebodies are also characterised by lower Cu concentrations (complete absence of late stage Cu sulphides observed towards the north), an increase in gold particle size (up to 150 μm), large amounts of magnetite replacement (rarely seen in the north, excluding P-125), and high degrees of supergene alteration. Furthermore, at Faraba a reverse ore paragenesis is seen (arsenopyrite \rightarrow pyrite) in comparison to the Yalea-style deposits. However, Faraba-style orebodies also show similarities to the northern Loulo orebodies. For example, P-64 (Fe-Cu-REE-Ni-W-As-Au-Pd) and Faraba (Fe-As-Cu-W-Au-Ag-Pb-Sb) contain typical metal signatures of Gara- and Yalea-style deposits, respectively.

The comparative mineralogy model developed here forms the basis of an ore deposit classification for Loulo. The likely reasons for the diverse ore petrogenesis are that multiple fluids of contrasting compositions were responsible for mineralisation at Loulo, as well as possible variations in pressure-temperature conditions across the permit. These models will be investigated in the forthcoming chapters.

4.6.3 Geothermometry

Ore assemblages documented in *sections 4.2 to 4.5* can be used to estimate mineralisation temperatures in a selection of the Loulo orebodies. Two geothermometers are used here: the arsenopyrite and telluride geothermometers (discussed below).

4.6.3.1 Arsenopyrite geothermometry

The composition of arsenopyrite varies as a function of temperature and sulphur fugacity (fS_2) (Clark, 1960), and can therefore be used as a useful geothermometer (Kretschmar & Scott, 1976; Sharp *et al.*, 1985). The arsenopyrite geothermometer is a commonly used method for determining mineralisation temperatures in As-bearing mineral deposits in a wide range of geological environments (e.g. Hammond & Shimazki, 1994; Chamberlain, 2003; Koh *et al.*, 2004; Zoheir, 2008b). In Yalea-style deposits, arsenopyrite-I (coeval pyrite and gold) show As contents between 29.49 to 31.37 at.%, while rare arsenopyrite inclusions in mineralised pyrite from Gara-style deposits (limited data) give higher As concentrations of 30.32 to 32.37 at.% (Fig. 4.20). Using the fS_2 -buffered arsenopyrite-pyrite-pyrrhotite equilibrium (Kretschmar & Scott, 1976; Sharp *et al.*, 1985), these compositions correspond to mineralisation temperatures in Yalea- and Gara-style deposits of 300-377 $^{\circ}\text{C}$ (mean of 325 $^{\circ}\text{C}$) and 320-447 $^{\circ}\text{C}$ (mean of 391 $^{\circ}\text{C}$), respectively (Fig. 4.21). Data from individual deposits are given in Table 4.23. No estimates were made on Faraba-style deposits as arsenopyrite is not in textural equilibrium with pyrite (at least at Faraba).

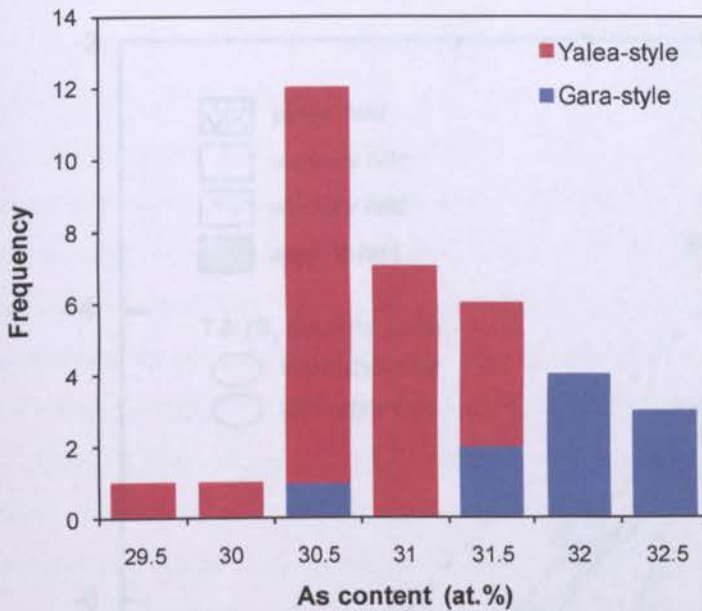


Fig. 4.20. Histogram showing the composition of the Gara- and Yalea-style arsenopyrites. Data in atomic weight % (at.%).

Table 4.23. Estimated mineralisation temperatures at Loulo based on the arsenopyrite geothermometer (Kretschmar & Scott, 1976; Sharp *et al.*, 1985).

Deposit	As content (at.%)	Estimated temperature
Gara	31.69-32.37 (3) mean of 32.02	400-447 °C mean = 418 °C
Yalea North	30.32-32.06 (7) mean of 31.41	320-424 °C mean = 383 °C
Yalea Main	30.31- 31.11 (8) mean of 30.56	320-367 mean = 326 °C
Loulo-3	29.89-31.37 (8) mean of 30.56	320-377 °C mean = 327 °C
Baboto	29.49-31.25 (8) mean of 30.40	300-372 °C mean = 320 °C

Note- brackets refer to number of analysed grains.

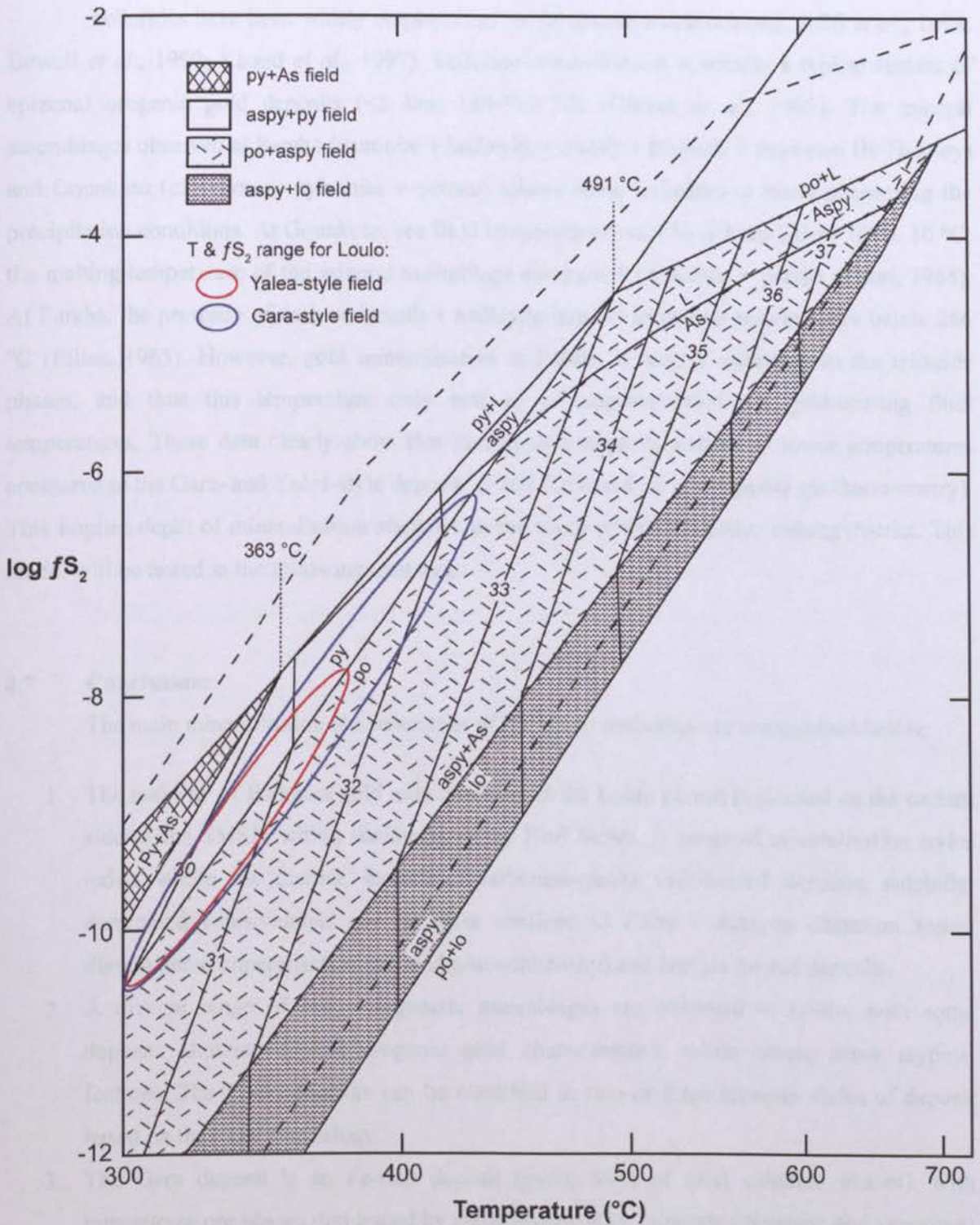


Fig. 4.21. Sulphidation curves in the system Fe-As-S in the stability range of arsenopyrite (Barton, 1969), with atomic wt.% As arsenopyrite-buffered curves from Kretschmar & Scott (1976). The effects of increase in pressure from 1 bar (solid lines) to 5 kbar (dashed lines) are also shown. The red and blue circles represent the temperature and fS_2 conditions of the auriferous sulphides at Loulo. As = arsenic, aspy = arsenopyrite, L = liquid, lo = loellingite, po = pyrrhotite, py = pyrite.

4.6.3.2 Telluride geothermometry

Tellurides have been widely employed as useful geothermometers (e.g. Afifi *et al.*, 1988; Howell *et al.*, 1990; Klemd *et al.*, 1997). Telluride mineralisation is usually a typical feature of epizonal orogenic gold deposits (<5 km; 150-300 °C) (Groves *et al.*, 1998). The mineral assemblages observed at Faraba (tsumoite + hedleyite + altaite + bismuth + unknown Bi-Te alloy) and Goukoto (calaverite + sylvanite + petzite) allows some estimates to be made concerning the precipitation conditions. At Goukoto, ore fluid temperatures must have been below 304 ± 10 °C; the melting temperature of the mineral assemblage electrum + calaverite + petzite (Cabri, 1965). At Faraba, the presence of native bismuth + hedleyite implies formation temperatures below 266 °C (Elliot, 1965). However, gold mineralisation at Faraba is largely unrelated to the telluride phases, and thus this temperature only acts as an approximation for gold-bearing fluid temperatures. These data clearly show that Faraba-style deposits formed at lower temperatures compared to the Gara- and Yalea-style deposits (>300 °C; based on arsenopyrite geothermometry). This implies depth of mineralisation shallows to the south within the Loulo mining district. This model will be tested in the following chapters.

4.7 Conclusions

The main mineralisation characteristics of the Loulo orebodies are summarised below:

1. The majority of Birimian gold mineralisation in the Loulo permit is situated on the eastern side of the SMSZ, within sediments of the Kofi Series. A range of mineralisation styles exists within the district, including: carbonate-quartz vein-hosted deposits, sulphide-dominated veins/veinlets and stringers confined to albite \pm ankerite alteration zones, disseminated mineralisation (pre and post-schistosity) and breccia-hosted deposits.
2. A diverse range of ore petrogenetic assemblages are observed at Loulo, with some deposits showing typical orogenic gold characteristics, while others show atypical features. The Loulo deposits can be classified as two or three separate styles of deposit based on their ore mineralogy.
3. The Gara deposit is an Fe-rich deposit (pyrite 99% of total sulphide phases), with minor/trace ore phases dominated by chalcopyrite, REE minerals (monazite and xenotime) and Ni-bearing sulphides (gersdorffite, pentlandite and Ni-bearing pyrrhotite). Native gold is situated in numerous locations mainly confined to pyrite (occluded and remobilised sites), and is Ag-poor (fineness >990).
4. Yalea Main contains more typical orogenic gold characteristics. Major sulphide phases include pyrite and arsenopyrite (~70:30 ratio). Minor/trace phases lack REE phosphates and Ni-bearing sulphides, and instead are dominated by chalcopyrite, scheelite, galena and rare Sb sulphides. Mineral paragenesis is more complex compared to Gara, with numerous

phases of pyrite, arsenopyrite and gold generation. Native gold is more Ag-rich with a fineness of 920-990.

5. Petrogenetic studies of the other orebodies show that a majority can be classified as either Gara-style deposits (Gara West, Yalea North & P-129) with a typical Fe-Cu-REE-Au-Ni-W-As \pm Co-Ag-Pd metal association, or Yalea-style deposits (majority of deposits associated with the Yalea-trend; e.g. P-125, Loulo-3 & Baboto) with Fe-As-Cu-W-Au-Pb-Sb-Ag metal signature.
6. Orebodies in the southern parts of the permit can be classified as a third style of Loulo gold mineralisation, termed Faraba-style deposits. Although these orebodies show Gara-style (P-64 & Goukoto) or Yalea-style features (Faraba), they also contain distinctive characteristics such as telluride mineralisation, lower Cu concentrations, increase in gold particle size, abundant magnetite replacement of sulphide phases, and high degrees of supergene alteration.
7. Estimates of precipitation temperatures, based on arsenopyrite geothermometry, suggest Gara-style sulphides form over a range of 320-447 °C (mean of 391 °C), while Yalea-style sulphides formed at lower temperatures between 300-377 °C (mean of 325 °C). Telluride assemblages in the Faraba-style deposits indicate temperatures below 300 °C, suggesting depth of mineralisation shallows to the south.
8. The variation in ore petrography at Loulo is likely caused by ore fluids of contrasting composition (i.e. a Gara-style fluid and Yalea-style fluid) and differences in pressure-temperature conditions at the site of mineralisation.
9. The various styles of deposits outlined here contain distinctly different alteration assemblages (discussed in *chapter 5*).

CHAPTER 5: HYDROTHERMAL ALTERATION AT LOULO

Wall-rock alteration halos are characteristic features of hydrothermal ore deposits and their study provides valuable information on the fluid properties associated with ore formation. Textural studies of alteration zones also help to understand the timing of mineralisation relative to stages of orogenesis (e.g. peak metamorphism and deformation). Thus, examining the processes involved in the interaction of hydrothermal fluids with their host rocks is an essential part of ore genetic studies. Furthermore, alteration patterns have been used as important exploration tools in many Archaean orogenic gold districts, at both regional- and mine-scale (e.g. Davis *et al.*, 1990; Groves & Foster, 1993). This chapter outlines the mineralogical and geochemical characteristics of hydrothermal alteration at Loulo, concentrating on the Gara and Yalea deposits.

5.1 Alteration characteristics of orogenic gold deposits

Hydrothermal alteration assemblages associated with orogenic gold deposits reflect the interaction of an H₂O-CO₂-H₂S (\pm N₂ & CH₄) ore fluid (Table 1.2) with different host lithologies at various temperatures and pressures (Ridley & Diamond, 2000). Auriferous fluids (especially in mesozonal and hypozonal deposits; >5 km) are often in equilibrium with their host rocks, having formed close to the ambient metamorphic pressure-temperature (P-T) conditions (Goldfarb *et al.*, 1986; Clark *et al.*, 1989). As a result, alteration halos are commonly more enigmatic and less well-developed than in other hydrothermal ore deposits, and harder to distinguish from mineral assemblages that form during regional metamorphism. This phenomenon is even more pronounced in siliciclastic sedimentary host rocks, which are typically less reactive than volcanic and granitic hosts (Bierlein *et al.*, 1998a).

The types of alteration assemblage that occur vary as a function of five factors: (1) temperature; (2) pressure; (3) host rock composition; (4) fluid composition; and (5) the fluid/rock ratio (Robb, 2005). Alteration halos of orogenic gold deposits, which typically form under greenschist facies conditions, are dominated by a variety of carbonate minerals; sulphides in the form of pyrite, pyrrhotite or arsenopyrite; and alkali-rich phases (K>Na) mainly in the form of sericite and less commonly as fuchsite, biotite, albite and/or chlorite (Ridley & Diamond, 2000). Alteration zones involve the addition of significant amounts of CO₂, S, K, H₂O, SiO₂ \pm Na and large ion-lithophile elements (LILE) (e.g. Kerrich, 1989). At progressively deeper crustal levels, amphibole or diopside become the dominant alteration phases, with a notable decrease in carbonate concentrations (Groves *et al.*, 1998).

5.2 Alteration characteristics at Loulo

5.2.1 Hydrothermal alteration

Alteration at Loulo differs to most other metasedimentary-hosted orogenic gold deposits (e.g. Bierlein *et al.*, 1998a). A range of alteration styles are present in the Loulo mining district, such as tourmalinisation, alkali metasomatism, carbonatisation and magnetite alteration, plus minor silication (conversion of a carbonate mineral or rock into a silicate mineral or rock) and silification (formation of new quartz or amorphous silica minerals). Such diversity probably reflects the variation in ore fluid compositions throughout the permit (as indicated by the diverse ore parageneses outlined in *chapter 4*) and differences in host lithologies (clastic to carbonate sediments). Together, these different types of alteration form four major distinctive alteration assemblages: (1) tourmaline alteration zones with minor quartz-ankerite-siderite-biotite; (2) pink albite alteration with associated ankerite and minor quartz-sericite-haematite; (3) a phyllic sericite-chlorite phase with accessory ankerite-quartz; and (4) a replacement magnetite phase. The width of the alteration zones at Loulo varies significantly between deposits from a few centimetres to several hundreds of metres.

5.2.2 Regional metamorphism

Sediments of the Kofi Series, as well as various generations of igneous rocks within the sedimentary basin and along the Falémé volcanic belt, have all undergone regional greenschist facies metamorphism. The metamorphic assemblage consists of sericite + Mg-rich chlorite + calcite + epidote, with the former three minerals present within the sediments and the latter three occurring within the volcanic and intrusive rocks. In terms of composition, the metamorphic assemblage is difficult to distinguish from the phyllic hydrothermal alteration. However, peak regional metamorphism pre-dates mineralisation and is not restricted to the alteration halos around mineralised zones, but instead occurs homogeneously throughout the host sequence. Regional metamorphism is also marked by the absence or limited extent of quartz-carbonate veins and the preservation of primary sedimentary and igneous features.

5.3 Alteration mineralogy

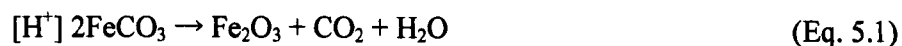
Alteration zones at Gara differ substantially to those at Yalea Main, which is in agreement with the different ore petrogenesis observed at both deposits (*chapter 4*). Gara is characterised by abundant tourmaline and sodic alteration, while the main Yalea orebody contains an alteration zone consisting of carbonate and phyllic assemblages, with the notable absence of tourmaline. However, widespread albitisation is still present at Yalea. This section discusses the alteration mineralogy present at these two main deposits, but comparisons are also made with other Loulo deposits where appropriate.

5.3.1 Gara

Two main alteration zones can be distinguished at Gara: (1) a proximal tourmaline alteration zone (50 m) confined to quartz-wacke sediments within and below the mineralised zone; and (2) a distal pink sodic alteration zone (<150 m) overprinting argillaceous greywacke wall-rock on both sides of the orebody. Previously, these pink altered rocks have been termed QR (quartz rosé) units (albite mistaken for quartz). The proximal and distal alteration zones at Gara are illustrated in Fig. 3.3a.

5.3.1.1 Sodic alteration

The distal alteration zone at Gara occurs as pink/orange bleached zones, which either targets particular beds (less pervasive zones) or whole rock units (more extensive zones) (Fig. 5.1). In the first scenario, alteration mainly targets the carbonate-rich arenaceous beds/laminae (<2 cm thick) within the argillaceous greywacke sediments (argillite beds are largely unaltered) (Fig. 5.1a). These altered layers represent a conversion of quartz + ankerite → albite + haematite (Fig. 5.2a,b), with the pink colouration caused by the following alteration process:



More pervasive pink sodic alteration zones (<3 m width) (Fig. 5.1b) are locally seen along second-order NNE-trending shears and are associated with the Gara West satellite orebody. These zones occur in both carbonate wall-rock (calcite + orthoclase → albite + quartz) and argillaceous greywackes (quartz + carbonate + sericite + chlorite → albite ± haematite ± ankerite). Ankerite is usually present as small (<2 cm), irregular lenses or as interstitial phases along albite grain boundaries (Fig. 5.2c). The distal alteration zone lacks sulphidation (sulphides confined to the mineralised veins); a common characteristic of alteration zones throughout the district. The timing of sodic alteration relative to gold mineralisation at Gara is difficult to interpret for two reasons: (1) albitisation largely effects argillaceous-greywackes (and occasionally carbonate units) rather than the more silica or feldspar-rich sandstones (i.e. the mineralised quartz-wacke unit); and (2) any albite alteration within the proximal alteration zone is likely to have been overprinted by multiple and widespread (in terms of strike length) tourmaline alteration events (discussed below). However, the spatial association between sodic alteration and gold mineralisation within the Loulo district suggests these zones are related to the gold-bearing hydrothermal fluid system (at least in some deposits). This type of alteration is discussed further in *section 5.3.2.1* (also present at Yalea Main).

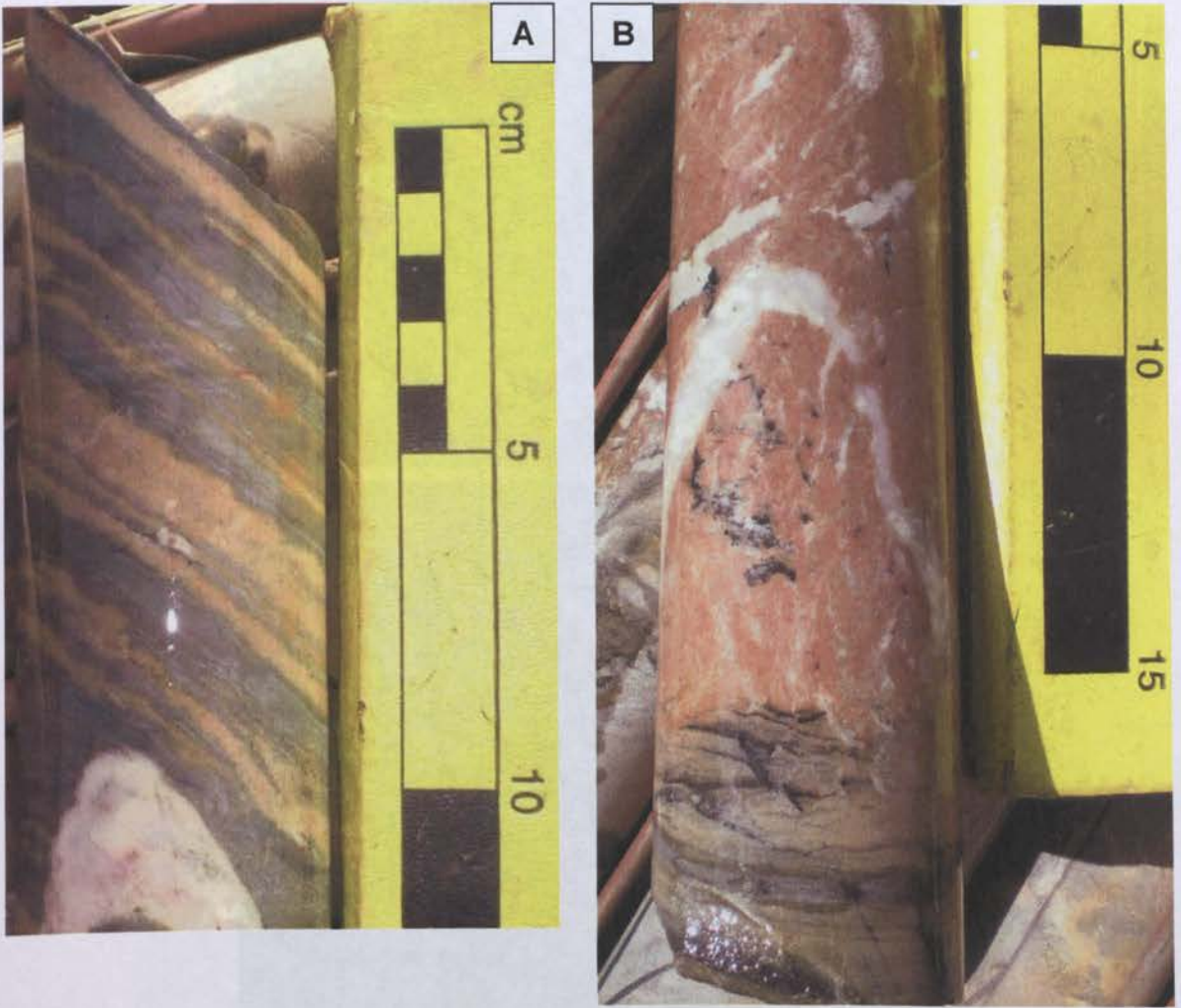


Fig. 5.1. Drill core images of the distal pink sodic alteration zones in wall-rock argillaceous greywacke sediments surrounding the Gara orezone. **A)** Less-pervasive zones where alteration targets ankerite-rich greywacke laminae. Green argillite layers remain largely hydrothermally unaltered as a result of porosity/permeability controls (LOCP90, 183.5 m). **B)** Pervasive pink sodic alteration overprinting both arenaceous and argillite layers, crosscut by late barren quartz veins (LOCP120, 414.2 m).

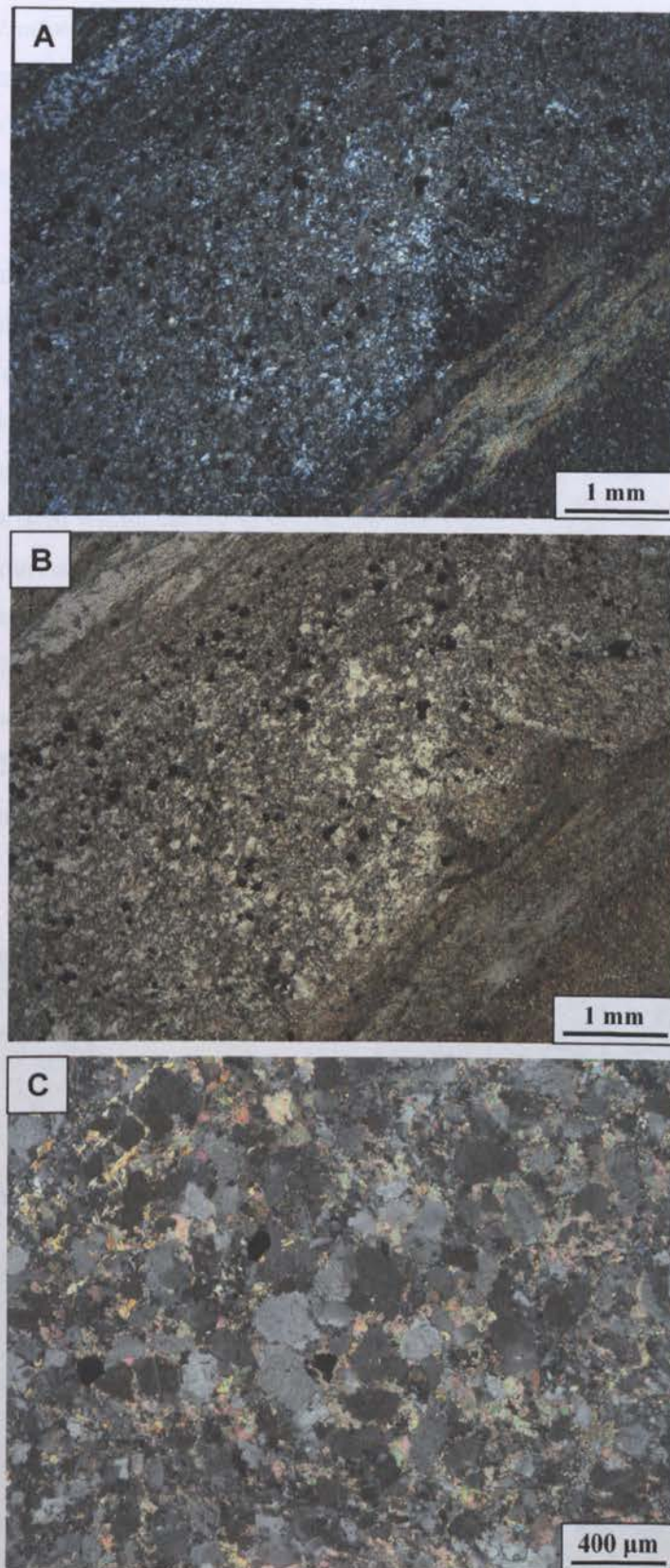


Fig. 5.2. Photomicrographs of the distal pink sodic alteration zone at Gara. **A)** XPL image of Fig. 5.1a showing greywacke laminae in the centre of the image and argillite layers in the top left and bottom right. Alteration targets arenaceous horizons with albite occurring as polycrystalline grains difficult to distinguish from sedimentary quartz. Abundant haematite (~10% of laminae; blocky opaques) is spatially associated with ankerite cement and is the cause of the pink colouration (LOCP90, 183.5 m). **B)** PPL image of the same field of view showing clearly the presence of haematite in the altered horizon. **C)** Higher magnitude XPL image of Fig. 5.1b (more pervasive alteration zone). Albite occurs as twinned and untwinned grains with interstitial ankerite (ankerite show high-order anomalous interference colours) (LOCP120, 414.2 m).

5.3.1.2 Tourmalinisation

The proximal alteration zone at Gara is confined to a 50 m thick quartz-wacke sediment. Two sub-zones can be distinguished (Fig. 3.3a): (1) an inner tourmalinite zone (5-20 m) towards the top of the quartz-wacke sequence (assuming beds are not overturned), which hosts the mineralisation; and (2) an outer weakly tourmalinised zone towards the base of the unit. Rock descriptions and images of the quartz-wacke unit are given in *section 3.3.3* and Fig. 3.9.

The tourmalinite zone is black in colour and confined to fine-sand (grain size $<200\ \mu\text{m}$) beds. These layers are composed of 30-80% tourmaline, which probably form at the expense of phyllic metamorphic mineral phases (e.g. chlorite + sericite). Locally, the tourmalinite zone grades into more weakly-tourmalinised layers over 0.5 to 0.75 m, associated with low-grade. The outer alteration zone is situated within coarse to very coarse sand beds ($500\ \mu\text{m}$ to 2 mm) and consist of lower degrees of tourmalinisation ($<30\%$ of the rock). This zone is moderate to dark grey in colour, is largely barren (fewer carbonate-quartz veins), and is associated with additional silica alteration. Although it is clear from textural studies (*section 5.3.1.2.1*) that tourmaline was associated with the mineralising fluids, the earliest tourmaline alteration event pre-dates mineralisation and F_2 folding (stratabound geometry). These early B-rich fluids are likely to have channelised along narrow (0.5-4 m), bedding parallel, ductile shears, which border the tourmalinite zone (Fig. 5.3).

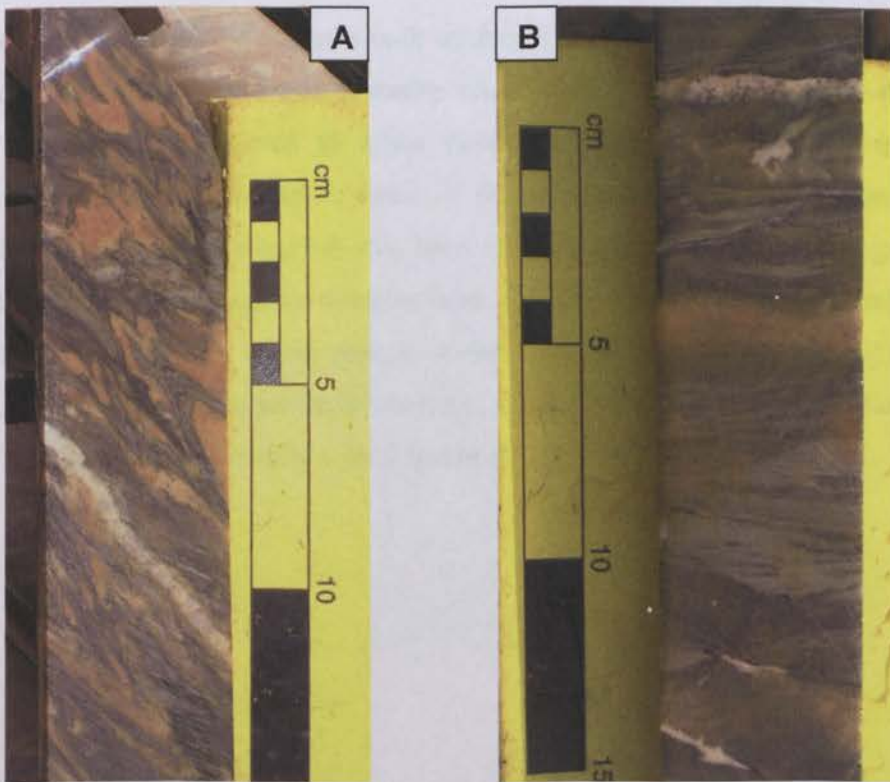


Fig. 5.3. Shear zones bounding the Gara tourmalinite alteration zone. **A)** The top shear zone along the lithological contact between the quartz-wacke and argillaceous greywacke (LOCP44, 85 m). **B)** The bottom, less-developed, shear zone located towards the base of the quartz-wacke sedimentary unit (LOWDH2O, 361.3 m). Both shear zones pre-date F_2 folding (parallel to bedding) and are likely fluid pathways for the earliest B-rich hydrothermal fluids.

5.3.1.2. 1 *Timing and nature of alteration*

Petrographic studies and microprobe analysis of the Gara tourmalines identify several tourmaline alteration events (pre-, syn- and post-mineralisation phases):

- (1) **E-stage-** The main tourmaline alteration event(s) occurs as a massive pre-mineralisation stage (an estimated 60-75% of the overall tourmaline) (Fig. 5.4a to c). E-stage tourmaline occurs as cryptocrystalline grains (mainly <10 μm) with no clear crystal habits.
- (2) **V-stage-** Syn-mineralisation tourmalines (5-10%) occur within auriferous veins or as narrow alteration selvages (<5 cm) around these veins (the latter is often difficult to distinguish because of pervasive E-stage tourmaline growth). Vein-hosted tourmalines occur as acicular grains (30-50 μm) perpendicular to the vein walls (Fig. 5.4c).
- (3) **L-stage-** A late replacement phase (20-35%) after pyrite in some (not all) mineralised veins, accounting for the highly-altered nature of the pyrite crystals (*section 4.2.4.2*). Replacement textures are shown in Fig. 5.4d to i.

The current exploration model is built on the premise that the E-stage tourmaline event(s) increased the brittleness of the quartz-wacke host. During D₂-D₃ deformation and hydraulic fracturing, this horizon deformed to allow development of a carbonate-quartz mineralised stockwork. Although misinterpreted in terms of timing relative to sediment deposition (*section 5.5.2.2*), this early tourmaline stage has long been reported by previous workers (e.g. Dommanget *et al.*, 1993). The V- and L-stage tourmalines have not been reported previously and represent an important discovery in terms of ore genetic studies at Loulo for two reasons: (1) it implies a hydrothermal, epigenetic origin for the tourmaline (contradicts with Dommanget *et al.*, 1993); and (2) tourmaline alteration was broadly coeval and related to gold mineralisation.

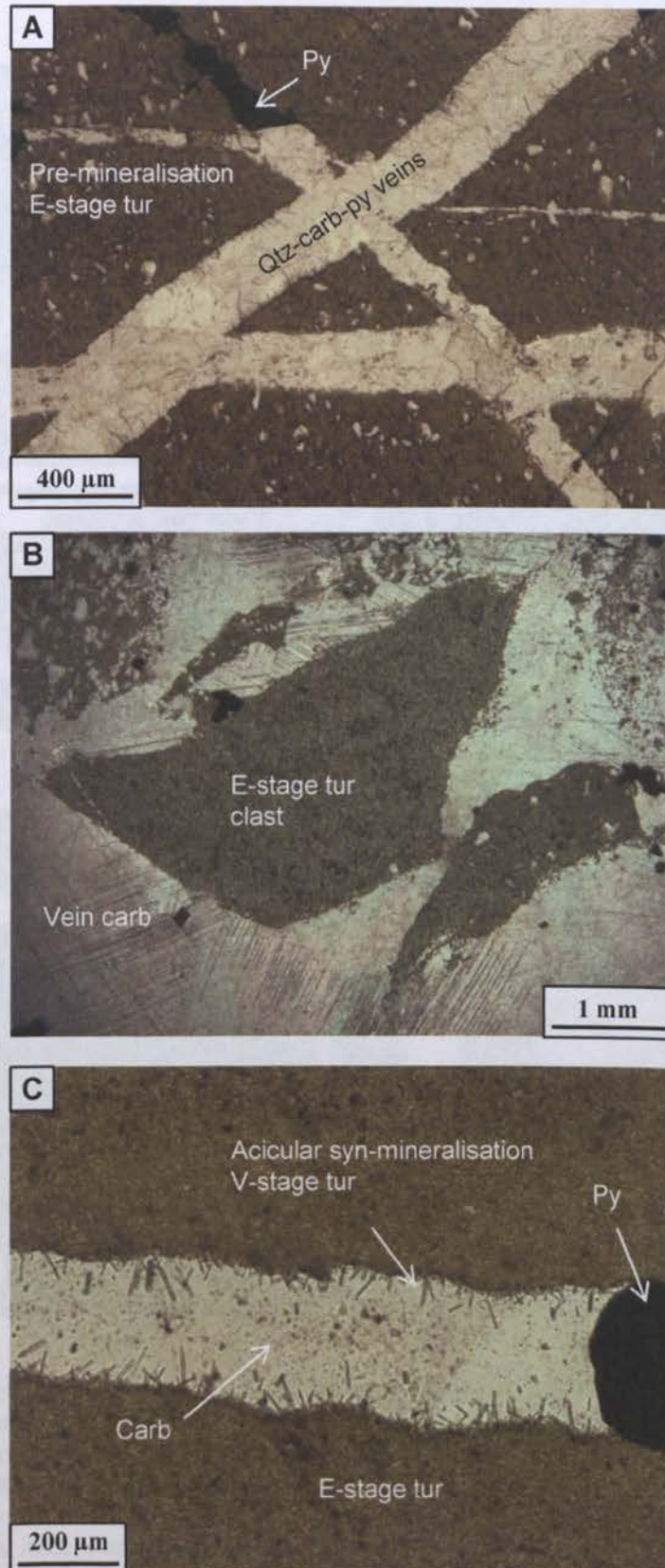


Fig. 5.4. Photomicrographs showing the relative timing of the various tourmaline phases at Gara. **A)** Early massive tourmalinisation (E-stage) predating mineralised quartz-carbonate-pyrite veins (PPL image) (LOCP81, 689.1 m). **B)** E-stage tourmalines also occur as angular clasts within mineralised carbonate veins (wall-rock broken off during vein formation) (XPL image) (LOWDH23, 436.8 m). **C)** Syn-mineralisation tourmalines within a quartz-pyrite vein (V-stage) cross cutting E-stage tourmalines (PPL image). V-stage tourmaline occurs as coarser-grained needles that lie perpendicular to the vein walls (LOWDH23, 436.8 m). Abbreviations same as in Fig. 4.3 and in text.

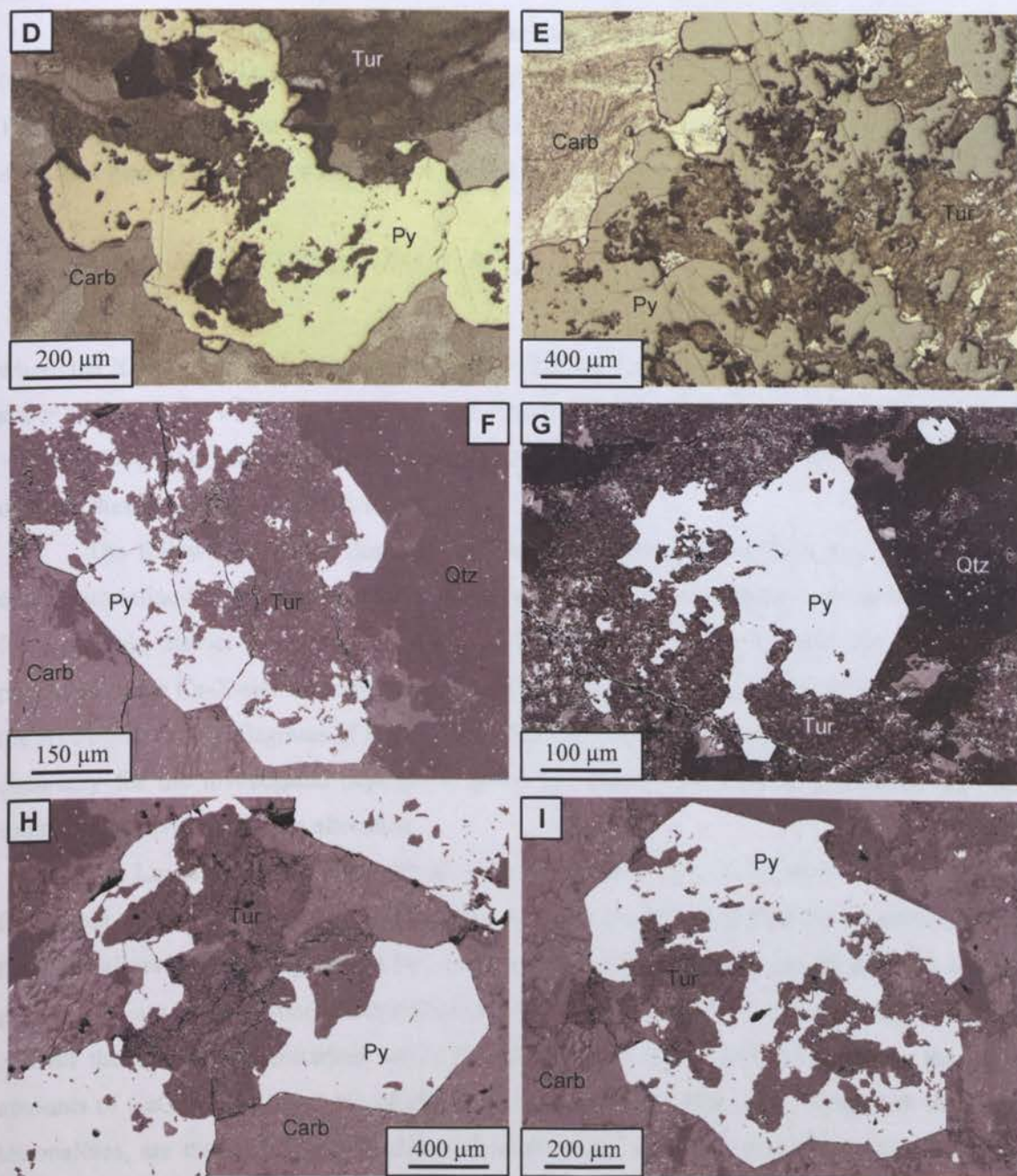


Fig. 5.4 cont. Polarised light images (D & E) and back-scattered electron (BSE) images (F to I) showing L-stage tourmalines replacing mineralised vein pyrite and disseminated pyrite along margins of gold-bearing veins. The polarised light images are shown with both transmitted and reflected light modes on (both in PPL) to show the full extent of the replacement textures. Polarised light images were taken from a sample collected from LOCP120 at 761.5 m, and BSE images from a sample taken from LOCP117 at 338.4 m. Abbreviations same as in Fig. 4.3.

5.3.1.2.2 Chemical compositions

Due to the complexity of the tourmaline mineral group, the compositions of the Loulo tourmalines were calculated using the WinClastour program developed by Yavuz *et al.* (2006). The various normalisation schemes used by WinClastour are described in the appendices (*section A-5*). The general formula for tourmaline may be expressed as:



where the X-site = Ca, Na, □ [vacancy]; Y-site = Li, Mg, Fe²⁺, Mn²⁺, Al, Cr³⁺, V³⁺, Fe³⁺, (Ti⁴⁺); Z-site = Mg, Al, Fe³⁺, V³⁺, Cr³⁺; T-site = Si, Al, (B); B-site = B, (□); V-site = OH, O≡[O(3)]; W-site = OH, F, O≡[O(1)]. Although the species in parentheses are accepted, they are yet to be proven to occur at these sites (Hawthorne & Henry, 1999).

The following sections describe the tourmaline chemistry at Gara, and for comparison other tourmaline-bearing deposits will also be examined. Representative tourmaline chemistries for the Loulo district are given in Table 5.1, Table 5.2 and Table 5.3, and the full dataset is presented in the Ca-X-site vacancy-Na + (K) ternary diagrams of Hawthorne & Henry (1999) and the Al-Fe-Mg ternary diagrams of Henry & Guidotti (1985) below. Interpretation of the tourmaline chemistry for the investigated deposits is given in *section 5.5.2.1*, accompanied by the likely substitutions involved during alteration.

The Loulo tourmalines classify as alkali tourmalines (Fig. 5.5a; Fig 5.7a; Fig. 5.8a) and fall within the dravite (NaMg₃Al₆Si₆O₁₈(BO₃)₃)-schorl (NaFe²⁺Al₆Si₆O₁₈(BO₃)₃) series; although, the tourmalines contain a significant Fe³⁺ content (*see below*). The three generations of tourmaline growth at Gara show distinct compositional variations (Fig. 5.5a, b). The E-stage tourmalines contain the lowest concentrations of Al₂O₃ (28.58-31.00 wt.%) and, less clearly, the highest amounts of CaO (0.29-0.69 wt.%) of all the three generations. This stage, along with the L-stage tourmalines, are the most Mg-rich (dravitic) tourmalines in the Loulo district (MgO 7.48-10.45 wt.%; Fe/[Fe + Mg] cation ratio of 0.174-0.348). However, the E-stage tourmalines contain the highest Fe³⁺ estimates (Fe²⁺/[Fe²⁺ + Fe³⁺] of 0.512-1.000) compared to the V- and L-stage tourmalines, where Fe³⁺ is largely absent. In contrast, the V-stage tourmalines are the most Al₂O₃ (32.29-33.96 wt.%) and Fe-rich (FeO_{total} 7.49-9.58 wt.%; Fe/[Fe + Mg] of 0.418-0.559) of the Gara tourmalines, classifying as Fe-rich dravites or Mg-rich schorls. The V-stage tourmalines are clearly distinguished from the E- and L-stage tourmalines in Fig. 5.5a, with noticeably higher X-site vacancies (□ of 0.364-0.486).

Table 5.1. Representative chemical composition of tourmaline phases at Gara by SEM-EDS analysis.

E-stage	1	2	3	4	5	6	7	8	9	10	11	12	13	14	15
SiO ₂	37.30	37.73	37.78	37.78	37.49	37.64	37.60	37.52	38.22	38.66	37.27	37.57	37.70	36.42	37.09
Al ₂ O ₃	31.00	30.31	28.98	29.69	29.76	29.21	29.65	28.58	28.77	30.68	29.71	29.60	30.13	28.62	29.07
TiO ₂	0.29	0.41	0.70	0.78	0.77	0.69	0.52	0.80	0.31	0.68	0.50	0.65	0.77	0.53	0.91
FeO _{total}	5.71	5.84	6.13	6.14	5.83	6.83	6.30	6.66	7.54	6.67	6.62	6.99	6.79	6.52	7.28
MgO	10.05	9.94	10.19	9.35	10.29	10.45	10.25	10.36	10.34	9.09	9.05	9.06	8.89	9.25	8.45
CaO	0.69	0.65	0.61	0.50	0.58	0.61	0.54	0.62	0.00	0.29	0.32	0.46	0.43	0.47	0.37
Na ₂ O	2.24	2.33	2.64	2.69	2.66	2.68	2.53	2.48	2.89	2.72	2.68	2.61	2.75	2.53	2.72
LiO ₂ *	0.00	0.06	0.15	0.24	0.01	0.00	0.00	0.03	0.02	0.25	0.15	0.17	0.19	0.11	0.24
B ₂ O ₃ *	10.82	10.81	10.74	10.74	10.79	10.82	10.78	10.70	10.80	10.97	10.63	10.70	10.78	10.39	10.55
H ₂ O*	3.63	3.64	2.82	2.82	3.69	2.82	3.68	3.68	2.84	2.85	2.75	2.78	2.80	3.58	2.77
Total	101.73	101.71	100.74	100.72	101.87	101.77	101.84	101.42	101.75	102.88	99.69	100.59	101.24	98.42	99.46
Structural formula on the basis of 24.5 oxygens															
B	3.00	3.00	3.00	3.00	3.00	3.00	3.00	3.00	3.00	3.00	3.00	3.00	3.00	3.00	3.00
Si ^T	5.99	6.07	6.12	6.11	6.04	6.05	6.06	6.09	6.15	6.12	6.10	6.10	6.08	6.09	6.11
Al ^T	0.01	0.00	0.00	0.00	0.00	0.00	0.00	0.00	0.00	0.00	0.00	0.00	0.00	0.00	0.00
T total	6.00	6.07	6.12	6.11	6.04	6.05	6.06	6.09	6.15	6.12	6.10	6.10	6.08	6.09	6.11
Al ^Z	5.86	5.75	5.53	5.66	5.65	5.53	5.63	5.47	5.25	5.73	5.73	5.67	5.73	5.64	5.54
Mg ^Z	0.14	0.26	0.47	0.34	0.35	0.47	0.37	0.53	0.75	0.27	0.27	0.33	0.27	0.36	0.47
Fe ³⁺ Z	0.00	0.00	0.00	0.00	0.00	0.00	0.00	0.00	0.00	0.00	0.00	0.00	0.00	0.00	0.00
Z total	6.00	6.00	6.00	6.00	6.00	6.00	6.00	6.00	6.00	6.00	6.00	6.00	6.00	6.00	6.00
Al ^Y	0.00	0.00	0.00	0.00	0.00	0.00	0.00	0.00	0.00	0.00	0.00	0.00	0.00	0.00	0.00
Ti ^Y	0.03	0.05	0.09	0.10	0.09	0.08	0.06	0.10	0.04	0.08	0.06	0.08	0.09	0.07	0.11
Fe ²⁺ Y	0.71	0.73	0.65	0.83	0.63	0.60	0.63	0.60	0.52	0.88	0.85	0.89	0.92	0.78	0.99
Fe ³⁺ Y	0.06	0.06	0.16	0.00	0.16	0.31	0.22	0.31	0.50	0.00	0.06	0.06	0.00	0.14	0.02
Mg ^Y	2.27	2.13	1.99	1.92	2.12	2.03	2.10	1.98	1.74	1.88	1.93	1.86	1.87	1.95	1.61
Li ^Y	0.00	0.04	0.10	0.16	0.00	0.00	0.00	0.02	0.01	0.16	0.10	0.11	0.12	0.07	0.16
Y total	3.07	3.00	3.00	3.00	3.00	3.03	3.01	3.00	2.80	3.00	3.00	3.00	3.00	3.00	2.89
Ca ^X	0.12	0.11	0.11	0.09	0.10	0.11	0.09	0.11	0.00	0.05	0.06	0.08	0.08	0.08	0.07
Na ^X	0.70	0.73	0.83	0.84	0.83	0.84	0.79	0.78	0.90	0.84	0.85	0.82	0.86	0.82	0.87
X total	0.82	0.84	0.93	0.93	0.93	0.94	0.88	0.89	0.90	0.89	0.91	0.90	0.93	0.90	0.94
X vacancy	0.18	0.16	0.07	0.07	0.07	0.06	0.12	0.11	0.10	0.11	0.09	0.10	0.07	0.10	0.06
Na/(Na + Ca)	0.85	0.87	0.89	0.91	0.89	0.89	0.89	0.88	1.00	0.94	0.94	0.91	0.92	0.91	0.93
Fe/(Fe + Mg)	0.24	0.25	0.25	0.27	0.24	0.27	0.26	0.27	0.29	0.29	0.29	0.30	0.30	0.28	0.33
Fe ²⁺ /(Fe ²⁺ +Fe ³⁺)	0.93	0.93	0.78	1.00	0.80	0.66	0.74	0.66	0.51	1.00	0.94	0.93	1.00	0.85	0.99
Σ Cations	18.89	18.91	18.05	18.04	18.97	18.02	18.95	18.98	18.85	18.01	18.00	18.01	18.02	18.00	18.94

Note- * calculated from WircIastour (see appendices section A-5); T, Z, Y and X refers to site positions.

Table 5.1. cont. Representative chemical composition of tourmaline phases at Gara by SEM-EDS analysis.

	L-stage																					
	V-stage	1	2	3	4	5	6	7	8	9	10	11	12									
SiO ₂	36.96	36.50	37.17	37.33	36.93	37.33	36.06	36.84	37.28	37.32	37.28	37.30	37.44	38.01	37.49	37.48	37.44	37.43	37.46	37.43	37.43	
Al ₂ O ₃	33.13	33.42	33.96	32.89	33.62	33.51	32.29	32.91	31.09	31.51	33.50	33.17	32.49	35.45	31.09	30.43	31.82	31.00	33.16	30.83	30.83	
TiO ₂	0.05	0.06	0.08	0.00	0.09	0.00	0.16	0.10	0.48	0.25	0.00	0.21	0.24	0.24	0.66	0.54	0.28	0.45	0.19	0.60	0.60	
FeO*	7.49	7.57	8.46	8.33	8.32	8.75	9.58	8.92	7.19	7.04	4.77	4.99	5.71	3.54	6.46	6.31	5.60	5.63	5.01	6.59	6.59	
MgO	5.84	5.92	4.69	4.81	4.61	5.10	4.24	5.20	7.55	7.48	8.92	9.01	8.50	9.45	7.82	9.16	8.72	9.19	8.92	8.45	8.45	
CaO	0.05	0.05	0.00	0.00	0.00	0.00	0.00	0.00	0.00	0.00	0.22	0.29	0.29	0.17	0.37	0.24	0.26	0.32	0.25	0.21	0.21	
Na ₂ O	1.98	1.94	1.70	1.85	1.61	1.84	1.76	1.83	2.73	2.42	2.20	2.32	2.55	1.68	2.45	2.68	2.46	2.49	2.16	2.69	2.69	
LiO ₂ *	0.22	0.07	0.26	0.43	0.29	0.23	0.23	0.16	0.22	0.19	0.00	0.00	0.05	0.00	0.29	0.10	0.05	0.09	0.00	0.11	0.11	
B ₂ O ₃ *	10.61	10.59	10.66	10.55	10.56	10.68	10.32	10.57	10.65	10.65	10.87	10.90	10.77	11.18	10.70	10.74	10.73	10.75	10.90	10.68	10.68	
H ₂ O*	3.38	3.31	3.31	3.40	3.27	3.37	3.25	3.32	3.63	3.54	3.51	3.55	3.57	3.47	3.62	3.66	3.55	3.61	3.50	3.62	3.62	
Total	99.71	99.44	100.29	99.60	99.29	100.80	97.88	99.85	100.83	100.40	101.27	101.71	101.01	102.94	100.96	101.34	100.61	100.96	101.56	100.91	100.91	
Structural formula on the basis of 24.5 oxygens																						
B	3.00	3.00	3.00	3.00	3.00	3.00	3.00	3.00	3.00	3.00	3.00	3.00	3.00	3.00	3.00	3.00	3.00	3.00	3.00	3.00	3.00	
Si ^{IV}	6.06	5.99	6.09	6.15	6.08	6.07	6.07	6.06	6.08	6.09	5.95	5.95	6.00	5.91	6.09	6.07	6.01	6.05	5.97	6.04	6.04	
Al ^{IV}	0.00	0.01	0.00	0.00	0.00	0.00	0.00	0.00	0.00	0.00	0.05	0.05	0.01	0.09	0.00	0.00	0.00	0.00	0.03	0.00	0.00	
T total	6.06	6.00	6.09	6.15	6.08	6.07	6.07	6.06	6.08	6.09	6.00	6.00	6.00	6.00	6.09	6.07	6.01	6.05	6.00	6.04	6.04	
Al ²⁺	5.89	5.87	5.93	5.92	5.94	5.87	5.87	5.83	5.70	5.73	6.00	6.00	6.00	6.00	5.96	5.81	6.00	5.91	6.00	5.91	5.91	
Mg ²⁺	0.11	0.13	0.07	0.08	0.06	0.13	0.14	0.17	0.30	0.28	0.00	0.00	0.00	0.00	0.05	0.19	0.00	0.09	0.00	0.09	0.09	
Fe ³⁺	0.00	0.00	0.00	0.00	0.00	0.00	0.00	0.00	0.00	0.00	0.00	0.00	0.00	0.00	0.00	0.00	0.00	0.00	0.00	0.00	0.00	
Z total	6.00	6.00	6.00	6.00	6.00	6.00	6.01	6.00	6.00	6.00	6.00	6.00	6.00	6.00	6.00	6.00	6.00	6.00	6.00	6.00	6.00	
Al ^{IV}	0.51	0.59	0.60	0.47	0.59	0.56	0.55	0.55	0.00	0.00	0.26	0.18	0.12	0.41	0.00	0.00	0.07	0.00	0.20	0.00	0.00	
Ti ^{IV}	0.01	0.01	0.01	0.00	0.01	0.00	0.02	0.01	0.06	0.03	0.00	0.03	0.03	0.00	0.08	0.07	0.03	0.05	0.02	0.07	0.07	
Fe ²⁺	1.03	1.04	1.15	1.15	1.15	1.19	1.35	1.23	0.98	0.96	0.64	0.67	0.77	0.46	0.88	0.83	0.76	0.76	0.67	0.90	0.90	
Fe ³⁺	0.00	0.00	0.00	0.00	0.00	0.00	0.00	0.00	0.00	0.00	0.00	0.00	0.00	0.00	0.00	0.02	0.00	0.00	0.00	0.00	0.00	
Mg ^{IV}	1.31	1.32	1.07	1.10	1.07	1.10	0.92	1.11	1.54	1.56	2.12	2.14	2.05	2.19	1.85	2.02	2.10	2.13	2.12	1.96	1.96	
Li ^{IV}	0.14	0.05	0.17	0.29	0.19	0.15	0.16	0.11	0.15	0.13	0.00	0.00	0.04	0.00	0.19	0.07	0.03	0.06	0.00	0.07	0.07	
Y total	3.00	3.00	3.00	3.00	3.00	3.00	3.00	3.00	2.72	2.66	3.02	3.01	3.00	3.06	3.00	3.00	3.00	3.00	3.01	3.00	3.00	
Ca ^X	0.01	0.01	0.00	0.00	0.00	0.00	0.00	0.00	0.00	0.00	0.04	0.05	0.05	0.03	0.06	0.04	0.05	0.06	0.04	0.04	0.04	
Na ^X	0.63	0.62	0.54	0.59	0.51	0.58	0.58	0.58	0.87	0.77	0.68	0.72	0.80	0.51	0.77	0.84	0.77	0.78	0.67	0.85	0.85	
X total	0.64	0.63	0.54	0.59	0.51	0.58	0.58	0.58	0.87	0.77	0.72	0.77	0.85	0.54	0.84	0.88	0.82	0.84	0.71	0.88	0.88	
X vacancy	0.36	0.37	0.46	0.41	0.49	0.42	0.43	0.42	0.14	0.24	0.28	0.24	0.15	0.46	0.16	0.12	0.16	0.16	0.29	0.12	0.12	
Na/(Na + Ca)	0.99	0.99	1.00	1.00	1.00	1.00	1.00	1.00	1.00	1.00	0.95	0.94	0.94	0.95	0.92	0.95	0.94	0.93	0.94	0.96	0.96	
Fe/(Fe + Mg)	0.42	0.42	0.50	0.49	0.50	0.49	0.56	0.49	0.35	0.35	0.23	0.24	0.27	0.17	0.32	0.28	0.27	0.26	0.24	0.30	0.30	
Fe ²⁺ /(Fe ²⁺ +Fe ³⁺)	1.00	1.00	1.00	1.00	1.00	1.00	1.00	1.00	1.00	1.00	1.00	1.00	1.00	1.00	1.00	0.97	1.00	1.00	1.00	1.00	1.00	
Σ Cations	18.69	18.63	18.63	18.74	18.59	18.65	18.66	18.64	18.67	18.52	18.74	18.77	18.85	18.59	18.93	18.95	18.83	18.89	18.73	18.93	18.93	

Note: * calculated from WinClasour (see appendices section A-5); T, Z, Y and X refers to site positions.

Fig. 5.5 A) The classification of tourmaline generations at Gara based on the X-site occupancy, using the Ca-X-site vacancy-Na+(K) ternary diagram (Hawthorne & Henry, 1999). E-, V- and L-stage tourmalines plot into separate clusters in the alkali field.

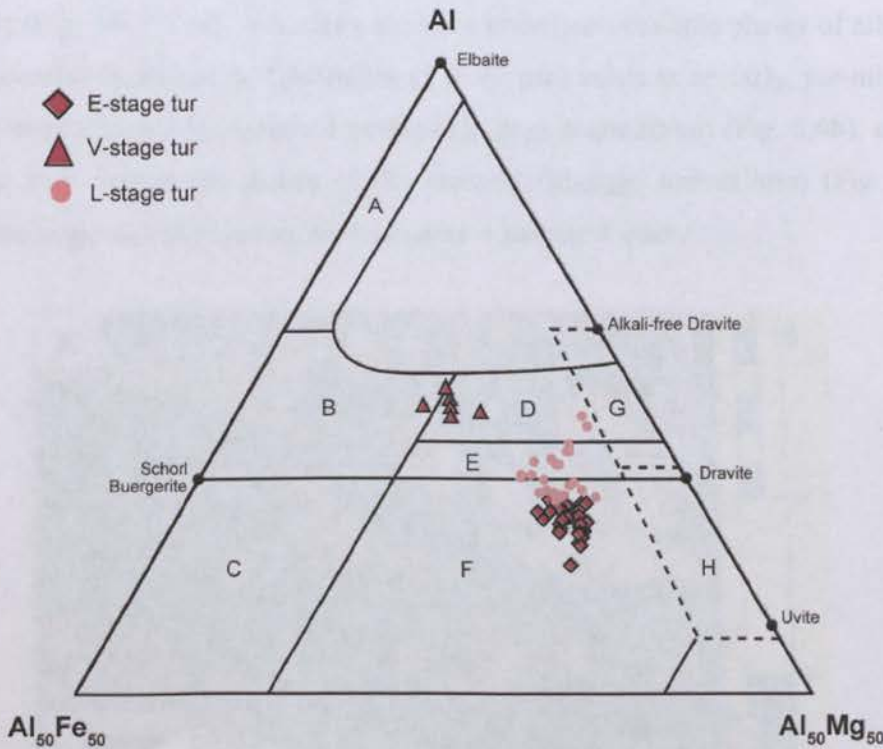
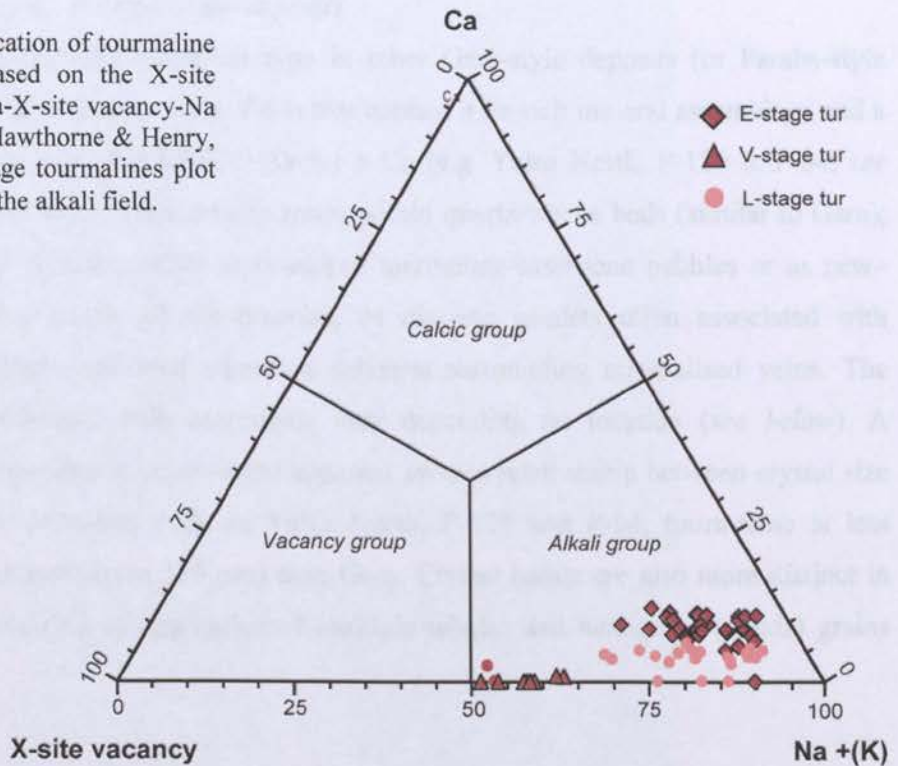


Fig. 5.5 B) Classification of Gara tourmalines based on Y- and Z-site occupancy, using the Al-Fe-Mg ternary diagram (Henry & Guidotti, 1985). Labelled fields: A- Li-rich granitoid pegmatites and aplites; B- Li-poor granitoids pegmatites and aplites; C- Fe^{3+} -rich quartz-tourmaline rocks (altered granitoids); D- metapelites and metapsammities with Al-saturating phase. E- metapelites and metapsammities lacking Al-saturating phase. F- Fe^{3+} -rich quartz-tourmaline rocks, calc-silicate rocks and metapelites; G- low-Ca metaultramafic rocks and Cr-V-rich metasediments; H- metacarbonates and metapyroxenites.

5.3.1.2.3 Comparisons to other Loulo deposits

Tourmaline is a common alteration type in other Gara-style deposits (or Faraba-style orebodies showing Gara-style features; e.g. P-64) that contain a Fe-rich mineral assemblage and a metal signature consisting of Fe-Cu-REE-Ni-As-Au \pm Co (e.g. Yalea North, P-129 & P-64; *see chapter 4*). Tourmaline occurs in metasomatic zones within quartz-wacke beds (similar to Gara); in hydrothermal-tectonic breccias, either as reworked tourmaline-sandstone pebbles or as new-growth tourmaline in the matrix of the breccias; as discrete veinlets often associated with mineralisation; or as narrow proximal alteration selvages surrounding mineralised veins. The mineral assemblages associated with tourmaline vary depending on location (*see below*). A distinctive feature of tourmaline at Loulo is the apparent inverse relationship between crystal size and volume. In smaller orebodies such as Yalea North, P-129 and P-64, tourmaline is less abundant and coarser-grained (up to 150 μm) than Gara. Crystal habits are also more distinct in these deposits, often occurring in aggregates of multiple tabular and hexagonal (c-axis) grains (Fig. 5.6d; Fig. 5.7).

Yalea North

Mineralisation at Yalea North is confined to the matrix of hydrothermal-tectonic breccias (*section 3.3.5*) (Fig. 5.6a). These breccias units have undergone multiple phases of albite (*section 5.3.2.1*) and tourmaline alteration. Tourmaline (5 to 40 μm) exists as an early, pre-mineralisation stage, as reworked tourmaline-sandstone pebbles (R-stage tourmalines) (Fig. 5.6b), or as a syn-mineralisation stage within the matrix of the breccias (M-stage tourmalines) (Fig. 5.6c). The alteration assemblage includes tourmaline + ankerite + siderite \pm quartz.



Fig. 5.6 A). Hydrothermal-tectonic breccia host rocks at Yalea North (modified from Fig. 3.11; rock descriptions in *section 3.3.5*). Tourmaline occurs within the matrix of the breccias along with mineralisation (M stage) or as reworked material (clast fragments between 200 μm to 5 cm; R-stage). Multiphase tourmaline growth is clearly distinguished in the photomicrographs shown below.

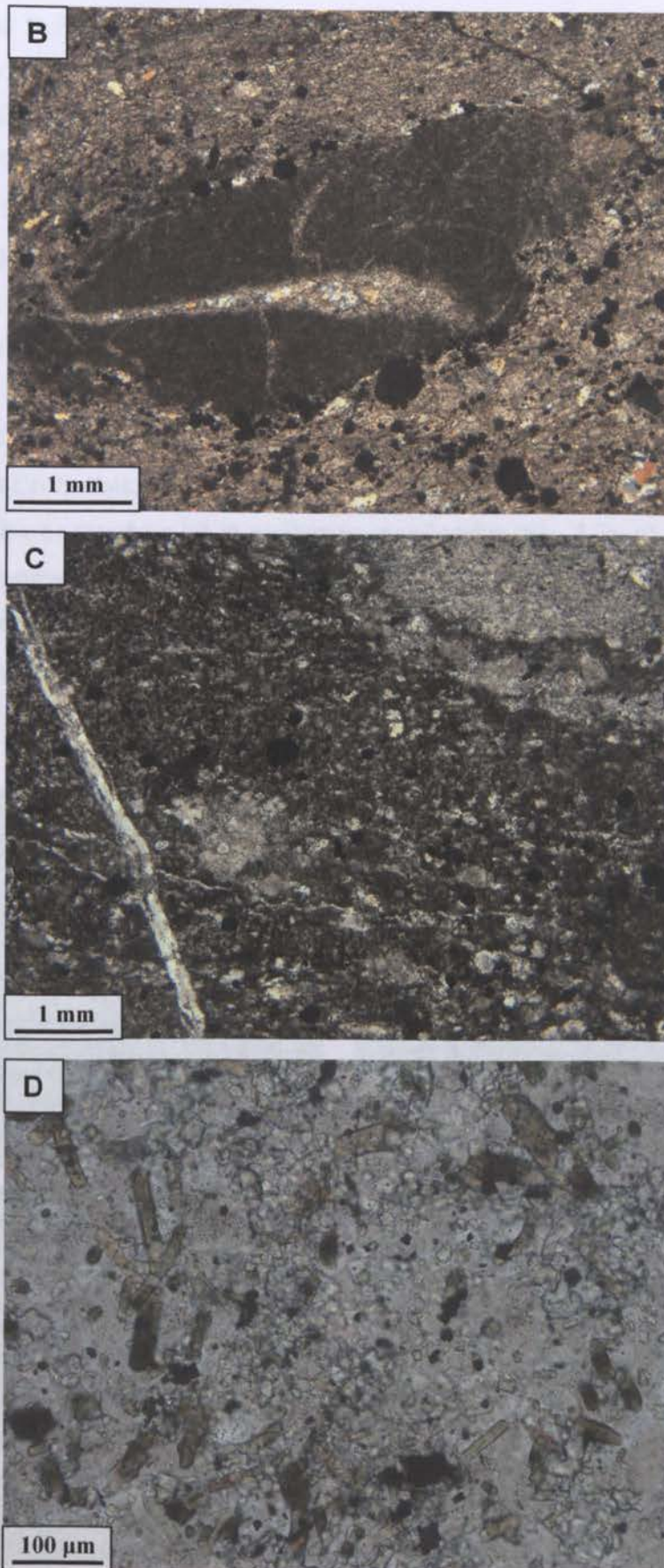


Fig. 5.6. cont. Photomicrographs of the tourmaline phases (brown-olive green minerals) at Yalea North. **B)** R-stage tourmaline clast surrounding a carbonate and pyrite (opaques) matrix (XPL image) (YDH149, 486.5 m). **C)** A later M-stage tourmaline growth within the matrix of the breccias, coeval with pyrite and gold mineralisation (XPL image) (YDH149, 468.8 m). **D)** A higher magnitude image showing prismatic M-stage tourmalines (PPL image) (YDH149, 476.8 m). Crystal habits are also shown in Fig. 5.7.

The Yalea North tourmalines contain more variable and Fe-rich compositions than the Gara tourmalines (5.57-19.23 wt.% FeO_{total}). Both R- and S-stages contain similar compositions (Table 5.2) and prominent rim-core zonation (Fig. 5.7). Crystal rims have higher Fe levels with Fe/(Fe + Mg) ratios of 0.444-0.591, and higher Fe³⁺ estimates with Fe²⁺/(Fe²⁺ + Fe³⁺) ratios of 0.368-0.640. On the other hand, the cores have lower Fe/(Fe + Mg) ratios of 0.249-0.485 and Fe²⁺/(Fe²⁺ + Fe³⁺) ratios >0.5. The Fe/(Fe + Mg) ratio difference between the cores and rims is restricted by the largely constant MgO levels (mainly from 7-9 wt.%). Another rim-core distinction is the variation in X-site vacancy. Tourmaline rims contain full or near full site occupancy (\square of 0-0.090) compared to the rim cores (\square of 0-0.206). Crystal rims also contain minor amounts of V₂O₃ (up to 0.8 wt.%) and Cr₂O₃ (up to 0.5 wt.%), which are absent from the cores (positive Fe-Cr-V relationship), and contain higher levels of K₂O (~0.5 wt.%) and TiO₂ (~1 wt.%). Similar patterns are observed in oscillatory zoned grains (Fig. 5.7a, c). As well as zoned grains, M-stage tourmalines intergrown with mineralised pyrite also show unzoned patterns (Fig. 5.7d). These grains show markedly lower MgO contents of 3.56-6.27 wt.%, and clearly plot into a separate cluster on the Al-Fe-Mg diagram (Fig. 5.8b). These Mg-poor tourmalines contain higher X-site vacancies (\square of 0.196-0.489) (Fig. 5.8a) and share similarities to Gara V-stage tourmalines.

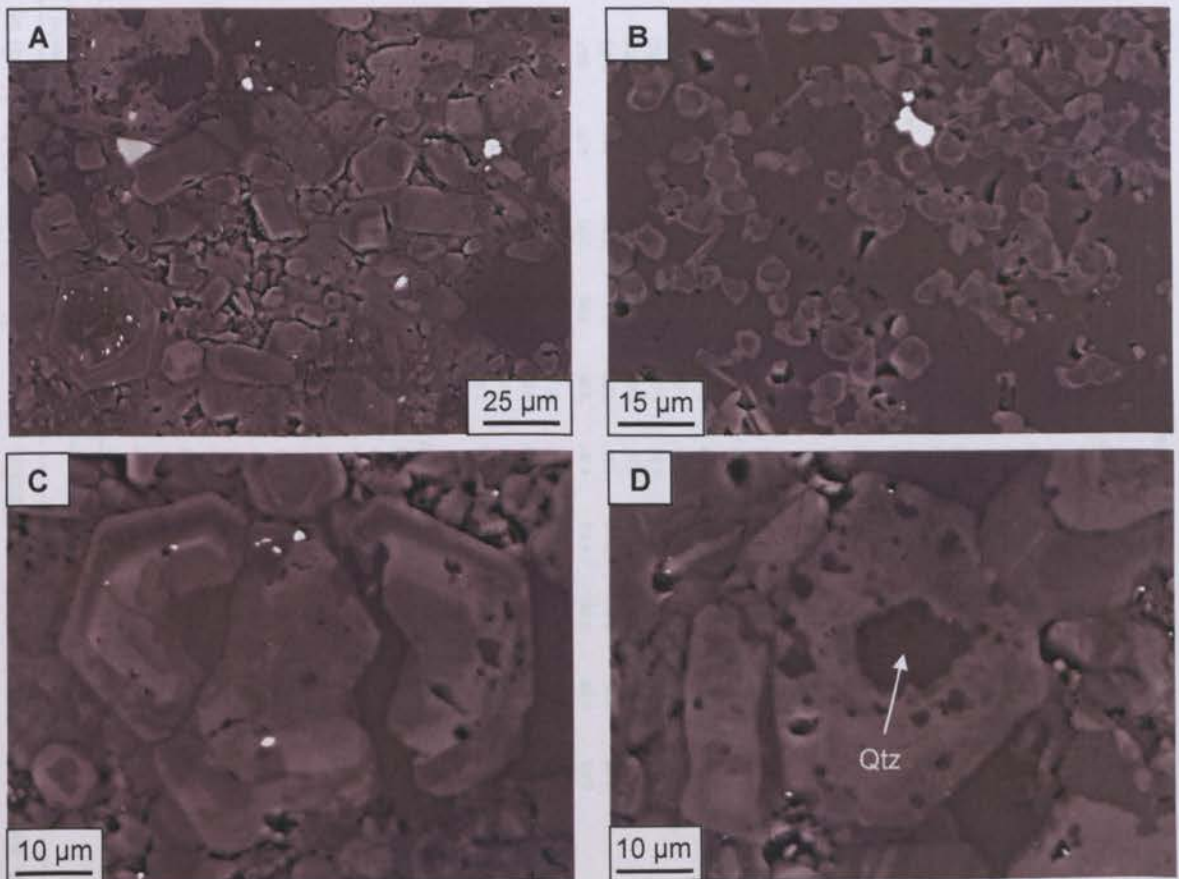


Fig. 5.7. BSE images showing the nature of the tourmaline crystals at Yalea North. **A)** Hexagonal (C-axis) tourmaline crystals within the matrix of the breccias (M-stage), showing both zoned and unzoned patterns (YDH149, 486.5 m). **B)** M-stage tourmalines showing rim-core zoning (2-zoned pattern), with higher Fe concentrations towards the rims (YDH149, 462.8 m). **C)** Larger oscillatory zoned R-stage tourmaline crystal. **D)** Unzoned M-stage tourmaline grains with a quartz nucleus and small quartz inclusions (C & D from YDH149, 486.5 m).

Table 5.2. Representative chemical composition of tourmaline phases at Yalea North by SEM-EDS analysis.

	R-stage										M-stage zoned grains										M-stage unzoned		
	1	2	3	4	5	6	7	8	1	2	3	4	5	6	7	8	9	1	2	3			
SiO ₂	36.34	35.60	36.68	36.00	35.51	37.24	37.63	35.41	36.21	38.08	35.73	35.83	36.12	36.30	36.46	36.76	35.83	36.99	36.64	37.59			
Al ₂ O ₃	29.08	20.88	25.18	22.82	20.28	28.83	31.34	24.97	23.54	29.11	29.76	23.74	21.77	23.48	24.22	28.59	24.46	30.24	33.28	32.45			
TiO ₂	0.34	0.98	1.03	0.98	0.63	0.24	0.49	1.67	0.80	0.29	0.00	0.99	1.50	1.08	0.80	0.00	0.95	0.65	0.00	0.00			
FeO*	11.31	17.67	12.34	15.64	19.23	9.56	5.57	12.34	13.54	5.97	7.25	13.35	15.20	13.56	13.09	6.75	12.94	15.18	11.74	8.53			
MgO	6.72	7.25	8.37	7.54	7.46	8.29	8.68	8.27	9.24	10.11	8.39	7.74	8.05	8.30	8.44	9.04	8.03	3.87	3.56	5.52			
Cr ₂ O ₃	0.00	0.50	0.26	0.39	0.00	0.00	0.00	0.00	0.00	0.00	0.00	0.44	0.80	0.36	0.00	0.00	0.00	0.00	0.00	0.00			
V ₂ O ₅	0.00	0.79	0.55	0.62	0.71	0.00	0.00	0.44	0.39	0.25	0.21	0.79	0.65	0.43	0.40	0.00	0.38	0.26	0.00	0.00			
CaO	0.36	0.50	0.50	0.50	0.68	0.42	0.41	0.44	2.44	2.50	2.66	2.53	2.46	2.65	2.67	3.07	2.36	1.67	1.60	2.02			
Na ₂ O	2.55	2.49	2.72	2.53	2.40	2.96	2.57	3.40	2.44	2.50	2.66	2.53	2.46	2.65	2.67	3.07	2.36	1.67	1.60	2.02			
K ₂ O	0.00	0.41	0.23	0.27	0.41	0.00	0.00	0.29	0.41	0.16	0.00	0.22	0.44	0.43	0.00	0.00	0.23	0.00	0.00	0.00			
Li ₂ O*	0.00	0.00	0.00	0.00	0.00	0.10	0.28	0.00	0.00	0.21	0.00	0.04	0.00	0.00	0.00	0.00	0.00	0.28	0.08	0.36			
B ₂ O ₃ *	10.43	9.90	10.39	10.11	9.87	10.61	10.78	10.22	10.15	10.71	10.32	10.10	10.13	10.21	10.23	10.49	10.07	10.44	10.56	10.63			
H ₂ O*	3.55	3.42	2.99	3.21	3.41	2.85	3.67	3.05	2.98	2.81	3.53	3.05	3.35	3.15	3.02	2.81	2.81	3.37	3.23	3.47			
Total	100.69	100.21	101.18	100.61	100.59	101.11	101.39	100.06	99.50	100.20	97.86	99.27	101.06	100.52	100.10	99.54	98.06	100.96	100.68	100.58			
Structural formula on the basis of 24.5 oxygens																							
B	3.00	3.00	3.00	3.00	3.00	3.00	3.00	3.00	3.00	3.00	3.00	3.00	3.00	3.00	3.00	3.00	3.00	3.00	3.00	3.00			
Si ¹	6.06	6.25	6.14	6.19	6.25	6.10	6.07	6.02	6.20	6.18	6.02	6.17	6.28	6.18	6.18	6.09	6.18	6.15	6.03	6.15			
Al ¹	0.00	0.00	0.00	0.00	0.00	0.00	0.00	0.00	0.00	0.00	0.00	0.00	0.00	0.00	0.00	0.00	0.00	0.00	0.00	0.00			
T total	6.06	6.25	6.14	6.19	6.25	6.10	6.07	6.02	6.20	6.18	6.02	6.17	6.28	6.18	6.18	6.09	6.18	6.15	6.03	6.15			
Al ²	5.45	4.28	4.96	4.62	4.21	5.37	5.96	5.00	4.75	5.57	5.50	4.82	4.41	4.71	4.85	5.29	4.97	5.72	5.83	5.83			
Mg ²	0.55	1.03	0.88	0.96	1.12	0.63	0.04	0.89	1.14	0.43	0.50	0.88	1.02	0.97	0.96	0.71	0.92	0.28	0.18	0.17			
Fe ³⁺²	0.00	0.52	0.08	0.28	0.57	0.00	0.00	0.10	0.11	0.00	0.00	0.16	0.39	0.21	0.14	0.00	0.11	0.00	0.00	0.00			
Cr ²	0.00	0.07	0.03	0.01	0.00	0.00	0.00	0.00	0.00	0.00	0.00	0.06	0.11	0.05	0.00	0.00	0.00	0.00	0.00	0.00			
V ²	0.00	0.11	0.07	0.09	0.10	0.00	0.00	0.00	0.00	0.00	0.00	0.07	0.08	0.06	0.05	0.00	0.00	0.00	0.00	0.00			
Z total	6.00	6.00	6.00	5.95	6.00	6.00	6.00	6.00	6.00	6.00	6.00	6.00	6.00	6.00	6.00	6.00	6.00	6.00	6.00	6.00			
Al ¹	0.27	0.00	0.00	0.00	0.00	0.20	0.00	0.00	0.00	0.00	0.41	0.00	0.00	0.00	0.00	0.29	0.00	0.22	0.63	0.42			
Ti ¹	0.04	0.13	0.13	0.13	0.08	0.03	0.06	0.21	0.08	0.04	0.00	0.13	0.19	0.14	0.10	0.00	0.12	0.08	0.00	0.00			
Fe ²⁺³	1.39	1.20	1.00	1.15	1.17	1.05	0.75	0.98	0.71	0.60	0.93	1.18	1.08	0.99	0.94	0.77	1.00	1.84	1.62	1.17			
Fe ³⁺³	0.18	0.88	0.67	0.80	1.09	0.26	0.00	0.67	1.12	0.21	0.09	0.59	0.74	0.73	0.78	0.45	0.76	0.00	0.00	0.00			
Mg ¹	1.12	0.87	1.21	0.98	0.84	1.38	2.04	1.20	1.22	2.02	1.61	1.10	1.04	1.14	1.18	1.52	1.15	0.86	0.70	1.18			
Li ¹	0.00	0.00	0.00	0.00	0.00	0.07	0.15	0.00	0.00	0.14	0.00	0.02	0.00	0.00	0.00	0.00	0.00	0.19	0.05	0.24			
Y total	3.01	3.08	3.01	3.07	3.18	3.00	3.00	3.07	3.12	3.00	3.04	3.00	3.03	3.00	3.00	3.03	3.03	3.00	3.00	3.00			
Ca ²	0.06	0.09	0.09	0.09	0.13	0.07	0.07	0.08	0.07	0.04	0.04	0.15	0.12	0.10	0.08	0.00	0.07	0.05	0.00	0.00			
Na ²	0.82	0.85	0.88	0.84	0.82	0.94	0.80	1.12	0.81	0.79	0.87	0.84	0.82	0.88	0.88	0.99	0.79	0.54	0.51	0.84			
K ²	0.00	0.09	0.05	0.06	0.09	0.00	0.00	0.06	0.09	0.03	0.00	0.05	0.10	0.09	0.07	0.00	0.05	0.00	0.00	0.00			
X total	0.89	1.03	1.02	1.00	1.04	1.02	0.88	1.28	0.97	0.86	0.91	1.04	1.04	1.07	1.03	0.99	0.91	0.59	0.51	0.84			
X vacancy	0.11	0.00	0.00	0.00	0.00	0.00	0.13	0.00	0.03	0.14	0.09	0.00	0.00	0.00	0.00	0.01	0.09	0.41	0.49	0.36			
Na/(Na + Ca)	0.93	0.90	0.91	0.90	0.86	0.93	0.92	0.93	0.92	0.95	0.96	0.85	0.87	0.90	0.92	1.00	0.92	0.66	0.65	0.48			
Fe/(Fe + Mg)	0.49	0.58	0.45	0.54	0.59	0.39	0.26	0.46	0.45	0.25	0.33	0.49	0.51	0.48	0.47	0.35	0.47	0.66	0.65	0.48			
Fe ²⁺³ /(Fe ²⁺³ +Fe ³⁺)	0.88	0.56	0.80	0.59	0.52	0.80	1.00	0.60	0.37	0.74	0.63	0.49	0.60	0.49	0.51	0.63	0.54	1.00	1.00	1.00			
Σ Cations	18.95	19.36	19.17	19.21	19.47	19.12	18.94	19.35	19.30	19.05	18.96	19.20	19.35	19.25	19.23	19.11	19.13	18.75	18.55	18.79			

Note- * calculated from WirtClastour (see appendices section A-5); T, Z, Y and X refers to site positions.

Fig. 5.8. Classification of Yalea North tourmalines. **A)** Ca-X-site vacancy-Na + (K) ternary diagram (Hawthorne & Henry, 1999). Both stages show full or near complete site occupancy at the X-site, apart from several unzoned M-stage grains.

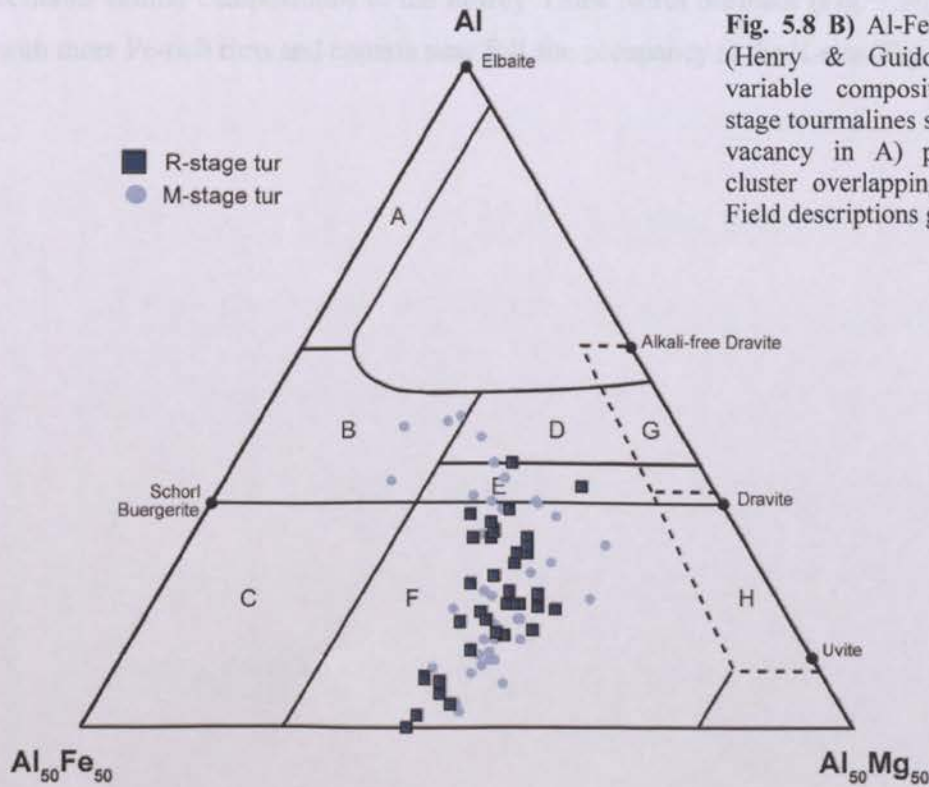
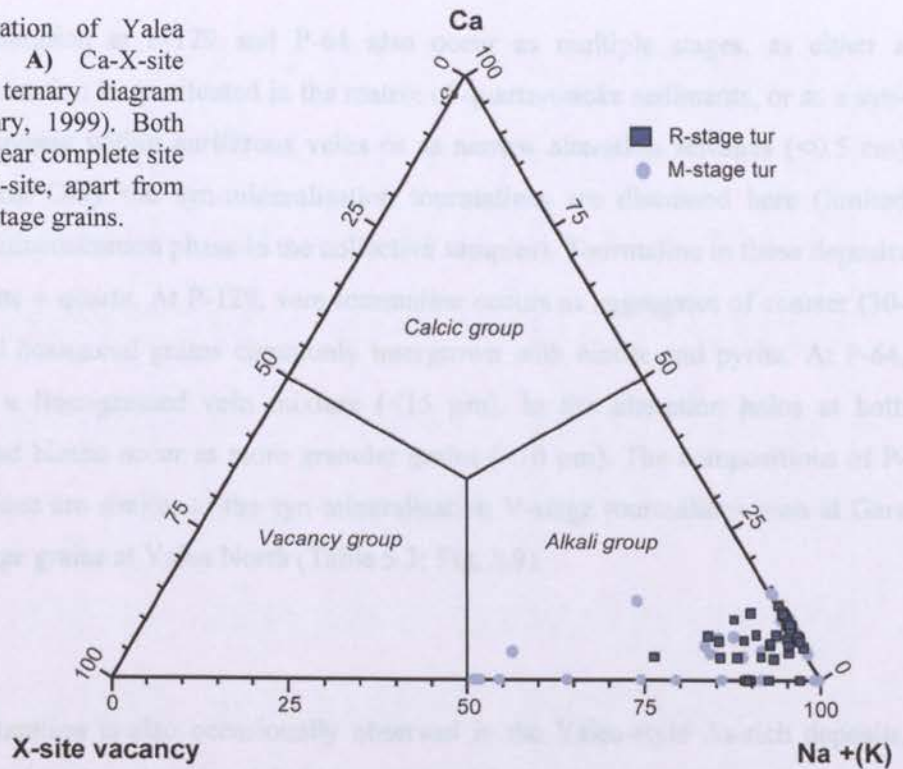


Fig. 5.8 B) Al-Fe-Mg ternary diagram (Henry & Guidotti, 1985) showing variable compositions. Unzoned M-stage tourmalines showing higher X-site vacancy in A) plot into a separate cluster overlapping fields B, D & E. Field descriptions given in Fig. 5.5b.

P-129 & P-64

Tourmaline alteration at P-129 and P-64 also occur as multiple stages, as either a widespread pre-mineralisation stage situated in the matrix of quartz-wacke sediments, or as a syn-mineralisation phase present within auriferous veins or as narrow alteration selvages (<0.5 cm) surrounding these veins. Only the syn-mineralisation tourmalines are discussed here (limited appearance of the pre-mineralisation phase in the collective samples). Tourmaline in these deposits is associated with biotite \pm quartz. At P-129, vein tourmaline occurs as aggregates of coarser (30-150 μm) prismatic and hexagonal grains commonly intergrown with biotite and pyrite. At P-64, tourmaline occurs as a finer-grained vein mixture (<15 μm). In the alteration halos at both deposits, tourmaline and biotite occur as more granular grains (<10 μm). The compositions of P-129 and P-64 tourmalines are similar to the syn-mineralisation V-stage tourmalines seen at Gara and the unzoned M-stage grains at Yalea North (Table 5.3; Fig. 5.9).

Other deposits

Tourmaline alteration is also occasionally observed in the Yalea-style As-rich deposits, but is generally unrelated to the mineralised fluid event(s). At P-125, tourmaline alteration occurs as a late replacement phase, often as patchy alteration within disseminated sulphide zones, or located along recrystallised zones on the margins of vein quartz. Tourmaline alteration at P-125 contains similar compositions to the nearby Yalea North oreshoot (Fig. 5.9b). Crystals are zoned with more Fe-rich rims and contain near full site occupancy at the X-site (Fig. 5.9a).

Table 5.3. Representative chemical composition of tourmaline at P-64, P-129 and P-125 orebodies by SEM-EDS analysis.

	P-64 syn-mineralisation tur						P-129 syn-mineralisation tur						P-125 post-mineralisation tur					
	1	2	3	4	5	6	1	2	3	4	5	6	1	2	3	4	5	6
SiO ₂	37.04	37.33	35.59	37.01	37.05	37.48	37.35	36.90	36.95	36.87	36.79	36.87	36.45	36.74	36.34	37.64	35.88	37.17
Al ₂ O ₃	30.94	31.93	23.87	31.54	31.76	31.59	31.96	30.32	30.50	31.65	29.91	31.05	28.08	27.87	26.63	29.57	25.20	28.80
TiO ₂	0.00	0.30	0.46	0.00	0.29	0.35	0.00	0.49	0.31	0.00	0.78	0.00	0.54	0.23	1.28	0.00	0.98	0.00
FeO _{total}	7.55	7.81	6.34	7.92	7.56	7.77	8.45	9.12	8.46	8.37	9.11	8.43	11.03	12.00	11.57	8.93	13.36	10.45
MgO	7.45	7.63	7.91	7.17	7.40	7.73	6.23	6.77	6.83	6.55	6.86	6.63	6.74	6.72	7.10	8.31	7.65	8.38
V ₂ O ₅	0.00	0.00	0.29	0.00	0.00	0.00	0.00	0.00	0.00	0.00	0.00	0.00	0.00	0.00	0.00	0.00	0.34	0.00
CaO	0.21	0.32	0.25	0.21	0.22	0.30	0.00	0.00	0.00	0.00	0.19	0.00	0.00	0.00	0.30	0.00	0.49	0.00
K ₂ O	2.50	2.43	2.62	2.43	2.55	2.33	0.00	0.00	0.00	0.00	0.00	0.00	0.00	0.00	0.00	0.00	0.00	0.00
Na ₂ O	0.00	0.00	0.28	0.00	0.00	0.00	2.19	2.67	2.43	2.40	2.69	2.43	2.97	2.98	2.72	2.47	2.62	2.81
LiO ₂ *	0.20	0.03	0.00	0.12	0.09	0.08	0.28	0.18	0.22	0.15	0.20	0.20	0.32	0.14	0.15	0.08	0.00	0.00
B ₂ O ₃ *	10.56	10.79	10.05	10.62	10.69	10.78	10.60	10.53	10.49	10.56	10.52	10.49	10.32	10.36	10.28	10.63	10.20	10.59
H ₂ O*	3.56	3.56	3.02	3.54	3.56	3.56	3.49	3.58	3.53	3.50	3.61	3.52	2.77	2.80	2.78	3.61	2.85	2.79
Total	100.01	102.13	99.48	100.57	101.19	101.95	100.23	100.56	99.73	100.04	100.66	99.63	99.07	99.85	99.17	101.23	99.57	100.99
Structural formula on the basis of 24.5 oxygens																		
B	3.00	3.00	3.00	3.00	3.00	3.00	3.00	3.00	3.00	3.00	3.00	3.00	3.00	3.00	3.00	3.00	3.00	3.00
Si ^T	6.10	6.01	6.16	6.06	6.02	6.04	6.12	6.09	6.12	6.07	6.08	6.11	6.14	6.16	6.14	6.16	6.11	6.10
Al ^T	0.00	0.00	0.00	0.00	0.00	0.00	0.00	0.00	0.00	0.00	0.00	0.00	0.00	0.00	0.00	0.00	0.00	0.00
T total	6.10	6.01	6.16	6.06	6.02	6.04	6.12	6.09	6.12	6.07	6.08	6.11	6.14	6.16	6.14	6.16	6.11	6.10
Al ^Z	5.66	5.65	4.82	5.66	5.69	5.64	5.78	5.61	5.65	5.71	5.60	5.68	5.45	5.40	5.31	5.42	5.06	5.28
Mg ^Z	0.34	0.35	1.02	0.32	0.31	0.36	0.22	0.39	0.35	0.29	0.40	0.32	0.55	0.60	0.65	0.56	0.85	0.72
Fe ³⁺ Z	0.00	0.00	0.12	0.00	0.00	0.00	0.00	0.00	0.00	0.00	0.00	0.00	0.00	0.00	0.05	0.00	0.04	0.00
V ^Z	0.00	0.00	0.04	0.00	0.00	0.00	0.00	0.00	0.00	0.00	0.00	0.00	0.00	0.00	0.00	0.00	0.05	0.00
Z total	6.00	6.00	6.00	6.00	6.00	6.00	6.00	6.00	6.00	6.00	6.00	6.00	6.00	6.00	6.00	6.00	6.00	6.00
Al ^Y	0.34	0.41	0.00	0.41	0.39	0.37	0.40	0.29	0.30	0.43	0.23	0.38	0.30	0.11	0.00	0.28	0.00	0.29
Tl ^Y	0.00	0.04	0.06	0.00	0.04	0.04	0.00	0.06	0.04	0.00	0.10	0.00	0.07	0.03	0.16	0.00	0.13	0.00
Fe ³⁺ Y	1.04	1.05	1.01	1.08	1.03	1.05	1.12	1.26	1.17	1.15	1.26	1.17	1.31	1.32	1.27	0.97	1.15	0.95
Fe ²⁺ Y	0.00	0.00	0.09	0.00	0.00	0.00	0.00	0.00	0.00	0.00	0.00	0.00	0.24	0.36	0.33	0.25	0.71	0.49
Mg ^Y	1.49	1.48	1.02	1.43	1.48	1.50	1.30	1.28	1.34	1.32	1.29	1.32	1.14	1.08	1.14	1.45	1.09	1.34
Li ^Y	0.13	0.02	0.00	0.08	0.06	0.05	0.16	0.12	0.15	0.10	0.13	0.14	0.12	0.10	0.11	0.05	0.00	0.00
Y total	3.00	3.00	3.18	3.00	3.00	3.00	3.00	3.00	3.00	3.00	3.00	3.00	3.00	3.00	3.00	3.00	3.00	3.06
Ca ^X	0.04	0.06	0.05	0.04	0.04	0.05	0.00	0.00	0.00	0.00	0.03	0.00	0.00	0.00	0.06	0.00	0.09	0.00
Na ^X	0.80	0.76	0.88	0.77	0.80	0.73	0.69	0.85	0.78	0.77	0.66	0.78	0.97	0.97	0.89	0.78	0.87	0.87
K ^X	0.00	0.00	0.06	0.00	0.00	0.00	0.00	0.00	0.00	0.00	0.00	0.00	0.00	0.00	0.00	0.00	0.00	0.00
X total	0.83	0.81	0.99	0.81	0.84	0.78	0.69	0.85	0.78	0.77	0.70	0.78	0.97	0.97	0.95	0.78	0.96	0.87
X vacancy	0.17	0.19	0.01	0.19	0.16	0.22	0.31	0.15	0.22	0.23	0.31	0.22	0.03	0.03	0.05	0.22	0.04	0.13
Nar/(Na + Ca)	0.96	0.93	0.95	0.95	0.95	0.93	1.00	1.00	1.00	1.00	0.95	1.00	1.00	1.00	0.94	1.00	0.91	1.00
Fe/(Fe + Mg)	0.36	0.36	0.52	0.38	0.36	0.36	0.42	0.43	0.41	0.42	0.43	0.42	0.48	0.50	0.48	0.38	0.49	0.41
Fe ²⁺ /(Fe ²⁺ +Fe ³⁺)	1.00	1.00	0.45	1.00	1.00	1.00	1.00	1.00	1.00	1.00	1.00	1.00	0.84	0.78	0.77	0.80	0.66	0.66
Σ Cations	18.89	18.91	19.05	18.04	18.97	19.02	18.82	18.95	18.90	18.84	18.77	18.89	19.11	19.13	19.09	18.94	19.15	19.03

Note: * calculated from WinClastour (see appendices section A-5); T, Z, Y and X refers to site positions.

Fig. 5.9 A) Ca-X-site vacancy-Na+(K) ternary diagram (Hawthorne & Henry, 1999) showing X-site occupancy of syn-mineralised tourmaline phases at P-129 and P-64, and the post-mineralisation tourmaline phase at P-125. Syn-mineralised tourmalines show higher X-site vacancy.

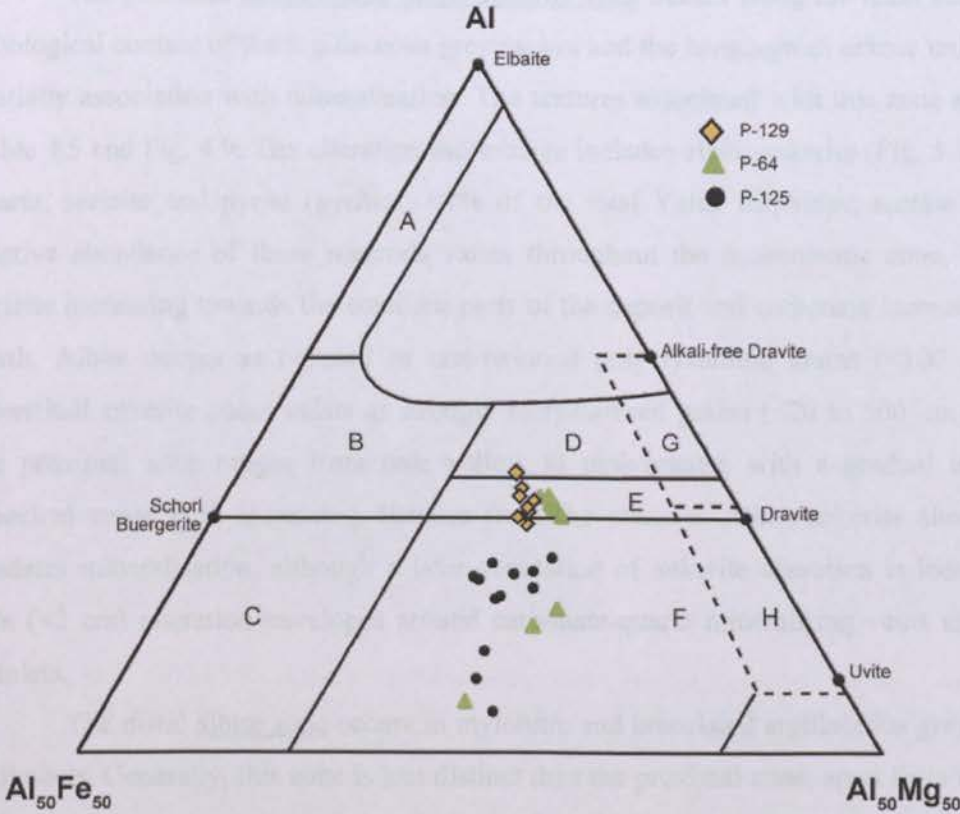
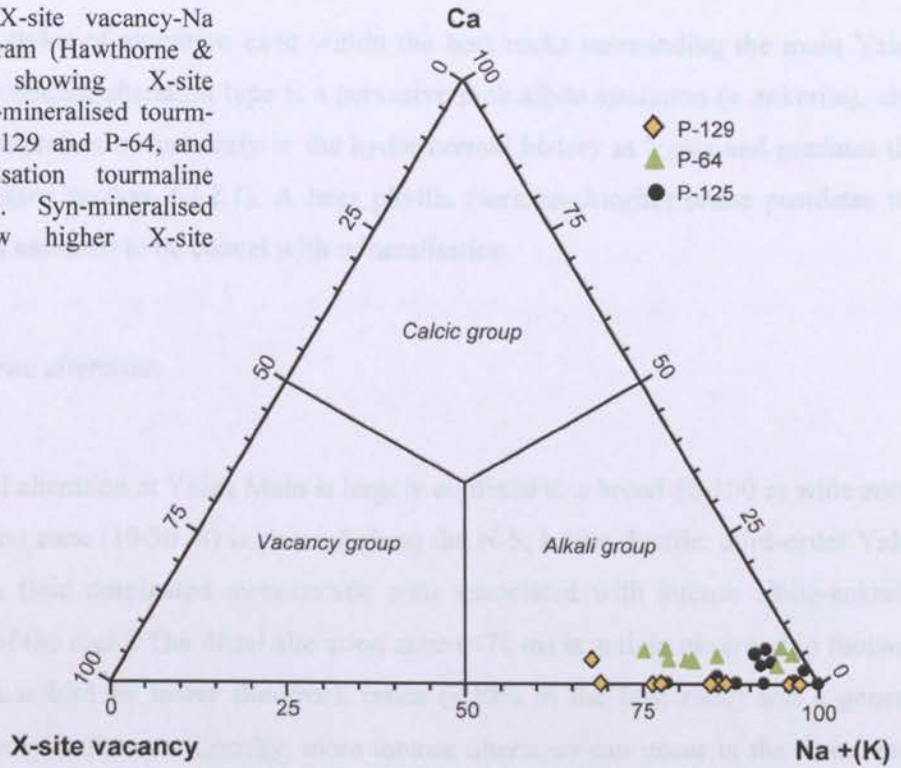


Fig. 5.9 B) Al-Fe-Mg ternary diagram (Henry & Guidotti, 1985) for P-64, P-129 and P-125 tourmalines. P-125 tourmalines plot into a separate cluster (more Fe-rich and Al-depleted). Field descriptions given in Fig. 5.5b.

5.3.2 *Yalea Main*

Two distinct styles of alteration exist within the host rocks surrounding the main Yalea orebody. The most dominant alteration type is a pervasive pink albite alteration (\pm ankerite), also seen at Gara. Sodic alteration occurs early in the hydrothermal history at Yalea and predates the mineralisation phase (*see section 4.3.2.1*). A later phyllic (sericite-chlorite) phase postdates the albite alteration and is assumed to be coeval with mineralisation.

5.3.2.1 *Sodic \pm ankerite alteration*

Yalea footwall

Hydrothermal alteration at Yalea Main is largely confined to a broad 50-100 m wide zone. The proximal alteration zone (10-30 m) is situated along the N-S, brittle-ductile, third-order Yalea shear. It represents a fluid dominated metasomatic zone associated with intense albite-ankerite alteration (80-100% of the rock). The distal alteration zone (<70 m) is mainly observed in footwall sediments, and characterised by lower fluid/rock ratios (<20% of the host rock) and a general decrease in hydrothermal carbonate. Locally, more intense alteration can occur in the distal zone along footwall splays (NNE-trending second-order structures).

The proximal metasomatic albite-ankerite zone occurs along the main shear between the lithological contact of the argillaceous greywackes and the hangingwall arkose units. Alteration is spatially associated with mineralisation. The textures associated with this zone are illustrated in Table 4.5 and Fig. 4.9. The alteration assemblage includes albite-ankerite (Fig. 5.11a), plus minor quartz, sericite and pyrite (pyrite-I; <1% of the total Yalea sulphides; *section 4.3.2.2.2*). The relative abundance of these minerals varies throughout the metasomatic zone, with albite and sericite increasing towards the southern parts of the deposit and carbonate increasing towards the north. Albite occurs as twinned or non-twinned polycrystalline grains (<100 μm), while the interstitial ankerite phase exists as strongly recrystallised grains (<20 to 500 μm). The colour of the proximal zone ranges from pale yellow to pink/orange, with a gradual increase in pink bleached zones with increasing distance from the orezone. Albite-ankerite alteration generally predates mineralisation, although a later generation of ankerite alteration is locally observed as thin (<2 cm) alteration envelopes around carbonate-quartz mineralising veins and sulphide-rich veinlets.

The distal albite zone occurs in mylonitic and brecciated argillaceous greywacke footwall sediments. Generally, this zone is less distinct than the proximal zone, apart from narrow (8-25 m) highly altered regions along footwall splays (Fig. 5.10). These latter zones are characterised by multiply deformed and altered hydrothermal-tectonic breccias. Breccias are composed primarily of pink albite-altered rock fragments and, less commonly, clasts of sedimentary wall-rock (Fig. 5.10b). Foliation development locally affects the breccias indicating that an early episode of ductile deformation postdates breccia formation and early sodic alteration. However, breccias are

also overprinted by a later pink albite alteration event implying brecciation, ductile shearing and alteration were broadly coeval and probably related (Allibone & Cameron, 2006). The alteration assemblage consists predominately of albite (Fig. 5.11b), with minor quantities of specular haematite (≤ 2 mm; often oxidised to goethite) + ankerite + quartz + minor tourmaline + pyrite (weakly mineralised; <1 g/t). The cause of the pink colouration in the proximal and distal zones is equivocal. The bleached zones may be result of fine-grained haematite, or in the absence of haematite, a change in Fe state ($\text{Fe}^{2+} \rightarrow \text{Fe}^{3+}$) of any Fe-bearing minerals during wall-rock interaction.



Fig. 5.10. Drill core photos of the pink distal albite alteration zone in footwall sediments at Yalea Main. **A)** Pervasive alteration of argillaceous greywacke sediments. Albite is accompanied by specular haematite (the uniformly distributed, fine-grained, black minerals) (YDH147, 86.5 m). **B)** Hydrothermal-tectonic breccias along footwall NNE splays. Clasts consist mainly of an early pink albitisation phase plus rarer reworked black tourmaline and unaltered argillaceous greywacke clasts. At the bottom of the image, a second phase of pink albite alteration overprints the breccias suggesting albitisation and brecciation was broadly coeval (YDH187, 371.3 m). These breccias are similar to the host sediments at Yalea North (Fig. 5.6), but with lower tourmaline concentrations.

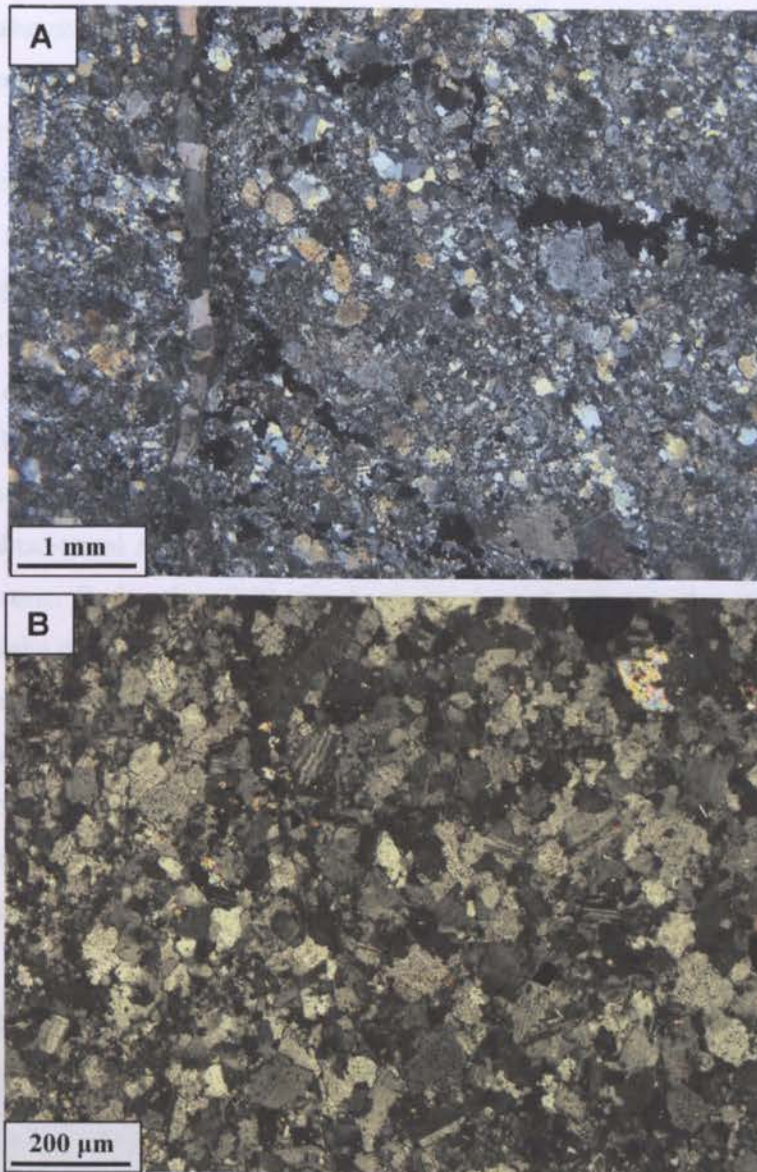


Fig. 5.11. Transmitted light images (XPL) of the albite \pm ankerite alteration zones at Yalea Main. **A)** Proximal metasomatic albite-ankerite zone along the main N-S Yalea mineralised shear. Untwinned albite and minor quartz occurs as aggregates within a finer grained ankerite cement (YDH132, 500.1 m). **B)** Distal albite zone along a NNW splay off the main N-S shear. Albite occurs as the dominant alteration material as twinned and untwined grains. Minor ankerite is observed in the top right of the image (YDH187, 265 m).

Yalea hangingwall

The Yalea hangingwall is less deformed and altered compared to the footwall. This can be explained by differences in rock compositions with hangingwall lithologies less reactive than argillaceous greywackes. The distal albite alteration zone is limited in extent (<20 m) and mainly affects arkose sediments and carbonates. Alteration is subtle and less distinct than footwall alteration, and varies in intensity (one of the reasons for the variable chemical compositions of the arkose units- see section 3.3.4). In the southern parts of the Yalea shear, the hangingwall carbonate unit has undergone localised red silication. Dolomite has transformed to a mineral assemblage consisting of albite-quartz-ankerite-haematite. Similar to the footwall, more intense albite alteration occurs along hangingwall splays, but no brecciation is observed.

5.3.2.2 Phyllic alteration

The second type of alteration surrounding the main Yalea orezone consists of a sericite-chlorite \pm minor ankerite-quartz assemblage. A similar alteration assemblage occurs at other Yalea-style orebodies, but is general absent from Gara-style deposits. Phyllic alteration at Yalea Main occurs in narrow (<5 cm) ductile shears, sub-parallel to main shear direction, in both footwall and hangingwall clastic sediments in close proximity to the orezone (Fig. 5.12a). These ductile shears are more commonly observed towards the northern parts of the deposit (also seen at P-125). Phyllic alteration also occurs as patchy yellow alteration in hangingwall carbonate sediments towards the south, as thin green-black alteration envelopes (<5 cm) around auriferous veins/veinlets, and as gangue material in quartz-ankerite veins, mainly situated along vein walls (Fig. 5.12b). Hydrothermal alteration progresses from chloritisation to sericitisation approaching the mineralised zone. Both mineral phases occur as weakly foliated, fine-grained (<150 μm) crystals, with sericite often pseudomorphously replaced by chlorite. Locally, chlorite can occur as massive radial grains. Phyllic alteration clearly postdates the pink albite \pm ankerite alteration phase (Fig. 5.12). Allibone & Cameron (2006) proposed that this alteration event was broadly coeval with the ductile/brittle shears that host the mineralisation. In fact, phyllic phases form a common component of mineralising veins in other Loulo orebodies (e.g. Faraba and Loulo-3; see chapter 4) reinforcing their link to mineralisation in the Loulo district.



Fig. 5.12. Drill core photos of phyllic alteration at Yalea Main. **A)** Green sericite-chlorite shears overprinting pink albite altered rock in proximity to the orezone (YDH132, 534 m). **B)** Chlorite-carbonate-quartz veins cross cutting albite-altered rock. (YDH187, 350 m).

Chlorite chemistry at Yalea Main-P125

Because chlorite acts as a useful geothermometer in epigenetic ore deposits (*section 5.5.4*), the composition of the Loulo chlorites is described below. According to the classification of Hey (1954), hydrothermal chlorites at Yalea Main and P-125 contain brunsvigite, pycnochlorite and ripidolite compositions (Fig. 5.13a). The variation in chemistry reflects the changing Fe/(Fe+Mg) cation ratios (0.41 to 0.70) within individual crystals (diffusive zonation patterns). In terms of chemistry, the Yalea Main and P-125 chlorites are clearly distinguished from metamorphic chlorites from surrounding sedimentary and intrusive wall-rock. Metamorphic chlorites contain notably lower Fe/(Fe+Mg) ratios of 0.24-0.28 signifying the high Fe content of the mineralised fluids. Metamorphic and hydrothermal chlorite chemistries from a variety of deposits are given in Table 5.4. For reference, the general formula for chlorite is:

*Chlorite chemistry at Loulo-3 and Faraba*

Chlorites chemistries from other Yalea-style orebodies or Faraba-style deposits showing Yalea-style affinities are plotted in Fig. 5.13. Loulo-3 share similar chlorite compositions to Yalea-P-125. However, Faraba chlorites are notably more Si-rich and Al-depleted compared to chlorite alteration zones to the north, classifying as diabantites (Fig. 5.13a). These minerals also show higher and more uniform Fe/(Fe+Mg) ratios between 0.70-0.74 (Fig. 5.13b). In polarised light, Faraba chlorites show low relief and stronger pleochroism compared to the brunsvigites and pycnochlorites from Yalea Main, P-125 and Loulo-3. The contrast in chlorite composition between Faraba and other deposits reflects the variation in precipitation conditions (*see section 5.5.4*).

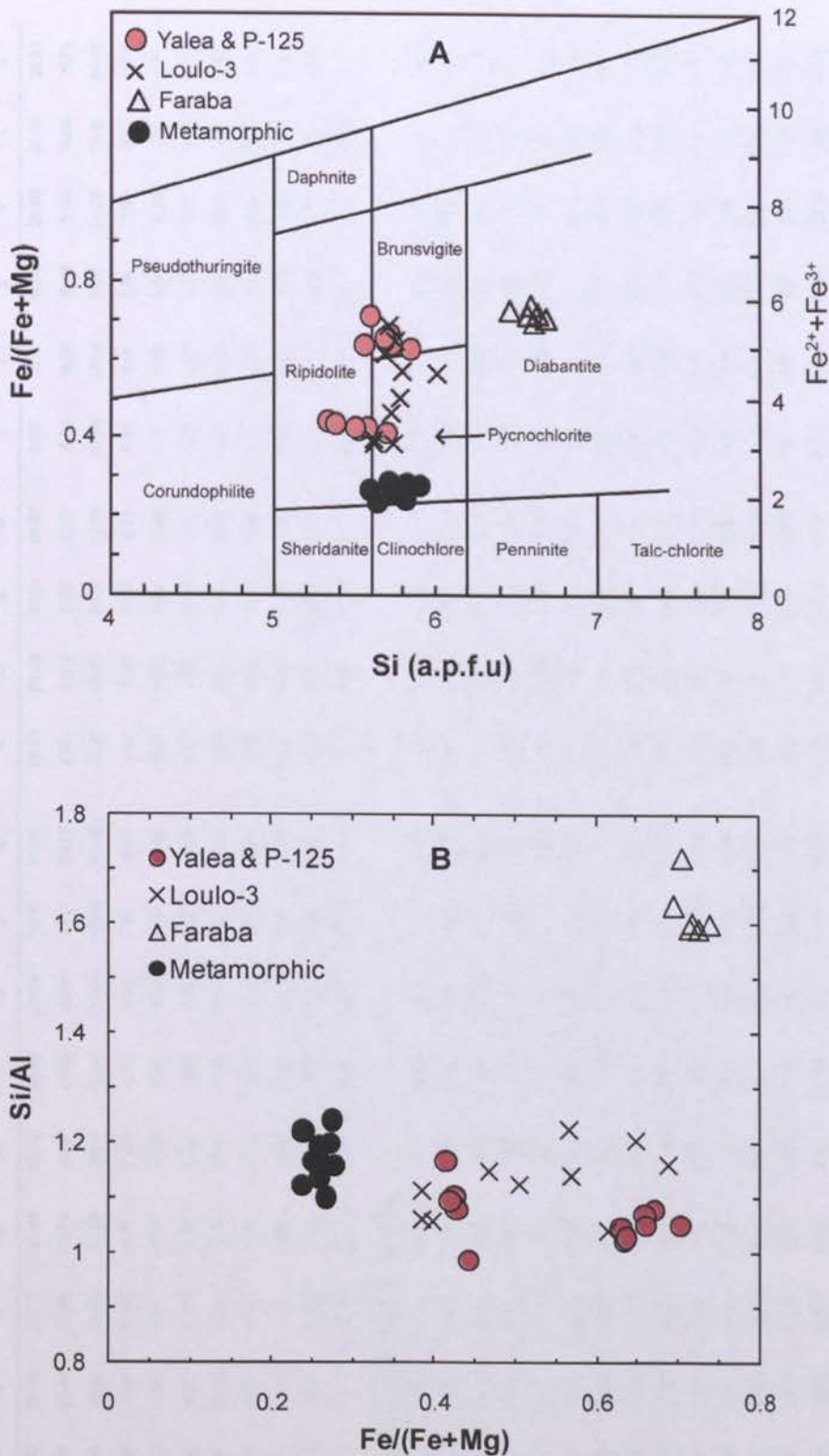


Fig. 5.13. Binary plots showing the compositions of the hydrothermal and metamorphic chlorites at Loulo. **A)** Fe/(Fe+Mg) vs. Si cation plot using the nomenclature of Hey (1954). **B)** Si/Al vs. Fe/(Fe+Mg) plot. Hydrothermal chlorites from Yalea-style deposits (Yalea, P125 & Loulo-3) show near constant Si/Al ratios but with variable Fe/(Fe+Mg) ratios. Metamorphic chlorites show similar Si/Al values but lower and more uniform Fe/(Fe+Mg) ratios. Hydrothermal chlorite from Faraba show higher Si/Al ratios and Fe contents compared to chlorites to the north.

Table 5.4. Chemical composition of hydrothermal and metamorphic chlorites at Loulo by SEM-EDS analysis.

	P-125										Faraba									
	1	2	3	4	5	6	7	8	9	10	11	12	13	14	1	2	3	4	5	6
SiO ₂	26.26	26.97	28.96	26.73	27.41	27.52	27.29	27.34	26.13	28.32	26.63	27.38	27.61	26.97	31.87	31.33	31.04	30.90	30.39	29.51
Al ₂ O ₃	22.60	21.23	23.49	22.96	22.70	21.17	21.59	21.39	21.0	20.57	21.95	21.53	21.37	21.79	15.69	16.24	16.41	16.43	16.09	15.71
FeO	23.99	32.88	30.08	24.00	30.22	23.51	32.01	23.60	33.63	23.02	31.12	23.43	23.18	32.05	34.70	33.39	33.17	34.20	34.13	34.95
MgO	16.91	9.02	9.90	16.92	9.75	17.84	9.26	17.82	7.95	18.23	9.92	17.57	17.97	9.21	8.05	8.14	7.25	7.59	6.67	7.34
CaO	0.00	0.49	0.00	0.00	0.00	0.00	0.00	0.00	0.00	0.00	0.00	0.00	0.00	0.00	0.73	0.79	0.84	0.70	1.02	0.71
Na ₂ O	0.00	0.00	0.00	0.00	0.00	0.00	0.00	0.00	0.00	0.00	0.37	0.00	0.00	0.00	0.00	0.00	0.00	0.00	0.00	0.00
K ₂ O	0.00	0.00	0.30	0.00	0.00	0.00	0.17	0.00	0.00	0.00	0.00	0.00	0.00	0.00	0.00	0.00	0.00	0.00	0.19	0.00
V ₂ O ₅	0.00	0.00	0.00	0.00	0.00	0.00	0.35	0.00	0.00	0.00	0.00	0.00	0.00	0.00	0.51	1.11	1.21	0.38	0.39	0.51
Cr ₂ O ₃	0.00	0.38	0.00	0.00	0.47	0.52	0.00	0.67	0.44	0.00	0.37	0.28	0.25	0.38	0.00	0.00	0.00	0.00	0.00	0.00
Co ₂ O ₃	0.10	0.25	0.00	0.00	0.21	0.00	0.00	0.16	0.33	0.00	0.00	0.00	0.00	0.00	0.00	0.00	0.00	0.00	0.00	0.00
Total	89.86	91.23	92.74	90.60	90.76	90.56	90.66	90.97	89.59	90.14	90.37	90.21	90.38	90.40	91.54	91.01	89.91	90.20	88.90	88.73
Structural formula on the basis of 28 oxygens																				
Si	5.34	5.67	5.81	5.37	5.68	5.55	5.72	5.50	5.63	5.69	5.59	5.53	5.55	5.67	6.68	6.61	6.63	6.57	6.59	6.46
Al ^(IV)	2.66	2.33	2.19	2.63	2.32	2.45	2.28	2.50	2.37	2.31	2.41	2.47	2.45	2.33	1.32	1.39	1.37	1.43	1.41	1.54
Al ^(VI)	2.75	2.93	3.36	2.81	3.23	2.57	3.05	2.58	3.00	2.55	3.02	2.65	2.61	3.07	2.56	2.65	2.77	2.69	2.70	2.51
Fe	4.08	5.78	5.05	4.03	5.24	3.96	5.61	3.97	6.07	3.87	5.46	3.95	3.90	5.64	6.09	5.89	5.93	6.08	6.19	6.40
Mg	5.12	2.83	2.96	5.07	3.01	5.36	2.90	5.35	2.56	5.46	3.11	5.29	5.39	2.89	2.52	2.56	2.31	2.41	2.16	2.39
Ca	0.00	0.11	0.00	0.00	0.00	0.00	0.00	0.00	0.00	0.00	0.00	0.00	0.00	0.00	0.16	0.18	0.19	0.16	0.24	0.17
Na	0.00	0.00	0.00	0.00	0.00	0.00	0.00	0.00	0.00	0.00	0.08	0.00	0.00	0.00	0.00	0.00	0.00	0.00	0.00	0.00
K	0.00	0.00	0.04	0.00	0.00	0.00	0.02	0.00	0.00	0.00	0.00	0.00	0.00	0.00	0.00	0.00	0.00	0.00	0.03	0.00
V	0.00	0.00	0.00	0.00	0.00	0.00	0.03	0.00	0.00	0.00	0.00	0.00	0.00	0.00	0.04	0.09	0.10	0.03	0.03	0.04
Cr	0.00	0.03	0.00	0.00	0.04	0.04	0.00	0.05	0.04	0.00	0.03	0.02	0.02	0.03	0.00	0.00	0.00	0.00	0.00	0.00
Co	0.01	0.02	0.00	0.00	0.02	0.00	0.00	0.01	0.03	0.00	0.00	0.00	0.00	0.00	0.00	0.00	0.00	0.00	0.00	0.00
Total	19.96	19.70	19.41	19.91	19.54	19.94	19.61	19.96	19.68	19.88	19.70	19.91	19.92	19.63	19.38	19.37	19.30	19.37	19.35	19.52
Al ^(IV) _c	2.97	2.80	2.63	2.94	2.76	2.75	2.74	2.80	2.86	2.60	2.86	2.77	2.74	2.79	1.81	1.88	1.87	1.93	1.93	2.05
T (°C) ^a	333.2	314.8	296.9	329.7	310.6	309.7	308.6	314.3	320.9	294.1	320.8	312.0	308.8	314.0	209.9	217.2	216.3	222.7	222.4	235.4
Fe/(Fe + Mg)	0.44	0.67	0.63	0.44	0.63	0.42	0.66	0.43	0.70	0.41	0.64	0.43	0.42	0.66	0.71	0.70	0.72	0.72	0.74	0.73

Note: Al^(IV)_c = Al in tetrahedral sites according to Krantidiotis & Maclean (1987); T (°C)^a = temperature estimates calculated from Cathelineau (1988).

Table 5.4. cont. Chemical composition of hydrothermal and metamorphic chlorites at Loulo by SEM-EDS analysis.

	Loulo-3										Metamorphic chlorite from intrusive & sedimentary w all-rocks									
	1	2	3	4	5	6	7	8	9	10	1	2	3	4	5	6	7	8	9	10
SiO ₂	27.62	26.16	28.19	27.97	28.53	27.77	29.70	27.68	26.51	27.82	29.52	30.85	29.60	29.76	29.66	29.85	28.90	28.86	29.61	30.21
Al ₂ O ₃	19.47	19.15	21.29	20.64	21.77	22.25	20.54	22.14	21.59	20.68	21.59	21.85	21.05	20.67	21.57	21.81	21.56	21.78	22.83	20.65
FeO	34.84	34.60	25.62	24.75	20.17	20.64	28.90	20.01	28.87	28.62	15.79	15.49	15.35	13.80	14.82	15.86	15.07	13.83	14.65	15.99
MgO	10.54	8.80	14.06	15.84	17.96	17.43	12.40	17.87	10.19	12.18	22.99	23.29	24.75	24.64	24.91	25.03	24.17	24.83	22.46	23.62
CaO	0.00	0.00	0.00	0.00	0.00	0.00	0.00	0.00	0.00	0.00	0.00	0.00	0.00	0.00	0.00	0.00	0.15	0.00	0.00	0.00
K ₂ O	0.00	0.00	0.00	0.00	0.00	0.17	0.00	0.09	0.00	0.05	0.85	0.00	0.00	0.00	0.13	0.13	0.47	0.00	0.74	0.00
Total	92.46	88.70	89.17	89.20	88.43	88.27	91.54	87.79	87.16	89.35	90.74	91.48	90.75	88.87	91.10	92.69	90.33	89.30	90.28	90.47
Structural formula on the basis of 28 oxygens																				
Si	5.75	5.71	5.79	5.73	5.74	5.62	6.01	5.62	5.69	5.80	5.69	5.84	5.67	5.77	5.65	5.61	5.58	5.58	5.69	5.81
Al ^(IV)	2.25	2.29	2.21	2.27	2.26	2.38	1.99	2.38	2.31	2.20	2.31	2.16	2.33	2.23	2.35	2.39	2.42	2.42	2.31	2.19
Al ^(VI)	2.53	2.64	2.94	2.71	2.90	2.94	2.91	2.92	3.15	2.88	2.60	2.71	2.42	2.50	2.49	2.45	2.49	2.54	2.85	2.50
Fe	6.07	6.32	4.40	4.24	3.39	3.50	4.89	3.40	5.18	4.99	2.55	2.45	2.46	2.24	2.36	2.49	2.43	2.24	2.35	2.57
Mg	3.27	2.86	4.30	4.83	5.39	5.26	3.74	5.41	3.26	3.79	6.61	6.57	7.07	7.13	7.07	7.02	6.96	7.16	6.43	6.78
CaO	0.00	0.00	0.00	0.00	0.00	0.00	0.00	0.00	0.00	0.00	0.00	0.00	0.00	0.00	0.00	0.00	0.03	0.00	0.00	0.00
K	0.00	0.00	0.00	0.00	0.00	0.02	0.00	0.01	0.00	0.01	0.10	0.00	0.00	0.00	0.02	0.02	0.06	0.00	0.09	0.00
Total	19.86	19.82	19.64	19.78	19.68	19.72	19.54	19.73	19.58	19.66	19.86	19.73	19.95	19.87	19.93	19.97	19.97	19.94	19.73	19.85
Al ^(IV) _c	2.71	2.77	2.57	2.60	2.53	2.66	2.39	2.85	2.74	2.60	2.50	2.35	2.51	2.40	2.53	2.57	2.60	2.59	2.50	2.38
T (°C) ^a	304.8	311.6	290.2	293.6	286.4	299.5	271.0	299.2	308.9	293.7	283.4	267.5	284.1	271.9	286.1	290.6	293.9	292.2	283.1	270.4
Fe/(Fe + Mg)	0.65	0.69	0.51	0.47	0.39	0.40	0.57	0.39	0.61	0.57	0.28	0.27	0.26	0.24	0.25	0.26	0.26	0.24	0.27	0.28

Note- Al^(IV)_c = Al in tetrahedral sites according to Krantidiotis & MacClean (1987); T (°C)^a = temperature estimates calculated from Cathelineau (1988).

5.3.3 Other types of alteration in the Loulo district

Silica alteration at Baboto

Quartz is mainly confined to veins and forms only a minor component of the alteration assemblages described above. However, in the northern parts of the permit, polycrystalline silicic alteration becomes the dominant alteration type (Fig. 5.14). Silica alteration forms under high fluid/rock conditions around the Baboto orebody, with an alteration zone increasing from south (average 15 m) to north (average 65 m). Ankerite is also present but mainly occurs in more proximal zones as narrow ankerite selvages (<5 mm) surrounding sulphide veinlets and stringers. Other minerals in the assemblage include minor albite and tourmaline (the latter occurs as reworked material unrelated to mineralisation). The high silica concentration in the alteration zones is consistent with the increase in quartz contents of the mineralised veins (decrease in carbonate) in the most northerly deposits along the Yalea-trend (e.g. Loulo-3 and Baboto).

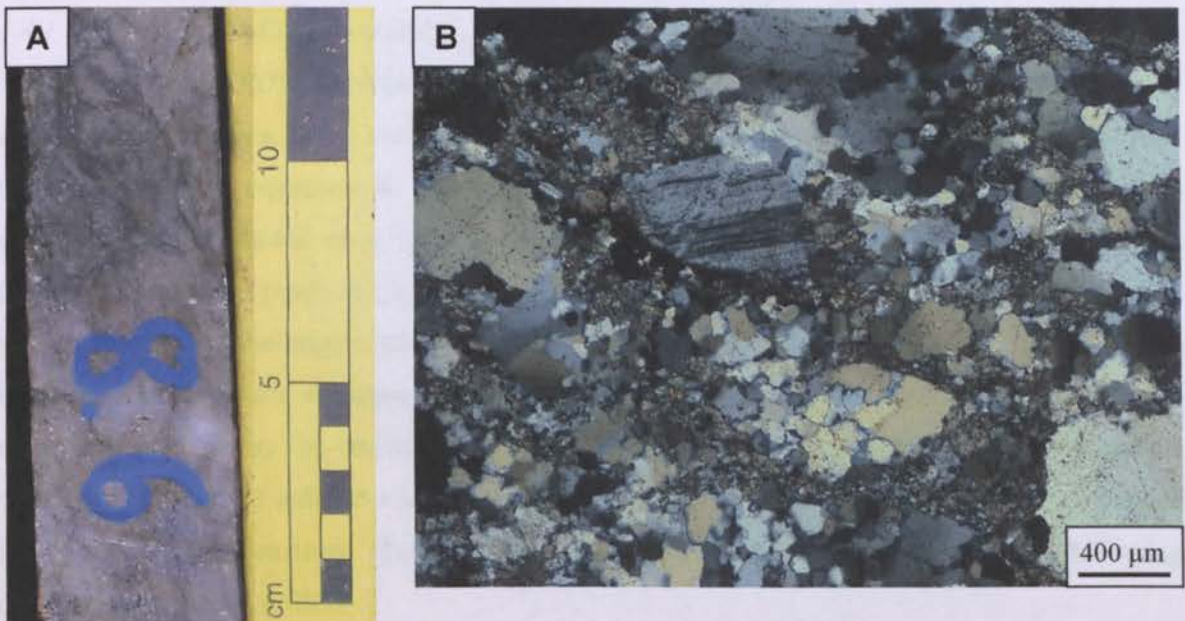


Fig. 5.14. Silica alteration at Baboto. **A)** A Drill core photo of the silica alteration surrounding the orezone (BADH20, 314.5 m). **B)** An XPL image of A) showing the appearance of polycrystalline quartz which makes up a large proportion of the altered rock, as well as minor coarser albite (twinned grain just above centre) and interstitial carbonate.

Magnetite replacement

A late magnetite alteration phase is a characteristic feature of the P-125, Faraba, P-64 and Goukoto deposits. Magnetite is a common replacement phase observed in the orezones, altering numerous sulphide phases (mainly pyrite and arsenopyrite). Due to their close association with mineralisation, this type of alteration is discussed in more detail in *chapter 4*. Magnetite is commonly associated with supergene minerals such as haematite, goethite and limonite. It represents a late, post-mineralisation, oxidised fluid phase that largely affected the southern parts of the Loulo district (excluding P-125).

5.4 Alteration geochemistry

The distinct mineral assemblages described in *section 5.3* form from the interaction of the hydrothermal fluids with the surrounding host rocks, and are accompanied by changes in bulk-rock chemistries. A geochemical analysis of the alteration zones at Gara and Yalea Main was carried out using ICP-AES and ICP-MS at Kingston University (geochemical data presented in appendices in Table A-5). The aim of the study was two-fold: (1) to determine the metasomatic behaviour of particular elements during the alteration process; and (2) to distinguish the alteration profiles around the orezones. The first objective is achieved by comparing the composition of unaltered or least-altered rocks with altered rocks of the same original lithology, using methods developed by Gresen (1967) and Grant (1986) (discussed below). To determine geochemical alteration profiles around the Yalea and Gara deposits, altered rocks were systematically sampled approximately every 10 m across a 300 m transverse from hangingwall into footwall sediments.

5.4.1 Isocon method of Grant (1986)

Gresens (1967) developed a method that utilised specific gravity data to determine compositional changes during alteration. To avoid calculating specific gravity data, Grant (1986) modified Gresens' equations to provide a graphical solution for determining compositional changes. Plotting altered rock (y-axis) against least-altered equivalents (x-axis), isochemical (conserved) elements (such as Al, Ti, Zr and Y; Rollinson, 1993) should plot along a straight line that passes through the origin, referred to as the isocon (Grant, 1986). The isocon diagram can be used to calculate the net volume-mass changes during alteration, as well as relative mass changes of particular elements. The isocon slope determines the mass changes involved. Isocon diagrams with a gradient (m) > 1 indicate a net loss in overall mass, $m < 1$ a net mass gain, and $m = 1$ implies isovolumetric metasomatism. The net mass change (ΔM^A) can be measured using the following calculation of Huston (1993):

$$\Delta M^A (\%) = 100[(1/m)-1] \quad (\text{Eq. 5.4})$$

Elements plotting away from the isocon exhibit mobile behaviour during alteration, with elements plotting below and above the isocon showing mass losses and mass gains, respectively. Elemental mass changes (ΔC_i^A) can be calculated using the following formula from Grant (1986):

$$\Delta C_i^A (\%) = 100[C_i^A/(mC_i^O)-1] \quad (\text{Eq. 5.5})$$

where m is the isocon slope, C_i^A is any oxide concentration in an altered sample, and C_i^O is any oxide concentration in the least-altered sample.

5.4.2 Mass transfers during alteration

Due to limited amount of material collected from the phyllic alteration zones, only the tourmaline and sodic alteration is analysed in the following sections.

5.4.2.1 Tourmalinisation

In the absence of an unaltered precursor, the most weakly-altered (5-30% tourmaline) quartz-wacke rocks ($n = 3$) are used as a proxy and plotted against the tourmalinite (>30% tourmaline) rocks ($n = 3$) to determine minimum mass changes. The isocon is defined by taking an average of the altered/least-altered ratio of each immobile element, which all plot close to an ideal isocon (i.e. a straight line). Tourmalinisation at Gara is associated with a minimum net mass loss of 12% (Fig. 5.15a). This mass loss implies the alteration process created porosity within the quartz-wacke probably through dissolving and removing of major components, such as Si, to precipitate the tourmaline.

Element mass changes are shown in Fig. 5.15b. As well as B addition (not measured), the alteration is characterised by mass gains in MgO (51%), Fe₂O₃ (24%) and NaO₂ (25%). Mass gains in Fe would be more significant in other tourmaline alteration zones at Loulo (e.g. Yalea North- more Fe-rich tourmalines). These rocks shows notable mass gains in CaO and although present in minor concentrations (~0.02 wt.%) significant increases in MnO (217%), which implies Mn-bearing carbonate (rhodochrosite) occurs as an accessory phase (not observed during petrographic studies). The alteration process involves mass losses in K₂O (62%) and SiO₂ (21%) indicating that tourmaline forms at the expense of an initial phyllic phase (as observed in other rock types). These significant mass changes in element chemistry suggest high fluid/rock conditions.

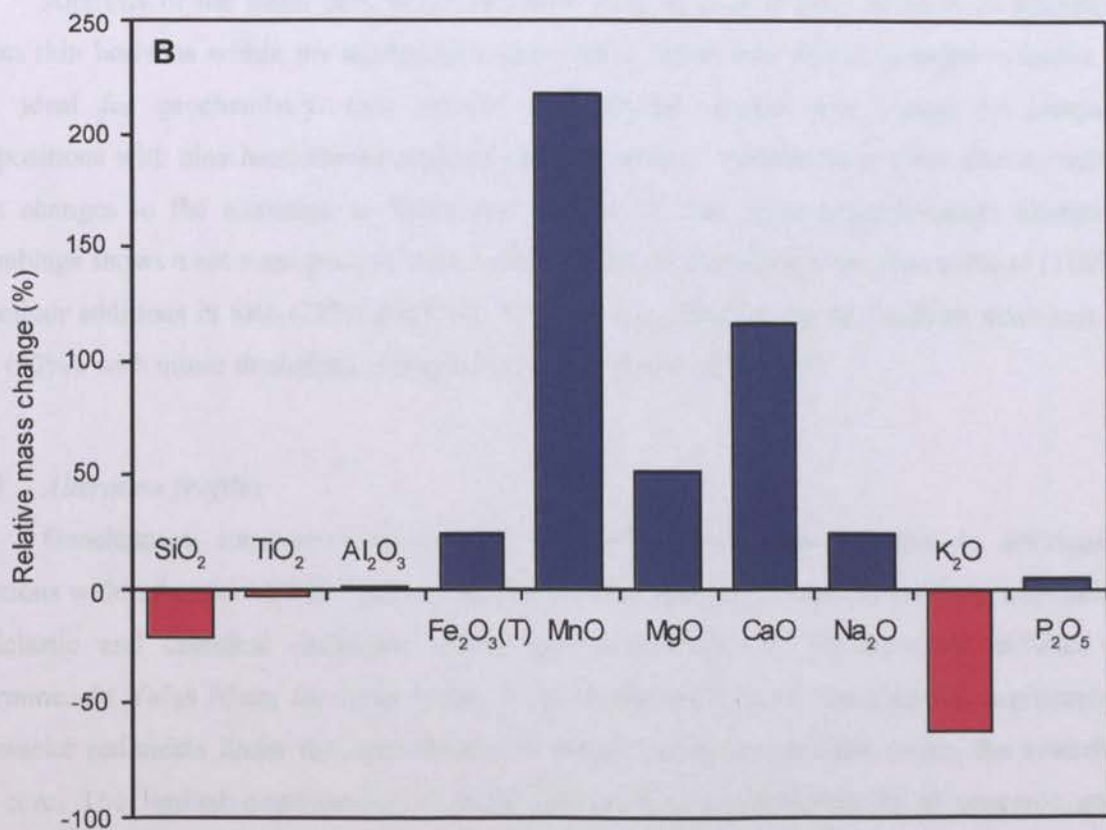
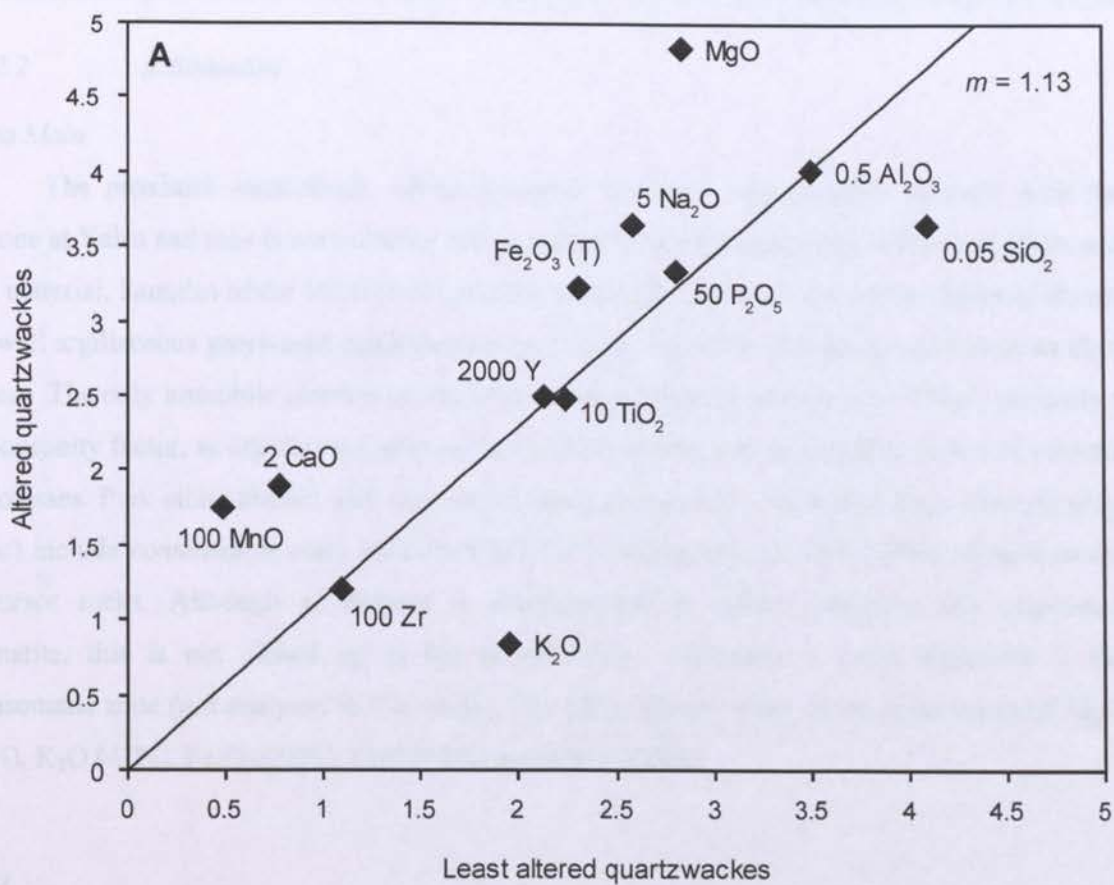


Fig. 5.15. A) Isocon diagram, after Grant (1986), showing mass changes involved during tourmalinisation at Gara. The most altered tourmalinite samples ($n = 3$) are plotted against the least-altered quartz-wacke samples ($n = 3$). B) Elemental mass changes involved during tourmaline alteration (blue = mass gain; red = mass loss).

5.4.2.2 Albitisation

Yalea Main

The proximal metasomatic albite-carbonate alteration zone broadly overlaps with the orezone at Yalea and thus is not included in this section to avoid contamination from sulphides and vein material. Samples of the footwall distal albite alteration zone are compared to the least-altered footwall argillaceous greywacke equivalents (Fig. 5.16a). Immobile elements plot close to an ideal isocon. The only immobile element to plot away from the regression line is Al. This is probably a homogeneity factor, as argillaceous greywackes contain arenaceous and argillite layers of variable thicknesses. Pink albite altered rock show a net mass gain of 10%. Elemental mass changes (Fig. 5.16c) include considerable mass gains in Na₂O (147%) and, less so, SiO₂ (38%), relative to the precursor rocks. Although albitisation is accompanied by minor carbonate and occasional haematite, this is not picked up in the geochemistry. Carbonate is more dominant in the metasomatic zone (not analysed in this study). The albite altered rocks shows mass losses of MgO (45%), K₂O (42%), Fe₂O₃ (38%), CaO (33%) and MnO (23%).

Gara

Analysis of the distal pink albite alteration zone at Gara is more difficult as alteration targets thin horizons within the argillaceous greywackes rather than affecting larger volumes of rock ideal for geochemistry. One thicker albite-altered sample was chosen to compare compositions with nine least-altered argillaceous greywackes. Albitisation at Gara shows similar mass changes to the alteration at Yalea (Fig. 5.16b, d). The albite-ankerite-quartz alteration assemblage shows a net mass gain of 13%, with a prominent elemental mass gain in Na₂O (116%) and minor additions in SiO₂ (20%) and CaO (11%). Sodic alteration shows a distinct mass loss of K₂O (47%), with minor depletions in MgO, Fe₂O₃ and MnO (<25% each).

5.4.3 Alteration profiles

Geochemical transverse across both Gara and Yalea Main deposits, to distinguish zonations within the altered rocks, proved ineffective for a number of reasons. At Gara, alternating siliciclastic and chemical sediments makes spatial variations in geochemistry difficult to determine. At Yalea Main, the large extent of albite alteration in the hangingwall argillaceous greywacke sediments limits the identification of distinct alteration profiles within the available drill-core. The limited development of metal zoning is a common feature of orogenic gold deposits, where ore fluids form close to the ambient metamorphic P-T conditions (Goldfarb *et al.*, 1986; Clark *et al.*, 1989).

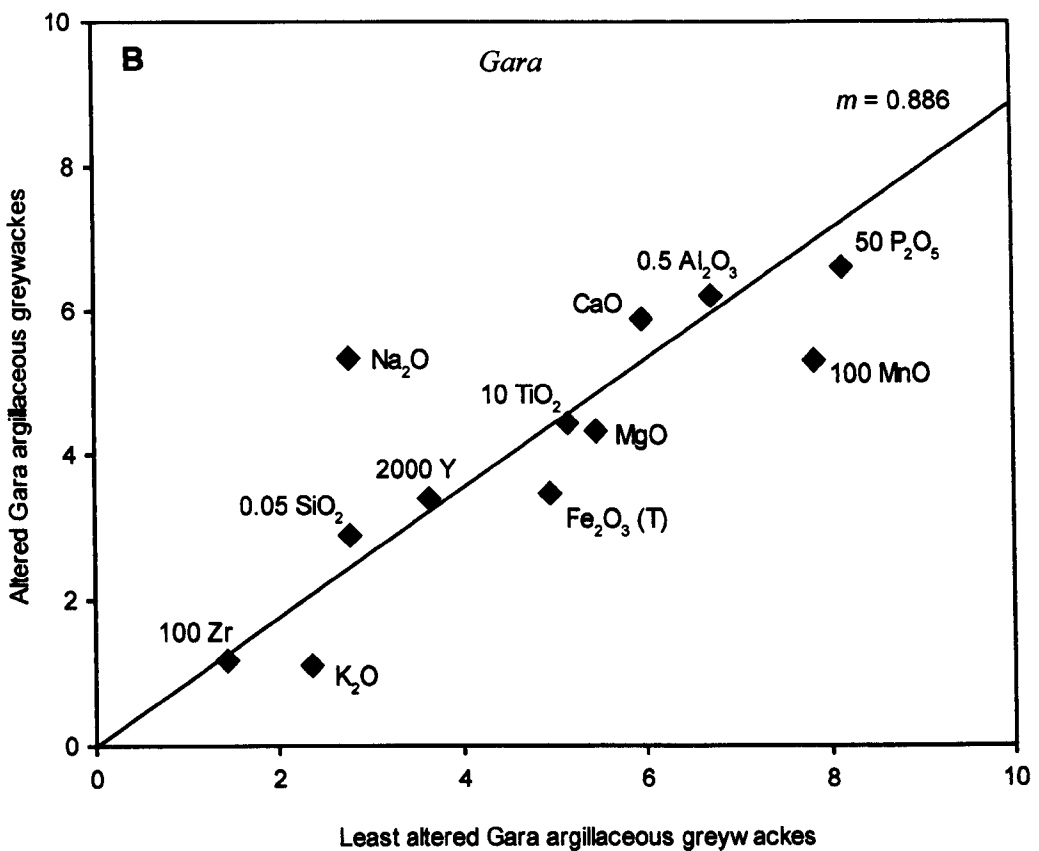
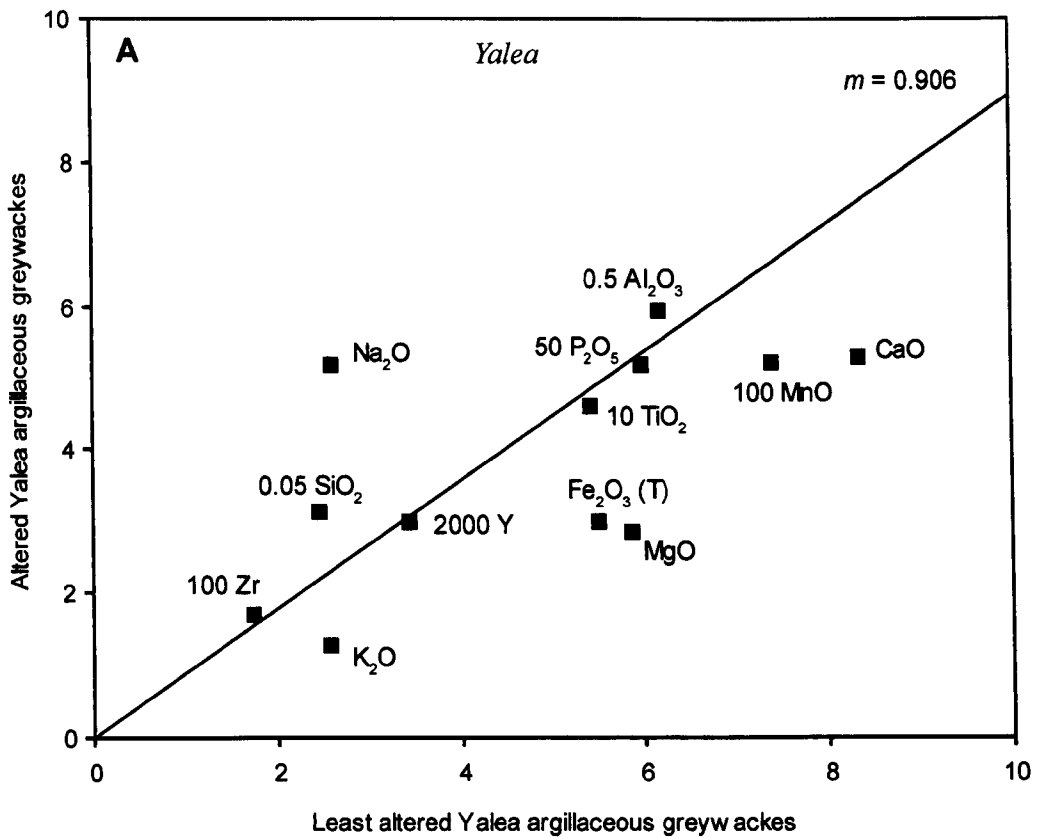


Fig. 5.16. Isocon diagrams, after Grant (1986), showing mass changes involved during albite alteration of argillaceous greywacke units. Average values of major oxides (wt.%) are given. **A)** Yalea albitised footwall rock ($n = 5$) plotted against unaltered footwall sediments ($n = 4$). **B)** Gara albitised sediments ($n = 1$) plotted against unaltered sediments ($n = 9$).

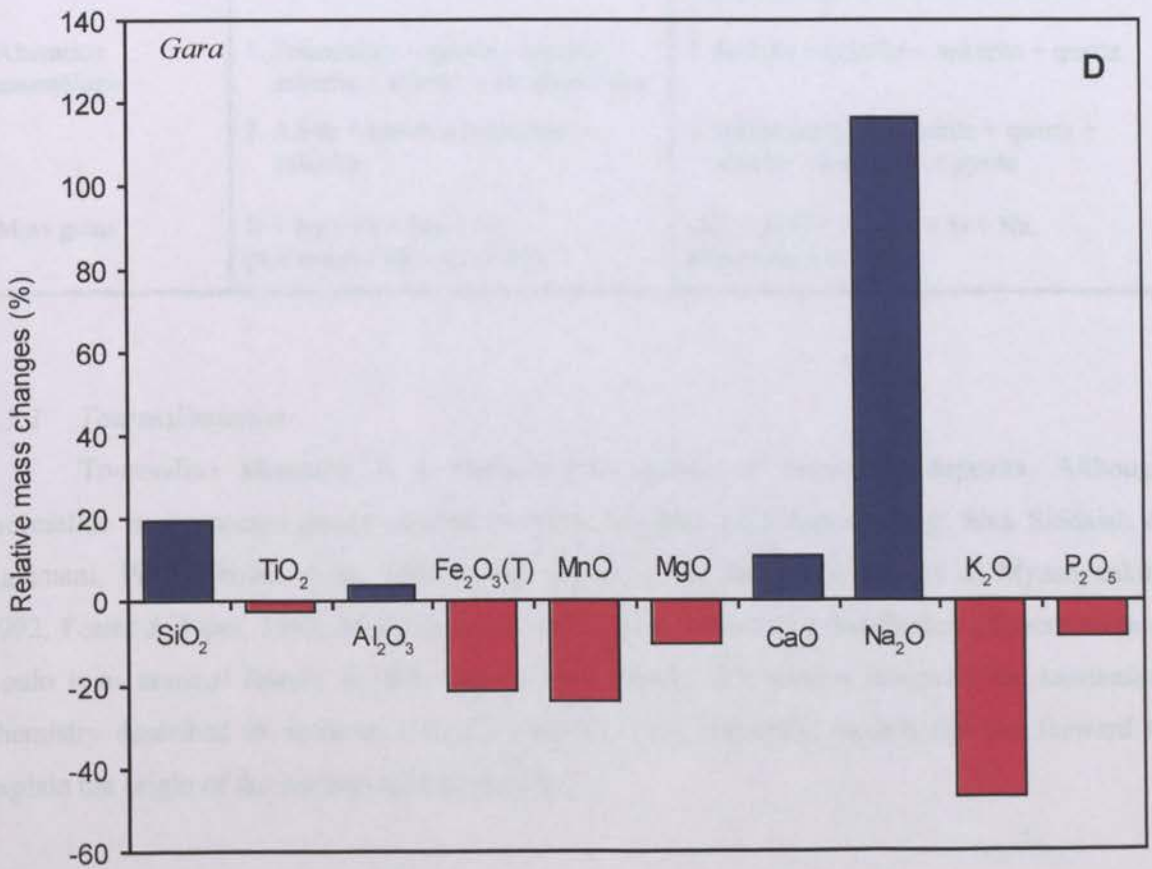
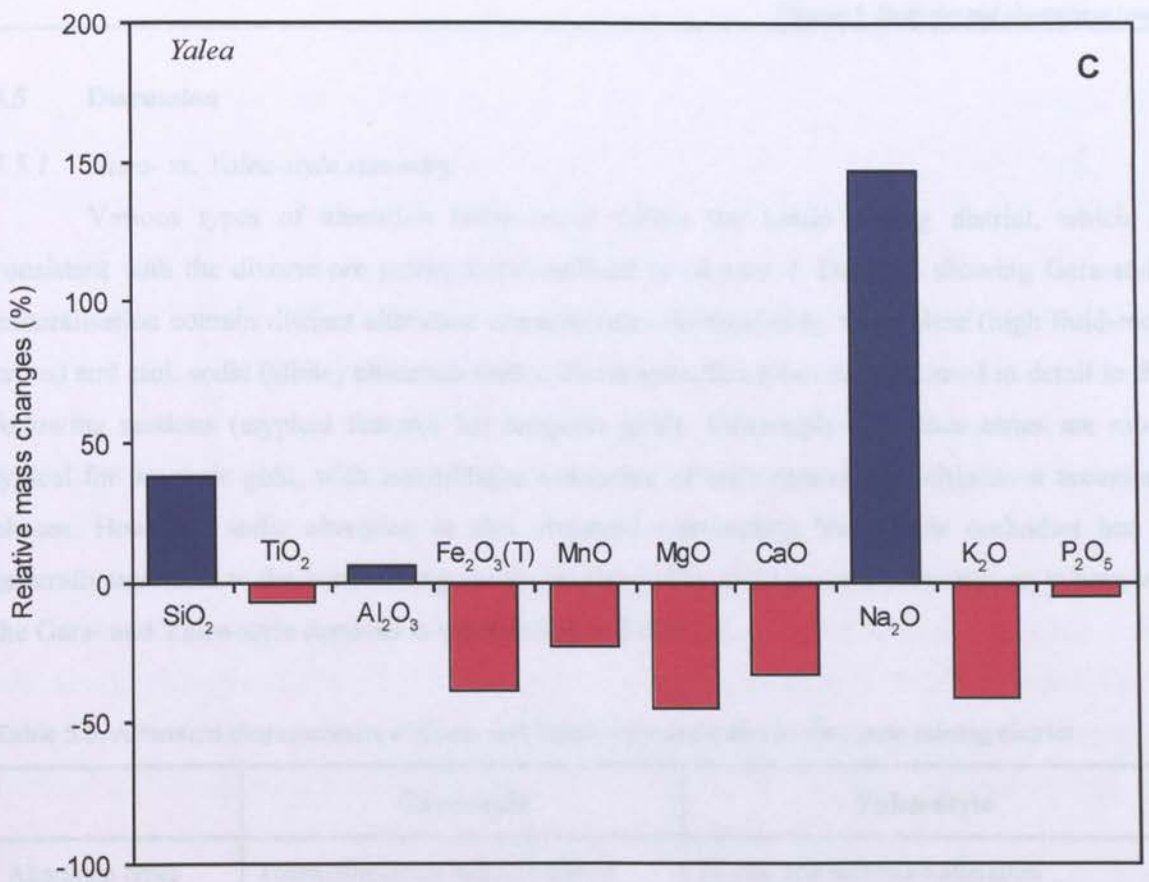


Fig. 5.16. cont. C) to D) Elemental mass changes involved during albitisation at Gara and Yalea. Mass changes calculated from isocon diagrams on previous page (blue = mass gain; red = mass loss).

5.5 Discussion

5.5.1 Gara- vs. Yalea-style summary

Various types of alteration halos occur within the Loulo mining district, which is consistent with the diverse ore petrogenesis outlined in *chapter 4*. Deposits showing Gara-style mineralisation contain distinct alteration characteristics dominated by tourmaline (high fluid-rock ratios) and pink sodic (albite) alteration zones. These alteration types are discussed in detail in the following sections (atypical features for orogenic gold). Yalea-style alteration zones are more typical for orogenic gold, with assemblages consisting of carbonate-sericite-chlorite \pm accessory phases. However, sodic alteration is also observed surrounding Yalea-style orebodies but is generally unrelated to the mineralising event (predates). The differences in alteration style between the Gara- and Yalea-style deposits is summarised in Table 5.5.

Table 5.5. Alteration characteristics of Gara- and Yalea-style orebodies in the Loulo mining district.

	Gara-style	Yalea-style
Alteration types	Tourmalinisation and albitisation	Phyllic and carbonate alteration Albitisation (predates mineralisation)
Alteration assemblages	1. Tourmaline + quartz + biotite + ankerite + siderite + rhodochrosite 2. Albite + quartz \pm haematite \pm ankerite	1. Sericite + chlorite + ankerite + quartz 2. Albite (early) + ankerite + quartz + sericite \pm haematite \pm pyrite
Mass gains	B + Na + Fe + Mg + Si, plus minor CO ₂ + Ca + Mn	CO ₂ + H ₂ O + K + Ca + Si + Na, plus minor Fe + Mg

5.5.2 Tourmalinisation

Tourmaline alteration is a characteristic feature of Gara-style deposits. Although tourmaline is a common gauge mineral in many orogenic gold deposits (e.g. Siva Siddaiah & Rajamani, 1989; Groves *et al.*, 1989, 1992; Jébrak *et al.*, 1990; Chernyshov & Myasnyankin, 1992; Foster & Piper, 1993; McCuaig *et al.*, 1993), the volume and distribution of tourmaline at Loulo is an unusual feature for this deposit type. Firstly, this section interprets the tourmaline chemistry described in *sections 5.3.1.2.2 and 5.3.1.2.3*. Secondly, models are put forward to explain the origin of the widespread tourmaline.

5.5.2.1 Chemical compositions

The tourmaline compositional dataset for Loulo is summarised in Fig. 5.17. The Al-Fe-Mg ternary diagram shows the appearance of two tourmaline groups corresponding to two types of Al substitution involving the X, Y and Z tourmaline sites (Eq. 5.2):



The former substitution is dominant (but not exclusive) to pre- and post-mineralisation tourmaline events, while the latter prevails in syn-mineralisation tourmalines. The first tourmaline group shows near constant Mg concentrations, with variable Fe and Al contents. This group mainly plot below the schorl-dravite join into the Fe^{3+} -rich quartz-tourmaline, calc-silicate rock and metapelite field of Henry & Guidotti (1985). High ferric iron concentrations are also observed in the cation proportions ($\text{Fe}^{2+}/[\text{Fe}^{2+} + \text{Fe}^{3+}]$ ratios as low as 0.37). The significant Fe^{3+} content of this tourmaline group indicate the minerals grew in equilibrium with an oxidised hydrothermal fluid. Tourmaline chemistries show similarities to granite-related tourmalines from $\text{Cu} \pm \text{Mo} \pm \text{Au}$ deposits (Koval *et al.*, 1991; Lubis *et al.*, 1994). The pre-mineralisation (E-stage) tourmalines at Gara plot in the Al-rich, Fe-depleted part of the spectrum. This can be explained by the leaching of Fe from the tourmaline sediments by later mineralising fluids, with Fe consumed to form the pyrite.

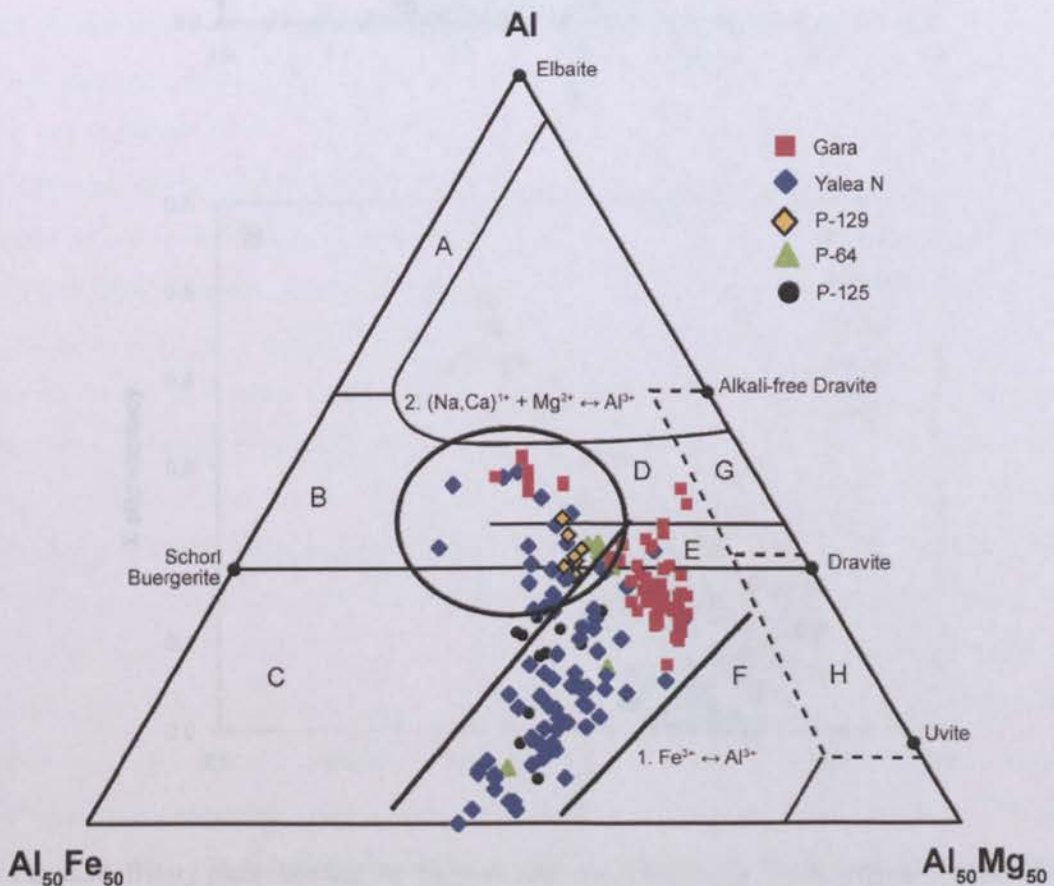


Fig. 5.17. Al-Fe-Mg ternary diagram (Henry & Guidotti, 1985) showing the full tourmaline compositional dataset for Loulo (summarised from Fig. 5.5a, Fig 5.8a and Fig. 5.9a). The marked areas show the two substitutions that are involved: (1) $\text{Fe}^{3+} \leftrightarrow \text{Al}^{3+}$; and (2) $(\text{Na,Ca})^{1+} + \text{Mg}^{2+} \leftrightarrow \text{Al}^{3+}$. The latter substitution is more dominant in the syn-mineralisation tourmalines. Fields given in Fig. 5.5b.

The second tourmaline group is confined to syn-mineralisation tourmalines from Gara, Yalea North (not all), P-129 and P-64. These tourmalines are Mg-poor, Al-rich, and show higher X-site vacancies (lower Ca and Na contents) and lower Fe^{3+} concentrations (mainly absent). The replacement of Ca, Na and Mg by Al is graphically shown in Fig. 5.18. These tourmalines plot above the schorl-dravite join (Fe present as Fe^{2+}) implying precipitation from more reduced fluids.

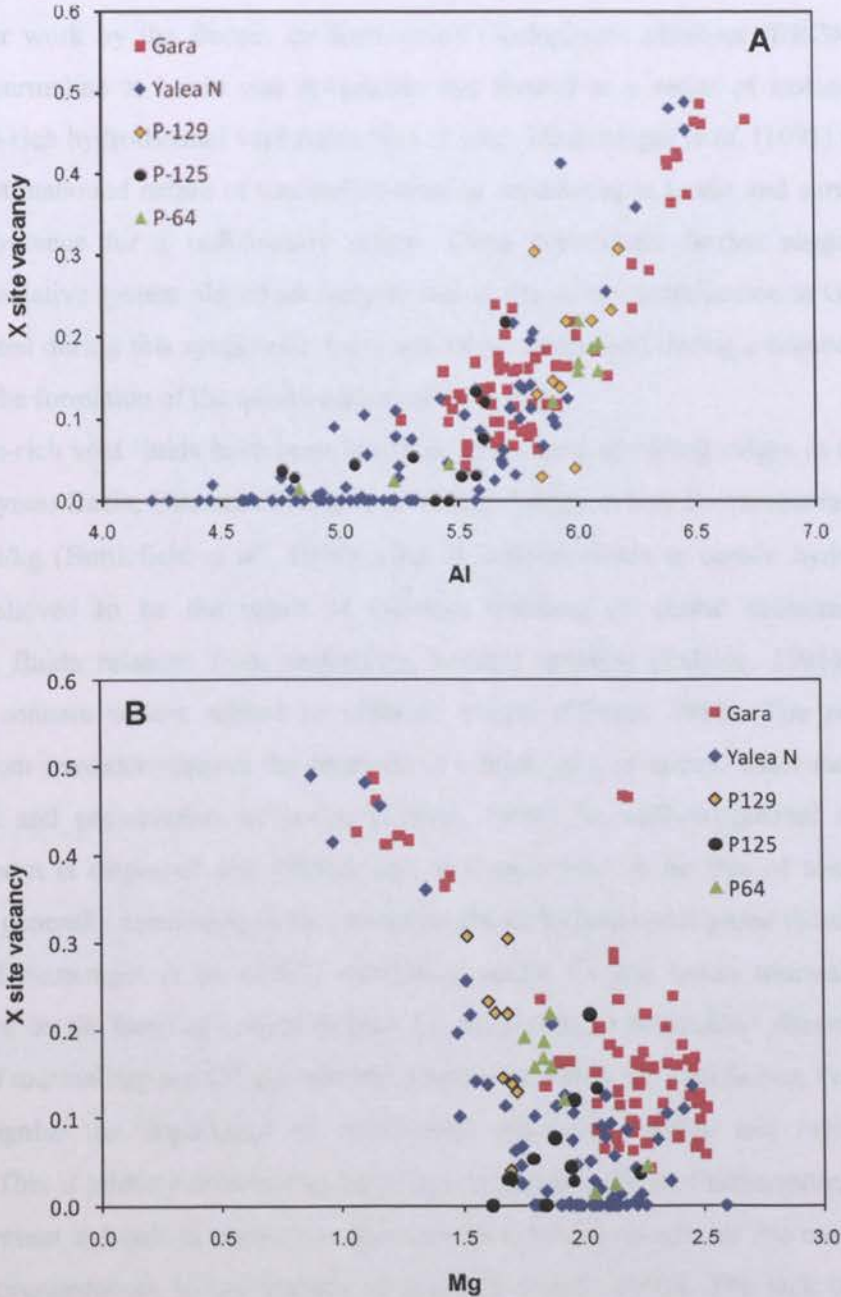


Fig. 5.18. Binary plots showing the major element chemistry of the Loulo tourmalines. **A)** Al vs. X-site vacancy plot showing a clear positive relationship (Al replacing Ca and Na). **B)** Mg vs. X-site vacancy binary plot showing a negative relationship between the two variables (Ca, Na & Mg replaced by Al).

5.5.2.2 Fluid source

Two possible models have been established to explain the widespread tourmaline growth at Loulo. A previous study by Dommanget *et al.* (1993) suggested that the tourmaline was deposited in an exhalative system (a syngenetic model). Data collected during this study implies B-rich fluids were derived from crystallising granitic magmas (an epigenetic model).

1. Exhalative model

Earlier work by the Bureau de Recherches Géologiques Minières (BRGM) argued the widespread tourmaline at Loulo was syngenetic and formed in a series of isolated hypersaline basins from B-rich hydrothermal vent fluids (Fig. 5.19a). Dommanget *et al.* (1993) suggested that the apparent stratabound nature of tourmaline-bearing sandstones at Loulo and surrounding areas is primary evidence for a sedimentary origin. These researchers further suggested that the submarine exhalative system played an integral part in the gold mineralisation at Gara, with gold pre-concentrated during this syngenetic event and later remobilised during a second metallogenic event during the formation of the quartz-carbonate stockwork.

Boron-rich vent fluids have been identified at modern spreading ridges in the NE Pacific Ocean at Guaymas Basin, Escanaba Trough and Middle Valley, where B contents range from 1550 to 2160 $\mu\text{mol/kg}$ (Buttlefield *et al.*, 1994). High B concentrations in certain hydrothermal vent fluids are believed to be the result of efficient leaching of clastic sedimentary units by hydrothermal fluids released from underlying basaltic magmas (Palmer, 1991); or from the presence of connate waters related to volcanic events (Plimer, 1986). The precipitation of tourmaline from seawater requires the presence of a brine pool or anoxic water mass to facilitate concentration and preservation of boron (Turner, 1992). In well-oxygenated normal-salinity seawaters, boron is dispersed and diluted, and sediments tend to be free of tourmaline. Thus, tourmaline is generally considered to be a metamorphic or hydrothermal phase (Slack, 1996).

The Dommanget *et al.* (1993) exhalative model for the Loulo tourmalines (+Au) is dismissed here on the basis of several factors: (1) the timing of tourmaline alteration events; (2) the volume of tourmaline; and (3) depositional conditions within the Kofi Series. Previous workers did not recognise the importance of vein-hosted syn-mineralisation and replacement stage tourmalines. This is primary evidence to discount a syngenetic origin. Furthermore, the volume of tourmaline present at Loulo is unlikely to represent an exhalative source as this model would need exceptional circumstances to concentrate so much B (Slack, 1996). The lack of evidence for hypersaline conditions within the Kofi basin during sedimentation (absence of evaporites) further suggests a non-exhalative source for the tourmaline. However, brine pools do not always form evaporites. There is also a notable absence in other types of exhalative ore deposits within the Kofi Series (e.g. massive sulphide deposits, banded iron formations- BIF's).

The stratabound geometry of tourmaline at Gara and other areas of the Loulo district do not necessarily signify a syngenetic origin. Many stratabound gold deposits, containing tourmaline in variable abundance, were formed during or after regional metamorphism. Examples include the Telfer deposit, Western Australia (Goellnicht *et al.*, 1989; Dimo, 1990); Passagem de Mariana and Cauê deposits, Brazil (Fleischer & Vial, 1991); and deposits associated with the Proterozoic Pine Creek inlier in the Northern Territory of Australia (e.g. Matthai & Henley, 1996). At Loulo, B-bearing fluids likely targeted specific horizons due to lithological contrasts (e.g. permeability) or bedding parallel structures (Fig. 5.3).

A. Exhalative Model (syngenetic)

B. Granitic Model (epigenetic)

Fig. 5.19. Schematic diagrams illustrating the two possible fluid source models for the widespread tourmaline observed in the Loulo district. **A)** Syngenetic exhalative model of Dommanget *et al.* (1993). **B)** Epigenetic granitic model adopted during the present study.

2. Granitic model

The model favoured by this study implies that tourmaline is an epigenetic mineral phase, related to mineralisation, and a part of a magmatic hydrothermal system (Fig. 5.19b). Tourmaline at Gara and other Gara-style deposits is one manifestation of a remarkable boron anomaly that extends for more than 200 km along the strike of the SMSZ (Fig. 5.20). The most likely explanation for the anomaly, and the pervasive growth of epigenetic tourmaline, is a release of B-rich fluids from crystallising granitic melts (Slack, 1996). The geometry of the boron anomaly suggests that B-rich, magmatically derived fluids were focussed over large distances along this shear zone.

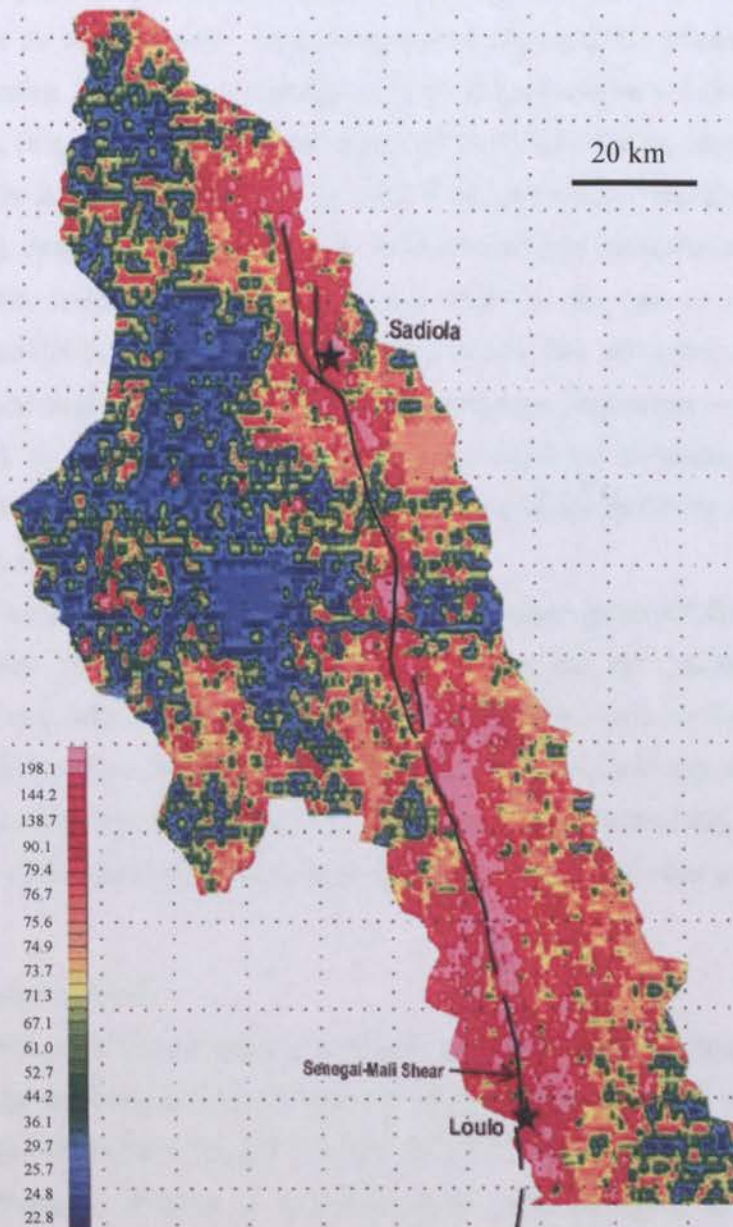


Fig. 5.20. Boron concentrations in the eastern parts of the Kédougou-Kéniéba inlier based on soil geochemistry surveys. High B anomalies are seen all way along the SMSZ (concentrations given in ppm). Image courtesy of Randgold Resources.

Boron is an incompatible element and strongly partitions into the fluid phase during crystallisation of granitic magmas (London *et al.*, 1996). Boron-rich granitic rocks tend to be peraluminous in nature, similar to the basin-type granitoids of the Kofi Series (*chapter 3*). Boron-rich magmas are likely melting products of metasediments containing large quantities of both biotite and muscovite, in addition to quartz and plagioclase (London *et al.*, 1996). Boron levels in micas range from 10 to 200 ppm, with higher concentrations in muscovite than biotite (Truscott *et al.*, 1986). Tourmaline-bearing fluids are a common feature of the late stage evolution of granitic hydrothermal systems (e.g. the Cornwall granites in SW England; Smith & Yardley, 1996).

5.5.3 Sodic alteration

The pervasive pink albite alteration halos surrounding the Loulo orebodies are not a common alteration type for orogenic gold. Alkali metasomatism in a majority of reported orogenic deposits show $K > Na$ ratios, with mineral assemblages consisting of sericite \pm fuchsite \pm biotite \pm chlorite \pm minor albite (e.g. Ridley & Diamond, 2000). In the Loulo district, albitisation is also observed along the strike length of the SMSZ in the form of albitites (eastern margin of the Falémé volcanic belt; Fig. 3.2), implying that Na-rich fluids were concentrated along this major suture as well as B-bearing fluids. Sodic alteration is also present further to the west as alteration zones surrounding the Falémé IOCG deposits and as more widespread, less pervasive, alteration seen throughout the granodiorites and diorites of the Balangouma plutons (plagioclase \rightarrow albite \pm minor sericite; *section 3.3.9*). In fact, sodic alteration is not uncommon for Birimian orogenic gold deposits. Pink albite alteration zones are associated with the tonalite-hosted Chirano deposit, along the Sefwi belt in Ghana (Allibone *et al.*, 2004).

Albitisation is a typical style of alteration of iron oxide-copper-gold (IOCG) deposits, such as Olympic Dam, South Australia (e.g. Bastrakov *et al.*, 2007); and the Candelaris-Punta del Cobre deposits, Chile (e.g. Marschik & Fontboté, 2001). The similar alteration halos around the Falémé iron deposits (Schwartz & Melcher, 2004) may imply the Loulo gold deposits (at least the Gara-style mineralisation) have possible links to IOCG deposits, with mineralising fluids crossing the SMSZ. The source of the Gara-style magmatic fluids will be discussed further in *chapter 8*.

5.5.4 Alteration geothermometry

The P-T conditions of mineralisation at Loulo can be estimated using the alteration mineral assemblages. In the Yalea-style orebodies, the alteration assemblage of sericite-chlorite-carbonate-quartz suggest alteration took place at 225 to 400 °C at <1 to 3 kbars (McCuaig & Kerrich, 1998). Additionally, chlorite is a widely used geothermometer in the study of hydrothermal ore deposits (e.g. Zhang *et al.*, 1997; Zoheir *et al.*, 2008; Zoheir & Akawy, in press; Atsuyuki *et al.*, 2010). Cathelineau & Nieva (1985) and Cathelineau (1988) showed that the $Al^{(iv)}$ content in the tetrahedral site of chlorites (*see Eq. 5.3*) has an empirical relationship with

temperature by the following formula:

$$T\text{ }^{\circ}\text{C} = 106\text{Al}^{(\text{iv})} + 18 \quad (\text{Eq. 5.8})$$

Further work by Kranidiotis & Maclean (1987) showed that the $\text{Al}^{(\text{iv})}$ content is also dependent on the $\text{Fe}/(\text{Fe}+\text{Mg})$ ratio, with $\text{Al}^{(\text{iv})}$ corrected ($\text{Al}^{\text{iv}}_{\text{c}}$) as follows:

$$\text{Al}^{\text{iv}}_{\text{c}} = \text{Al}^{(\text{iv})} + 0.7\text{Fe}/(\text{Fe}+\text{Mg}) \quad (\text{Eq. 5.9})$$

Hydrothermal chlorites were measured from Yalea Main, Loulo-3 and Faraba (Table 5.4). The calculated temperatures of chlorite formation for Yalea Main occur between 294-333 °C (mean of 315 °C), Loulo-3 from 271-313 °C (mean of 296 °C), and Faraba between 201-235 °C (mean of 221 °C) (Fig. 5.20). The lower formation temperatures at Faraba are consistent with the telluride geothermometry data in section 4.6.3.2. Metamorphic chlorites (lower $\text{Fe}/[\text{Fe}+\text{Mg}]$ ratios) from across the Loulo permit show estimated temperatures of 268-294 °C (mean of 282 °C). No P-T estimates could be achieved on Gara-style mineralisation as chlorite is largely absent from these orebodies

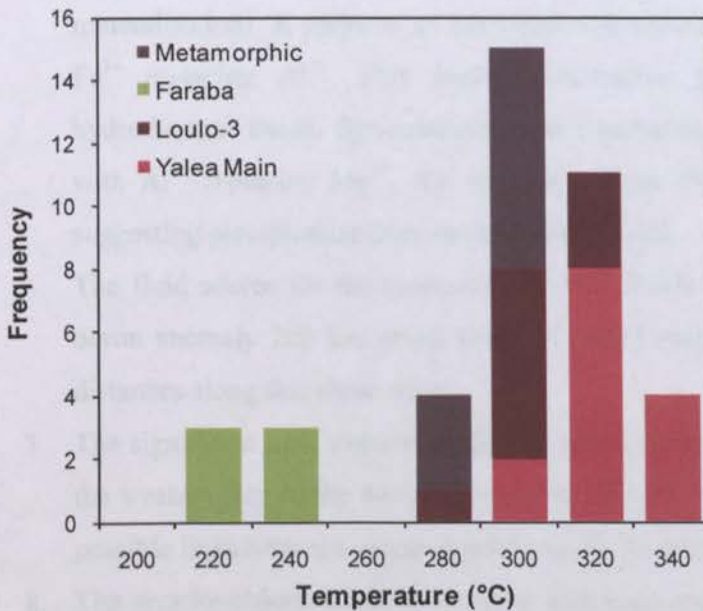


Fig. 5.21. Histogram showing the formation temperatures of hydrothermal chlorite at Yalea Main, Loulo-3 and Faraba, and metamorphic chlorite from sedimentary and intrusive rocks from the Loulo district. Temperatures calculated from Cathelineau (1988).

5.6 Conclusions

The alteration characteristics of the Loulo orebodies are summarised below:

1. Three distinctive alteration assemblages are observed at Loulo: (1) tourmaline-quartz-biotite-carbonates; (2) albite-ankerite-quartz-haematite-sericite; and (3) sericite-chlorite-ankerite-quartz. Other, more local, styles of alteration include silica and magnetite alteration.
2. Alteration zones at Loulo lack sulphidation, with sulphides mainly confined to mineralised zones.
3. Tourmaline alteration forms typical alteration halos around Gara-style orebodies (largely absent from Yalea-style), while sericite-chlorite-ankerite alteration is generally associated with deposits showing Yalea-style mineralisation. Pink sodic alteration is a common feature in all styles of Loulo mineralisation (although seems to predate the mineralisation event in Yalea-style orebodies).
4. Alteration zones associated with Gara-style mineralisation show mass gains in B + Na + Fe + Mg + Si, plus minor CO₂ + Ca + Mn; while Yalea-style deposits show increases in CO₂ + H₂O + K + Ca + Si + Na, plus minor Fe + Mg. These variations can be attributed to ore fluids of contrasting compositions.
5. Multiple tourmaline events can be observed in individual deposits (pre-, syn- and post-mineralisation). A majority of the Loulo tourmalines show high Fe³⁺ compositions, with Fe³⁺ replacing Al³⁺. This implies tourmaline grew in equilibrium with oxidised hydrothermal fluids. Syn-mineralisation tourmaline show slightly different chemistries, with Al³⁺ replacing Mg²⁺, Na⁺ and Ca⁺. These tourmalines are largely absent of Fe³⁺ suggesting precipitation from more reduced fluids.
6. The fluid source for the tourmaline-bearing fluids is likely granitic in origin. The large boron anomaly 200 km along strike of SMSZ suggests magmatic fluids travelled large distances along this shear zone.
7. The significant pink albite alteration surrounding the Loulo orebodies is also observed on the western side of the SMSZ associated with the Falémé IOCG deposits and may imply possible links between orogenic gold and IOCG development in the Loulo district.
8. The sericite-chlorite-carbonate-quartz alteration assemblage associated with Yalea-style mineralisation suggest alteration took place at 225 to 400 °C at <1 to 3 kbars. Chlorite chemistries show more restricted temperatures between 270-335 °C. Chlorite formation temperatures decrease towards the south at Faraba (200-235 °C) implying shallower levels of ore emplacement.

CHAPTER 6: FLUID INCLUSION STUDIES AT LOULO

6.1 Introduction

Fluids responsible for the growth or recrystallisation of hydrothermal minerals may be trapped and preserved as microscopic fluid-filled cavities. Examination of these fluid inclusions form a key part of any ore genetic study (e.g. Koděra, 2000; Chamberlain, 2003; Allan, 2006; Zoheir *et al.*, 2008; Zoheir & Akawy, 2009). The two most common techniques in investigating fluid inclusions are optical microscopy and microthermometry. Transmitted light petrography is the first and most integral step in any fluid inclusion study. The timing of fluid inclusion formation relative to the host crystal, and the classification and occurrence of fluid inclusions can all be achieved during this stage. Microthermometry is the most widely used method for analysing fluid inclusions. This non-destruction technique measures phase transformations that occur within inclusions during heating and cooling, which in turn can provide semi-quantitative to quantitative data on fluid composition and vital information on the temperature and pressure of fluids at the time of entrapment (e.g. Roedder, 1984; Touret, 2001; Yao *et al.*, 2001; Zoheir, 2008a, b). For further information on microthermometry the reader is referred to Shepherd *et al.* (1985) and Samson *et al.* (2003).

Laser Raman spectroscopy has also been applied to fluid inclusion studies since the mid 1970's (e.g. Rosasco & Roedder, 1975; 1979). The laser Raman is a sensitive, non-destructive tool for the identification of molecular species (solid, liquid and gaseous phases). Raman spectroscopy is based on the inelastic scattering of light by the vibrations of molecular bonds or the lattice motions of crystalline materials. An inclusion sample can be excited by a monochromatic laser beam to cause emission of backscattered Raman radiation, characteristic of the species present (for further details *see* Burruss, 2003). Solid phases in fluid inclusions can also be measured using the Scanning Electron Microscope (SEM) (e.g. Anthony *et al.*, 1984; Campbell *et al.*, 2001).

6.2 Aims and objectives

The aim of this chapter is to document the petrographic, electron microprobe, microthermometric and laser Raman properties of fluid inclusions from the Loulo gold deposits. If it can be demonstrated that fluid inclusions are coeval with mineralisation and representative of the ore-bearing fluid, data obtained from this study can be used in several ways: (1) to help distinguish the nature and source of the fluid and metal components; (2) to give estimates on P-T-X conditions at time of ore deposition; and (3) to provide information on metal transport and depositional mechanisms (e.g. Helmy *et al.*, 2004; Zoheir, 2008b; Coulibaly *et al.*, 2008).

This fluid inclusion study largely concentrates on the Gara and Yalea deposits; however, a selection of other Gara-style deposits (Yalea North) and Yalea-style deposits (Loulo-3 and Baboto) are also investigated to determine a realistic fluid evolution model for the Loulo district. Comparisons between Gara- and Yalea-style deposits will test whether these two different styles

of deposit (based on ore and alteration mineralogy) formed from different hydrothermal ore fluids. Faraba-style deposits are not studied and represent a topic for future research. Barren veins (<0.1 g/t) from the Gara and Yalea orebodies are also measured to examine any differences between the fluid inclusion characteristics of gold-bearing and barren veins at Loulo. On a wider-scale, comparisons can be made with other Birimian gold deposits and other orogenic gold deposits worldwide, providing valuable information on the composition and origin of such ore fluids.

6.3 Previous fluid inclusion studies

This section briefly summaries the fluid inclusion characteristics of orogenic gold deposits and previous fluid inclusion studies on the Birimian terranes of West Africa. The fluid compositions of orogenic gold deposits are outlined in Table 1.2. Fluid inclusion studies show orogenic gold deposits of all ages (Precambrian to Phanerozoic) have a uniform fluid composition typified by a low-salinity (<10 wt% NaCl equiv.), mixed H₂O-CO₂ (5-50 mol % CO₂) fluid, with minor amounts of CH₄ and N₂ (e.g. Groves *et al.*, 2000; Ridley & Diamond, 2000; Goldfarb *et al.*, 2005). However, a variety of end-member fluid inclusion types are commonly observed in this deposit type; a prime example being the Birimian gold deposits of West Africa. Previous studies have shown that Birimian auriferous veins exhibit a range of fluid inclusion types (all spatially and temporally related): (1) low-salinity (generally <5 wt.% NaCl equiv.) H₂O-CO₂ inclusions; (2) abundant high-density (up to 1.15 g/cm³) CO₂-N₂-(CH₄) inclusions; and (3) less common, low-salinity (generally <5 wt.% NaCl equiv.) H₂O-rich inclusions. This range in fluid inclusion types have been interpreted to be the result of either fluid unmixing of a primary H₂O-CO₂ fluid (Yao *et al.*, 2001; Coulibaly *et al.*, 2008) or from selective leakage of H₂O from H₂O-CO₂ inclusions post-entrapment (e.g. Schwartz *et al.*, 1992; Klemd & Hirdes, 1997; Klemd *et al.*, 1997; Willie & Klemd, 2004). These models are discussed in detail in *section 6.7*.

Fluid inclusion studies on Birimian gold mineralisation are limited in extent. A majority of the investigations have been carried out in Ghana (Bowell *et al.*, 1990; Schwartz *et al.*, 1992; Manu, 1993; Hammond & Shimazaki, 1994; Oberthür *et al.*, 1994; Schmidt Mumm *et al.*, 1997; Yao *et al.*, 2001; Willie & Klemd, 2004) and Burkina Faso (Klemd & Ott, 1997; Klemd *et al.*, 1997; Bourges *et al.*, 1998; Dubois *et al.*, 2007). One published study has been carried in the Côte d'Ivoire (Coulibaly *et al.*, 2008). To date, no published data exist for the highly gold-endowed Kédougou-Kéniéba inlier (KKI), which highlights the need for fluid inclusion studies at Loulo.

The fluid inclusion populations previously reported in quartz veins from Birimian orogenic gold deposits are presented in Fig. 6.1, showing the dominance of CO₂-rich fluids. Similar distributions are observed in detrital auriferous quartz pebbles from the older Tarkwaian paleoplacers (Klemd & Olesch, 1991; Klemd *et al.*, 1993). Klemd *et al.* (1993) proposed that the original lode deposits for the Tarkwaian gold contained similar fluid characteristics to the younger Birimian orogenic gold deposits. The Morila deposit, in southern Mali, is the only Birimian gold deposit to show notable differences in fluid inclusion characteristics (Fig. 6.1), with the

predominance of mixed-salinity (1 to 27 wt.% NaCl equiv.) aqueous inclusions and the complete absence of CO₂-bearing inclusions (Hammond & Robb, 2009). Mcfarlane *et al.* (2008) classified Morila as a separate style of deposit compared to many other reported Birimian gold deposits (section 2.6.1.2) with fluids closely matching shallow-level (~5 km) reduced intrusion-related gold systems (RIRGS) (Baker, 2002).

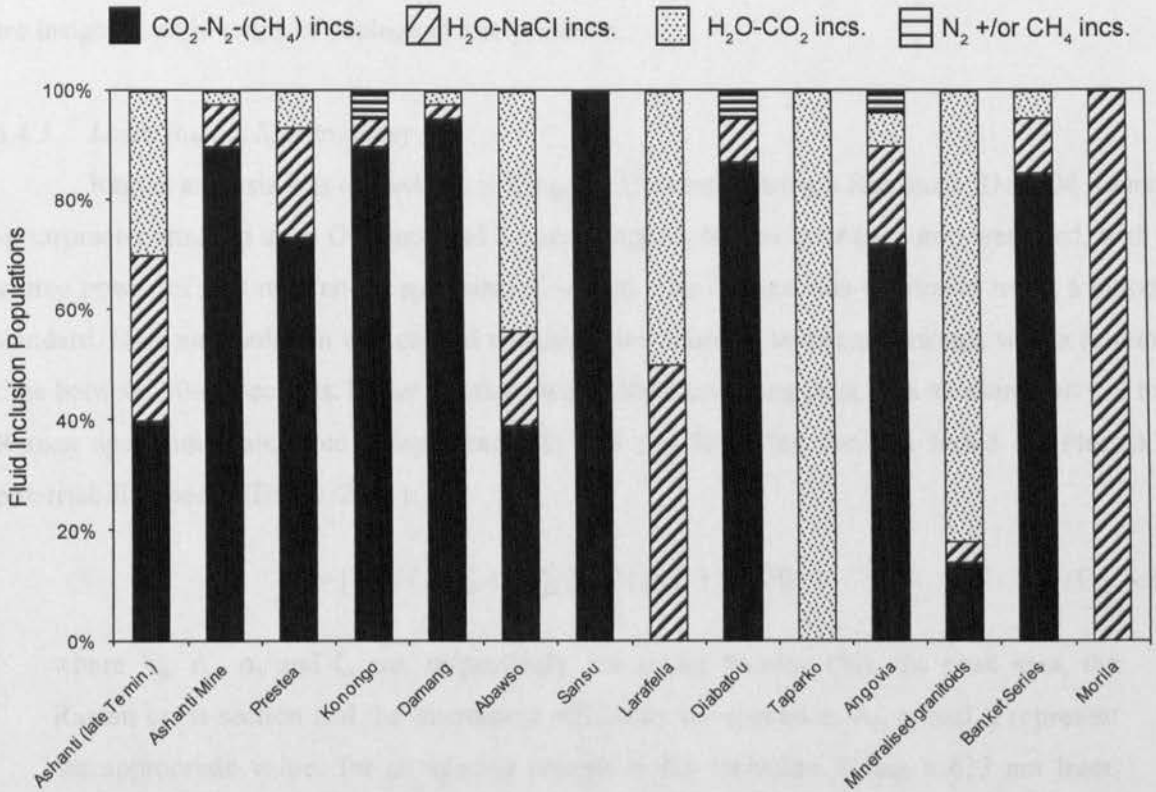


Fig. 6.1. Fluid inclusion populations for various Birimian gold deposits (see Fig. 2.4 for locations). Many deposits show the dominance of CO₂-rich fluid inclusions. Larafella, Taparko and mineralised granitoids (Ghanaian belt- & basin-type intrusions) show higher percentages of H₂O-CO₂ fluid inclusions. Morila shows the predominance of aqueous inclusions without CO₂. Deposit types: Banket Series refers to Tarkwaian paleoplacer deposits; Morila- RIRGS; other deposits- orogenic gold deposits. Subordinate N₂ and/or CH₄-bearing inclusions are occasionally observed but interpreted to be late and post-mineralisation. See text for references.

6.4 Methodology

6.4.1 Sample preparation

For the fluid inclusion studies reported here, samples were prepared as doubly-polished wafers approximately 150 μm in thickness, following the procedures outlined by Beeskov (2007). All material chosen for analysis were quartz vein samples. Quartz is generally considered the most applicable material for fluid inclusion analysis because of its widespread geological appearance, transparency, the tendency to trap relatively large inclusions, and the ability to withstand internal fluid pressures during heating experiments (Shepherd *et al.*, 1985). Carbonate vein material was not measured because these soft easily-cleaved minerals were much more susceptible to leakage and necking down of fluid inclusions.

6.4.2 Microthermometry

Microthermometry experiments were carried out at Kingston University using a Linkam LMS600 heating and freezing stage attached to a Nikon Optiphot microscope. The stage was regularly calibrated using FLINC synthetic standards of CO₂ (pure CO₂ triple point at -56.6 °C) and H₂O (pure H₂O critical point at +374.2 °C) fluid inclusions. The reproducibility of the measurements was approximately ± 0.2 °C below 30 °C and ± 2 °C up to 400 °C. Analytical errors are insignificant in terms of geological interpretation.

6.4.3 Laser Raman Spectroscopy

Raman analysis was carried out at Kingston University using a Reinshaw RM1000 Raman spectrometer attached to an Olympus BH-2 microscope. A Ne-ion laser (633 nm) was used, with a source power of 500 mW and a spot size of ~5 µm. The Raman was calibrated using a silicon standard. Data manipulation was carried out using the Grams32 software package, with a running time between 30-60 seconds. Molar fractions were calculated using peak area measurements of the Raman spectrum (calculated using Grams32) and the following formula based on Placzek's polarisability theory (Burke, 2001):

$$X_a = [A_a / (\sigma_a \zeta_a)] / \sum [A_i / (\sigma_i \zeta_i)] * 100 \quad (\text{Eq. 6.1})$$

where X_a , A_a , σ_a and ζ_a are, respectively, the molar fraction (%), the peak area, the Raman cross-section and the instrument efficiency for species a; A_i , σ_i and ζ_i represent the appropriate values for all species present in the inclusion. Using a 633 nm laser, Raman cross-section values for CO₂, N₂, CH₄ are 2.7, 1.0 and 7.2, respectively (Burke, 2001). The instrument efficiency was calculated by Beeskov *et al.* (2005) at 0.65. Peaks positions for CO₂ (twinned peaks), N₂ and CH₄ occur at ~1282 cm⁻¹ (ν_1) and ~1386 cm⁻¹ (ν_2); 2330 cm⁻¹; and 2913 cm⁻¹, respectively (Fig. 6.7; Fig. 6.8).

6.4.4 SEM analysis of opened inclusions

The identification of daughter minerals within fluid inclusions can be carried out optically, by Raman spectroscopy (in Raman active phases), or by semi-quantitative analyses using the energy-dispersive X-ray spectrometer (EDS) microanalyser on the scanning electron microscope (SEM). This latter technique involves the removal and evaporation of the fluid phases by cracking the host quartz minerals and opening the inclusions prior to analysis. The advantage of this method is that as well as identifying solid phases within the inclusions, the dissolved components of the aqueous fluid can also be determined by the precipitation of minerals during the evaporation process (Fig. 6.4). Electron microprobe identification of solid phases is commonly used in cases where daughter minerals are too small to be recognised by other techniques (e.g. Anthony *et al.*, 1984; Campbell *et al.*, 2001).

6.5 Fluid inclusion petrography

6.5.1 Classification schemes

There are many ways to classify fluid inclusions (e.g. Roedder, 1984; Goldstein, 2003). One of the most useful classification schemes relates the timing of formation of an inclusion relative to that of the host crystal, i.e. the primary, secondary and pseudosecondary inclusion classification (e.g. Roedder, 1984). In many cases, such as Loulo, determining the temporal distribution of inclusions within a given sample is difficult and equivocal. Goldstein & Reynolds (1994) proposed an alternative classification scheme, whereby analysis of inclusions should be restricted to a group of inclusions that were trapped coevally, termed the Fluid Inclusion Assemblage (FIA) concept. The FIA classification is now considered the preferred approach as they define the most finely discriminated fluid inclusion trapping event that can be recognised based on petrography (Goldstein, 2003). The FIA approach is used in this study.

6.5.2 Timing and origin of inclusions

Transmitted light petrography of vein quartz at Loulo show variable degrees of recrystallisation. The most re-crystallised, deformed and strained quartz occur along discrete zones and exhibit diagnostic features such as polycrystalline, undulose, stylolite and triple-point textures. The abundance of fluid inclusions in these crystals is extremely high, which is typical of deformed quartz (Shepherd *et al.*, 1985). Limited work was carried out on these samples as the inclusions are unlikely to represent the original gold-bearing fluid.

Between these areas of strain accumulation, the quartz veins are relatively undeformed, as shown by cathodoluminescence studies which show recrystallised zones are largely concentrated along grain boundaries. The majority of fluid inclusions in quartz cores are assumed to be primary in origin (termed 'early' inclusions here) and coeval with mineralisation. These early inclusions form parallel to growth zones or more commonly as random clusters within the cores of the host grains (two styles of FIA). Secondary inclusions (termed 'late' inclusions here) are also observed and generally follow healed micro-fracture planes, which either start and terminate within a given quartz crystal (intergranular trails; rare textures) or crosscut quartz grain boundaries (transgranular trails). These inclusions were measured but were not considered a priority as they are likely to post-date mineralisation. Late inclusions were also observed as zones along recrystallised grain boundaries (inclusions too small to measure, $<2 \mu\text{m}$). The occurrence of early and late fluid inclusions at Gara and Yalea Main are shown schematically in Fig. 6.2. Even within the less recrystallised quartz crystals, deformation may have caused post-entrapment modification of the inclusions, such as necking down, partial leakage of selective components, or total leakage (see Bodnar, 2003 for information on re-equilibration textures and Table 6.3 for terminology descriptions). Where possible, inclusions suspected of being modified post-entrapment were ignored.

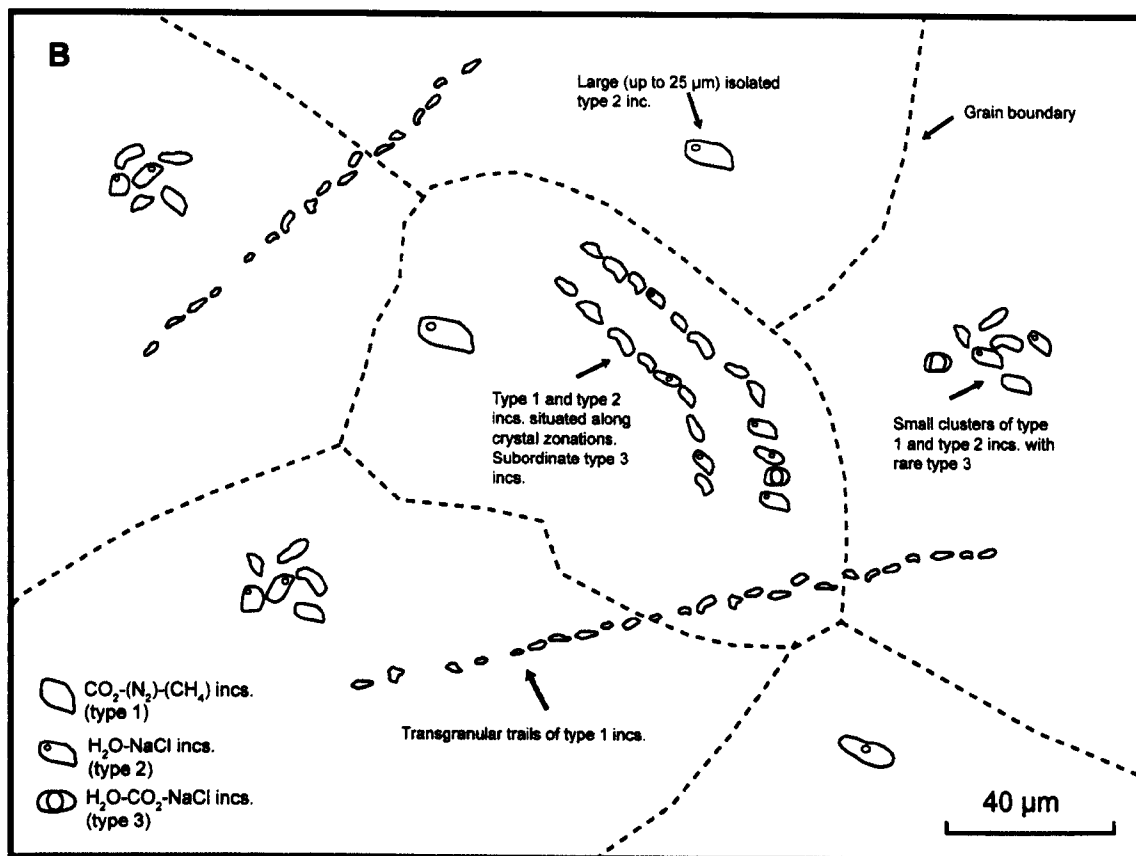
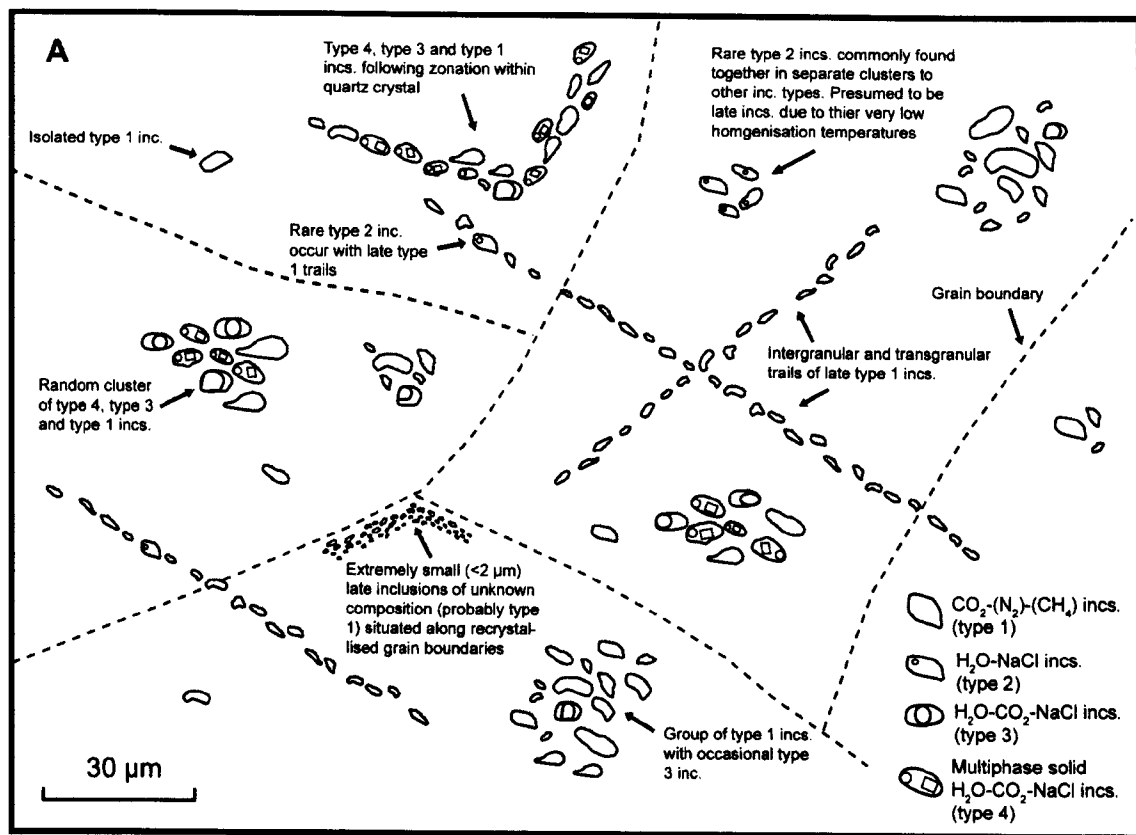


Fig. 6.2. Schematic drawings showing the distribution of the four fluid inclusion types at Gara (A) and Yalea Main (B).

6.5.3 Fluid inclusion types and occurrence

In transmitted light, the recognition of different inclusion types and different phases within an inclusion (i.e. liquid, vapour and solid phases) was carried out using the criteria stated in Goldstein (2003). The volumetric proportions of the different phases were visually estimated (approximate error $\pm 10\%$) at room temperature using the volumetric charts of Shepherd *et al.* (1985). Four types of fluid inclusions are present in the Loulo quartz veins (summarised in Table 6.1):

type 1- CO₂-(N₂)-(CH₄) inclusions (dominant type)



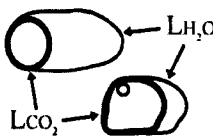
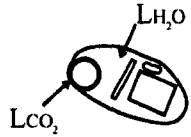
type 2- H₂O-NaCl inclusions

type 3- H₂O-CO₂-NaCl inclusions (\pm N₂-CH₄)

type 4- hypersaline H₂O-CO₂-NaCl (\pm CH₄-N₂) multiphase solid inclusions

Such an array of fluid inclusion types is common for Birimian orogenic gold deposits (*section 6.3*) but Loulo shows a notable addition of hypersaline inclusions (type 4) not yet reported elsewhere in the Birimian crust.

Table 6.1. Compositional classification of fluid inclusions present in the Loulo district, based on phases identified at room temperature and by laser Raman.

Type	Schematic	System	Notes
Type 1		CO ₂ -(N ₂)-(CH ₄)	LCO ₂ \pm VCO ₂ \pm S Graphite present in CH ₄ -bearing incs.
Type 2		H ₂ O-NaCl	LH ₂ O + VH ₂ O Vapor bubble <25 vol.%
Type 3		H ₂ O-CO ₂ -NaCl	LH ₂ O + LCO ₂ \pm VCO ₂ Variable CO ₂ proportions (15 to 85 vol.%). Graphite detected in gas phase in CH ₄ -bearing incs.
Type 4		Multiphase solid H ₂ O-CO ₂ -NaCl	LH ₂ O + LCO ₂ \pm VCO ₂ + DMS + NDMS 1 to 4 visible daughter minerals CO ₂ phase <20 vol.%

Note- L + V = liquid & vapour of a particular species; S = solid phase; DMS = dissolvable solids; NDMS = non-dissolvable solids (captured minerals). Graphite detected by Raman spectroscopy (*section 6.6*).

Type 1 CO₂-rich inclusions are predominant (discussed in *section 6.5.4*) and occur both as early and late high relief inclusions. Early inclusions occur as small (diameter <5 to 10 μm), rounded to oblate inclusions or as larger (10-30 μm) irregular-shaped inclusions, mainly within random orientated clusters (Fig. 6.3a, b). Late type 1 inclusions are commonly elongate in shape (<1 μm to 5 μm in size) and occur along planar trails. Within FIAs, both early and late inclusions are mono- (LCO₂) (dominant) or bi-phase (LCO₂ + VCO₂) at room temperature.

Aqueous inclusions (type 2) are easily distinguished from CO₂-bearing inclusions by their transparency and low relief boundaries (Fig. 6.3c, d). These inclusions are bi-phase at room temperature (LH₂O + VH₂O) and have rounded and rare negative shapes (inclusions that take on the shape of their host crystal). The occurrence of type 2 inclusions is as follows: as isolated grains or in small clusters with type 3 inclusions (occasionally showing necking down or natural decrepitation textures; inclusions ignored); as small aggregates (3 to 6 inclusions) situated away from other inclusion types; or as rare grains along fracture planes with type 1 inclusions (Fig. 6.2). The latter two locations are seen at Gara (Fig. 6.2) and are presumed to represent late inclusions (as showed by their low homogenisation temperatures; *section 6.6.2.2*).

Immiscible H₂O-CO₂ type 3 inclusions show a near continuum of modal proportions from 10 to 90 vol.% CO₂ within individual FIAs (Fig. 6.3e, f). At room temperature, these inclusions are both two- (LH₂O + LCO₂) and, less commonly, three-phase inclusions (LH₂O + LCO₂ + VCO₂). Type 3 inclusions are oblate to well-rounded in shape, between 5-15 μm in diameter and occur in random groups or along crystal zonations with type 1 inclusions (Fig. 6.2).

Type 4 multiphase solid aqueous-rich inclusions commonly contain a liquid bubble of CO₂ (5 to 25 vol.%; mainly ≤ 10 vol.%) (Fig. 6.3g, h). Inclusions are rounded and characteristically small (<5 to 10 μm), which makes their analysis difficult. Type 4 inclusions contain one to four visible daughter minerals (5 to 35 vol.%; mainly between 15 and 20 vol.%) and the various mineral phases are described below. These inclusions have a sporadic distribution within the Loulo district (discussed in *section 6.5.4*). At Gara and Yalea North, this inclusion type is spatially associated in the same FIAs with early type 3 and, less so, early type 1 inclusions (Fig. 6.2a). Necking down of this inclusion type is occasionally observed, with ultra-fine CO₂ inclusions (<3 μm) surrounding larger CO₂-absent inclusions (inclusions ignored).

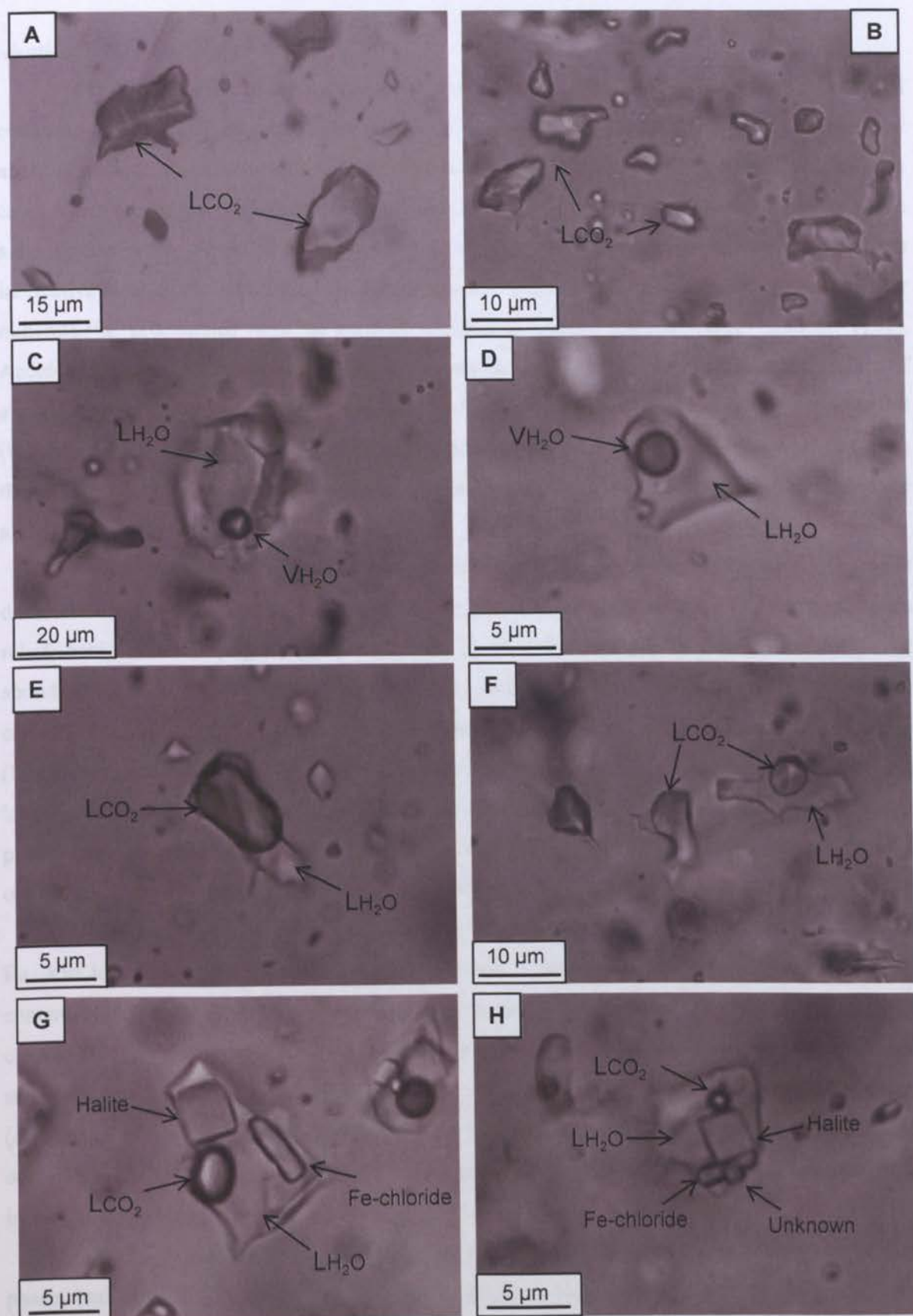


Fig. 6.3. Photomicrographs of the four fluid inclusion types at Loulo (at room temperature). **A)** Two large, irregular-shaped, mono-phase CO_2 inclusions (type 1). **B)** A cluster of irregular-shaped and smaller rounded type 1 inclusions, with distinctly dark rims. **C)** Transparent, low relief, aqueous inclusion (type 2) with a darker vapour bubble occupying 5 vol.% of the inclusion. **D)** Bi-phase type 2 inclusion showing a larger vapour bubble (~15 vol.%). **E)** Mixed type 3 inclusion with nearly equal proportions of CO_2 and H_2O . **F)** A cluster of type 3 inclusions showing variation in CO_2 content between inclusions. **G)** Hypersaline aqueous-rich inclusion (type 4) with a small CO_2 bubble (10 vol.%). Halite and Fe-chloride occupy ~20-25 vol.% of the inclusion. **H)** Type 4 inclusion with similar daughter phases to G) and lower concentrations of CO_2 (<5 vol.%).

Identification of the solid phases

The identification of the various solid phases present within type 4 inclusions was carried out using transmitted light microscopy (using criteria of Van den Kerkhof & Hein, 2001), or by analysis of open fluid inclusions on the SEM (*section 6.4.4*). The latter technique was used in cases where the optical properties are insufficient to correctly identify the daughter minerals or the solid phases were too small to observe ($<1 \mu\text{m}$) by optical methods. Raman analysis was ineffective due to the small size of the inclusions. Solid phases can represent true daughter minerals (i.e. precipitated from the aqueous fluid) or accidentally trapped solids (Roedder, 1984). Accidentally trapped solids occur when mineral contaminants settle or precipitate onto the surface of a growing crystal and were incorporated into the fluid inclusion as the host crystal grew around it (Goldstein, 2003). The frequent appearance and relative proportions of many of the solid phases in these inclusions implies they represent true daughter minerals. Accidentally trapped solid phases are also seen and are discussed further below.

Halite and Fe-chloride could be correctly identified optically. Halite forms the most dominant solid phase (present in all type 4 inclusions) and occurs as small ($<3 \mu\text{m}$), moderate relief, cubic minerals (Fig. 6.3g, h; Fig. 6.4a, b). Fe-chloride minerals form the second most abundant chloride (10:1 halite/Fe chloride ratio), existing as green, high birefringent, prismatic crystals (Fig. 6.3g h; Fig. 6.4c). They may represent lawrencite (FeCl_2) or Fe-chloride hydrates (Shepherd *et al.*, 1985; Kwak *et al.*, 1986). Due to their small size ($\leq 1 \mu\text{m}$), other solid phase were identified by electron microprobe analysis. As well halite and Fe-chloride, a range of other mineral phases were observed such as rare crystals of sylvite (KCl) (Fig. 6.4f), rare Ca-bearing chlorides, oxides, carbonates, silicates and extremely rare sulphates.

Numerous metals were detected in all the chloride phases, most notably Cu, Ni, W, Sr and Ba, and less commonly Pb and Zn (concentrations $>5000 \text{ ppm}$), symbolising the high metal content of this fluid type. In a few cases, these metals concentrate at the apex of the chloride crystals (Fig. 6.4h). Chlorides (mainly halite) were also observed in mounds along quartz fracture surfaces, representing the precipitation of the dissolved components of the aqueous phase (dominance of Na^+ cations) (Fig. 6.4e). Electron microprobe images also document the existence of solid halite crystals that appear to be intergrown with the host quartz (no evidence of an inclusion cavity) (Fig. 6.4g).

Type 4 inclusions also contain carbonate minerals, which commonly occur as Ca-rich phases (calcite) and Ca-Fe-Mg bearing phases (ankerite) (Fig. 6.4b, d). Haematite and magnetite (in separate inclusions) were also detected; the latter distinguished from the former by its octahedral habit (Fig. 6.4 b to d). Muscovite and rare barite were also observed (Fig. 6.4d). No sulphides (common ore mineral phases) were detected in these hypersaline inclusions. Muscovite and barite show an irregular appearance and the former especially shows inconsistent liquid: solid ratios indicating they represent accidentally trapped mineral phases. The compositions and properties of the solid phases within type 4 inclusions are summarised in Table 6.2.

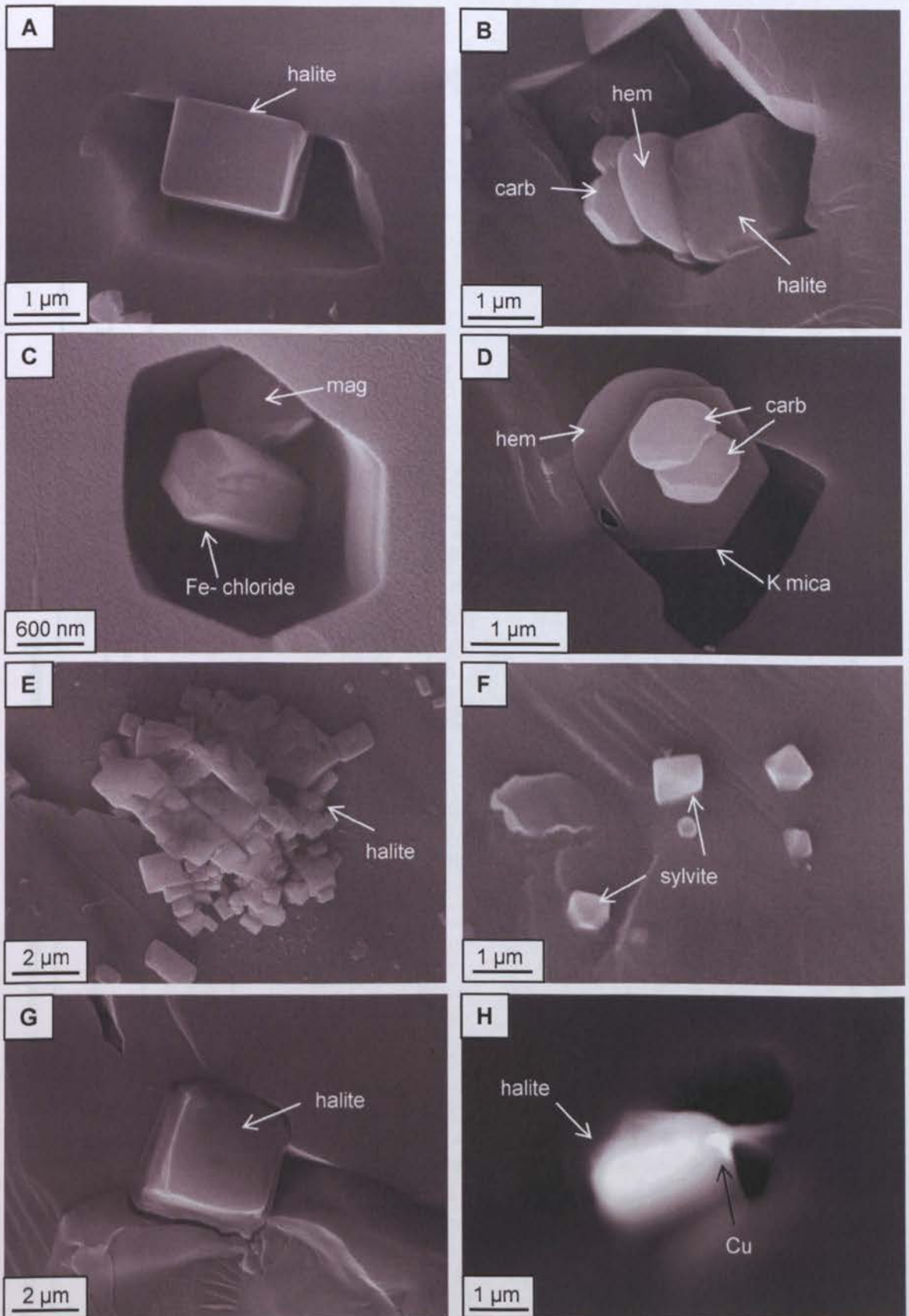
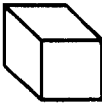
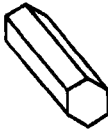


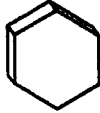





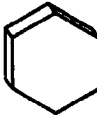

Fig. 6.4. Electron microprobe images of opened, quartz-hosted type 4 inclusions (gold coated samples) from Gara and Yalea North (A to G are secondary electron images and H is a back-scattered electron image). **A)** Single cube of halite. **B)** Halite surrounded by platy grains of haematite and carbonate. **C)** Hexagonal prism of Fe chloride and an octahedral crystal of magnetite. **D)** A range of solid phases including platy haematite and muscovite and anhedral grains of calcite and ankerite. Small individual halite cubes are observed outside the inclusion cavity in C and D (not shown). **E)** Mounds of halite cubes precipitated onto fracture surface during evaporation of the fluid (dissolved components). **F)** Octahedral crystals of sylvite on quartz surface. **G)** Halite intergrown with quartz. **H)** BSE image of halite showing Cu concentration on the apex of the cube (poor quality image due to an unpolished fracture surface).

Table 6.2. Identification of solid phases by optical microscopy and electron microprobe analysis.

Mineral System	Schematic	Frequency	Optical and physical properties	SEM-EDS		Identification	
				Comments	Elements detected	Name	Formula
Chlorides		MD	Cubic minerals with some crystals showing rounded corners. Largest daughter mineral (up to 3 µm). Low to moderate relief with weak to no birefringence.	Occurs as daughter minerals in open inclusions (Fig. 6.4a, b) and multiple smaller grains precipitated from the evaporated fluid (Fig. 6.4e). Crystals also seen intergrown in vein quartz (Fig. 6.4g). Numerous metals are detected in this chloride phase.	Na, Cl ± Cu ± Ni ± Ba ± Sr ± As ± Zn	Halite	NaCl
		C	Prismatic crystals with moderate to high relief, colourless to light green in colour and highly birefringent (blue interference colours).	Distinct hexagonal prism shape (Fig. 6.4c). Spatially associated with other chlorides, especially halite. Cu is detected in this chloride.	Fe, Cl ± Cu ± Mn	Fe-chloride	FeCl ₂ or Fe-chloride hydrates
		R	Not seen optically	Octahedral to rarely hexagonal crystals. Also seen in clusters precipitated from evaporated fluid (Fig. 6.4f).	K, Cl	Sylvite	KCl
		VR	Not seen optically	Ca-bearing chloride of variable composition. Often forming cubic habits, smaller than halite crystals.	Ca, Na, Cl ± Mg ± Fe	Ca-bearing chlorides	?
		C	Not seen optically	Sub-micron anhedral to hexagonal platy grains (Fig. 6.4b, d). Plates commonly attach themselves to the margins of halite cubes. Mn and Cu also detected.	Fe, Mn, O ± Cu	Haematite	Fe ₂ O ₃
		R	Not seen optically	Octahedral grains, larger than haematite (up to 1 µm) (Fig. 6.4c).	Fe, Mn, O	Magnetite	Fe ²⁺ Fe ³⁺ O ₄

Note- MD = most dominant, C = common, R = rare, VR = very rare.

Table 6.2. cont. Identification of solid phases by optical microscopy and electron microprobe analysis.

Mineral System	Schematic	Frequency	Optical and physical properties	SEM-EDS		Identification	
				Comments	Elements detected	Name	Formula
Carbonates		C	Extremely small, anhedral, high relief minerals. Strongly birefringent.	Sub-micron anhedronal grains (Fig. 6.4b,d), slightly larger than Fe oxides (not shown in Fig. 6.4). Crystals commonly attached to inclusions walls and spatially associated with Fe oxides.	Ca, O	Calcite	CaCO ₃
		C	Extremely small, anhedral, high relief minerals. Strongly birefringent.	Sub-micron anhedronal grains (Fig. 6.4b,d), slightly larger than Fe oxides. Crystals commonly attached to inclusions walls and spatially associated with Fe oxides. Contain peaks for Fe & Mg.	Ca, Fe, Mg, O	Ankerite	Ca(Fe,Mg)(CO ₃) ₂
Silicates		C	Not seen optically	Thin rectangular to hexagonal plates (Fig. 6.4d). Halite, plus other solid phases, commonly nucleated to mica surface.	K, Si, Al, O	Muscovite	KAl ₃ (Si ₃ Al)O ₁₀ (OH,F) ₂
Sulphates		C	Not seen optically	One sub-micron sulphate grain seen. Spatially associated with carbonate and magnetite.	Ba, S, O, Sr	Barite	BaSO ₄

Note- MD = most dominant, C = common, R = rare, VR = very rare.

6.5.4 Fluid inclusion populations

The modal proportions of the different fluid inclusion types in a given sample were calculated using a point count procedure (100-300 inclusions counted per sample) over random fields of view (at least ten per sample), rather than using percentages from measured inclusions during microthermometry. This was to avoid bias towards the CO₂-bearing inclusions, which are typically easier to measure microthermometrically compared to aqueous-bearing inclusions. The distribution of the four fluid inclusion types varies between deposits and between mineralised and barren veins (Fig. 6.5). Carbonic type 1 inclusions are the most dominant inclusion type in the ore zones (generally >70%), but decrease in abundance in barren quartz (42-75%). The most striking relationship is the common appearance (3-67%; mainly <20%) of type 4 inclusions within auriferous veins at the Fe-rich Gara-style deposits and the complete absence of this inclusion type from Yalea-style deposits and barren veins throughout the permit (including Gara). Aqueous-bearing type 2 inclusions are the second most dominant inclusion type in mineralised veins at Yalea Main, Loulo-3 and Baboto (mainly between 15-35%). They are also common in barren veins (3-51%), but occur in subordinate amounts at the Gara-style orebodies (0-5%). Mixed H₂O-CO₂ type 3 inclusions are less common than other fluid inclusions types (≤10%); however their abundance increases in some of the barren quartz veins (7-42%).

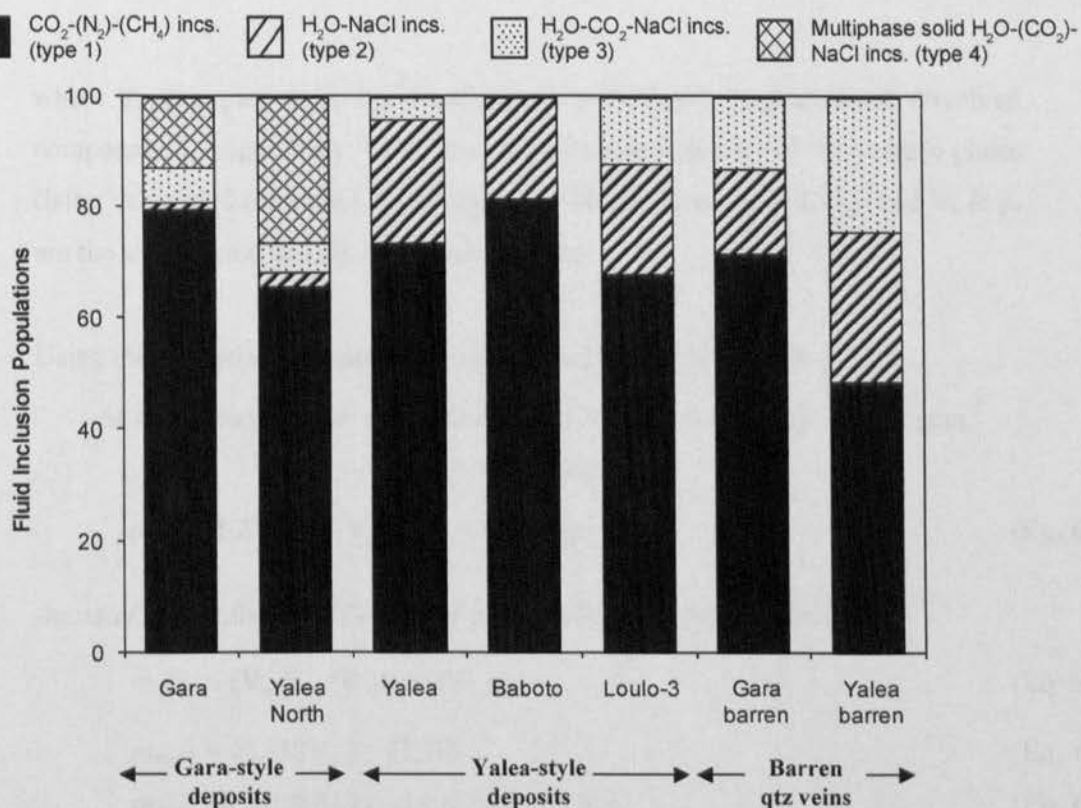


Fig. 6.5. Fluid inclusion populations in the Loulo mining district from analysis of 35 quartz vein samples (mean values given) (14 samples from Gara-style deposits, 16 from Yalea-style orebodies and 5 barren veins). *Note-* the complete absence of type 4 inclusions from Yalea-style deposits and barren quartz veins, and the dominance of type 1 and type 2 inclusions at Yalea-style deposits.

6.6 Microthermometry and Raman spectroscopy

6.6.1 Equations of state

Calculations of salinity, density of carbonic phase (ρ_{CO_2}) and bulk fluids (ρ_{tot}), molar fractions ($X_{\text{H}_2\text{O}}$; X_{CO_2} , X_{NaCl}) and pressure estimates (based on the microthermometric data-section 6.6.2) were made using the following equations of state (using the FLINCOR software): Brown & Lamb (1989) for carbonic fluid inclusions; Zhang & Frantz (1987) for H_2O -NaCl fluid inclusions; and Bowers & Helgeson (1983a,b) for inclusions in the H_2O - CO_2 -NaCl system. The abbreviations and terminology used in the following sections are summarised in Table 6.3.

Salinity was calculated using several equations: (1) from ice melting temperatures (type 2 inclusions) (Hall *et al.*, 1998); (2) from clathrate melting temperatures (type 3 inclusions) (Diamond, 1992); (3) from the dissolution of the solid phases (type 4 inclusions) (Zhang & Frantz, 1987); and (4) in the absence of (3), from estimations on the volumetric proportions of different phase present within the inclusions (*see below*). In the absence of the dissolution and/or homogenisation temperatures (*see section 6.6.2.4*), bulk density and salinity of type 4 inclusions can be calculated using the following equations:

-bulk density (ρ_{tot}) calculation:

$$\rho_{\text{tot}} = (V_{\text{aq}} \rho_{\text{aq}}) + (V_{\text{CO}_2} \rho_{\text{CO}_2}) + (V_{\text{s}} \rho_{\text{s}}) \quad (\text{Eq. 6.2})$$

where V_{aq} & ρ_{aq} are the volume and density of the aqueous phase (incl. dissolved components), respectively; V_{CO_2} ρ_{CO_2} are volume and density of the volatile phase (latter calculated from the CO_2 homogenisation temperature; T_{hCO_2}); and V_{s} & ρ_{s} are the volume and density of the solid phases.

Using the following assumptions given in Shepherd *et al.* (1985):

-At room temperature- ρ of saline water (26 wt.% NaCl equiv.) = 1.2 gcm^{-3}

- ρ of halite = 2.16 gcm^{-3}

$$\rho_{\text{tot}} = (1.2V_{\text{aq}}) + (V_{\text{gas}} \rho_{\text{gas}}) + (2.16V_{\text{s}}) \quad (\text{Eq. 6.3})$$

-mass of NaCl (dissolved [26 wt.%] and solid components) calculation:

$$m_{\text{NaCl}} = (V_{\text{aq}} \rho_{\text{aq}} * 0.26) + (V_{\text{s}} \rho_{\text{s}}) \quad (\text{Eq. 6.4})$$

$$m_{\text{NaCl}} = (0.312V_{\text{aq}}) + (2.16V_{\text{s}}) \quad (\text{Eq. 6.5})$$

$$m_{\text{NaCl}} \% = [(0.312V_{\text{aq}}) + (2.16V_{\text{s}})] / \rho_{\text{tot}} \quad (\text{Eq. 6.6})$$

- mass of H_2O and CO_2 :

$$m_{\text{H}_2\text{O}} \% = (0.888V_{\text{H}_2\text{O}}) / \rho_{\text{tot}} \quad (\text{Eq. 6.7})$$

$$m_{\text{CO}_2} \% = (T_{\text{hCO}_2} * V_{\text{CO}_2}) / \rho_{\text{tot}} \quad (\text{Eq. 6.8})$$

Table 6.3. Notations and terminology used in this chapter (as used by Diamond, 2003).

Abbrev.	Terminology	Description
	Early inclusion	A fluid inclusion trapped while the host crystal was growing.
	Late inclusion	A fluid inclusion trapped after the host crystal finished growing. Commonly located along healed microfractures.
	Clathrate	Clathrates or gas hydrates are non-stoichiometric crystalline compounds of H ₂ O molecules and gas molecules.
	True daughter minerals	Minerals precipitated from solution upon cooling of the fluid.
	Accidentally trapped minerals	Solid phases incorporated in the inclusion during fluid entrapment (not precipitated from the fluid upon cooling).
	Necking down	A post-entrapment process. Large, irregular shaped inclusions split into numerous smaller inclusions to minimise surface-free energy. These inclusions should be avoided if necking textures are clearly seen.
FIA	Fluid inclusion assemblage	A group of cogenetic inclusions occupying an individual petrographic feature or particular area of a crystal.
T _m CO ₂	Melting temperature of the CO ₂ phase	Pure CO ₂ melting point is at -56.6 °C. Inclusions showing melting temperatures below this critical temperature implies the presence of N ₂ +/or CH ₄ .
T _e	Eutectic melting temperature	This temperature refers to the first signs of liquid formation upon heating of a frozen aqueous phase. This temperature can be used to estimate the types of salt within the fluid (<i>see</i> text).
T _m ice	Ice melting temperature	The temperature at which ice completely dissolves into liquid. T _m ice is used to calculate the salinity of an aqueous fluid.
T _m cl	Clathrate melting temperature	Temperature of CO ₂ clathrate dissociation. This temperature is used to calculate salinity in mixed carbonic-aqueous inclusions.
T _h	Homogenisation temperature	The temperature at which a fluid inclusion transforms from a multiphase (heterogeneous) to a one-phase (homogeneous) state. This can occur into the liquid phase (LV→L), the vapour phase (LV→V) or homogenisation via a critical transition to a supercritical fluid (LV→SCF). This temperature represents the minimum trapping temperature.
T _h CO ₂	Homogenisation of CO ₂	In gas inclusions, T _h CO ₂ can represent partial homogenisation in mixed H ₂ O-CO ₂ inclusions (L _{CO2} L _{aq} V→LV), or final homogenisation in inclusions without a visible aqueous phase (LV→L or LV→V), at low temperatures. This temperature can be used to calculate the density of the CO ₂ phase.
T _h tot	Final homogenisation temperature	In mixed H ₂ O-CO ₂ inclusions, the final homogenisation temperature is marked by the disappearance of the aqueous liquid, or carbonic phase, or dissolution of the solid phases (T _s)
T _s	Dissolution temperature of daughter minerals	Upon heating, true daughter minerals will dissolve and the final dissolution temperature can be used to estimate salinity, if the solid phase(s) are known. During this study, halite was the only solid phase to dissolve completely prior to decrepitation.
T _d	Decrepitation temperature	The temperature at which an inclusion irreversibly ruptures or decrepitates, due to build up of internal pressure. A common phenomenon in CO ₂ -bearing inclusions.

6.6.2 Microthermometry and Raman results

The microthermometric and Raman study included detailed analysis of over 1400 fluid inclusions from 35 quartz vein samples. In this section, each inclusion type is described separately with distinctions made between auriferous and barren quartz. Comparisons are also made between deposits and deposit-styles (Gara- vs. Yalea-style) where appropriate. The full dataset for each deposit is given in the appendices (Tables A-10 to A-14) and each inclusion type is summarised in the following tables. Interpretation of the microthermometric and Raman data is given in *section 6.7*.

6.6.2.1 CO_2 -(N_2)-(CH₄) inclusions (type 1)

Gold-bearing quartz

Microthermometric data for CO_2 -(N_2)-(CH₄) inclusions are summarised in Table 6.4. Type 1 inclusions are gaseous-only inclusions (no water detected by Raman analysis or by clathrate melting). The melting temperature of CO_2 ($T_m CO_2$) varies throughout the Loulo district, which implies variable concentrations of N_2 and/or CH_4 within this inclusion type. In the Gara-style deposits, milky quartz synchronous with vein carbonate formation at Gara (termed here Gara Main vein phase) and vein quartz from the Yalea North oreshoot contain a narrow $T_m CO_2$ range from -58.5 to -56.6 °C, with a majority of inclusions showing near pure CO_2 compositions (mainly between -57.2 °C to -56.6 °C) (Fig. 6.6a). In contrast, the late grey quartz stage at Gara, which reactivate early milky quartz-carbonate veins (termed here Gara Reactivation vein phase), show more variable $T_m CO_2$ values between -75 to -57 °C, indicating the presence of additional species (Fig. 6.6a). This is revealed by Raman spectroscopy, which show the Gara Main phase and Yalea North either contain pure CO_2 compositions or minor $N_2 \pm CH_4$ concentrations (<10 mol.%), while the Gara Reactivation quartz phase show higher CH_4 contents with CO_2 - N_2 - CH_4 molar fractions of 58.3 to 100 mol.%; 0 to 18.5 mol.% (mainly <10 mol.%); and 0 to 32.7 mol.%, respectively. Representative Raman spectra from Gara are shown in Fig. 6.7 and the full dataset are presented in the CO_2 - N_2 - CH_4 ternary diagram in Fig. 6.9a.

Unlike the Gara-style deposits, type 1 inclusions from Yalea-style orebodies always contain depressed CO_2 melting temperatures (below -56.6 °C) (Fig. 6.6b). Quartz analysed from the central parts of the Yalea Main orebody (termed here Yalea Central) and from Loulo-3 shows $T_m CO_2$ mainly between -59.3 to -57.0 °C. Type 1 inclusions from the southern parts of Yalea Main (termed here Yalea South) and from Baboto show lower and more widespread CO_2 melting temperatures between -65.7 to -57.7 °C. Raman analyses reveal variable CO_2 - N_2 - CH_4 compositions, with markedly higher N_2 levels than type 1 inclusions at Gara and Yalea North. Yalea Central and Loulo-3 contain CO_2 - N_2 - CH_4 molar fraction ratios (%) of 79.7 to 95.7, 4.3 to 20.0, and 0 to 1.1, respectively. Yalea South and Baboto type 1 inclusions exhibit higher CH_4 concentrations, with CO_2 from 49.1 to 93.3 mol.%, N_2 between 0 to 45.7 mol.%, and CH_4 between

0 to 28.7 mol.%. Representative Raman spectra from Yalea Main are shown in Fig. 6.8 and the full dataset for Yalea-style deposits is graphically shown in Fig. 6.9b. In summary, type 1 inclusions in the Gara-style deposits contain $\text{CO}_2 \pm \text{CH}_4$ (\pm minor N_2) compositions, while similar inclusions in the Yalea-style orebodies contain $\text{CO}_2\text{-N}_2 \pm \text{CH}_4$ compositions.

The homogenisation of CO_2 ($T_h \text{ CO}_2$) show a wide temperature range in all the studied deposits (Fig. 6.6c, d). A majority of early type 1 inclusions homogenise into the liquid phase ($T_h \text{ CO}_2$ (L)) between 0 to +30.0 °C, representative of densities (ρ_{tot}) ranging from 0.596 to 0.928 g/cm^3 . This density range can be observed within individual FIAs (particularly in the Gara-style deposits). Late type 1 inclusions show no systematic microthermometric differences to early inclusions; however the density spread is slightly more confined within individual FIAs (± 10 °C $T_h \text{ CO}_2$ variation). Lower CO_2 homogenisation temperatures of -14.3 to +12.8 °C (to the liquid phase) can be observed towards the northern parts of the Loulo property at Baboto (Fig. 6.6d), equivalent to higher densities of 0.840 to 1.005 g/cm^3 (mainly $>0.900 \text{ g/cm}^3$). These high-density inclusions are subordinate in other deposits (e.g. Gara- maximum densities of 1.014 to 1.168 g/cm^3). High-density ($>1 \text{ g/cm}^3$) carbonic inclusions are a distinctive feature of Birimian orogenic gold deposits in Ghana and Burkina Faso (Hammond & Shimazaki, 1994; Schmidt Mumm *et al.*, 1997; Dubois *et al.*, 2001; 2007; Willie & Klemd, 2004). Extremely rarely (3 inclusions from Yalea South), type 1 inclusions homogenise into the vapour phase ($T_h \text{ CO}_2$ (V)) from +20.1 to +23.9 °C, indicative of bulk densities as low as 0.195 g/cm^3 (probably leaked inclusions).

As well as the identification of the gaseous components in type 1 inclusions, Raman spectroscopy also detected the presence of graphite/amorphous carbon as coatings on the inclusion walls (Fig. 6.7b). Graphite is exclusive to CH_4 -bearing inclusions (i.e. Gara Reactivation quartz phase, Yalea South and Baboto).

Barren quartz

Measurements of type 1 inclusions from barren Gara and Yalea quartz veins are confined to early inclusions because late inclusions were too small to measure ($<2 \mu\text{m}$). $T_m \text{ CO}_2$ occurs between -59.3 to -56.9 °C and $T_h \text{ CO}_2$ (L) from -0.4 to +30.1 °C (mainly from 10 to 25 °C), with estimated bulk densities between 0.672 to 0.930 g/cm^3 . Type 1 inclusions from barren quartz show a few distinctive features in comparison to the mineralised quartz veins: (1) a distinct lack of high-density ($>1 \text{ g/cm}^3$) inclusions; (2) $T_h \text{ CO}_2$ is more homogenous (± 5 °C) within FIAs (vary between different FIA's or more commonly between different samples); (3) Raman analysis shows high N_2 contents (particularly in Yalea barren veins) and the complete absence of CH_4 , with $\text{CO}_2\text{-N}_2$ compositions between 63.6-96.0 mol.% and 4.0-36.4 mol.%, respectively (Fig. 6.7c, Fig. 6.8c, Fig. 6.9c); and (4) no graphite/amorphous carbon was detected in the inclusions.

Table 6.4. Summary of microthermometric and Raman results for CO₂-(N₂)-(CH₄) (type 1) inclusions.

	Fl occurrence	Range	T _m CO ₂ °C	T _h CO ₂ (L) °C	T _h CO ₂ (V) °C	ρ _{tot} g/cm ³	CO ₂ * mol.%	N ₂ * mol.%	CH ₄ * mol.%
Gara-style	Early	Min	-75.0	-53.8		0.513	58.3	0.0	0.0
		Max	-56.6	31.0		1.168	100.0	18.5	32.7
		Mean	-57.4	9.4		0.866	91.9	3.8	4.2
		N	295	450		450	57	57	57
	Late	Min	-57.4	-0.1		0.707			
		Max	-56.6	25.3		0.929			
		Mean	-56.7	14.2		0.829			
		N	68	75		75			
Yalea-style	Early	Min	-65.7	-14.3	23.9	0.195	49.1	4.3	0.0
		Max	-56.7	29.3	20.1	1.005	95.7	45.7	28.2
		Mean	-59.3	9.8	21.3	0.863	79.6	14.8	5.7
		N	215	211	3	214	65	65	65
	Late	Min	-57.9	9.1		0.654			
		Max	-56.9	28.1		0.868			
		Mean	-57.3	17.6		0.798			
		N	8	8		8			
Barren qtz	Early	Min	-59.3	-0.4		0.672	63.6	4.0	0.0
		Max	-56.9	27.3		0.930	96.0	36.4	0.0
		Mean	-57.8	15.4		0.819	81.5	18.5	0.0
		N	114	160		160	38	38	38

Note- CO₂*, N₂* and CH₄* estimated from Raman analysis. Other abbreviations same as in text.

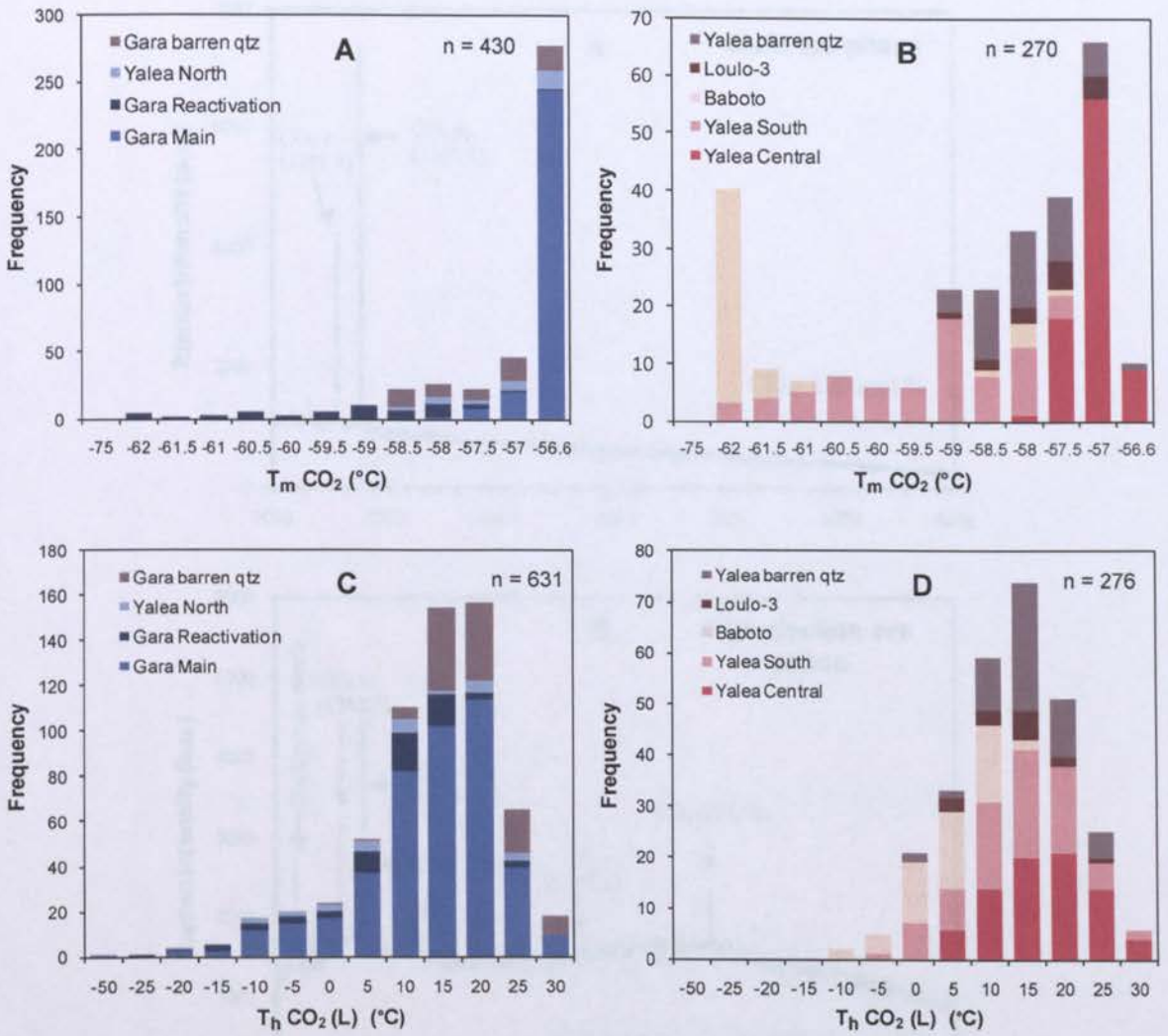


Fig. 6.6. The melting and homogenisation temperatures of CO₂-(N₂)-(CH₄) inclusions (type 1) at Loulo (early and late inclusions are not distinguished as they show similar T_m CO₂ and T_h CO₂ - see Table 6.4 for distinctions). **A)** CO₂ melting temperatures for Gara-style deposits. **B)** CO₂ melting temperatures for Yalea-style deposits. **C)** CO₂ homogenisation temperatures (into the liquid phase) for Gara-style deposits. **D)** CO₂ homogenisation temperatures (into the liquid phase) for Yalea-style deposits.

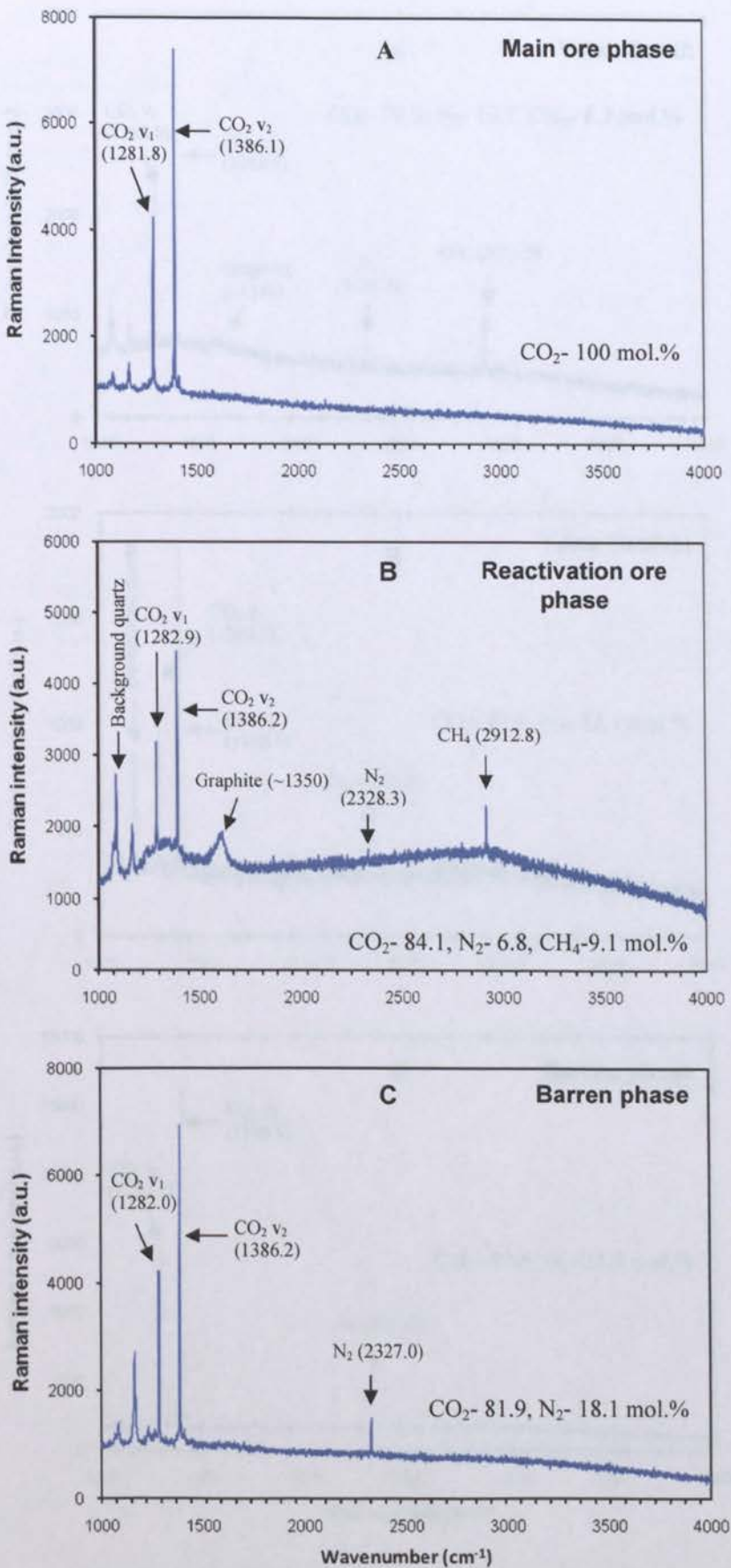


Fig. 6.7. Representative Raman spectra of CO₂-(N₂)-(CH₄) inclusions from auriferous and barren quartz at Gara. **A)** CO₂ inclusion from the main ore phase. **B)** CO₂-CH₄-N₂ inclusion from reactivated quartz, with the presence of graphite/carbonaceous matter. **C)** CO₂-N₂ fluid from barren veins. Molar fractions are given for each spectrum using Eq. 6.1.

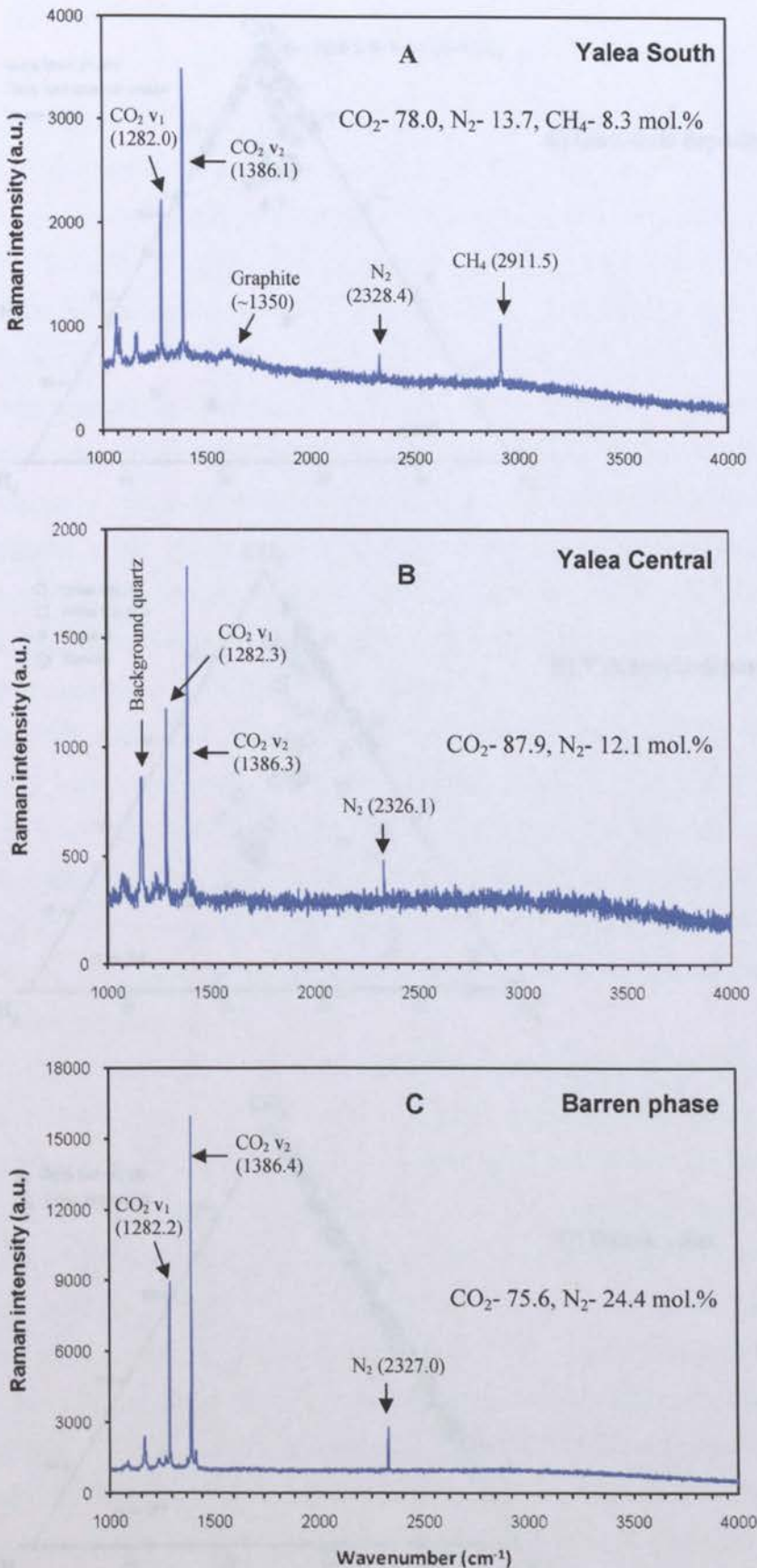


Fig. 6.8. Representative Raman spectra of CO₂-(N₂)-(CH₄) inclusions from auriferous and barren quartz at Yalea Main. **A)** CO₂-N₂-CH₄ inclusion from Yalea South, with the presence of graphite/carbonaceous matter. **B)** CO₂-N₂ inclusion from Yalea Central. **C)** CO₂-N₂ fluid from barren veins (similar composition to Yalea Central). Molar fractions are given for each spectrum using Eq. 6.1.

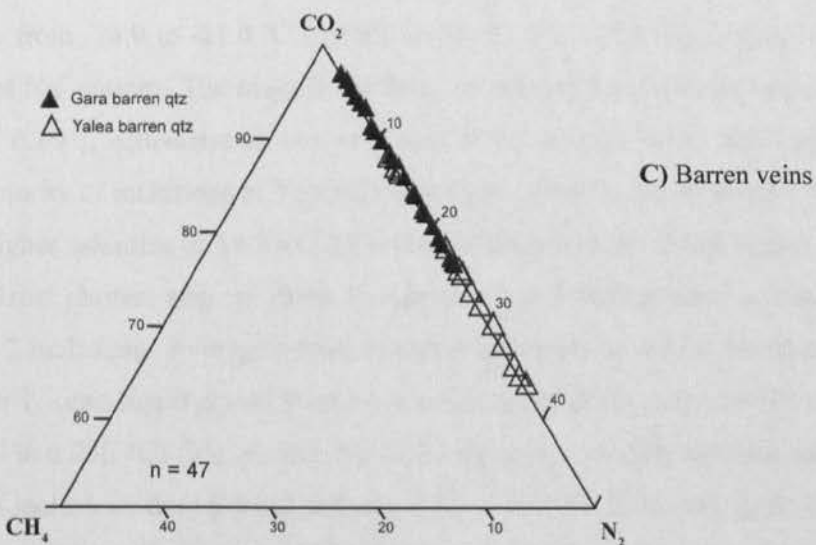
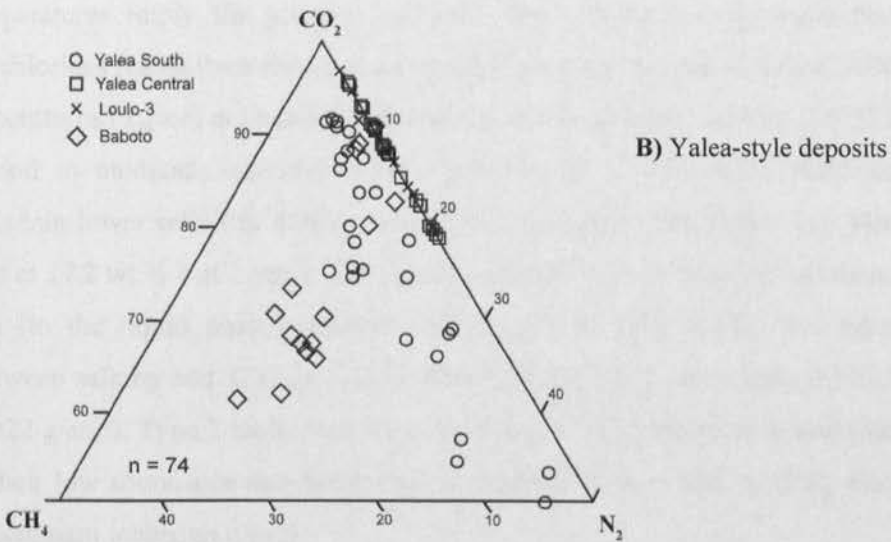
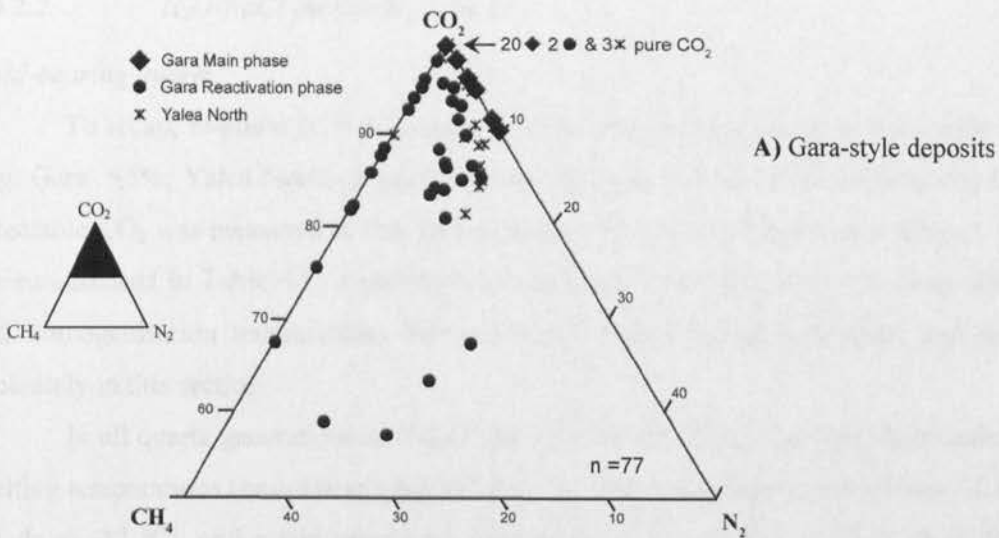


Fig. 6.9. CO₂-N₂-CH₄ ternary diagrams showing the gas fluid compositions of type 1 and type 3 inclusions at Loulo (mol.%). No systematic difference are observed between type 1 and type 3 inclusions within individual FIAs or samples (see section 6.6.2.3). Gara-style deposits are characterised by CO₂ ± CH₄ compositions (± minor N₂); Yalea-style deposits by CO₂-N₂ ± CH₄ compositions; and barren veins by CO₂-N₂ compositions.

6.6.2.2 *H₂O-NaCl inclusions (type 2)*

Gold-bearing quartz

To recap, bi-phase (L + V) aqueous inclusions are subordinate in Gara-style quartz veins (e.g. Gara- $\leq 5\%$; Yalea North- absent) but are common in Yalea-style deposits (up to 35%). No detectable CO₂ was measured in this inclusion type. Microthermometric data for type 2 inclusions are summarised in Table 6.5. Aqueous inclusions show clear differences in composition, salinity and homogenisation temperatures between Gara- and Yalea-style deposits and are discussed separately in this section.

In all quartz generations at Gara, type 2 inclusions show a bimodal distribution of first ice melting temperatures (or eutectic temperatures; T_e), with a dominant cluster from -38.8 to -31.6 °C (mode at -37 °C), and a less expressed grouping between -26.7 to -25.9 °C (Fig. 6.10a). These eutectic temperatures imply the presence of additional dissolved components besides NaCl, probably Fe chlorides (using the eutectic property table given in Van den Kerkhof, 2008). Final ice melting temperatures (T_m ice) at Gara are extremely variable between -20.4 to -2.6 °C (Fig. 6.10c) and correspond to moderate salinities mainly between 13 to 22.6 wt.% NaCl equiv. Three inclusions contain lower salinities down to 4.0 wt.% (inclusions with higher T_e). Mean salinities are estimated at 17.2 wt.% NaCl equiv. The homogenisation (T_h) of these inclusions occurs at low temperatures (to the liquid phase) between 140 to 197 °C (Fig. 6.10e). No correlation was observed between salinity and T_h (Fig. 6.11a). Bulk densities (ρ_{tot}) occur from 0.935-1.066 g/cm³ (mean of 1.022 g/cm³). Type 2 inclusions are considered to be unrelated to mineralisation at Gara because of their low abundance and occurrence in isolated clusters (not spatially associated with other more dominant inclusion types).

Type 2 inclusions from Yalea-style auriferous quartz veins exhibit uniform eutectic temperatures from -24.9 to -21.0 °C (mainly from -24.0 to -22.0 °C) (Fig. 6.10b), indicating the dominance of Na⁺ cations. The majority of final ice melting temperatures occur between -7.3 to -0.4 °C (Fig. 6.10d), equivalent to low salinities of 0.7 to 12.7 wt.% NaCl equiv. (mean at 6.9 wt.%). A minority of inclusions at Yalea Central show lower T_m ice between -15.9 to -20.7 °C and ultimately higher salinities of 19.3 to 22.8 wt.% NaCl equivalent. These higher-salinity inclusions occur in isolated clusters and are likely to represent a different generation compared to the low-salinity type 2 inclusions. Average homogenisation temperatures are higher than similar inclusions at Gara, with T_h (into liquid phase) showing a major temperature range of 176 to 350 °C (majority between 200 and 270 °C) (Fig. 6.10f). No relationship is observed between salinity and T_h (Fig. 6.11b). Five inclusions decrepitated between 253 to 320 °C. Estimated bulk densities are lower than aqueous inclusions in Gara-style deposits from 0.606 to 1.041 g/cm³ (mean of 0.896 g/cm³).

Barren quartz

Aqueous inclusions from barren quartz across Loulo show uniform characteristics. Eutectic melting temperatures range from -27.9 to -20.8 °C (Fig. 6.10a, b). Final ice melting temperatures occur from -8.0 to -0.1 °C (Fig. 6.10c, d), corresponding to estimated salinities between 0.2 to 11.7 wt.% NaCl equiv (Fig. 6.11c). These salinity values closely match salinities calculated from auriferous veins in the Yalea-style deposits and are typically lower and more uniform than those measured from Gara. Homogenisation temperatures are intermediate between Yalea- and Gara-style type 2 inclusions, with T_h from 167 to 254 °C (mean of 207 °C) (Fig. 6.10e, f).

Table 6.5. Summary of microthermometric results for H₂O-NaCl (type 2) inclusions at Loulo.

	FI occurrence	Range	T_e °C	$T_{m \text{ ice}}$ °C	T_h (L) °C	T_d °C	Salinity			
							(wt.% NaCl)	ρ_{tot}	XH ₂ O	XNaCl
Gara-style	Late?	Min	-38.8	-20.4	140		4.0	0.935	0.917	0.013
		Max	-25.9	-2.6	197		22.6	1.066	0.987	0.083
		Mean	-33.3	-13.3	158		17.2	1.022	0.941	0.059
		N	23	24	24		24	24	24	24
Yalea-style	Early	Min	-24.9	-8.9	176	250	0.7	0.606	0.957	0.002
		Max	-21.0	-0.4	350	320	12.7	0.980	0.998	0.043
		Mean	-22.4	-4.5	234	291	7.1	0.877	0.977	0.023
		N	37	53	51	5	53	51	51	51
	Late?	Min	-29.9	-20.7	176		17.8	0.937	0.916	0.062
		Max	-21.2	-14.0	270		22.8	1.041	0.938	0.084
		Mean	-23.5	-17.9	217		20.9	1.002	0.925	0.075
		N	9	11	11		11	11	11	11
Barren qtz	Early	Min	-27.9	-8	167		0.2	0.816	0.961	0.001
		Max	-20.8	-0.1	254		11.7	0.980	0.999	0.039
		Mean	-23.6	-4.2	205		6.7	0.908	0.979	0.021
		N	38	56	54		56	54	54	54

Note- XH₂O and XNaCl = mole fractions of H₂O and NaCl estimated from microthermometric data. Other abbreviations same as in text.

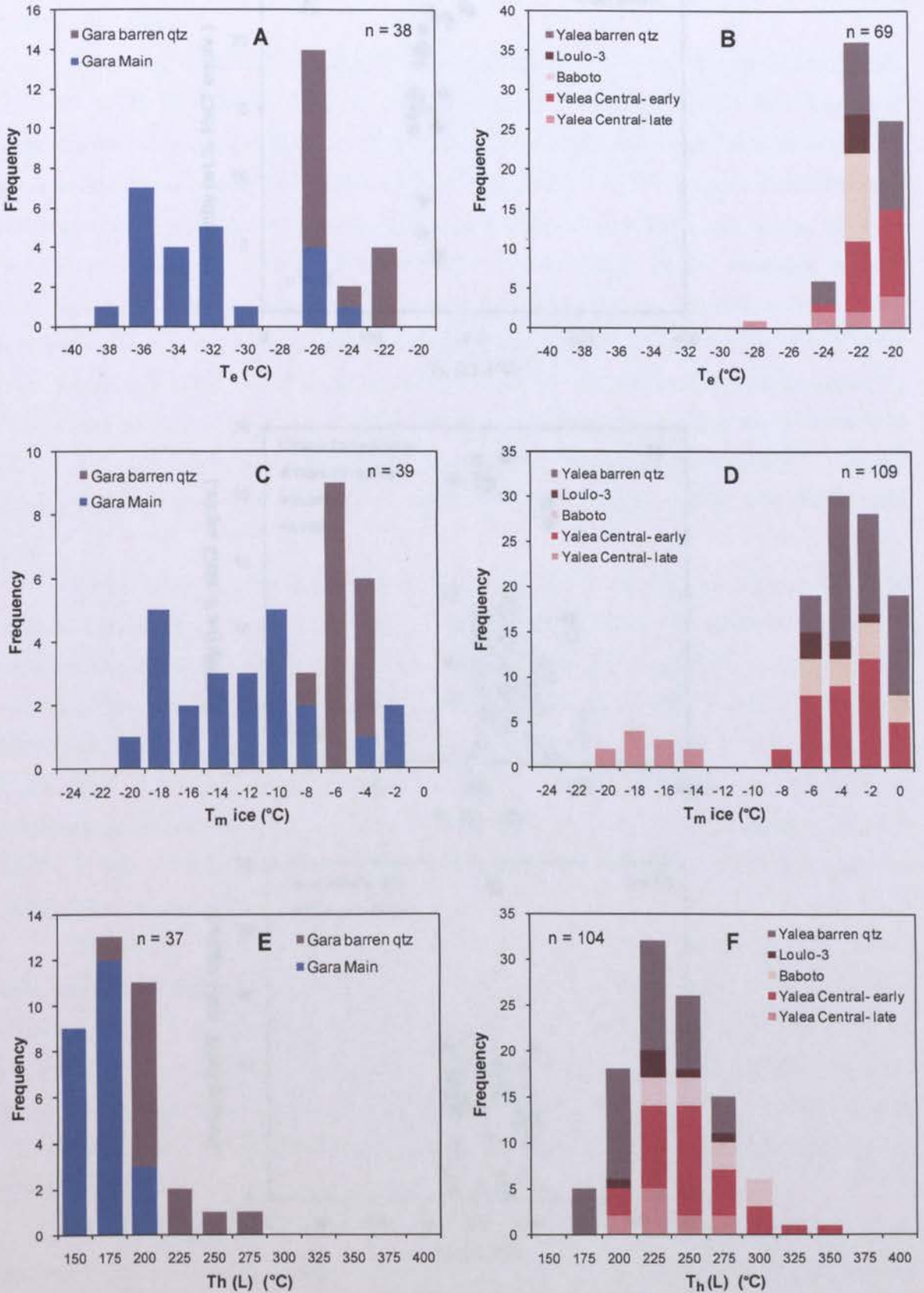


Fig. 6.10. Freezing and heating measurements for $H_2O-NaCl$ inclusions (type 2) at Loulo. **A)** Eutectic melting temperatures for Gara-style deposits. **B)** Eutectic melting temperatures for Yalea-style deposits. **C)** Final ice melting temperatures for Gara-style deposits. **D)** Final ice melting temperatures for Gara-style deposits. **E)** Homogenisation temperatures (to the liquid phase) for Gara-style deposits. **F)** Homogenisation temperatures (to the liquid phase) for Gara-style deposits.

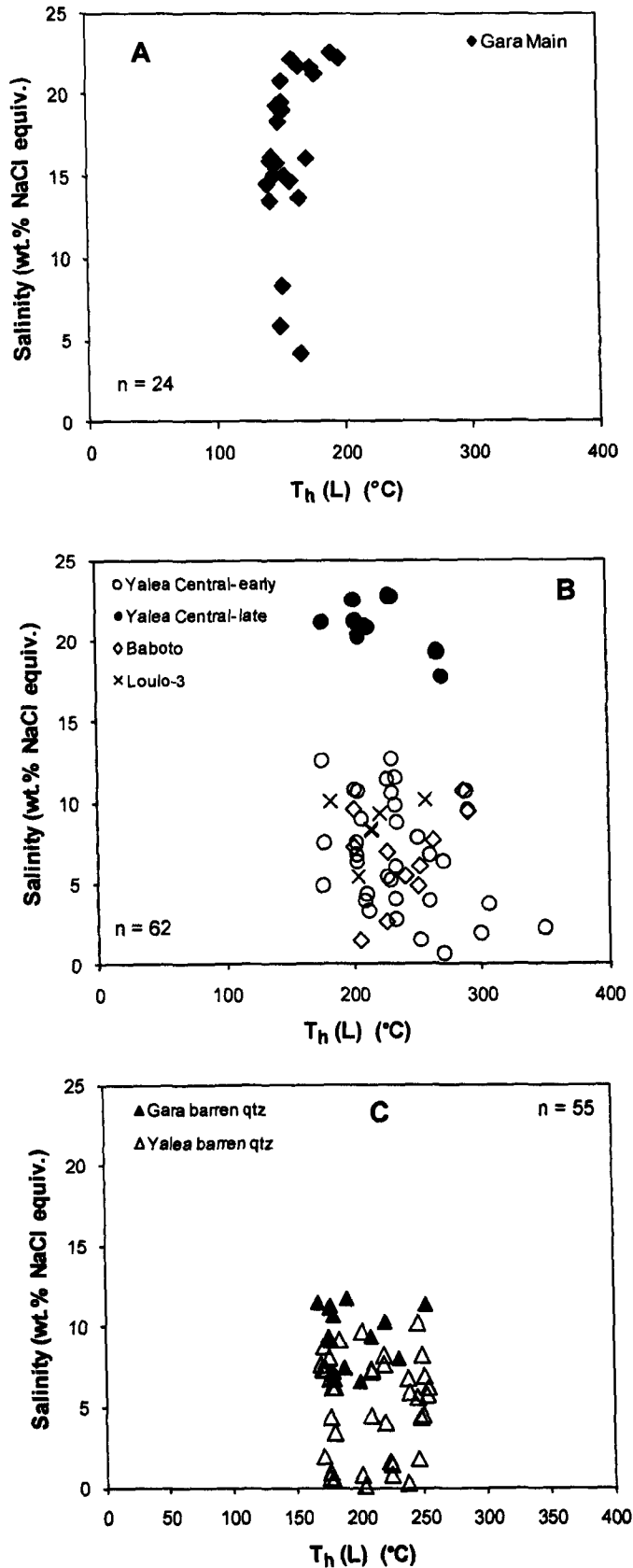


Fig. 6.11. Homogenisation temperatures vs. salinity binary plots for H_2O -NaCl inclusions at Loulo. **A)** Gara-style deposits contain moderate salinity (mainly 13-23 wt.% NaCl equiv.), low-temperature (<200 $^{\circ}\text{C}$) inclusions. **B)** Yalea-style deposits contain mainly low-salinity (<13 wt.% NaCl equiv.) inclusions with T_h occurring over a wide range from 175 to 350 $^{\circ}\text{C}$. **C)** Barren veins show similar salinities to Yalea-style deposits, with more restricted T_h between 170-270 $^{\circ}\text{C}$. No relationship is observed between salinity and T_h throughout the Loulo district for this inclusion type (in contrast to type 3 inclusions; see Fig. 6.13a).

6.6.2.3 H_2O - CO_2 - $NaCl$ inclusions (type 3)

Gold-bearing quartz

Mixed H_2O - CO_2 - $NaCl$ inclusions show a wide continuum of volumetric proportions from 10 to 90 vol.% CO_2 (V_{CO_2}) in all the studied deposits. Microthermometric data for type 3 inclusions are summarised in Table 6.6. The melting and homogenisation temperatures of the CO_2 phase are analogous to type 1 inclusions within the same FIA, or on a wider-scale within the same quartz generation (e.g. Gara Main or Gara Reactivation phase) or deposit. This is good evidence that CO_2 - (N_2) - (CH_4) and H_2O - CO_2 - $NaCl$ inclusions are genetically linked. Gara-style deposits show high T_m CO_2 mainly between -57.0 to -56.6 °C (Fig. 6.12a); an exception being the Gara Reactivation quartz, which show widespread melting temperatures between -96.0 to -57.1 °C (due to the presence of CH_4). Type 3 inclusions in the Yalea-style deposits always show depressed T_m CO_2 values (-58.5 to -57.0 °C) (Fig. 6.12b) indicating the presence of additional species apart from CO_2 . T_h CO_2 (L) occurs over a wide range in all deposits between -15.8 to $+30.0$ °C (mainly between $+5.0$ to $+30.0$ °C) (Fig. 6.12c, d), equivalent to CO_2 densities (ρ_{CO_2}) of 0.596 to 1.013 g/cm³.

Raman data show the gaseous phase of type 3 inclusions at Gara and Yalea North to be composed primarily of CO_2 (57.0-100 mol.%) \pm CH_4 (0-27.6 mol.%), with minor N_2 observed in some inclusions (0-15.5 mol.%). In contrast, Yalea-style deposits show CO_2 - N_2 compositions, with mole fractions as follows: X_{CO_2} - 79.9 to 96.8 % and X_{N_2} - 3.2 to 20.1 %. These data closely match measurements collected from type 1 inclusions. Methane present in type 1 inclusions at Yalea South and Baboto is not observed in Yalea-style type 3 inclusions because H_2O - CO_2 inclusions are absent from these two orebodies. Gas fluid compositions are presented in Fig. 6.9. Similar to type 1 inclusions, Raman analysis detected graphite/amorphous carbon in the gaseous phase within CH_4 -bearing inclusions.

The salinity of the aqueous phase in this inclusion type varies between Gara- and Yalea-style deposits (similar to type 2 inclusions). At Gara and Yalea North, melting temperatures of clathrates (T_m cl) show a scattered pattern between -6.0 to $+7.9$ °C (Fig. 6.12e), indicative of a wide salinity range from 4.5 to 21.3 wt.% NaCl equiv. (mean of 15.6 wt.%). H_2O - CO_2 - $NaCl$ inclusions measured in the Yalea-style orebodies show distinctly higher and more uniform T_m cl of $+4.2$ to $+9.0$ °C (Fig. 6.12f), corresponding to low salinities of 2.0 to 10.2 wt.% NaCl equiv. (mean of 6.0 wt.% NaCl equiv.).

The final homogenisation temperatures (T_h tot) of type 3 inclusions were difficult to measure because a majority (~50% of inclusions) decrepitated prior to homogenisation between 200 - 328 °C (Fig. 6.12k, l). Decrepitation upon heating is a common occurrence in mixed H_2O - CO_2 inclusions due to the build up of internal pressures caused by the presence of CO_2 (Shepherd *et al.*, 1985). Type 3 inclusions homogenised into both the liquid and vapour phase (due to the range in CO_2 modal proportions) between 243 to 309 °C at Yalea Central and Loulo-3 (mean of 273 °C)

(Fig. 6.12h, j), and from 251 to 351 °C at Gara and Yalea North (higher average temperatures of 300 °C) (Fig. 6.12g, i). In Gara-style deposits, this inclusion type shows a positive correlation between $T_{h\ tot}$ and salinity (Fig. 6.13a), while Yalea-style orebodies show no correlation (Fig. 6.13b); although the latter style of Loulo deposits do show a positive correlation between salinity and X_{H_2O} (Fig. 6.19). Bulk densities (ρ_{tot}) vary from 0.676-1.010 g/cm³ at Gara and Yalea North, while type 3 inclusions at Yalea Central and Loulo-3 exhibit a narrower ρ_{tot} range from 0.850-0.958 g/cm³.

Barren quartz

Mixed H₂O-CO₂-NaCl inclusions form a common inclusion type in barren veins and in places (Yalea barren quartz) comprise the most dominant inclusion type (up to 50% of the fluid inclusion population in some samples). A majority of inclusions show more homogeneous compositions compared to the mineralised veins, with CO₂ volumetric proportions between 20-35 vol.%. Microthermometric results from this inclusion type show similar CO₂ melting and homogenisation temperatures to type 1 inclusions within the same FIAs. $T_m\ CO_2$ occurs mainly from -59.8 to -57.0 °C (Fig. 6.11a, b) and $T_h\ CO_2$ (to the liquid phase) from -3.4 to +27.2 °C (Fig. 6.11c, d). A few inclusions exhibit lower CO₂ homogenisation temperatures down to -11.6 °C. Carbon dioxide densities range from 0.674 to 0.992 g/cm³ (mean of 0.832 g/cm³).

Type 3 inclusions from barren quartz show positive clathrate melting temperatures between +3.2 to +9.4 °C (higher in Yalea barren veins) (Fig. 6.11e, f), corresponding to salinities from 1.2 to 11.7 wt.% NaCl equiv (i.e. similar salinities to Yalea-style auriferous veins, but much lower than salinities calculated from Gara-style gold-bearing veins). Type 3 salinities from barren quartz closely match salinities calculated from H₂O-NaCl inclusions from the same FIA. These inclusions display a narrow range of final homogenisation temperatures, mainly to the liquid phase, between 249 to 289 °C (Fig. 6.11g, h). A minority of inclusions contain higher V_{CO_2} from 80-90 vol.% and ultimately homogenise into the vapour phase between 197 to 257 °C (Fig. 6.11i,j). These inclusions are assumed to have re-equilibrated (necked down or partially leaked). Approximately 50% of type 3 inclusions decrepitated prior to final homogenisation from 250 to 291 °C (Fig. 6.11 k, l). Bulk densities occur from 0.804 to 0.993 g/cm³. The composition of the gaseous phase, determined by laser Raman analysis of nine inclusions, show the following CO₂-N₂ gas mixtures of 73.1-96.9 mol.% and 3.1-26.9 mol.%, respectively (CH₄ completely absent) (Fig. 6.9c).

Table 6.6. Summary microthermometric and Raman results for H₂O-CO₂-NaCl (type 3) inclusions at Loulo.

Fi occurrence	Range	V CO ₂ %	T _m CO ₂ °C	T _m cl °C	T _h CO ₂ (L) °C	T _h tot (L) °C	T _h tot (V) °C	T _d °C	Salinity			ρ _{tot} g/cm ³	XH ₂ O	XNaCl	XCO ₂	CO ₂ * mol.%	N ₂ * mol.%	CH ₄ * mol.%
									(wt.% NaCl)	ρCO ₂ g/cm ³	(wt.% NaCl)							
Gara-styfe	Min	10	-96.0	-6.0	-15.8	251	261	200	4.1	0.596	0.676	0.322	0.007	0.028	57.0	0.0	0.0	
	Max	85	-56.6	7.9	30.0	351	334	328	21.3	1.073	1.010	0.952	0.071	0.667	100.0	15.5	27.6	
	Mean	35	-57.5	0.0	14.0	299	334	286	15.6	0.830	0.930	0.753	0.044	0.206	90.7	3.1	6.3	
	N	155	149	48	155	20	10	18	48	155	155	48	48	48	20	20	20	
Yalea-styfe	Min	20	-58.5	4.2	3.4	243	279	247	2.0	0.689	0.850	0.241	0.002	0.07	79.9	3.2	0.0	
	Max	90	-57.0	9.0	26.2	309	284	284	10.2	0.907	0.958	0.912	0.031	0.757	96.8	20.1	0.0	
	Mean	40	-57.7	6.7	18.4	271	282	265	6.0	0.785	0.916	0.759	0.016	0.225	89.1	10.9	0.0	
	N	18	18	18	18	8	2	8	18	18	18	18	18	18	9	9	9	
Barren qtz	Min	15	-59.8	3.2	-116	249	197	250	12	0.674	0.804	0.239	0.003	0.065	73.1	3.1	0.0	
	Max	90	-56.6	9.4	27.2	289	259	291	11.2	0.992	0.993	0.924	0.039	0.756	96.9	26.9	0.0	
	Mean	30	-57.7	6.8	13.8	261	224	274	6.1	0.832	0.938	0.811	0.016	0.172	86.5	13.5	0.0	
	N	69	63	36	71	16	4	16	36	69	69	36	36	36	9	9	9	

Note- XH₂O, XNaCl and XCO₂ = mole fractions of H₂O, NaCl and CO₂ estimated from microthermometric data. CO₂*, N₂* and CH₄* estimated from Raman analysis. Other abbreviations same as in text.

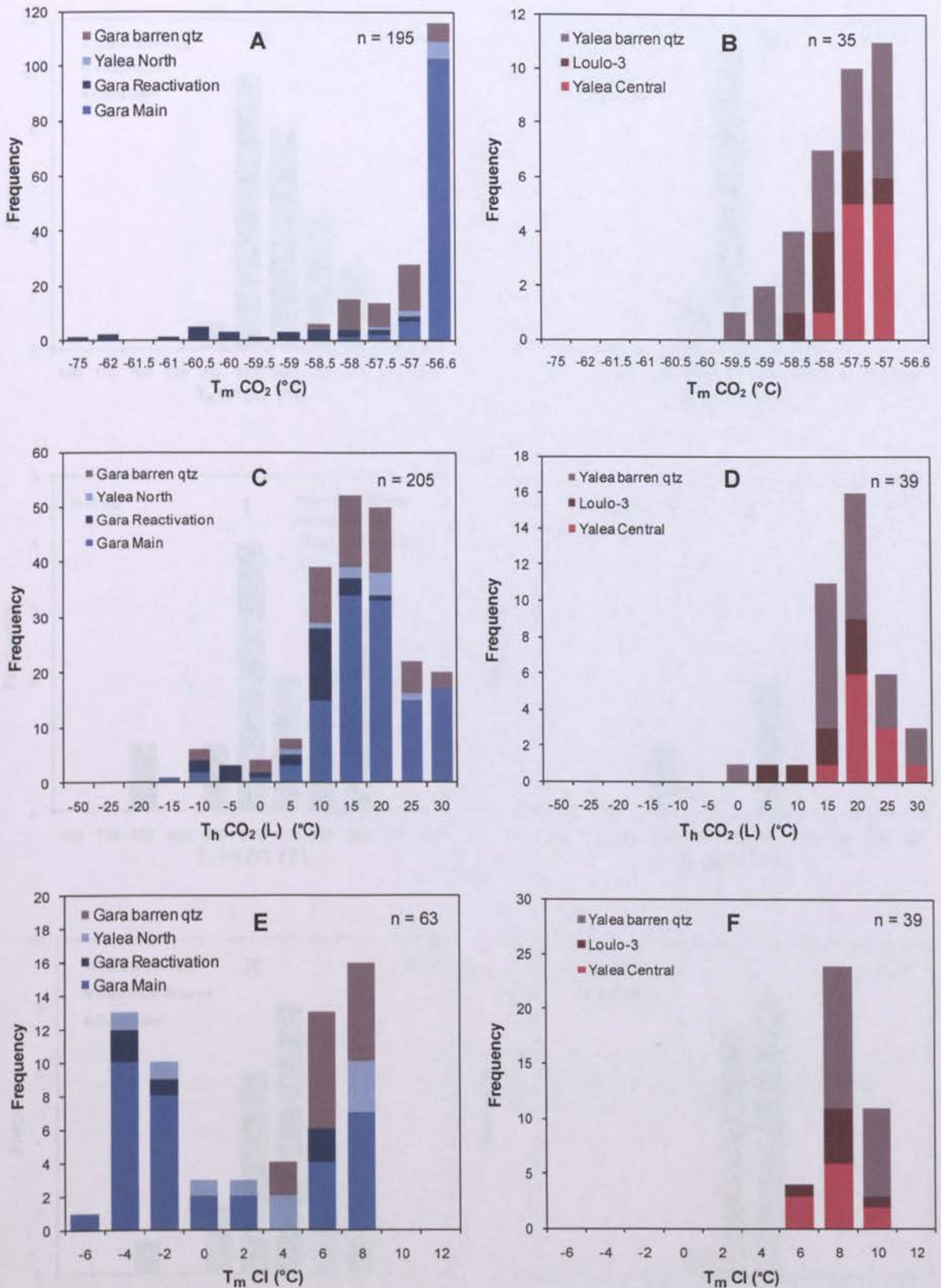


Fig. 6.12. Freezing and heating measurements for $\text{H}_2\text{O}-\text{CO}_2-\text{NaCl}$ inclusions (type 3) at Loulo. Continued on the next page. **A)** CO_2 melting temperatures for Gara-style deposits. **B)** CO_2 melting temperatures for Yalea-style deposits. **C)** CO_2 homogenisation temperatures (into the liquid phase) for Gara-style deposits. **D)** CO_2 homogenisation temperatures (into the liquid phase) for Yalea-style deposits. **E)** Clathrate melting temperatures for Gara-style deposits. **F)** Clathrate melting temperatures for Yalea-style deposits.

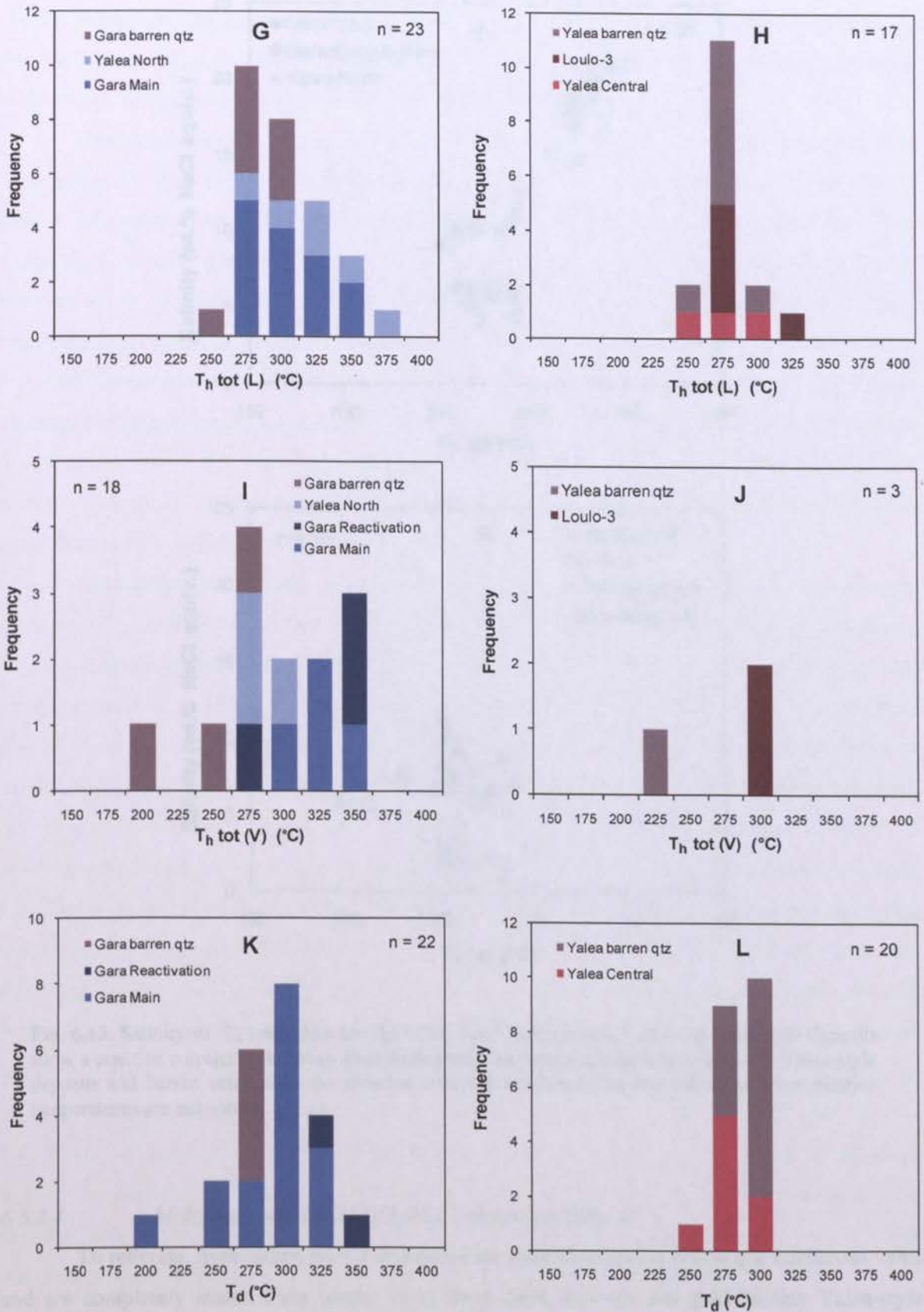


Fig. 6.12. cont. Freezing and heating measurements for $\text{H}_2\text{O-CO}_2$ inclusions (type 3) at Loulo. **G**) Homogenisation temperatures (into the liquid phase) for the Gara-style deposits. **H**) Homogenisation temperatures (into the liquid phase) for the Yalea-style deposits. **I**) Homogenisation temperatures (into the vapour phase) for the Gara-style deposits. **J**) Homogenisation temperatures (into the vapour phase) for the Yalea-style deposits. **K**) Decrepitation temperatures for Gara-style deposits. **L**) Decrepitation temperatures for Yalea-style deposits.

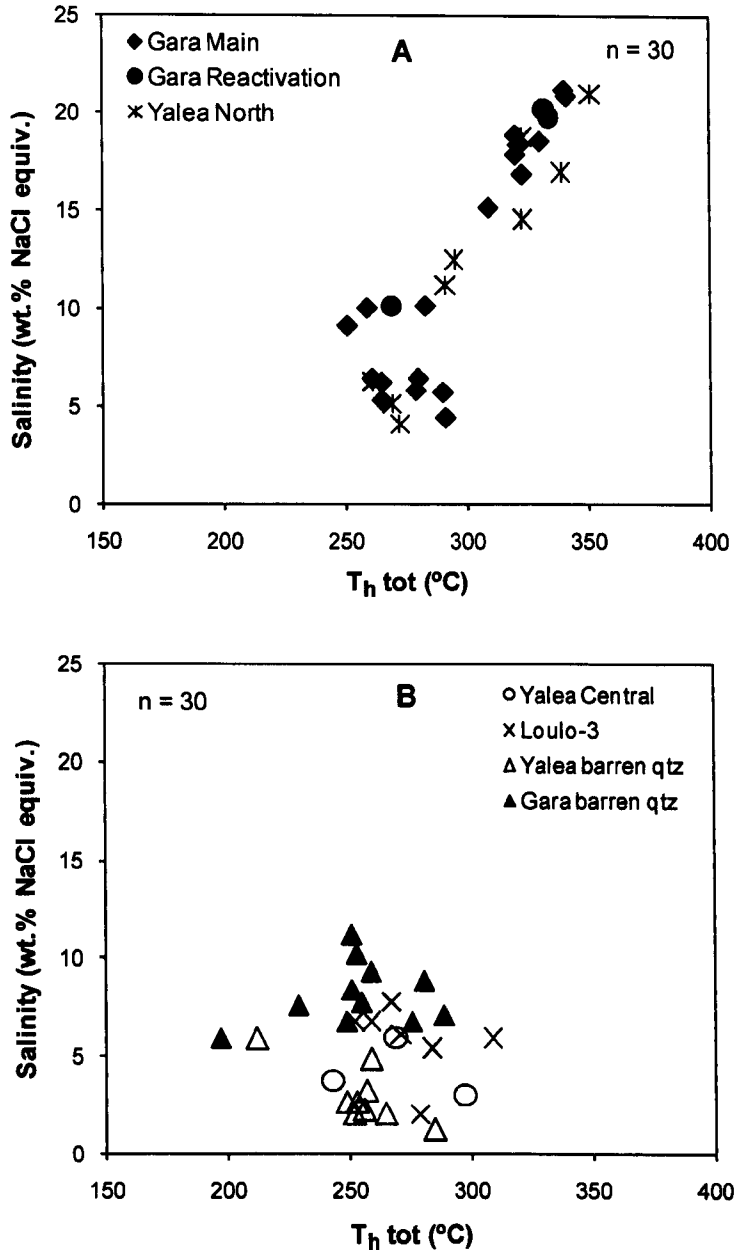


Fig. 6.13. Salinity vs. T_h total plots for H_2O-CO_2-NaCl inclusions at Loulo. **A)** Gara-style deposits show a positive correlation between final homogenisation temperatures and salinity. **B)** Yalea-style deposits and barren veins show no apparent correlation between the two variables. Decrepitation temperatures are not shown.

6.6.2.4 Multiphase solid H_2O-CO_2-NaCl inclusions (type 4)

To reiterate, hypersaline type 4 inclusions are only observed in Gara-style auriferous veins and are completely absent from barren veins from these deposits and gold-bearing Yalea-style quartz veins. These brines were extremely difficult to analyse for several reasons: (1) their small size (usually $<10 \mu m$) makes it difficult to measure phase transformations within these inclusions; and (2) inclusions often decrepitated during heating. Melting measurements on the gaseous phase closely match type 1 and type 3 inclusions within the same assemblage, with $T_m CO_2$ in the Gara

Main vein phase showing near pure CO₂ compositions (mean of -56.7 °C) and Yalea North slightly lower temperatures between -57.8 to -56.6 °C (Fig. 6.14a). The Gara Reactivation phase show a scattered T_m CO₂ pattern down to -62.8 °C, similar to other carbonic-bearing inclusions within this late auriferous vein phase, indicating the presence of CH₄ and/or N₂.

Homogenisation temperatures of the CO₂ phase show more uniform values compared to other inclusion types in the Gara-style deposits, with a majority falling between +13 and +28 °C (Fig. 6.14b), equivalent to lower CO₂ densities of 0.654-0.836 g/cm³ (mean at Gara Main and Yalea North of 0.745 g/cm³). However, brines in the Gara Reactivation phase show lower T_h CO₂ between 4.1 to 14.1 °C (Fig. 6.14b) and ultimately higher ρCO₂ of 0.830 to 0.903 g/cm³. These higher densities could be attributed to errors in the density calculation due to the presence of CH₄ ± N₂ (similar correlation observed in type 1 and type 3 inclusions; Fig. 6.6c & Fig. 6.12c). Raman analyses of the gaseous phase is limited due to the small size of the CO₂ bubble (<5 μm). Two type 4 inclusions from Gara Main quartz phase show predominately CO₂ compositions (93.7-100 mol.%) with minor N₂ (0-6.3 mol.%), while two inclusions from the latter reactivation phase exhibit mean CO₂-N₂-CH₄ contents of 86.5, 7.9 and 5.6 mol.%, respectively.

Dissolution temperatures of the solid phases (T_s) are restricted as 70% of the inclusions decrepitated prior to complete dissolution. Only inclusions with a single 'visible' grain of halite (≤ 10 vol.%) dissolved, while more multiphase solid (2 to 4 visible daughter minerals; higher salinity) inclusions contain T_s greater than T_d (although Fe chlorides were close to complete dissolution at T_d). T_s measurements of halite occur between 283 and 372 °C (Fig. 6.14c), corresponding to salinities of 36.9 to 44.5 wt.% NaCl equiv. (Fig. 6.14e). These salinities are only estimates as they do not take into account the presence of FeCl₂, which may have been in solution (difficult to determine Na:Fe ratio). To determine the full range of salinities of type 4 inclusions (salinities based on T_s biased towards the lower salinity inclusions), crude estimates can be calculated using the volumetric proportions of the salts and T_m CO₂ values (*see section 6.6.1*; Eq. 6.6) (Fig. 6.14f). Type 4 inclusions show a salinity range from 36.9 to 62.6 wt.% NaCl equiv. (mean of ~50 wt.% NaCl). Salinities calculated using the second method closely match T_s salinity values from individual inclusions (± 4 wt.% NaCl) confirming the reliability of the salinity dataset. No inclusions showed complete homogenisation before decrepitation (T_d between 250 and 380 °C; Fig. 6.14d). In the absence of T_h tot, bulk densities were calculated using the degree of fill and a number of assumptions (*see section 6.6.1*; Eq. 6.3). This inclusion type contains the highest density fluids in the Loulo district between 1.235 and 1.531 g/cm³ (mean of 1.351 g/cm³). The complete microthermometric dataset for type 4 inclusions is presented in Table 6.7.

Table 6.7. Summary of the microthermometric and Raman spectrometric data for multiphase H₂O-CO₂ (type 4) inclusions at Loulo.

Deposit/ vein phase	Range	V CO ₂ %	T _m CO ₂ °C	T _h CO ₂ (L) °C	T _h CO ₂ (V) °C	T _s °C	T _h tot (L) °C	T _h tot (V) °C	T _d °C	Salinity ¹		pCO ₂ g/cm ³	ρ _{tot} g/cm ³	XH ₂ O	XNaCl	XCO ₂	CO ₂ * mol.%	N ₂ * mol.%	CH ₄ * mol.%
										(wt.% NaCl)	(wt.% NaCl)								
Gara	Min	5	-57.8	13.7	283	258	36.9	37.3	0.654	1235	0.610	0.162	0.017	93.7	0.0	0.0			
Main phase	Max	25	-56.6	28.1	372	380	44.5	62.6	0.833	1481	0.805	0.357	0.104	100.0	6.3	0.0			
	Mean	10	-56.7	23.0	341	316	41.7	48.8	0.732	1342	0.710	0.245	0.046	96.9	3.1	0.0			
	N	22	22	22	10	22	10	22	22	22	22	22	22	2	2	2			
Gara	Min	10	-62.8	4.1	250	334	42.0	57.1	0.830	1292	0.616	0.197	0.039	86.4	6.6	4.3			
Reactivation phase	Max	20	-56.7	14.1	303	303	49.2	49.2	0.903	1436	0.764	0.316	0.095	86.7	9.1	7.0			
	Mean	16	-60.5	9.7	8	8	8	8	0.864	1364	0.688	0.252	0.060	86.5	7.9	5.6			
	N	8	8	8	8	8	8	8	8	8	8	8	8	2	2	2			
Yalea North	Min	5	-57.8	13.3	341	281	41.6	37.2	0.702	1251	0.585	0.162	0.018						
	Max	20	-56.9	25.6	353	360	42.7	62.4	0.836	1513	0.803	0.347	0.088						
	Mean	10	-57.4	19.7	347	317	42.2	50.1	0.774	1361	0.692	0.258	0.051						
	N	10	10	10	2	10	2	10	10	10	10	10	10	10	10	10			

Note- Salinity¹ estimates calculated from T_s; salinity² estimates calculated from volumetric proportions (equation 6); ρ_{tot} and XH₂O, XNaCl & XCO₂ calculated from combination of microthermometric data and volumetric estimates (section 6.6.1); CO₂*, N₂* & CH₄* estimated from Raman analysis. Abbreviations as in text.

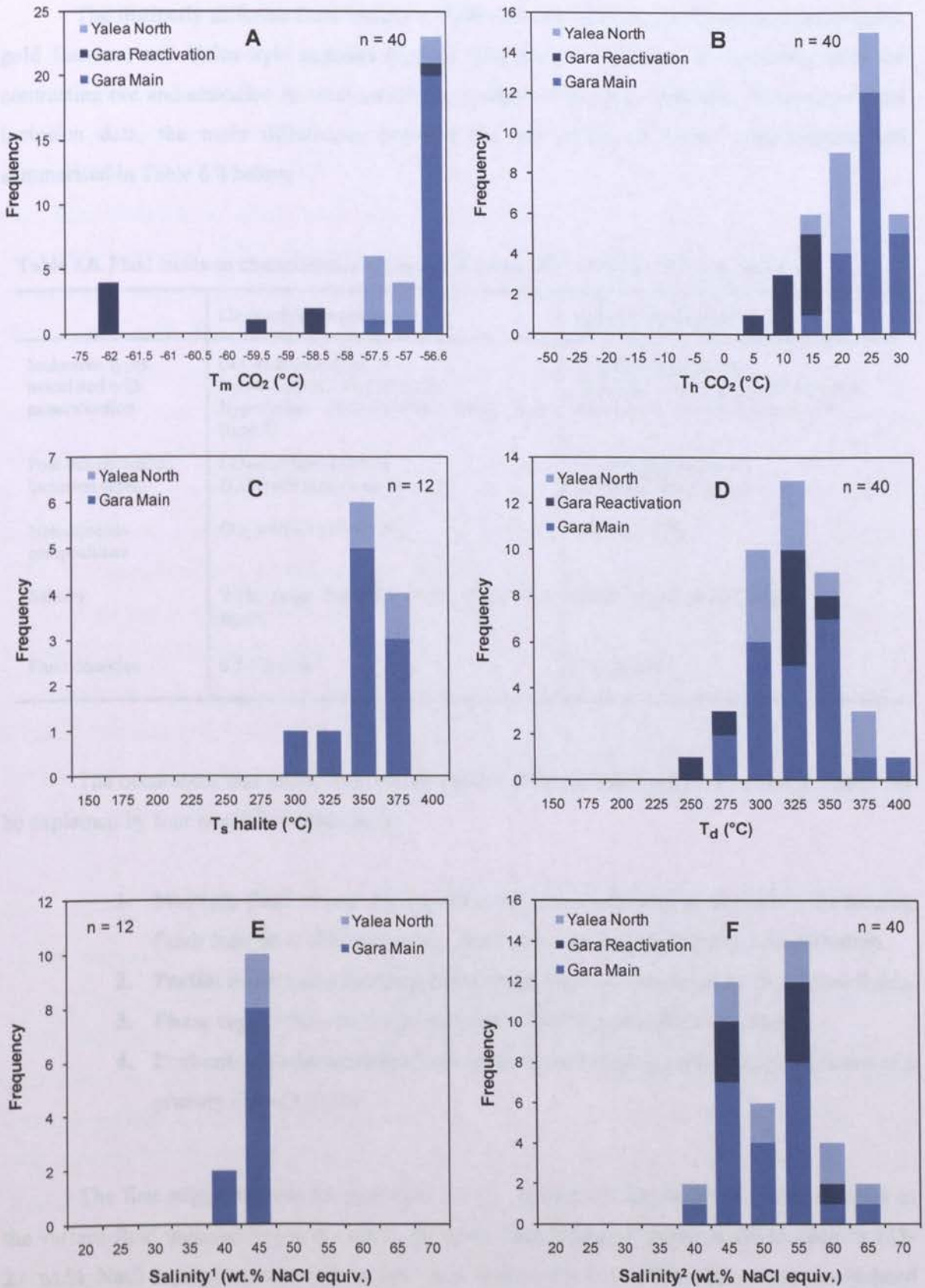


Fig. 6.14. Freezing and heating measurements for hypersaline, multiphase solid, H₂O-CO₂ inclusions (type 4) at the Gara-style deposits. **A)** CO₂ melting temperatures. **B)** CO₂ homogenisation temperatures (into the liquid phase). **C)** Dissolution temperatures of halite. **D)** Decrepiation temperatures. **E)** Salinities calculated from halite dissolution temperatures (T_s). **F)** Salinities based on visual estimates based on the volumetric proportions at room temperature and T_h CO₂ (Eq. 6.6).

6.7 Discussion

The distinctly different fluid inclusion characteristics of the Gara-style (atypical orogenic gold features) and Yalea-style deposits (typical orogenic gold features) is consistent with the contrasting ore and alteration mineral assemblages observed at these orebodies. In terms of fluid inclusion data, the main differences between the key styles of Loulo mineralisation are summarised in Table 6.8 below.

Table 6.8. Fluid inclusion characteristics of Gara- and Yalea-style orebodies in the Loulo district.

	Gara-style deposits	Yalea-style deposits
Inclusions types associated with mineralisation	CO ₂ -rich incs. (type 1) H ₂ O-CO ₂ -NaCl incs. (type 3) Hypersaline H ₂ O-CO ₂ -NaCl-FeCl ₂ incs. (type 4)	CO ₂ -rich incs. (type 1) H ₂ O-NaCl incs. (type 2) with no FeCl ₂ Minor H ₂ O-CO ₂ -NaCl incs. (type 3)
Post-mineralisation inclusion types	CO ₂ -rich incs. (type 1) H ₂ O-NaCl incs. (type 2)	CO ₂ -rich incs. (type 1) H ₂ O-NaCl incs. (type 2)
Non-aqueous compositions	CO ₂ ± CH ₄ (± minor N ₂)	CO ₂ -N ₂ ± CH ₄
Salinity	Wide range from 4.1 to 60 wt.% NaCl equiv.	Mainly <10 wt.% NaCl equiv.
Fluid densities	0.5-1.5 g/cm ³	0.6-1.0 g/cm ³

The occurrence and distribution of the various fluid inclusion types observed at Loulo can be explained by four possible mechanisms:

1. **Multiple fluid events** distinguished by chemically and/or physically contrasting fluids trapped at different stages, some of which are unrelated to mineralisation.
2. **Partial mixing and heterogeneous trapping** of two separate hydrothermal fluids.
3. **Phase separation** (fluid unmixing) of a homogeneous H₂O-CO₂ fluid.
4. **Post-entrapment modifications**, such as water leakage and/or necking down of a primary H₂O-CO₂ fluid.

The first suggestion can be dismissed for the majority of the analysed quartz samples as the various fluid inclusion types coexist in the same FIA. However, minor moderate-salinity (13-23 wt.% NaCl equiv.) aqueous inclusions from both Gara and Yalea Main occur in isolated clusters and are suggested to be unrelated to the major inclusion types and mineralisation. Late type 1 inclusions are discussed in the sections below. The origin of the major inclusion types are examined in the following sections, with seemingly different mechanisms occurring at the Gara-style (fluid mixing) and Yalea-style deposits (fluid immiscibility). Re-equilibration of the

inclusions also played minor roles in both deposit-styles.

Additionally, the dominance of carbonic inclusions (type 1) in a majority of Birimian gold deposits (Fig. 6.1) has been suggested by Schmidt Mumm *et al.* (1997, 1998) to represent the primary ore fluid expelled from deep levels of the crust or mantle. These authors suggested orogenic gold deposits, which form over a range of crustal levels, should show different fluid compositions, with H₂O-rich fluids expelled under low-grade metamorphic conditions and CO₂-rich fluids forming at higher grade conditions, as seen in many metamorphic terranes (e.g. Crawford & Hollister, 1986). However, this hypothesis fails to stand true for many orogenic gold deposits worldwide, which show uniform fluid compositions over a range of P-T conditions (e.g. Groves *et al.*, 1998, 2003; Kerrich *et al.*, 2000; Ridley & Diamond, 2000).

A primary ore fluid model for type 1 inclusions at Loulo is dismissed for the following reasons: (1) it does not explain the coexistence of other fluid inclusion types; (2) wall-rock alteration zones surrounding the orebodies are not in thermal equilibrium with a solely CO₂-bearing fluid (does not account for the tourmalinisation, chloritisation and sericitisation present in the alteration zones); (3) little is known about gold solubility in CO₂-rich fluids at depth (Klemd, 1998; Williams-Jones *et al.*, 2009); and (4) although it explains the dominance of carbonate veins in some deposits, it does not account for the precipitation of vein quartz, as SiO₂ solubility is very limited in CO₂-rich fluids (Water & Orville, 1983). The predominance of CO₂-rich fluid inclusions in orogenic belts is not particularly uncommon and is documented elsewhere in West Africa, within the Pan-African belts (Garba & Akande, 1992); in the Limpopo mobile belt, South Africa (van Reenen *et al.* (1994); and gold deposits along the Rio Itapicuru greenstone belt, Brazil (Xavier & Foster, 1999; Teixeira *et al.*, 1990).

6.7.1 Fluid immiscibility

Mineralised zones

The two major coexisting inclusion types present in the Yalea-style deposits are a CO₂-N₂ ± CH₄ fluid (type 1 inclusions) and a low-salinity (1-12.5 wt.% NaCl) aqueous fluid (type 2 inclusions). The petrographic and microthermometric data collected from these inclusions imply they are end-member fluids of a low-salinity (≤10 wt.% NaCl equiv.) mixed H₂O-CO₂ fluid. This fluid composition is typical for orogenic gold fluids (Table 1.2) and considered to be metamorphic in origin.

The likely explanations for the two end-member fluids are either fluid unmixing (phase separation) of a homogeneous parent fluid prior to entrapment or selective water leakage from mixed H₂O-CO₂ inclusions post-entrapment. In the case of the Yalea-style deposits, the major factor controlling the appearance of the various inclusion types appears to be the phase separation model (evidence given below). In the H₂O-CO₂-NaCl system, fluid immiscibility occurs when the P-T-X path of a homogenous fluid crosses the solvus surface into the two phase region (liquid and

vapour) during changes in temperature or pressure (Robert & Kelly, 1987; Diamond, 1990) (Fig. 6.15) or via expansion of solvus during interaction with graphitic sediments (Naden & Shepherd, 1989; Mernagh & Witt, 1994). The coexistence of rare H₂O-CO₂ (type 3) inclusions at Yalea Central and Loulo-3 with variable XCO₂ concentrations can be explained by the mixed entrapment of the aqueous- and carbonic end-member fluids, rather than representing the original homogenous parent fluid. This style of heterogeneous trapping is a common feature of fluid immiscibility (Robert & Kelly, 1987; Yao *et al.*, 2001).

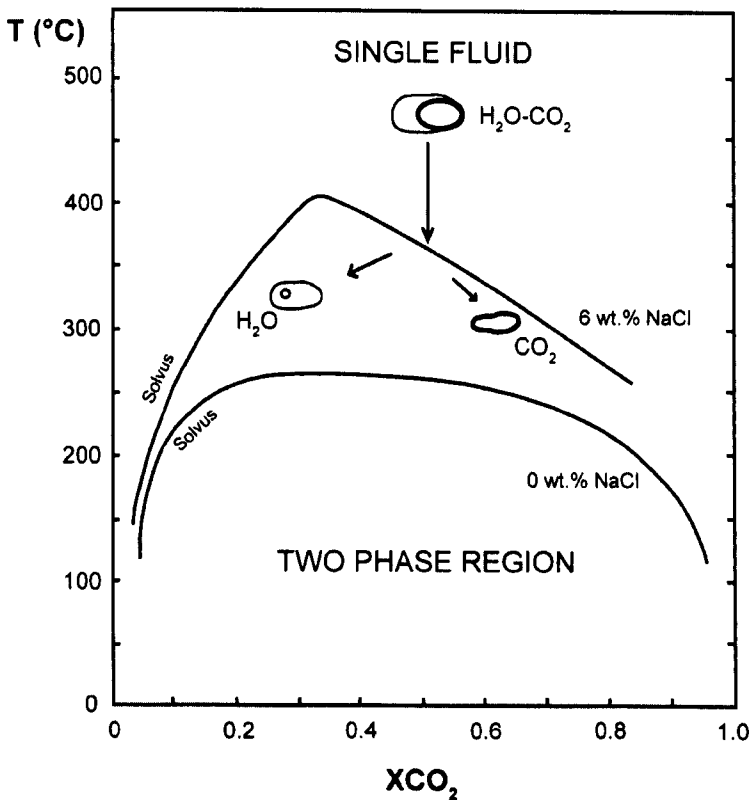


Fig. 6.15. Composition-temperature phase diagram for the system H₂O-CO₂-NaCl at 2 kbar, and 0 and 6 wt.% NaCl equiv. The position and shape of the solvus varies with increasing salinity. The exact patch of the Yalea-style primary homogenous fluids is unclear as the XCO₂ of the original fluid is unknown (not present within the inclusion assemblage- trapped below the solvus). Figure modified from Bowers & Helgeson (1983a).

Evidence for fluid immiscibility of a low-salinity H₂O-CO₂ fluid in the Yalea-style deposits following criteria outlined by Ramboz *et al.* (1982) and others is summarised below:

1. Type 1 and type 2 inclusions coexist in the same FIAs. The dominance of type 1 inclusions over type 2 inclusions can be explained by the contrasting wetting properties of H₂O compared to CO₂, with respect to quartz. The strong polarity of H₂O means that it can wet the quartz surface and remains outside the advancing crystal front during quartz growth and migrate along grain boundaries (Crawford & Hollister, 1986). Also at P-T conditions lower than 450 °C at 4 kbar, H₂O has a lower wetting angle (<60°) than CO₂ (>60°) and is more likely to be expelled from the system along grain boundaries (Watson & Brenan, 1987; Hollister, 1990; Holness, 1993) and as a result type 1 inclusions appear to be more dominant. The

predominance of type 1 inclusions at Yalea South is not consistent with fluid immiscibility but its close proximity to Yalea Central and the similar deposit characteristics to other Yalea-style orebodies suggest a similar mineralisation process was involved.

2. Type 2 inclusions show a similar salinity range (1 to 12.5 wt.% NaCl equiv.) to type 3 inclusions (2-10 wt.% NaCl equiv.), which suggests they are genetically related.
3. Type 3 inclusions show an evolutionally salinity trend, with more aqueous-rich inclusions showing higher salinities than carbonic-rich inclusions (positive X_{H_2O} vs. salinity relationship; Fig. 6.16). This is consistent with phase separation, as salt is preferential fractionated into the aqueous phase (Ramboz *et al.*, 1982; Frantz *et al.*, 1992).
4. T_m CO₂ and T_h CO₂ for type 1 and type 3 inclusions fall within the same T range, further implying a genetic link between the two fluid inclusion types.
5. Final homogenisation temperatures for type 3 inclusions are higher than T_h for type 2 inclusions, which is consistent with fluid immiscibility (more pure CO₂ and H₂O end-members trapped at lower temperatures) (Roedder, 1984).
6. In general, many researchers believe H₂O values are too low in carbonic inclusions to be compatible with phase separation of a H₂O-CO₂ fluid (Gehrig, 1980). However, these inclusions may contain microscopically undetectable H₂O (up to 15 vol.%) along the inclusion walls, especially in small inclusions (<15 μ m) (Burrus, 1981; Hollister, 1990). It must be noted, however, that no H₂O was observed during heating or by Raman analysis in this inclusion type.

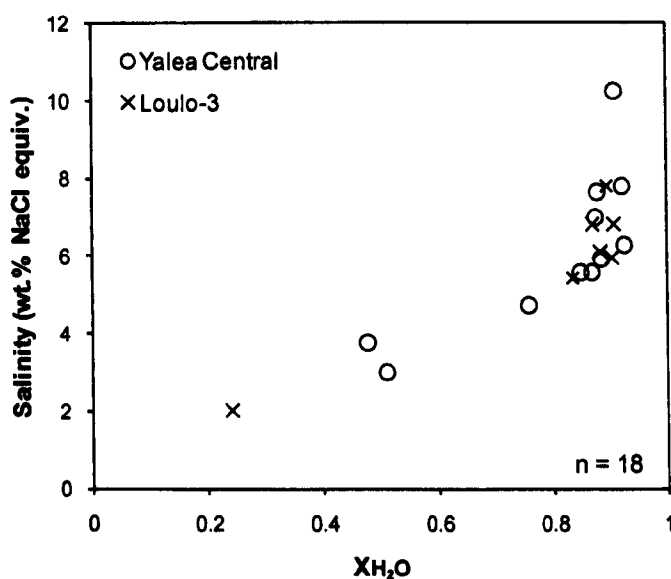


Fig. 6.16. Bulk X_{H_2O} vs. salinity plot for H₂O-CO₂ type 3 inclusions from Yalea-style gold-bearing veins. The higher salinities recorded in aqueous-rich inclusions is indicative of fluid immiscibility, as salt is fractionated in the aqueous phase rather than the carbonic phase.

Due to the variable deformation features observed in the quartz veins, re-equilibration of the fluid inclusions cannot be ignored (e.g. water leakage, necking down). Loss of water from mixed H₂O-CO₂ inclusions can occur via wicking during plastic deformation of quartz, where H₂O is driven to grain boundaries (Hollister, 1988), or by diffusion through the quartz vein via crystal defects (Bakker & Jansen, 1994). Selective leakage of H₂O fluids can occur due to the contrasting wetting properties of H₂O and CO₂, by a process known as grain boundary migration (discussed in fluid immiscibility evidence (1)), to account for the dominance of carbonic inclusions present in Yalea-style deposits. This water leakage water can also explain the wide range in T_h CO₂, densities (especially lower densities <0.6 g/cm³) and homogenisation temperatures (T_h and T_h tot). This model has been used to explain the dominance of CO₂-bearing fluids in several gold deposits in Ghana and Burkina Faso (Schwartz *et al.*, 1992; Hammond & Shimazaki, 1994; Klemd & Hirdes, 1997; Klemd *et al.*, 1997; Klemd, 1998; Willie & Klemd, 2004).

Although water leakage cannot be ruled out completely for the Yalea-style bodies, any re-equilibration of inclusions used in this study is likely to be limited in extent due to: (1) measured quartz cores are largely undeformed and analysed inclusions show little evidence of necking down; (2) the similar density range calculated for CO₂ from type 1 and type 3 inclusions within the same FIA argue against a water leakage model. If type 1 inclusions mainly form from selective water leakage of type 3 inclusions, then the former should show lower carbonic densities than the latter inclusion type, as some CO₂ will be invariably lost along with water during this process (e.g. Yao & Robb, 2000; Yao *et al.*, 2001); and (3) water leakage on such a regional scale across the whole Birimian crust seems unlikely (also suggested by Schmidt *et al.*, 1997).

Barren veins

Fluid inclusion studies on barren quartz veins from Birimian terranes in Ghana, Burkina Faso and Cote d'Ivoire (Hunken *et al.*, 1994; Klemd & Hirdes, 1997; Klemd & Ott, 1997; Coulibaly *et al.*, 2008) have shown remarkably different fluid inclusion populations to the mineralised veins. Barren veins show the predominance of aqueous and/or aqueous-carbonic inclusions, with CO₂-rich inclusions occurring as a minor phase (<15%) or are completely absent. Klemd *et al.* (1993; 1996) therefore believed the CO₂-rich inclusions can be used as important an exploration tool in the Birimian terranes of West Africa. Although aqueous bearing inclusions (type 2 and type 3) are more common in barren veins than mineralised veins at Loulo (not exclusive everywhere), CO₂-rich (type 1) inclusions are still abundant (Fig. 6.5), and therefore the above hypothesis does not appear to hold for Birimian rocks in the eastern parts of the KKI.

Fluid inclusion assemblages in the Loulo barren veins show evidence for fluid immiscibility (following criteria stated in the previous pages). However, they differ to the mineralised veins in two ways: (1) type 3 inclusions are more common and homogenous in composition, and it is suggested that this fluid represents the original fluid phase rather than heterogeneous mixtures of the two end-member fluids as indicated in the mineralised veins; and

(2) no methane was detected in the gaseous phase of the different inclusion types (more oxidised fluid). Barren fluids contain a low-salinity (mean of 6 wt.% NaCl) H₂O-CO₂-N₂ (6.5 to 17.2 mol.% CO₂-N₂) composition. The appearance of this parent fluid in the same FIAs as the two immiscible phases (type 1 and type 2 inclusions) implies the barren fluids were trapped along or close to the solvus. The absence of the original fluid phase in the mineralised veins suggests these fluids were trapped exclusively below the solvus.

6.7.2 Fluid mixing

A fluid mixing model is proposed for the Gara-style deposits to explain the coexistence of hypersaline (37 to 63 wt.% NaCl equiv.) H₂O-CO₂-NaCl-FeCl₂ inclusions (type 4) and H₂O-CO₂-NaCl inclusions (type 3) of variable compositions (5-21 wt.% NaCl equiv.; 0.040-0.667 mol.% CO₂). The bulk composition of these major inclusion types are shown in Fig. 6.18. The two fluid types are unlikely to represent two immiscible phases (as suggested for the Yalea-style bodies) as they contain notably different homogenisation temperatures and compositions (essential criteria for fluid immiscibility as outlined by Ramboz *et al.*, 1982). The observed fluid inclusion assemblage can be explained by the heterogeneous trapping of different mixtures (partial mixing) in the two-phase, sub-solvus, region. Evidence for heterogeneous trapping in the Gara and Yalea North auriferous veins is shown in the following points, using criteria established by Ramboz *et al.* (1982):

1. Simultaneous trapping of all the inclusions types of interest.
2. No clear evidence of leakage and/or necking down in the measured inclusions.
3. Scattered degree of filling, homogenisation temperatures and compositions

The precise composition of the two end-member fluids is unclear. The brine end-member is a high temperature (>400 °C; using maximum T_d values), high-density (1.35-1.5 g/cm³), aqueous-rich (X_{H₂O} of 0.7-0.8), CO₂-poor (X_{CO₂} <0.1), NaCl-FeCl₂-rich fluid, with a salinity of ~45-55 wt.% NaCl equiv. This fluid composition is typical for a magmatic derived fluid (Hedenquist & Lowenstern, 1994). The presence of both magnetite and haematite in the daughter assemblages implies *f*O₂ was close to the haematite-magnetite (HM) buffer. The second end-member fluid is a more reduced, low-density (< 1.0 g/cm³), low-salinity (<10 wt.% NaCl equiv.) H₂O-CO₂ fluid. The exact composition of this fluid type (H₂O/CO₂ ratio) is unknown as the mixing process masks the original composition of this fluid (a range of H₂O-CO₂ proportions is seen). However, it is clearly more carbonic-rich than the hypersaline fluid. The latter fluid type is likely to be similar to in composition to the Yalea-style ore fluids (metamorphic fluids) and thus temperatures can be inferred to be between 270-350 °C (using ore and alteration geothermometers, and fluid inclusion data; *see section 6.7.3* for the latter). Strong evidence for fluid mixing can be observed in type 3 inclusions, which show a positive correlation between final homogenisation temperatures and salinity (Fig. 6.17). This fluid mixing model is developed further in *chapter 8*.

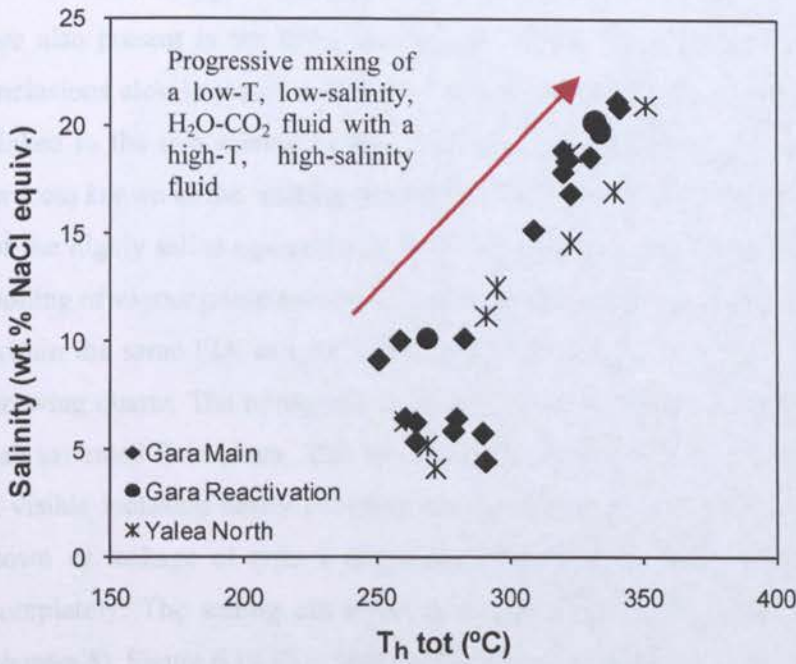


Fig. 6.17. Salinity vs. T_h total plot for H_2O - CO_2 (type 3) inclusions from Gara-style auriferous veins (redrawn from Fig. 6.13a). The plot shows a compositional trend with higher temperature fluids associated with higher salinities. This correlation reflects different degrees of mixing with a hypersaline H_2O -rich, CO_2 -poor fluid. This trend could be extended to include the high T (>400 °C), high-salinity (~ 50 wt.% NaCl equiv.) type 4 inclusions; however they failed to homogenise completely before decrepitating.

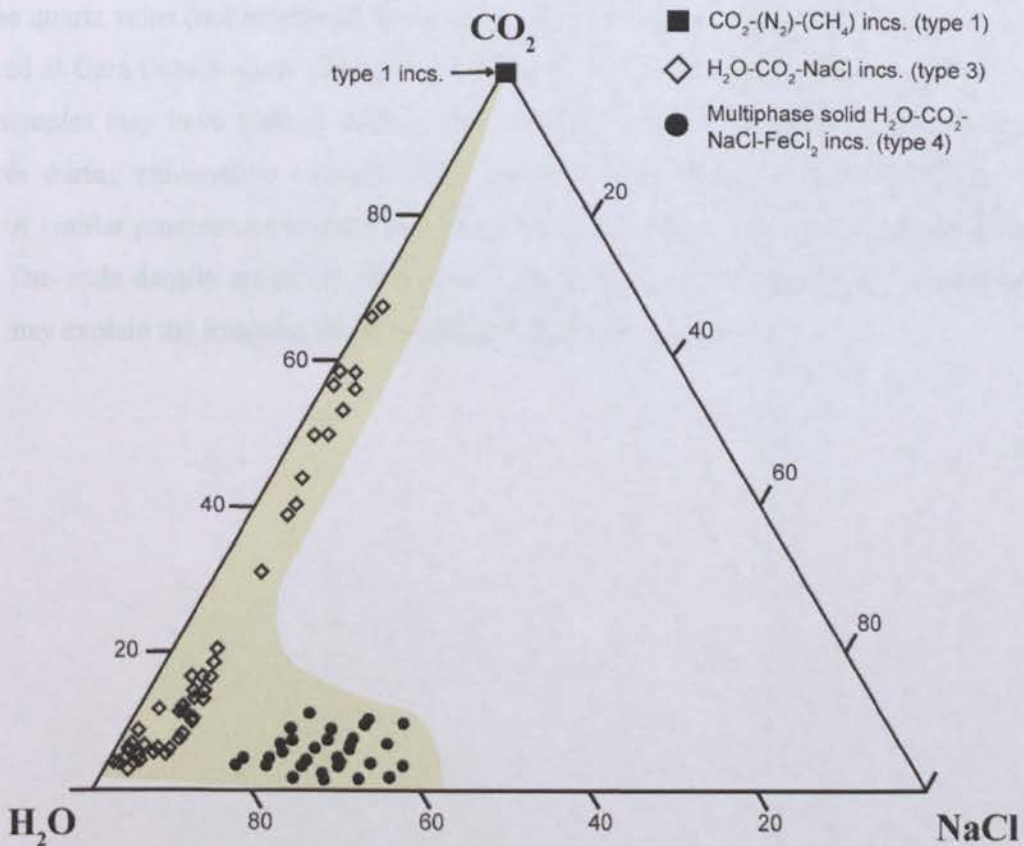


Fig. 6.18. H_2O - $NaCl$ - CO_2 ternary diagram showing the bulk molar compositions of type 1, type 3 and type 4 inclusions in the Gara-style deposits. The wide compositional range for type 3 inclusions is a distinctive feature. CO_2 -rich type 3 inclusions are common but are more difficult to measure in terms of salinity and T_h tot, and thus there is a slight bias in the dataset towards more H_2O -rich type 3 inclusions. The gap between 70% CO_2 and 100% CO_2 (i.e. type 1 inclusions) is probably due to the difficulty in detecting the aqueous phase in CO_2 -rich type 3 inclusions (mistaken for type 1). As a result, type 3 inclusions probably show a continuum from 3 to >90 mol.% CO_2 , with the CO_2 -rich inclusions forming through a process known as the 'salting out effect' during fluid mixing (see text). The shaded area represents the zone of mixing.

As well type 4 and type 3 inclusions, abundant $\text{CO}_2 \pm \text{CH}_4$ (\pm minor N_2) type 1 inclusions are also present in the FIAs. $T_m\text{CO}_2$ and $T_h\text{CO}_2$ measurements recorded for type 3 and type 4 inclusions closely match with type 1 inclusions, implying the latter inclusion type is genetically linked to the two mixing fluids. Carbonic-rich inclusions can form via fluid mixing through a process known as the ‘**salting out effect**’ (Anderson *et al.*, 1992). Due to salinity contrasts, mixing of the highly saline aqueous-rich fluid with the low-salinity $\text{H}_2\text{O}-\text{CO}_2$ fluid will cause retrograde boiling of vapour phase to form CO_2 -rich inclusions. These fluids could be trapped instantaneously within the same FIA as type 3 and type 4 inclusions, or form isolated clusters elsewhere in the growing quartz. The retrograde boiling of the CO_2 phase (in both fluid types) can leave behind a salt saturated fluid phase. This mechanism could possibly explain the solid halite crystals without a visible inclusion cavity observed during microprobe studies (Fig. 6.4g). Alternatively, necking down or leakage of type 4 inclusions could leave a halite remnant, and cannot be ruled out completely. The salting out effect is a significant gold precipitation mechanism (discussed in *chapter 8*). Figure 6.19 illustrates the fluid mixing model proposed for the Gara-style orebodies.

Re-equilibration of the fluid inclusions in the Gara-system cannot be ruled out completely as some quartz veins (not measured) show strong recrystallisation textures. Late type 1 inclusions observed at Gara (which show similar $T_m\text{CO}_2$ and $T_h\text{CO}_2$ values to early type 1 inclusions in the same sample) may have formed during selective leakage and re-trapping of CO_2 along microfractures during exhumation into the brittle realm (CO_2 leakage via hydrofracturing; Klemd, 1998). A similar process can be used to explain the appearance of late type 1 inclusions at Yalea Main. The wide density spread in early type 1 inclusions could be the result of necking down, which may explain the irregular shape of some of the larger inclusions.

Zone of partial mixing and heterogeneous trapping

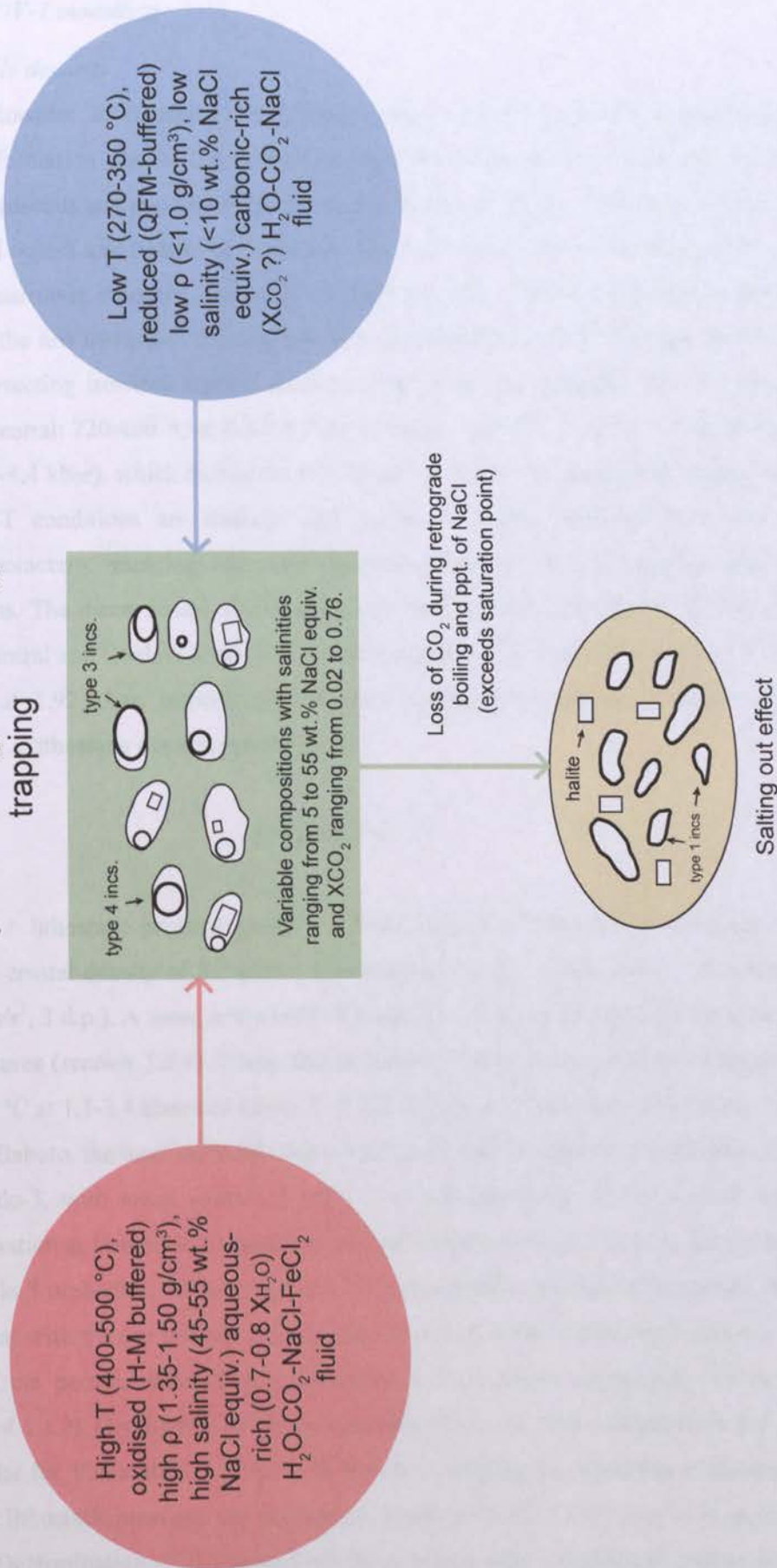


Fig. 6.19. A schematic sketch of the fluid mixing model proposed for the Gara-style deposits. Model developed further in Fig. 8.3.

6.7.3 P-V-T modelling

Yalea-style deposits

Roedder & Bodnar (1980) demonstrated that pressure and temperature estimates on mineral formation can be determined through the intersection of isochores of coexisting end-member gaseous and aqueous fluid inclusions. Isochores of type 1 and type 2 inclusions for Yalea Central, Loulo-3 and Baboto are shown in Fig. 6.20. In the case of Yalea Central, where densities show a narrower standard deviation to other deposits, a 95% confidence level was used (i.e. ignoring the few inclusions showing low and high densities outside the range shown in Fig. 6.21a). The intersecting isochore method shows a large zone of entrapment for all Yalea-style deposits (Yalea Central: 220-460 °C at 0.8-2.8 kbar; Loulo-3: 245-425 °C at 1.1-2.6 kbar; Baboto: 300-610 °C at 1.6-4.4 kbar), which makes the P-T ranges irrelevant for geological interpretation. However, mean P-T conditions are realistic and similar to values obtained from ore and alteration geothermometers, implying that they represent good estimates of average gold mineralisation conditions. The mean values also demonstrate the cogenetic trapping of the two inclusion types. Yalea Central and Loulo-3 share similar P-T conditions for mineralisation: 340 °C at 1.8 kbar and 335 °C at 1.92 kbar, respectively. Pressure estimates correspond to depths of 6.8-7.25 km, assuming a lithostatic overburden (Eq. 6.9).

$$P = z * \rho(z) * g \quad (\text{Eq. 6.9})$$

where P = lithostatic pressure (bar); z = depth (m); $\rho(z)$ = density of overlying rock at depth z (average crustal density of 2.7 g/cm³; Hawkesworth *et al.*, 2010); and g = acceleration of gravity (9.813 m/s², 3 d.p.). A more restricted P-T range can be obtained using the intersections of chlorite temperatures (*section 5.5.4*). Using this technique, Yalea shows estimated trapping conditions of 294-333 °C at 1.1-2.4 kbar and Loulo-3 of 271-312 °C at 1.2-2.2 kbar (Fig. 6.20a, b).

Baboto, the most northerly deposit at Loulo, shows higher P-T conditions than Yalea Main and Loulo-3, with mean values of 440 °C at 2.9 kbar (Fig. 6.20c). Crustal emplacement for mineralisation at Baboto is estimated at 10.9 km, approximately 3.5-4 km deeper than Yalea Main and Loulo-3 orebodies, suggesting depth of mineralisation shallow to the south. This model is in agreement with the ore mineral assemblages observed in the Faraba-style deposits in the southern parts of the permit, which imply precipitation from lower temperature fluids (<260-300 °C) (*section 4.6.3.2*). Geothermal gradients calculated from the mean temperature and depth estimates are similar for Yalea Main, Loulo-3 and Baboto, verifying the reliability of the dataset. Assuming constant lithostatic pressure, the geothermal gradient for the Loulo district is approximately 40-50 °C/km. Determination of P-T conditions from mixed type 3 inclusions proved ineffective due to heterogeneous trapping of this inclusion type.

The wide range of P-T conditions observed in the Yalea-style orebodies (Fig. 6.20) could be the result of several factors. Firstly at Yalea, a decrease in pressure is likely as fluids entered the dilational N-S Yalea shear. Secondly, the fault valve model of Sibson (1987) and Sibson *et al.* (1988) implies that fluid pressures in active shear zones may fluctuate from near lithostatic to near hydrostatic conditions (the latter accounting for the lower P-T values). Minerals trapped during this process will record variations in P-T-X properties of the fluid (Hagemann & Cassidy, 2000; Sibson, 2001; Yao *et al.*, 2001; Coulibaly *et al.*, 2008; Zoheir *et al.*, 2008; Zoheir & Akawy, 2009). Evidence for fault-valve behaviour can be seen at Loulo, with many mineralised vein showing multiply stages of reactivation and brecciation (although laminated veins are limited in extent). These processes outlined in the first two points could be the cause of the fluid phase separation in the Yalea-style deposits, as determined by microthermometric work. However, pressure fluctuations alone are unlikely to cause such a spread in bulk densities. Some degree of re-equilibration of the inclusions could be a contributing factor (e.g. Schwartz *et al.*, 1992; Willie & Klemd, 2004). Furthermore, calculated density inaccuracies of type 1 inclusions could be present if these inclusions contain undetectable H₂O along the inclusion walls (underestimation of bulk densities in some inclusions).

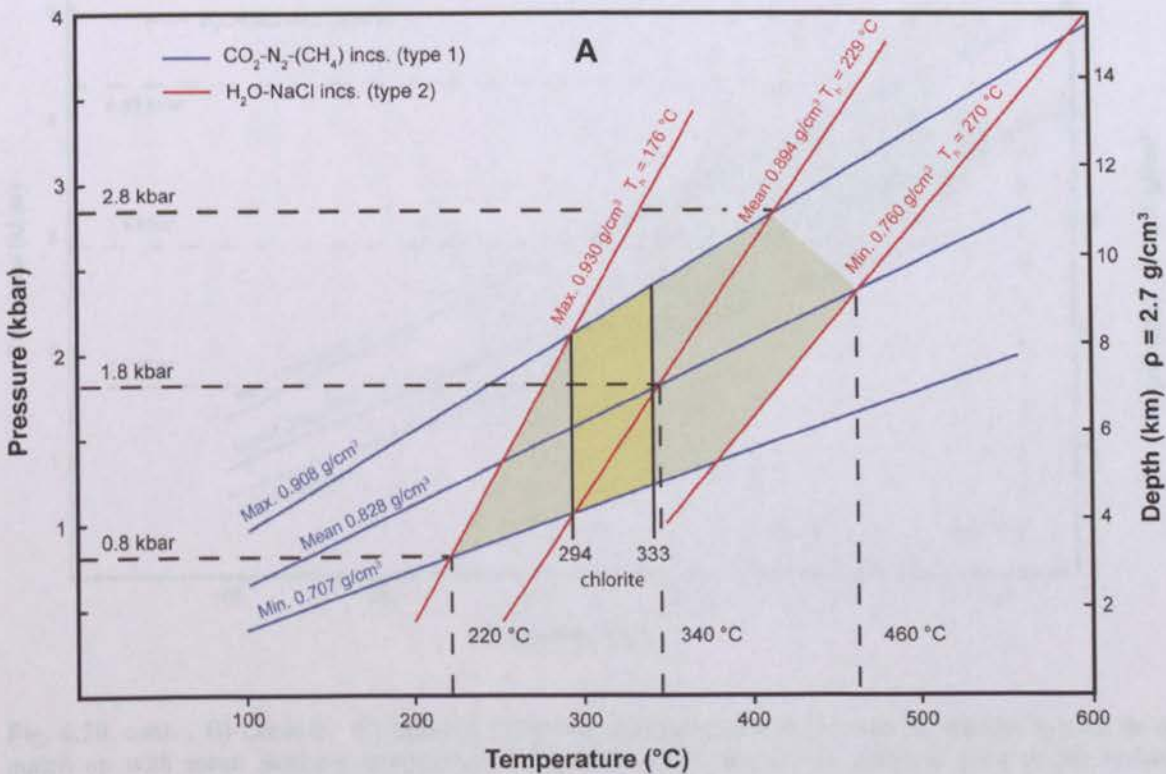


Fig. 6.20. Isochores for minimum, maximum and mean bulk densities for type 1 and type 2 inclusions from Yalea-style mineralised quartz veins. Intersections are also shown with chlorite temperatures determined in section 5.5.4, which are assumed to be coeval with mineralisation. The zone of trapping is shown by the shaded fields. Intersection of maximum isochore of type 1 with minimum isochore of type 2 inclusions is ignored because of the unrealistically high P-T conditions (inclusions mostly likely to have leaked). **A)** Yalea Central.

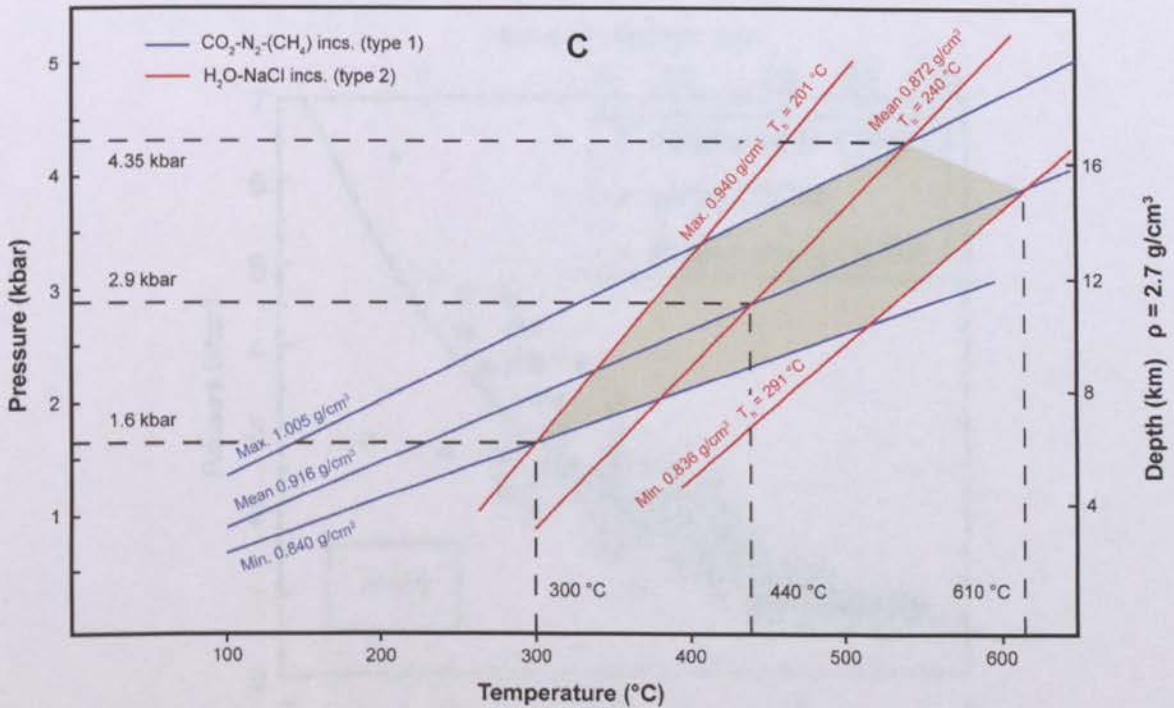
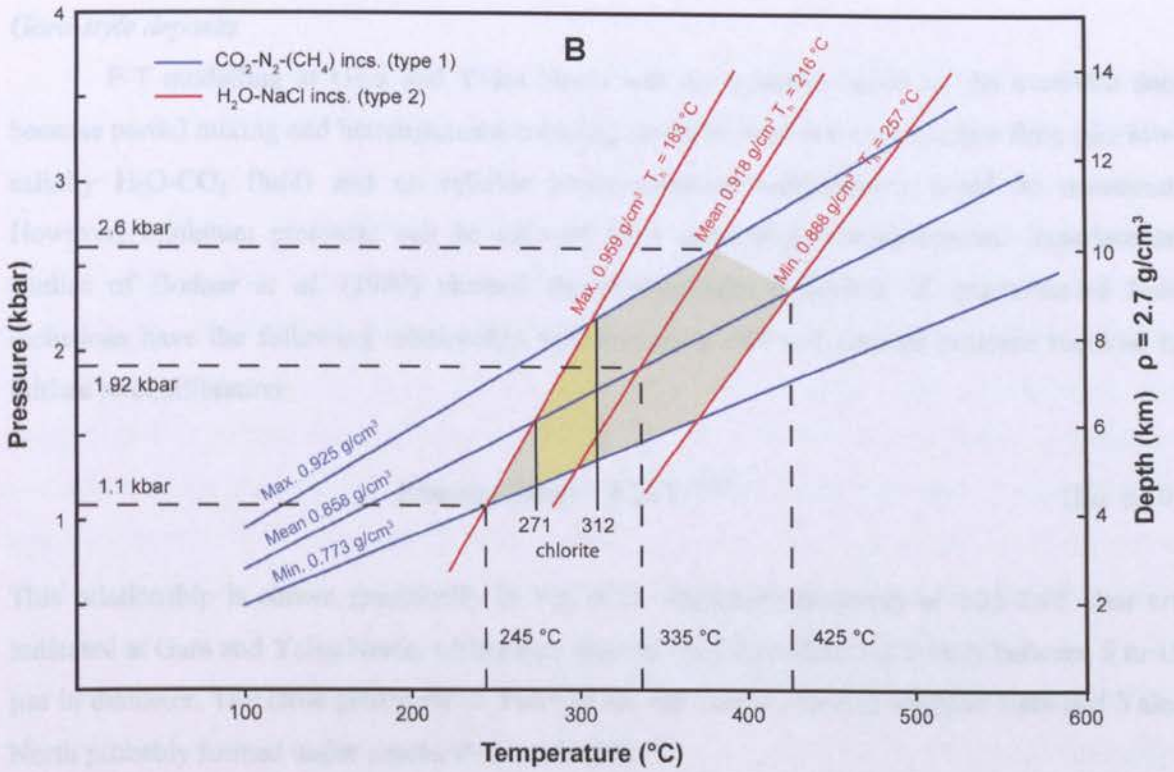


Fig. 6.20. cont. . **B)** Loulo-3. **C)** Baboto. Chlorite temperatures are not shown for Baboto as they do not match up with mean isochore intersections (chlorite samples taken from different parts of the orebody compared to the fluid inclusion samples).

Gara-style deposits

P-T modelling at Gara and Yalea North was not possible based on the available data because partial mixing and heterogeneous trapping masks at least one end-member fluid (the low-salinity H₂O-CO₂ fluid) and no reliable homogenisation temperatures could be measured. However, minimum pressures can be inferred from decrepitation temperatures. Experimental studies of Bodnar *et al.* (1989) showed the decrepitation behaviour of quartz-hosted fluid inclusions have the following relationship with inclusion size and internal pressure required to initiate re-equilibration:

$$\text{Pressure (kbar)} = 4.26 D^{-0.423} \quad (\text{Eq. 6.10})$$

This relationship is shown graphically in Fig. 6.21. Minimum pressures of 1.35-2.15 kbar are indicated at Gara and Yalea North, taking into account fluid inclusions are mainly between 5 to 15 μm in diameter. The close proximity to Yalea Main and Loulo-3 bodies suggests Gara and Yalea North probably formed under similar P-T conditions.

Fig. 6.21. Relationship between inclusion size and the pressure required to initiate re-equilibration in quartz-hosted fluid inclusions under atmosphere confining pressure. Data from Swanenburg (1980), Leroy (1979) and Bodnar *et al.* (1989). Figure from Bodnar (2003).

Barren veins

The fact that fluid inclusions from barren veins were trapped close to the solvus suggests P-T fluctuations were limited during vein formation compared to the mineralised veins. However, this is not observed in the isochore plots (re-equilibration overprint?). Isochores of type 1 and type 2 inclusions show a wide zone of emplacement similar to Yalea-style mineralised veins (Fig. 6.22a). Mean isochore intersections correspond to lower P-T conditions than the mineralised veins at 295 °C at 1.55 kbar. True trapping conditions are best estimated using bulk densities measured from type 3 inclusions, as these inclusions represent the original fluid. Accordingly, final homogenisation temperatures of this inclusion type provide minimum trapping temperature conditions of the hydrothermal fluid (e.g. Touret & Dietvorst, 1983). Minimum T_h tot of 249 °C and maximum T_d of 291 °C represent the best temperature range approximation of the barren fluids (ignoring inclusions which show evidence of necking down and stretching). This range is slightly lower than trapping temperatures calculated from the two immiscible fluid phases (295 °C). Isochores of minimum and maximum bulk densities suggest pressure estimates 0.75 to 2.15 kbar (Fig. 6.22b), with depths of vein formation occurring between 3-8 km. P-T modelling implies barren veins formed under lower P-T conditions compared to the mineralising veins, and thus pressure and temperature may play an important role in gold transport and deposition in the Loulo district (discussed in *chapter 8*).

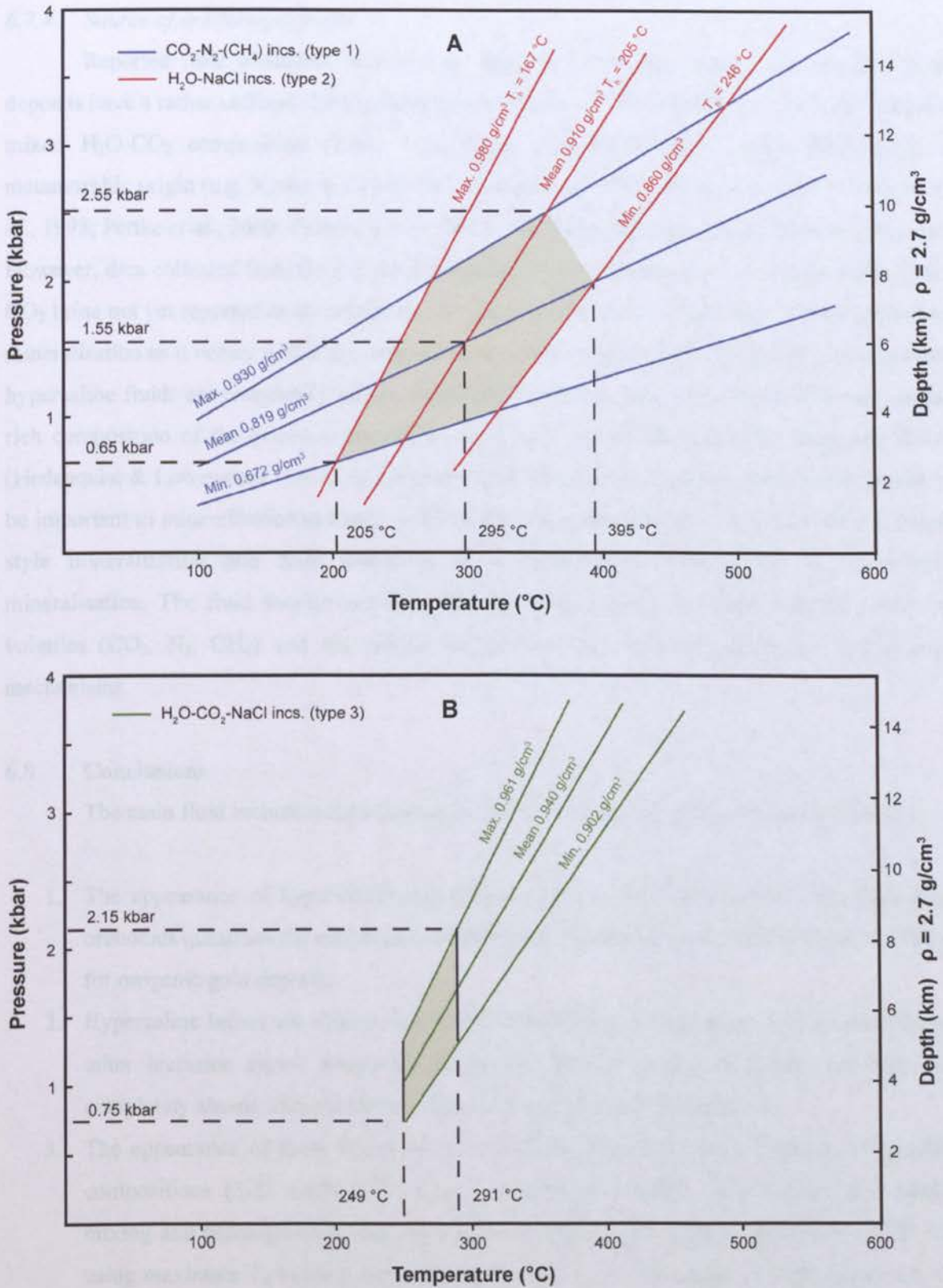


Fig. 6.22. Isochore plots of barren veins from Gara and Yalea. **A)** Isochores of type 1 and type 2 inclusions using minimum, maximum and average bulk densities (type 2 inclusions- 95% confidence level). Shaded zone represents zone of entrapment. **B)** Isochores of the highest and lowest bulk density of type 3 inclusions. The shaded field represents intersections with maximum and minimum T_h tot (L) and T_d (249-291 °C) measured from this inclusion type (zone of entrapment). Bulk density values ignore the few inclusion that homogenised into the vapour phase and inclusions showing densities up to 0.993 g/cm³ (due to dense CO₂ phase). Scale on right side of both diagrams refers to depth in km at rock density of 2.7 g/cm³ for lithostatic overburden.

6.7.4 Source of ore-forming fluids

Reported fluid inclusions studies from deposits of all ages imply most orogenic gold deposits have a rather uniform fluid composition, typified by a low-salinity (<10 wt% NaCl equiv) mixed H₂O-CO₂ composition (Table 1.2). Many researchers believe these fluids have a metamorphic origin (e.g. Koons & Craw, 1991; Powell *et al.* 1991; Stüwe *et al.*, 1993; Jamison *et al.*, 1998; Pettke *et al.*, 2000; Pitcairn *et al.*, 2006). Such fluid compositions are observed at Loulo. However, data collected from Gara-style deposits also show the occurrence of a hypersaline H₂O-CO₂ brine not yet reported in other Birimian orogenic gold deposits. This brine is clearly linked to mineralisation as it occurs within the same FIAs as the low-salinity H₂O-CO₂ inclusions, and these hypersaline fluids are completely absent from barren veins at Gara. The Na-Fe-Ca-K-base metal rich composition of the brines is analogous to mineral deposits derived from magmatic fluids (Hedenquist & Lowenstern, 1994). In summary, both metamorphic and magmatic fluids appear to be important to mineralisation at Loulo, with fluid mixing between the two fluids linked to Gara-style mineralisation and fluid unmixing of a metamorphic fluid linked to Yalea-style mineralisation. The fluid sources are discussed further in *chapter 8*, along with the source of volatiles (CO₂, N₂, CH₄) and ore related components, and metal transport and depositional mechanisms.

6.8 Conclusions

The main fluid inclusion characteristics of the Loulo orebodies are summarised below:

1. The appearance of hypersaline H₂O-CO₂-NaCl-FeCl₂ fluid inclusions in the Gara-style orebodies questions the established metamorphic fluid model (low-salinity H₂O-CO₂ fluid) for orogenic gold deposits.
2. Hypersaline brines are clearly linked to mineralisation as they occur in the same FIA as other inclusion types, numerous metals are detected in the chlorides, and they are completely absent from the barren veins surrounding Gara-style deposits.
3. The appearance of these brines with low-salinity H₂O-CO₂-NaCl inclusions of variable compositions (5-21 wt.% NaCl equiv.; 0.040-0.667 mol.% CO₂) implies that partial mixing and heterogeneous trapping occurred between: (1) a high temperature (>400 °C; using maximum T_d values), high-salinity (~45-55 wt.% NaCl equiv.), high-density (1.35-1.5 g/cm³), aqueous-rich (X_{H₂O} of 0.7-0.8), CO₂-poor (X_{CO₂} <0.1) fluid; and (2) a lower temperature (270-350 °C), low-density (< 1.0 g/cm³), low-salinity (<10 wt.% NaCl equiv.) H₂O-CO₂ fluid with an unknown H₂O/CO₂ ratio.
4. The favoured and likely sources of these two end-member fluids are a magmatic and metamorphic fluid, respectively.
5. Fluid mixing between these two fluids caused retrograde boiling of a gaseous phase to form abundant CO₂-dominant inclusions.

6. In Yalea-style deposits, fluid inclusion populations are markedly different, with the complete absence of hypersaline fluids and the dominance of low-salinity (1-12.5 wt.% NaCl) aqueous inclusions and CO₂-N₂ inclusions.
7. Petrographic and microthermometric data imply these fluids are two immiscible phases of a low-salinity (≤ 10 wt.% NaCl equiv.) mixed H₂O-CO₂ metamorphic fluid.
8. P-T modelling of two end-member fluids (using mean isochore intersections) related to Yalea Main and Loulo-3 deposits suggest trapping conditions of 340 °C at 1.8 kbar and 335 °C at 1.92 kbar, respectively (using mean values). This corresponds to depths of formation between 6.8-7.25 km (mesozonal deposits), assuming lithostatic conditions.
9. P-T modelling at Baboto gives higher P-T trapping conditions at 440 °C at 2.9 kbar, equivalent to depths of 10.9 km, implying the depth of mineralisation shallows to the south.
10. Barren veins show similar fluid inclusion assemblages to Yalea-style fluids but with the significant addition of homogeneous, low-salinity (mean of 6 wt.% NaCl), H₂O-CO₂-N₂ (6.5 to 17.2 mol.% CO₂-N₂) fluid inclusions representative of the original ore fluid. The appearance of this parent fluid in the same FIAs as the two immiscible phases (aqueous and carbonic inclusions) implies the barren fluids were trapped along or close to the solvus.
11. P-T modelling of barren veins indicate lower P-T trapping conditions compared to mineralised veins (i.e. post-date mineralisation), with mean isochore intersections of the two immiscible fluids giving P-T values of 295 °C at 1.55 kbar. Homogenisation temperatures and isochores of minimum and maximum bulk densities of the H₂O-CO₂-NaCl inclusions give a P-T range from 249-291 °C and 0.75 to 2.15 kbar. Barren veins formed at depths between 3 and 8 km.
12. Re-equilibration (water leakage and necking down) of the Loulo fluid inclusions are likely to have played some role and may account for the wide composition and density ranges observed.

CHAPTER 7: STABLE ISOTOPE STUDIES AT LOULO

7.1 Introduction and objectives

Stable isotope geochemistry is a widely applied technique in the study of hydrothermal mineral deposits (Rye & Ohmoto, 1974; Ohmoto & Rye, 1979; Ohmoto, 1986; Ohmoto & Goldhaber, 1997). Isotope studies can assess the behaviour and source of certain components in the mineralising fluid and give insights into the possible fluid source(s). In this study, stable isotopes (O, C, S), in conjunction with fluid inclusion data (*chapter 6*), were used: (1) to provide information on the physiochemical conditions of the ore fluid (e.g. temperature, pH and redox state (fO_2)) (e.g. Xavier & Foster, 1999; Juliani *et al.*, 2005; Zoheir *et al.*, 2008); (2) to determine the source(s) of the fluid (metamorphic vs. magmatic) and ore-related components; (3) to distinguish similarities/differences between the key styles of Loulo mineralisation; and (4) to understand the role of wall-rock interactions. The data in this chapter are compared with those from a previous study on the first discovered Loulo deposits (Fouillac *et al.*, 1993), and largely concentrate on Gara and the main Yalea deposit (Yalea North not studied here); however a few samples from the minor orebodies were also analysed (Faraba, Loulo-3 and P-64). Finally, comparisons are made with other orogenic gold and Birimian stable isotope studies.

7.2 Methodology

Oxygen, carbon and sulphur isotope analysis were carried out at the Scottish Universities Environmental Research Centre (S.U.E.R.C) at East Kilbride, Scotland. Samples were separated and prepared using the facilities at Kingston University.

7.2.1 Mineral separation

Samples were separated using a combination of crushing, sieving and hand picking down to a 250 μm mineral fraction. No heavy liquids or gravity separation was needed. For sulphur analysis, approximately 5-10 mg of sulphides was separated, while 2-5 mg of silicates and carbonates were utilised for carbon and oxygen isotopes. The purity of each sulphide sample was greater than 80% (in most cases >90%); while silicate and carbonate separates were almost totally pure.

7.2.2 Analytical procedures

Oxygen, $\delta^{18}\text{O}$

Quartz and albite separates were analysed using a laser fluorination procedure, involving total sample reaction with excess ClF_3 using a CO_2 laser as a heat source (in excess of 1500 $^\circ\text{C}$; following Sharp, 1990). All combustions resulted in 100% release of O_2 from the silica lattice. Oxygen was then converted to CO_2 by reaction with hot graphite, which was then analysed on-line

by a VG SIRA 10 spectrometer. Laboratory reproducibility is better than ± 0.3 ‰ (1σ). Results are reported in standard notation ($\delta^{18}\text{O}$) as per mil (‰) deviations from the Vienna Standard Mean Ocean Water (V-SMOW) standard. Oxygen isotopes were also measured from carbonate minerals (see below for description on analytical procedures).

Carbon, $\delta^{13}\text{C}$

Carbonate minerals and whole-rock powders were analysed by conventional procedures. Carbon dioxide was quantitatively released from the samples during an overnight reaction *in vacuo* with 100% phosphoric acid at 100 °C. Gases produced were analysed on a VG SIRA 10 mass spectrometer, monitoring mass:charge ratios 44, 45 and 46. Analytical raw data were corrected using standard procedures (Craig, 1957). Carbon and oxygen isotope data are reported in standard notation as per mil (‰) deviations relative to V-PDB (Vienna PeeDee belemnite) and V-SMOW standards, respectively. Reproducibility, based on complete analysis of internal standards (including acid digestion), was ± 0.1 ‰ for $\delta^{13}\text{C}$, and ± 0.2 ‰ for $\delta^{18}\text{O}$.

Sulphur, $\delta^{34}\text{S}$

Sulphide separates were analysed by standard techniques (Robinson & Kusakabe, 1975) in which SO_2 gas was liberated by combusting the sulphides with excess Cu_2O at 1075 °C, *in vacuo*. Liberated gases were analysed on a VG Isotech SIRA II mass spectrometer, and standard corrections applied to raw $\delta^{66}\text{SO}_2$ values to produce true $\delta^{34}\text{S}$. The standards employed were the international standards NBS-123 (sphalerite) and IAEA-S-3 (silver sulphide, Ag_2S), and the S.U.E.R.C standard CP-1 (chalcopyrite). These gave $\delta^{34}\text{S}$ values of +17.1 ‰, -31.5 ‰ and -4.6 ‰ respectively, with 1σ lab reproducibility around ± 0.2 ‰. Data are reported in $\delta^{34}\text{S}$ notation as per mil (‰) variations from the Vienna Cañon Diablo Troilite (V-CDT) standard.

7.3 Oxygen isotope studies

The oxygen, carbon and sulphur isotope data collected in this study are shown in Table 7.1. The previous stable isotope data of Fouillac *et al.* (1993) are presented in Table 7.2. The following sections summarise the data collected in both studies, with comparisons made with other orogenic gold deposits. The results are then discussed in *section 7.6*.

Oxygen isotopes are commonly used as fluid tracers in many types of mineral deposits (e.g. de Ronde *et al.*, 1992; Matsuhisa & Aoki, 1994; Stenger *et al.*, 1998; Juliani *et al.*, 2005; Nutt & Hofstra, 2007). Hydrothermal quartz is the most widely analysed material for oxygen isotopes in orogenic gold deposits because quartz is generally the dominant vein material and the mineral is also resistant to retrograde exchange (e.g. Ridley & Diamond, 2000). Measured oxygen isotopes of the quartz are specifically dependent on fluid temperature and the $\delta^{18}\text{O}$ signature of the fluid from which they precipitate, assuming equilibrium (an assumption which is valid at the temperatures

under consideration in this area) (Taylor, 1997). In order to determine the isotopic composition of the fluid, ($\delta^{18}\text{O}_{\text{fluid}}$), isotopic fractionation factors need to be applied to the measured $\delta^{18}\text{O}_{\text{mineral}}$ data, in conjunction with an estimate for the temperature of mineralisation. Uncertainties in the calculated $\delta^{18}\text{O}_{\text{fluid}}$ values may exist for numerous reasons: (1) uncertainties in defining the true temperature of deposition; (2) the effects of fluid chemistry on mineral-water fractionation; and (3) likely errors in the equations of isotope fractionation (Ohmoto, 1986). The fractionation equations used for the Loulo dataset are listed below:

$$\delta^{18}\text{O}_{\text{quartz}} - \delta^{18}\text{O}_{\text{fluid}} = (3.34 \cdot 10^6 / T^2) - 3.31 \quad (\text{Matsuhisa } et al., 1979) \quad (\text{Eq. 7.1})$$

$$\delta^{18}\text{O}_{\text{albite}} - \delta^{18}\text{O}_{\text{fluid}} = (4.33 \cdot 10^6 / T^2) - (6.15 \cdot 10^3 / T) + 1.98 \quad (\text{Zheng, 1993a}) \quad (\text{Eq. 7.2})$$

$$\delta^{18}\text{O}_{\text{ankerite}} - \delta^{18}\text{O}_{\text{fluid}} = (4.12 \cdot 10^6 / T^2) - (4.62 \cdot 10^3 / T) + 1.71 \quad (\text{Zheng, 1999}) \quad (\text{Eq. 7.3})$$

$$\delta^{18}\text{O}_{\text{dolomite}} - \delta^{18}\text{O}_{\text{fluid}} = (4.06 \cdot 10^6 / T^2) - (4.65 \cdot 10^3 / T) + 1.71 \quad (\text{Zheng, 1999}) \quad (\text{Eq. 7.4})$$

$$\delta^{18}\text{O}_{\text{calcite}} - \delta^{18}\text{O}_{\text{fluid}} = (4.01 \cdot 10^6 / T^2) - (4.66 \cdot 10^3 / T) + 1.71 \quad (\text{Zheng, 1999}) \quad (\text{Eq. 7.5})$$

where T is temperature in Kelvin (K).

7.3.1 Previous studies

Oxygen isotopes are relatively uniform for orogenic gold hydrothermal systems. Oxygen isotope compositions occur over a consistently narrow range of values (Kerrick, 1987), with calculated $\delta^{18}\text{O}_{\text{fluid}}$ compositions between +6 and +11‰ for Precambrian deposits (e.g. Kerrich & Fryer, 1979; Golding & Wilson, 1982; Kerrich, 1983; de Ronde *et al.*, 1992) and between +7 and +13‰ for Phanerozoic deposits (Kontak *et al.*, 1990; Goldfarb *et al.*, 1991; Bierlein & Crowe, 2000). Oxygen isotopes from vein quartz in the Ashanti district, in Ghana, show $\delta^{18}\text{O}_{\text{fluid}}$ compositions typical of Precambrian deposits from +5.9 to +11.5‰ (Mumin *et al.*, 1996; Oberthür *et al.*, 1996). These heavy isotope values imply a deep-seated fluid source for orogenic gold deposits, overlapping the magmatic (+5 to +10‰) or metamorphic fields (+4 to +25‰) (Ohmoto & Goldhaber, 1997).

Table 7.1. Isotopic compositions (O, C, S) of the Gara, Yalea Main and Faraba orebodies (data collected from present study).

Sample No.	Lithology	Silicates		Carbonates			Sulphides		
		$\delta^{18}\text{O}$ (‰ vs. V-SMOW)		$\delta^{18}\text{O}$ (‰ vs. V-SMOW)			$\delta^{13}\text{C}$ (‰ vs. V-PDB)	$\delta^{34}\text{S}$ (‰ vs. V-CDT)	
		albite	quartz	calcite	ankerite	dolomite		pyrite	arsenopyrite
Gara									
<i>Mineralisation:</i>									
PT5	Ankerite-quartz-pyrite vein	-	-	-	+15.2	-	-10.5	+15.2	-
PT6	Quartz-ankerite-pyrite vein	-	+16.1	-	-	-	-	+15.5	-
PT8	Quartz-ankerite-pyrite vein	-	+16.6	-	-	-	-	-	-
PT9	Ankerite-pyrite vein	-	-	-	15.4	-	-11.9	-	-
G5	Brecciated ankerite vein filled by late quartz	-	+16.1	-	-	-	-	-	-
G7	Weakly mineralised quartz vein	-	+16.2	-	-	-	-	-	-
LD13	Ankerite-pyrite vein	-	-	-	+15.4	-	-13.7	+14.1	-
LD20	Brecciated ankerite vein with abundant pyrite	-	-	-	+15.6	-	-11.6	+13.6	-
LD27	Sigmoidal quartz veins	-	+16.5	-	-	-	-	-	-
LD28	Quartz-ankerite-pyrite vein	-	+16.5	-	-	-	-	-	-
LD30	Pyrite-rich vein	-	-	-	-	-	-	+13.8	-
LD31	Ankerite-pyrite vein	-	-	-	+15.5	-	-13.1	-	-
LD32	Ankerite-quartz-pyrite vein	-	+16.4	-	+15.5	-	-9.7	-	-
LD38	Late pyrite veinlets cutting brecciated ankerite vein	-	-	-	-	-	-	+14.5	-
LD41	Quartz-rich vein, patchy pyrite	-	+16.8	-	-	-	-	-	-
LD44	Ankerite-pyrite vein	-	-	-	+15.6	-	-14.4	+11.7	-
LD45	Quartz-ankerite-pyrite vein	-	+16.2	-	+15.1	-	-11.6	+13.3	-
LD46	Pyrite-rich ankerite vein	-	-	-	+15.2	-	-8.6	+11.5	-
LD51	Pyrite veinlets	-	-	-	-	-	-	+14.3	-
LD53	Brecciated ankerite vein with late patchy pyrite	-	-	-	-	-	-	+12.5	-
<i>Host sediments:</i>									
LD11	Barren quartz vein	-	+16.4	-	-	-	-	-	-
G39	Barren quartz-calcite vein	-	+17.0	+17.4	-	-	-0.2	-	-
G40	Barren quartz-calcite vein	-	-	+21.1	-	-	-1.7	-	-
G13	Schistose limestone	-	-	+23.2	-	-	+1.3	-	-
LD16	Schistose limestone	-	-	+20.7	-	-	-0.4	-	-
LD26	Schistose limestone	-	-	+23.3	-	-	+0.1	-	-

Note- Schistose limestone sediment samples exclude carbonaceous matter.

Table 7.1 cont. Isotopic compositions (O, C, S) of the Gara, Yalea Main and Faraba orebodies (data collected from present study).

Sample No.	Lithology	Silicates		Carbonates			Sulphides		
		$\delta^{18}\text{O}$ (‰ vs. V-SMOW)		$\delta^{18}\text{O}$ (‰ vs. V-SMOW)			$\delta^{13}\text{C}$ (‰ vs. V-PDB)	$\delta^{34}\text{S}$ (‰ vs. V-CDT)	
		albite	quartz	calcite	ankerite	dolomite		pyrite	arsenopyrite
Yalea Main									
<i>Mineralisation:</i>									
PT18	Sulphide veinlets	-	-	-	-	-	-	+7.3	+6.4
PT20	Sulphide veinlets	-	-	-	-	-	-	+8.0	+6.6
PT26	Quartz-pyrite vein	-	+15.8	-	-	-	-	+8.8	-
07YD17	Quartz-sulphide vein	-	+16.3	-	-	-	-	-	+9.6
07YD18	Quartz-sulphide vein	-	+16.1	-	-	-	-	-	-
07YD60	Quartz-pyrite veinlets	-	+16.0	-	-	-	-	+8.3	-
07YD65	Massive sulphides	-	-	-	-	-	-	+7.1	+5.8
07YD69	Ankerite-sulphide veinlet	-	-	-	+23.2	-	-15.8	-	-
07YD71	Ankerite alteration	-	-	-	+14.4	-	-21.5	-	-
07YD76	Ankerite alteration with later sulphides	-	-	-	+14.2	-	-21.7	+7.7	-
07YD80	Albite alteration	+15.6	-	-	-	-	-	-	-
08YD10	Ankerite-quartz-sulphide vein	-	+16.0	-	+15.1	-	-19.5	-	-
08YD24	Ankerite alteration	-	-	-	+13.5	-	-15.9	-	-
08YD29	Quartz-sulphide vein	-	+16.3	-	-	-	-	-	-
08YD30	Quartz-sulphide vein	-	+16.2	-	-	-	-	-	-
08YD31	Albite alteration	+15.6	-	-	-	-	-	-	-
08YD33	Ankerite alteration	-	-	-	+14.8	-	-16.1	-	-
<i>Host sediments:</i>									
07YD90	Barren calcite-quartz vein	-	+15.9	+16.4	-	+24.6	-1.7	-	-
07YD52	Schistose dolomite with syngenetic pyrite	-	-	-	-	+20.0	-2.9	+9.0	-
07YD53	Schistose dolomite	-	-	-	-	+19.9	+0.4	-	-
07YD89	Syngenetic pyrite in schistose dolomite	-	-	-	-	-	-	+6.4	-
Faraba									
<i>Mineralisation:</i>									
FA5	Massive, weakly mineralised, disseminated arsenopyrite	-	-	-	-	-	-	-	+11.5
FA6	Ankerite-sulphide vein	-	-	-	+20.5	-	-13.2	-	+8.2
FA7	Ankerite vein	-	-	-	+18.2	-	-12.2	-	-
FA12	Dolomite vein	-	-	-	-	+18.5	-10.9	-	-

Note- Schistose dolomite sediment samples exclude carbonaceous matter.

Table 7.2. Selected data (O, C & S) from the Fouillac *et al.* (1993) stable isotope study.

Lithology	Silicates	Carbonates		Sulphides
	$\delta^{18}\text{O}_{\text{qtz}}$	$\delta^{18}\text{O}$	$\delta^{13}\text{C}$	$\delta^{34}\text{S}$
	(‰ vs. V-SMOW)	(‰ vs. V-SMOW)	(‰ vs. V-PDB)	(‰ vs. V-CDT)
<u>Gara</u>				
Mineralised carbonate-quartz stockwork	+16.1 to +16.6 (2)	+16.0 to +19.5 (2)	-5.9 to -4.5 (2)	+12.5 to +12.9 (3)
Mineralised disseminated pyrite	–	–	–	+12.1 to +12.9 (2)
Carbonate alteration	–	+15.5 to +17.7 (3)	-7.2 to -5.1 (3)	–
Limestones	–	+22.2 (1)	+0.5 (1)	–
Barren veins	–	+15.1 to +16.9 (2)	-2.0 to +3.8 (2)	–
<u>P-64</u>				
Mineralised carbonate-quartz-magnetite stockwork	–	+16.9 to +19.1 (2)	-8.5 to -7.0 (2)	+6.7 to +9.7 (10)
Disseminated sulphides	–	–	–	+6.0 to +10.5 (12)
<u>Loulo-3</u>				
Stockwork & disseminated sulphides	–	–	–	+7.8 to +9.2 (3)

Note- (1) Number of samples in brackets; (2) $\delta^{18}\text{O}_{\text{carb}}$ data are corrected to dolomites for both hydrothermal and syngenetic carbonates. However, this study shows that carbonates associated with mineralisation classify as ankerites from across the permit. Also, barren veins and host rock carbonates are composed primarily of calcite, with only local dolomitisation.

7.3.2 Sample selection and objectives

The oxygen isotope study includes analyses of 16 mineralised quartz veins from Gara and Yalea. These samples are representative of the Gara and Yalea mineralised systems, with samples selected from different parts of the orebodies. In the case of the Gara stockwork, different vein generations were analysed including early milky quartz and late grey quartz generations. Three barren quartz veins were selected from both deposits for comparison with mineralised veins. Five of these vein samples were also selected for carbonate analysis, with petrographic studies implying cogenetic precipitation of these two minerals. The silicate oxygen isotope dataset also includes two samples of hydrothermal albite from the proximal alteration zone at Yalea Main. Lastly, as well as carbon isotopes (section 7.4), oxygen isotopes were also measured in the carbonate samples. The samples were selected in order: (1) to determine the $\delta^{18}\text{O}$ composition of the various hydrothermal minerals and the mineralising fluids that they precipitated from; (2) to obtain an estimate for the temperature of mineralising and barren fluids, using cogenetic mineral phases (e.g. quartz-carbonate); and (3) to compare the isotopic compositions of mineralised and barren veins.

7.3.3 Results

$\delta^{18}\text{O}$ hydrothermal silicates

The $\delta^{18}\text{O}_{\text{quartz}}$ values are remarkably homogenous (Fig. 7.1) (within error of reproducibility in each deposit) despite clear differences in location and generation. Gara and Yalea Main mineralised quartz veins show measured $\delta^{18}\text{O}$ of +16.1 to +16.8‰ ($n = 9$; mean of $+16.4 \pm 0.2\text{‰}$) and +15.8 to +16.3‰ ($n = 7$; mean of $+16.1 \pm 0.2\text{‰}$), respectively. These data agree well with two analyses by Fouillac *et al.* (1993) on quartz mineralised veins from Gara (+16.1 to +16.6‰). Barren veins from both deposits are indistinguishable from the mineralised veins, with $\delta^{18}\text{O}_{\text{quartz}}$ of +15.9 to +17.0‰ ($n = 3$; mean of +16.4‰). Hydrothermal albite from the Yalea alteration zone exhibits slightly lower, but not significantly different $\delta^{18}\text{O}$ values of +15.6‰ ($n = 2$).

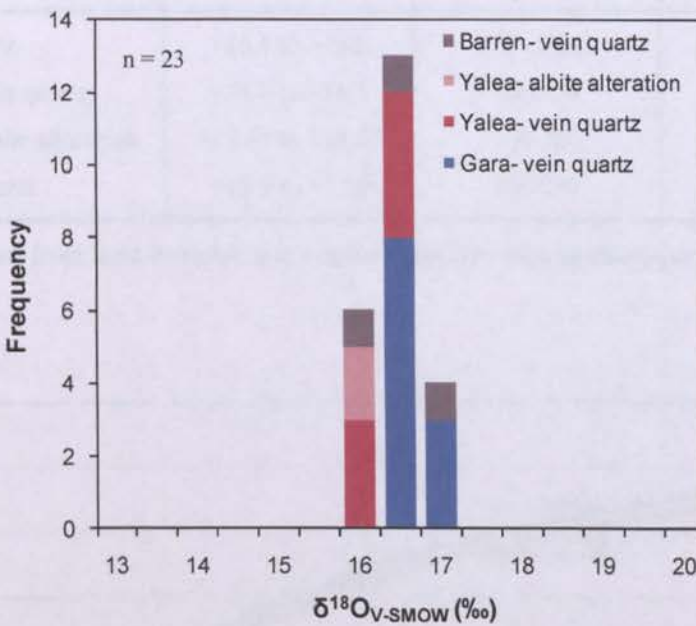


Fig. 7.1 A histogram showing the uniform silicate $\delta^{18}\text{O}$ compositions at Gara and the main Yalea orebody. The dataset includes two analyses from the previous study of Fouillac *et al.* (1993).

The $\delta^{18}\text{O}_{\text{fluid}}$ compositions derived from the silicate dataset can be calculated using the measured quartz $\delta^{18}\text{O}$ values, the fractionation equations of Matsuhisa *et al.* (1979) and Zheng (1993b), and estimated temperatures of vein formation. The temperature of mineralisation at Yalea Main, using data collected during fluid inclusion studies (section 6.7.3), and from ore (section 4.6.3) and alteration geothermometers (section 5.5.4), mainly range from 300-350 °C. This temperature range is consistent with isotopic geothermometer calculations using cogenetic quartz and ankerite (see section 7.6.1). A 300-350 °C temperature range is used as a reasonable estimate for albite crystallisation temperatures, although sodic alteration generally predates the main mineralisation event at Yalea Main. Mineralisation temperature measurements at Gara are not clear cut from fluid inclusion work because of the role of fluid mixing. However, as a Yalea-style

fluid is proposed to be an end-member fluid at Gara (the cooler fluid), a temperature of 350 °C is used as the minimum temperature to calculate $\delta^{18}\text{O}_{\text{fluid}}$ (i.e. the $\delta^{18}\text{O}_{\text{fluid}}$ is also a minimum). Fluid inclusion studies on barren quartz veins imply lower vein formation temperatures between 250 to 295 °C. Despite this apparent temperature distinction, it is notable, however, that the measured quartz $\delta^{18}\text{O}$ values in the barren veins are essentially identical to auriferous vein quartz. The calculated $\delta^{18}\text{O}_{\text{fluid}}$ compositions for Gara and Yalea Main are shown in Table 7.3 and illustrated in Fig. 7.2. Calculated fluid $\delta^{18}\text{O}$ in this system varies from around 7 to 12‰.

Table 7.3. Measured silicate $\delta^{18}\text{O}_{\text{V-SMOW}}$ (‰) and calculated values for coexisting fluid (all data from this study).

Type	$\delta^{18}\text{O}_{\text{mineral}}$	T (°C)	$\delta^{18}\text{O}_{\text{fluid}}$
Gara vein quartz	+16.1 to +16.8	350 (min.)	+10.8 to +11.5
Yalea Main vein quartz	+15.8 to +16.3	300-350	+8.9 to +11.0
Yalea Main albite alteration	+15.61 to +15.63	300-350	+11.2 to +12.3
Barren vein quartz	+15.9 to +17.0	250-295	+7.0 to +10.1

Note- T calculated from fluid inclusion work and ore and alteration geothermometers.

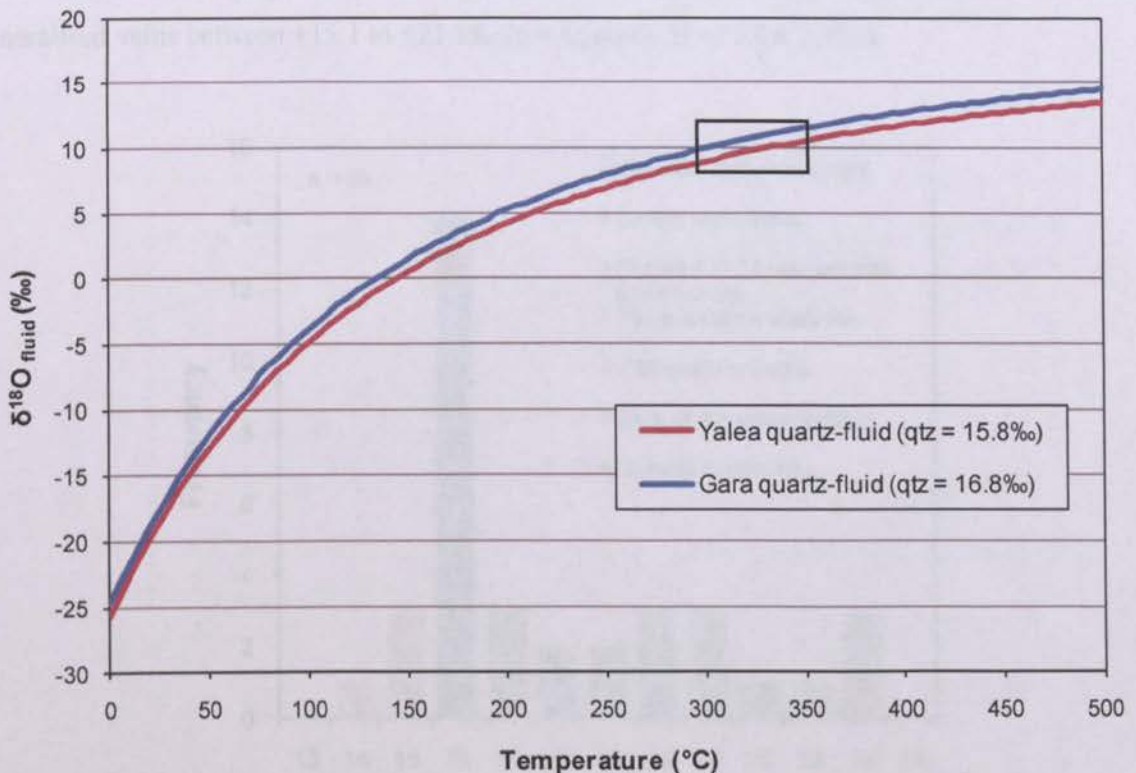


Fig. 7.2. $\delta^{18}\text{O}_{\text{fluid}}$ vs. temperature plot using the measured $\delta^{18}\text{O}_{\text{quartz}}$ values of 15.8‰ and 16.8‰ (min. and max. compositions from Gara and Yalea Main mineralised veins) and the fractionation equation of Matsuhisa *et al.* (1979). The square box refers to the mineralisation temperature range obtained by fluid inclusion studies, and ore and alteration geothermometers.

$\delta^{18}\text{O}$ carbonates

On the whole, the $\delta^{18}\text{O}_{\text{carbonate}}$ data are slightly more heterogeneous than the $\delta^{18}\text{O}_{\text{quartz}}$ data (Fig. 7.3). However, Gara mineralised veins again display a remarkably uniform $\delta^{18}\text{O}_{\text{ankerite}}$ of +15.1 to +15.6‰ (n = 9; mean of $+15.4 \pm 0.2\%$). Gara carbonates measured by Fouillac *et al.* (1993) show a wider scatter, with vein carbonates showing $\delta^{18}\text{O}$ values of +16.0 to +19.5‰ (n = 2; the higher value is slightly anomalous compared to the current dataset) and carbonate alteration material analysed from host quartz-wacke and argillaceous greywacke sediments displaying $\delta^{18}\text{O}$ compositions of +15.5 to +17.7‰ (n = 3; mean of +16.3‰).

Only two mineralised veins were measured at Yalea Main due to the lack of carbonate veining at this deposit. Sample 08YD10 shows an isotopic composition comparable to the Gara vein carbonates (+15.1‰). However, sample 07YD69 shows an anomalous $\delta^{18}\text{O}_{\text{ankerite}}$ value of +23.2‰. Hydrothermal ankerite from the proximal Yalea Main alteration zone exhibits slightly lower $\delta^{18}\text{O}$ mineral compositions compared to the mineralised veins between +13.5 to +14.8‰ (n = 4; mean of +14.2‰). Slight enrichment of the hydrothermal $\delta^{18}\text{O}_{\text{carbonate}}$ signal occurs towards the southern parts of the Loulo mining camp, with gold-bearing ankerite-dolomite veins at Faraba (this study) and P-64 (previous study) showing an isotopic range from +18.2 to +20.5‰ (mean +19.1‰) and +16.9 to +19.1‰ (mean +18.0‰), respectively. However, this observation is based on limited data (n = 5) and further work is needed on these deposits. Barren calcite veins from Gara and Yalea display more heterogeneous $\delta^{18}\text{O}$ mineral compositions compared to the mineralised veins between +15.1 to +21.1‰ (n = 5; mean of $+17.4 \pm 2.3\%$).

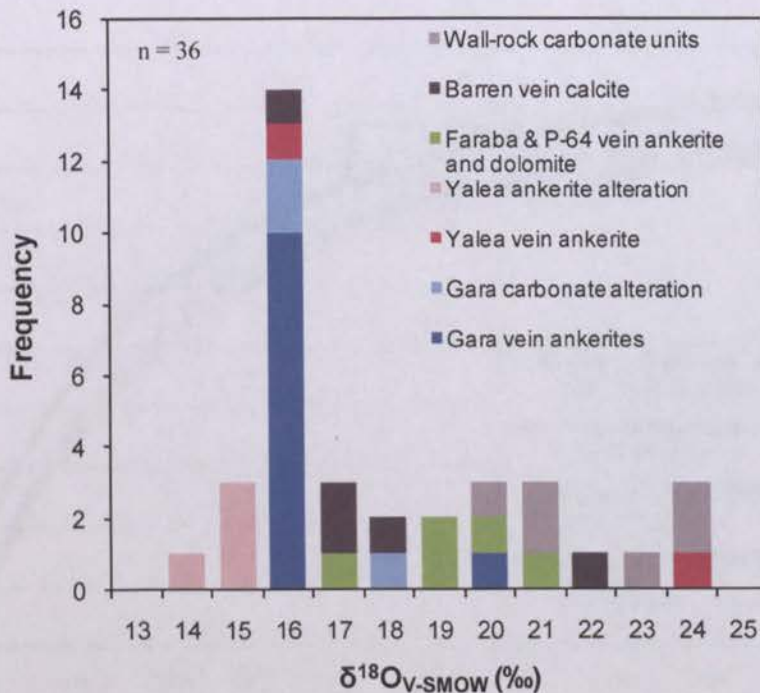


Fig. 7.3. A histogram showing the carbonate $\delta^{18}\text{O}$ compositions at Loulo. The dataset includes 10 analyses from the previous study of Fouillac *et al.* (1993). A majority of the hydrothermal $\delta^{18}\text{O}$ compositions fall within a range of +13.5 to +21.1‰, while sedimentary carbonates from the host limestones/dolostones show heavier $\delta^{18}\text{O}$ values between +19.9 to 23.2‰.

The $\delta^{18}\text{O}_{\text{fluid}}$ compositions calculated from the $\delta^{18}\text{O}_{\text{carbonate}}$ data collected in this study are shown in Table 7.4 and illustrated in Fig. 7.4. Temperature estimates for Yalea Main and Gara mineralised and barren carbonates are the same as those stated for the quartz dataset. In the absence of fluid inclusion data from Faraba, a mineralisation temperature range of 200-266°C can be assumed based on the telluride and chlorite geothermometers (section 4.6.3.2; section 5.5.4). Mineralised and alteration carbonates from Gara and Yalea Main show a dominantly uniform composition from +7.3 to +10.7‰. The lower temperature Faraba gold-bearing veins and barren calcite veins show more compositional variety between +7.9 to +15.7‰. Isotopic fractionations are not applied to the Fouillac *et al.* (1993) dataset to avoid correction errors (all carbonate analyses corrected to dolomite in the previous study) and these data are not discussed further here.

Table 7.4. Measured carbonate $\delta^{18}\text{O}_{\text{V-SMOW}}$ (‰) and calculated values for coexisting fluid (all data from this study).

Type	$\delta^{18}\text{O}_{\text{mineral}}$	T (°C)	$\delta^{18}\text{O}_{\text{fluid}}$
Gara vein ankerite	+15.1 to +15.6	350 (min.)	+10.2 to +10.7
Yalea Main vein ankerite	+15.1 to +23.2	300-350	+8.9 to +18.3
Yalea Main ankerite alteration	+13.5 to +14.8	300-350	+7.3 to +9.9
Faraba ankerite-dolomite veins	+18.2 to +20.5	201-266	+7.9 to +13.2
Barren vein calcite	+16.4 to +21.1	250-295	+9.0 to +15.7

Note- T calculated from fluid inclusion work or mineral assemblages (Faraba).

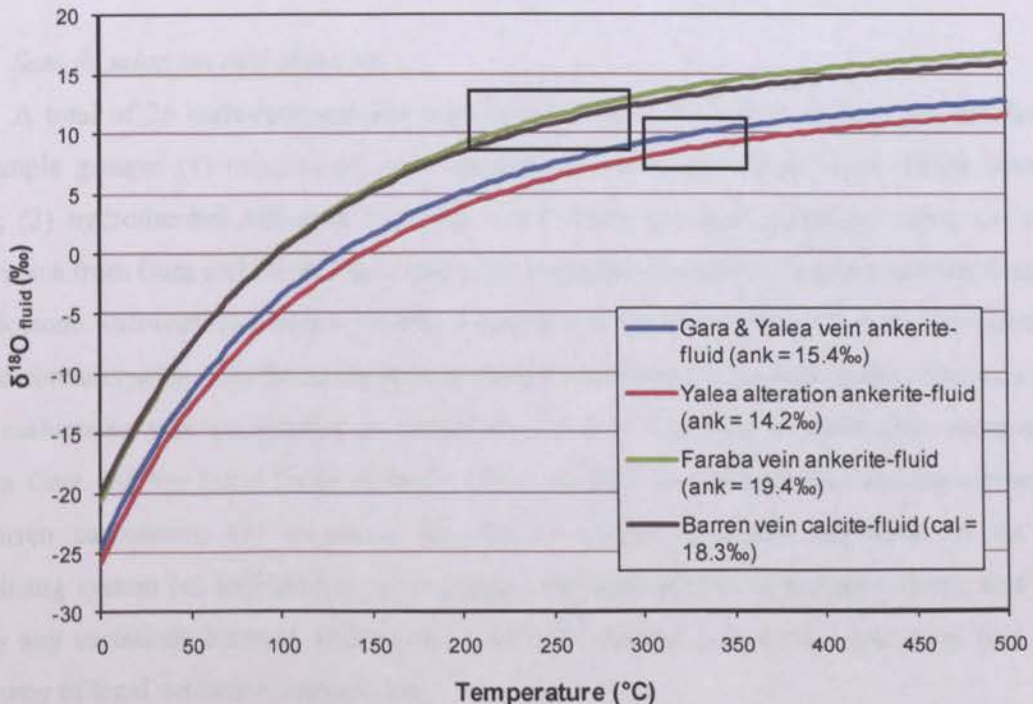


Fig. 7.4. $\delta^{18}\text{O}_{\text{fluid}}$ vs. temperature plot for the Loulo carbonates using the measured $\delta^{18}\text{O}_{\text{carbonate}}$ (mean values) and fractionation equations of Zheng (1999). The square boxes refer to the formation temperature ranges obtained by fluid inclusion studies, and ore and alteration geothermometers.

7.4 Carbon isotope studies

The appearance of carbonate minerals within the Loulo orebodies imply the mineralising hydrothermal fluids contained oxidised carbon compounds. The carbon isotope compositions of these carbonates can be used as a potential tracer for fluid sources at Loulo (Ohmoto, 1986; Ohmoto & Goldhaber, 1997). Carbonate $\delta^{13}\text{C}$ values are dependent on temperature, Eh and pH at time of deposition, as well as the carbon isotope compositions of the carbon species in solution (Ohmoto & Rye, 1979). Thus, interpretation of the carbon isotope data is based upon the knowledge of possible carbon reservoirs, and the physiochemical conditions of the mineralising fluid. The latter can be obtained by analysis of the ore and alteration mineral assemblages (chapter 4 & 5), and from fluid inclusion studies (chapter 6).

7.4.1 Previous studies

Orogenic gold deposits of all ages show a large spread of average $\delta^{13}\text{C}$ values from approximately -23 to +2‰, with a majority of deposits falling in the range -11 to +2‰ (McCuaig & Kerrich, 1998). Restricted ranges are observed in individual deposits (Kerrich, 1987). This spread of $\delta^{13}\text{C}$ values has been interpreted in several ways: (1) crustal C derived from devolatilisation of greenstone terranes (Kerrich & Fyfe, 1981; Groves & Phillips, 1987); (2) a magmatic origin for CO_2 (-7 to -3‰; e.g. Burrows *et al.*, 1986; Burrows, 1991; Spooner, 1991b); (3) a mantle CO_2 source (~-3‰; Cameron, 1988; Colvine *et al.*, 1988); (4) mixing of different fluids with contrasting redox states (Kerrich, 1987; 1990); or (5) interaction with reduced sediments (depleted $\delta^{13}\text{C}$ values; Kontak *et al.*, 1990; Oberthür *et al.*, 1996).

7.4.2 Sample selection and objectives

A total of 26 carbonate samples were selected for $\delta^{13}\text{C}$ analysis. These are divided into four sample groups: (1) mineralised vein ankerites and dolomites from Gara, Yalea Main and Faraba; (2) hydrothermal ankerites from the Yalea Main proximal alteration zone; (3) barren calcite veins from Gara and Yalea Main; and (4) a selection of whole-rock samples from limestone and dolostone wall-rock sediments. Careful separation of the carbonate wall-rock was carried out to avoid contamination with the carbonaceous matter contained within these rocks. Analysis of the Loulo carbonates was undertaken to constrain: (1) any variation in carbonate compositions between Gara and the main Yalea orebody; (2) to identify any differences between mineralised and barren carbonates; (3) to assess the role of magmatic-related carbonate in the Gara mineralising system (as indicated by petrography, alteration and fluid inclusion data); and (4) to identify any variations between sedimentary and hydrothermal carbonate, which may hint at the importance of local wall-rock interactions.

7.4.3 Results

The carbon isotope dataset measured in this study and the previous study by Fouillac *et al.* (1993) show a wide range of carbonate isotopic compositions ($\delta^{13}\text{C}$) at Loulo from -21.7 to +3.8‰ (Fig. 7.5). However, there are some clear distinctions between deposits, barren and mineralised veins, and hydrothermal and sedimentary/metamorphic carbonate. Firstly, the Gara vein carbonates in this study show a $\delta^{13}\text{C}$ range from -14.4 to -8.6‰, with slightly lower values recorded by the previous study of -5.9 to -4.5‰. Fouillac *et al.* (1993) also measured the carbonate cement of the mineralised tourmalinite host, as well as from argillaceous greywackes and quartzwackes in proximity to the orebody. These carbonates are isotopically different to host carbonate wall-rocks (see below) and display similar values to the mineralised carbonates between -7.2 to -5.1‰ (part of the alteration zone). These data give a spread of $\delta^{13}\text{C}$ compositions at Gara from -14.4 to -4.5‰ ($n = 14$; mean of $-9.6 \pm 3.3\%$), regardless of the location of the carbonate (no clear systematic differences in $\delta^{13}\text{C}$ were observed along strike of the tourmalinite host). The P-64 orebody shows similar values from -8.5 to -7.0‰ ($n = 2$).

Unlike the oxygen isotope dataset, there are clear differences between the $\delta^{13}\text{C}$ isotopic compositions at Yalea Main compared to Gara, which is expected due to the contrasting ore, alteration and fluid inclusion characteristics of these deposits. Representative mineralised vein and alteration ankerites from Yalea Main exhibit light $\delta^{13}\text{C}$ signatures of -19.5 to -15.8‰ and -21.7 to -15.9‰, respectively ($n = 6$; mean of $-18.40 \pm 2.8\%$), and clearly plot into a separate cluster in Fig. 7.5. Faraba vein ankerites-dolomites show intermediate $\delta^{13}\text{C}$ compositions of -13.2 to -10.8‰ ($n = 3$; mean of -12.2%). Barren calcite veins from Gara and Yalea show notably different isotopic compositions to the mineralised veins. Barren veins show heavier and more homogeneous $\delta^{13}\text{C}$ values between -2.0 to -0.2‰; however one sample shows a higher value of +3.8‰ ($n = 5$; mean of $-0.2 \pm 2.3\%$). Barren carbonate veins share similar compositions to the limestone and dolostone wall-rock sediments, with $\delta^{13}\text{C}$ between -2.9 to +1.3‰ ($n = 6$; mean of $-0.16 \pm 1.4\%$).

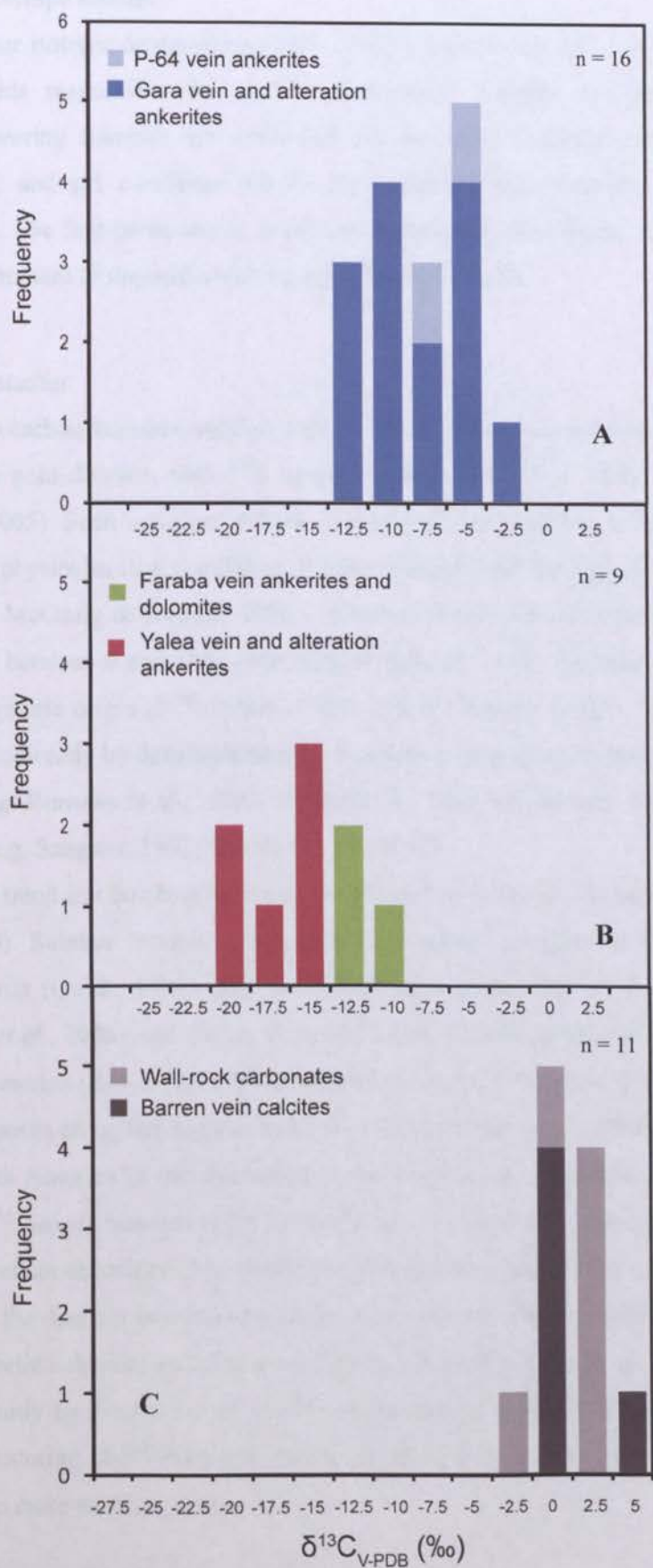


Fig. 7.5. A stacked histogram showing the scattered distribution of $\delta^{13}\text{C}$ compositions of the Loulo carbonates, using data from the present study and the previous study by Fouillac *et al.* (1993). **A)** Gara-style deposits. **B)** Yalea and Faraba deposits. **C)** Host rock carbonates and barren calcite veins.

7.5 Sulphur isotope studies

The sulphur isotopic composition of the Loulo sulphides can also serve as a tracer for the hydrothermal fluids responsible for gold mineralisation. Sulphur isotope compositions of hydrothermal S-bearing minerals are controlled by the total S isotope composition ($\delta^{34}\text{S}_{\Sigma\text{S}}$), temperature, $f\text{O}_2$, and pH conditions of the mineralising fluid (Ohmoto, 1986; Ohmoto & Goldhaber, 1997). The first parameter is considered a source characteristic, while the other three relate to the environment of deposition (McCuaig & Kerrich, 1998).

7.5.1 Previous studies

Similar to carbon isotopes, sulphur isotopes tend to show compositional variety between different orogenic gold districts, with $\delta^{34}\text{S}$ values ranging from -20 to +25‰ (as summarised in Goldfarb *et al.*, 2005). Such variation reflects local crustal contributions to the ore fluids and/or differences in the physiochemical conditions of hydrothermal fluid during gold deposition (Groves & Phillips, 1987; McCuaig & Kerrich, 1998). However, a majority of deposits contain $\delta^{34}\text{S}$ in a restricted interval between 0 and +9‰ (McCuaig & Kerrich, 1998). Sulphur of this composition could have a magmatic origin ($\delta^{34}\text{S}$ values of 0‰ \pm 5‰; Ohmoto & Rye, 1979) either directly from magmas or indirectly by desulphidation or dissolution of magmatic sulphide minerals during fluid transport (e.g. Burrows *et al.*, 1986). Alternatively, these values may reflect average crustal sulphur sources (e.g. Sangster, 1992; Goldfarb *et al.*, 1997).

A similar trend can be observed using a comparative study of Palaeoproterozoic lode gold deposits (Fig. 7.6). Sulphur isotopic compositions are mainly confined to the 0 to +10‰ $\delta^{34}\text{S}$ interval: e.g. Morila (Quick, 1999); deposits associated with the Rio Itapicuru greenstone belt, Brazil (Geraldes *et al.*, 2006); and Tartan Lake and Homestake deposits within the Trans Hudson orogeny, North America (Rye & Rye, 1974; Fedorowich *et al.*, 1991). Exceptions are the Birimian orogenic gold deposits along the Ashanti belt in Ghana (Oberthür *et al.*, 1996) and within the São Luis Craton, South America (a rifted remnant of the Birimian crust) (Klein *et al.*, 2005b), which show depleted $\delta^{34}\text{S}$ values between -12.6 to -4.6‰ and -11 to -0.5‰, respectively. These lighter $\delta^{34}\text{S}$ values may reflect deposition from oxidised hydrothermal fluids (Klein *et al.*, 2005b). For the Ashanti deposits, the data are interpreted as showing source inheritance, with similar signatures to syngenetic-diagenetic sulphides in the surrounding wall-rock (Oberthür *et al.*, 1996; Fig. 7.6). The sulphur isotope study by Fouillac *et al.* (1993) on the earliest discovered Loulo deposits show a relatively tight clustering of $\delta^{34}\text{S}$ between +6.0 to +12.9‰, with heavier compositions observed at Gara (discussed in more detail in *section 7.5.3*).

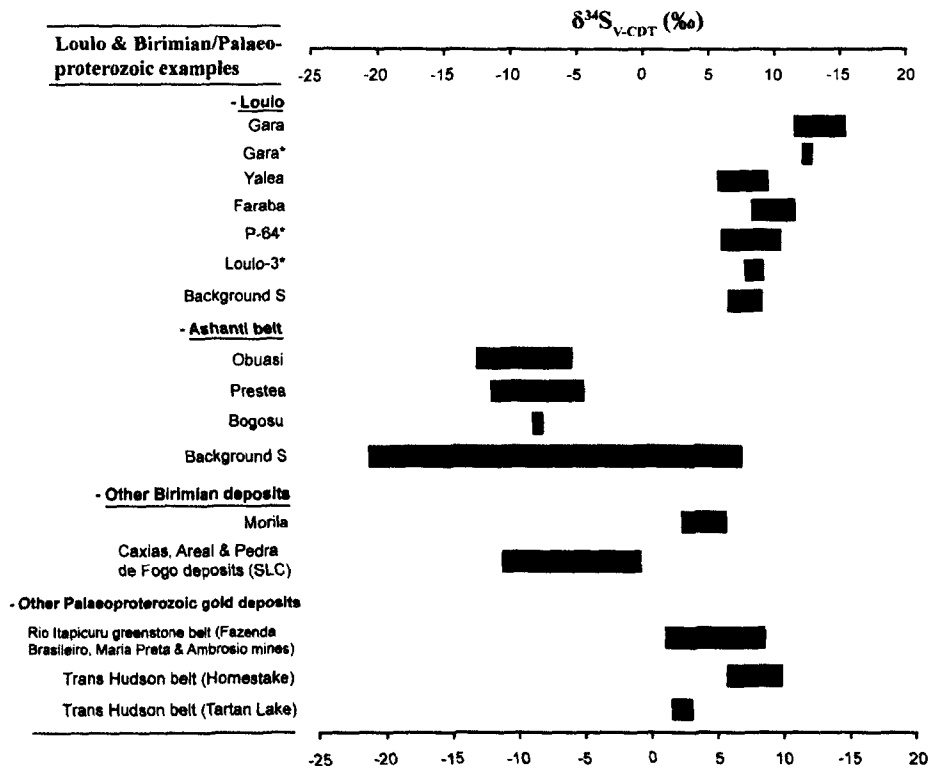


Fig. 7.6. Sulphur isotope compositions of Birimian and other Palaeoproterozoic orogenic gold deposits. The Loulo dataset is also included here for comparison (presented in section 7.5.3). Note- * refers to previous isotope study at Loulo by Fouillac *et al.* (1993); SLC refers to São Luis Craton. See text on previous page for references.

7.5.2 Sample selection and objectives

A total of 25 analyses were carried out on 22 sulphide samples. At Gara, pyrite samples ($n = 11$) were collected from various drill-core 1 km along strike. Mineralised pyrite was selected from ankerite \pm milky quartz veins, sulphide-dominated veinlets and from the late phase grey-quartz veins (reactivation phase). At Yalea, both the pyrite-II and arsenopyrite-II phases ($n = 10$) were measured from across the main orebody. Sulphides were mainly selected from sulphide stringers along the main shear, but rare mineralised quartz-pyrite veins were also measured in the surrounding wall-rock. A few Faraba samples (disseminated and vein stage) were also included in the dataset. Lastly, two samples of syngenetic-diagenetic pyrite from the host sediments were collected from hangingwall dolostones at Yalea.

The samples were selected in order: (1) to show any compositional variations between the orebodies; (2) to test for variations in composition between different sulphide/vein phases; (3) to examine for any isotopic differences along strike at Gara and Yalea Main (limited data to determine this); (4) to test for any distinctions between the Te-Bi arsenopyrite phases at Faraba in relation to the gold mineralised events at Gara and Yalea; and (5) to compare the $\delta^{34}\text{S}$ signatures of ore-stage sulphides and background syngenetic-diagenetic pyrite. Analysis of the complete sulphide paragenesis was not within the scope of this study and may be a topic for further research to determine isotopic variations during the fluid evolution of an individual Loulo deposit

(variations are suggested by subtle, but significant differences between stages- see below).

7.5.3 Results

The $\delta^{34}\text{S}$ data is uniform in terms of individual orebodies; however there are significant isotopic differences between deposits. Yalea Main sulphides show $\delta^{34}\text{S}$ signatures between +5.8 to +9.6‰ (mean of $+7.5 \pm 1.2\text{‰}$). Despite this tight cluster, there are clear systematic differences between mineral phases and vein mineralogy. Pyrite-II exhibit $\delta^{34}\text{S}$ values between +7.1 to +8.8‰, with the two heaviest values (+8.3 & +8.8‰) from quartz-bearing veins. Sulphides representative of the arsenopyrite-II ore stage mainly show lower compositions of +5.8 to +6.6‰; however, a quartz vein phase sample gave the highest value of +9.6‰. The $\delta^{34}\text{S}$ range obtained at Yalea Main closely matches sulphides collected from P-64 and Loulo-3 by Fouillac *et al.* (1993) (+6.0 to +10.5‰).

Gara sulphides display distinctly heavier $\delta^{34}\text{S}$ compositions from +11.5 to +15.5‰ (mean of $+13.6 \pm 1.3\text{‰}$). This range is wider than the sulphide data obtained by Fouillac *et al.* (1993) at Gara, based on a smaller dataset ($n = 5$) (+12.1 to +12.9‰). The Gara sulphur dataset shows no clear trend with respects to different vein phases (i.e. similar signatures for early milky quartz veins and late grey reactivated veins) and to isotopic compositions along strike (the latter observation also seen at Yalea Main). The $\delta^{34}\text{S}$ values from Gara are slightly higher than the majority of sulphur isotope studies on lode gold deposits (*section 7.5.1*; Fig. 7.7). Disseminated and vein stage telluride-bearing arsenopyrite at Faraba shows no real systematic differences compared to the gold-bearing sulphides (intermediate between sulphides at Gara and Yalea Main- +8.2 to +11.5‰). Syngenetic-diagenetic pyrite from Yalea wall-rock show similar compositions (+6.4 to +9.0‰) to hydrothermal sulphides in the adjacent mineralised zone.

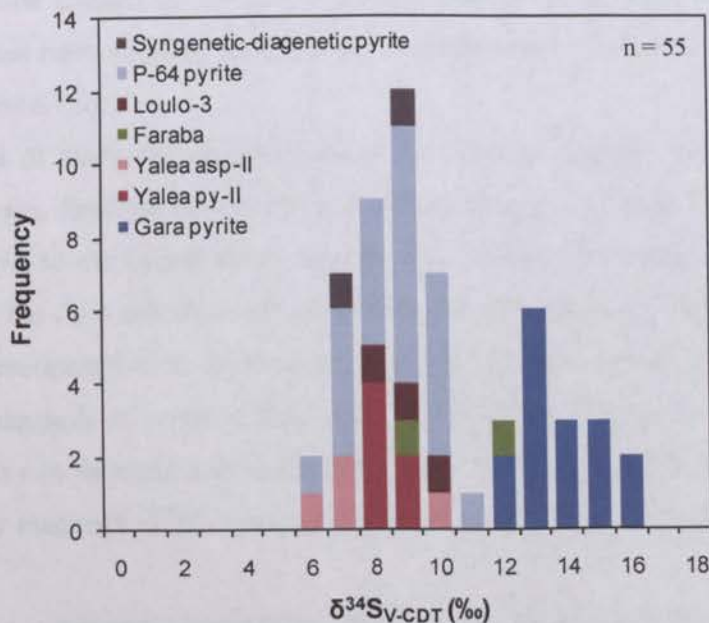


Fig. 7.7. A histogram showing the bimodal isotopic compositions of the Loulo sulphides using data from the present study and the previous study by Fouillac *et al.* (1993).

7.6 Discussion

7.6.1 Oxygen isotopes

There is a remarkable uniformity of $\delta^{18}\text{O}_{\text{silicate}}$ and $\delta^{18}\text{O}_{\text{carbonate}}$ values from gold-bearing veins at Gara and Yalea Main. Indeed, the mean $\delta^{18}\text{O}$ values from the quartz veins are within analytical error. This suggests a corresponding homogeneity of the hydrothermal $\delta^{18}\text{O}_{\text{fluid}}$, coupled with a relatively consistent temperature of deposition (the alternative being a fortuitous and unlikely co-variation in $\delta^{18}\text{O}_{\text{fluid}}$ and T, resulting in the homogeneity of measured values). Estimated $\delta^{18}\text{O}_{\text{fluid}}$ compositions (using only data collected in this study) are similar for both mineral types, with values ranging between +9 to +12‰ (sample 07YD69 shows an anomalous $\delta^{18}\text{O}_{\text{fluid}}$ of +18.3‰), which indicates that vein quartz and ankerite were in isotopic equilibrium. These values are analogous (albeit more homogenous) to oxygen isotope studies at Ashanti (Oberthür *et al.*, 1996) and other Precambrian orogenic gold deposits (*section 7.3.1*). Broadly, the $\delta^{18}\text{O}_{\text{fluid}}$ compositions at Gara and Yalea Main are consistent with a magmatic fluid (magmatic field +5 to +9‰ and metamorphic field +4 to +25‰; Ohmoto & Goldhaber, 1997), although a contribution from an anomalously $\delta^{18}\text{O}$ -enriched magmatic fluid cannot be ruled out, particularly for Gara (see below) (Sheppard, 1986).

Assuming coeval precipitation of vein quartz and ankerite, as suggested by petrographic studies in a majority of Gara and Yalea Main veins (*chapter 4*; excluding late grey quartz at Gara), paired quartz-ankerite $\delta^{18}\text{O}_{\text{fluid}}$ values can be used as a geothermometer. At Gara, two vein samples (LD32 & LD45) were measured for both $\delta^{18}\text{O}_{\text{quartz}}$ and $\delta^{18}\text{O}_{\text{ankerite}}$, with $\Delta\delta^{18}\text{O}_{\text{fluid}}$ (isotopic fractionation differences between quartz and ankerite) of 0.5 and 0.6‰, respectively. These correspond to crystallisation temperatures of 329 and 311 °C (Matsuhisa *et al.*, 1979; Zheng, 1999). One paired quartz-ankerite sample at Yalea Main (08YD10) shows $\Delta\delta^{18}\text{O}_{\text{fluid}}$ of 0.5‰, equivalent to a similar temperature of 329 °C (using max. $\delta^{18}\text{O}_{\text{fluid}}$ values for both). This value closely matches mean mineralisation temperatures measured from fluid inclusion studies at Yalea Main (340°C; *section 6.7.3*).

In the case of Gara, the oxygen isotope data do not appear consistent with ore and alteration assemblages, fluid inclusion data and carbon isotopes (*section 7.6.2*), which imply a clear magmatic input to the hydrothermal system. The similar $\delta^{18}\text{O}$ values for Gara and Yalea Main suggests that the fluid mixing event(s) at Gara, between a cooler (~340 °C) CO_2 -rich fluid (Yalea-style fluid; metamorphic in origin) and a higher temperature (>400 °C) aqueous-rich brine (presumed to be magmatic in origin) (*chapter 6*), had little effect on the overall temperature of mineralisation. This can be explained by the dominance of the regional CO_2 -rich fluids over the brines and thus any magmatic $\delta^{18}\text{O}$ signature at Gara may have been diluted by the metamorphic fluids.

Nonetheless, a magmatic contribution should not be ruled out on the basis of the oxygen isotope data. A view of what is meant by a magmatic fluid is worth consideration. As outlined by

Sheppard (1986): (1) a magmatic fluid is a fluid which is in equilibrium with rocks at high temperature; (2) the definition of magmatic waters carries no implication concerning its origin. Fluids released from peraluminous, S-type, granitic rocks are likely to be enriched in $\delta^{18}\text{O}$ (similar compositions to the sediment protolith) compared to ordinary magmatic rocks (I-type granites, basalts etc.) which contain $\delta^{18}\text{O}$ between +5 to +9‰ (Sheppard, 1986). So, if the Gara $\delta^{18}\text{O}$ data are in fact magmatic, then we would predict that the magmatic rocks from which the fluids emerged had to be peraluminous in nature. Peraluminous granitic bodies are observed within the Kofi Series, in proximity to the Loulo district (e.g. Yatea pluton or the B-rich Gamaye pluton; Fig. 3.1) (discussed further in *chapter 8*).

Oxygen isotopes measured from alteration zones and barren veins (especially $\delta^{18}\text{O}$ from carbonates) show more compositional variety. The quartz-calcite (cogenetic phases) barren veins at Gara and Yalea show $\delta^{18}\text{O}_{\text{fluid}}$ for quartz between +7.0 to +10.1‰ and for calcite from +9.0 to +15.7‰. Paired values from samples G39 and O7YD90 ($\Delta\delta^{18}\text{O}_{\text{fluid}}$ of 1.9 and 2.0) give temperatures of 196 and 184 °C, respectively. These are notably lower than temperatures modelled from fluid inclusion data (250-295 °C). The albite-ankerite proximal alteration zone at Yalea Main shows a varied isotopic composition (albite- +11.2 to +12.3; ankerite- +7.3 to +9.9‰). Given that the albite-ankerite appears to be cogenetic, the likely reason for the variation in the $\delta^{18}\text{O}_{\text{fluid}}$ data is that the two mineral phases were not precipitated in isotopic equilibrium (a similar story may be true for the barren veins to account for the inconsistency in vein formation temperatures). Alternatively, the isotopic composition of one, or both, minerals may have changed post-deposition (Ohmoto, 1986). From a study of Archaean orogenic gold deposits, Kerrich (1987) suggested the compositional variety of $\delta^{18}\text{O}$ in carbonates, compared to uniform $\delta^{18}\text{O}$ values of quartz, is due to varying degrees of re-equilibration at temperatures below the quartz-carbonate precipitation temperature during later mineral-fluid interaction (i.e. carbonates are more susceptible to modification post-deposition). A similar process can be used to explain the variation in $\delta^{18}\text{O}$ in the alteration zone at Yalea and possibly within the barren veins (although in mineralised veins, no such re-equilibration is evident).

7.6.2 Carbon isotopes

Many orogenic gold deposits are considered to be characterised by fluids containing $f\text{O}_2$ close to the QFM buffer, above the CO_2/CH_4 buffer, and temperatures >270 °C (Kerrich, 1987). At these conditions, carbon isotope fractionation due to changing redox effects or temperature is minor and $\delta^{13}\text{C}$ values are likely to be close to fluid compositions (Ohmoto & Rye, 1979; Kerrich, 1987). Mineral assemblages (pyrite-arsenopyrite dominated) and fluid inclusion data ($\text{CO}_2 > \text{CH}_4$; $T = 300\text{-}350$ °C) suggest the dominant mineralising fluid at Loulo falls under similar conditions. Magnetite increases in concentration to the south but appears to be unrelated to the mineralisation events (although oxidising fluids appear to remobilise gold in some deposits), occurring late in the Loulo hydrothermal history.

The spread of $\delta^{13}\text{C}$ values at Loulo is best explained by mixing of different carbon sources. The depleted $\delta^{13}\text{C}$ values observed at Yalea Main and Faraba (-21.7 to -10.8‰) implies a reduced carbon source for these deposits. Similar light carbon isotope compositions have been recorded elsewhere in the Birimian, in deposits along the Ashanti belt in Ghana (-15.7 to -9.5‰; Mumin *et al.*, 1996; Oberthür *et al.*, 1996). Oberthür *et al.* (1996) suggested that the carbon source for the Ashanti deposits was reduced carbon in the Birimian sediments (graphitic sediments showing $\delta^{13}\text{C}$ values of -28 to -11‰). A similar interpretation can be applied to Yalea Main and Faraba. Wall-rock surrounding the Loulo orebodies consists of reduced chemical sediments such as limestones and dolostones rich in carbonaceous matter (*chapter 3*). Extensive interaction of the mineralising fluids with these sediments can explain the depleted $\delta^{13}\text{C}$ signatures. Given that organic carbon generally contains $\delta^{13}\text{C}$ compositions of -25‰ (Hoefs, 1987) and sedimentary carbonate in the Loulo district show $\delta^{13}\text{C}$ values close to zero, a mixing trend can be established for Yalea Main and Faraba with a 43-87% carbon input from an organic carbon source. The carbon could have been leached into solution by inorganic oxidation ($\text{C} + \text{O}_2 \rightarrow \text{CO}_2$) or by hydrolysis reactions (e.g. $2\text{C} + 2\text{H}_2\text{O} \rightarrow \text{CO}_2 + \text{CH}_4$) (Oberthür *et al.*, 1996). The latter reaction could explain the appearance of CH_4 and amorphous carbon in the fluid inclusions in veins in close proximity to the carbonate host rocks (e.g. Yalea South; *chapter 6*). The former reaction would result in CO_2 isotopic compositions close to the parental carbon material, while the CO_2 produced by the latter reaction, above temperatures of 300 °C, could have $\delta^{13}\text{C}$ values 3 to 12‰ heavier than the carbon in the host rocks (Ohmoto & Rye, 1979) (thus, will affect the mixing trends mentioned above).

Carbon isotope compositions for mineralised carbonate veins at Gara and P-64 show heavier, and for Gara, more heterogeneous $\delta^{13}\text{C}$ values between -14.4 to -4.5‰. These compositions imply a magmatic contribution (magmatic field from -7 to -3‰; Burrows *et al.*, 1986; Colvine *et al.*, 1988) as well as more a reduced carbon source (similar to Yalea Main). There is also likely to be a sedimentary carbon contribution from the host rocks. Fluid mixing is proposed for Gara and deposits with similar characteristics (e.g. P-64) between a magmatic fluid and a regional CO_2 -rich metamorphic fluid (*chapter 6*). The spread of the $\delta^{13}\text{C}$ data implies carbon was sourced from both end-member fluids. Fluid inclusion studies has shown the magmatic brine end-member to be an oxidised fluid, with a redox state close to the HM buffer (presence of haematite and magnetite daughter phases). Under these conditions, isotopic fractionation (small effects) will occur between the carbonates and the original fluid (Ohmoto & Rye, 1979), and the $\delta^{13}\text{C}$ values measured will not exactly reflect the carbon isotopic compositions of the magmatic fluid.

Barren calcite veins contain relatively high $\delta^{13}\text{C}$ signatures of -2 to +3.8‰. These values closely match the isotopic compositions of the carbonate wall-rock, which contain typical chemical sediment signatures (Schidlowski *et al.*, 1983) with constant $\delta^{13}\text{C}$ values close to zero (seawater derived carbon). The lack of a reduced carbon signature implies the barren fluids did not interact with carbonaceous material within the country rock (evidence that wall-rock interaction

played an important role in gold deposition), but instead probably formed from the devolatilisation/ decarbonisation of the sedimentary carbonate grains during metamorphism. The distinct differences in the carbon isotopic compositions of mineralised and barren veins suggest carbon isotopes can be used as a potential exploration tool in the Loulo district (discussed in section 8.5.3).

7.6.3 Sulphur isotopes

Excluding the Gara sulphides, the relatively narrow range of $\delta^{34}\text{S}$ values at Loulo from +5.8 to +10.5‰ (Fig. 7.5) implies the sulphur source was isotopically uniform. The redox state of the Loulo mineralising fluid was above the CO_2/CH_4 buffer, which is evident from fluid inclusion analysis ($\text{CO}_2 > \text{CH}_4$). Ore assemblages indicate that mineralisation took place under reducing conditions with sulphur largely present as H_2S (there are limited sulphates within the orezones; exclusively supergene in origin). Equilibrium isotopic fractionation between H_2S and most sulphides are small ($\pm 2\%$) at temperatures above 250 °C (Ohmoto & Rye, 1979). Thus, the uniform $\delta^{34}\text{S}$ values at Loulo are likely to closely represent the overall sulphur isotope composition of the fluid.

The source of sulphur at Yalea Main, P-64, Loulo-3 and Faraba is probably from sedimentary pyrites in the host Kofi sediments. Sulphides from these deposits closely match the $\delta^{34}\text{S}$ values of syngenetic-diagenetic pyrites measured from the Yalea hangingwall dolostones (+6.4 to +9.0‰). A magmatic sulphur source is unlikely for these orebodies (magmatic sulphides are typically close to zero; Ohmoto & Rye, 1979). Chang *et al.* (2008) noticed that many sediment-hosted orogenic gold deposits contain sulphur isotopes that mirror the seawater sulphate curve through geological time (Fig. 7.8). This trend can be observed at Loulo. The sulphur was initially fixed as pyrite by reduction of seawater during early diagenesis of the host sediment and subsequently converted to other sulphides during interaction with hydrothermal fluids (Ohmoto & Goldhaber, 1997).

At Yalea Main, the slight differences in the pyrite-II $\delta^{34}\text{S}$ compared to arsenopyrite-II could be explained by phase separation of the mineralising fluid (as indicated by fluid inclusion work). During fluid unmixing, H_2S will partition into the vapour phase (e.g. Mikucki, 1998; Williams Jones *et al.*, 2009) and be locally consumed to form the early pyrite-II phase. The residual fluid will be depleted in H_2S and sulphides forming late in the paragenesis (e.g. arsenopyrite-II phase) will contain lower $\delta^{34}\text{S}$ (as suggested by Drummond & Ohmoto, 1985). This offset may be balanced by changes in the physiochemical conditions of the fluids during the evolution of the Yalea mineralised system (e.g. temperature, $f\text{O}_2$). But, whilst there are measurable and subtle differences between these stages (albeit on a limited database), there is a general clear $\delta^{34}\text{S}$ signature from Yalea-type ores of +6 to +10.5‰.

Fig. 7.8. The variation of sulphide $\delta^{34}\text{S}$ compositions in sediment-hosted orogenic gold deposits, in correlation with the seawater sulphate curve through geological time. Loulo (2028 ± 10 Ma; Vielreicher, 2006) – majority of $\delta^{34}\text{S}$ data fall within the median zone for Palaeoproterozoic deposits, but Gara contains slightly higher values close to seawater sulphate compositions (but not outside ranges stated in other sediment-hosted deposits; e.g. Olimpiada and Homestake). Figure from Chang *et al.* (2008) using the seawater sulphate curve of Claypool *et al.* (1980) and Strauss (1997). For orogenic gold references see Chang *et al.* (2008) and references therein.

Sulphides at Gara have distinct and heavier $\delta^{34}\text{S}$ compositions of +11.5 to +15.5‰, compared to Yalea Main, and thus may have different sulphur source(s), despite having essentially similar host rocks. Fluid inclusion work implies Gara formed from the result of fluid mixing, between a magmatic brine and metamorphic fluid end-members, while at Yalea Main only the metamorphic fluid is present. We know from the work at Yalea that the dominant $\delta^{34}\text{S}$ signal in the metamorphic fluid was around +6 to +10.5‰. This implies that if Gara contains a magmatic S contribution, a magmatic source would have to be greater than +10.5‰; this is not typical of magmatic rocks, which are dominantly around 0 ± 5 ‰ (Ohmoto & Rye, 1979). However, as with the discussion above regarding oxygen isotope systematics in peraluminous granitoids, anomalously high $\delta^{34}\text{S}$ are seen in such granitoids, having inherited the high $\delta^{34}\text{S}$ from the sedimentary protolith (Ohmoto & Rye, 1979; Laouar *et al.*, 1990; Lowry *et al.*, 2005).

On the other hand, the lack of S-bearing phases from the daughter assemblages in the brines and the fact that $\delta^{34}\text{S}$ compositions do not reflect normal magmatic signatures could suggest the S was largely sourced from the metamorphic fluids at Gara. Given the dominance of reducing conditions in the metamorphic fluids, and thus H_2S in the ore fluid, it is unlikely that the higher

$\delta^{34}\text{S}$ signal from Gara reflects variations in the redox state of the fluid (Ohmoto & Goldhaber, 1997). Therefore, the variation in $\delta^{34}\text{S}$ compositions at Gara is source inherited and reflects local variations in the crustal S signature within the Kofi Series. The isotope composition of sedimentary sulphides, which is dominated by reduction of seawater sulphate by bacteria, show a considerable natural range of $\delta^{34}\text{S}$ values (around $\pm 10\text{‰}$; e.g. Ohmoto, 1986; Seal, 2006) and which could account for the differences between Gara and the other deposits. Clearly, this could be tested by further measurements of syngenetic-diagenetic pyrite from Gara wall-rocks, offering scope for future work.

The $\delta^{34}\text{S}$ compositions at Loulo (+5.8 to + 15.5‰) differ significantly to the $\delta^{34}\text{S}$ signatures in the Ashanti belt (-12.6 to -4.6‰; Oberthür *et al.*, 1996), despite similar interpretations (leached from metasedimentary wall-rock). This indicates a significant $\delta^{34}\text{S}$ shift across the Birimian crust, with lighter values found in older rocks to the east.

7.7 Conclusions

The main isotopic characteristics of the Loulo orebodies are summarised below:

1. $\delta^{18}\text{O}_{\text{silicate}}$ compositions are extraordinarily homogenous at Loulo: Gara gold-bearing quartz veins = $+16.4 \pm 0.2\text{‰}$; auriferous Yalea Main quartz veins = $+16.1 \pm 0.2\text{‰}$; albite alteration at Yalea Main = $+15.6\text{‰}$ (n = 2); and barren veins = $+16.4\text{‰}$ (n = 3).
2. $\delta^{18}\text{O}_{\text{carbonate}}$ values are slightly more heterogeneous: Gara mineralised veins = $+15.4 \pm 0.2\text{‰}$; Yalea Main carbonates = $+14.4 \pm 0.6\text{‰}$; Faraba-P64 veins = $17.7 \pm 1.4\text{‰}$; and barren calcite veins = $+17.4 \pm 2.3\text{‰}$.
3. Estimated $\delta^{18}\text{O}_{\text{fluid}}$ compositions mainly fall in range of +8 to +12‰ implying a dominant metamorphic fluid signature. However, in the case of the Gara-style deposits, where magmatic signatures are observed in mineralogy and fluid inclusion characteristics, a potential $\delta^{18}\text{O}$ -enriched fluid derived from peraluminous granitic rocks cannot be ruled out.
4. Paired quartz-ankerite equilibria for mineralised veins imply crystallisation temperatures of 311-329 °C for Gara and Yalea Main. Cogenetic mineral phases in barren veins and alteration zones appear not to be in isotopic equilibrium, or carbonate grains have re-equilibrated during exhumation.
5. The Loulo orebodies show a wide spread in $\delta^{13}\text{C}$ compositions. Yalea Main and Faraba display light $\delta^{13}\text{C}$ compositions of -21.7 to -10.8‰, which indicate a reduced C source (caused by interaction with host-rocks rich in carbonaceous matter). Gara carbonates show heavier $\delta^{13}\text{C}$ compositions between -14.4 to -4.5‰, suggesting a magmatic and a reduced C contribution (C sourced from both end-member fluids).
6. Barren veins show distinctly different $\delta^{13}\text{C}$ signatures to mineralised veins, with values

close to zero and analogous to wall-rock carbonates and dolostones. Thus, barren veins show no evidence of interacting with the reduced sediments and likely formed from the dissolution of sedimentary carbonate.

7. The significant differences in $\delta^{13}\text{C}$ signatures between mineralised and barren carbonates suggests carbon isotopes can be a potentially useful exploration tool at Loulo, with negative $\delta^{13}\text{C}$ values linked to gold occurrence.
8. Sulphur isotope compositions show typical features for sediment-hosted orogenic gold deposits. Reduced $\delta^{34}\text{S}$ values at Loulo range from +5.8 to +15.5‰ (higher at Gara), closely matching syngenetic-diagenetic pyrites from the host sediments (+6.4 to +9.0 ‰). Sulphur was originally fixed as pyrite in the host sediments by reduction of seawater and later leached by fluid-rock interactions.

CHAPTER 8: ORE GENETIC MODEL FOR LOULO

The mineralogical and geochemical data presented in *chapters 4 to 7* have provided a number of key constraints on the fluid evolution of the Loulo hydrothermal system. In this chapter, these data are used to develop a precise ore genetic model for Loulo. Data collected at Loulo are also considered in a wider context, such as the implications for orogenic gold mineralisation in general and Birimian metallogenesis, together with possible local and regional exploration strategies along the SMSZ.

8.1 Introduction

The Loulo gold deposits show typical orogenic gold characteristics in terms of geological setting (associated with an accretionary orogeny), structural setting (shear hosted, with mineralisation situated within 2nd or higher order splays off a major terrane-bounding shear zone); host geology (situated within greenschist facies rocks); and timing of mineralisation (emplacement towards the late stages of the Eburnean orogeny; Vielreicher, 2006) (*see* Table 1.2 for comparison with reported orogenic gold deposits). However, several Loulo orebodies contain atypical features in terms of ore mineralogy, wall-rock alteration and ore fluid composition. Consequently, ore genetic studies at Loulo can help in the ongoing development and understanding of orogenic gold systems.

8.2 The northern Loulo orebodies

8.2.1 Gara- vs. Yalea-style orebodies

Previous chapters have clearly shown that contrasting styles of gold mineralisation occur at Loulo. In this section, orebodies in the northern half of the Loulo permit are discussed. Orebodies associated with the Gara subarea (*section 3.2.2*) (Gara, Gara West, P129) and the Yalea North oreshoot are termed Gara-style deposits. These deposits contain unusual orogenic gold features, typified by Fe-rich mineralised zones, high concentrations of REE minerals, widespread tourmaline and sodic alteration, and hypersaline (~45 wt.% NaCl equiv.) H₂O-CO₂- NaCl-FeCl₂ fluid inclusions. In contrast, a majority of the deposits associated with the Yalea-trend (termed Yalea-style deposits) show typical metasediment-hosted orogenic gold characteristics (*c.f.* Groves *et al.*, 2000; Ridley & Diamond, 2000; Goldfarb *et al.*, 2005). Mineralised zones are As-rich, with pyrite and arsenopyrite the dominant sulphide phases (~70:30 ratio); alteration assemblages consisting of sericite-chlorite-ankerite and a notable lack of tourmaline (although sodic alteration is still common); and an ore fluid composition characterised by a low-salinity (<10 wt.% NaCl equiv.) H₂O-CO₂ fluid. The gold-grade in these deposits varies but shows no significant difference between the two different styles. The ore mineralogy, wall-rock alteration, fluid inclusion and isotope characteristics of Gara- and Yalea-style orebodies are summarised in Table 8.1.

Table 8.1. Mineralogical and geochemical characteristics of the Gara- and Yalea-style orebodies at Loulo (data taken from Table 4.22, Table 5.5 & Table 6.8).

	Gara-style	Yalea-style
Examples	Gara, Gara West, Yalea North, P-129 & P-64?	Yalea Main, P-125, Loulo-3 & Baboto
- Ore Mineralogy		
Mineralisation styles	Ankerite-quartz vein-hosted, breccia-hosted & disseminated orebodies	Quartz vein-hosted, ankerite-quartz vein-hosted, sulphide veinlets/ stringers & massive disseminated styles
Major sulphides	Pyrite (>90%; mainly >99%)	Pyrite & arsenopyrite (>90%)
Minor sulphides	Chalcopyrite + gersdorffite + pentlandite + pyrrhotite + arsenopyrite ± cobaltite	Chalcopyrite + tennantite + pyrrhotite + galena ± tetrahedrite ± jamesonite ± bourmonite ± ullmannite
Other ore minerals of interest	Monazite + xenotime + scheelite ± minor magnetite	Range of tungstates (mainly scheelite) + sayrite ± magnetite
Metal association	Fe-Cu-REE-W-Ni-As-Au ± Co-Ag-Pd	Fe-As-Cu-W-Au-Pb-Sb-Ag
Gold location	Gold mainly confined to pyrite in numerous sites. Free gold is minor (except P-64).	Gold situated in a range of sulphide phases.
Gold fineness	>980 (mainly <1 wt.% Ag). Some rare Pd-bearing grains.	840-960 (5 to 15 fold increase in Ag with respects to Gara-style deposits).
- Alteration		
Alteration types	Tourmalinisation & albitisation	Phyllic & carbonate alteration Albitisation (predates mineralisation)
Alteration assemblages	1. Tourmaline + quartz + biotite + ankerite + siderite + rhodochrosite 2. Albite + quartz ± haematite ± ankerite	1. Sericite + chlorite + ankerite + quartz 2. Albite (early) + ankerite + quartz + sericite ± haematite ± pyrite
Mass gains	B + Na + Fe + Mg + Si, plus minor CO ₂ + Ca + Mn	CO ₂ + H ₂ O + K + Ca + Si + Na, plus minor Fe + Mg
- Fluid Inclusions		
Major inclusion types	CO ₂ (58.3-100 mol.%) ± CH ₄ (0-32.7 mol.%) incs. (type 1), with traces of N ₂ (mainly 0-5 mol.%). Mixed-salinity (5-21 wt.% NaCl equiv.) H ₂ O-NaCl-CO ₂ ± CH ₄ incs. (type 3), with traces of N ₂ (CO ₂ -N ₂ -CH ₄ ratios of 57-100, 0-15.5 & 0-27.6 mol.%). Hypersaline (40-60 wt.% equiv.) H ₂ O-NaCl-FeCl ₂ -CO ₂ ± CH ₄ incs. (type 4).	CO ₂ -N ₂ ± CH ₄ incs. (type 1) (CO ₂ -N ₂ -CH ₄ ratios of 49.1-95.7, 4.3-45.7 & 0-28.2 mol.%). Low-salinity (<12 wt.% NaCl equiv.) H ₂ O-NaCl incs. (type 2).
Minor inclusion types	Moderate-salinity (~13-22.6 wt.% NaCl equiv.) H ₂ O-NaCl incs. (type 2) (unrelated to mineralisation).	Low-salinity (<10 wt.% NaCl equiv.) H ₂ O-CO ₂ -N ₂ incs. (type 3) (CO ₂ -N ₂ ratios of 79.1-96.8 & 3.2-20.1 mol.%). Moderate-salinity (17.8-22.8 wt.% NaCl equiv.) H ₂ O-NaCl incs. (type 2) (unrelated to mineralisation).
- Stable Isotopes		
	δ ¹⁸ O from +10.2 to +11.5‰; δ ¹³ C from -14.4 to -4.5‰; & δ ³⁴ S +11.5 to +15.5‰	δ ¹⁸ O from +7.3 to +12.3‰; δ ¹³ C from -21.7 to -15.9‰; & δ ³⁴ S +5.8 to +9.6‰

8.2.2 Yalea-style orebodies

8.2.2.1 Ore mineralisation

Mineralisation in the Yalea-style deposits is hosted in ankerite or quartz-dominated veins, sulphide veinlets/stringers and/or in disseminated sulphide zones. These orebodies contain a uniform ore paragenesis, although minor differences are observed in the trace mineral assemblages of individual orebodies. The two dominant sulphide phases are pyrite and arsenopyrite, with the latter showing a polyphase growth history. Arsenopyrite-I occurs in textural equilibrium with pyrite, as inclusions and intergrowths, while the more dominant arsenopyrite-II phase post-dates pyrite generation, either pseudomorphously replacing pyrite or occurring as overgrowth phases. Minor and trace phases include pyrrhotite, galena and scheelite, plus sporadic appearances of Sb-Pb minerals (jamesonite, bournonite and ullmannite) which increase in abundance towards the north at Baboto. The last stage of sulphide paragenesis is marked by Cu sulphidation (also common for Gara-style deposits), with chalcopyrite + tennantite \pm tetrahedrite formation (<10% of total sulphide generation). Ore paragenesis in the Yalea-style orebodies implies a fluid chemistry evolving from Fe through to As to Cu-rich fluids.

Gold (1-70 μm) is associated with all stages of sulphide growth (multiple mineralisation events). However, the majority of visible gold particles are located in pyrite, either occluded or situated in remobilised sites (*see chapter 4*). Despite the widespread appearance of arsenopyrite in high-grade zones, visible gold in both arsenopyrite phases is limited compared to pyrite. Wavelength dispersive spectra (WDS) analysis of individual arsenopyrite grains showed no evidence of refractory gold (lattice bound “invisible gold”). It is therefore suggested that gold associated with arsenopyrite formation mainly occurs as patchy zones of invisible gold (discussed further in *section 8.2.2.6*), or that gold is selectively remobilised from arsenopyrite and deposited locally along micro-fracture planes that tend to concentrate in pyrite crystals. Additionally, gold in arsenopyrite could be present as nanoparticles. Gold nanoparticles have recently been envisaged as an important component of hydrothermal gold systems (Hough *et al.*, 2009). Gold fineness for Yalea-style bodies is typical for orogenic gold deposits hosted in metasedimentary rocks (Goldfarb *et al.*, 2005), with fineness values between 840 and 960.

The source of the sulphur in Yalea-style orebodies was determined by isotope analysis (*section 7.5; section 7.6.3*). Sulphur isotope compositions of mineralised pyrite and arsenopyrite-II from Yalea and Loulo-3 ($\delta^{34}\text{S}$ +5.8 to +9.6‰) closely match isotopic signatures of syngenetic-diagenetic pyrites from the S-depleted host sediments (+6.4 to +9.0‰). Sulphur was initially fixed as marine pyrite, largely within the carbonate units of the Kofi Series, by the reduction of Birimian seawater. During orogenesis, efficient leaching of these sediments by Yalea-style hydrothermal fluids removed the S (+Fe) to form the hydrothermal sulphides.

8.2.2.2 *Fluid origin and chemistry*

Fluid inclusion and isotope studies have successfully ascertained the composition of the Yalea-style ore fluids. Fluid inclusion populations are dominated by carbonic and aqueous inclusions, which show strong evidence of phase separation from a primary low-salinity (≤ 10 wt.% NaCl equiv.) $\text{CO}_2\text{-H}_2\text{O-NaCl-N}_2 \pm \text{CH}_4$ fluid ($\text{CO}_2\text{-N}_2\text{-CH}_4$ ratios of 49.1-96.8, 3.2-45.7 and 0-28.2 mol.%, respectively). Although these fluids are CO_2 -rich, the exact CO_2 concentration is unknown as primary inclusions are absent from the inclusion assemblage. The redox state of the ore fluid is close to the QFM buffer (*see chapter 7*). The composition of the Yalea-style ore fluid is similar to other Birimian gold deposits and orogenic gold deposits reported elsewhere (*section 6.3*). The $\delta^{18}\text{O}$ composition of the mineralising fluid at Yalea Main shows uniform values between +8.9 to +11.0‰ (obtained from quartz-ankerite vein material). These compositions indicate a metamorphic fluid source for Yalea-style deposits, which is considered by many researchers to be the fluid model most favoured for orogenic gold deposits (discussed in detail in *section 8.5.1*).

The temperature of the mineralising fluids can be inferred from mineral and alteration assemblages, as well as from fluid inclusion and isotope data. Emplacement conditions for Yalea Main and Loulo-3 are bracketed between 271-377 °C (Table 8.2), with the majority of the data indicating temperatures of 300-350 °C at 1-2 kbar (i.e. mesozonal orogenic gold deposits; Groves *et al.*, 1998). The uniform $\delta^{18}\text{O}$ measured from quartz and carbonate veins at Yalea Main implies a near constant ambient fluid temperature for mineralisation. Ore fluid temperatures at Baboto are more enigmatic. Arsenopyrite geothermometry indicate formation temperatures in the range of 300-372 °C, while trapping conditions calculated from fluid inclusion modelling imply higher temperatures of 440 °C at 2.9 kbar (mean values).

Table 8.2. P-T estimates for Yalea-style mineralisation.

Deposit	Arsenopyrite geothermometry	Chlorite geothermometry	P-T modelling of fluid inclusions (mean values)	$\delta^{18}\text{O}$ paired quartz-ankerite equilibria
Yalea Main	320-367 °C (mean = 326 °C)	294-333 °C (mean of 315 °C)	340 °C at 1.8 kbar	329 °C
Loulo-3	320-377 °C (mean = 327 °C)	271- 313 °C (mean of 296 °C)	335 °C at 1.9 kbar	—
Baboto	300-372 °C (mean = 320 °C)	—	440 °C at 2.9 kbar	—

Note- see previous chapters for information on these techniques.

8.2.2.3 *Source of volatile components*

The source of the large CO₂ concentrations in the Yalea-style metamorphic fluids is debatable. Carbon dioxide may have been sourced from decarbonation reactions at depth during regional metamorphism or by internal buffering of the ore fluid by interaction with limestones/dolostones and/or host sediments rich in carbonaceous matter. The reduced δ¹³C values observed at Yalea Main (-21.7 to -15.9‰) imply a 43-87% carbon input from an organic carbon source. Carbon dioxide could have been leached into solution by inorganic oxidation (C + O₂ → CO₂) or by hydrolysis reactions (e.g. 2C + 2H₂O → CO₂ + CH₄). The latter equation could also explain the appearance of CH₄ and amorphous carbon/graphite (in situ equilibration) observed in some carbonic-bearing inclusions (*section 6.6*). Nitrogen is a common component of Birimian mineralising fluids. According to Yao *et al.* (2001), nitrogen is fixed in K-bearing sedimentary minerals as ammonia (NH₃) and released during metamorphism. Alternatively, N could be sourced from carbonaceous sediments which are common in the Birimian (e.g. black shales in Ghana and Burkina Faso; Křibek *et al.*, 2008). Nitrogen is a good indicator for a metamorphic fluid in the Loulo district (largely absent from Gara-style veins, which are proposed to have a significant magmatic input; *section 8.2.3*).

8.2.2.4 *Source of metals*

The source of many of the metals in the Yalea hydrothermal system (e.g. Fe, As, Cu) is likely to have a background crustal origin. However, the gold source is more debatable. Several studies have shown orogenic gold deposits (> 1 Moz) can form from efficient leaching of 10-125 km³ of crustal rocks that contain normal concentrations of gold around 1-2 ppb (e.g. Fyfe & Kerrich, 1984; Pitcairn *et al.*, 2006). Pyrite situated in marine sediments and greenstones is a likely leachable source mineral with high background concentrations of gold (Groves *et al.*, 2003) (i.e. marine pyrite may be the source of S + Fe + Au). Alternatively, some researchers believe a pre-concentration of gold is needed to form a significant size orogenic gold deposit (e.g. Henley *et al.*, 1976; McKeag *et al.*, 1989; Bierlein *et al.*, 1998b) (discussed further in *section 8.5.2*).

8.2.2.5 *Metal transport*

Metal solubilities of simple aqueous ions (such as Zn²⁺, Pb²⁺, Au⁺) in hydrothermal solution are too low for the transport of significant quantities of ore metals (Barnes, 1979). To obtain solubilities necessary for ore deposit formation, metals must form complexes (Wood & Samson, 1998). In nature, gold dominantly occurs as Au⁺, which is generally considered to be a soft metal (weakly charged, strongly polarisable ions) (Pearson, 1963). Thus, gold will preferentially bond with soft ligands. In hydrothermal fluids up to 350 °C (applicable for the majority of Yalea-style deposits; excluding Baboto), the most important gold ligand is HS⁻ (Seward, 1973) (Fig. 8.1), which is consistent with the reduced nature of the Yalea-style ore fluid

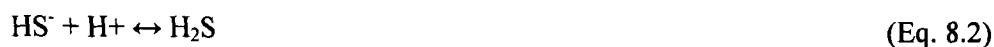
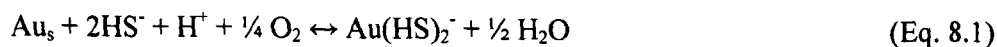
and the textural evidence of cogenetic formation of sulphides and gold (at least partially). At low pH, the predominant complex is AuHS° , while $\text{Au}(\text{HS})_2^-$ is common in neutral to alkaline pH fluids (Fig. 8.2) (Benning & Seward, 1996; Stefánsson & Seward, 2004). Although the exact pH of the Yalea-style fluid is unclear, the majority of orogenic gold deposits contain a neutral to slightly alkaline pH, indicating that $\text{Au}(\text{HS})_2^-$ is the dominant ligand in such deposits (Mikucki, 1998).

Fig. 8.1. Gold solubility (in molality, m , and in parts per billion) and speciation at 1 kbar, as a function of temperature for aqueous solution containing 1.5 molal (m) NaCl and 0.5 m KCl, with pH buffered by the assemblage K-feldspar-muscovite-quartz. **A)** $f\text{O}_2$ buffered by the haematite-magnetite (HM) assemblage ($\Sigma\text{S} = 0.01$ m). **B)** ΣS and $f\text{O}_2$ buffered by the assemblage pyrite-pyrrhotite-magnetite ($\Sigma\text{S} = 0.1$ m). Black dashed lines (ΣAu) represent total solubility of gold (figure from Williams-Jones *et al.*, 2009).

Fig. 8.2. Gold solubility (in part per billion; solid lines) and speciation at 0.5 kbar and 250 °C, as a function of $\log f\text{O}_2$ and pH in a solution containing 1 m NaCl and ΣS of 0.01 m. Dashed lines separate regions of predominance of certain complexes. Coloured zones represent high gold solubilities (figure from Williams-Jones *et al.*, 2009).

8.2.2.6 Gold precipitation

In the case of the Yalea-style deposits, the dissolution and deposition of gold at temperatures up to ~350 °C is controlled by the following reactions (Williams-Jones *et al.*, 2009):



Applying Le Châtelier's principle to this equation, the principal factors affecting gold precipitation are a decrease in the activity of HS^- and $f\text{O}_2$, and an increase in pH (i.e. consumption of H^+) (Mikucki, 1998; Williams-Jones *et al.*, 2009).

Numerous mechanisms appear to be responsible for gold deposition in the Yalea-style hydrothermal system. The principal cause is phase separation of the ore fluid (Fig. 8.3), which is evident from fluid inclusion studies (*section 6.7.1*). The cause of fluid unmixing could be three-fold: (1) cooling of the fluid to below the solvus; (2) fluctuations in pressure, for example due to fault-valve mechanisms (Sibson, 1987; Sibson *et al.*, 1988) or fluid movement into dilational zones (e.g. the N-S Yalea Reidel shear); or (3) expansion of the solvus due to fluid interaction with carbonaceous-rich sediments (as suggested by carbon isotopes) (Naden & Shepherd, 1989; Mernagh & Witt, 1994). Fluid unmixing of a H_2O - CO_2 ore fluid would preferentially fractionate the H_2S in the vapour phase (i.e. the CO_2 phase) and ultimately lower the HS^- activity in the aqueous fluid, and therefore promote gold precipitation. As well as causing phase separation, fluid interaction with the carbonaceous-rich Kofi limestones/dolostones can also have a direct effect on gold deposition by reducing the $f\text{O}_2$ activity of the ore fluid (e.g. Gebre *et al.*, 1997).

The interaction between H_2S -rich auriferous fluids and Fe-rich host rocks has been suggested to be an important depositional mechanism in many orogenic gold districts (e.g. Neal & Phillips, 1987; Groves & Phillips, 1987; Cox *et al.*, 1995). In this scenario, gold drops out of solution because the bi-sulphide complex is destabilised as H_2S is lost from the system during sulphide formation (e.g. pyrite). Although this explains the close association between gold and sulphides, this style of fluid-rock interaction is only considered a minor depositional mechanism in vein-hosted deposits at Loulo, because sulphides + Au are largely absent from the alteration zones (focussed vein emplacement). However, in disseminated-hosted deposits, such as P-125, de-sulphidation reactions may play an important role in gold mineralisation. Chemisorption processes may also be operative at Loulo, whereby gold absorbs onto the surface of coevally or previously precipitated sulphide minerals, by half cells reactions (Jean & Bancroft, 1985; Starling *et al.*, 1989; Michel & Giuliani, 1996):



Surface chemistry-driven processes have been suggested to be responsible for the high contents of invisible gold in arsenian pyrite, arsenopyrite and loellingite in certain lode gold deposits (Cathelineau *et al.*, 1989; Neumayr *et al.*, 1993a). This process may explain the patchy appearance of invisible gold in the Yalea-style arsenopyrites. Extensive studies of sulphide minerals in Carlin-type deposits reveal that incorporation of Au into the sulphide structure is facilitated by the presence of As (Hough *et al.*, 2009).

8.2.2.7 *Alteration associated with Yalea-style mineralisation*

Two styles of alteration assemblages are associated with Yalea-style orebodies (*section 5.3.2*). Pink albite-ankerite-quartz-haematite alteration halos are common and extend up to 100 m away from the mineralised zones. Sodic alteration is widespread throughout the Loulo district and largely predates the mineralisation in this style of deposit. Distal alteration zones at Yalea show an overall mass gain of 10%, with significant elemental mass gains in Na₂O (~150%) and SiO₂ (~40%) and losses in MgO, K₂O, Fe₂O₃ and MnO. Carbonate concentrations increase towards the orezones and generally outlast albite formation, often forming alteration selvages around quartz ankerite-sulphide veins or sulphide-rich veinlets and stringers, as well as occurring as an early interstitial phase between larger albite grains. Oxygen isotopic signatures of coeval albite-ankerite alteration material from the proximal metasomatic zone at Yalea Main show more compositional variety ($\delta^{18}\text{O}$ between +7.3 to +12.3‰) than mineralised vein material, which probably relates to modifications through fluid-rock interactions. Silicification and sulphidation are limited in many of the alteration halos surrounding Yalea-style deposits (mainly vein focussed), although silica alteration becomes predominant in the Baboto deposit to the north. This is a common characteristic of deeper level orogenic gold deposits (decrease in carbonisation; Groves *et al.*, 1998).

A second, less common, alteration assemblage associated with Yalea-style orebodies is sericite-chlorite-ankerite-quartz alteration, which appears to be coeval with mineralisation (Allibone & Cameron, 2006). This style of alteration is sometimes difficult to distinguish from regional greenschist facies metamorphic assemblages. Phyllic alteration overprints the sodic alteration zones and either occurs in ductile shears sub-parallel to the main shear direction, as thin green-black alteration envelopes (<5 cm) around auriferous veins, or as gangue material with quartz-ankerite veins. Sericitisation increases towards the orezones. The addition of CO₂, H₂O Ca, K, and Si observed at Yalea-style deposits is typical for alteration zones associated with orogenic gold mineralisation (e.g. Kerrich, 1989; *section 5.1*).

8.2.3 Gara-style orebodies

8.2.3.1 Ore mineralisation

Gara style deposits are associated with a range of mineralisation styles including quartz-ankerite stockworks (e.g. Gara), breccia-hosted (Yalea North) and disseminated pyrite zones (e.g. P-64 & Gara West). These deposits contain remarkably different petrogenetic assemblages in comparison to Yalea-style bodies (Table 8.1) and many reported orogenic gold deposits (see Table 1.2). The main distinctions of Gara-style mineralisation are listed below:

1. Vein-hosted deposits are ankerite-rich (most orogenic vein-hosted deposits are quartz-dominated and few are ankerite-rich).
2. Orebodies are Fe-rich and As-depleted, with pyrite as the principal sulphide phase (95-99%) (most metasedimentary-hosted gold deposits are arsenopyrite rich; Groves *et al.*, 2000).
3. Ore assemblages are rich in REE phosphates and Ni-bearing sulphides (former more dominant).
4. A metal association of Fe-Cu-REE-W-Ni-As-Au ± Co-Ag-Pd.
5. Gold fineness is extremely high (>990). Most reported orogenic gold deposits hosted in metamorphic rocks have fineness values of 800 to 900 (i.e. gold grains up to 20 wt.% Ag; Goldfarb *et al.*, 2005).

The Fe-Cu-REE-W-Ni metal signature of the Gara-style deposits is an atypical metal association for orogenic gold deposits. The large amount of Fe, abundant monazite, xenotime and scheelite imply a possible magmatic input to the formation of these Loulo orebodies (*c.f.* intrusion-related gold deposits; e.g. Lang & Baker, 2001; Hart, 2007). Similar metal signatures are associated with nearby granitoids (see chapter 3). The Yalea North orebody shows slightly different ore assemblages to other Gara-style deposits. This deposit is characterised by trace sulphide phases dominated by Co-Ni sulphides, the presence of native gold and native silver, and a lower gold fineness (920-990). This orebody could represent a more mafic end-member of the Gara-style hydrothermal system.

Sulphur isotope compositions of mineralised pyrites from Gara are slightly higher than, but not significantly different to, the Yalea-style deposits (+11.5 to +15.5‰), and do not show a magmatic source. This can be explained by the appearance of a second, S-rich fluid (“Yalea-style fluid”) in the Gara-style hydrothermal system, with fluid mixing responsible for mineralisation (discussed further below).

8.2.3.2 Fluid chemistry, origin and evolution

Two primary mineralising fluids have been identified in the Fe-rich Gara-style orebodies: (1) a lower temperature (300-350 °C), low-salinity (<10 wt.% NaCl equiv.) CO₂-H₂O-NaCl fluid, rich in H₂S-N₂ ± CH₄; and (2) a high temperature (>400 °C), hypersaline (~45-55 wt.% NaCl equiv.) H₂O-NaCl-FeCl₂-B-CO₂ ± CH₄ fluid. These fluids contain noticeably different chemistries and are clearly derived from two separate fluid sources. The first fluid type is a low-density (< 1 g/cm³), reduced (QFM buffered), CO₂-rich fluid (the exact CO₂ molality unclear due to the mixing process); identical to the mineralising fluid responsible for Yalea-style mineralisation (“a Yalea-style metamorphic fluid”). The second Gara-style fluid is a high-density (1.35-1.5 g/cm³), aqueous-rich (X_{H₂O} of 0.7-0.8), CO₂-poor (X_{CO₂} <0.1), S-depleted, oxidised, acidic brine. Fluid inclusions representative of this brine are multiphase with a daughter assemblage consisting of halite and Fe-chloride (probably lawrencite; FeCl₂) (10:1 ratio), rare K-Ca chlorides, haematite, calcite, ankerite and magnetite (Fig. 6.4; Table 6.2). The presence of both haematite and magnetite suggests that deposition conditions were near those of the HM buffer.

Sources of high-salinity fluids

The discovery of hypersaline fluids at Loulo is significant in terms of the understanding of fluid evolution in orogenic gold systems, as these fluids have been sparsely recognised in this deposit type (at least as fluids related to mineralisation). The Na-Fe-Ca-K-rich composition of these fluids is analogous to mineral deposits derived from magmatic fluids (Hedenquist & Lowenstern, 1994). However, there are numerous other possible sources for the high-salinity fluids: (1) they could represent an evolved seawater fluid that has interacted with evaporite host rocks (basinal brines) (Boullier *et al.*, 1998; Wilkinson *et al.*, 1999; Oberthür *et al.*, 2000); (2) or form by extreme fluid unmixing of a low-salinity H₂O-CO₂ fluid (Bowers & Helgeson, 1983a, b); or (3) form through hydrolysis reactions (i.e. sericitisation, which removes H₂O from the system leaving behind a salt saturated phase) (e.g. Bennet & Barker, 1995).

The basinal brine model is unlikely as such fluids are typically of low temperature and Ca-rich in composition. Furthermore, no evaporite units have been recorded in the Kofi Series. Extreme fluid unmixing and hydrolysis reactions are unlikely to produce such high-salinity fluids. In addition, the different homogenisation temperatures of the low-salinity H₂O-CO₂ fluids and the brines exclude fluid immiscibility for the Gara-style deposits (*c.f.* Ramboz *et al.*, 1982). Thus, a magmatic fluid is the most favoured model to explain the appearance of these hypersaline fluids, which is consistent with the magmatic signature observed in the ore and alteration assemblages at these deposits (latter discussed in section 8.2.3.5). Bromine/chlorine ratios and chlorine isotopes (δ³⁷Cl) would accurately determine the origin of salinity in these fluids (e.g. Banks *et al.*, 2000); and is a scope for future work.

Fluid mixing model

The distinct characteristics of the Gara-style deposits are controlled by the partial mixing of the high temperature (>400 °C), Fe-rich magmatic brines and the circulating regional, cooler (300-350 °C), CO₂-rich metamorphic fluid. Fluid mixing is unlikely to be a single pass system resulting in catastrophic precipitation of gold, but rather repeated pulses of fluid movement (e.g. via seismic pumping; Sibson, 1987; Sibson *et al.*, 1988). The best (but not only) trigger for gold precipitation is when these two fluids interact and mix (gold depositional mechanisms discussed in *section 8.2.3.4*). Carbon isotope signatures for this style of deposit show good evidence for fluid mixing, with $\delta^{13}\text{C}$ compositions (-14.4 to -4.5‰) overlapping the metamorphic and magmatic fields (carbon sourced from both fluid types). However, the oxygen isotope composition of the mineralising fluid at Gara show remarkably uniform $\delta^{18}\text{O}$ values between +10.0 to +11.2 ‰ (similar to Yalea Main), which are not typical for magmatic fluids (magmatic oxygen signature generally between +5 to +9‰; Ohmoto & Goldhaber, 1997). However, these higher values could reflect contributions from a more $\delta^{18}\text{O}$ -enriched magmatic source, such as fluids derived from peraluminous granitoids (Sheppard, 1986) (discussed in *section 7.6.1*). Paired quartz-ankerite $\delta^{18}\text{O}$ equilibria indicate crystallisation temperatures of 311-329 °C for mineralised veins at Gara. This suggests mixing between the more dominant, cooler, metamorphic fluid and the high temperature brine had little effect on the overall temperature of the fluid. However, higher temperatures for mineralisation at Gara are inferred from arsenopyrite geothermometry (400-447 °C; limited data).

The extent of the magmatic Gara-style fluid is indicated by the regional-scale boron anomaly which extends 200 km along strike of the SMSZ (Fig. 5.20). Strong seismic pumping must have been in place to drive and focus magmatic fluids over such large distances and to restrict conductive cooling during interaction with the country rock. A schematic of the fluid mixing model applied to Loulo is shown in Fig. 8.3.

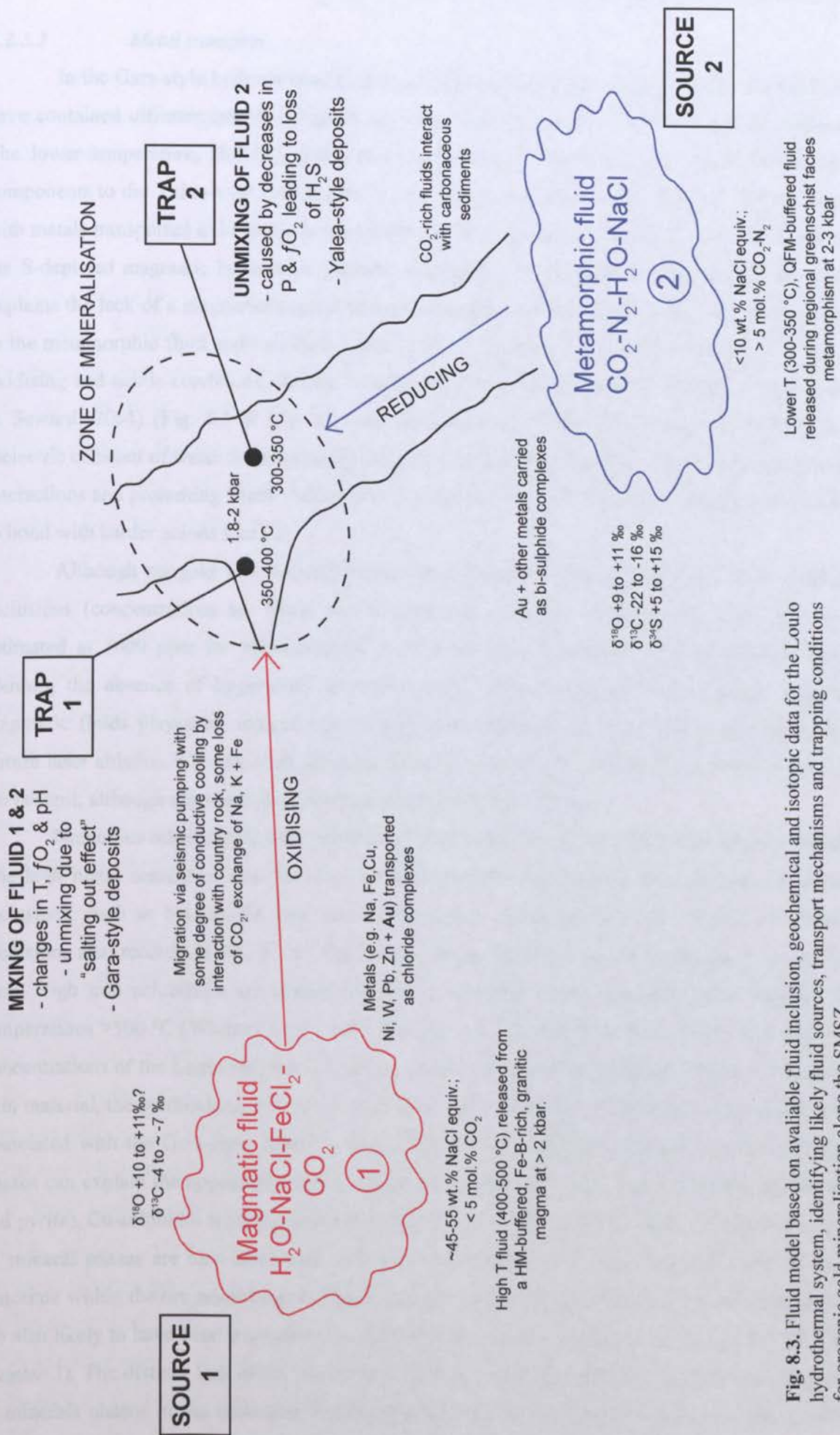


Fig. 8.3. Fluid model based on available fluid inclusion, geochemical and isotopic data for the Loulo hydrothermal system, identifying likely fluid sources, transport mechanisms and trapping conditions for orogenic gold mineralisation along the SMSZ.

8.2.3.3 Metal transport

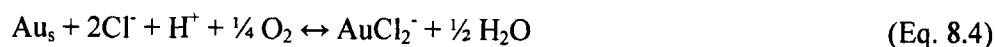
In the Gara-style hydrothermal system, the magmatic and metamorphic fluids are likely to have contained different transport ligands and consequently carried different metals in solution. The lower temperature, H₂S-CO₂-rich metamorphic fluid is likely to have transported similar components to the Yalea-style fluid (some Fe, As, W, Au, Ag and volatiles such as CO₂, N₂ etc), with metals transported as bi-sulphide complexes. In contrast, metals (including Au) carried within the S-depleted magmatic brine were probably transported as oxidised chloride complexes. This explains the lack of a magmatic sulphur isotope signature within this style of deposit (S confined to the metamorphic fluid end-member). Under higher temperature (>350 °C), high-salinity, more oxidising and acidic conditions, the AuCl₂⁻ complex will predominate over Au(HS)₂⁻ (Stefansson & Seward, 2004) (Fig. 8.1 & Fig. 8.2). As documented by Williams-Jones *et al.* (2009), the dielectric constant of water decreases with increasing temperature, therefore favouring electrostatic interactions and promoting “hard” behaviour. This then allows a soft metallic element such as Au⁺ to bond with harder anions like Cl⁻.

Although no gold was detected in the brine inclusions during SEM analysis of opened inclusions (concentrations are likely to be lower than detection limits of the EDS analyser; estimated at 5000 ppm for measurements taken from uneven fracture surfaces; Giddens pers. comm.), the absence of hypersaline inclusions from barren veins surrounding Gara suggests magmatic fluids played an integral role in gold mineralisation and most likely gold transport. Future laser ablation ICP-MS work on these inclusions would give indications as to the levels of Au present, although the small inclusion size may inhibit such studies.

Numerous other metals were transported as chloride complexes within the magmatic fluid. The high metal content of this fluid can be inferred from the daughter assemblages within the inclusions, such as Na and Fe, and less so, Ca and K. Broad beam EDS analysis of opened inclusions also record Cu, Ni, W, Sr, Ba, Pb and Zn concentrations in chloride phases of >5000 ppm. High iron solubilities are typical features of oxidised, acidic magmatic fluids released at temperatures >500 °C (Whitney *et al.*, 1985; Kwak *et al.*, 1986; Rankin *et al.*, 1992). The high Fe concentrations of the Loulo magmatic fluid can account for the widespread occurrence of ankerite vein material, the predominance of pyrite, and the Fe-rich nature of the tourmaline alteration zones associated with the Gara-style deposits. The Ni-Cu-W metal signature observed in the chloride phases can explain the appearance of Ni-sulphides (gersdorffite pentlandite, Ni-bearing pyrrhotite and pyrite), Cu-sulphides (chalcopyrite and tennantite) and widespread scheelite; although the Cu-W mineral phases are also associated with the metamorphic fluid. The abundant monazite and xenotime within the ore assemblages at these deposits implies REE's (usually immobile elements) are also likely to have been transported by the magmatic fluids (nearby intrusions rich in LREE's; *chapter 3*). The distinct lack of Sr, Ba, Pb and Zn (other metals detected by microprobe analysis) as mineral phases in the orebodies implies that selective deposition of metals took place, with some metals transported further along the plumbing system.

8.2.3.4 Gold precipitation

Gold precipitation in Gara-style deposits is controlled by fluid mixing between two compositional contrasting fluids (Fig. 8.3). In the chloride-rich magmatic fluid, gold solubility is governed by the reaction (Williams-Jones *et al.*, 2009):



As is the case for Eq. 8.1, gold deposition is controlled by the decrease in ligand activity (Cl^-) and $f\text{O}_2$, and an increase in pH. Therefore, fluid mixing with a more reduced, alkaline-bearing metamorphic fluid will lead to gold deposition in the brine (drop in $f\text{O}_2$ and increase in pH). Although a decrease in temperature has little effect on deposition when gold is transported as a bi-sulphide complex, the opposite is true for a fluid where gold is transported as a chloride complex (Fig. 8.1) (Mikucki, 1998; Williams-Jones *et al.*, 2009). Thus, fluid mixing between a hotter magmatic fluid and a cooler regional metamorphic fluid will decrease the AuCl_2^- activity in the former fluid type. Consumption of H^+ during tourmalinisation could also be a further precipitation mechanism.

Gold present as a bi-sulphide complex (metamorphic fluid) is probably precipitated during fluid mixing by a process known as the salting out effect (Fig. 6.19; Fig. 8.3) (Anderson *et al.*, 1992). An increase in salinity will cause effervescence of the CO_2 component. During phase separation, H_2S will fractionate into the vapour phase and destabilise the $\text{Au}(\text{HS})_2^-$ complex. In the late grey quartz mineralised phase at Gara (CH_4 bearing fluids), reduction of one or both fluid types by interaction with carbonaceous-rich wall-rock could have acted as a further mineralisation trap (Naden & Shepherd, 1989; Gebre *et al.*, 1997).

8.2.3.5 Alteration associated with Gara-style mineralisation

The magmatic fluid partially responsible for mineralisation in the Gara-style deposits is associated with widespread tourmaline alteration, signifying a high boron content in the fluid. Although linked to mineralisation, tourmaline alteration is typically a broader event(s) (section 5.3.1.2). Tourmaline takes on many forms: such as cryptocrystalline grains within metasomatic zones (tourmaline 10-70% of the rock) (e.g. Gara & P-64), usually confined to quartz-wacke sediments (physical and chemical controls); as multiple phases in hydrothermal-tectonic breccias (e.g. Yalea North); as discrete veinlets often associated with mineralisation (P-64 & P-129); or as narrow proximal alteration selvages surrounding mineralised veins (seen in the majority of deposits). Tourmaline generally classifies as alkali, Fe-rich dravites and Mg-rich schorls, with high Fe^{3+} concentrations ($\text{Fe}^{2+}/[\text{Fe}^{2+} + \text{Fe}^{3+}]$ ratios as low as 0.37). The significant Fe^{3+} content of the tourmalines reinforces the idea that the magmatic fluid had a high $f\text{O}_2$. Syn-mineralisation tourmalines within auriferous veins show lower Fe^{3+} contents which is strong primary evidence that fluid mixing with the cooler metamorphic fluid during mineralisation resulted in the reduction

of the magmatic brine. Other minerals associated with tourmaline include quartz + biotite + ankerite + siderite + rhodochrosite. Geochemical analyses of the tourmaline-bearing quartz-wacke at Gara indicate a minimum net mass loss of 12% is associated with alteration. During the alteration process, porosity was created in the rock by the dissolving and removing of the major components, such as Si, to precipitate the tourmaline. Significant elemental mass changes also occurred reflecting the high fluid-rock ratio, with gains in B (not measured), MgO, Fe₂O₃, Na₂O, MnO and CaO, and losses in K₂O and SiO₂.

Pink albitisation is also a dominant alteration type observed surrounding Gara-style deposits. This style of alteration is associated with all styles of gold mineralisation in the Kofi Series, and also occurs within the granodiorites-diorites of the Falémé belt to the west of the SMSZ where it is linked to Fe skarn mineralisation. This widespread albitisation could be explained by the interaction of host rocks of different lithology with Na-rich magmatic fluids (developed further in *sections 8.2.3.6 and 8.4.1*).

8.2.3.6 Possible sources for magmatic fluids

Although the presence of a magmatic fluid has been established for the Loulo hydrothermal system, the exact source of this fluid is unclear. The strong Ni ± Co (latter observed at Yalea North) metal association at Gara-style deposits imply a dioritic-granodioritic source (e.g. Leblanc & Billaud, 1982). Three possible granitic bodies could be responsible for these fluids (*see Fig. 3.1 & Fig. 3.2 for locations*):

1. Metaluminous, I-type, granodiorites and quartz-diorites of the Balangouma and/or other belt-type plutons along the Falémé volcano-plutonic belt.
 - These plutons are associated with the Falémé Fe skarn deposits, supposedly of iron oxide copper-gold (IOCG) affinity (Schwartz & Melcher 2004).
 - This model would infer mineralising fluids crossed the SMSZ and could have possible links to IOCG/skarn deposits.
 - Pluton ages could constrain timing of mineralisation as belt-type plutons are generally considered as syn-orogenic intrusions; however, no geochronological data are available for the Balangouma plutons to compare with mineralisation dates at Loulo obtained by Vielreicher (2006) (2028 Ma ± 10 Ma).
2. The peraluminous Gamaye basin-type pluton, 20 km to the south of the Loulo mining camp.
 - If the δ¹⁸O data at Gara represent a magmatic fluid then a peraluminous granitic source is inferred to explain the enriched δ¹⁸O compositions.
 - This pluton is the only known B-rich intrusion in this part of the KKI and

could explain the widespread tourmaline in the Loulo district.

- This model would infer northward migrating fluids along the SMSZ.

3. A possible deep-seated granitic source.

- A recent geophysical survey has shown a significant gravity low beneath the Loulo mining camp (Fig. 8.4).

To develop this magmatic model further, it is important that future work concentrates on determining the exact source of the hypersaline fluids. Further mineralogical, fluid inclusion and isotopes studies are advised to test models 1 to 3, especially looking at the granitic rocks.

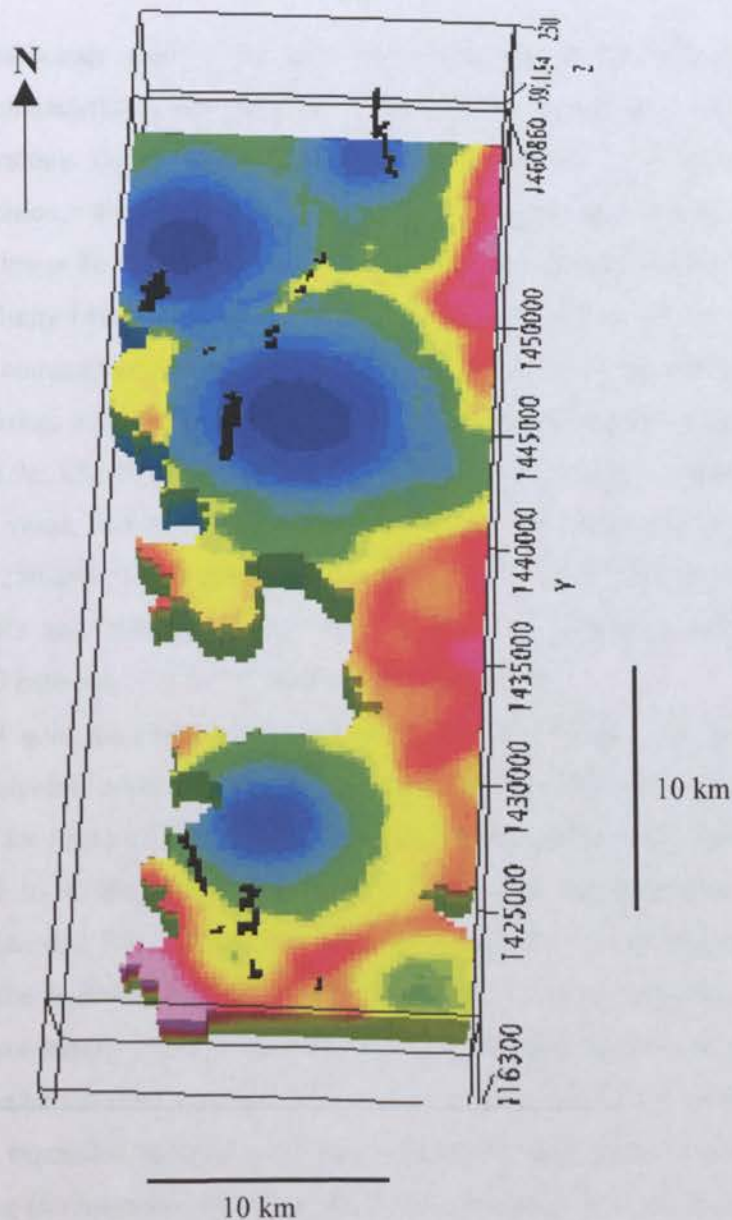


Fig. 8.4. A 2009 gravity map of the Loulo permit showing numerous low density anomalies in the northern part of the permit and in the south at Goukoto and P-64, indicating deep-seated granitic bodies exist within the Kofi sedimentary package. **Blues** = low density and **reds** = high density. Image courtesy of Randgold Resources.

8.2.4 *Post-mineralisation fluids*

Fluid inclusion studies at Gara and Yalea show the appearance of late, mixed salinity (mainly between 13.0 to 22.8 wt.% NaCl equiv.) aqueous fluids with no detectable CO₂, which appear to post-date mineralisation. Low eutectic melting temperatures of inclusions at Gara (T_e from -38.8 to -31.6 °C) imply a significant FeCl component to this fluid, although similar temperatures were not observed at Yalea Main (-24.0 to -22.0 °C; dominance of Na⁺ cations). The origin of these low temperature fluids (T_h mainly between 140-200 °C) is unknown. They could be linked to the late Cu mineralisation observed in the northern Loulo orebodies (late stage chalcopyrite ± tennantite ± tetrahedrite), although there is no clear evidence to support this.

8.2.5 *Barren fluids*

Barren quartz-carbonate veins (<0.1 g/t) show clear systematic differences in fluid inclusion and isotopic characteristics compared to mineralised veins, and also show pronounced variations in vein mineralogy. Barren veins are dominated by quartz +/- calcite, with a notable lack of ankerite precipitation, which constitutes the predominant carbonate phase in the auriferous veins. This reflects the lower Fe + Mg contents of the barren hydrothermal fluids. Barren Loulo fluids contain a low-salinity (mean of 6 wt.% NaCl) H₂O-CO₂-N₂ (6.5 to 17.2 mol.% CO₂-N₂) composition. This fluid composition is similar to the Yalea-style ore fluids. However, barren fluids appear to be more oxidising, with the complete absence of CH₄ and amorphous carbon within the fluid inclusions (Fig. 6.9c; CO₂-N₂ ratios of 63.6-96.9 and 3.1-36.4 mol.%, respectively). P-T conditions of barren veins, inferred from fluid inclusion data, suggest lower formation temperatures between 250-295 °C, at pressures of 0.75 to 2.15 kbar (*section 6.7.3*). Oxygen isotope data from quartz and carbonate phases show a wider compositional range than gold-bearing veins, with δ¹⁸O between +7.0 to +15.7‰ (metamorphic field).

The absence of gold mineralisation associated with these fluids could be the result of several factors. Low sulphide content in the barren veins suggests there was a lack of suitable ligands (e.g. Au[HS]₂) for gold transport in these particular metamorphic fluids. Secondly, carbon isotopes (δ¹³C from -2 to +3.8‰) imply CO₂ was sourced from metamorphism of the Kofi limestones/dolostones (*section 7.6.2*), rather than from the interaction of carbonaceous sediments (i.e. no reduction of the hydrothermal fluid, which appears to be an important depositional mechanism in the Loulo district). Thirdly, fluid inclusion evidence implies fluid immiscibility was less extensive within the barren fluids (*section 6.7.1*), which may be due to lack of interaction with reduced sediments (no expansion of the solvus) and limited P-T fluctuations. Lastly, the lack of evidence of fluid mixing (no magmatic fluid) could be a further cause for limited gold potential in these fluids.

8.3 The southern Loulo orebodies

Gold deposits in the southern parts of the Loulo district (Faraba, Goukoto & P-64) were investigated only briefly during this project. This section discusses the mineralogy of these orebodies, accompanied by limited stable isotope data. Further geochemical studies will need to be undertaken to confirm the preliminary interpretations outlined here.

8.3.1 Ore mineralisation

Similarities to the northern Loulo deposits

The southern Loulo orebodies show similarities and differences when compared to the Gara- and Yalea-style deposits. P-64 shows strong similarities to the Gara-style orebodies with Fe-rich assemblages (pyrite the principle sulphide phase), a metal signature consisting of Fe-Ni-REE-As-Au-Pd, Ag-depleted gold (fineness >990), and widespread tourmaline alteration. Faraba show similarities to the Yalea-style deposits (As-rich orebodies, Fe-As-Pb-Au-Ag metal association), while Goukoto is more difficult to classify (Gara-style ore mineralogy but limited tourmaline alteration). During this study I only had access to first core ever drilled at Goukoto. A more detailed study of this deposit would be worthwhile as it could be used to test models set out elsewhere in this thesis. For further information on the parageneses of these deposits, the reader is referred to *chapter 4 and appendices A-7*.

Differences from the northern Loulo deposits

The southern Loulo orebodies also show features that make them distinct from the northern Loulo orebodies, and are therefore classified as a third style of Loulo gold mineralisation (termed **Faraba-style deposits**). These deposits are characterised by the frequent appearance of telluride mineralisation (Te-Bi-Pb \pm Au-Ag bearing phases). Telluride mineral phases are described in *sections 4.4.3, 4.3.4 and 4.5.5*, and their compositions are presented in Table 4.16 and Table 4.20. A summary of the telluride assemblages present in the Faraba-style deposits is shown in Table 8.3. At Faraba, tellurides are mainly associated with barren to weakly-mineralised arsenopyrite phases, with tellurides confined to the Te-Bi system. At Goukoto and P-64, tellurides are Au-bearing and assigned to the Au-Ag-Te system.

Table 8.3. Te-Au mineral phases associated with Faraba style deposits.

Orebody	Telluride and related ore assemblages
Faraba	tsumoite + hedleyite + altaite + native bismuth + unknown Bi-Te alloy + native gold
Goukoto	calaverite + sylvanite + petzite + native gold
P-64	calaverite + native bismuth + native gold (Au, Ag, Pd alloy)

Faraba-style deposits also contain several other features that distinguish them from the northern Loulo deposits and these are listed below:

1. Lower Cu concentrations- complete absence of the late Cu sulphides seen in the northern orebodies.
2. High degrees of oxidation of the sulphides (sulphides → magnetite); only seen extensively in the north at P-125.
3. Higher degrees of supergene alteration (although the laterite profiles are not significantly different to the northern parts of the district):
 - FeS_2 (pyrite) + FeAsS (arsenopyrite) + $\text{Fe}^{3+}_2\text{Fe}^{2+}\text{O}_4$ (magnetite) → Fe_2O_3 (haematite) + $\text{Fe}^{3+}\text{O}[\text{OH}]$ (goethite)
 - FeS_2 (pyrite) → FeTiO_3 (ilmenite) → TiO_2 (leucoxene) (common for Loulo)
 - CaWO_4 (scheelite) → $\text{WO}_3 \cdot [\text{H}_2\text{O}]$ (tungstite)
 - $(\text{Ce,La,Nd})\text{PO}_4$ (monazite) → $(\text{Ce, La})_2[\text{CO}_3]_3 \cdot 4\text{H}_2\text{O}$ (calkinsite)
4. In As-rich orebodies (e.g. Faraba), a reverse paragenesis is established (arsenopyrite → pyrite), compared to the Yalea-style deposits (pyrite → arsenopyrite).
5. Gold particle size is greater than deposits to the north (up to 150 μm). Possibly a function of supergene processes.
6. Chlorites from alteration assemblages are more Si-rich and Al-depleted (classify as diabantites) compared to ripidolite + pynochlorites + brunsvigite compositions observed to the north (Fig. 5.13). This is typical for low temperature chlorites (Cathelineau & Nieva, 1985; Cathelineau, 1988).

8.3.2 Geochemical characteristics

Fluid inclusion studies were not carried out on the Faraba-style deposits during this project because vein samples were either too highly recrystallised or inclusions were too small to measure. Oxygen isotopes collected from mineralised carbonates at Faraba (this study) and P-64 (Fouillac *et al.*, 1993) show slightly more enriched measured $\delta^{18}\text{O}$ compositions than the northern deposits of between +16.9 to +20.5‰ (typically of low-T deposits), with $\delta^{18}\text{O}_{\text{fluid}}$ values between +7.9 to +13.2‰. Carbon isotopes differ between deposits, with Faraba displaying Yalea-style metamorphic $\delta^{13}\text{C}$ values (-13.2 to -10.8‰) and P-64 showing Gara-style characteristics with heavier compositions overlapping the magmatic and metamorphic fields (-8.5 to -7.0‰). Sulphur isotope data are analogous to the northern Loulo orebodies showing crustal $\delta^{34}\text{S}$ compositions (+6.0 to +11.5‰).

8.3.3 P-T conditions of mineralisation at Loulo

The differences in ore mineralogy between Faraba-style deposits and the northern orebodies can be explained by the variation in depth of mineralisation across the Loulo permit, with shallower-level mineralisation towards the south. According to Groves *et al.* (1998), telluride mineralisation is a typical feature of shallower-level epizonal deposits (<6 km; 150-300 °C). This is consistent with the telluride geothermometry data (*section 4.6.3.1*), which indicate maximum mineralisation temperatures at Faraba and Goukoto of 266 °C and 304 ± 10 °C, respectively. Chlorite geothermometry at Faraba (*section 5.5.4*) indicate crystallisation temperatures between 201-235 °C (mean of 221 °C) and therefore a temperature range between 201-266 °C can be inferred for this deposit.

In the absence of fluid inclusion data from the Faraba-style deposits, approximations of emplacement depths can be established by applying the geothermal gradient ($\sim 45^\circ\text{C}/\text{km}$) determined by P-T modelling towards the north (uniform for mineralised and barren veins from several deposits). This corresponds to depths of 4.5-5.9 km for mineralisation at Faraba, and depths below 6.7 km for mineralisation at Goukoto (epizonal deposits). The shallower level mineralisation conditions of the Faraba-style deposits could explain the widespread appearance of replacement magnetite (late circulating surface-derived oxidised fluids) and the high degrees of supergene alteration (more prolonged exposure). The similarities to the northern orebodies documented in *sections 8.3.1 and 8.3.2* indicate that Faraba-style mineralisation represents shallow-level expressions of Gara- and Yalea-style deposits. The depth of formation of the Loulo orebodies is illustrated in Fig. 8.5.

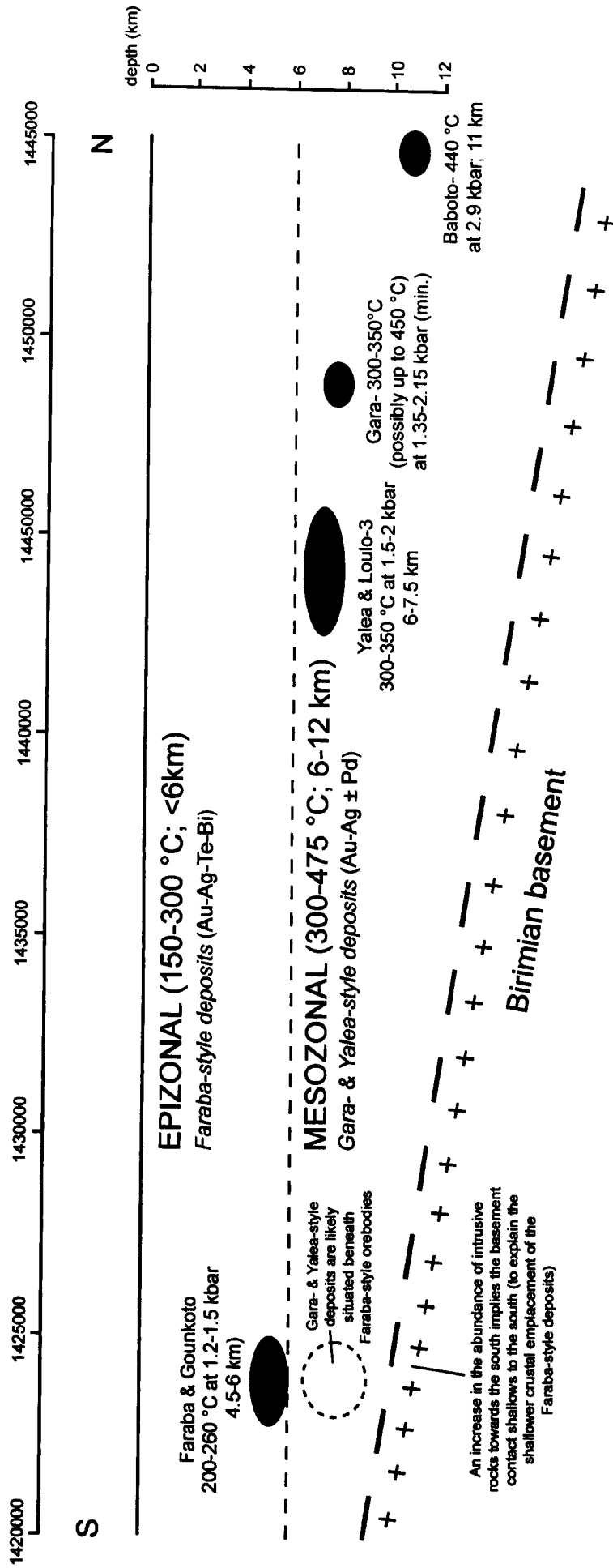


Fig. 8.5. Depth of ore emplacement in the Loulo district based on mineralogy and fluid inclusion studies, showing shallower mineralisation conditions to the south. The Kofi sedimentary package in the Loulo district is believed to have tilted to the south post-mineralisation to account for the present day position of the orebodies (all relatively at similar levels in the shallow subsurface).

8.4 Controls on mineralisation at Loulo

The high gold endowment of the Loulo district is controlled by numerous factors that work on a range of scales. The world-class orogenic gold deposits present along the SMSZ, and other parts of the Birimian (e.g. the Ashanti region), suggest that the crust was initially enriched with respects to gold (see section 8.5.2). Coupling of numerous other local factors would then have a significant role in mineralisation at Loulo, including: (1) several fluid and metal sources; (2) high heat flow from emplacement of nearby granitoids; (3) the close proximity to the major SMSZ; (4) efficient fluid focussing along second and higher order structures; (5) multiple mineralisation and/or remobilisation events; (6) favourable host-rocks (physically and chemically); and (7) multiple mechanisms for deposition (e.g. fluid mixing, phase separation, decrease in T and fO_2). Similar factors have been used to explain the size and distribution of orogenic gold deposits/districts in the Yilgarn Craton, Australia and Superior Province, Canada (Phillips *et al.*, 1996; Bierlein *et al.*, 2006b; Morey *et al.*, 2007).

8.5 Implications

8.5.1 Implications for orogenic gold mineralisation

The fluid source for orogenic gold mineralisation is a highly debated subject (see summary papers by Ridley & Diamond, 2000; Groves *et al.*, 2003; Goldfarb *et al.*, 2005). The generally uniform characteristics of this deposit type (Table 1.2) have been previously suggested to imply one common source. The release of low-salinity metamorphic H_2O-CO_2 fluids during greenschist facies regional metamorphism is the generally accepted model (e.g. Stüwe, 1998; Goldfarb *et al.*, 1988; 1991b; Kerrich & Wyman, 1990; Jemielita *et al.*, 1990; Koons & Craw, 1991; Powell *et al.* 1991; Stüwe *et al.*, 1993; Jamison *et al.*, 1998; Pettke *et al.*, 2000; Pitcairn *et al.*, 2006). However, exsolution of fluids from granitic magmas has also been suggested as a potential fluid source (Burrows *et al.*, 1986; Patrick *et al.*, 1988; Campbell & Hill, 1988; Burrow & Spooner, 1989; Spooner, 1993; de Ronde *et al.*, 2000). Alternative fluid sources include mantle fluids (Cameron, 1988; 1993); fluid derived from shoshonitic lamprophyre magmas (Rock & Groves, 1988; Rock *et al.*, 1989); a meteoric fluid model (Nesbitt *et al.*, 1989; Nesbitt & Muehlenbachs, 1991); or fluids derived from an external source, such as the subducting slab (Breeding & Ague, 2002).

There are a number of lines of evidence to suggest a significant magmatic contribution to the fluids that controlled the evolution of the Loulo orogenic gold deposits. These include, in the Gara-style deposits: (1) the presence of Ni ± Co bearing sulphides, abundant REE phosphates; (2) the extensive growth of syn-mineralisation epigenetic tourmaline (3) the remarkable boron anomaly that extends 200 km along strike of SMSZ; (4) the presence of metalliferous hypersaline fluid inclusions; and (5) $\delta^{13}C$ values that overlap the magmatic field. Thus, orogenic gold mineralisation at Loulo brings into question the sole metamorphic fluid paradigm for orogenic gold deposits. The mineralogical and chemical data collected here points towards the potential role of both metamorphic and magmatic fluids in the formation of orogenic gold deposits.

The granitic fluid model

Traditionally, the magmatic model for orogenic gold has been dismissed for several reasons:

- The low-salinity and high CO₂ concentration of the ore fluids
- The lack of a genetic relationship between mineralisation and granitoid emplacement

Moderate to hypersaline (10 to 60 wt.% NaCl), aqueous-rich fluids are typical features of magmatic derived fluids, e.g. shallow-level (<5 km) reduced intrusion-related gold systems (RIRGS) (Petersen & Fitzmeyer, 1998; Ebert *et al.*, 2000; Rombach & Newberry, 2001), and skarn and porphyry gold systems (e.g. Hedenquist & Lowenstern, 1994; Ulrich *et al.*, 1999). However (excluding Loulo), high-salinity fluids are rarely interpreted to be the primary mineralising fluids in orogenic gold deposits (Höppner, 1994; Pan & Fleet, 1995; Mishra & Panigrahi, 1999; Vallance *et al.*, 2003).

Recent studies of deep-seated (>5 km) RIRGS (e.g. deposits associated with the Tombstone-Tungsten belt, Yukon, Canada) suggest that low-salinity and high CO₂ concentrations are not robust arguments to discount a magmatic fluid model for orogenic gold deposits. Baker & Lang (2001) show that these RIRGS, which are found at similar crustal levels to orogenic gold lodes, are typified by low-salinity (<10 wt.% NaCl equiv.) H₂O-CO₂ (up to 33 mol.% CO₂) fluids. Baker (2002) suggests that the composition of magmatic-derived ore fluids is dependent on pressure. Magmatic ore fluids released at greater depths (>5-10 km) will generally show low-salinity and enriched CO₂ compositions, while fluids exsolved at shallower levels (e.g. skarn and porphyry gold systems) will be depleted in CO₂ and enriched in Cl⁻ and H₂O. The variation in fluid compositions with respects to crustal depth is due to the increase in CO₂ solubility in granitic melts with increasing pressure (Lowenstern, 2001).

The most important factor in dismissing the magmatic fluid model for orogenic gold is the lack of evidence for genetic links between mineralisation and granitoid emplacement. Many Archaean deposits are spatially associated with granitic intrusions; however, in nearly all cases, intrusions either pre-date (e.g. Duuring *et al.*, 2007) or post-date mineralisation (e.g. Goldfarb *et al.*, 1986, 1988; Bierlein *et al.*, 2001). The large structural networks of orogenic gold districts, coupled with post-mineralisation disruption of the terrane, means it's sometimes difficult to pinpoint the exact source of the mineralising fluid. Furthermore, Powell *et al.* (1991) suggests the high concentrations of CO₂ in these systems is indicative of a deep-seated source (potential granitic sources could be well below the current level of any gold deposit). Also, the full subsurface architecture of any terrane is not known (Ridley & Diamond, 2000). For the magmatic model to gain further interest, genetic links between mineralisation and coeval granitoids need to

be established. However, informal discussions at the European Current Research on Fluid Inclusions (ECROFI) Conference 2007, with key workers in the field, demonstrate that the magmatic model is receiving lots of recent interest.

Gara-style deposits- a new subclass of orogenic gold deposit

It is proposed here that the Gara-style orebodies represent a new subclass of orogenic gold deposit. These orebodies contain distinct characteristics (Table 8.1; *section 8.2.3*) that differ from all other reported orogenic gold deposits. The high Fe content of the fluid, the large concentrations of sodic alteration associated with mineralisation, and the spatial association with the Falémé iron deposits, could imply that this style of orogenic gold deposit has genetic links with IOCG or iron skarn systems (Marschik & Fontboté, 2001; Bastrakov *et al.*, 2007). In this scenario, IOCG/skarn deposits form in proximal zones around I-type, oxidised, HM-buffered intrusions, through the interaction with wall-rocks. In more distal zones, cooling granitic fluids readily mix with regional metamorphic fluids to form the distinct Gara-style orogenic gold bodies. To strengthen this model, further work is needed to determine the precise source of the Gara-style brines (a range of magmatic sources are proposed at Loulo- *see section 8.2.3.6*).

8.5.2 Insights into Birimian gold mineralisation

The Birimian terrane of West Africa is highly enriched with respects to gold and, although less well-explored, is comparable to the well-known gold-districts of Western Australia (Yilgarn Craton) and Canada (e.g. Superior Province). As well as regional and deposit-scale controls (*section 8.4*), mineralisation at Loulo is also controlled by orogen to lithospheric-scale factors, which contribute to the overall gold endowment of the Birimian crust. These include: (1) a thin sub-continental lithospheric mantle (SCLM); and (2) subduction of a large oceanic basin. Bierlein *et al.* (2006a) and Bateman & Bierlein (2007) argue that the pre-mineralisation history of an orogen is a critical factor in deciding whether an orogen contains world-class (3 to 9 Moz) to giant (9 to 75 Moz) orogenic gold deposits. Juvenile orogens, such as the Birimian, will contain a thin SCLM compared to more long-lived orogens, and therefore receive a greater heat input from the asthenosphere to drive hydrothermal circulation through the crust. Alternatively, Leahy *et al.* (2005) suggested that large oceanic closure orogens, like the Birimian, will contain thicker continental crust and a greater radiogenic input. Consequently, these orogens will have a larger heat engine compared to orogens with shorter-lived subduction histories.

The lack of research into the Birimian means that little is known about the sources of ore-bearing fluids and the exact the timing of mineralisation within the Eburnean orogeny. Mineralogical and geochemical studies at Loulo give the first indication of the role of Birimian magmas in orogenic gold mineralisation. However, magmatic fluids have been considered important in other types of Birimian mineralisation, such as the Morila gold deposit (reduced

intrusion-related gold system; Mcfarlane *et al.*, 2008) and the Falémé iron ore deposits in Senegal (IOCG deposits; Schwartz & Melcher, 2004). Further research is needed (including geochronology studies) to establish genetic links between orogenic gold mineralisation and Birimian granitoid emplacement.

8.5.3 Exploration strategies

Isotopes

As mentioned in *section 8.2.5*, barren quartz-carbonate veins show clear systematic differences in fluid inclusion and isotopic characteristics compared to mineralised veins. Measured oxygen isotopes show little variation in the current database and thus are not a useful exploration tool in the Loulo mining district. However, the exploration potential for carbon isotopes is very good, with significant differences between deposits (Gara- vs. Yalea-style) and mineralised and barren veins, with negative $\delta^{13}\text{C}$ values linked to gold occurrence. There are a number of advantages for the use of carbonate isotopes over silicate analysis: (1) fluorination for oxygen in silicates is slower and therefore more expensive than carbonate work; and (2) carbonates can be run automatically and can be cost effective in regional exploration. Sulphur isotopes could be potentially useful in discriminating a Yalea- from a Gara-type prospect (notwithstanding the P-64 deposit, which contains similar compositions to Yalea-style deposits).

Fluid inclusions

Fluid inclusion analysis can also determine different styles of mineralisation and discriminate between mineralised and barren zones. The identification of hypersaline inclusions in Gara-style deposits could be used as an important exploration tool as these inclusions are exclusively confined to mineralised veins (completely absent from barren veins). Mapping of these inclusions by random sampling of quartz veins from across the Loulo property would give indications into the fluid migration pathways of the magmatic brines and insights into potential zones of fluid mixing and sites of mineralisation. In the case of Yalea-style deposits, where hypersaline inclusions are absent, there are still clear differences in fluid inclusion assemblages between mineralised and barren zones. In auriferous quartz veins, fluid inclusions populations are dominated by aqueous and carbonic inclusion, which represent unmixing of a low-salinity (<10 wt.% NaCl) $\text{H}_2\text{O}-\text{CO}_2-\text{N}_2-(\text{CH}_4)$ primary ore fluid. In barren veins, evidence for fluid immiscibility is less extensive. As well as the presence of aqueous and carbonic end-member inclusions, primary, low-salinity (mean of 6 wt.% NaCl equiv.), homogenous $\text{H}_2\text{O}-\text{CO}_2-\text{N}_2$ inclusions are also observed (such inclusions are absent from mineralised zones). Raman analysis of quartz samples could also be utilised as exploration criteria for future work as CH_4 can be used as a useful indicator for mineralisation (this study shows that barren fluids contain no detectable CH_4).

CHAPTER 9: CONCLUSIONS

The data collected during this research project gives a precise description of the mineralogy and alteration chemistry of the Loulo orogenic gold deposits, and permits insights into the controlling factors and origin of mineralisation. The data also has important implications for global-scale studies of orogenic gold deposits, in that it makes an important contribution to the current understanding on the fluid source(s) of orogenic gold-bearing fluids. In this chapter, the project aims are reviewed and the main conclusions summarised. Important areas for future work are also suggested based on the results obtained during this study.

9.1 Project objectives and conclusions

The project objectives set out in *section 1.4.2* are resolved in this section. Each objective is addressed separately accompanied by a list of the main findings.

9.1.1 Aim 1

To determine the mineralogical characteristics of mineralisation and alteration, and to establish paragenetic sequences for individual orebodies.

- Detailed petrographic and electron microprobe studies indicate the Loulo district is comprised of three styles of deposit with contrasting ore and alteration assemblages.
- **Gara-style deposits** (Gara, Gara-West, P-129, Yalea North) exhibit atypical orogenic gold features. Orebodies are Fe-rich (pyrite principal sulphide phase) with minor/trace ore phases dominated by chalcopyrite, REE minerals (monazite and xenotime) and Ni-bearing sulphides (gersdorffite, pentlandite and Ni-bearing pyrrhotite). Native gold is situated in numerous locations (occluded and remobilised sites) mainly confined to pyrite, and is Ag-poor (fineness >990). Metal signatures are typically Fe-Cu-REE-Au-Ni-W-As ± Co-Ag-Pd.
- Alteration zones associated with Gara-style mineralisation involve significant additions of B + Na + Fe + Mg + Si. Albite and Fe³⁺-rich tourmaline form the two most dominant mineral phases.
- The mineralogy of Gara-style deposits implies a granitic contribution to the hydrothermal fluids.
- **Yalea-style deposits** (Yalea Main; P-125, Loulo-3, Baboto) show more typical orogenic gold characteristics. Orebodies are As-rich with major sulphides phases dominated by pyrite and arsenopyrite (~70:30 ratio). Minor/trace phases lack REE phosphates and Ni-bearing sulphides, and are instead dominated by chalcopyrite, scheelite, galena and rare Sb sulphides. Mineral paragenesis is more complex compared to Gara-style orebodies, with

multi-stage pyrite, arsenopyrite and gold generation. Native gold is more Ag-rich with a fineness of 920-990. These orebodies contain a Fe-As-Cu-W-Au-Pb-Sb-Ag metal association.

- Alteration zones are characterised by albitisation, sericitisation, chloritisation and ankerite formation, with a notable absence of tourmalinisation.
- **Faraba-style deposits** in the southern part of the Loulo district show similar features to both Gara- and Yalea-style orebodies, but also noteworthy differences such as common telluride mineralisation, lower Cu concentrations, oxidation of the major sulphide phases and widespread supergene alteration.
- Detailed paragenesis charts of individual orebodies are given in *chapter 4* and in the appendices (*section A-4*).

9.1.2 Aim 2

To develop a comprehensive dataset of fluid chemistries and PVT properties to model the various hydrothermal mineralising fluids.

- Fluid inclusion and isotopic data imply Gara- and Yalea-style deposits formed from ore fluids of contrasting composition.
- Two primary mineralising fluids have been identified in the Fe-rich Gara-style orebodies: (1) a lower temperature (300-350 °C), low-density (<1 g/cm³), reduced (QFM-buffered), low-salinity (<10 wt.% NaCl equiv.) CO₂-H₂O-NaCl fluid, rich in H₂S-N₂ ± CH₄; and (2) a high temperature (>400 °C), high-density (1.35-1.5 g/cm³), oxidised (HM-buffered), hypersaline (~45-55 wt.% NaCl equiv.) H₂O-NaCl-FeCl₂-B-CO₂ ± CH₄ fluid. These fluids contain noticeably different chemistries and are clearly derived from two separate fluid sources (discussed in *aim 3*).
- Fluid inclusions representative of the brine are multiphase with a daughter assemblage consisting of halite and Fe-chloride (probably lawrencite; FeCl₂) (10:1 ratio), rare K-Ca chlorides, haematite, calcite, ankerite and magnetite.
- The coexistence of two fluid phases in vein quartz is best explained by the partial mixing and heterogeneous trapping of these fluids. Fluid mixing is unlikely to be a single pass system resulting in catastrophic precipitation of gold, but rather repeated pulses of fluid movement (e.g. via seismic pumping).
- CO₂-rich fluid inclusions without a visible aqueous phase are also observed in Gara-style mineralised veins. This inclusion type can be modelled as a remnant of the mixing process ("salting-out effect").
- Isotopic compositions of the Gara-style fluids include remarkably uniform δ¹⁸O of +10.2 to +11.5‰, δ¹³C between -14.4 to -4.5‰, and δ³⁴S from +6.0 to +15.5‰.

- Estimates of the P-T conditions of mineralisation in Gara-style deposits are hindered by the fluid mixing process. However, decrepitation temperatures of CO₂-bearing inclusions imply minimum pressures of 1.35-2.15 kbar.
- Fluid inclusion assemblages in Yalea-style deposits are dominated by carbonic and aqueous inclusions, which show strong evidence of phase separation from a primary, reduced (QFM buffered), low-salinity (≤ 10 wt.% NaCl equiv.) CO₂-H₂O-NaCl-N₂ \pm CH₄ fluid. This fluid is similar in composition to the low-salinity end-member fluid in the Gara-style deposits.
- Isotopic compositions of the Yalea-style fluids include $\delta^{18}\text{O}$ of +7.3 to +12.3‰, $\delta^{13}\text{C}$ between -21.7 to -10.8‰, and $\delta^{34}\text{S}$ from +5.6 to +9.6‰. C isotopes are markedly lighter in Yalea-style orebodies in comparison to Gara-style bodies.
- P-T conditions at site of mineralisation in Yalea-style deposits, estimated from fluid inclusion modelling, mineral equilibria and oxygen isotope compositions of cogenetic phases, are between 300-350 °C at 1-2 kbar. Average estimates of depths of formation for Yalea Main and Loulo-3 orebodies are between 6.8-7.25 km (mesozonal deposits). Fluid inclusion modelling at Baboto gives higher P-T trapping conditions at 440 °C at 2.9 kbar, equivalent to depths of 10.9 km.
- Mineral equilibria from the Faraba deposits in the south indicate epizonal gold emplacement (200-260 °C at <1.5 kbar; 4.5-6 km). This implies that depth of gold formation shallows to the south within the Loulo property, which could explain the distinct mineralogical characteristics of the Faraba-style orebodies.
- Post-mineralisation fluids from both Gara- and Yalea-styles deposits include mixed salinity (13.0 to 22.8 wt.% NaCl equiv.) aqueous fluids with no detectable CO₂. These fluids may have remobilised some of the gold and could be linked to the late Cu mineralisation seen in the northern Loulo orebodies.
- Barren fluids contain lower Fe contents and are typified by a low-salinity (mean of 6 wt.% NaCl) H₂O-CO₂-N₂ composition. This fluid is similar in composition to the Yalea-style ore fluids. However, barren fluids appear to be more oxidising, with the complete absence of CH₄ and amorphous carbon within the fluid inclusions. In addition, fluid immiscibility appears less extensive. Isotopic compositions are clearly distinct from auriferous zones with $\delta^{18}\text{O}_{\text{fluid}}$ between +7.0 to +15.7‰ and $\delta^{13}\text{C}$ signatures similar to host rock carbonates (close to zero). P-T conditions of barren vein formation occur between 250-295 °C at pressures of 0.75 to 2.15 kbar.

9.1.3 Aim 3

To constrain the potential source(s) of fluid and ore-related components.

- The mineralogical and chemical data collected at Loulo bring into question the metamorphic fluid paradigm for orogenic gold mineralisation and points towards the role of both magmatic and metamorphic fluids in the formation of these deposits.
- There are a number of lines of evidence to suggest a significant magmatic contribution to the fluids that controlled the evolution of the Loulo orogenic gold deposits. These include, in the Gara-style deposits: (1) the presence of Ni ± Co bearing sulphides, abundant REE phosphates and widespread W minerals; (2) the extensive growth of syn-mineralisation epigenetic tourmaline; (3) the remarkable boron anomaly that extends 200 km along strike of SMSZ; and (4) the presence of metalliferous hypersaline fluid inclusions.
- Fluid inclusion studies show that Gara-style deposits form through fluid mixing of an Na-Fe-Cl rich magmatic fluid, carrying abundant metals in solution such as Cu + Ni + W + Au ± Co, with a CO₂-N₂-H₂S-rich regional metamorphic fluid transporting metals such as As + Fe + Cu + Au + Ag + Sb + Pb. In the Yalea-style orebodies, which show more typical orogenic gold characteristics, only the metamorphic fluid appears to control gold mineralisation (no magmatic signature).
- Carbon isotopes support the potential magmatic component to the Loulo hydrothermal system. δ¹³C values from mineralised ankerite veins at Gara-style orebodies range from -14.4 to -4.5‰ overlapping the magmatic field.
- Carbon isotopic studies from mineralised and alteration carbonates from Yalea Main show lighter δ¹³C from -21.7 to -15.8‰. These isotopic values, as well as the presence of CH₄-bearing inclusions and amorphous carbon along inclusion walls, imply fluid-rock interactions with the reduced Kofî carbonate sediments sourced some of the fluid components and had significant effects on gold deposition (*see below*).
- Estimated δ¹⁸O_{fluid} compositions for both Gara- and Yalea-style deposits fall mainly in the range of +8 to +12‰ implying a dominant metamorphic fluid signature. However, in the case of the Gara-style deposits, where magmatic signatures are observed in mineralogical and fluid inclusion characteristics, a potential δ¹⁸O-enriched fluid derived from peraluminous granitic rocks cannot be ruled out.
- Sulphur isotopes imply S in all types of Loulo mineralisation was initially fixed as pyrite in the host sediments by reduction of seawater and later leached by fluid-rock interactions.
- Three granitic bodies have been suggested as potential sources for the magmatic fluids in the Loulo area: (1) belt-type, I-type, metaluminous granodiorites and diorites of the Balangouma pluton that crop out on the western side of the SMSZ, and are associated with the Falémé IOCG deposits; (2) the B-rich, basin-type, peraluminous, Gamaye granitoid to

the south of the Loulo district; or (3) a deep-seated granitic source beneath Loulo (as suggested by geophysical surveys). These models need to be tested in future studies (section 9.2).

- The Gara-style orebodies could represent a new sub-class of orogenic gold deposit, with genetic links to IOCG systems.

9.1.4 Aim 4

To understand the controls on fluid migration, subsequent alteration and mineralisation.

- The metamorphic and magmatic fluids responsible for mineralisation in the Loulo district are likely to have contained different transport ligands.
- Metals within the reduced, lower temperature (300-350 °C) metamorphic fluid are likely to have been transported as bi-sulphide complexes, while metals carried in the higher temperature (>400 °C), S-depleted magmatic brine were probably transported as oxidised chloride complexes.
- Different mechanisms for gold deposition took place at the various deposit styles. At Yalea-style deposits, fluid inclusion and carbon isotope data indicate the principal mineralisation trap is phase separation of the H₂O-CO₂ ore fluid during fluctuations in pressure and/or temperature, and interaction with reduced wall-rocks. Chemisorption processes may also be important to account for the supposedly high amounts of refractory gold in arsenopyrite.
- In the Gara-style deposits, changing temperature, pH and *f*O₂ conditions during fluid mixing could have contributed to gold deposition. Additionally, an increase in salinity of the metamorphic fluids during fluid mixing led to retrograde boiling of the CO₂ and destabilisation of the bi-sulphide complex. Consumption of H⁺ during wall-rock interaction and tourmalinisation could also be a further precipitation mechanism.
- The high gold endowment of the Loulo district is controlled by numerous factors that work on a range of scales. Local factors include: (1) several fluid and metal sources; (2) high heat flow from emplacement of nearby granitoids; (3) the close proximity to the major SMSZ; (4) efficient fluid focussing along second and higher order structures; (5) multiple mineralisation and/or remobilisation events; (6) favourable host-rocks (physically and chemically); and (7) multiple mechanisms for deposition.

9.1.5 Aim 5

To use these data to develop local and regional exploration strategies.

- Carbon isotopes can be a potentially useful exploration tool at Loulo and other parts of the

SMSZ. There are distinct isotopic differences between mineralised ($\delta^{13}\text{C}$ from -21.7 to -4.5‰) and barren ($0 \pm 3\%$) veins, with negative $\delta^{13}\text{C}$ values linked to gold occurrence.

- It is clear from the data collected in this study that magmatic fluids played an important role in gold mineralisation at Loulo. Further fluid inclusion studies from across the permit could give indications into the fluid migration pathways of the magmatic brines and insights into potential zones of fluid mixing and sites of mineralisation.
- Fluid inclusion assemblages differ between deposit-styles and between gold-bearing and barren veins. Identification of certain inclusion types can give indications into the type of mineralisation present or whether a potential target is mineralised or not. See *chapter 6* or *section 8.5.3* for description on the types of fluid inclusions present within Gara-style, Yalea-style and barren veins.

9.2 Suggestions for future work

A key component of future work at Loulo would be to develop more fully the extent of the magmatic contribution to orogenic gold mineralisation in the district. To do this, the exact fluid source needs to be determined. Although three possible granitoids have been pinpointed as possible sources during this study, these models still need to be tested. Fluid inclusion and isotopic work on these granitoids would be an essential part of a future research program aimed to build on data collected during this study. A geochronological study of these plutons would also be advised in order to determine genetic links with gold mineralisation. Furthermore, detailed work on the Falémé iron skarn deposits in Senegal would assess the possible link between IOCG and orogenic gold mineralisation within the Loulo area.

Expansion of the stable isotope database is also recommended. Carbon isotopes on the amorphous carbon matter from wall-rock sediments should be carried out to enable comparison with the reduced signatures measured from the mineralised veins. A more extensive O, C & S isotope dataset is needed to determine any isotopic variations during the paragenetic history of the main deposits. Boron isotopes on the epigenetic tourmalines phases from across the Loulo district would give further insights into the source of the hydrothermal fluids. The magmatic model could be tested by analysing tourmaline from the B-rich Gamaye pluton to the south of the Loulo permit. Additionally, chlorine isotopes could be measured by thermal ionisation mass spectrometry in order to accurately ascertain the source of the salinity in these fluids (e.g. Banks *et al.*, 2000).

Future work should also concentrate on the exciting new discovery at Goukoto, which is located on a late NNW trending structure. During this study I only had access only to the first core ever drilled at Goukoto. A more detailed study (including structural, mineralogical, fluid inclusion and geochemical analysis) at this deposit will test the models proposed during this study. They would also test the hypothesis that the Goukoto and Faraba deposits are epizonal rather than mesozonal deposits. Comparative data from as yet unanalysed samples from NNW trending high-

grade zone in the Yalea underground could test a model that late stage fluids scavenged gold from Gara/Yalea type deposits and re-deposited it in high grade bodies hosted by late NNW trending structures.

On a more regional scale, developing a new exploration paradigm for this prospective part of the Birimian crust is of strategic importance. To date, there is no regionally coherent model for mineralisation and this hinders the development of sensible exploration strategies. Existing remote sensing, geophysical and geochemical datasets should be re-examined. Particular emphasis should be placed on developing enhanced structural models for mineralisation. Collection of new geochemical, mineral chemical and fluid inclusion data will constrain variations in mineralisation styles along strike of the SMSZ.

REFERENCES

- ABOUCHAMI, W., BOHER, M., MICHARD, A. & ALBAREDE, F., 1990. A major 2.1 Ga event of mafic magmatism in West Africa: an early stage of crustal accretion. *Journal of Geophysical Research*, 95: 17605-17629.
- AFIFI, A.B., KELLY, W.C. & ESSENE, E.J., 1988. Phase relations among tellurides, sulphides and oxides: I. Thermochemical data and calculated equilibria. *Economic Geology*, 83: 377-394.
- ALLAN, M.M., 2006. *Hydrothermal Processes in the Mount Leyshon Intrusive Complex, Australia*. Ph.D Thesis, University of Leeds School of Earth and Environment, Leeds, 321 pp.
- ALLIBONE, A., 2004. *Geological setting of mineralisation in the Loulo district, western Mali. Implications for targeting further gold deposits*. Randgold Resources Ltd, Internal Report.
- ALLIBONE, A. & CAMERON, G., 2006. *Geological setting of mineralisation in the Loulo district, western Mali #2. Implications for targeting further gold deposits*. Randgold Resources Ltd, Internal Report 23 pp.
- ALLIBONE, A., TEASDALE, J., CAMERON, G., ETHERIDGE, M., UTTLEY, P., SOBOH, A., APPIAH-KUBI, J., ADANU, A., ARTHUR, R., MAMPHEY, J., ODOOM, B., ZUTA, J., TSIKATA, A., PATAYE, F. & FAMIYEH, S., 2002a. Timing and structural controls on gold mineralisation at the Bogoso gold mine, Ghana, West Africa. *Economic Geology*, 97: 949-969.
- ALLIBONE, A., MCCUAIG, T.C., HARRIS, D., ETHERIDGE, M., MUNROE, S., BYRNE, D., AMMANOR, J. & GYAPONG, W., 2002b. Structural controls on gold mineralisation at the Ashanti deposit, Obuasi, Ghana. *Society of Economic Geologists Special Publications*, 9: 65-92.
- ALLIBONE, A., HAYDEN, P., CAMERON, G. & DUKU, F., 2004. Palaeoproterozoic Gold Deposits Hosted by Albite- and Carbonate-Altered Tonalite in the Chirano District, Ghana, Ghana, West Africa. *Economic Geology*, 99: 479-497.
- ALRIC, G., 1990. Géochimie du volcanisme birimien (Protérozoïque inférieur) de l'Unité de la Haute-Comoé, N-E de la Côte d'Ivoire: premiers résultats. *Journal of African Earth Sciences*, 10: 669-681.
- ANDERSON, M.R., RANKIN, A.H. & SPIRO, B., 1992. Fluid mixing in the generation of mesothermal gold mineralisation in the Transvaal Sequence, Transvaal, South Africa. *European Journal of Mineralogy*, 4: 933-948.
- ANGLOGOLD ASHANTI LTD, 2008. Obuasi country report 2008. Available at: <http://www.anglogold.com/about+our+business/our+operations/ghana.htm>. [Accessed 15 May 2010].
- ANTHONY, E.Y., REYNOLDS, T.J. & BEANE, R.E., 1984. Identification of daughter minerals in fluid inclusions using scanning electron microscopy and energy dispersive analysis. *American Mineralogist*, 69: 1053-1057.
- ASIEDU, D.K., DAMPARE, S.B., ASAMOAH SAKYI, P., BANOENG-YAKUBO, B., OSAE, S., NYARKO, B.J.B. & MANU, J., 2004. Geochemistry of Palaeoproterozoic metasedimentary rocks from the Birim diamondiferous field, southern Ghana: Implications for provenance and crustal evolution at the Archaean-Proterozoic boundary. *Geochemical Journal*, 38: 215-228.
- ATSUYUKI, I., KUROKAWA, K. & HATTA, T., 2010. Application of chlorite geothermometry to hydrothermal alteration in Toyoha geothermal system, southwestern Hokkaido, Japan. *Resource Geology*, 60: 52-70.
- ATTOH, K. & EKWUEME, B.N., 1997. The West African Shield. In: de Wit, M.J. & Ashaal, L.D., (Editors), *Greenstone belts*. Oxford Monographs on Geology and Geosciences no. 35, Oxford Science Publications, pp. 517-528.

- ATTOH, K. & NUDE, P.M., 2008. Tectonic significance of carbonatite and ultrahigh-pressure rocks in the Pan-African Dahomeyide suture zone, southeastern Ghana. *In: Ennih, N. & Liégeois, J.P. (Editors), The Boundaries of the West African Craton*. Geological Society of London Special Publication No 297, pp. 217-231.
- ATTOH, K., EVANS, M.J. & BICKFORD, M.E., 2006. Geochemistry of an ultramafic-rodingite rock association in the Palaeoproterozoic Dixcove greenstone belt, southwestern Ghana. *Journal of African Earth Sciences*, 45: 333-346.
- AVION GOLD CORP, 2009. Tabakoto and Segala gold projects, Mali (West Africa). Available at: <http://www.aviongoldcorp.com/Projects/Current-Projects/default.aspx>. [Accessed 15 May 2010].
- AVNEL GOLD MINING LTD, 2009. The Kalana mine and permit background and existing resources. Available at: <http://www.avnelgold.com>. [Accessed 15 May 2010].
- BAKER, T., 2002. Emplacement depth and carbon dioxide-rich fluid inclusions in intrusion-related gold deposits. *Economic Geology*, 97: 1111-1117.
- BAKER, T. & LANG, J.R., 2001. Fluid inclusion characteristics of intrusion-related gold mineralisation, Tombstone-Tungsten magmatic belt, Yukon Territory, Canada. *Mineralium Deposita*, 36: 563-582.
- BAKKER, R.J. & JANSEN, J.B.H., 1994. A mechanism for preferential H₂O leakage from fluid inclusions in quartz, based on TEM observations. *Contributions to Mineralogy and Petrology*, 116: 7-20.
- BANKS, D.A., GLEESON, S.A. & GREEN, R., 2000. Determination of the origin of salinity in granitic-related fluids: evidence from chlorine isotopes in fluid inclusions. *Journal of Geochemical Exploration*, 69: 309-312.
- BARKER, F., 1979. Trondhjemite: definition, environment and hypotheses of origin. *In: Barker, F. (Editor), Trondhjemites, dacites and related rocks*. Elsevier, Amsterdam, pp. 1-12.
- BARKER, F. & ARTH, J.G., 1976. Generation of trondhjemitic-tonalitic liquids and Archaean bimodal trondhjemite-basalt suites. *Geology*, 4: 596-600.
- BARNES, H.I., 1979. Solubilities of ore minerals. *In: Barnes, H.I. (Editor), Geochemistry of hydrothermal ore deposits*. Wiley, New York, pp. 404-460.
- BARTON, P.B., 1969. Thermometric study of the system Fe-As-S. *Geochimica et Cosmochimica Acta*, 33:841-857.
- BASSOT, J.P., 1987. Le complexe volcano-plutonique calcoalcalin de la rivière Dalema (Est Sénégal): discussion de sa signification géodynamique dans le cadre de l'orogénie eburnéenne (Protérozoïque inférieur). *Journal of African Earth Science*, 6: 505-519.
- BASSOT, J.P. & CAEN-VACHETTE, M., 1984. Données géochronologiques et géochimiques nouvelles sur les granitodes de l'Est du Sénégal: implications sur l'histoire géologique du Birrimien de cette région. *In: Klerkx, J. & Michot, J. (Editors), African Geology*. Tervuren, Belgium, pp. 196-209.
- BASTRAKOV, E.N., SKIRROW, R.G. & DAVIDSON, B., 2007. Fluid evolution and origin of iron oxide Cu-Au prospects in the Olympic Dam district, Gawler Craton, South Australia. *Economic Geology*, 102: 1415-1440.
- BATEMAN, R. & BIERLEIN, F.P., 2007. On Kalgoorlie (Australia), Timmins-Porcupine (Canada), and factors in intense gold mineralisation. *Ore Geology Reviews*, 32: 187-206.
- BEESKOW, B., 2007. *The occurrence, distribution and origin of hydrocarbons in the Knibiny nepheline syenite complex, Kola Peninsula, Russia*. Ph.D Thesis, Kingston University, London, 262 pp.
- BEESKOW, B., RANKIN, A.H., MURPHY, P.J. & TRELOAR, P.J., 2005. Mixed CH₄-CO₂ fluid inclusions in quartz from the South Wales Coalfield as suitable natural calibration standards for microthermometry and Raman spectroscopy. *Chemical Geology*, 223: 3-15.

- BENNETT, D.G. & BARKER, A.J., 1992. High salinity fluids: The result of retrograde metamorphism in thrust zones. *Geochimica et Cosmochimica Acta*, 56: 81-95.
- BENNING, L.G. & SEWARD, T.M., 1996. Hydrosulphide complexing of Au (I) in hydrothermal solutions from 150–400°C and 500–1500 bar. *Geochimica et Cosmochimica Acta*, 60: 1849-1871.
- BERMUDEZ-LUGO, O., 2003. The mineral history of Mali. *U.S. Geological Survey Yearbook*, 22.1-22.5.
- BERMUDEZ-LUGO, O., 2006. The mineral history of Mali. *U.S. Geological Survey Yearbook*, 28.1-28.7.
- BESSELES, B., 1977. *Géologie de l'Afrique, Le Craton de l'Ouest Africain*. Bureau de Recherches Géologique et Minières Mémoires No 88, 402 pp.
- BÉZIAT, D., BOURGES, F., DEBAT, P., FUCHS, Y., LOMPO, M., MARTIN, F., NIKIÉMA, S. & TOLLON, F., 1999. The Guibaré and Fété Kolé gold-bearing tourmaline-quartz veins in the Birimian greenstone belts of Burkina Faso. *Canadian Mineralogist*, 37: 75-591.
- BÉZIAT, D., BOURGES, F., DEBAT, P., LOMPO, M., MARTIN, F. & TOLLON, F., 2000. A Palaeoproterozoic ultramafic-mafic assemblage and associated volcanic rocks of the Boromo greenstone belt: fractionates originating from island-arc volcanic in the West African Craton. *Precambrian Research*, 101: 25-47.
- BÉZIAT, D., DUBOIS, M., DEBAT, P., NIKIÉMA, S., SALVI, S. & TOLLON, F., 2008. Gold metallogeny in the Birimian craton of Burkina Faso (West Africa). *Journal of African Earth Sciences*, 50: 215-233.
- BHATIA, M.R., 1983. Plate tectonics and geochemical composition of sandstones. *Journal of Geology*, 91: 611-627.
- BHATIA, M.R. & CROOK, K.A.W., 1986. Trace element characteristics of greywackes and tectonic setting discrimination of sedimentary basins. *Contributions to Mineralogy and Petrology*, 92: 181-193.
- BIERLEIN, F.P. & CROWE, D.E., 2000. Phanerozoic orogenic lode gold deposits. *Reviews in Economic Geology*, 13: 103-139.
- BIERLEIN, F.P., FULLER, T., STÜWE, K., ARNE, D.C. & KEAYS, R.R., 1998a. Wall-rock alteration associated with turbidite-hosted gold deposits. Examples from the Paleozoic Lachlan Fold belt in central Victoria, Australia. *Ore Geology Reviews*, 13: 345-380.
- BIERLEIN, F.P., ARNE, D.C., BROOME, J.M.N. & RAMSAY, W.R.H., 1998b. Metatholeiites and interflow sediments from the Cambrian Heathcote greenstone belt, Australia: Sources for gold mineralisation in Victoria. *Economic Geology*, 93: 84-101.
- BIERLEIN, F.P., ARNE, D.C., FOSTER, D.A. & REYNOLDS, P., 2001. A geochronology framework for orogenic gold mineralisation in central Victoria, Australia. *Mineralium Deposita*, 36: 741-767.
- BIERLEIN, F.P., GROVES, D.I., GOLDFARB, R.J. & DUBE, B., 2006a. Lithospheric controls on the formation of provinces hosting giant orogenic gold deposits. *Mineralium Deposita*, 40: 874-886.
- BIERLEIN, F.P., MURPHY, F.C., WEINBERG, R.F. & LEES, T., 2006b. Distribution of orogenic gold deposits in relation to fault zones and gravity gradients: targeting tools to the Eastern Goldfields, Yilgarn Craton, Western Australia. *Mineralium Deposita*, 41: 107-126.
- BLACK, R., 1980. Precambrian of West Africa. *Episodes*, 4: 3-8.
- BLACK, R. & LIEGEOIS, J.P., 1993. Cratons, mobile belts, alkaline rocks and continental lithospheric mantle: the Pan-African testimony. *Journal of Geological Society London*, 150: 89-98.
- BLACK, R., CABY, R. & MOUSSINE-POUCHKINE, A., 1979. Evidence for Late Precambrian plate tectonics in West Africa. *Nature*, 279: 223-227.

- BLACK, R., LATOUCHE, L., LIEGEOIS, J.P., CABY, R. & BERTRAND, J.M., 1994. Pan-African displaced terranes in the Tuareg shield (central Sahara). *Geology*, 22: 641-644.
- BLENKINSOP, T., SCHMIDT MUMM, A., KUMI, R. & SANGNOR, S., 1994. Structural geology of the Ashanti gold mine. *Geologische Jahrbuch*, 100: 131-153.
- BODNAR, R.J., 2003. Re-equilibration of fluid inclusions. In: Samson, I., Anderson, A. & Alderton, D.H.M. (Editors), *Fluid Inclusions: Interpretation and Analysis*. Mineralogical Association of Canada. Short Course Series Volume 32, Vancouver, British Columbia, pp. 213-231.
- BODNAR, R.J., BINNS, P.R. & HALL, D.L., 1989. Synthetic fluid inclusions. VI. Quantitative evaluation of the decrepitation behaviour of fluid inclusion in quartz at one atmosphere confining pressure. *Journal of Metamorphic Geology*, 7: 229-242.
- BOHER, M., ABOUCHAMI, W., MICHARD, A., ALBAREDE, F. & ARNDT, N.T., 1992. Crustal growth in West Africa at 2.1 Ga. *Journal of Geophysical Research*, 97: 345-369.
- BOLTRUKEVITCH, B.N., 1973. *Notice explicative sur la carte des gisements et indices auriferes de la Republique du Mali*. Unpublished report, SONAREM, Kati.
- BONHOMME, M., 1962. *Contribution à l'étude géochronologique de la plate-forme de l'Ouest africain*. Ph.D. Thesis, University of Clermont-Ferrand, France, 62 pp.
- BOSSIÈRE, G., BONKOUNGOU, I., PEUCAT, J. & PUPIN, J., 1996. Origin and age of Palaeoproterozoic conglomerates and sandstones of the Tarkwaian Group in Burkina Faso, West Africa. *Precambrian Research*, 80: 153-172.
- BOULLIER, A.M., FIRDAOUS, K. & ROBERT, F., 1998. On the significance of aqueous fluid inclusions in gold-bearing quartz vein deposits from the southeastern Abitibi Subprovince (Quebec, Canada). *Economic Geology*, 93: 216-223.
- BOURGES, F., DEBAT, P., TOLLON, F., MUMOZ, M. & INGLES, J., 1998. The geology of the Taparko gold deposit, Birimian greenstone belt, Burkina Faso, West Africa. *Mineralium Deposita*, 33: 591-605.
- BOWELL, R.J., FOSTER, R.P. & STANLEY, C.J., 1990. Telluride mineralisation at Ashanti gold mine, Ghana. *Mineralogical Magazine*, 54: 617-627.
- BOWERS, T.S. & HELGESON, H.C., 1983a. Calculations of the thermodynamic and geochemical consequences of non-ideal mixing in the system H₂O-CO₂-NaCl on phase relations in geological systems. Equation of state for H₂O-CO₂-NaCl fluids at high pressures and temperatures. *Geochimica et Cosmochimica Acta*, 47: 1247-1275.
- BOWERS, T.S. & HELGESON, H.C., 1983b. Calculations of the thermodynamic consequences of non-ideal mixing in the system H₂O-CO₂-NaCl on phase relations in geological systems. *American Mineralogist*, 68: 1059-1075.
- BREEDING, C.M. & AGUE, J.J., 2002. Slab-derived fluids and quartz vein formation in an accretionary prism, Otago schist, New Zealand. *Geology*, 30: 499-502.
- BROONER, G., CHAUVEL, J.J. & TRILBOULET, C., 1990. Geochemistry and knowledge of banded-iron formations in the West African shield, an example. In: Chauvel, J.J., Yuqi, CH., El Shazly, E.M., Gross, G.A., Laajoki, K., Markov, M.S., Rai, K.L., Stulchikov, V.A. & Augusthithis, S.S. (Editors), *Ancient Banded Iron-formations (Regional Presentations)*. Theophrastus, Athens, 462 pp.
- BROWN, P.E. & LAMB, W.M., 1989. P-V-T properties of fluids in the system H₂O ± CO₂ ± NaCl: New graphical presentations and implications for fluid inclusion studies. *Geochimica et Cosmochimica Acta*, 53: 1209-1221.
- BURKE, E.A.J., 2001. Raman microspectrometry of fluid inclusions. *Lithos*, 55: 139-158.

- BURROWS, D.R., 1991. *Relationships between Archaean lode gold quartz vein deposits and igneous intrusions in the Timmins and Val d'Or areas, Abitibi sub-province, Canada*. Ph.D Thesis, University of Toronto, Canada, 217 pp.
- BURROWS, D.R. & SPOONER, E.T.C., 1989. Relationships between Archaean gold vein-shear zone mineralisation and igneous in the Val d'Or and Timmins areas, Abitibi Subprovince, Canada. *Economic Geology Monograph*, 6: 424-444.
- BURROWS, D.R., WOOD, P.C. & SPOONER, E.T.C., 1986. Carbon isotope evidence for a magmatic origin for Archaean gold-quartz vein ore deposits. *Nature*, 321: 851-854.
- BURRUSS, R.C., 1981. Analysis of phase equilibrium in C-O-H-S fluid inclusions. *Mineralogical Association of Canada Short Course Handbook*, 6: 39-74.
- BURRUSS, R.C., 2003. Raman spectroscopy of fluid inclusions. In: Samson, I., Anderson, A. & Alderton, D.H.M. (Editors), *Fluid Inclusions: Interpretation and Analysis*. Mineralogical Association of Canada. Short Course Series Volume 32, Vancouver, British Columbia, pp. 279-289.
- BUTTERFIELD, D.A., MCDUFF, R.E., FRANKLIN, J. & WHEAT, C.G., 1994. *Geochemistry of hydrothermal vent fluids from Middle Valley, Juan de Fuca Ridge*. Proceedings Ocean Drilling Program, 139: 395-410.
- CABRI, L.J., 1965. Phase relations in the Au-Ag-Te system and their mineralogical significance. *Economic Geology*, 60: 1569-1606.
- CABY, R., 2003. Terrane assembly and geodynamic evolution of central-western Hoggar: a synthesis. *Journal of African Earth Sciences*, 37: 133-159.
- CABY, R. & KIENAST, J.R., 2009. Neoproterozoic and Hercynian metamorphism events in the Central Mauritanides: Implications for the geodynamic evolution of West Africa. *Journal of African Earth Sciences*, 53: 122-136.
- CAMPBELL, A.R., LUNDBERG, S.A.W. & DUNBAR, N.W., 2001. Solid inclusions of halite in quartz: evidence for the halite trend. *Chemical Geology*, 173: 179-191.
- CAMERON, E.M., 1988. Archaean gold: Relation to granulite formation and redox zoning in the crust. *Geology*, 16: 109-112.
- CAMERON, E.M., 1993. Precambrian Gold: Perspectives from the top and bottom of shear zones. *Canadian Mineralogist*, 31: 917-944.
- CAMERON, G., 2006. *Tectonic evolution and distribution of orogenic gold deposits in Africa*. Randgold Resources Ltd, Internal Report, 61pp.
- CAMERON, G. & MOOLMAN, R., 2004. *Loulo Generative Report: Incorporating new data from Aster Imagery*. Randgold Resources Ltd. Internal Report, 16 pp.
- CAMIL, J., 1984. *Pétrographie, chronologie des ensembles granulitiques Archéens et formations associées de la région de Man (Côte d'Ivoire). Implications pour l'histoire géologique du craton Ouest African*. Ph.D. Thesis, Abidjan University, Abidjan, Cote d'Ivoire.
- CAMPBELL, I.H. & HILL, R.I., 1988. A two-stage model for the formation of the granite-greenstone terrains of the Kalgoorlie-Norseman area, Western Australia. *Earth and Planetary Science Letters*, 90: 11-25.
- CARD, K.D., 1990. A review of the Superior Province of the Canadian Shield, a product of Archean accretion. *Precambrian Research*, 48: 99-156.

- CASTAING, C., BILLA, M., MILÉSI, J.P., THIÉBLEMONT, D., LE MÉTOUR, J., EGAL, E., DONZEAU, M., GUÉROT, C., COCHERIE, A., CHÉVREMONT, P., TEGYÉY, M., ITARD, Y., ZIDA, B., OUEDRAOGO, I., KOTE, S., KABORE, B.E., OUEDRAOGO, C., KI, J.C. & ZUNINO, C., 2003. *Notice explicative de la carte géologique et minière du Burkina Faso à 1/1 000 000*. Ministère des Mines, des Carrières et de l'Energie, Burkina Faso.
- CASTELLANA, C.H. & LONG, L., 1998. Origin of the Coronel Joao Sa pluton: implications for the tectonic evolution of NE Brazil. *Geological Society of America Abstracts*, 30: 236.
- CASTILLO, J., BATIZA, R. & STERN, J., 1986. Petrology and geochemistry of the Naura basin igneous complex: large-volume, off-ridge eruptions of MORB-like basalts during the Cretaceous. *Initial Reports of the Deep Sea Drilling Project*, 39: 555-576.
- CATHELINEAU, M., 1988. Cation site occupancy in chlorides and illites as a function of temperature. *Clay Minerals*, 23: 471-485.
- CATHELINEAU, M. & NIEVA, D., 1985. A chlorite solid solution geothermometer. The Los Azufres geothermal system (Mexico). *Contributions to Mineralogy and Petrology*, 91: 235-244.
- CATHELINEAU, M., BOIRON, M.C., HOLLIGER, P., MARION, P. & DENIS, M., 1989. Gold in arsenopyrites: crystal chemistry, location and state, physical and chemical conditions of deposition. *Economic Geology Monograph*, 6: 328-341.
- CHAMBERLAIN, C.M., 2003. *Geology and genesis of the Bulyanhulu gold deposit, Sukumaland greenstone belt, Tanzania*, Royal School of Mines, Imperial College, London, 343 pp.
- CHALOKWU, C.I., GHAZI, M.A. & FOORD, E.E., 1997. Geochemical characteristics and K-Ar ages of rare-metal bearing pegmatites from the Birimian of southeastern Ghana. *Journal of African Earth Sciences*, 24: 1-9.
- CHANG, Z., LARGE, R.L. & MASELENNIKOV, V., 2008. Sulphur isotopes in sediment-hosted orogenic gold deposits: evidence for an early timing and seawater sulphur source. *Geology*, 36: 971-974.
- CHAPPELL, B.W. & WHITE, A.J.R., 1974. Two contrasting granite types. *Pacific Geology*, 8: 173-174.
- CHEILLETZ, A., BARBEY, P., LAMA, C., PONS, J., ZIMMERMANN, J.L. & DAUTEL, D., 1994. Age de refroidissement de la croûte juvénile birimienne d'Afrique de l'Ouest. Données U-Pb, Rb-Sr, et K-Ar sur les formations à 2.1 Ga du SW-Niger. *Comptes Rendus de l'Académie des Sciences Paris Séries II*, 319: 435-442.
- CHERNYSHOV, N.M. & MYASNYANKIN, V.I., 1992. Gold potential of the early Precambrian greenstone structures of the KMA. *International Geology Reviews*, 33: 639-651.
- CLARK, L.A., 1960. The Fe-As-S system: phase relations and applications. *Economic Geology*, 55: 1345-1381.
- CLARK, M.E., CARMICHAEL, D.M., HODGSON, C.J. & FU, M., 1989. Wall-rock alteration, Victory gold mine, Kambalda, Western Australia: Processes and P-T-XCO₂ conditions of metasomatism. *Economic Geology Monograph*, 6: 445-459.
- CLAYPOOL, G.E., HOLSER, W.T., KAPLAN, I.R., SAKAI, H. & ZAKI, I., 1980. The age curves of sulphur and oxygen in marine sulphate and their initial interpretation. *Chemical Geology*, 28: 199-206.
- CLUFF GOLD PLC, 2009. Angovia reserves and resources. Available at: http://www.cluffgold.com/pages/projects_angovia.asp. [Accessed 15 May 2010].
- COHEN, H.A. & GIBBS, A.K., 1989. Is the equatorial Atlantic discordant? *Precambrian Research*, 42: 353-369.

- COLVINE, A.C., FYON, J.A., HEATHER, K.B., MARMONT, S., SMITH, P.M. & TROOP, D.G., 1988. Archaean lode gold deposits in Ontario. *Ontario Geological Survey Miscellaneous Paper*, 139: 136 p.
- CONDIE, K.C., 1989. Geochemical changes in basalts and andesites across the Archaean-Proterozoic boundary: identification and significance. *Lithos*, 23: 1-18.
- CONDIE, K.C., 1993. Chemical compositions and evolution of the upper continental crust: contrasting results from surface samples and shales. *Chemical Geology*, 104: 1-37.
- CONDIE, K.C., 2000. Episodic continental growth models: Afterthoughts and extensions. *Tectonophysics*, 322: 153-162.
- COULIBALY, Y., BOIRON, M.C., CATHELINEAU, M. & KOUAMELAN, A.N., 2008. Fluid immiscibility and gold deposition in the Birimian quartz veins of the Angovia deposit (Yaouré, Ivory Coast). *Journal of African Earth Sciences*, 50: 234-254.
- COX, K.G., BELL, J.D. & PANKHURST, R.J., 1979. *The interpretation of igneous rocks*. George, Allen & Unwin, London, 450 pp.
- COX, S.F., SUN, S.S., ETHERIDGE, M.A., WALL, V.J. & POTTER, T.F., 1995. Structural and geochemical controls on the development of turbidite-hosted gold quartz vein deposits, Wattle Gully Mine, Central Victoria, Australia. *Economic Geology*, 90: 1722-1746.
- CRAIG, H., 1957. Isotopic standards and isotopic correction factors for mass spectrometric analysis of carbon dioxide. *Geochimica et Cosmochimica Acta*, 12: 133-149.
- CRAWFORD, M.L. & HOLLISTER, L.S., 1986. Metamorphic fluids: The evidence from fluid inclusions. In: Walther, J.V. & Wood, B.J. (Editors), *Fluid rock interaction during metamorphism*. Springer-Verlag, Berlin, pp. 1-35.
- CULLERS, R.L., 2000. The geochemistry of shales, siltstones and sandstones of Pennsylvanian-Permian age, Colorado, USA: implications for provenance and metamorphic studies. *Lithos*, 51: 181-203.
- CULLERS, R.L., BASU, A. & SUTTNER, L.J., 1988. Geochemical signature of provenance in sand-mixed material in soil and stream sediments near the Tobacco Root batholith, Montana, USA. *Chemical Geology*, 70: 335-348.
- DALLMEYER, R.D. & LECORCHE, J.P., 1991. *The West African Orogens and Circum-Atlantic Correlatives*. 1st Edition, Springer-Verlag, Berlin, 405 pp.
- DAMPARE, S.B., SHIBATA, T., ASIEDU, D.K., OSAE, S. & BANOENG-YAKUBO, B., 2008. Geochemistry of Palaeoproterozoic metavolcanic rocks from the southern Ashanti volcanic belt, Ghana: Petrogenetic and tectonic setting implications. *Precambrian Research*, 162: 403-423.
- DAVIDSON, B., 2005. *Africa in history*. Simon & Schuster, New York.
- DAVIES, G.F., 1995. Penetration of plates and plumes through the mantle transition zone. *Earth and Planetary Science Letters*, 133: 507-516.
- DAVIES, J.F., WHITHEAD, R.E.S., HUANG, J. & NAWARATNE, S., 1990. A comparison of progressive hydrothermal carbonate alteration in Archaean metabasalts and metaperidotites. *Mineralium Deposita*, 25: 65-72.
- DAVIS, G.H. & REYNOLDS, S.J., 1996. *The structural geology of rocks and regions*. 2nd Edition, Wiley, New York, 800 pp.
- DAVIS, D.W., HIRDES, W., SCHALTEGGER, U. & NUNOO, E.A., 1994. U-Pb age constraints on deposition and provenance of Birimian and gold-bearing Tarkwaian sediments in Ghana, West Africa. *Precambrian Research*, 67: 89-107.

- DEBAT, P., NIKIÉMA, S., MERCIER, A., LOMPO, M., BÉZIAT, D., BOURGES, F., RODDAZ, M., SALVI, S., TOLLON, F. & WENMENGA, U., 2003. A new metamorphic constraint for the Eburnean orogeny from Palaeoproterozoic formations of the Man shield (Aribinda and Tampelga countries, Burkina Faso). *Precambrian Research*, 123: 47-65.
- DELOR, C., SIMEON, Y., KOUAMELAN, A. & PEUCAT, J.J., 1994. *Persistence de processus archaïques de création crustale au Birimien (Paléoprotérozoïque) en Côte d'Ivoire (Afrique de l'Ouest)*. XV RST Meeting, Nancy, France, p 10.
- DE RONDE, C.E.J., SPOONER, E.T.C., DE WIT, M.J. & BRAY, C.J., 1992. Shear zone-related, Au quartz vein deposits in the Barberton greenstone belt, South Africa: field and petrographic characteristics, fluid properties, and light stable isotope geochemistry. *Economic Geology*, 87: 366-402.
- DE RONDE, C.E.J., FAURE, K., BRAY, C.J. & WHITFORD, D.J., 2000. Round Hill shear zone-hosted gold deposit, Macraes flat, Otago, New Zealand: Evidence of a magmatic ore fluid. *Economic Geology*, 95: 1025-1048.
- DIA, A., 1988. *Caractères et signification des complexes magmatiques et métamorphiques du secteur de Sandikounda- Lamina (Nord de la boutonnière de Kédougou; Est du Sénégal): un modèle géodynamique du Birimien de l'Afrique de l'Ouest*. Ph.D. Thesis, Université de Dakar, Sénégal, 350 pp.
- DIA, A., VAN SCHMUS, W.R. & KRÖNER, A., 1997. Isotopic constraints on the age and formation of a Palaeoproterozoic volcanic arc complex in the Kédougou inlier, eastern Senegal, West Africa. *Journal of African Earth Sciences*, 24: 197-213.
- DIAMOND, L.W., 1990. Fluid inclusion evidence for P-V-T-X evolution of hydrothermal solutions in Late-Alpine gold-quartz veins at Brusson, Val D'Ayas, Northwest Italian Alps. *American Journal of Science*, 290: 912-958.
- DIAMOND, L.W., 1992. Stability of CO₂-clathrate-hydrate + CO₂ liquid + CO₂ vapour + aqueous KCl-NaCl solutions: Experimental determination and application to salinity estimates of fluid inclusions. *Geochimica et Cosmochimica Acta*, 55: 273-280.
- DIAMOND, L.W., 2003. Glossary: terms and symbols used in fluid inclusion studies. In: Samson, I., Anderson, A. & Alderton, D.H.M. (Editors), *Fluid Inclusions: Interpretation and Analysis*. Mineralogical Association of Canada. Short Course Series Volume 32, Vancouver, British Columbia, pp. 365-374.
- DIALLO, D.P., 2001. Le paléovolcanisme de la bordure occidentale de la boutonnière de Kédougou, Paléoprotérozoïque du Sénégal oriental: incidences géotectoniques. *Journal of African Earth Sciences*, 32: 919-940.
- DIOH, E., BÉZIAT, D., DEBAT, P., GRÉGOIRE, M. & NGOM, P.M., 2006. Diversity of the Palaeoproterozoic granitoids of the Kédougou inlier (eastern Senegal): Petrographical and geochemical constraints. *Journal of African Earth Sciences*, 44: 351-371.
- DIESSEL, C.F.K., BROTHERS, R.N. & BLACK, P.M., 1978. Coalification and graphitization in high-pressure schists in New Caledonia. *Contributions to Mineralogy and Petrology*, 68: 63-78.
- DIMO, G., 1990. Telfer gold deposits. *Australia's Institute of Mining Metallurgy Monograph*, 14: 643-651.
- DOMMANGET, A., MILESI, J.P. & DIALLO, M., 1993. The Loulo gold and tourmaline-bearing deposit. *Mineralium Deposita*, 28: 253-263.
- DOUMBIA, S., POUCLLET, A., KOUAMELAN, A., PEUCAT, J.J., VIDAL, M. & DELOR, C., 1998. Petrogenesis of juvenile-type Birimian (Palaeoproterozoic) granitoids in Central Cote-d'Ivoire, West Africa: geochemistry and geochronology. *Precambrian Research*, 87: 33-63.
- DRUMMOND, S.E. & OHMOTO, H., 1985. Chemical evolution and mineral deposition in boiling hydrothermal systems. *Economic Geology*, 80: 126-147.

- DUBE, B., WILLIAMSON, K., MCNICOLL, V., SKULSKI, T., TWOMEY, T. & SANBIRN-BARRIE, M., 2004. Timing of gold mineralisation at Red Lake, Northwestern Ontario, Canada: New constraints from U-Pb Geochronology at the Goldcorp high-grade zone, Red Lake mine, and the Madsen mine. *Economic Geology*, 99: 1611-1641.
- DUBOIS, M., BÉZIAT, D., DEBAT, P., SAVARY, V., LOMPO, M., NIKIEMA, S. & TOLLON, F., 2001. *A fluid inclusion study in the Proterozoic (2.0 Ga) gold deposits of Burkina Faso*. ECROFI-XVI European Current Research on Fluid Inclusions, pp. 135-136.
- DUBOIS, M., STEFANO, S. & BÉZIAT, D., 2007. *Peculiar fluids at the origin of orogenic gold deposits in Burkina Faso, West Africa*. ECROFI-XIX European Current Research on Fluid Inclusions, pp. 248.
- DUURING, P., CASSIDY, K.F. & HAGEMANN, S.G., 2007. Granitoid-associated orogenic, intrusion-related, and porphyry style metal deposits in the Archaean Yilgarn Craton, Western Australia. *Ore Geology Reviews*, 32: 157-186.
- EBERT, S., MILLER, L., PETSSEL, S., DODD, S. & KOWALEZYK, P., 2000. Geology, mineralisation, and exploration at the Donlin Creek project, southwest Alaska. In: Tucker T.L. & Smith, M.T. (Editors), *The Tintina gold belt: concepts, exploration, and discoveries*. British Columbia and Yukon Chamber of Mines, Cordillera Roundup, pp. 99-114.
- EGAL, E., THIÉBLEMONT, D., LAHONDÈRE, D., GUERROT, C., COSTEA, C.A., ILIESCU, D., DELOR, C., GOUJOU, J., LAFON, J.M., TEGYEY, M., DIABY, S. & KOLIÉ, P., 2002. Late Eburnean granitisation and tectonics along the western and northwestern margin of the Archaean Kénéma–Man domain (Guinea, West African Craton). *Precambrian Research*, 117: 57-84.
- EISENLOHR, B.N. & HIRDES, W., 1992. The structural development of the early Proterozoic Birimian and Tarkwaian rocks of southwest Ghana, West Africa. *Journal of African Earth Sciences*, 14: 313-325.
- ELLIOT, R.P., 1965. *Constitution of binary alloys*. McGraw Hill, New York, 875 pp.
- FEDO, C.M., NESBITT, H.W. & YOUNG, G.M., 1995. Unraveling the effects of potassium metasomatism in sedimentary rocks and palaeosoils, with implications for palaeoweathering conditions and provenance. *Geology*, 23: 921-924.
- FEDOROWICH, J., STAUFFER, M. & KERRICH, R., 1991. Structural setting and fluid characteristics of the Proterozoic Tartan Lake gold deposit, Trans-Hudson orogeny, Northern Manitoba. *Economic Geology*, 86: 1434-1467.
- FEYBESSE, J. & MILÉSI, J.P., 1994. The Archaean/Proterozoic contact zone in West Africa: a mountain belt of decollement thrusting and folding on a continental margin related to 2.1 Ga convergence of Archean cratons? *Precambrian Research*, 69: 199-227.
- FEYBESSE, J., BILLA, M., GUERROT, C., DUGUEY, E., LESCUYER, J., MILÉSI, J.P. & BOUCHOT, V., 2006. The Palaeoproterozoic Ghanaian province: Geodynamic model and ore controls, including regional stress modelling. *Precambrian Research*, 149: 149-196.
- FLEISCHER, R. & VIAL, D.S., 1991. Surface and underground geological excursion around and in the Passagem de Mariana gold mine, Minas Gerais, Brazil. *U.S. Geological Survey Bulletin*, 1980-A: A49-A62.
- FOSTER, R.P. & PIPER, D.P., 1993. Archaean lode gold deposits in Africa: Crustal setting, metallogenesis and cratonisation. *Ore Geology Reviews*, 8: 303-347.
- FOSTER, R.P., LEAHY, K., HUNNS, S.R., PELHAM, D.A., LAWRENCE, S.R. & HARRISON, A.E., 2000. Pan-African terranes: realizing the metal potential. *Transactions of the Institution of Mining and Metallurgy*, 110: B15-B23.
- FOUILLAC, A.M., DOMMANGET, A. & MILESI, J.P., 1993. A carbon, oxygen, hydrogen and sulphur isotopic study of the gold mineralization at Loulo, Mali. *Chemical Geology*, 106: 47-62.

- FRANTZ, J.D., POOP, R.K. & HOERING, T.C., 1992. The compositional limits of fluid immiscibility in the system H₂O-NaCl-CO₂ as determined with the use of synthetic fluid inclusion inclusions conjunction with mass spectrometry. *Chemical Geology*, 98: 237-255.
- FRIMMEL, H.E. & MINTER, W.E.L., 2002. Recent development concerning the geological history and genesis of the Witwatersrand gold deposits, South Africa. *Society of Economic Geologists Special Publications*, 9: 17-45.
- FYFE, W.S. & KERRICH, R., 1984. Gold: Natural concentration processes. In: Foster, R.P. (Editor), *Gold '82: The geology, geochemistry, and genesis of gold deposits*. Balkema, Rotterdam, pp. 99-127.
- GALIPP, K., KLEMD, R. & HIRDES, W., 2003. Metamorphism and geochemistry of the Palaeoproterozoic Birimian Sefwi volcanic belt (Ghana, West Africa). *Geologisches Jahrbuch Reihe D*, 151-191.
- GARBA, I. & AKANDE, S., 1992. The origin and significance of non-aqueous CO₂ fluid inclusions in the auriferous veins of Bin Yauri, northwestern Nigeria. *Mineralium Deposita*, 27: 249-255.
- GASQUET, D., BARBEY, P., ADOU, M. & PAQUETTE, J.L., 2003. Structure, Sr-Nd isotope geochemistry and zircon U-Pb geochronology of the granitoids of the Dabakala area (Cote d'Ivoire): evidence for a 2.3 Ga crustal growth event in the Palaeoproterozoic of West Africa? *Precambrian Research*, 127: 329-354.
- GEBRE-MARIAM, M., GROVES, D.I. & MCNAUGHTON, N.J., 1997. Aqueous and CO₂- and CH₄- rich inclusions at the Archaean Golden Kilometre gold deposit: multiple fluid sources and depositional mechanisms. *Chronique de la Recherche Miniere*, 529: 59-73.
- GEHRIG, M., 1980. Phasengleichgewichte und PVT-Daten ternarer Mischungen aus Wasser, Kohlendioxid und Natriumchlorid bis 3 kbar und 550 °C. *Freiburg, Hochschulverlag, Hochschulsammlung Naturewissenschaften*, 1: 1-109.
- GERALDES, M.C., DE ABREU, G.C., PIRES, P.R., MELLO, E.F. & IYER, S.S., 2006. Sulphur isotope characteristics of mesothermal gold deposits: results of an investigation of the Rio Itapicuru region, Bahia, Brazil. *International Geology Reviews*, 43: 110-119.
- GIBBS, A.K. & OLSZEWSKI, J., WILLIAM J., 1982. Zircon U-Pb ages of Guyana greenstone-gneiss terrane. *Precambrian Research*, 17: 199-214.
- GOELLNICH, N.M., GROVES, D.I., MCNAUGHTON, N.J. & DIMO, G., 1989. An epigenetic origin for the Telfer gold deposit, Western Australia. *Economic Geology Monograph*, 6: 151-167.
- GOLD FIELDS LTD, 2009. Mineral resources and reserves. Available at: http://www.goldfields.co.za/ops_res_res.php. [Accessed 15 May 2010].
- GOLDEN STAR RESOURCES LTD, 2009. Golden Star 2009 annual report. Available at: http://www.gsr.com/Investment/Financial_Information. [Accessed 2 August 2010].
- GOLDFARB, R.J., LEACH, D.L., MILLER, M.L. & PICKTHORN, W.J., 1986. Geology, metamorphic setting and genetic constraints of epigenetic lode-gold mineralisation within the Cretaceous Valdez Group, south-central Alaska. In: Keppie, J.D., Boyle R.W. & Haynes, S.J. (Editors), *Turbidite-hosted gold deposits: Geological Association of Canada Special Paper 32*. pp. 97-105.
- GOLDFARB, R.J., LEACH, D.L., PICKTHORN, W.J. & PATERSON, C.J., 1988. Origin of lode-gold deposits of the Juneau gold belt, southeastern Alaska. *Geology*, 16: 440-443.
- GOLDFARB, R.J., NEWBERRY, R.J., PICKTHORN, W.J. & GENT, C.A., 1991. Oxygen, hydrogen, and sulphur isotope studies in the Juneau Gold Belt, Southeastern Alaska: constraints on the origin of hydrothermal fluids. *Economic Geology*, 86: 66-80.
- GOLDFARB, R., MILLER, L.D., LEACH, D.L. & SNEE, L.W., 1997. Gold deposits in metamorphic rocks of Alaska. *Economic Geology Monograph*, 9: 151-190.

- GOLDFARB, R.J., GROVES, D.I. & GARDOLL, S., 2001a. Orogenic gold and geologic time: a global synthesis. *Ore Geology Reviews*, 18: 1-75.
- GOLDFARB, R.J., GROVES, D.I. & GARDOLL, S., 2001b. Rotund versus skinny orogens: Well-nourished or malnourished gold. *Geology*, 29: 539-542.
- GOLDFARB, R.J., BAKER, T., DUBE, B., GROVES, D.I., HART, C.J.R. & GOSSELIN, P., 2005. Distribution, character, and genesis of gold deposits in metamorphic terranes. *Economic Geology*, 100: 407-450.
- GOLDING, S.D. & WILSON, A.F., 1982. Geochemical and stable isotope studies of the Crown and Mararoa Reefs, Noresman, Western Australia. *Rev. Brans. Geoscience*, 12: 445-456.
- GOLDSTEIN, R.H., 2003. Petrographic analysis of fluid inclusions. In: Samson, I., Anderson, A. & Alderton, D.H.M. (Editors), *Fluid Inclusions: Interpretation and Analysis*. Mineralogical Association of Canada. Short Course Series Volume 32, Vancouver, British Columbia, pp. 9-53.
- GOLDSTEIN, R.H. & REYNOLDS, T.J., 1994. *Systematics of fluid inclusions in diagenetic minerals*. SEPM Short Course 31. Society for Sedimentary Geology, Oklahoma.
- GRANT, J.A., 1986. The isocon diagram- a simple solution to Gresens' equation for metasomatic alteration. *Economic Geology*, 81: 1976-1982.
- GRAU, G., MARTIN, H., LEVEQUE, B. & CAPDEVILLA, R., 1985. Rb-Sr and Sm-Nd geochronology of Lower Proterozoic granite-greenstone terranes in French Guiana, South America. *Precambrian Research*, 30: 63-80.
- GRESENS, R.L., 1967. Composition-volume relationships of metasomatism. *Chemical Geology*, 2: 47-55.
- GRICE, J.D. & ERCIT, T.S., 1993. Ordering of Fe and Mg in the tourmaline crystal structure: the correct formula. *Neues Jahrbuch für Mineralogy*, 165: 245-266.
- GROVES, D.I. & FOSTER, R.P., 1993. Archaean lode gold deposits. In: Foster, R.P. (Editor), *Gold metallogeny and exploration*. Chapman & Hall, London, pp. 63-103.
- GROVES, D.I. & PHILLIPS, G.N., 1987. The genesis and tectonic control on Archaean gold deposits of the Western Australian Shield: A metamorphic replacement model. *Ore Geology Reviews*, 2: 287-322.
- GROVES, D.I., BARLEY, M.E. & HO, S.E., 1989. Nature, genesis, tectonic setting of mesothermal gold mineralisation in the Yilgarn Block, Western Australia. *Economic Geology Monograph*, 6: 151-167.
- GROVES, D.I., BARLEY, M.E., BARNICOAT, A.C., CASSIDY, K.F., FARE, R.J., HAGEMANN, S.G., HO, S.E., HRONSKY, J.M.A., MIKUCKI, E.J., MUELLER, A.G., MCNAUGHTON, N.J., PERRING, C.S., RIDLEY, J.R. & VEARNCOMBE, J.R., 1992. Sub-greenschist to granulite-hosted Archaean lode-gold deposits of the Yilgarn Craton: A depositional continuum from deep sourced hydrothermal fluids in crustal-scale plumbing systems. *University of Western Australia Special Publications*, 22: 325-338.
- GROVES, D.I., GOLDFARB, R.J., GEBRE-MARIAM, M., HAGEMANN, S.G. & ROBERT, F., 1998. Orogenic gold deposits: A proposed classification in the context of their crustal distribution and relationship to other gold deposit types. *Ore Geology Reviews*, 13, 7-27.
- GROVES, D.I., GOLDFARB, R.J., KNOX-ROBINSON, C.M., OJALA, J., GARDOLL, S., YUN, G.Y. & HOLYLAND, P., 2000. Late-kinematic timing of orogenic gold deposits and significance for computer-based exploration techniques with emphasis on the Yilgarn Block, Western Australia. *Ore Geology Reviews*, 17: 1-38.
- GROVES, D.I., GOLDFARB, R.J., ROBERT, F. & HART, C.J.R., 2003. Gold Deposits in metamorphic belts: Overview of current understanding, outstanding problems, future research, and exploration significance. *Economic Geology*, 98: 1-29.

- GROVES, D.I., CONDIE, K.C., GOLDFARB, R.J., HRONSKY, J.M.A. & VIELREICHER, R.M., 2005a. Secular changes in global tectonic processes and their influence on the temporal distribution of gold-bearing mineral deposits. *Economic Geology*, 100: 203-224.
- GROVES, D.I., VIELREICHER, R.M., GOLDFARB, R.J. & CONDIE, K.C., 2005b. Controls on the heterogeneous distribution of mineral deposits through time. *Geological Society Special Publications*, 248: 71-101.
- GREW, E.S., 1974. Carbonaceous material in some metamorphic rocks of New England and other areas. *Journal of Geology*, 82: 50-73.
- GUEYE, M., SIEGESMUND, S., WEMMER, K., PAWLIG, S., DROBE, M., NOLTE, N. & LAYER, P., 2007. New evidence for an early Birimian evolution in the West African Craton: an example from the Kédougou-Kéniéba inlier, southeast Senegal. *South African Journal of Geology*, 110: 511-534.
- GUEYE, M., NGOM, P.M., DIENE, M., THIAM, Y., SIEGESMUND, S., WEMMER, K. & PAWLIG, S., 2008. Intrusive rocks and tectono-metamorphic evolution of the Mako Palaeoproterozoic belt (Eastern Senegal, West Africa). *Journal of African Earth Sciences*, 50: 88-110.
- HAGEMANN, S.G. & CASSIDY, K.F., 2000. Archaean orogenic lode gold deposits. *Reviews in Economic Geology*, 13: 9-68.
- HALL, D.L., STERNER, S.M. & BODNAR, R.J., 1988. Freezing point depression of NaCl-KCl-H₂O solutions. *Economic Geology*, 83: 197-202.
- HAMMOND, N.Q. & ROBB, L.J., 2009. *Gold mineralisation at the Morila mine, Mali: petrographic, mineral-chemical, and fluid aspects*. The Society of Geology Applied to Mineral Deposits (SGA) Conference, 17-20th August.
- HAMMOND, N.Q. & SHIMAZAKI, H., 1994. Geology and geochemical aspects of ore formation at the Prestea mesothermal vein gold deposit in the Birimian system of Ghana. *International Geology Reviews*, 36: 15-31.
- HARRIS, R.W., 1998. *An Assessment of the structural geology of the Loulo 0, Yalea Shear, and Yalea Ridge gold prospects, Mali*. Randgold Resources Ltd, Internal Report, 74 pp.
- HARRIS, N.B., PEARCE, J.A. & TINDLE, A.G., 1986. Geochemical characteristics of collision-zone magmatism. In: Coward, M.P. & Reis, A.C. (Editors), *Collision tectonics*. Geological Society of London Special Publications, pp. 67-81.
- HART, C.J.R., 2007. Reduced intrusion-related gold systems. In: Goodfellow, W.D. (Editor), *Mineral deposits of Canada: A synthesis of major deposit types, district metallogeny, the evolution of geological province, and exploration methods*. Geological Association of Canada, Mineral Deposits Division, Special Publication No 5, pp. 95-112.
- HAWKESWORTH, C.J., DHUIME, B., PIETRANIK, A.B., CAWOOD, P.A., KEMP, A.I.S. & STOREY, C.D., 2010. The generation and evolution of the continental crust. *Journal of Geological Society London*, 167: 229-248.
- HAWTHORNE, F.C. & HENRY, D.J., 1999. Classification of the minerals of the tourmaline group. *European Journal of Mineralogy*, 11: 201-215.
- HEDENQUIST, J.W. & LOWENSTERN, J.B., 1994. The role of magmas in the formation of hydrothermal ore deposits. *Nature*, 370: 519-527.
- HEIN, K.A.A., MOREL, V., KAGONE, O., KIEMDE, F. & MAYES, K., 2004. Birimian lithological succession and structural evolution in the Goren segment of the Boromo-Goren Greenstone Belt, Burkina Faso. *Journal of African Earth Sciences*, 39: 1-23.
- HELMY, H.M., KAINDI, R., FRITZ, H. & LOIZENBAUER, J., 2004. The Sukari gold mine, Eastern Desert- Egypt: structural setting, mineralogy and fluid inclusion study. *Mineralium Deposita*, 39: 495-511.

- HENLEY, R.W., NORRIS, R.J. & PATERSON, C.J., 1976. Multistage ore genesis in the New Zealand Geosyncline: A history of post-metamorphic lode emplacement. *Mineralium Deposita*, 11: 180-196.
- HENRY, D.J. & DUTROW, B.L., 1996. Metamorphic tourmaline and its petrologic applications. *Reviews in Mineralogy*, 33: 275-279.
- HENRY, D.J. & GUIDOTTI, C.V., 1985. Tourmaline as a petrogenetic indicator mineral- an example from the staurolite-grade metapelites of NW Maine. *American Mineralogist*, 70: 1-15.
- HERBERT, S. & SENGHOR, D., 2007. *Bambadji overall concession appraisal*. Randgold Resources Ltd, Internal Report, 46 pp.
- HERRON, M.M., 1988. Geochemical classification of terrigenous sands and shales from core and log data. *Journal of Sedimentology and Petrology*, 58: 820-829.
- HEY, M.H., 1954. A new review of the chlorites. *Mineralogical Magazine*, 30: 277-292.
- HIRDES, W. & DAVIS, D.W., 1998. First U-Pb zircon age of extrusive volcanism in the Birimian Supergroup of Ghana/West Africa. *Journal of African Earth Sciences*, 27: 291-294.
- HIRDES, W. & DAVIS, D.W., 2002. U-Pb Geochronology of Palaeoproterozoic rocks in the southern part of the Kédougou-Kéniéba inlier, Senegal, West Africa: evidence for diachronous accretionary development of the Eburnean Province. *Precambrian Research*, 118: 83-99.
- HIRDES, W. & NUNOO, B., 1994. The Proterozoic paleoplacers of Tarkwa gold mine/SW Ghana: sedimentology, mineralogy, and precise age dating of the Main Reef and West Reef, and bearing of the investigations on source area aspects. *Geologische Jahrbuch*, 100: 247-311.
- HIRDES, W., SAAGER, R. & LEUBE, A., 1987. *The Tarkwaian Group of Ghana: new aspects relating to its tectonic setting, structural evolution, gold mineralisation and provenance area*. International Conference on Metallogeny Related to Tectonics, Arusha, pp. 19-20.
- HIRDES, W., DAVIS, D.W. & EISENLOHR, B.N., 1992. Reassessment of Proterozoic granitoid ages in Ghana on the basis of U/Pb zircon and monazite dating. *Precambrian Research*, 56: 89-96.
- HIRDES, W., DAVIS, D.W., LUDTKE, G. & KONAN, G., 1996. Two generations of Birimian (Palaeoproterozoic) volcanic belts in northeastern Cote d'Ivoire (West Africa): consequences for the 'Birimian controversy'. *Precambrian Research*, 80: 173-191.
- HOEFS, J., 1987. *Stable isotope geochemistry*. Springer-Verlag, Berlin, 241 p.
- HOLLAND, H.D., 1978. *The chemistry of the atmosphere and oceans*. Wiley, New York, 351 pp.
- HOLLIDAY, J., 2007. Gold helps Mali shine. *Mining Journal*, 26th October.
- HOLLIDAY, J., 2008. Golden Mali needs a boost. *Mining Journal*, 28th November.
- HOLLIDAY, J., 2009. West Africa: Mali has room for more. *Mining Journal*, 23rd October.
- HOLLISTER, L.S., 1988. On the origin of CO₂-rich fluid inclusions in migmatites. *Journal of Metamorphic Geology*, 6: 467-474.
- HOLLISTER, L.S., 1990. Enrichment of CO₂ in fluid inclusions in quartz by removal of H₂O during crystal-plastic deformation. *Journal of Geology*, 12: 895-901.
- HOLNESS, M.B., 1993. Temperature and pressure dependence of quartz-aqueous fluid dihedral angles: the control of adsorbed H₂O on the permeability of quartzites. *Earth and Planetary Science Letters*, 117: 363-377.
- HÖPPNER, M., 1994. The Eureka gold deposit in Northern Zimbabwe: an example of Archaean gold-quartz shear zone mineralisation derived from magmatic fluids. *Geologisches Jahrbuch*, 100: 391-421.

- HOUGH, R.M., BUTT, C.R.M. & BUHNER, J.F., 2009. The crystallography, metallography and composition of gold. *Elements*, 5: 297-302.
- HUNKEN, U., KLEMD, R. & OLESCH, M., 1994. Fluid inclusions in quartz pebbles of Proterozoic Tarkwaian conglomerates in Ghana. *Geologisches Jahrburg*, 100: 313-343.
- HUSTON, D.L., 1993. The effect of alteration and metamorphism on wall rocks to the Balcooma and Dry River South volcanic-hosted massive sulphide deposits, Queensland, Australia. *Journal of Geochemical Exploration*, 48: 277-307.
- IRVINE, T.N. & BARAGAR, W.R.A., 1971. A guide to the classification of the common volcanic rocks. *Canadian Journal of Earth Sciences*, 8: 523-549.
- JAMIESON, R.A., BEAUMONT, C., FULLSACK, P. & LEE, B., 1998. Barrovian regional metamorphism: where's the heat? *Geological Society Special Publications*, 138: 23-51.
- JEAN, G.E. & BANCROFT, G.M., 1985. An XPS and SEM study of gold deposition at low temperatures on sulphide mineral surfaces: concentration of gold by absorption/reduction. *Geochimica et Cosmochimica Acta*, 49: 979-987.
- JEBRAK, M., MINEAU, R., BARDOUX, M. & GOULET, N., 1990. Boron cycle in the Abitibi greenstone belt, and compositional variations in tourmaline associated with gold deposits. In: Robert, F., Sheahan, P.A. & Green, S.B. (Editors), *Greenstone gold and crustal evolution*. Geological Association of Canada, 177 pp.
- JEMIELITA, R.A., DAVIS, D.W. & KROGH, T.E., 1990. U-Pb evidence for Abitibi gold mineralisation postdating greenstone magmatism and metamorphism. *Nature*, 346: 831-834.
- JOHN, T., KLEMD, R., HIRDES, W. & LOH, G., 1999. The metamorphic evolution of the Palaeoproterozoic (Birimian) volcanic Ashanti belt (Ghana, West Africa). *Precambrian Research*, 98: 11-30.
- JULIANI, C., RYE, R.O., NUNES, C.M.D., SNEE, L.W., CORREA SILVA, R.H., MONTEIRO, L.V.S., BETTENCOURT, J.S., NEUMANN, R. & NETO, A.A., 2005. Palaeoproterozoic high-sulphidation mineralisation in the Tapajos gold province, Amazonian Craton, Brazil: geology, mineralogy, alunite argon age, and stable isotope constraints. *Chemical Geology*, 215: 95-125
- JUNNER, N.R., 1935. *Gold in the Gold Coast*. Ghanaian Geological Survey, Memoirs No 5, 67 pp.
- JUNNER, N.R., 1940. Geology of the Gold Coast and Western Togoland. *Gold Coast Geological Survey Bulletin*, 11: 1-40.
- KERRICH, R., 1983. Geochemistry of gold deposits in the Abitibi greenstone belt. *Canadian Institute Mining and Metallurgy Special Paper*, 27: 75p.
- KERRICH, R., 1987. *The stable isotope geochemistry of Au-Ag vein deposits in metamorphic rocks*. Mineralogical Association of Canada Short Course Handbook. pp. 287-336.
- KERRICH, R., 1989. Lithophile element systematics of gold vein deposits in Archaean greenstone belts: Implications for source processes. *Economic Geology Monograph*, 6: 508-519.
- KERRICH, R., 1990. Carbon isotope systematics of Archaean Au-Ag vein deposits in the Superior Province. *Canadian Journal of Earth Sciences*, 27: 40-56.
- KERRICH, R. & FRYER, B.J., 1979. Archaean precious metal hydrothermal systems, Dome Mine, Abitibi greenstone belt: II. REE and oxygen isotope relations. *Canadian Journal of Earth Sciences*, 16: 440-458.
- KERRICH, R. & FYFE, W.S., 1981. The gold-carbonate association: Source of CO₂ fixation reactions in Archaean lode gold deposits. *Chemical Geology*, 33: 265-294.

- KERRICH, R. & WYMAN, D., 1990. Geodynamic setting of mesothermal gold deposits: An association with accretionary tectonic regimes. *Geology*, 18: 882-885.
- KERRICH, R. & WYMAN, D., 1994. The mesothermal gold-lamprophyre association: significance for an accretionary geodynamic setting, supercontinent cycles, and metallogenic processes. *Mineralogy and Petrology*, 51: 147-172.
- KERRICH, R., GOLDFARB, R.J., GROVES, D.I. & GARWIN, S., 2000. The geodynamics of world class gold deposits: Characteristics, space-time distribution, and origins. *Reviews in Economic Geology*, 13: 501-551.
- KESLER, S.E. & WILKINSON, B.H., 2006. The role of exhumation in the temporal distribution of ore deposits. *Economic Geology*, 101: 919-922.
- KESSE, G.O., 1985. *The mineral and rock resources of Ghana*. Balkema, Rotterdam, 610 pp.
- KEY, R.M., LOUGHLIN, S.C., GILLESPIE, M., DEL RIO, M., HORSTWOOD, M.S.A., CROWLEY, Q.G., DARBYSHIRE, D.P.F., PITFIELD, P.E.J. & HENNEY, P.J., 2008. Two Mesoarchaeic terranes in the Reguibat shield of NW Mauritania. In: Ennih, N. & Liégeois, J.P. (Editors), *The Boundaries of the West African Craton*. Geological Society of London Special Publication No 297, pp. 33-52.
- KIRK, J., RUIZ, J., CHESLEY, J., TITLEY, S. & WALSHE, J., 2001. A detrital model for the origin of gold and sulphides in the Witwatersrand basin based on Re-Os isotopes. *Geochimica et Cosmochimica Acta*, 13: 2149-2159.
- KITSON, A.E., 1928. *Provisional geological map of the Gold Coast and western Togoland, with brief descriptive notes thereon*. Gold Coast Geological Survey Bulletin No 2, 13 pp.
- KLEIN, E.L. & MOURA, C.A.V., 2001. Age constraints on granitoids and metavolcanic rocks of the São Luis Craton and Gurupi Belt, northern Brazil: implications for lithostratigraphy and geological evolution. *International Geology Reviews*, 43: 237-253.
- KLEIN, E.L. & MOURA, C.A.V., 2008. São Luis Craton and Gurupi Belt (Brazil): possible links with the West African Craton and surrounding Pan-African belts. In: Pankhurst, R.J., Trouw, R.A.J., Brito Neves, B.B. & de Wit, M.J., (Editors), *West Gondwana: Pre-Cenozoic correlations across the South Atlantic region*. Geological Society London, Special Publications, pp. 137-151.
- KLEIN, E.L., MOURA, C.A.V. & PINHEIRO, B.L.S., 2005a. Palaeoproterozoic crustal evolution of the São Luis Craton, Brazil: evidence from zircon geochronology and Sm-Nd isotopes. *Gondwana Research*, 8: 177-186.
- KLEIN, E.L., MOURA, C.A.V., HARRIS, C. & GIRET, A., 2005b. Reconnaissance stable isotope (C, O, H, S) study of Palaeoproterozoic gold deposits of the São Luis Craton and country rocks, Northern Brazil: implications for gold metallogeny. *International Geology Reviews*, 47: 1131-1143.
- KLEIN, E.L., LUZARDO, R., MOURA, C.A.V., LOBATO, D.C., BRITO, R.S.C. & ARMSTRONG, R., 2009. Geochronology, Nd isotopes and reconnaissance geochemistry of volcanic and metavolcanic rocks of the São Luis Craton, northern Brazil: Implications for tectonic setting and crustal evolution. *Journal of South American Earth Sciences*, 27: 129-145.
- KLEMD, R., 1998. Comment on the paper by Schmidt Mumm *et al.* High CO₂ content of fluid inclusions in gold mineralisations in the Ashanti Belt, Ghana: a new category of ore forming fluids? (*Mineralium Deposita* 32: 107-118, 1997). *Mineralium Deposita*, 33: 317-319.
- KLEMD, R. & HIRDES, W., 1997. Origin of an unusual fluid composition in Early Proterozoic palaeoplacer and lode-gold deposits in Birimian greenstone terranes of West Africa. *South African Journal of Geology*, 100: 405-414.
- KLEMD, R. & OLESCH, M., 1991. Flüssigkeitseinschlüsse in goldführenden Meta-Konglomeraten des Tarkwaian von Ghana. *Berichte zur Lagerstätten und Rthstofforschung*, 5: 84 S.

- KLEMD, R. & OTT, S., 1997. Compositional characteristics of fluid inclusions as exploration tool for Au-mineralisation at Larafella, Burkina Faso. *Journal of Geochemical Exploration*, 59: 251-258.
- KLEMD, R., HIRDES, W., OLESCH, M. & OBERTHÜR, T., 1993. Fluid inclusions in quartz-pebbles of the gold-bearing Tarkwaian conglomerates of Ghana as guides to their provenance area. *Mineralium Deposita*, 28: 334-343.
- KLEMD, R., HUNKEN, U. & OLESCH, M., 1996. Fluid composition and source of early Proterozoic lode gold deposits of the Birimian volcanic belt, West Africa. *International Geology Reviews*, 38: 22-32.
- KLEMD, R., OBERTHÜR, T. & OUEDRAGO, A., 1997. Gold-telluride mineralisation in the Birimian at Diabatu, Burkina Faso. *Journal of African Earth Sciences*, 24: 227-239.
- KLEMD, R., HÜNKEN, U. & OLESCH, M., 2002. Metamorphism of the country rocks hosting gold-sulphide-bearing quartz veins in the Palaeoproterozoic southern Kibi-Winneba belt (SE-Ghana). *Journal of African Earth Sciences*, 35: 199-211.
- KODERA, P., 2000. *Mineralisation processes in the Central Zone of the Banska Striavnic stratovolcano (Slovakia) associated with a subvolcanic granodiorite pluton*. Ph.D Thesis, Kingston University, London, 340 pp.
- KOH, Y.K., CHOI, S.G., SO, C.S., CHOI, S.H. & UCHIDA, E., 2004. Application of arsenopyrite geothermometry and sphalerite geobarometry to the Taebaek Pb-Zn(-Ag) deposit at Yeonhwa I mine, Republic of Korea. *Mineralium Deposita*, 27: 58-65.
- KOONS, P.O. & CRAW, D., 1991. Gold mineralisation as a consequence of continental collision: an example from the Southern Alps, New Zealand. *Earth and Planetary Science Letters*, 103: 1-9.
- KONTAK, D.J., SMITH, P.M., KERRICH, R. & WILLIAMS, P.F., 1990. An integrated model for Meguma Group lode gold deposits, Nova Scotia, Canada. *Geology*, 18: 238-242.
- KOUAMELAN, A.N., DELOR, C. & PEUCAT, J., 1997. Geochronological evidence for reworking of Archean terrains during the Early Proterozoic (2.1 Ga) in the western Cote d'Ivoire (Man Rise-West African Craton). *Precambrian Research*, 86: 177-199.
- KOVAL, P.V., ZORINA, L.D., KITAJEV, N.A., SPIRIDONOV, A.M. & ARIUNBILEG, S., 1991. The use of tourmaline in geochemical prospecting for gold and copper mineralisation. *Journal of Geochemical Exploration*, 40: 349-360.
- KRANIDIOTIS, P. & MACLEAN, W.H., 1987. Systematics of chloride alteration at the Phelps Dodge massive sulphide deposit, Matagami, Quebec. *Economic Geology*, 82: 1898-1911.
- KRETSCHMAR, U. & SCOTT, S.D., 1976. Phase relations involving arsenopyrite in the system Fe-As-S and their application. *Canadian Mineralogy*, 14: 364-386.
- KŘÍBEK, B., SÝKOROVÁ, I., MACHOVIČ, V. & LAUFEK, F., 2008. Graphitisation of organic matter and fluid-deposited graphite in Palaeoproterozoic (Birimian) black shales of the Kaya-Goren greenstone belt (Burkina Faso, West Africa). *Journal of Metamorphic Geology*, 26: 937-958.
- KUSNIR, I., 1999. Gold in Mali. *Acta Montanistica Slovaca*, 4: 311-318.
- KUSNIR, I. & DIALLO, M., 1986. *Résultats des travaux de prospection*. Projet MLI/82/007. Unpublished report, UNDP/DNGM, Bamako, 159 pp.
- KWAK, T.A.P., BROWN, W.M., ABEYSINGHE, P.B. & TEONG, H.T., 1986. Fe solubilities in very saline hydrothermal fluids: their relation to zoning in some ore deposits. *Economic Geology*, 81: 447-465.
- LAHONDÈRE, D., THIÉBLEMONT, D., TEGYEV, M., GUERROT, C. & DIABATE, B., 2002. First evidence of early Birimian (2.21 Ga) volcanic activity in Upper Guinea: the volcanics and associated rocks of the Niani suite. *Journal of African Earth Sciences*, 35: 417-431.

- LANDIS, C.A., 1971. Graphitization of dispersed carbonaceous material in metamorphic rocks. *Contributions to Mineralogy and Petrology*, 30: 34-45.
- LANG, J.R. & BAKER, T., 2001. Intrusion-related gold systems: the present level of understanding. *Mineralium Deposita*, 36: 477-489.
- LAOUAR, R., BOYCE, A., FALLICK, A.E. & LEAKE, B.E., 1990. A sulphur isotope study on selected Caledonian granites of Britain and Ireland. *Geological Journal*, 25: 359-369.
- LEAHY, K., BARNICOAT, A.C., FOSTER, R.P., LAWRENCE, S.R. & NAPIER, R.W., 2005. Geodynamic processes that control the global distribution of giant gold deposits. *Geological Society of London Special Publications*, 248: 119-132.
- LEBLANC, M. & BILLAUD, P., 1982. Cobalt arsenide orebodies related to an upper Proterozoic ophiolite; Bou Azzer (Morocco). *Economic Geology*, 77: 162-175.
- LEBLANC, M. & SAUVAGE, J.F. 1986. Un gisement polymétallique en milieu volcano-sédimentaire du Protérozoïque supérieur, Tessalit (Ardrard des Iforas, Mali). *Journal of African Earth Sciences*, 15: 201-207.
- LEDRU, P., MILESI, J.P., VINCHON, C., ANKRAH, P.T., JOHAN, V. & MARCOUX, E., 1988. *Geology of the Birimian series of Ghana*. International conference and workshop on the geology of Ghana with special emphasis on gold; geology and exploration in Ghana and in selected other Precambrian Terrains, Ghana Geological Survey Department.
- LEDRU, P., JOHAN, V., MILÉSI, J.P. & TEGYEY, M., 1994. Markers of the last stages of the Palaeoproterozoic collision: evidence for a 2 Ga continent involving circum-South Atlantic provinces. *Precambrian Research*, 69: 169-191.
- LEMOINE, S., 1988. *Evolution géologique de la région de Dabakala (NE Côte d'Ivoire) au Protérozoïque inférieur*. Unpublished Ph.D. Thesis, University of Clermont-Ferrand, France, 338 pp.
- LEPAGE, N., 2007. *Mining in West Africa*. CIM Mining Conference & Exhibition, May 2007.
- LEROY, J., 1979. Contribution à l'étalonnage de la pression interne des inclusions fluides lors de leur décrépiation. *Bulletin de Mineralogie*, 102: 584-593.
- LEUBE, A. & HIRDES, W., 1986. *The Birimian Supergroup of Ghana- depositional environment, structural development and conceptual model of an early Proterozoic suite*. Federal Ministry for Economic Cooperation, Hanover, 259 pp.
- LEUBE, A., HIRDES, W., MAUER, R. & KESSE, G.O., 1990. The early Proterozoic Birimian Supergroup of Ghana and some aspects of its associated gold mineralisation. *Precambrian Research*, 46: 139-165.
- LIÉGEOIS, J.P., CLAESSENS, W., CAMARA, D. & KLERKX, J., 1991. Short-lived Eburnean orogeny in southern Mali. Geology, tectonics, U-Pb and Rb-Sr geochronology. *Precambrian Research*, 50: 111-136.
- LIHIR GOLD LTD, 2009. Bonikro site overview. Available at: <http://www.lgldgold.com/asp/index.asp?pgid=10858>. [Accessed 15 May 2010].
- LONDON, D., MORGAN, G.B. & WOLF, M.B., 1996. Boron in granitic rocks and their contact aureoles. In: Grew, E.S. & Anovitz, L.M. (Editors), *Reviews in Mineralogy, Boron: mineralogy, petrology and geochemistry*, Reviews in Mineralogy, Mineralogical Society of America, 33: 299-330.
- LOWENSTERN, J.B., 2001. Carbon dioxide in magmas and implications for hydrothermal systems. *Mineralium Deposita*, 36: 490-502.

- LOWRY, D., BOYCE, A.J., FALLICK, A.E., STEPHENS, W.E. & GRASSINEAU, N.V., 2005. Terrane and basement discrimination in northern Britain using sulphur isotopes and mineralogy of ore deposits. In: McDonald, I., Boyce, A.J., Butler, I.B., Herrington, R.J. & Polya, D.A. (Editors), *Mineral Deposits and Earth Evolution*. Geological Society Special Publications, 248: 133-151.
- LUBIS, H., PRIHATMOKO, S. & JAMES, L.P., 1994. Bulagidum prospect: a copper, gold and tourmaline bearing porphyry and breccia system in northern Sulawesi, Indonesia. *Journal of Geochemical Exploration*, 50: 257-278.
- LYNCH, G. & ORTEGA, J., 1997. Hydrothermal alteration and tourmaline-albite equilibria at the Coxheath porphyry Cu-Mo-Au deposit, Nova Scotia. *Canadian Mineralogist*, 35: 79-94.
- MANNING, D., 1982. Chemical and morphological variation in tourmalines from the Hub Kapong batholith of Peninsular Thailand. *Mineralogical Magazine*, 45: 139-147.
- MANU, J., 1993. *Gold deposits of Birimian Greenstone Belt in Ghana: hydrothermal alteration and thermodynamics*, Dissertation, Braunschweiger Geol.-Palaontol, Germany, 166 pp.
- MARCOUX, E. & MILESI, J.P., 1993. Lead isotope signature of Early Proterozoic ore deposits in Western Africa: comparisons with gold deposits in French Guiana. *Economic Geology*, 88: 1862-1879.
- MARSHIK, R. & FONTBOTE, L., 2001. The Candelaria-Punta del Cobre iron oxide Cu-Au(-Zn-Ag) deposits, Chile. *Economic geology*, 96: 1799-1826.
- MARTIN, H., 1987. Petrogenesis of Archaean trondhjemites, tonalites and granodiorites from eastern Finland: major and trace elements geochemistry. *Journal of Petrology*, 28: 921-953.
- MATSUHISA, Y. & AOKI, M., 1994. Temperature and oxygen isotope variations during vein formation of the Hishikari epithermal gold-silver veins, southern Kyushu, Japan. *Economic Geology*, 89: 1608-1613.
- MATSUHISA, Y., GOLDSMITH, J.R. & CLAYTON, R.N., 1979. Oxygen isotopic fractionation in the system quartz-albite-anorthite-water. *Geochimica et Cosmochimica Acta*, 43: 1131-1140.
- MATTHÄI, S.K. & HENLEY, R.W., 1996. Geochemistry and depositional environment of the gold-mineralized Proterozoic Koolpin Formation, Pine Creek Inlier, Northern Australia: a comparison with modern shale sequences. *Precambrian Research*, 78: 211-235.
- MCCUAIG, T.C. & KERRICH, R., 1998. P-T-t deformation-fluid-characteristics of lode gold deposits: Evidence from alteration systematics. *Ore Geology Reviews*, 12: 381-454.
- MCCUAIG, T.C., KERRICH, R., GROVES, D.I. & ARCHER, N., 1993. The nature and dimensions of regional and local gold-related hydrothermal alteration in tholeiitic metabasalts in the Norsman goldfields: The missing link in a crustal continuum of gold deposits. *Mineralium Deposita*, 28: 420-435.
- MCFARLANE, C., LENTZ, D. & MAVRONGENES, J., 2008. *Refining mineralisation models at Morila integrating regional and local geology, petrophysical properties, chemostratigraphy, geochronology, and geophysics*. Randgold Resources Ltd, 25 pp.
- MCKEAG, S.A., CRAW, D. & NORRIS, R.J., 1989. Origin and deposition of a graphitic schist-hosted metamorphogenic Au-W deposit, Marcaes, East Otago, New Zealand. *Mineralium Deposita*, 24: 124-131.
- MCLENNAN, S.M., HEMMING, S. & MCDANIEL, D.K.H., 1993. Geochemical approaches to sedimentation, provenance, and tectonics. In: Johnson, M.J. & Basu, A. (Editors), *Processes controlling the composition of clastic sediment*. Geological Society of America, Boulder, Colorado, pp. 21-40.
- MERNAGH, T.P. & WITT, W.K., 1994. Early, methane-rich fluids and their role in Archaean gold mineralisation at the Sand King and Missouri deposits, Eastern Goldfields Province, Western Australia. *Journal of Australian Geology & Geophysics*, 15: 297-312.

- MERREZ GOLD INC, 2009. West Mali- Gold. Available at: <http://www.merrexgold.com/Default.aspx?tabid=74>. [Accessed 15 May 2010].
- MICHEL, D. & GIULIANI, G., 1996. Habit and composition of gold grains in quartz veins from greenstone belts: Implications for mechanisms of precipitation of gold. *Canadian Mineralogist*, 34: 513-528.
- MIKUCKI, E.J., 1998. Hydrothermal transport and depositional processes in Archaean lode-gold systems: A review. *Ore Geology Reviews*, 13: 307-321.
- MILÉSI, J.P., LEDRU, P., DOMMANGET, A., JOHAN, V. & DIALLO, M., 1989a. Lower Proterozoic succession in Senegal and Mali (West Africa): position of sediment hosted Au and Fe deposits of the Loulo area and significance in terms of crustal evolution. 28th International Geology Congress, Washington, pp. 433-434.
- MILÉSI, J.P., FEYBESSE, J.L., LEDRU, P., DOMMANGET, A., OUEDRAGO, M., MARCOUX, E., PROST, A., VINCHON, C., SYLVAIN, J.P., JOHAN, V., TEGYEV, M., CALVEZ, J.Y. & LAGNY, P., 1989b. West African gold deposits in their Lower Proterozoic lithostructural setting. *Chronique de la Recherche Minière*, 497: 3-98.
- MILÉSI, J.P., LEDRU, P., FEYBESSE, J., DOMMANGET, A. & MARCOUX, E., 1992. Early Proterozoic ore deposits and tectonics of the Birimian orogenic belt, West Africa. *Precambrian Research*, 58: 305-344.
- MINERAL DEPOSITS LTD, 2009. Mineral Deposits Ltd Business Review 2009. Available at: http://www.mineraldeposits.com.au/publication/annual_reports. [Accessed 15 May 2010].
- MISHRA, B. & PANIGRAHI, M.K., 1999. Fluid evolution in the Kolar Gold Field: evidence from fluid inclusion studies. *Mineralium Deposita*, 34: 173-181.
- MOREY, A.A., WEINBERG, R.F. & BIERLEIN, F.P., 2007. The structural controls of gold mineralisation within the Bardoc Tectonic Zone, Eastern Goldfields Province, Western Australia: implications for gold endowment in shear systems. *Mineralium Deposita*, 42: 583-600.
- MOURA, C.A.V., ABREU, F.A.M., KLEIN, E.L., PALHETA, E.S.M. & PINHEIRO, B.L.S., 2003. Geochronology of the Sao Luis Craton and the Gurupi Belt, Brazil. *IV South American Symposium on Isotope Geology*. Salvador, Brazil Short Papers, pp. 225-228.
- MUCKE, A., 2005. The Nigerian manganese-rich iron formations and their host rocks- from sedimentation to metamorphism. *Journal of African Earth Sciences*, 41: 407-436.
- MUMIN, A.H. & FLEET, M.E., 1995. Evolution of gold mineralisation in the Ashanti Gold Belt, Ghana: evidence from carbonate compositions and paragenesis. *Mineralogy and Petrology*, 55: 265-280.
- MUMIN, A.H., FLEET, M.E. & LONGSTAFFE, F.J., 1996. Evolution of hydrothermal fluids in the Ashanti gold belt, Ghana: stable isotope geochemistry of carbonates, graphite and quartz. *Economic Geology*, 91: 135-148.
- NABA, S., LOMPO, M., DEBAT, P., BOUCHEZ, J.L. & BÉZIAT, D., 2004. Structure and emplacement model for late-orogenic Palaeoproterozoic granitoids: the Tenkodogo-Yamba elongate pluton (Eastern Burkina Faso). *Journal of African Earth Sciences*, 38: 41-57.
- NADEN, J. & SHEPHERD, T.J., 1989. Role of methane and carbon dioxide in gold deposition. *Nature*, 342: 793-795.
- NDIAYE, P.M., DIA, A., VIALETTE, Y., DIALLO, D.P., NGOM, P.M., SYLLA, M., WADE, S. & DIOH, E., 1997. Données pétrographiques, géochimiques et géochronologiques nouvelles sur les granitoïdes du Paléoprotérozoïque du Supergroupe de Dialé-Daléma (Sénégal Oriental): implications pétrogénétiques et géodynamiques. *Journal of African Earth Sciences*, 25: 193-208.
- NEALL, F.B. & PHILLIPS, G.N., 1987. Fluid-wall rock interaction in an Archaean hydrothermal gold deposit: a thermodynamic model for the Hunt Mine, Kambalda. *Economic Geology*, 82: 1679-1694.

- NÉDÉLIC, A., AFFATON, P., FRANC-LANFORD, C., CHARRIERE, A. & ALVARO, J., 2007. Sedimentology and chemostratigraphy of the Bwipe Neoproterozoic cap dolostones (Ghana, Volta Basin): a record of microbial activity in a petridal environment. *Comptes Rendus Geosciences*, 339: 223-239.
- NESBITT, B.F. & MUEHLENBACHS, K., 1991. Stable isotopic constraints on the nature of the syntectonic fluid regime of the Canadian Cordillera. *Geophysical Research Letters*, 18: 963-966.
- NESBITT, B.F., MUROWCHICK, J.B. & MUEHLENBACHS, K., 1986. Dual origins of lode gold deposits in the Canadian Cordillera. *Geology*, 14: 506-509.
- NESBITT, B.F., MUEHLENBACHS, K. & MUROWCHICK, J.B., 1989. Genetic implications of stable isotopes characteristics of mesothermal Au deposits and related Sb and Hg deposits in the Canadian Cordillera. *Economic Geology*, 84: 1489-1506.
- NESBITT, H.W. & YOUNG, G.M., 1982. Early Proterozoic climates and plate motions inferred from major element chemistry of lutites. *Nature*, 279: 715-717.
- NEUMAYR, P., CABRI, L.J., GROVES, D.I., MIKUCKI, E.J. & JACKMAN, J.A., 1993a. The mineralogical distribution of gold and relative timing of gold mineralisation in two Archaean settings of high metamorphic grade in Australia. *Canadian Mineralogist*, 31: 711-725.
- NEYBERGH, H., LADURON, D., MARTIN, H. & VERKAEREN, J., 1980. The vanadiferous-magnetite deposits of the Oursi region, Upper-Volta. *Economic Geology*, 75: 1042-1052.
- NEWMONT MINING CORP, 2009. Newmont 2009 annual report. Available at: <http://www.newmont.com/our-investors>. [Accessed 2 August 2010].
- NOMADE, J., CHEN, Y., FERAUD, G., POUCKET, A. & THEVENIAUT, H., 2001. First paleomagnetic and $^{40}\text{Ar}/^{39}\text{Ar}$ study of Palaeoproterozoic rocks from the French Guayana (Camopi and Oypok rivers), northeastern Guyana Shield. *Precambrian Research*, 109: 230-256.
- NUTT, C.J. & HOFSTRA, A.H., 2007. Bald Mountain gold mining district, Nevada: a Jurassic Reduced Intrusion Related Gold System. *Economic Geology*, 102: 1129-1155.
- NYAME, F.K., 2008. Petrography and geochemistry of intraclastic manganese-carbonates from the ~2.2 Ga Nstua deposit of Ghana: significance for manganese sedimentation in the Palaeoproterozoic of West Africa. *Journal of African Earth Sciences*, 50: 133-147.
- OBERTHÜR, T., VETTER, U., SCHMIDT MUMM, A., WEISER, T., AMANOR, J.A., GYAPONG, W.A., KUMI, R. & BLECKINSOP, T.G., 1994. The Ashanti gold mine at Obuasi in Ghana. *Geologische Jahrbuch*, 100: 31-131.
- OBERTHÜR, T., SCHMIDT MUMM, A., VETTER, U., SIMON, K. & AMANOR, J.A., 1996. Gold mineralisation in the Ashanti Belt of Ghana: genetic constraints of the stable isotope geochemistry. *Economic Geology*, 91: 289-301.
- OBERTHÜR, T., VETTER, U., DAVIS, D.W. & AMANOR, J.A., 1998. Age constraints on gold mineralisation and Palaeoproterozoic crustal evolution in the Ashanti belt of southern Ghana. *Precambrian Research*, 89: 129-143.
- OBERTHÜR, T., BLENKINSOP, T.G., HEIN, U.F., HOPNER, M., HOHNDORF, A. & WEISER, T.W., 2000. Gold mineralization in the Mazowe area, Harare-Bindura-Shamva greenstone belt, Zimbabwe: II. Genetic relationships deduced from mineralogical, fluid inclusion and stable isotope studies, and the Sm-Nd isotopic composition of scheelites. *Mineralium Deposita*, 35: 138-156.
- OHMOTO, H., 1986. Stable isotope geochemistry of ore deposits. In: Valley, J.E., Taylor, H.P. & O'Neil, J.R. (Editors), *Stable isotopes in high temperature geological processes*. Mineralogical Society of America Reviews in Mineralogy, 16: 491-560.

- OHMOTO, H. & GOLDBERGER, M.B., 1997. Sulphur and carbon isotopes. In: Barnes, H.I. (Editor), *Geochemistry of hydrothermal ore deposits*. 3rd Edition. John Wiley & Sons, New York, pp. 517-612.
- OHMOTO, H. & RYE, R.O., 1979. Isotopes of sulphur and carbon. In: Barnes, H.I. (Editor), *Geochemistry of hydrothermal ore deposits*. 2nd Edition, John Wiley & Sons, New York, pp. 509-567.
- OLSON, S.F., 2000. The Proterozoic evolution of Africa. *Economic Geology Research Unit Information Circular*, 343: 1-61.
- OLSON, S.F., DIAKITE, K., OTT, L., GUINDO, A., FORD, C.R.B., WINER, N., HANSEN, E., LAY, N., BRADLEY, R. & POHL, D., 1992. Regional setting, structure, and descriptive geology of the Middle Proterozoic Syama gold deposit, Mali, West Africa. *Economic Geology*, 87: 310-331.
- ONSTOTT, T.C. & HARGRAVES, R.B., 1981. Proterozoic transcurrent tectonics: palaeomagnetic evidence from Venezuela and Africa. *Nature*, 289: 131-136.
- PALMER, M.R., 1991. Boron isotope systematics of hydrothermal fluids and tourmalines: A synthesis. *Isotope Geoscience*, 14, 111-121.
- PAN, Y. & FLEET, M.E., 1995. The late Archaean Helmo gold deposit, Ontario, Canada: a review and synthesis. *Ore Geology Reviews*, 9: 455-488.
- PAPON, A., 1973. *Géologie et Minéralisations du Sud-Ouest de la Côte d'Ivoire*. Bureau de Recherches Géologique et Minières Mémoires No 80, 284pp.
- PATRICK, R.A.D., BOYCE, A. & MACINTYRE, R.M., 1988. Gold and silver mineralisation at Tyndrum, Scotland. *Mineralogy and Petrology*, 38: 61-76.
- PAWLIG, S., GUEYE, M., KLISCHES, R., SCHWARZ, S., WEMMER, K. & SIEGESMUND, S., 2006. Geochemical and Sr-Nd isotopic data on the Birimian of the Kédougou-Kéniéba Inlier (Eastern Senegal): Implications on the Palaeoproterozoic evolution of the West African Craton. *South African Journal of Geology*, 109: 411-427.
- PEARCE, J.A., 1983. Role of the sub-continental lithosphere in magma genesis at active continental margins. In: Hawkesworth, C.J. & Norry, M.J. (Editors), *Continental basalts and mantle xenoliths* Shiva, Nantwich, pp. 230-249.
- PEARCE, J.A., HARRIS, N.B. & TINDLE, A.G., 1984. Trace element discrimination diagrams for the tectonic interpretation of granitic rocks. *Journal of Petrology*, 25: 956-983.
- PEARSON, R.G., 1963. Hard and soft acids and bases. *Journal of the American Chemical Society*, 85: 3533-3539.
- PETERSEN, E.U. & FITZMAYER, J.R., 1998. The alunite-sericite association: a new type of epithermal precious metal deposits. *Geological Society of America Program and Abstracts*, 30: A127.
- PETTKE, T., DIAMOND, L.W. & KRAMERS, J.D., 2000. Mesothermal gold lodes in the north-western Alps: A review of genetic constraints from radiogenic isotopes. *European Journal of Mineralogy*, 12: 213-230.
- PHILLIPS, G.N., GROVES, D.I. & KERRICH, R., 1996. Factors in the formation of the giant Kalgoorlie gold deposit. *Ore Geology Reviews*, 10: 295-317.
- PIGOIS, J.P., GROVES, D.I., FLETCHER, I.R., MCNAUGHTON, N.J. & SNEE, L.W., 2003. Age constraints on Tarkwaian palaeoplacer and lode-gold formation in the Tarkwa-Damang district, SW Ghana. *Mineralium Deposita*, 38: 695-714.
- PITCAIRN, I.K., TEAGLE, D.A., CRAW, G.R., OLIVO, G.R., KERRICH, R. & BREWER, T.S., 2006. Sources of metals and fluids in orogenic gold deposits: Insights from the Otago and Alpine Schists, New Zealand. *Economic Geology*, 101: 1525-1546.

- PLIMER, I.R., 1986. Tourmalinites from the Golden Dyke dome, northern Australia. *Mineralium Deposita*, 21: 263-270.
- PONS, J., OUDIN, O.C. & VALERO, J., 1992. Kinematics of large syn-orogenic intrusions: example of the Lower Proterozoic Saraya batholith (Eastern Senegal). *Geologische Rundschau*, 81: 473-486.
- POTREL, A., PEUCAT, J.J., FANNING, C.M., AUVRAY, B., BURG, J.J. & CARUBA, C., 1996. 3.5 Ga old terranes in the West African Craton, Mauritania. *Journal of the Geological Society of London*, 153: 507-510.
- POUCLET, A., VIDAL, M., DELOR, C., SIMEON, Y. & ALRIC, G., 1996. Le volcanisme Birimien du nord-est la Côte-d'Ivoire, mise en évidence de deux phases volcano-tectoniques distinctes dans l'évolution géodynamique du Paléoprotérozoïque. *Bulletin de la Societe Geologique de France*, 167: 529-541.
- POUCLET, A., ALLIALY, M., DAOUDA-YAO, B. & ESSO, B., 2004. Discovery of a diamond-bearing kimberlite diatreme at Séguéla in Ivory Coast. *Comptes Rendus Geosciences*, 336: 9-17.
- POUCLET, A., DOUMBIA, S. & VIAL, D.S., 2006. Geodynamic setting of the Birimian volcanism in central Ivory Coast (western Africa) and its place in the Palaeoproterozoic evolution of the Man Shield. *Bulletin Societe Geologique de France*, 177: 105-121.
- POUDJOM-DJOMANI, Y., O'REILLY, S., GRIFFIN, W.L. & MORGAN, P., 2001. The density structure of subcontinental lithosphere through time. *Earth and Planetary Science Letters*, 184: 605-621.
- POWELL, R., WILL, T.M. & PHILLIPS, G.N., 1991. Metamorphism in Archaean greenstone belts: calculated fluid compositions and implications for gold mineralisation. *Journal of Metamorphic Geology*, 9: 141-150.
- PRIESTLEY, K., MCKENZIE, D., DEBAYLE, E. & PILIDOU, S., 2008. The African upper mantle and its relationship to tectonics and surface geology. *Geophysical Journal International*, 175: 1108-1126.
- QUICK, R., 1999. *The Morila gold deposit, Southern Mali, West Africa*. Ph.D. Thesis, Leicester University.
- RAMBOZ, C., PICHAVANT, M. & WEISBROD, A., 1982. Fluid immiscibility in natural processes: use and misuse of fluid inclusion data. II. Interpretation of fluid inclusion data in terms of immiscibility. *Chemical Geology*, 37: 29-48.
- RANGOLD RESOURCES LTD, 2009. Annual resource and reserve declaration. Available at: <http://www.randgoldresources.com/randgold/view/randgold/en/page6107>. [Accessed 15 May 2010].
- RANKIN, A.H., RAMSEY, M.H., COLES, B., VAN LANGEVELDE, F. & THOMAS, C.R., 1992. The composition of hypersaline, iron-rich granitic fluids based on laser-ICP and Synchrotron-XRF microprobe analysis of individual fluid inclusions in topaz, Mole granite, eastern Australia. *Geochimica et Cosmochimica Acta*, 56: 67-79.
- REDBACK MINING INC, 2009. Chirano mineral reserves and resources. Available at: <http://www.redbackmining.com/s/Chirano.asp?ReportID=142514>. [Accessed 15 May 2010].
- RESOLUTE MINING LTD, 2009. Operations overview- Syama. Available at: http://www.resolute-ltd.com.au/operations_overview_syama.html. [Accessed 15 May 2010].
- REYNER, A. & SCHUBERT, G., 1984. Phanerozoic addition rates to the continental crust and crustal growth. *Tectonics*, 3: 63-77.
- RIDLEY, J.R. & DIAMOND, L.W., 2000. Fluid chemistry of orogenic lode gold deposits and implications for genetic models. *Reviews in Economic Geology*, 13: 141-162.
- ROBB, L.J., 2005. *Introduction to ore-forming processes*. Blackwell Publishing, USA, 373 pp.

- ROBERT, F. & KELLY, W.C., 1987. Ore-forming fluids in Archaean gold-bearing quartz veins at the Sigma Mine, Abitibi greenstone belt, Quebec, Canada. *Economic Geology*, 82: 1464-1482.
- ROBINSON, B.W. & KUSAKABE, M., 1975. Quantitative preparation of SiO₂ for ³⁴S/³²S analysis from sulphides by combustion with cuprous oxide. *Analytical Chemistry*, 47: 1179-1181.
- ROCK, N.M.S. & GROVES, D.I., 1988. Do lamprophyres carry gold as well as diamonds? *Nature*, 332: 253-255.
- ROCK, N.M.S., GROVES, D.I. & PERRING, C.S., 1989. Gold, Lamprophyres, and Porphyries: What does their association mean? *Geology Monograph*, 6: 609-625.
- ROEDDER, E., 1984. *Fluid inclusions*. Reviews in Mineralogy, Mineralogical Society of America, 12: 646 pp.
- ROEDDER, E. & BODNAR, R.J., 1980. Geologic pressure determinations from fluid inclusion studies. *American Reviews of Earth & Planetary Science*, 8: 263-301.
- ROCCI, G., BRONNER, G. & DESCHAMPS, M., 1991. Crystalline basement of the West African Craton. In: Dallmeyer, R.D. & Lecorche, J.P. (Editors), *The West African Orogens and circum-Atlantic correlatives*. Springer-Verlag, Berlin, pp. 31-64.
- RODDAZ, M., DEBAT, P. & NIKIÉMA, S., 2007. Geochemistry of Upper Birimian sediments (major and trace elements and Nd-Sr isotopes) and implications for weathering and tectonic setting of the Late Palaeoproterozoic crust. *Precambrian Research*, 159: 197-211.
- ROLLINSON, H., 1993. *Using geochemical data: evaluation, presentation, interpretation*. Longman Group Ltd, England, 352 pp.
- ROMBACH, C.S. & NEWBERRY, R.J., 2001. Genesis and mineralisation of the Shotgun deposit, southwest Alaska. *Mineralium Deposita*, 36: 607-621.
- ROSASCO, G.J. & ROEDDER, E., 1975. Laser excited Raman spectroscopy. *Science*, 190: 557-560.
- ROSASCO, G.J. & ROEDDER, E., 1979. Application of a new Raman microprobe spectrometer to non-destructive analysis of sulphate and other ions in individual phases in fluid inclusions in minerals. *Geochimica et Cosmochimica Acta*, 43: 1907-1915.
- RYE, D.M. & OHMOTO, H., 1974. Sulphur and carbon isotopes and ore genesis: a review. *Economic Geology*, 69: 826-842.
- RYE, D.M. & RYE, R.O., 1974. Homestake gold mine, South Dakota: I. Stable isotope studies. *Economic Geology*, 69: 293-317.
- SAMSON, I., ANDERSON, A. & MARSHALL, D., 2003. *Fluid Inclusions: Interpretation and Analysis*. Mineralogical Association of Canada. Short Course Series Volume 32, Vancouver, British Columbia, 374 pp.
- SANOOGO, A.D. & PROST, A.E., 1993. Evolution synchrone des déformations et des minéralisation dans le filon aurifère de Poura (province de Mohoun, Burkina Faso). *Pangea*, 20: 23-29.
- SANSGETER, A.L., 1992. Light stable isotope evidence for a metamorphogenic orogen for bedding-parallel, gold-bearing veins in Cambrian flysch, Meguma Group, Nova Scotia. *Exploration and Mining Geology*, 1: 69-79.
- SCHIDLOWSKI, M., HAYES, J.M. & KAPLAN, I.R., 1983. Isotopic inferences of ancient biochemistries: carbon, sulphur, hydrogen and nitrogen. In: Schopf, J.W. (Editor), *Earth's earliest biosphere: it's origin and evolution*. Princeton University Press, New York, pp. 149-186.
- SCHMIDT MUMM, A., OBERTHÜR, T. & VETTER, U., 1997. High CO₂ content of fluid inclusions in gold mineralisations in the Ashanti Belt, Ghana: a new category of ore forming fluids. *Mineralium Deposita*, 32: 107-118.

- SCHMIDT MUMM, A., OBERTHÜR, T., VETTER, U. & BLENKINSOP, T.G., 1998. High CO₂ content of fluid inclusions in gold mineralisations in the Ashanti belt, Ghana: a new category of ore forming fluid- a reply. *Mineralium Deposita*, 33: 320-322.
- SCHWARTZ, M.O. & MELCHER, F., 2003. The Perkoa Zinc deposit, Burkina Faso. *Economic Geology*, 98: 1463-1485
- SCHWARTZ, M.O. & MELCHER, F., 2004. The Falémé Iron District, Senegal. *Economic Geology*, 99: 917-939.
- SCHWARTZ, M.O., OBERTHÜR, T., AMANOR, J. & GYAPONG, E.A., 1992. Fluid inclusion re-equilibration and P-T-x constraints on fluid evolution in the Ashanti gold deposit, Ghana. *European Journal of Mineralogy*, 4: 1017-1034.
- SEAL, R.R., 2006. Sulphur isotope geochemistry of sulphide minerals. *Reviews in Mineralogy and Geochemistry*, 61: 633-677.
- SESTINI, G., 1973. Sedimentology of a paleoplacer: the gold-bearing Tarkwaian of Ghana. In: Amstutz, G.C. & Bernard, A.J. (Editors), *Ores in Sediments*. Springer, Berlin, pp. 275-306.
- SEWARD, T.M., 1973. Thio complexes of gold in hydrothermal ore solutions. *Geochimica et Cosmochimica Acta*, 37: 379-399.
- SHACKLETON, R.M., 1986. Precambrian collision tectonics in Africa. In: Coward, M.P. & Ries A.C. (Editors), *Collision tectonics*. Geological Society America Special Publication No 19, pp. 329-349.
- SHARP, Z.D., 1990. A laser-based microanalytical method for the in situ determination of oxygen isotope ratios in silicates and oxides. *Geochimica et Cosmochimica Acta*, 54: 1353-1357.
- SHARP, Z.D., ESSENE, E.J. & KELLY, W.C., 1985. A re-examination of the arsenopyrite geothermometer: pressure consideration and applications to natural assemblages. *Canadian Mineralogy*, 23: 517-534.
- SHEPPARD, S.M.F., 1986. Characterisation and isotopic variations in natural waters. In: Valley, J.W., Taylor, H.P. & O'Neil, J.R. (Editors), *Stable isotopes in high temperature geological processes*. Mineralogical Society of America Reviews in Mineralogy, 16: 165-183.
- SHEPHERD, T.J., RANKIN, A.H. & ALDERTON, D.H.M., 1985. *A practical guide to fluid inclusion studies*. Blackie, Glasgow, 239 pp.
- SIBSON, R.H., 1987. Earthquake rupturing as mineralising agent in hydrothermal systems. *Geology*, 15: 701-704.
- SIBSON, R.H., 2001. Seismogenic framework for hydrothermal transport and ore deposition. *Society of Economic Geology Reviews*, 14: 25-50.
- SIBSON, R.H., ROBERT, F. & POULSEN, K.H., 1988. High angle reverse faults fluid pressure cycling and mesothermal gold-quartz deposits. *Geology*, 16: 551-555.
- SIGNATURE METALS LTD, 2010. Konongo Gold Project. Available at: <http://www.signaturemetals.com.au>. [Accessed 2 August 2010].
- SIVA SIDDAIAH, N. & RAJAMANI, V., 1989. The geologic setting, mineralogy, geochemistry, and genesis of gold deposits of the Archaean Kolar schist belt, India. *Economic Geology*, 84: 2155-2172.
- SLACK, J.F., 1996. Tourmaline association with hydrothermal ore deposits. In: Grew, E.S. & Anovitz, L.M. (Editors), *Boron: mineralogy, petrology and geochemistry*. Reviews in Mineralogy, Mineralogical Society of America, 33: 559-643.

- SMITH, M.P. & YARDLEY, B.W.D., 1996. The boron isotopic composition of tourmaline as a guide to fluid processes in the southwestern England ore field: An ion microprobe study. *Geochimica et Cosmochimica Acta*, 60: 1415-1427.
- SPOONER, E.T.C., 1991b. The magmatic model for the origin of Archaean Au-quartz vein ore systems; an assessment of the evidence. In: Ladeira, E.A. (Editor), *Brazil Gold '91*. Balkema, Rotterdam, pp. 279-286.
- SPOONER, E.T.C., 1993. Magmatic sulphide/volatile interaction as a mechanism for producing chalcophile element enriched, Archaean Au-quartz, epithermal Au-Ag and Au skarn hydrothermal ore fluids. *Ore Geology Reviews*, 7: 359-379.
- STARLING, A., GILLIGAN, J.M., CARTER, A.H.C., FOSTER, R.P. & SANDERS, R.A., 1989. High-temperature hydrothermal precipitation of precious metals on the surface of pyrite. *Nature*, 340: 298-300.
- STEFANSSON, A. & SEWARD, T.M., 2004. Gold(I) complexing in aqueous sulphide solutions to 500 °C at 500 bar. *Geochimica et Cosmochimica Acta*, 68: 4121-4143.
- STENGER, D.P., KESLER, S.E. & VENNEMANN, T., 1998. Carbon and oxygen isotope zoning around Carlin-type gold deposits: a reconnaissance survey at Twin Creeks, Nevada. *Journal of Geochemical Exploration*, 63: 105-121.
- STRAUSS, H., 1997. The isotopic composition of sedimentary sulphur through time. *Palaeoceanography, Palaeoclimatology, Palaeoecology*, 132: 97-118.
- STROGEN, P., 1988. *The sedimentology, stratigraphy and structure of the Tarkwaian, Western Region, and its relevance to gold exploration and development*. International Conference for Geology of Ghana with Special Emphasis on Gold, Accra, pp. R/1-R/39.
- STÜWE, K., 1998. Tectonic constraints on the timing relationships of metamorphism, fluid production and gold-bearing quartz vein emplacement. *Ore Geology Reviews*, 13: 219-228.
- STÜWE, K., WILL, T.M. & ZHOU, S., 1993. On the timing relationship between fluid production and metamorphism in metamorphic piles: some implications for the origin of post-metamorphic gold mineralisation. *Earth and Planetary Science Letters*, 114: 417-430.
- SUN, S.S. & MCDONOUGH, W.F., 1989. Chemical and isotopic systematics of oceanic basalts: implications for mantle composition and processes. In: Saunders, A.D. & Norry, M.J. (Editors), *Magmatism in ocean basins*. Geological Society of London Special Publications, pp. 313-345.
- SWANENBURG, H.F.C., 1980. *Fluid inclusions in high-grade metamorphic rocks from SW Norway*. Ph.D. Thesis edn. University of Utrecht, The Netherlands.
- SYLVESTER, P.J. & ATTOH, K., 1992. Lithostratigraphy and composition of 2.1 Ga greenstone belts of the West African Craton and their bearing on crustal evolution and the Archean-Proterozoic boundary. *Journal of Geology*, 100: 377-393.
- TAYLOR, H.P., 1997. Oxygen and hydrogen isotope relationships in hydrothermal mineral deposits. In: Barnes, H.I. (Editor), *Geochemistry of hydrothermal ore deposits*. 3rd Edition, John Wiley & Sons, New York, pp. 229-302.
- TAYLOR, S.R. & MCLENNAN, S.M., 1985. *The continental crust: its composition and evolution*. Blackwell Scientific Publications, London.
- TAYLOR, P.N., MOORBATH, S., LEUBE, A. & HIRDES, W., 1992. Early Proterozoic crustal evolution in the Birimian of Ghana: constraints from geochronology and isotope geochemistry. *Precambrian Research*, 56: 97-111.
- TEJADA, M.L.G., MAHONEY, J.J., DUNCAN, R.A. & HAWKINS, M.P., 1996. Age and geochemistry of basement and alcaic rocks of Malaita and Santa Isabel, Solomon Islands, southern margin of the Ontang-Java plateau. *Journal of Petrology*, 37: 361-394.

- TEIXCIRA, J.B.G., KISHIDA, A., MARIMON, M.P.C., XAVIER, R.P. & MCREATH, I., 1990. The Fazenda Brasileiro gold deposit: geology, Hydrothermal alteration, and fluid inclusion studies. *Economic Geology*, 85: 990-1009.
- THIÉBLEMONT, D., DELOR, C., COCHERIE, A., LAFON, J.M., GOUJOU, J.C., BALDÉ, A., BAH, M., SANÉ, H. & MARK FANNING, C., 2001. A 3.5 Ga granite–gneiss basement in Guinea: further evidence for early Archean accretion within the West African Craton. *Precambrian Research*, 108: 179-194.
- TOURET, J.L.R., 2001. Fluids in metamorphic rocks. *Lithos*, 55: 1-25.
- TOURET, J.L.R. & DIETVORST, P., 1983. Fluid inclusions in high-grade anatectic metamorphites. *Journal of Geological Society London*, 140: 635-649.
- TRUSCOTT, M.G., SHAW, D.M. & CRAMER, J.J., 1986. Boron abundance and localisation in granulites and the lower continental crust. *Bulletin of Geological Survey Finland*, 58: 169-177.
- TUNKS, A.J., SELLEY, D., ROGERS, J.R. & BRABHAM, G., 2004. Vein mineralisation at the Damang Gold Mine, Ghana: controls on mineralisation. *Journal of Structural Geology*, 26: 1257-1273.
- TURNER, R.J.W., 1992. Formation of Phanerozoic stratiform sediment-hosted zinc-lead deposits: Evidence for the critical role for ocean anoxia. *Chemical Geology*, 99: 165-188.
- ULRICH, T., GUNTHER, D. & HEINRICH, C.A., 1999. Gold concentrations of magmatic brines and the metal budget of porphyry copper deposits. *Nature*, 399: 676-679.
- U.S. CENTRAL INTELLIGENCE AGENCY, 2010. The World Factbook- Mali. Available at: <https://www.cia.gov/library/publications/the-world-factbook/geos/ml.html>. [Accessed 2 August 2010].
- VALLANCE, J., CATHELINÉAU, M., BOIROM, M.C., FOURCADE, S., SHEPHERD, T.J. & NADEN, J., 2003. Fluid-rock interactions and the role of late Hercynian aplite intrusion in the genesis of the Castromil gold deposit, northern Portugal. *Chemical Geology*, 194: 201-224.
- VALLANCE, J., BOIROM, M., CATHELINÉAU, M., FOURCADE, S., VARLET, M. & MARIGNAC, C., 2004. The granite hosted deposit of Moulin de Cheni (Saint-Yrieix district, Massif Central, France): petrographic, structural, fluid inclusion and oxygen isotope constraints. *Mineralium Deposita*, 39: 265-281.
- VAN DEN KERKHOFF, A., 2008. *Fluid Inclusions*. ISES course, Netherlands Research School of Sedimentary Geology, 43 pp.
- VAN DEN KERKHOFF, A. & HEIN, U.F., 2001. Fluid inclusion petrography. In: Anderson, T., Frezzotti, M.L. & Burke, E.A.J. (Editors), *Fluid inclusions: phase relationship- methods-applications*. *Lithos (special issue)*, 320 pp.
- VAN REENEN, D.D., PRETORIUS, A.I. & ROERING, C., 1994. Characterisation of fluids associated with gold mineralisation and with regional high-temperature retrogression of granulites in the Limpopo belt, South Africa. *Geochimica et Cosmochimica Acta*, 58: 1147-1159.
- VELTON, R., 2009. Mali- Bradt Travel Guide. 3rd Edition, Bradt Travel Guides, 320 pp.
- VIDAL, M. & ALRIC, G., 1994. The Palaeoproterozoic (Birimian) of Haute-Comoé in the West African Craton, Ivory Coast: a transtensional back-arc basin. *Precambrian Research*, 65: 207-229.
- VIELREICHER, N.M., 2006. *Reconnaissance SHRIMP xenotime and monazite geochronology on mineralised samples from Loulo 0 (LOCP22/106.4-106.5) gold deposit, Kédougou-Kéniéba Inlier, western Mali*. Randgold Resources Ltd, Internal Report, 13 pp.

- VILLENEUVE, M., 2008. Review of the orogenic belts on the western side of the West African craton: the Bassarides, Rokelides and Mauritanides. In: Ennih, N. & Liégeois, J.P. (Editors), *The Boundaries of the West African Craton*. Geological Society of London Special Publication No 297, pp. 169-201.
- VILLENEUVE, M. & CORNÉE, J.J., 1994. Structure, evolution and paleoceanography of the West African Craton and bordering belts during the Neoproterozoic. *Precambrian Research*, 69: 307-326.
- WALTHER, J.V. & ORVILLE, P.M., 1983. The extraction-quench technique for determination of the thermodynamic properties of solute complexes: application to quartz solubility in fluid mixtures. *American Mineralogist*, 68: 731-741.
- WATSON, E.B. & BRENNAN, J.M., 1987. Fluids in the lithosphere. 1. Experimentally-determined wetting characteristics of CO₂-H₂O fluids and their implications for fluid transport, host-rock physical properties, and fluid inclusion formation. *Earth and Planetary Science Letters*, 85: 497-515.
- WHITE, R.V., TARNEY, J., KERR, A.C., SAUNDERS, A.D., KEMPTON, P.D., PRINGLE, M.S. & KLAVER, G.T., 1999. Modification of an oceanic plateau, Arubu, Dutch Caribbean: implications for the generation of continental crust. *Lithos*, 46: 43-68.
- WHITNEY, J.A., HEMLEY, J.J. & SIMON, F.O., 1985. The concentration of iron in chloride solutions equilibrated with synthetic granitic compositions: the sulfur-free system. *Economic Geology*, 80: 444-460.
- WILKINSON, J.J., BOYCE, A.J., EARLS, G. & FALLICK, A.E., 1999. Gold remobilization by low-temperature brines: Evidence from the Curraghinalt gold deposit, Northern Ireland. *Economic Geology*, 94: 289-296.
- WILLIAMS-JONES, A.E., BOWELL, R.J. & MIGDISOV, A.A., 2009. Gold in solution. *Elements*, 5: 281-287.
- WILLIE, S.E. & KLEMD, R., 2004. Fluid inclusion studies of the Abawso gold prospect, near the Ashanti Belt, Ghana. *Mineralium Deposita*, 39: 31-45.
- WILSON, M., 1989. *Igneous petrogenesis: a global tectonic approach*. Unwin Hyman, London, 461 pp.
- WOOD, S.A. & SAMSON, I.M., 1998. Solubility of ore minerals and minerals and complexation of ore metals in hydrothermal systems. *Reviews in Economic Geology*, 10: 33-80.
- XAVIER, R.P. & FOSTER, R.P., 1999. Fluid evolution and chemical controls in the Fazenda Maria Preta (FMP) gold deposit, Rio Itapicuru Greenstone Belt, Bahia, Brazil. *Chemical Geology*, 154: 133-154.
- YAO, Y. & ROBB, L.J., 1999. *Gold mineralisation associated with the Birimian granitoids of Ghana*. Johannesburg, University of Witwatersrand, final report to Gold Fields of South Africa.
- YAO, Y. & ROBB, L.J., 2000. Gold mineralisation in Palaeoproterozoic granitoids at Obusai, Ashanti region, Ghana: ore geology, geochemistry and fluid characteristics. *South African Journal of Geology*, 103: 255-278.
- YAO, B.D., DELOR, C., SIMÉON, Y., DIABY, I., GADOU, G., KOHOU, P., OKOU, A., KONATE, S., KONAN, G., VIDAL, M., COCHERIE, A., DOMMANGET, A., CAUTRU, J.P. & CHIRON, J.C., 1995. *Carte géologique de la Côte d'Ivoire à 1/200 000; feuille No. 6, Dimbokro*, Abidjan, Cote d'Ivoire.
- YAO, Y., MURPHY, P.J. & ROBB, L.J., 2001. Fluid characteristics of granitoid-hosted gold deposits in the Birimian terrane of Ghana: A fluid inclusion microthermometric and Raman spectroscopic study. *Economic geology*, 96: 1611-1643.
- YAVUZ, F., YAVUZ, V. & SASMAZ, A., 2006. WinClastour- a Visual Basic program for tourmaline formula calculation and classification. *Computers & Geosciences*, 32: 1156-1168.

- ZHANG, Y.G. & FRANTZ, J.D., 1987. Determination of homogenisation temperatures and densities of supercritical fluids in the system NaCl-KCl-CaCl₂-H₂O using synthetic fluid inclusions. *Chemical Geology*, 64: 335-350.
- ZHANG, Y., MUCHEZ, P. & HEIN, U.F., 1997. Chlorite geothermometry and the temperature conditions at the Variscan thrust front in eastern Belgium. *Geologie en Mijnbouw*, 76: 267-270.
- ZHENG, Y.F., 1993a. Calculation of oxygen isotope fractionation in anhydrous silicate minerals. *Geochimica et Cosmochimica Acta*, 57: 1079-1091.
- ZHENG, Y.F., 1999. Oxygen isotope fractionation in carbonate and sulphate minerals. *Geochemical Journal*, 33: 109-126.
- ZOHEIR, B.A., 2008a. Characteristics and genesis of shear zone-related gold mineralization in Egypt: A case study from the Um El Tuyor mine, south Eastern Desert. *Ore Geology Reviews*, 34: 445-470.
- ZOHEIR, B., 2008b. Structural controls, temperature-pressure conditions and fluid evolution of orogenic gold mineralisation at the Betam mine, south Eastern Desert, Egypt. *Mineralium Deposita*, 43: 79-95.
- ZOHEIR, B.A. & AKAWY, A., (in press). Genesis of the Abu Marawat gold deposit, central Eastern Desert of Egypt. *Journal of African Earth Sciences*.
- ZOHEIR, B., AKAWY, A. & HASSAN, I., 2008. Role of fluid mixing and wall-rock sulphidation in gold mineralization at the Semna mine area, central Eastern Desert of Egypt: Evidence from hydrothermal alteration, fluid inclusions and stable isotope data. *Ore Geology Reviews*, 34: 580-596.

APPENDICES

A-1 Microprobe analysis

Major and trace-element mineral compositions were determined using an X-ACT Energy Dispersive System (EDS) detector and WAVE Wavelength Dispersive spectrometer (WDS) mounted on a Zeiss EVO 50 Scanning Electron Microprobe (SEM) at Kingston University. The analytical software used was an Oxford Instruments INCA analytical suite. Operating parameters for the EDS include an accelerating voltage 20 kV, a beam current of 1.5 na, and a detector process time of 4; and for the WDS an accelerating voltage of 20 kV and a beam current 50–100 na. For combined trace/major element analyses, the WDS conditions were employed and the EDS detector moved further away from the sample in order to reduce the number of counts and dead time. Cobalt was used as a general quality control testing standard for the EDS analyser. For chlorite and arsenopyrite geothermometry, albite (similar Al contents to chlorite) and arsenopyrite standards were utilised, respectively. A 100% Au standard was used for WDS analysis of refractory gold. The detection limit for all elements using the EDS analyser was approximately 0.2 wt.%. The detection limit for Au on the WDS was 40 ppm.

A-2 Geochemical sample preparation and analysis

Sample preparation

Rock powders were oven dried overnight at 60 °C, re-ground using a pestle and mortar, and stored in glass vials until fusion the following day. Approximately 0.5 g of each sample was mixed with 1.25 g of lithium metaborate (LiBO₂) flux and fused in graphite crucibles at 1050 °C. The melt was then poured directly into clean plastic beakers containing 150 ml of 0.5M nitric acid (HNO₃) and then placed onto magnetic stirrers for 30 minutes to 1 hour, until the melt completely dissolved. The solutions were then filtered to remove carbon particles through a Whatman 41 filter paper and added to 250 ml volumetric flasks. Deionised water was added to reach a final acid concentration of 0.3M HNO₃. Proportions of each sample were then transferred to 50 ml centrifuge tubes for storage.

ICP-AES method

Analysis of major- (Si, Ti, Fe, Mn, Mg, Ca, Na, K and P) and trace- (Ba, Cr, Nb, Ni, Sr, V, Y, and Zr) elements was achieved by inductively coupled plasma atomic emission spectrometry (ICP-AES) using a JY Ultima 2C spectrometer at Kingston University. Calibration was carried out before each analytical run using the following reference materials (series devised by Prof. Ian Jarvis): GIT-IWG AC-E (granite), GIT-IWG AN-G (anorthosite), GSJ JG-3 (granodiorite), USGS BIR-1 (basalt), GSJ JCh-1 (chert), GSJ JLs-1 (limestone) and NRCC BCSS-1 (marine sediments).

Seven international standards were chosen for both ICP-AES and ICP-MS analysis to

cover the full range of geochemical compositions expected in the samples. These include GSJ JG-2 (granite), USGS AGV-2 (Guano Valley andesite), XIGMR DZE-1 (ultrabasic rock), USGS SGR-1 (Green River Shale), USGS SCo-1 (Cody Shale), GSJ JDo-1 (dolomite) and GSJ JLs-1 (limestone). These quality control standards were prepared in the same way as the samples. The accuracy of the standards for ICP-AES were typically better than 5% for the major elements, except K_2O (10-30%), and trace elements (Ba, Nb, Sr, V and Zr) were generally better than 20%. Ni, Cr and Y gave extreme inaccuracies >100%. For these three elements the ICP-MS data were used, which showed accuracies typically below 15%. The precision of the standard data is typically within a 10% error, excluding elements which showed high inaccuracies (Ni, Cr and Y). Emission lines and detection limits are given in Table A-1, and accuracy and precision values are presented in Table A-2.

An external drift monitor, USGS W-2 (Centerville Diabase), was run after every five samples. Instrumental drift was corrected by pinning data to the reference values of W-2 at its first analysis, calculating the percentage change independently for each element and for each subsequent analysis of the monitor, and then applying a linear correction to the intervening samples. The whole sample suite was analysed over four analytical runs on four separate days, with each sample measured three times within a particular run. Six of the samples were measured in all four runs to give a reproducibility of approximately 5% for major elements (except P_2O_5 ~20%) and 10% for trace elements (excluding Ni- >100%). Data was drift corrected and calibrated using the reference materials to give concentrations as weight % for major elements and parts per million (ppm) for trace elements.

Table A-1. Emission lines used for ICP-AES and association limits of detection.

Constituent	Analytical wavelength (nm)	Spectrometer	Detection limits (3 σ)	Rock quantitation limits (10 σ)
SiO ₂ (wt.%)	288.158	poly	0.015	0.050
TiO ₂	337.279	poly	0.003	0.010
Al ₂ O ₃	308.215	poly	0.013	0.043
Fe ₂ O ₃ (T)	259.940	poly	0.006	0.120
MnO	257.610	poly	0.001	0.003
MgO	279.079	poly	0.029	0.097
CaO	317.933	poly	0.004	0.013
Na ₂ O	589.592	poly	0.056	0.186
K ₂ O	766.490	poly	0.190	0.633
K ₂ O	766.490	mono	0.014	0.046
P ₂ O ₅	178.225	poly	0.100	0.333
P ₂ O ₅	178.229	mono	0.017	0.057
Ba (ppm)	455.403	mono	7.9	26.3
Cr	267.716	poly	21.1	70.3
Cr	267.716	mono	17.9	59.6
Nb	316.340	mono	10.9	36.3
Ni	231.604	poly	28.7	94.7
Sr	407.771	poly	1.0	3.3
V	290.882	mono	5.6	18.5
Y	371.029	poly	16.9	55.8
Zr	343.823	poly	3.9	12.9

Note- Fe₂O₃T = total Fe; poly = polychromator; mono = monochromator.
 Detection limits are 3 σ in test solutions; quantitation limits are 10 σ in rock samples.

Table A-2. Quality controls on the ICP-AES data.

Standard:	USGS AGV-2				XIGMR DZE-1			
	Measured (av.)	Ref.	Accuracy (%)	Precision (%)	Measured (av.)	Ref.	Accuracy (%)	Precision (%)
SiO ₂ (wt.%)	59.4	59.3	0.09	3.2	34.4	34.3	0.25	5.4
TiO ₂	1.07	1.05	1.8	2.9	0.013	0.008	66	24
Al ₂ O ₃	16.8	16.91	0.66	3.2	0.677	0.67	1.0	7.8
Fe ₂ O ₃ (T)	6.85	6.69	2.4	3.0	6.95	na	na	7.4
MnO	0.104	0.099	4.7	3.0	0.069	0.068	1.9	7.7
MgO	1.94	1.79	8.4	1.7	44.2	41	7.7	6.5
CaO	5.84	5.20	12	4.9	0.050	0.100	46	97
Na ₂ O	3.91	4.19	6.8	6.0	0.044	na	na	16
K ₂ O	2.49	2.88	13	10	—	na	na	na
K ₂ O (m)	2.18	2.88	24	3.3	0.006	na	na	64
P ₂ O ₅	0.431	0.48	10	6.1	—	0.004	na	na
Ba (ppm)	1160	1140	2.3	8.3	6.91	na	na	46
Cr	55.4	17	230	33	9650	10070	9.8	7.1
Nb	13.9	15	7.7	44	—	na	na	na
Ni	75.6	19	300	21	2690	2500	7.7	22
Sr	721	658	9.5	3.5	4.13	na	na	63
V	117	120	2.4	2.4	37.2	40	7.0	11
Y	29.2	20	46	2.1	—	na	na	na
Zr	252	230	9.6	5.0	26.2	na	na	130

Blank- below detection limits given in Table A-1.

Table A-2 cont. Quality controls on the ICP-AES data.

Standard:	USGS SCo-1				USGS SGR-1			
	Measured (av.)	Ref.	Accuracy (%)	Precision (%)	Measured (av.)	Ref.	Accuracy (%)	Precision (%)
SiO ₂ (wt.%)	63.2	62.8	0.65	3.6	29.2	28.2	3.6	8.2
TiO ₂	0.614	0.63	2.6	4.6	0.270	0.25	5.5	10
Al ₂ O ₃	13.6	13.7	0.42	4.3	6.76	6.52	3.6	9.9
Fe ₂ O ₃ (T)	5.28	5.13	3.0	4.7	3.14	3.03	3.7	11
MnO	0.053	0.053	0.11	5.1	0.034	0.035	0.13	10
MgO	2.98	2.72	9.7	4.8	4.98	4.44	12	10
CaO	2.98	2.62	14	4.0	9.72	8.38	16	10
Na ₂ O	0.876	0.90	2.6	12	2.85	2.99	4.8	5.1
K ₂ O	2.28	2.77	18	20	1.37	1.66	17	6.7
K ₂ O (m)	1.90	2.77	31	29	1.18	1.66	29	5.4
P ₂ O ₅	0.182	0.21	13	3.0	0.267	0.33	19	11
Ba (ppm)	572	570	0.52	12	280	290	3.3	1.8
Cr	100	68	47	26	63.7	30	110	10
Nb	11.9	11	8.5	47	—	5.2	na	na
Ni	74.3	29	180	60	89.7	29	210	19
Sr	189	420	4.3	4.7	447	420	6.3	10
V	162	130	25	8.1	134	130	3.4	12
Y	32.7	13	25	7.8	19.6	13	51	14
Zr	202	53	26	5.7	58.4	53	10	10

Standard:	GSJ JDo-1				GSJ JLs-1			
	Measured (av.)	Ref.	Accuracy (%)	Precision (%)	Measured (av.)	Ref.	Accuracy (%)	Precision (%)
SiO ₂ (wt.%)	—	0.216	na	na	—	0.12	na	na
TiO ₂	—	na	na	na	0.009	na	na	54
Al ₂ O ₃	0.017	0.017	31	33	0.032	na	na	170
Fe ₂ O ₃ (T)	—	0.201	na	na	0.031	na	na	31
MnO	0.006	0.007	2.0	12	—	0.002	na	na
MgO	18.5	18.47	0.56	2.6	0.760	0.61	25	5.9
CaO	33.2	33.96	2.3	2.7	54.95	55.09	0.25	2.1
Na ₂ O	—	na	na	na	0.053	na	na	28
K ₂ O	—	na	na	na	0.022	na	na	79
K ₂ O (m)	—	na	na	na	0.018	na	na	91
P ₂ O ₅	0.038	0.03	10	12	0.039	na	na	32
Ba (ppm)	8.82	6.14	44	19	466	476	2.1	12
Cr	44.6	7.93	460	23	28.6	3.37	749	81
Nb	—	0.4	na	na	—	1	na	na
Ni	70.3	2.9	2300	46	47.2	0.36	13000	89
Sr	114	116	1.5	1.8	325	295	10	1.7
V	6.53	3.14	100	30	35.8	3.59	900	15
Y	24.1	10.3	130	10	—	0.22	na	na
Zr	6.95	6.21	12	23	6.17	4.19	47	35

Blank- below detection limits given in Table A-1.

ICP-MS method

Analysis of trace and REE elements was achieved by inductively coupled plasma mass spectrometry (ICP-MS) using an Agilent 7500c quadrupole mass spectrometer at Kingston University. Firstly, the samples, standards and blanks were diluted x25. Next, a synthetic calibration line was prepared using a multi element solution cocktail to give 0, 1, 5, 10, and 20 ppb standards, all containing the same aliquot of the blank for matrix-matching standards and samples. The running procedure included blanks, standards and then samples, with a drift monitor measured every 5 samples (usually the 10 ppb standard). In between samples, a two minute washout time with 2% nitric acid was utilised to prevent cross contamination.

Standards typically showed accuracy and precession levels better than 10% and 25% respectively, apart from XIGMR DZE-1 which displayed poor quality controls for REE elements (Table A-4). In some standards, accuracies for Zn, Ga and Mo were greater than 50%. The sample data was drift corrected and calibrated with the standards for concentration determination (all done by computer programs). Detection limits are shown in Table A-3 and accuracy/precession values are stated in Table A-4.

Table A-3. Detection limits for the ICP-MS.

Element	Lower limits of detection (LLD) (ppb)	Element	Lower limits of detection (LLD) (ppb)
V ₅₁	0.009	Nd ₁₄₃	0.006
Cr ₅₂	0.189	Nd ₁₄₆	0.002
Co ₅₉	0.002	Sm ₁₄₇	0.003
Ni ₆₀	0.079	Sm ₁₄₉	0.005
Cu ₆₃	0.038	Eu ₁₅₁	0.001
Cu ₆₅	0.056	Gd ₁₅₇	0.012
Zn ₆₆	0.255	Tb ₁₅₉	0.005
Zn ₆₈	0.120	Dy ₁₆₁	0.004
Ga ₆₉	0.008	Dy ₁₆₃	0.002
Ga ₇₁	0.006	Ho ₁₆₅	0.004
Rb ₈₅	0.014	Er ₁₆₆	0.003
Sr ₈₈	0.010	Er ₁₆₇	0.002
Y ₈₉	0.004	Tm ₁₆₉	0.006
Zr ₉₀	0.014	Yb ₁₇₂	0.001
Nb ₉₃	0.006	Yb ₁₇₃	0.001
Mo ₉₅	0.020	La ₁₇₅	0.001
Cs ₁₃₃	0.001	Hf ₁₇₇	0.006
Ba ₁₃₅	0.050	Hf ₁₇₈	0.004
Ba ₁₃₇	0.026	Ta ₁₈₁	0.002
La ₁₃₉	0.008	Th ₂₃₂	0.001
Ce ₁₄₀	0.005	U ₂₃₈	0.001
Pr ₁₄₁	0.001		

Table A-4. Quality controls on the ICP-MS data.

Standard:	GSJ JG-2				USGS AGV-2			
	Measured (av.)	Ref.	Accuracy (%)	Precision (%)	Measured (av.)	Ref.	Accuracy (%)	Precision (%)
V ₅₁	-	3	na	na	119	120	0.64	31
Cr ₅₂	-	7.6	na	na	-	17	na	na
Co ₅₉	3.79	4.3	12	6.4	15.4	16	3.7	27
Ni ₆₀	2.36	2.1	12	18	21.8	19	15	33
Cu ₆₃	0.70	0.4	75	3.0	54.2	53	2.3	24
Zn ₆₆	-	12.7	na	na	75.7	86	12	38
Ga ₆₉	17.7	19	7.0	7.1	54.9	na	na	9.8
Ga ₇₁	16.1	na	na	14	20.2	20	1.0	28
Rb ₈₅	253	297	15	9.7	60.4	68.6	12	19
Sr ₈₈	15.8	16	1.5	12	669	658	1.7	32
Y ₈₉	68.5	88.2	22	6.1	17.9	20	11	32
Zr ₉₀	74.8	101	26	7.1	197	230	14	20
Nb ₉₃	11.8	15	21	0.25	12.2	15	18	25
Mo ₉₅	1.21	0.23	430	65	2.78	na	na	19
Cs ₁₃₃	5.45	7.5	27	9.4	0.98	1.16	16	18
Ba ₁₃₅	50.8	67	24.	7.6	1090	1140	4.7	24
La ₁₃₉	18.1	20.1	10	7.0	42.3	38	11	27
Ce ₁₄₀	42.4	49.5	14	6.2	68.8	68	1.2	25
Pr ₁₄₁	5.41	6.01	10	6.9	8.04	8.3	3.2	24
Nd ₁₄₃	22.9	25.8	11	6.3	30.3	30	0.96	24
Sm ₁₄₇	6.94	7.72	10	8.6	5.38	5.7	5.6	22
Eu ₁₅₁	0.10	0.09	15	18	1.67	1.54	8.3	26
Gd ₁₅₇	8.81	7.10	24	14	4.79	4.69	2.1	21
Tb ₁₅₉	1.64	1.50	9.3	14	0.68	0.64	6.3	26
Dy ₁₆₁	11.0	11.5	4.5	2.6	3.66	3.60	1.6	32
Ho ₁₆₅	1.36	1.40	2.9	5.8	0.65	0.71	8.3	29
Er ₁₆₆	5.21	4.95	5.3	5.1	1.76	1.79	1.5	34
Tm ₁₆₉	0.81	0.7	16	10	0.25	0.26	5.1	25
Yb ₁₇₂	7.51	7.34	2.3	12	1.64	1.60	2.3	29
Lu ₁₇₅	1.10	1.22	10	4.0	0.25	0.25	0.24	30
Hf ₁₇₇	3.49	5.36	35	6.2	4.21	5.08	17	23
Ta ₁₈₁	1.99	1.9	4.5	2.4	0.83	0.89	7.2	26
Th ₂₃₂	28.7	29.7	3.5	7.6	6.07	6.10	0.45	31
U ₂₃₈	9.40	12.5	25	12	1.82	1.88	3.2	33

Blank- below detection limits given in Table A-3.

Table A-4 cont. Quality controls on the ICP-MS data.

Standard:	XIGMR DZE-1				USGS SCo-1			
	Measured (av.)	Ref.	Accuracy (%)	Precision (%)	Measured (av.)	Ref.	Accuracy (%)	Precision (%)
V ₅₁	40.1	40	0.32	16	164	131	25	16
Cr ₅₂	11500	10700	7.3	14	67.1	68	1.3	6.3
Co ₅₉	109	90	21	16	11.2	10.5	6.8	21
Ni ₆₀	2880	2500	15	15	32.1	27	19	19
Cu ₆₃	8.90	na	na	1.5	31.3	28.7	9.1	15
Zn ₆₆	29.9	68	56	80	72.8	103	29	32
Ga ₆₉	1.45	na	na	20	32.8	15	120	9.5
Ga ₇₁	1.08	na	na	54	16.2	na	na	21
Rb ₈₅	—	na	na	na	108	112	3.7	15
Sr ₈₈	2.30	na	na	38	177	174	1.6	16
Y ₈₉	0.15	na	na	4.7	23.5	26	9.7	13
Zr ₉₀	—	na	na	na	159	160	0.72	9.0
Nb ₉₃	3.24	na	na	51	11.7	11	6.2	7.4
Mo ₉₅	5.03	na	na	54	2.90	1.37	110	3.1
Cs ₁₃₃	0.04	0.09	55	17	7.31	7.80	6.2	9.4
Ba ₁₃₅	2.64	na	na	37	581	570	1.9	9.2
La ₁₃₉	0.38	0.19	100	12	36.8	29.5	25	11
Ce ₁₄₀	0.34	0.36	6.4	34	60.3	62	2.8	10
Pr ₁₄₁	0.09	na	na	24	7.16	6.6	8.6	7.2
Nd ₁₄₃	0.12	0.15	31	56	27.8	26	7.0	14
Sm ₁₄₇	—	0.02	na	na	5.26	5.30	0.70	3.9
Eu ₁₅₁	0.01	0.004	50	24	1.20	1.19	0.72	26
Gd ₁₅₇	—	0.024	na	na	4.82	4.60	4.8	19
Tb ₁₅₉	0.03	0.002	1300	37	0.77	0.7	9.8	18
Dy ₁₆₁	0.05	na	na	15	4.35	4.20	3.6	17
Ho ₁₆₅	0.03	0.005	540	5.9	0.85	0.97	12	20
Er ₁₆₆	0.06	na	na	8.6	2.53	2.50	1.1	16
Tm ₁₆₉	0.04	0.003	1100	7.5	0.33	0.42	22	26
Yb ₁₇₂	0.05	0.02	140	55	2.40	2.27	5.7	10
Lu ₁₇₅	0.04	0.004	890	3.3	0.34	0.34	0.40	15
Hf ₁₇₇	0.29	na	na	17	4.20	4.60	8.7	17
Ta ₁₈₁	0.24	na	na	7.5	0.87	0.92	6.0	16
Th ₂₃₂	0.30	na	na	55	9.35	9.70	3.7	22
U ₂₃₈	—	na	na	na	3.06	3.00	1.9	30

Blank- below detection limits given in Table A-3.

Table A-4 cont. Quality controls on the ICP-MS data.

Standard:	USGS SGR-1				GSJ JDo-1			
	Measured (av.)	Ref.	Accuracy (%)	Precision (%)	Measured (av.)	Ref.	Accuracy (%)	Precision (%)
V ₅₁	131	128	2.0	10	2.14	na	na	30
Cr ₅₂	—	30	na	na	—	7.00	na	na
Co ₅₉	12.5	11.8	6.1	14	0.43	na	na	6.1
Ni ₆₀	33.1	29	14	15	3.16	2.9	9.0	13
Cu ₆₃	64.2	66	2.8	7.6	3.50	1.4	150	35
Zn ₆₆	46.1	74	38	75	30.4	34.4	12	1.6
Ga ₆₉	17.4	11	58	0.85	—	na	na	na
Ga ₇₁	8.73	na	na	na	—	na	na	na
Rb ₈₅	76.9	83	7.4	18	—	na	na	na
Sr ₈₈	410	420	2.4	16	130	119	8.9	10
Y ₈₉	11.5	13	11	14	11.0	11.2	1.9	5.1
Zr ₉₀	42.6	53	20	16	—	na	na	na
Nb ₉₃	5.02	5.2	3.5	15	—	na	na	na
Mo ₉₅	40.7	35.1	16	16	0.97	na	na	24
Cs ₁₃₃	4.81	5.2	7.4	18	—	na	na	na
Ba ₁₃₅	275	290	5.0	11	5.85	na	na	2.1
La ₁₃₉	21.3	20.3	5.0	15	8.25	7.87	4.9	6.5
Ce ₁₄₀	35.2	36	2.2	12	1.91	2.54	25	14
Pr ₁₄₁	4.07	3.9	4.4	15	1.11	0.90	23	1.9
Nd ₁₄₃	15.1	15.5	2.9	8.1	4.44	5.33	17	19
Sm ₁₄₇	2.61	2.7	3.2	16	0.71	0.84	16	14
Eu ₁₅₁	0.57	0.56	1.7	9.3	0.15	0.19	23	37
Gd ₁₅₇	2.19	2.0	9.6	13	0.91	na	na	9.1
Tb ₁₅₉	0.34	0.36	6.9	15	0.14	0.12	15	10
Dy ₁₆₁	1.86	1.90	2.1	13	0.79	1.0	21	0.44
Ho ₁₆₅	0.39	0.38	1.6	24	0.19	0.2	7.2	7.0
Er ₁₆₆	1.01	1.11	8.9	14	0.47	na	na	7.5
Tm ₁₆₉	0.19	0.17	9.8	11	0.05	0.06	20	8.7
Yb ₁₇₂	1.03	0.94	9.6	16	0.30	0.36	18	11
Lu ₁₇₅	0.16	0.14	14	0.05	0.05	0.05	1.1	5.78
Hf ₁₇₇	1.52	1.39	9.0	0.41	—	0.10	na	na
Ta ₁₈₁	0.45	0.42	5.9	1.8	—	na	na	na
Th ₂₃₂	4.99	4.78	4.5	12	0.09	na	na	30
U ₂₃₈	5.59	5.40	3.6	16	0.83	na	na	28

Blank- below detection limits given in Table A-3.

A-3 Geochemistry data presented in chapter 3 and chapter 5

Table A-5. Whole rock geochemistry of the intrusive and sedimentary rock samples from Loulo.

Sample	Balangouma belt-type plutons									
	R5	R8	R21	R25	LR4	LR5	R35	R36	R37	R41
SiO ₂	60.3	67.8	57.7	59.7	66.3	64.1	64.8	62.6	60.0	62.1
TiO ₂	0.756	0.794	0.496	0.637	0.538	0.799	0.427	0.730	0.850	0.642
Al ₂ O ₃	16.2	16.1	14.7	16.4	16.5	15.7	15.7	15.6	16.7	15.3
Fe ₂ O ₃ (T)	6.15	0.792	2.89	3.41	2.17	5.73	3.81	5.60	6.62	5.18
MnO	0.023	0.009	0.012	0.027	0.039	0.068	0.078	0.072	0.075	0.068
MgO	0.972	1.09	2.48	3.22	3.08	3.08	1.66	2.80	3.58	2.67
CaO	1.63	1.03	4.99	6.30	2.75	4.38	4.99	4.28	5.10	4.02
Na ₂ O	4.62	8.07	8.10	7.92	8.40	4.17	4.00	3.97	4.39	4.01
K ₂ O	2.20	0.771	0.079	0.599	0.353	2.39	2.65	2.99	2.25	3.12
P ₂ O ₅	0.292	0.013	0.156	0.326	0.182	0.200	0.168	0.203	0.244	0.170
Total	93.2	96.4	91.6	98.6	100.2	100.6	98.2	98.9	99.8	97.3
V	79.0	24.4	59.3	84.5	67.2	87.6	55.3	88.5	124	78.0
Cr	47.3	104	39.4	59.5	88.9	92.3	42.9	79.4	101	78.2
Co	5.91	3.52	11.7	11.9	7.24	16.6	11.7	16.6	21.7	14.5
Ni	60.2	26.9	16.7	33.1	11.8	37.6	10.7	35.2	45.5	34.3
Cu	14.7	6.10	14.2	44.1	4.58	10.5	5.62	16.8	29.4	15.8
Zn	67.6	26.5	33.4	18.6	39.2	78.3	6.64	288	90.5	173
Ga	19.9	19.7	16.6	15.9	21.7	25.0	28.7	29.7	32.7	26.5
Rb	92.0	7.48	2.00	26.3	7.11	143	121	121	108	128
Sr	312	265	93.4	234	206	382	453	419	538	377
Y	18.1	5.19	12.2	21.2	14.0	11.2	9.59	16.2	16.4	16.5
Zr	156	275	107.6	146	149	196	132	253	212	190
Nb	6.53	5.49	5.97	6.45	7.61	12.1	6.55	12.2	10.6	13.0
Mo	0.59	—	26.4	—	0.96	3.24	2.35	2.05	1.62	5.28
Cs	0.42	0.26	0.34	2.22	0.10	6.81	1.90	5.02	7.90	4.82
Ba	1540	395	14.5	80.7	183	360	491	668	590.8	589
Hf	4.12	6.95	3.15	3.58	3.92	5.63	3.59	6.27	5.07	4.96
Ta	0.51	0.80	0.60	0.48	0.89	1.21	0.90	1.12	0.98	1.10
Th	6.22	3.61	4.79	4.36	10.4	9.39	2.91	11.3	7.69	13.7
U	2.09	1.83	1.91	2.14	5.13	5.12	1.40	3.32	2.27	2.63
La	46.9	6.02	6.12	15.9	29.3	24.9	24.7	35.5	35.0	32.2
Ce	98.7	13.5	15.9	50.7	52.1	51.4	47.9	69.0	64.9	62.1
Pr	12.4	1.54	2.78	7.97	6.40	5.82	5.31	7.71	7.34	6.88
Nd	49.9	6.86	14.0	36.0	22.3	21.8	20.9	28.8	29.3	25.9
Sm	8.44	1.39	3.71	7.89	4.06	3.16	3.30	5.01	5.55	4.66
Eu	2.48	0.30	0.95	2.36	1.12	1.11	1.01	1.32	1.51	1.24
Gd	6.90	1.32	3.12	6.54	3.53	3.40	3.12	4.79	5.23	4.24
Tb	0.82	0.17	0.41	0.94	0.54	0.47	0.39	0.63	0.64	0.60
Dy	3.99	1.02	2.42	4.93	2.75	2.19	1.76	3.35	3.37	2.81
Ho	0.68	0.18	0.46	0.82	0.49	0.46	0.38	0.57	0.58	0.54
Er	1.95	0.57	1.31	2.24	1.63	1.24	0.98	1.72	1.70	1.46
Tm	0.25	0.10	0.19	0.29	—	—	—	0.18	0.21	0.16
Yb	1.69	0.65	1.16	1.94	1.49	1.15	1.06	1.48	1.57	1.44
Lu	0.25	0.10	0.17	0.23	0.21	0.20	0.16	0.25	0.24	0.22
(La/Lu)N	19.8	6.30	3.84	7.39	14.9	13.5	16.9	15.3	15.5	15.9
ΣREE	235.3	33.7	52.7	138.7	125.8	117.3	111.0	160.3	157.1	144.4
Eu/Eu*	0.96	0.67	0.83	0.97	0.88	1.03	0.95	0.81	0.84	0.83

Note- major elements given in wt.% and trace/REE elements in ppm; Fe₂O₃ (T) = total Fe; (La/Lu)N = chondrite normalised La/Lu ratios; blank- <LLD. Sample locations shown in Fig. 3.2.

Table A-5. Continued

Sample	Basin-type plutons					Felsic Birimian dykes			Mafic Birimian dykes			
	PTG1	R42	R43	R39	R40	P129.10	UYP1	GPI	LD9	LD14	LD23	UYP2
SiO ₂	70.5	76.8	76.7	74.5	76.7	65.6	61.2	59.0	52.9	50.4	54.2	56.1
TiO ₂	0.285	0.038	0.031	0.279	0.028	0.599	0.664	0.999	0.781	1.06	0.804	0.629
Al ₂ O ₃	15.3	13.8	13.9	15.7	12.9	16.1	14.9	15.8	18.0	13.0	18.5	15.0
Fe ₂ O ₃ (T)	1.89	0.422	0.524	2.20	1.05	4.21	4.66	2.19	9.09	8.77	9.30	6.76
MnO	0.029	0.007	0.006	0.069	0.011	0.051	0.014	0.045	0.013	0.018	0.013	0.028
MgO	0.802	0.067	0.080	0.771	0.079	1.64	3.16	2.84	6.68	7.75	6.84	4.36
CaO	1.43	0.271	0.315	0.133	0.019	3.43	2.80	4.95	1.00	5.97	1.05	5.94
Na ₂ O	4.10	3.54	4.05	0.161	0.149	5.42	7.65	9.00	3.67	4.01	3.77	5.00
K ₂ O	4.19	5.42	4.94	3.21	3.76	1.63	0.74	0.41	2.04	2.22	2.08	0.763
P ₂ O ₅	0.118	0.010	0.021	0.069	0.050	0.285	0.254	0.27	0.280	1.044	0.279	0.195
Total	98.7	100.3	100.6	97.1	94.7	98.9	96.0	95.5	94.4	94.2	96.8	94.7
V	25.9	1.89	2.70	17.8	3.86	75.4	96.9	10.5	137	171	141	101
Cr	18.8	11.3	15.8	24.9	10.2	23.9	123	69.5	214	215	225	237
Co	4.19	1.83	1.96	5.45	1.05	9.73	14.3	10.4	16.8	32.1	17.6	2180
Ni	8.01	5.42	3.72	11.8	5.89	13.4	54.3	4.73	10.3	63.1	14.6	1240
Cu	6.78	1.27	5.03	11.9	5.03	81.5	24.2	24.7	3.18	38.7	3.61	247
Zn	78.2	125	—	298	236	81.4	6.93	26.0	114	136	208	50.4
Ga	34.4	21.6	23.7	32.1	23.2	31.3	18.4	9.52	28.0	28.4	28.2	17.7
Rb	79.1	266	271	429	352	34.0	10.1	3.43	55.4	57.8	54.3	21.1
Sr	692	53.4	74.6	54.6	13.1	693	104	188	455	187	452	169
Y	5.76	7.83	4.40	8.58	9.04	9.18	13.4	18.3	10.3	25.4	10.2	14.8
Zr	120	38.4	28.4	155	19.1	141	143	124	139	274	137	118
Nb	5.99	8.35	8.59	9.15	8.37	10.5	8.40	10.6	11.5	8.01	8.80	10.5
Mo	1.24	1.46	3.03	2.31	2.08	1.30	0.83	1.03	4.72	2.24	2.44	5.59
Cs	2.63	3.30	13.6	15.9	8.99	0.78	0.60	0.22	1.89	1.37	1.73	1.07
Ba	955	133	164	421	29.5	637	31.3	49	595	753	566	94.2
Hf	3.09	1.80	1.80	4.16	1.49	3.65	3.62	3.03	3.92	6.41	3.71	3.04
Ta	0.51	1.45	1.74	1.31	2.13	0.64	0.67	0.62	0.74	0.66	0.62	0.56
Th	4.80	6.40	15.4	34.9	12.2	2.68	3.82	4.97	4.81	9.59	4.59	4.21
U	1.68	2.73	2.82	5.68	2.86	0.92	1.16	2.82	1.74	4.32	1.76	1.19
La	25.1	20.6	7.26	52.8	6.39	27.8	32.7	30.3	11.6	57.8	12.1	28.9
Ce	49.6	30.0	13.6	106	8.25	60.0	77.7	65.5	26.1	143	25.4	57.3
Pr	5.82	4.14	1.74	11.6	1.31	7.47	10.1	7.89	3.26	19.2	3.17	6.67
Nd	22.8	14.6	6.49	41.0	4.17	30.8	40.2	30.5	12.4	81.0	12.6	25.5
Sm	4.12	2.52	1.74	6.58	0.95	5.23	7.76	5.71	2.91	15.8	2.82	4.44
Eu	1.04	0.42	0.31	0.73	0.10	1.31	2.08	1.36	0.72	4.39	0.73	1.08
Gd	3.11	2.45	1.39	5.00	1.16	4.12	6.27	4.93	2.58	12.1	2.51	4.20
Tb	0.33	0.28	0.22	0.48	0.18	0.50	0.73	0.65	0.36	1.41	0.39	0.56
Dy	1.38	1.47	0.83	2.02	1.19	2.19	3.60	3.46	1.82	6.07	2.13	3.05
Ho	0.19	0.24	0.16	0.30	0.30	0.35	0.50	0.66	0.38	0.98	0.38	0.61
Er	0.59	0.58	0.42	0.85	1.01	0.84	1.20	2.08	1.15	2.46	1.20	1.64
Tm	—	—	—	—	—	—	—	0.29	—	0.25	—	0.21
Yb	0.47	0.46	0.44	0.85	1.01	0.59	0.95	2.12	1.54	2.00	1.36	1.47
Lu	0.05	0.05	0.05	0.12	0.17	0.10	0.18	0.29	0.23	0.28	0.17	0.20
(La/Lu) _N	53.7	44.2	15.6	47.2	3.97	29.7	19.1	11.2	5.39	22.5	7.84	15.3
ΣREE	114.5	77.8	34.7	228.1	26.2	141.2	184.0	155.7	65.0	347.1	65.0	135.7
Eu/Eu*	0.85	0.51	0.58	0.36	0.29	0.83	0.88	0.76	0.79	0.94	0.82	0.75

Note- Sample location of basin type plutons shown in Fig. 3.1 & Fig. 3.2 (PTG1 = Yatea pluton; R42 & R43 = isolated outcrop to NE of the Gara deposit; R39 & R40 = Moussala pluton). Felsic Birimian dykes collected from drill core P129DH12 (P129.10); the northern face of the Gara pit (GPI); and from the Yatea underground shaft (UYP1). Mafic Birimian dyke samples collected from Gara drill cores LOCP120 (LD9), LOCP124 (LD14), and LOCP90 (LD23); and from Yatea underground (UYP2).

Table A-5. Continued

Post-Birimian mafic dyke		Gara argillaceous greywacke wall-rock								
Sample	YD36	G14	G16	G17	G19	G21	G25	G29	G30	G33
SiO ₂	52.0	56.5	54.5	59.2	56.2	53.0	54.9	56.0	51.0	53.0
TiO ₂	1.05	0.603	0.515	0.401	0.448	0.574	0.402	0.354	0.474	0.586
Al ₂ O ₃	14.3	15.7	13.9	12.6	12.2	13.5	11.3	11.6	11.9	14.1
Fe ₂ O ₃ (T)	10.6	7.36	5.56	3.33	4.20	5.29	4.05	4.57	4.22	4.86
MnO	0.174	0.064	0.082	0.070	0.077	0.081	0.056	0.115	0.076	0.079
MgO	7.60	5.69	5.65	4.43	6.43	4.48	4.47	7.14	4.37	7.68
CaO	10.5	3.49	5.21	6.07	5.93	7.65	8.88	7.44	9.55	6.07
Na ₂ O	1.92	2.46	2.44	3.29	3.64	3.15	3.17	3.32	3.30	2.37
K ₂ O	0.668	2.94	2.87	1.98	1.76	1.72	1.79	1.23	1.94	2.47
P ₂ O ₅	0.133	0.175	0.145	0.109	0.143	0.193	0.159	0.105	0.152	0.195
Total	99.0	95.0	91.0	91.5	91.0	89.6	89.2	91.9	86.9	91.4
V	201	87.9	89.9	103	102	104	65.0	57.4	83.6	84.4
Cr	361	107	117	90.5	122	92.1	72.0	64.9	73.6	82.6
Co	38.1	15.7	21.4	10.4	12.5	16.0	9.48	19.6	12.7	14.2
Ni	76.4	45.3	47.0	55.3	40.4	53.7	33.6	53.1	46.6	43.7
Cu	81.0	3.40	25.4	26.9	21.0	3.82	3.36	4.82	15.1	3.57
Zn	10.7	488	599	—	15.9	490	692	695	744	622
Ga	15.7	19.8	18.6	23.9	28.1	24.4	16.0	17.1	20.9	21.9
Rb	14.6	56.2	43.7	50.7	72.9	56.0	49.5	31.1	51.4	64.0
Sr	176	114	72.6	95.9	247	106	266	154	122	63.0
Y	16.0	17.3	13.3	22.7	11.3	19.6	19.9	18.3	19.8	21.9
Zr	74.6	77.8	111	242	150	130	168	143	114	129
Nb	8.65	4.47	7.00	6.92	8.84	6.28	6.96	6.65	6.13	10.4
Mo	1.42	1.46	3.60	1.15	3.73	0.74	2.69	3.05	1.51	5.27
Cs	0.54	2.35	1.48	—	2.20	1.31	1.38	0.60	0.75	1.75
Ba	144	320	210	582	961	508	286	299	466	409
Hf	2.27	2.21	2.88	6.07	4.35	3.49	4.33	3.61	3.14	3.30
Ta	0.72	0.36	0.58	0.47	0.74	0.52	0.53	0.81	0.51	0.70
Th	1.97	3.91	3.69	4.75	4.61	4.43	3.24	3.53	3.95	4.18
U	0.43	1.37	1.46	1.70	1.87	1.68	1.06	1.35	1.52	1.21
La	11.0	28.1	23.8	20.4	19.4	21.6	19.2	23.0	20.8	23.4
Ce	23.5	54.4	47.4	44.3	42.5	46.0	41.9	49.3	45.3	47.5
Pr	2.81	6.64	5.68	5.25	5.39	5.62	5.29	5.98	5.61	5.92
Nd	12.2	26.5	22.2	22.1	22.9	22.7	22.0	24.2	22.5	23.5
Sm	2.64	5.49	4.29	4.01	4.30	4.41	4.60	4.75	4.52	4.56
Eu	0.99	1.43	1.27	1.26	1.17	1.28	1.09	1.27	1.28	1.33
Gd	3.14	5.08	4.02	3.80	4.01	4.44	4.30	4.08	4.45	4.26
Tb	0.50	0.69	0.58	0.56	0.60	0.61	0.59	0.63	0.65	0.68
Dy	3.16	3.76	3.46	3.37	3.40	3.72	3.59	3.35	3.66	3.87
Ho	0.63	0.79	0.70	0.72	0.72	0.80	0.78	0.77	0.81	0.82
Er	1.74	2.21	1.82	1.95	2.09	2.19	2.03	2.03	2.13	2.18
Tm	0.25	0.33	0.27	0.27	0.29	0.26	0.23	0.33	0.31	0.30
Yb	1.71	1.98	1.72	2.16	2.05	2.08	1.83	1.95	2.22	2.19
Lu	0.29	0.33	0.29	0.32	0.30	0.30	0.31	0.34	0.35	0.34
(La/Lu) _N	4.06	9.13	8.67	8.78	8.84	7.80	6.54	7.18	6.36	7.34
ΣREE	67.4	143.2	101.2	87.5	77.6	103.8	65.0	122.1	114.6	120.9
Eu/Eu*	1.04	0.81	0.92	0.97	0.85	0.87	0.74	0.86	0.86	0.91

Note- Post-Birimian dyke taken from Yalea drill core YDH187; Gara argillaceous greywacke samples from drill cores CO92 (G14 to G21) and LOCP116 (G25-G33).

Table A-5. Continued

Sample	Yalea footwall argillaceous greywackes						Yalea hangingwall arkoses				
	YD23	YD25	YD28	YD33	YD35	YD45	YD42	YD51	YD56	YD58	YD59
SiO ₂	45.1	47.5	52.8	56.6	53.5	46.5	63.0	69.0	70.6	59.7	60.9
TiO ₂	0.474	0.552	0.557	0.539	0.593	0.540	0.442	0.417	0.206	0.736	0.469
Al ₂ O ₃	12.0	13.6	13.4	13.08	10.5	12.9	10.3	10.6	9.71	16.8	10.7
Fe ₂ O ₃ (T)	5.67	5.99	4.48	6.34	5.10	3.80	5.07	3.81	1.53	5.08	4.07
MnO	0.056	0.075	0.067	0.115	0.099	0.091	0.061	0.020	0.056	0.021	0.066
MgO	4.27	7.36	6.41	6.39	4.94	6.84	2.81	3.17	2.72	3.93	4.44
CaO	13.8	6.48	5.79	7.33	8.38	10.0	7.28	0.87	4.28	0.93	6.39
Na ₂ O	1.82	1.45	2.83	3.89	3.11	2.53	3.77	3.43	2.79	2.28	2.13
K ₂ O	2.25	3.12	2.10	3.46	2.06	2.71	1.03	4.06	1.54	4.32	4.14
P ₂ O ₅	0.061	0.154	0.135	0.181	0.129	0.144	0.101	0.096	0.039	0.117	0.093
Total	85.5	86.2	88.5	98.0	88.4	86.1	93.8	95.5	93.5	93.9	93.4
V	87.9	100	89.9	103	86.8	102	88.0	89.7	34.5	176	88.8
Cr	107	80.2	117	90.5	161	122	116	65.9	24.3	161	117
Co	15.7	20.0	21.4	10.4	8.44	12.5	5880	10.4	5.27	14.2	15.3
Ni	45.3	52.1	47.0	55.3	24.2	40.4	3440	37.7	10.9	66.7	41.3
Cu	3.40	4.08	25.4	26.9	8.13	21.0	824	5.43	65.3	104	254
Zn	488	622	599	—	624	15.9	—	—	272	688	686
Ga	19.8	20.3	18.6	23.9	15.2	28.1	10.7	24.9	21.0	49.4	23.3
Rb	56.2	71.3	43.7	50.7	41.8	72.9	18.1	81.0	25.2	99.4	59.7
Sr	114	32.9	72.6	95.9	84.8	247	126	83.4	74.7	87.3	98.7
Y	17.3	19.0	13.3	22.7	19.5	11.3	14.3	15.4	9.75	13.9	17.2
Zr	77.8	98.9	111	242	416	150	296	111	73.1	122	224
Nb	4.46	7.26	7.00	6.92	8.99	8.84	19.9	6.06	4.58	8.02	12.6
Mo	1.46	1.82	3.60	1.15	6.02	3.73	14.1	42.7	2.99	2.76	8.43
Cs	2.35	2.04	1.48	—	0.93	2.20	0.63	1.91	0.26	2.49	1.29
Ba	320	272	210	582	291	961	81.8	496	691	1410	482
Hf	2.21	2.85	2.88	6.07	10.3	4.35	7.03	3.10	1.77	3.34	5.73
Ta	0.36	0.55	0.58	0.47	0.79	0.74	0.60	0.56	0.48	0.63	0.81
Th	3.91	3.79	3.69	4.75	5.25	4.61	7.30	3.83	1.96	5.63	5.34
U	1.37	1.65	1.46	1.70	1.65	1.87	2.05	1.46	0.46	2.07	1.50
La	36.3	24.1	7.05	27.9	16.0	15.6	19.8	23.0	16.2	31.8	21.9
Ce	75.3	51.6	16.5	61.4	37.0	28.4	41.4	44.9	33.5	62.1	41.1
Pr	8.99	6.46	2.19	7.40	4.75	3.58	4.99	5.19	3.96	7.27	4.73
Nd	34.0	26.5	8.46	31.0	19.9	14.1	22.1	20.8	15.4	28.0	18.5
Sm	5.94	5.55	2.05	6.45	4.19	2.85	4.13	3.62	3.05	4.87	3.86
Eu	1.62	1.53	0.61	1.72	1.11	1.03	1.06	1.04	0.88	1.47	1.19
Gd	4.97	4.96	2.25	6.39	3.86	2.95	3.51	3.56	2.59	4.85	3.93
Tb	0.60	0.72	0.40	0.83	0.72	0.39	0.47	0.49	0.38	0.54	0.59
Dy	3.47	3.95	2.47	4.13	3.64	2.17	2.67	2.66	1.95	2.59	3.02
Ho	0.70	0.71	0.53	0.83	0.80	0.43	0.54	0.59	0.35	0.52	0.65
Er	1.81	2.00	1.42	2.17	2.32	1.27	1.61	1.75	1.03	1.58	1.69
Tm	0.28	0.24	—	0.31	0.28	0.21	0.21	0.26	—	0.21	0.25
Yb	1.88	1.78	1.51	2.19	2.20	1.54	1.50	1.55	1.02	1.56	1.56
Lu	0.29	0.28	0.25	0.37	0.34	0.28	0.26	0.25	0.16	0.27	0.32
(La/Lu)N	13.4	9.15	3.05	8.09	5.03	6.00	8.05	10.0	11.1	12.6	7.40
ΣREE	176.2	130.4	45.7	153.0	97.1	74.7	104.2	109.6	80.4	147.5	103.2
Eu/Eu*	0.88	0.88	0.86	0.81	0.83	1.07	0.83	0.88	0.93	0.91	0.93

Note—Yalea argillaceous greywacke samples collected from drill core YDH187; Yalea arkoses from YDH187 (YD42) and YDH188 (YD51 to YD59).

Table A-5. Continued

Sample	Yalea hangingwall feldspathic greywackes			Gara carbonate wall-rock				Yalea hangingwall carbonates		
	YD43	YD47	YD48	G11	G12	G13	G24	YD44	YD52	YD53
SiO ₂	57.1	59.0	54.8	13.6	12.4	5.42	16.0	15.9	38.4	3.96
TiO ₂	0.459	0.435	0.512	0.139	0.140	0.064	0.192	0.100	0.349	0.05
Al ₂ O ₃	13.3	12.5	12.9	3.61	3.48	1.41	4.67	3.41	10.1	1.03
Fe ₂ O ₃ (T)	3.63	3.72	3.85	1.54	1.42	0.651	1.82	1.04	1.54	1.55
MnO	0.048	0.061	0.078	0.022	0.036	0.021	0.018	0.053	0.063	0.111
MgO	3.16	2.73	4.09	1.13	0.900	0.558	1.37	1.57	9.91	19.6
CaO	6.15	7.54	6.82	43.4	42.8	49.8	42.0	42.2	14.0	28.8
Na ₂ O	2.67	3.57	2.86	0.868	0.792	0.550	0.62	0.868	0.085	0.025
K ₂ O	2.73	1.92	2.64	1.03	0.735	0.171	1.20	0.765	3.94	0.400
P ₂ O ₅	0.089	0.115	0.131	0.051	0.048	0.028	0.05	0.032	0.102	0.023
Total	89.4	91.7	88.7	65.3	62.8	58.7	68.0	65.9	78.4	55.6
V	94.8	77.8	87.9	25.3	29.7	12.4	36.5	18.9	54.1	12.2
Cr	76.7	102	113	—	15.3	0.67	30.2	2.50	34.2	8.38
Co	15.8	9.03	10.5	4.73	6.87	3.59	5.66	5.02	7.70	4.07
Ni	36.2	27.6	31.7	20.7	24.2	15.8	28.2	11.1	8.17	10.2
Cu	81.8	3.75	5.92	22.4	49.8	29.4	19.3	40.7	2430	12.7
Zn	—	—	11.7	786	796	843	1100	—	—	64.2
Ga	23.2	21.2	25.0	12.1	30.3	12.3	20.8	13.6	48.4	2.93
Rb	63.7	55.8	70.5	21.1	23.9	3.34	29.1	21.6	68.0	8.17
Sr	136	161	98.2	1920	2960	2450	1410	292	37.2	19.1
Y	18.6	17.2	18.1	6.23	5.70	2.94	5.78	8.73	11.6	4.14
Zr	148	165	134	36.2	30.3	11.2	31.8	34.2	105	9.34
Nb	5.85	5.93	8.73	2.42	2.01	1.53	6.73	2.64	7.69	2.91
Mo	1.65	1.45	4.39	1.11	1.73	2.31	5.82	1.30	6.67	4.64
Cs	0.88	1.24	2.19	—	1.99	—	0.41	0.33	0.38	0.15
Ba	344	529	572	482	652	268	274	125	713	39.3
Hf	4.14	4.15	3.69	1.11	0.89	0.39	1.04	1.21	3.06	0.35
Ta	0.50	0.66	0.67	0.18	0.19	0.14	0.37	0.23	0.63	0.17
Th	4.42	3.37	3.92	1.83	1.12	0.60	1.23	2.60	6.46	0.47
U	1.68	1.41	1.94	3.33	3.18	3.22	2.51	2.98	5.70	2.52
La	24.9	19.8	21.1	8.03	4.23	2.48	5.66	10.4	8.01	5.14
Ce	50.4	41.9	44.4	16.6	9.57	6.00	13.0	21.2	18.1	8.98
Pr	6.07	5.47	5.82	1.86	1.21	0.88	1.67	2.49	2.18	1.20
Nd	24.5	21.8	25.3	7.73	5.45	2.70	6.80	9.65	9.42	4.71
Sm	4.67	4.48	5.46	1.34	2.11	1.40	2.67	1.86	2.04	1.03
Eu	1.26	1.10	1.39	6.34	0.39	0.27	0.39	0.40	0.65	0.31
Gd	4.57	4.36	4.88	1.36	1.09	0.79	1.26	1.88	2.51	0.93
Tb	0.63	0.58	0.65	0.17	0.20	0.15	0.24	0.24	0.36	0.14
Dy	3.82	3.25	3.47	0.92	1.01	0.52	1.26	1.40	1.99	0.79
Ho	0.67	0.60	0.71	0.25	0.25	0.15	0.24	0.30	0.40	0.15
Er	2.13	1.60	2.05	0.61	0.59	0.37	0.66	0.79	1.07	0.31
Tm	0.30	0.27	0.24	0.09	0.13	0.10	0.14	0.13	0.16	—
Yb	2.03	1.74	2.07	0.67	0.72	0.36	0.63	0.90	0.91	0.30
Lu	0.31	0.28	0.29	0.09	0.12	0.08	0.14	0.13	0.14	—
(La/Lu)N	8.52	7.53	7.67	9.31	3.62	3.22	4.45	8.87	6.09	—
∑REE	126.3	107.3	117.8	39.5	27.1	16.3	34.8	51.8	48.0	24.0
Eu/Eu*	0.82	0.75	0.80	0.77	0.71	0.73	0.57	0.65	0.88	0.94

Note- Yalea arkose samples collected from drill cores YDH187 (YD43) and YDH188 (YD47 & YD48); Gara carbonate sediments from CO92 (G11 to G13) and LOCP116 (G24); and Yalea carbonate wall-rock from YDH187 (YD44) and YDH188 (YD52 & YD53).

Table A-5. Continued

Sample	Gara quartz-wacke wall-rock			Gara tourmalinite wall-rock			Pink albite-altered argillaceous greywackes					
	G35	G37	G38	G22	G23	G36	G20	YD26	YD30	YD54	YD55	YD57
SiO ₂	81.1	87.9	76.8	74.2	72.2	72.9	58.4	65.3	55.0	59.0	69.8	61.7
TiO ₂	0.458	0.166	0.247	0.225	0.217	0.302	0.446	0.661	0.694	0.444	0.254	0.238
Al ₂ O ₃	7.09	6.64	10.3	7.42	6.64	10.0	12.4	12.3	13.76	13.0	10.4	9.85
Fe ₂ O ₃ (T)	4.22	1.50	1.78	3.24	1.76	2.64	3.46	1.87	2.81	2.91	2.48	4.82
MnO	0.005	0.004	0.005	0.009	0.019	0.024	0.053	0.029	0.043	0.061	0.050	0.077
MgO	2.69	2.59	3.23	3.43	4.89	4.21	4.34	2.52	3.85	3.29	1.94	2.59
CaO	0.289	0.389	0.480	0.714	4.86	2.22	5.88	3.61	7.12	5.85	3.86	5.85
Na ₂ O	0.117	1.75	0.686	0.606	0.487	1.10	5.34	4.68	6.90	4.27	4.54	5.41
K ₂ O	1.64	0.463	2.76	0.844	0.005	2.10	1.11	2.41	0.880	1.92	0.888	0.195
P ₂ O ₅	0.061	0.045	0.062	0.055	0.063	0.082	0.132	0.087	0.200	0.113	0.071	0.052
Total	97.6	101.4	96.3	90.7	91.1	95.6	91.6	93.4	91.3	90.9	94.3	90.8
V	95.4	32.9	32.1	32.3	30.3	52.7	91.4	112	100	85.1	58.6	29.2
Cr	67.4	21.2	23.5	25.5	18.1	42.0	-	170	11.1	-	-	-
Co	5.64	2.63	3.83	14.8	4.05	9.87	8.85	3.86	3.58	7.20	7.97	49.5
Ni	20.3	17.6	13.5	39.6	24.3	33.0	44.1	60.1	24.6	25.7	28.2	33.5
Cu	5.8	4.18	2.39	24.4	6.87	36.9	2.39	7.51	2.51	199	43.6	24.3
Zn	674	35.2	52.1	681	676	33.7	750	19.4	-	1963	8140	230
Ga	12.6	7.01	16.0	11.3	6.77	14.9	22.5	20.6	15.0	17.7	14.7	8.71
Rb	41.5	10.0	60.5	20.6	-	44.5	30.1	44.1	12.2	39.4	13.3	1.43
Sr	12.4	37.1	19.0	79.9	93.8	29.5	143	58.0	77.6	121	121	181
Y	10.2	9.95	11.9	11.7	15.7	13.8	17.0	14.5	16.9	17.9	15.9	8.95
Zr	214	81.7	171	116	109	140	118	183	296	172	111	84.9
Nb	12.9	4.07	6.51	5.86	6.33	5.05	5.92	8.24	7.67	5.92	4.12	4.56
Mo	6.05	2.51	2.47	3.70	3.80	1.23	1.46	3.49	1.03	70.1	3.01	4.44
Cs	0.65	0.33	1.06	1.24	0.06	0.90	0.87	0.55	-	0.66	0.23	-
Ba	280	43.5	377	157	8.02	331	445	162	40.2	237	277	50.6
Hf	5.24	2.08	3.97	3.00	2.54	3.35	5.74	4.51	7.87	4.46	2.92	1.95
Ta	1.39	0.49	0.57	0.60	0.61	0.63	0.66	0.62	0.63	0.51	0.51	0.55
Th	9.75	2.20	2.97	2.75	2.57	3.79	4.09	1.15	5.73	3.42	1.93	2.47
U	1.54	0.38	0.60	0.86	0.83	0.90	1.61	1.27	1.46	1.73	1.01	0.71
La	24.8	15.4	19.9	34.7	7.83	17.2	12.0	12.9	24.0	25.7	4.27	19.9
Ce	53.1	28.7	40.4	66.9	17.9	35.3	42.1	27.9	54.2	55.4	6.75	40.5
Pr	6.51	3.42	5.01	7.64	2.36	4.30	5.19	3.50	7.01	6.64	0.91	4.90
Nd	24.8	12.9	19.4	28.8	10.4	16.6	20.7	13.8	28.4	26.1	3.46	18.2
Sm	4.78	2.26	3.34	4.21	2.36	3.01	4.04	2.90	5.08	4.89	1.09	3.23
Eu	1.10	0.59	0.91	0.85	0.65	0.76	1.14	0.68	1.24	1.03	0.48	0.69
Gd	3.62	2.47	3.09	4.00	2.81	2.97	3.56	2.72	4.24	4.40	1.67	2.74
Tb	0.43	0.35	0.38	0.46	0.48	0.44	0.56	0.42	0.49	0.61	0.45	0.32
Dy	2.19	2.06	2.35	2.25	2.78	2.72	3.32	2.69	3.24	3.43	2.80	1.78
Ho	0.45	0.42	0.45	0.42	0.61	0.50	0.67	0.49	0.68	0.70	0.55	0.37
Er	1.14	1.19	1.38	1.26	1.71	1.50	2.05	1.45	2.11	1.89	1.80	1.07
Tm	-	-	-	-	0.20	0.16	0.33	0.16	0.31	0.27	0.24	-
Yb	1.23	1.15	1.49	1.29	1.41	1.37	2.02	1.37	2.18	1.89	1.91	0.99
Lu	0.23	0.15	0.23	0.17	0.24	0.21	0.33	0.28	0.34	0.30	0.30	0.14
(La/Lu)N	11.4	10.8	9.09	21.5	3.57	8.66	6.44	5.00	7.61	9.15	1.55	14.8
ΣREE	124.4	71.0	98.3	153.0	51.8	87.0	106.0	71.3	133.6	133.2	26.7	94.8
Eu/Eu*	0.78	0.75	0.85	0.62	0.77	0.77	0.90	0.73	0.80	0.67	1.09	0.69

Note- Gara quartz-wacke samples collected from dill core LOCP116; Gara tourmalinite samples from CO92 (G22 & G23) and LOCP116 (G36); and pink albite-altered samples from Gara drill core CO92 (G20) and Yalea drill cores YDH187 (YD26 & YD30) and YDH188 (YD54, YD55 & YD57).

A-4 Paragenesis charts for the smaller Loulo prospects

The following charts show the paragenesis at Loulo-3, Baboto, P-129 and P-64 ore bodies discussed in *section 4.5*.

Table A-6. Summary vein and sulphide paragenesis for the Loulo-3 orebody.

Mineral	Pre-ore stage	Main ore stage 1	Main ore stage 2	Post-main ore stage	Supergene
Vein material					
Carbonate	██████████	██████████			
Quartz		██████████			
Chlorite		██████████			
Sulphides/Opaques					
Pyrite		██████████			
Arsenopyrite-I		██████████			
Pyrrhotite		██████████			
Chalcopyrite-I		██████████			
Scheelite		██████████			
Arsenopyrite-II			██████████		
Galena			██████████		
Chalcopyrite-II				██████████	
Tennantite				██████████	
Gold		██████████		██████████	
Supergene					
Goethite					██████████
Limonite					██████████

Table A-7. Summary wall-rock alteration, vein and sulphide paragenesis for the Baboto orebody.

Mineral	Pre-ore stage	Main ore stage 1	Main ore stage 2	Post-main ore stage	Supergene
Wall-rock alteration					
Quartz	██████████	██████████			
Albite		██████████			
Tourmaline	██████████				
Carbonate		██████████			
Veining					
Quartz		██████████			
Carbonate		██████████			
Sulphides/Opaques					
Pyrite	-----	██████████			
Arsenopyrite-I		██████████			
Chalcopyrite-I		██████████			
Pyrrhotite		██████████			
Tetrahedrite-I		██████████			
Ullmannite		██████████			
Arsenopyrite-II			██████████		
Galena			██████████		
Ardaite			██████████		
Bournonite			██████████		
Chromite	-----				
Chalcopyrite-II				██████████	
Tetrahedrite-II				██████████	
Gold		██████████		██████████	
Supergene					
Limonite					██████████

Table A-8. Summary vein and sulphide paragenesis for the P-129 orebody.

Mineral	Main ore stage		Post-main ore stage	Supergene
	Carbonate-quartz	Chlorite-tourmaline		
Vein material				
Carbonate	████████			
Quartz	████████			
Chlorite		████████		
Tourmaline		████████		
Sulphides/Opaques				
Pyrite	████████	████████		
Arsenopyrite		████████		
Pyrrhotite		████████		
Scheelite		████████		
Gersdorffite		████████		
Pentlandite		████████		
Monazite		████████		
Chalcopyrite			████████	
Gold			████████	
Supergene				
Goethite				████████

Table A-9. Summary wall-rock alteration, vein and sulphide paragenesis for the P-64 orebody.

Mineral	Pre-ore stage	Main ore stage		Post-main ore stage	Supergene
		Dis.	Vein		
Wall-rock alteration					
Tourmaline	████████	████████	████████		
Chlorite	████████	████████	████████		
Veining					
Carbonate			████████		
Quartz			████████		
Tourmaline			████████		
Sulphides/Opaques					
Pyrite		████████	████████		
Arsenopyrite		████████			
Scheelite		████████			
Monazite		████████			
Chalcopyrite			████████		
Pyrrhotite			████████		
Gersdorffite			████████		
Pentlandite			████████		
Native bismuth			████████		
Calaverite			████████		
Gold		████████	████████		
Magnetite				████████	
Chromite				████████	
Supergene					
Haematite					████████
Goethite					████████
Lanthanite/Calcinsite					████████

Note- Dis = disseminated pyrite stage; Vein = vein stage.

A-5 WinClastour methodology

Due to the complexity of the tourmaline mineral group, the chemical formula for the Loulo tourmalines were calculated using the WinClastour program developed by Yavuz *et al.* (2006). The program allows the input of electron microprobe data or wet chemical analyses to estimate tourmaline stoichiometry, as well as classifying the minerals using the Hawthorne & Henry (1999) tourmaline classification scheme. The crystal chemistry of tourmaline is difficult to calculate fully because several components, such as B, Li, Fe³⁺ and H₂O cannot be determined by electron microprobe analysis. However, the complete tourmaline chemistry can be estimated using several normalisation schemes. Firstly, the data are normalised to 24.5 oxygens (Manning, 1982) to calculate the unit cell contents of the tourmalines. Then, B₂O₃ and LiO₂ can be estimated assuming full site occupancy at the B-site (3.000 per formula unit or *apfu*) and any vacancy at the Y-site (Li = 3- $\sum Y$; Henry & Dutrow, 1996), respectively. Water contents can also be calculated assuming OH + F = 4 *apfu*. However, F was not determined during this study (beyond capabilities of the microprobe) and thus, H₂O concentrations are overestimated. As a result, the classification of tourmalines based on the W-site occupancy is not possible (i.e. oxy-, hydroxyl- or fluor-subgroup classification).

The use of Micro-Mössbauer analyses or Micro-Xanes (using synchrotron radiation) are the most common procedures in obtaining precise data on Fe oxidation. In the absence of these techniques, Fe³⁺ can be estimated using the Lynch & Ortega (1997) calculation:

$$\text{Fe}^{3+} = \text{Fe}_{\text{total}} - ((3-\text{Mg})-\text{Ca}) \quad (\text{Eq. A.1})$$

It must be noted that this calculation, along with the combination of other normalisation procedures, can cause considerable error in the amount Fe³⁺ present in relation to Fe²⁺. The WinClastour program also contains an Al-Mg disorder function, which estimates the relative amount of Al and Mg at the Y and Z-sites. Grice & Ercit (1993) proposed that in the absence of cell volume measurements, Mg in the Y and Z-sites can be estimated for tourmalines with >7 wt.% FeO by the following expressions:

$${}^Y\text{Mg} = 3[1 - \text{Fe}/(\text{Fe} + \text{Mg})] \quad (\text{Eq. A.2})$$

$${}^Z\text{Mg} = (\sum \text{Mg}) - {}^Y\text{Mg} \quad (\text{Eq. A.3})$$

For the Loulo tourmalines, this Al-Mg disorder function overestimates the amount of Mg present in Z-site. It is clear from the electron microprobe data that Fe (Fe³⁺) is a more important substitution for ^ZAl than Mg (*see section 5.5.2.1*).

A-6 Microthermometric data

The following tables present the microthermometric and Raman data collected at individual deposits at Loulo. Summary tables are given in *section 6.6*.

Table A-10. Summary of the microthermometric and Raman spectrometric data for fluid inclusions from mineralised and barren veins at Gara.

Main ore phase	Type	Range	V CO ₂ %	T _m CO ₂ °C	T _o °C	T _m ice °C	T _m cl °C	T _h CO ₂ (L) °C	T _h CO ₂ (V) °C	T _o °C	T _h (L) °C	T _h (V) °C	T _d °C	Salinity ¹		pCO ₂ g/cm ³	ρ _{tot} g/cm ³	X _{H₂O}	X _{NaCl}	X _{CO₂}	CO ₂ * mol.%	N ₂ * mol.%	CH ₄ * mol.%
														(wt.% NaCl)	(wt.% NaCl)								
Type 1 early	Min		-58.2		-53.5											0.513					90.7	0.0	0.0
	Max		-56.6		30.0											1.168					100.0	9.3	0.0
	Mean		-56.8		10.5											0.858					98.6	14	0.0
	N		206		360											360					20	20	20
Type 1 late	Min		-57.4		-0.1											0.707							
	Max		-56.6		25.3											0.929							
	Mean		-56.7		14.2											0.829							
	N		68		75											75							
Type 2 early	Min		-39	-20.4				140								0.935	0.917	0.013					
	Max		-26	-2.6				197								1.066	0.987	0.083					
	Mean		-33.3	-13.3				168								1.022	0.941	0.059					
	N		23	24				24								24	24	24					
Type 3 early	Min		-58.1		-6.0			251	279	200	4.5					0.596	0.676	0.322	0.008	0.028	65.7	0.0	0.0
	Max		-56.6		7.7			341	330	325	21.3					1.013	1.010	0.952	0.071	0.577	100.0	34.3	0.0
	Mean		-56.7		-0.4			291	313	281	16.0					0.814	0.932	0.753	0.043	0.173	94.3	5.7	0.0
	N		13	13	34			14	4	16	34.0					121	121	34	34	34	6	6	6
Type 4 early	Min		-57.6		13.7					283	36.9					0.654	1.235	0.610	0.162	0.017	93.7	0.0	0.0
	Max		-56.6		28.1					372	44.5					0.833	1.481	0.805	0.357	0.104	100.0	6.3	0.0
	Mean		-56.7		23.0					341	41.7					0.732	1.342	0.710	0.245	0.046	96.9	3.1	0.0
	N		22	22	22					10	10					22	22	22	22	22	2	2	2

Note- Salinity¹ estimates calculated from T_i; salinity² estimates calculated from volumetric proportions; CO₂*, N₂* & CH₄* estimated from Raman analysis.

Table A-10. cont. Summary of the microthermometric and Raman spectrometric data for fluid inclusions from mineralised and barren veins at Gara.

Vein phase	Fl type	Range	V CO ₂ %	T _m CO ₂ °C	T _e °C	T _{m ice} °C	T _{m cl} °C	T _h CO ₂ (L) °C	T _h CO ₂ (V) °C	T _s °C	T _h (L) °C	T _h (V) °C	T _d °C	Salinity ¹		p _{wt}	X _{H₂O}	X _{NaCl}	X _{CO₂}	CO ₂ mol.%	N ₂ mol.%	CH ₄ * mol.%
														(wt.% NaCl)	(wt.% NaCl)							
Reactivation ore phase	Type 1	Min	-75.0					-25.1								0.729				58.3	0.0	0.0
	early	Max	-56.6					23.8								1056				100.0	18.5	32.7
		Mean	-59.7					4.8								0.848				85.1	5.0	9.9
		N	60					61								60				20	20	20
Type 3	Min	-96.0						-11.5			289	320		9.6	0.776	0.815	0.322	0.011	0.060	57.0	0.0	2.5
	early	Max	-57.1				-4.7	9.2			334	328		20.2	0.991	0.996	0.910	0.059	0.667	95.8	15.5	27.6
		Mean	-60.8				-0.7	2.4			312	324		16.4	0.894	0.946	0.590	0.034	0.377	85.3	3.6	11.1
		N	27				5	25			3	2		5	25	25	5	5	5	11	11	11
Type 4	Min	-62.8						4.1			250			42.0	0.830	1.292	0.616	0.197	0.039	86.4	6.6	4.3
	early	Max	-56.7					11.1			334			57.1	0.903	1.436	0.764	0.318	0.095	86.7	9.1	7.0
		Mean	-60.5					9.7			303			49.2	0.864	1.364	0.688	0.252	0.060	86.5	7.9	5.6
		N	8					8			8			8	8	8	8	8	8	2	2	2
Barren phase	Type 1	Min	-58.9					-0.4								0.93				76.0	4.0	0.0
	early	Max	-56.6					27.3								0.672				96.0	24.0	0.0
		Mean	-57.6					16.7								0.806				86.0	14.0	0.0
		N	67					106								106				22	22	22
Type 2	Min	-28						-8.0			167			6.5	0.848	0.961	0.021					
	early	Max	-22.0					-4.1			252			11.7	0.980	0.979	0.039					
		Mean	-25.6					-6.4			185			9.7	0.940	0.968	0.032					
		N	6					6			13			6	13	13	13					
Type 3	Min	-58.8						-11.6			249	187	250	5.1	0.674	0.804	0.324	0.006	0.055	79.3	3.1	0.0
	early	Max	-56.9					27.2			289	259	274	11.2	0.992	0.993	0.909	0.039	0.668	96.9	20.7	0.0
		Mean	-57.6					13.0			263	228	262	8.1	0.839	0.935	0.760	0.021	0.219	88.2	11.8	0.0
		N	46					50			8	3	4	6	50	50	5	5	5	8	8	8

Note- Salinity¹ estimates calculated from T_s; salinity² estimates calculated from volumetric proportions; CO₂*, N₂* & CH₄* estimated from Raman analysis.

Table A-11. Summary of the microthermometric and Raman spectrometric data for fluid inclusions from mineralised and barren veins at Yalea Main.

Vein phase	Fl type	Range	V CO ₂ %	T _m CO ₂ °C	T _e °C	T _m ice °C	T _m cl °C	T _h CO ₂ (L) °C	T _h CO ₂ (V) °C	T _s °C	T _h (L) °C	T _h (V) °C	T _d °C	Salinity		XH ₂ O	XNaCl	XCO ₂	CO ₂ * mol.%	N ₂ * mol.%	CH ₄ * mol.%	
														(wt.% NaCl)	pCO ₂ g/cm ³							
Yalea South ore phase	Type 1	Min		-65.7				-5.5	20.1						0.95				49.1	4.6	2.6	
	early	Max		-57.8				29.3	23.9						0.960				914	45.7	2.3	
		Mean		-59.6				10.6	21.8						0.854				763	17.8	5.9	
		N		74				75	3						78				27	27	27	
Yalea Central ore phase	Type 1	Min		-58.1				0.6							0.707				799	4.3	0	
	early	Max		-56.7				25.3							0.924				957	20.1	0	
		Mean		-57.3				14.3							0.828				87.8	12.4	0	
		N		76				71							71				8	8	8	
Type 1 late	Type 1	Min		-57.9				9.1							0.654							
	late	Max		-56.9				28.1							0.868							
		Mean		-57.3				17.6							0.798							
		N		8				8							8							
Type 2 early	Type 2	Min		-24.9	-8.9						176		280	0.7	0.606	0.002	0.957					
	early	Max		-21.0	-0.4						350		300	12.7	0.98	0.043	0.998					
		Mean		-22.0	-4.4						236		290	7.0	0.873	0.022	0.978					
		N		21	36						34		2	36	34	34	34					
Type 2 late?	Type 2	Min		-29.9	-20.7						176			17.8	0.937	0.916	0.062					
	late?	Max		-21.2	-14						270			22.8	1.041	0.938	0.084					
		Mean		-23.5	-17.9						217			20.9	1.002	0.925	0.075					
		N		9	11						11			11	11	11	11					
Type 3 early	Type 3	Min		-58.1				12.2			243		247	3.0	0.689	0.85	0.492	0.005	0.086	79.9	7.3	0
	early	Max		-57.0				26.2			297		284	10.2	0.850	0.958	0.891	0.031	0.503	92.7	20.1	0
		Mean		-57.4				6.7	19.3		270		264	6.1	0.777	0.916	0.795	0.017	0.88	88.9	11.1	0
		N		11	11			11	11		3		8	11	11	11	11	11	11	7	7	7

Note: CO₂*, N₂* & CH₄* estimated from Raman analysis. Abbreviations as in text.

Table A-11. cont. Summary of the microthermometric and Raman spectrometric data for fluid inclusions from mineralised and barren veins at Yalea Main.

Barren phase	Fl type	Range	V CO ₂ %	T _m CO ₂ °C	T _e °C	T _{m ice} °C	T _{m cl} °C	T _h CO ₂ (L) °C	T _h CO ₂ (V) °C	T _e °C	T _h (L) °C	T _h (V) °C	T _d °C	Salinity		ρ _{CO₂} g/cm ³	ρ _{tot} g/cm ³	XH ₂ O	XNaCl	XCO ₂	CO ₂ * mol.%	N ₂ * mol.%	CH ₄ * mol.%
														(wt.% NaCl)	(wt.% NaCl)								
Type1 early	Min		-59.3					-0.3								0.76				63.6	2.2	0	
	Max		-56.9				24.7									0.93				87.8	36.4	0	
	Mean		-58.1				12.8									0.84				75.3	24.7	0	
	N		47				54									54				16	16	16	
Type2 early	Min		-25.3	-6.8							169			0.2		0.816	0.966	0.001					
	Max		-20.8	-0.1							273			10.2		0.960	0.999	0.034					
	Mean		-22.3	-3.5							210			5.6		0.898	0.982	0.018					
	N		23	42							42			42		42	42	42					
Type3 early	Min		-59.8				6.1	-3.4			249	212	254	12		0.702	0.852	0.239	0.003	0.068	73.1	26.9	0
	Max		-57.0				9.4	25.6			285		291	7.3		0.948	0.984	0.924	0.021	0.756			
	Mean		-58.1				7.7	16.7			260		277	4.5		0.816	0.941	0.848	0.011	0.139			
	N		21	17			21	21			8	1	12	21		21	21	21	21	21	1	1	1

Note- CO₂*, N₂* & CH₄* estimated from Raman analysis. Abbreviations as in text.

Table A-12. Summary of the microthermometric and Raman spectrometric data for fluid inclusions from mineralised veins at Yalea North.

Fl type	Range	V CO ₂ %	T _m CO ₂ °C	T _e °C	T _m ice °C	T _m cl °C	T _h CO ₂ (L) °C	T _h CO ₂ (V) °C	T _s °C	T _h (L) °C	T _h (V) °C	T _d °C	Salinity ¹		pCO ₂ g/cm ³	ρ _{tot} g/cm ³	XH ₂ O	XNaCl	XCO ₂	CO ₂ * mol.%	N ₂ * mol.%	CH ₄ * mol.%
													(wt.% NaCl)	(wt.% NaCl)								
Type 1	Min		-58.5				-218								0.727				81.4	0.0	0.0	
early	Max		-56.6				23.9								10.41				100.0	10.9	10.0	
	Mean		-57.2				6.3								0.888				92.0	5.4	2.5	
	N		29				29								29				17	17	17	
Type 3	Min	10	-57.6		-5.8		15			272	261			4.1	0.756	0.829	0.338	0.007	89.2	0.0	0.0	
early	Max	85	-56.6		7.9		216			351	295			211	0.919	0.978	0.952	0.066	98.7	9.1	2.0	
	Mean	40	-57.0		2.0		14.1			317	275			13.2	0.830	0.926	0.728	0.035	92.9	6.0	1.1	
	N	9	9		9		9			6	3			9	9	9	9	9	3	3	3	
Type 4	Min	5	-57.8				13.3					281		416	0.702	1.251	0.585	0.162	0.018			
early	Max	20	-56.9				25.6			360	360			42.7	0.836	1.513	0.803	0.347	0.088			
	Mean	10	-57.4				19.7			317	347			42.2	0.774	1.361	0.692	0.258	0.051			
	N	10	10				10			2	2			10	10	10	10	10	10	10	10	

Note- Salinity¹ estimates calculated from T_s; salinity² estimates calculated from volumetric proportions; CO₂*, N₂* & CH₄* estimated from Raman analysis.

Table A-13. Summary of the microthermometric and Raman spectrometric data for fluid inclusions from mineralised veins at Loulo-3.

Fl type	Range	V CO ₂ %	T _m CO ₂ °C	T _o CO ₂ °C	T _m ice °C	T _m cl °C	T _h CO ₂ (L) °C	T _h CO ₂ (V) °C	T _m halite °C	T _h (L) °C	T _h (V) °C	T _d °C	Salinity			ρ _{br} g/cm ³	XH ₂ O	XNaCl	XCO ₂	CO ₂ * mol.%	N ₂ * mol.%	CH ₄ * mol.%
													(wt.% NaCl)	ρCO ₂ g/cm ³	(wt.% NaCl)							
Type 1 early	Min	-59.3																	79.7	5.3	0.0	
	Max	-57.2	0.5																94.7	20.3	11	
	Mean	-58.0	20.1																87.3	12.5	0.2	
	N	5	5																5	5	5	
Type 2 early	Min			-23.7	-6.8					83				5.5	0.888	0.966	0.018					
	Max			-22.3	-3.4					257			10.2	0.959	0.982	0.034						
	Mean			-23.2	-5.6					216			8.6	0.918	0.972	0.028						
	N			5	6					6			6	6	6	6						
Type 3 early	Min	-58.5				5.8				252	279		2.0	0.715	0.859	0.241	0.002	0.07	83.1	3.2	0.0	
	Max	-57.4	3.4			9				309	284		7.8	0.907	0.948	0.912	0.022	0.757	96.8	16.9	0.0	
	Mean	-58.0	24.8			6.9				272	282		5.8	0.797	0.917	0.702	0.015	0.284	90.0	10.0	0.0	
	N	7	7			7				5	2		7	7	7	7	7	7	2	2	2	

Note- CO₂*, N₂* & CH₄* estimated from Raman analysis. Abbreviations as in text.

Table A-14. Summary of the microthermometric and Raman spectrometric data for fluid inclusions from mineralised veins at Baboto.

Flitype	Range	V CO ₂ %	T _m CO ₂ °C	T _e °C	T _m ice °C	T _m cl °C	T _h CO ₂ (L) °C	T _h CO ₂ (V) °C	T _s °C	T _h (L) °C	T _h (V) °C	T _d °C	Salinity				ρ _{tot} g/cm ³	XH ₂ O	XNaCl	XCO ₂	CO ₂ * mol.%	N ₂ * mol.%	CH ₄ * mol.%
													(wt.% NaCl)	ρCO ₂ g/cm ³	ρ _{tot} g/cm ³	XH ₂ O							
Type 1	Min	-64.9													0.84				60.6	8.9	0.0		
early	Max	-57.7													1005				88.9	16.5	28.2		
	Mean	-62.1													0.916				73.3	13.1	14.1		
	N	50													50				15	15	15		
Type 2	Min			-23.8	-7.2					201		253	15		0.836	0.964	0.005						
early	Max			-22.0	-0.9					291		320	10.7		0.940	0.995	0.036						
	Mean			-22.9	-4.2					240		291	6.7		0.872	0.978	0.022						
	N			11	14					11		3	14		11	11	11						

Note- CO₂*, N₂* & CH₄* estimated from Raman analysis. Abbreviations as in text.